CRANFIELD INSTITUTE OF TECHNOLOGY

SCHOOL OF MECHANICAL ENGINEERING

Academic Year 1985 - 1988

Ph.D Thesis

I.R.W. McLUCKIE

INSTABILITY STUDIES OF AN 'O'-RING FLEXIBLY SUPPORTED, GAS BEARING, MOUNTED, COOL AIR UNIT.

Supervisors: Mr. B. R. Reason
Dr. C. R. MacFarlane

September 1990

This Thesis is submitted for the Degree of Doctor of Philosophy.

I dedicate this Thesis to my wife Valerie and my two beautiful children, Keith and Jenna. "Thank you for your understanding."

I must also express my deepest appreciation to my Mother and Father and Mother and Father-in-law, for their support and encouragement throughout.

I would also like to dedicate this work to friends who have encouraged me along the way in my career. Some of you are no longer with us but I will never forget you. God Bless.

SUMMARY

A Cool Air unit (C.A.U.) is powered by air bled from the engine and supplies cool air to the avionics and cockpit of the aircraft. Essentially a small turbo machine, the rotor is mounted upon two plain (gas) air bearings, which are flexibly supported by elastomeric 'O'-Rings.

The project objectives were to investigate, experimentally and theoretically, the mechanism of dynamic instability, half frequency whirl (HFW) observed in the C.A.U design, and hence evaluate methods by which it can be best controlled. Two main areas of study were embarked upon.

Firstly a steady state aerodynamic study, based on an existing single bearing rig, to evaluate the extent of aerodynamic operation and single bearing instability (HFW). This Test Rig did not have 'O'-Ring flexibility. Bearing L/D tested were 2, 1·5 and 1·0, with variable loading of 18·1 → 51·2N and speeds of 6000 → 40000 Rpm in approximately 5000 Rpm intervals. the theoretical study investigated non-linear effects of air film pressure distribution.

Secondly a Dynamic instability study of HFW was carried out on a newly designed Test Rig, simulating small turbo machines and the C.A.U.. Three bearing types were evaluated, Aerodynamic, Hybrid and Hybrid porous. With L/D of 1·0. 'O'-Ring Centres varied from 0·17 → 0·83 of bearing length. Viton and Silicon materials were tested with 70 shore hardness. Rotor mass, inertia, asymmetry and unbalance were investigated along with 'O'-Ring stiffness and damping variation from air pressure (0 → 120psi). Theory was developed to determine whirl onsets and effects of unbalance, and damping of the support.

Non-linear (stagnant areas) of air film detected experimentally, are not explained by Raimondi's theory. Experiments show that Raimondi's theory seriously over estimates the applicable area of fully developed aerodynamic operation. Pressure Profile at onset of Instability tends to a Sommerfeld condition. Temperature was a good indication of lubrication regime. Linear temperature rise curve denotes Aerodynamic operation, and transition to non-linear curve represents onset of Instability (HFW). Authors theory considers non-linearity of air film and suggests a new method of evaluation to improve convergence.

Dynamic study of dual bearing rig concludes, first instability onset speed (RSW) can be passed through due to residual unbalance and damping in the 'O'-Ring support. Theory developed shows relationship of RSW and HFW effects due to unbalance and damping and results agree well. Viton offered better damping than Silicon. RSW not present in Viton at'O'-Ring centres above 10 mm. HFW not present with Viton below 55,000 rpm. RSW observed with ω_n/ω = 1·0 and HFW occurred with ω_n/ω = 0·493 → 0·58. hybrid porous bearings had lower performance than hybrid, but better than aerodynamic. Hybrid bearings mounted in Viton 'O'-Rings offer best performance long term. Aerodynamic bearings can be concluded to be inherently unstable and have limited aerodynamic operation, so should see little use in high speed turbo machinery, including C.A.U. or aircraft applications where zero g loading likely.

II

ACKNOWLEDGEMENTS

I would like to thank my Supervisor Mr. Brian Reason, for his thoughtful guidance and encouragement during my Studies.

I should also like to extend my appreciation to the Members of Staff of the School of Mechanical Engineering, and in particular the following members: Dr. Colin MacFarlane. Mr. Brian Moffit, Mike Devonshire and Andy of the Instrumentation Department. Mr. Ray Wilson, Dick, Alan and Liz of the Drawing Office. David, George, Henry and all the members of the SME Workshops.

I must also thank the Science and Engineering Research Council and the School of Mechanical Engineering for their Financial Support of my Studies, and to British Aerospace for their Financial Support of the Project.

Finally I would like to thank my wife, Valerie, for her patient and meticulous translation of my work into an excellent Manuscript.

LIST OF FIGURES

LIST OF FIGURES

LIST OF FIGURES

LIST OF FIGURES

LIST OF FIGURES

LIST OF FIGURES

LIST OF FIGURES

LIST OF FIGURES

LIST OF TABLES

LIST OF TABLES

LIST OF PLATES

LIST OF PLATES

NOMENCLATURE

A = Area

C = Bearing Radial Clearance

C_s = Smooth Side Clearance

C_T = Tip Clearance

C_v = Vane Side Clearance

C_p = Pressure Coefficient

C_{EL} = $E_1 \;/\; \frac{1}{2}\rho\omega^2 R^4$

E_1 = End Load Coefficient

F = Force, Unbalance Force $F = m\omega^2 X_u$

G = $(2\pi R/L)^2$

H = $(1 + \varepsilon\cos\theta) = h/c$

I = Integer

I_T = Transverse Inertia

I_1 = Rotor or Journal Inertia

I_2 = Bearing 1 Inertia

I_3 = Bearing 2 Inertia

J = Integer

K = Stiffness Matrix

K_1 = Air Film Stiffness

K_2 = 'O'-Ring Support Stiffness

K_2^* = $K_2\ (1 + j\eta)$ = Complex Support Stiffness

Kg_2 = Gas Film Stiffness Bearing 1

Kg_3 = Gas Film Stiffness Bearing 2

K_{1c} = Critical Air Film Stiffness

k_s = Smooth Side Correction Factor

kv = Vane Side Correction Factor

L = Bearing Length

M = Moment and Mass Matrix

N = Journal Rotational Speed Rpm

N' = Journal Rotational Speed Rev/Sec

P = Absolute Pressure

Pr = Radial Pressure Profile

$\bar{P}$ = P/pa

Pa = Atmospheric Pressure

P' = $P - Pa$

Ps = Supply Pressure

$P_1 \rightarrow P_{10}$ = Pressure Tappings in Hydrodynamic Disc Seal

Q = $\bar{P}^2$

R = Journal Radius

S = Sommerfeld Number

So = Marsh's Bearing Support Stiffness

T = Temperature

$T_1 \rightarrow T_4$ = Thermocouple Tappings in Hydrodynamic Disc Seal

V = $(Vx + Vy + Vz)$ = Velocity Vector Matrix

$\forall$ = Volume

X, Y, Z } Fixed Co-ordinates of Machine Centre

X_1 = Journal Displacement

X_2 = Bearing Displacement

X_{12} = $X_1 - X_2$

X_{12c} = Critical Relative Displacement

X_{12r} = Relative Vector

X_u = Unbalance Displacement

β = Angle BGR Between Centre of Gravity and Rotor Centre

δx = $C - \Delta x$

δy = $C - \Delta y$ } Anti-Clockwise Rotation

ε = Eccentricity Ratio = e/c

η = Viscosity (Reyns) and Loss Angle or Coefficient

θ = Angle around Journal Struck from Attitude Angle

Line of Centres

θ = $\theta/2\pi$

λ = Compressibility Number (Raimondi)

Λ = Compressibility Number $12\eta\pi\omega (R/c)^2/Pa$

μ = Friction Coefficient

ν = nu = Poisson Ratio

π = Pi = 3·14156

ρ = Density

ρc = Convergence Criteria

σxx, σyy, σzz } x, y and z Components of Normal Stress

τxy, τyz, τxz } x, y and z Components of Shear Stress

Φ = Attitude Angle and Phase Angle

χ = Φ/ω = Frequency Ratio

ω = Angular Velocity

ω_n = Instability or Natural Frequency

ω_{n1} = First Instability or Natural Frequency

ω_{n2} = Second Instability or Natural Frequency

ωo = Bearing Support Natural Frequency (Marsh) = $(So/mB)^{\frac{1}{2}}$

Δx and Δy = x and y Displacements Respectively

Δ = Frequency Equation

e = Eccentricity

f = Force or Function

g = Gravitation Force ie. gx, gy and gz
in x, y and z Planes Respectively

h = Oil Film Thickness = $C(1 + \varepsilon\cos\theta) = HC$

i, j, k } Unit Vectors

l, la, lb, l_1, l_2 } Rotor Length Dimensions

m = Mass of Fluid

m_1 = Journal or Rotor Mass = mR (Marsh)

m_2 = Bearing or Bush Mass mB (Marsh)

R = Rotor Radius

t = Time Sec.

u = x Velocity Component (Horizontal)

ur = Journal Horizontal Velocity Component

u_2 = Bearing Horizontal Velocity Component

v = y Velocity Component

v_1 = Journal Vertical Velocity Component

v_2 = Bearing Vertical Velocity Component

w = z Velocity Component

x, y, z } Co-ordinates of Rotating Axis Set (Bush)

z z/L

CONTENTS

CONTENTS PAGE

CONTENTS

CONTENTS PAGE

CONTENTS

CONTENTS PAGE

CONTENTS

CONTENTS

CONTENTS PAGE

CHAPTER 1

INTRODUCTION

1·1·1 INTRODUCTION TO STUDIES

Cool Air Units (C.A.U.) supply regulated cool air to the Cockpit and Avionics of Aircraft. C.A.U.'s consist of a Compressor and an Impeller mounted axially either end of a common Shaft or Rotor. Historically the Rotor was mounted between two Rolling Element Bearings. Air bled from the engine turns the Compressor and hence turns the Impeller. The Impeller passes air via a refrigerant cycle into the Cockpit and Avionics. It was not uncommon for the devices to encompass three of the systems natural frequencies, the units being expected to run at speeds up to 100,000 Rpm.

Due to the dire vibrational behaviour which prematurely failed ball bearing units, an alternative bearing system was sought such that increased reliability and reduced maintenance costs could be obtained. B.Ae. decided upon a Rotor system mounted in self energised air bearings. After building and testing several devices they discovered a vibrational problem manifest itself which was later highlighted as half frequency whirl. The Instability occurred over a wide speed spectrum but was most severe at approximately 30,000 Rpm.

C.A.U.'s are required to operate, over a wide speed range, and in excess of 100,000 Rpm trouble free. C.A.U.'s are also called upon to dwell at any rotational speed in a stable manner.

B.Ae. after a long period of consultation with workers in this field of Tribology and Dynamics contacted Cranfield, such that Ph.D and M.Sc studies were initiated. The B.Ae C.A.U. system comprised a Rotor/Bearing design which was first tested by Kerr (48). The Rotor (Compressor and Impeller) was mounted in self energised air bearings. The air bearings were flexibly supported in Elastomeric 'O'-Rings. B.Ae were initially to supply a C.A.U. such that

Cranfield staff and students could fit Instrumentation and study its Tribological and Dynamic Characteristics . B.Ae were never able to deliver a unit due to the Instability problems and hence an alternative approach to the Ph.D research was embarked upon initiated by Cranfield, which would aid the understanding of the C.A.U.'s Instability problem.

Extensive literature reviews were carried out on Aerodynamic Bearing characteristics, Chapter 2, and Instability and Dynamic characteristics of Flexibly Supported Gas Bearings, Chapter 7. The Chapters indicate the Theoretical and Experimental work carried out by past workers.

The Project Objectives were to investigate, Experimentally and Theoretically, the mechanism of Dynamic Instability, Half Frequency Whirl (HFW) observed in the C.A.U. design, and hence evaluate methods by which it can best be controlled. Two main areas of study were embarked upon.

Firstly a Steady State Aerodynamic Study, based on an existing Test Rig used in Aerostatic and Hybrid Tests modified to evaluate the extent of Aerodynamic operation and Single Bearing Instability (HFW). The Test Rig does not have support flexibility. Bearing L/D Ratios tested were 2·0, 1·5 and 1·0, with variable loading of 18·1 → 51·2 N and speeds of 6,000 → 40,000 Rpm in approximately 5,000 Rpm intervals. Also to be investigated were the pressure profiles at Instability threshold. A parallel Theoretical study was undertaken to evaluate non-linear effects of Air Film pressure distribution and Convergence improvements.

Secondly a Dynamic Instability study of HFW is to be carried out on a newly designed Test Rig, simulating small Turbo Machines and the C.A.U. The Author designed and supervised manufacture and building of the Rig. Three Bearing types were evaluated, Aerodynamic, Hybrid, (jetted) and Hybrid Porous (Phospher Bronze), with an L/D of 1·0. Variable 'O'-Ring Centres of 0·17 → 0·83 of Bearing length. Viton

and Silicon materials were tested with 70 shore hardness. Rotor Mass, Inertia, Asymmetry and Unbalance along with 'O'-Ring Stiffness and Damping Variation from Air Pressurization (0 → 120 psi). Theory was to be developed to determine the effects of Unbalance and Damping of the 'O'-Ring Support upon the Instability onsets (HFW) and (RSW) and was corollated against theory for undamped model without unbalance.

The non-linear effects of Aerodynamic operation (stagnant area) was first observed by MacFarlane whilst undertaking Aerostatic and Hybrid Bearing Tests on the Single Bearing Rig. First highlighting that Raimondi's Aerodynamic Theory did not explain the stagnated areas of the pressure profile. To this end a theoretical program in conjunction with an extensive experimental program would enable the useful extent of Aerodynamic behaviour to be assayed. On one hand would be Low Speed, Metallic Contact (mixed or boundary lubrication) and on the other Dynamic Instability (HFW). The study would also allow the construction of improved Boundary conditions and valuable observations of the Stagnant area delineation within the pressure field. Also of great value would be observations of pressure profile at the onset of Instability which would clarify assumptions that effective load carrying capacity disappears at HFW. The theoretical approach of the Author is approached with the knowledge that Raimondi's Theory does not fully explain events taking place in the pressure field and will therefore address the non-linearity and search for a more mathematically rigorous solution to the compressible Reynold's equation.

Much work has been done on Instability of Spring Mass Systems where a Rotor is mounted between two Air Bearings which are assumed to impart no damping and support flexibility is due to Stiffness only, Damping being neglected. This approach allows prediction that flexible systems indeed contain two onset speeds in a Symmetric Rotor System but goes little towards understanding why with suitable damping ('O'-Ring), that the first onset can be passed through without metallic contact. To a much more stable condition of whirl between the First

and Second Instabilities. The present C.A.U. design, although mounted in 'O'-Rings has been modelled by previous workers in this area as a Spring Mass System. This can be assumed correct if the 'O'- Rings do not impart damping, but does not explain why previous workers with 'O'-Ring mounted bearings, Powell and Tempest, with the high speed electric motor, had trouble free operation at over 100,000 Rpm and why the Dental Turbine happily buzzes away at 500,000 Rpm.

Therefore to fully understand such a parody between the dire conditions of the C.A.U. and the above examples an extensive study is required with a Rig that can accommodate many Test Variables and allow the trial of new methods of Instability control and optimisation. Therefore the aim would be to have solved the present C.A.U. problem, and have derived a system which would be reliable and allow safe operation under all operating conditions within the Aircraft.

The following Chapters comment on the Experimental Methods and Results and also the Theoretical models proposed.

Chapter 1 considers the requirements for an improved design and increased understanding of the C.A.U. Chapter 2 is a literature review of the Steady State Bearing characteristics of Self Acting Aerodynamic Bearings to date. Chapter 3 is a Theroretical Analysis of the Steady State Air Bearing beginning with a fundamental derivation and discussion of the limitations of previous worker's approaches with recommendations of the improved Theoretical approach.

In Chapter 4 the Design and Modification of the Single Bearing Test Rig is discussed. The development of the Rig and the Calibration procedures are thoroughly dealt with. Chapter 5 contains the Experimental Results obtained from the Single Gas Bearing Rig. Variable Speed and Load against L/D of 1, 1½ and 2·0 are recorded for 94 Tests. Chapter 6 resulted from the need of an improved Sealing Technique on the Single Bearing Test Rig, and an investigation of High Speed Non-Contact Sealing Methods.

Chapter 7 is a literature review of Instability and Dynamic characteristics of High Speed Aerodynamic and Hybrid behaviour, for Flexibly Mounted Bearing Systems. The Design and Development of the Dual Bearing Test Rig is discussed in Chapter 8. The Rig is designed to simulate C.A.U. behaviour. Chapter 9 explains in detail the Calibration Methods of the Dual Bearing Rig's major components ie. Pressure Transducer, Telemetry Equipment, Proximity Probes and Slip Ring Assembly. Chapter 10 is an investigation into the Stiffness Variations of 'O'-Ring Centres under varying Pressure and Loadings (reactions).

The Instability Measurements and Tests of the Single Bearing Rig are discussed in great detail in Chapter 11, where Sommerfeld pressure conditions are highlighted at the onset of Instability. Chapter 12 is concerned with the Experimental Results recorded from the Dual Bearing Rig, where Instability Speeds and Loci are captured for varying Rotor Masses, 'O'-Ring Centre and 'O'-Ring Material variation. A Theoretical approach towards HFW and RSW is contained in Chapter 13. The approach is based on a Spring, Mass, Damper System which includes residual unbalance and further highlights HFW and RSW manifestation. Chapter 14 is the Conclusion and Chapter 15 the Recommendations for Further Work.

CHAPTER 2

STEADY STATE CHARACTERISTICS

2·1·1 LITERATURE REVIEW

As long ago as 1855 Hirn (1) proposed in a paper in Engineering that "Air under certain circumstances and in sufficient quantities becomes the best lubricator the coefficient falling as low as 0·00001." Also at this time the lubricating effect of air trapped between two well fitted surface plates was frequently observed.

However, not until 1896, when Professor A. Kingsbury (2) whilst fitting a piston into a close toleranced sleeve, did the aerodynamic effect of a journal bearing become recognised. Kingsbury found that the piston, weighing some 22lb (10Kg), 6" in diameter, 6 1/4" long and operating with a diametral clearance of 16/10000", could support its own weight, whilst spinning.

Kingsbury made three important observations:-

(i) The surfaces were completely separated by the Air film.

(ii) Radial clearance whilst the piston was spinning was not constant within the film, being dependent upon the direction and speed of Rotation.

(iii) The pressure distribution of the air film varied with rotational speed.

Also found at this time was that the Journal centre did not remain coincident with the bush centre, but operated at some displacement defined the eccentricity. Kingsbury made Pressure Curve comparisons, at 5 different axial locations. It can be noted that with increased speed, central pressure magnitudes decrease.

In 1913, W.J. Harrison (3) produced a paper which although having a different approach to that of Somerfeld, arrived at the same resultant equations for the infinite bearing. Harrison pointed out that he could not arrive at an explicit solution for the incompressible case.

He also compared his results with those of Kingsbury and noted that an obvious discrepancy in results were obtained if assuming air to be incompressible. Obviously another discrepancy was his boundary conditions since Kingsbury conducted experiments on a bearing of L/D ⇒ 1 not L/D ⇒ ∞

Katto and Soda (4) in 1952 produced an approximate approach to the solution of the infinite bearing, their solution was not accurate for large values of eccentricity and clearance.

Ausman (5) in 1957 published a perturbation method which was accurate for small eccentricity values and for the infinite bearing (L/D ⇒ ∞). He later improved the method to include the finite Journal bearing.

Osterle and Hughes (6) also in 1957 carried out a theoretical study on the high speed effects of Pneumodynamic lubrication for a 180 degree partial bearing. Their paper considered inertial effects of a gas bearing operating at elevated speeds. Their results disclose that at speeds of 10,000 Rpm inertia effects of the lubricant were negligible. However at speeds approaching 200,000 Rpm these effects cannot be safely neglected since 10 - 11 % reduction in load capacity was found and errors in attitude angle up to 13 degrees. The influence of inertia was also seen at speeds of 50,000 Rpm, not to be negligible, but this was an area which needed further investigation.

Cole and Kerr 1957 (7) carried out experiments on Self Acting Glass Air Bearings with L/D ⇒ 1·0, with clearance ratios of 0·001", and running up to 60,000 Rpm. They claim that loads of up to 1 lb/in^2 per 1,000 Rpm were sustained. At $\varepsilon < 0{\cdot}2$ HFW occurred.

Cole and Kerr investigated 5 areas, notably:

(1) Maximum steady load.

(2) Limitations imposed by out-of-balance at high speeds.

(3) Condition producing Whirl.

(4) Bearing material requirements.

(5) Influence of compressibility on Bearing performance.

They measured the mid plane circumferential pressure profile, and found the Airfilm temperature to follow more closely the Isothermal process. Temperature varying by less than ± 2°C. Also observed was humidity effect, condensation forming on the glass bearing inside surface. This they assumed due to Isothermal compression causing saturation.

On integration of the above pressure profile, having assumed a parabolic axial distribution, a 15 → 20% error of load was found (low). They assumed this to be due to the departure of the axial profile from a parabolic distribution. This agrees with the Author's findings.

Burgdorfer in 1958 (8) presented a theoretical approach on the influence of molecular mean free path on the performance of self acting gas bearings.

He stated that when the ratio of molecular mean free path to film thickness is between 0 and 1 then as a first approximation the flow can be treated as a continuum rather than a molecular medium. However, the boundary conditions must be modified to include the slip velocities at the boundaries. He applied his theory to the Rayleigh stepped bearing. For ratios of molecular free path to film thickness approaching unity, the effects of slip increased and the pressure profile was reduced, and hence load capacity. He mentioned that this

effect was negligible for bearings of high bearing number (approaching the incompressible case). A reviewer of Burgdorfer's paper, McNeilly, mentioned that this slip effect would be most appropriate for machines operating at high altitudes, where the air is rarefied.

In 1958 Elrod and Burgdorfer (9) produced a solution for all journal displacements for the plain bearing with an $L/D \Rightarrow \infty$.

Michael 1959 (10) and Gross 1959 (11) have all given numerical solutions for plane slider bearings of finite widths whilst Sternlicht et al (12) 1958 give solutions for the finite journal bearing for small values of compressibility.

In 1960 Raimondi (13) produced a paper for the steady state numerical solution of the finite self acting journal bearing employing the finite difference technique. His solution was suitable for both the isothermal and adiabatic gas film. He compared his results with those of Ausman and others showing their results to be inaccurate for large eccentricity ratios, breaking down at $\varepsilon > 0{\cdot}2$. He carried out studies on the effect of compressibility on the central pressure profile. His results compared very favourably with the experimental results of Whitley and Betts 1959 (14).

Whitley and Betts (14) observed that air follows most closely the isothermal characteristics than adiabatic. Whitley and Betts also studied the effects of instability closely.

CHAPTER 3

STEADY STATE BEARING ANALYSIS

3·1·1 EQUATION OF CONTINUITY (DERIVATION OF REYNOLD'S EQUATION)

The basic equation can be derived by considering the Law of conservation of mass flow through a control volume.

Experimental observations indicate that in the absence of Relativity and Nuclear Effects, the net rate of mass eflux from the control volume through its control surface equals the rate of decrease of mass inside the control volume. Considering, firstly the mass conservation of the system which occupies the C.V at time t. then by using the Transformation Law as shown below:-

$$\frac{Dm}{Dt} = \oiint_{c.s.} \rho V.\, dA + \frac{\partial}{\partial t} \iiint_{c.v.} \rho d\forall \qquad (3\cdot1)$$

Since $\frac{Dm}{Dt} \rightarrow 0$ Total mass must remain invariant (no change).

$$\oiint_{c.s.} \rho V.\, dA = - \frac{\partial}{\partial t} \iiint_{c.v.} \rho d\forall \qquad (3\cdot2)$$

Using Gauss Theorem to transform surface integral to a volume integral.

Equation 3·2 is termed the Equation of Continuity which states that the Fluid mass flow can neither be created nor destroyed, within any control volume of fixed size at time t.

Using Gauss Theorem equation 3·2 becomes where $\nabla.\rho V$ is rate of mass eflux per unit volume.

$$\iiint_{c.v.} \left[(\nabla.\rho V) + \frac{\partial \rho}{\partial t}\right] d\forall = 0$$

As volume is assumed constant integrals vanish leaving:-

$$\left[(\nabla.\rho V) + \frac{\partial \rho}{\partial t}\right] = 0 \qquad (3\cdot3)$$

This is the Differential Equation of Mass Flow at any point in a flow field.

For incompressible flow equation 3·3 becomes the Laplace Equation.

$$\nabla . V = 0 \qquad (3\cdot4)$$

Also for a steady flow field $\frac{\partial \rho}{\partial t} \rightarrow 0$

$$\therefore \quad \nabla \rho V = 0 \qquad (3\cdot4)$$

3·1·2 STEADY FLOW FIELD

If the flow field is steady with respect to time t the total mass inside remains constant R.H.S. of 3·2

$$\therefore \quad \iint_{c.s.} \rho V dA \rightarrow 0 \qquad (3\cdot5a)$$

Therefore incoming and outgoing ratio of mass remain the same.

$$\text{i.e.} \quad \iint_{Ai} \rho_{in} V_{in} dA_{in} = \iint_{Ao} \rho_{out} V_{out} dA_{out} \qquad (3\cdot5b)$$

Using Gauss Theorem

$$\iint_{c.s.} \rho V dA = \iiint_{c.v.} (\nabla . \rho V)\, dV$$

Where $\nabla . \rho V$ = Rate of eflux of mass per unit volume , which becomes since volume assumed not to change (in bearing).

$$\left[(\nabla . \rho V) + \frac{\partial \rho}{\partial t}\right] = 0 \qquad (3\cdot3)$$

3·1·3 CONSERVATION OF MOMENTUM - (Euler's Equations)

From Newton's second law of motion we have that the resultant of all body and external forces becomes:

$$F = \frac{D\rho}{Dt} = \frac{D}{Dt} \iiint_{system} V\rho d\forall$$

After applying the Transformation Law:

$$F = \frac{D\rho}{Dt} = \iint_{c.s} V(\rho V.\, dA) + \frac{\partial}{\partial t} \iiint_{c.v} V\rho d\forall \qquad (3\cdot6)$$

F = Net rate of Eflux of momentum through control surface at time t. + Rate of change of momentum inside the control volume at time t.

Using Gauss Theorem to transform the surface integral once again to a volume integral such that :

$$\iint_{c.s.} V(\rho V.\, dA) = \iiint_{c.v.} [\nabla.\, \rho VV]\, d\forall$$

Where VV is a dyadic VV = I

$$\therefore F = \iiint_{c.v.} [\nabla.\, \rho VV]\, d\forall + \frac{\partial}{\partial t} \iiint_{c.v.} V.\, \rho d\forall \qquad (3\cdot7)$$

Letting $F = \iiint_{c.v.} f\, d\forall$

We obtain $\iiint_{c.v.} f\, dV = \iiint_{c.v.} [\nabla.\, \rho VV]\, d\forall + \frac{\partial}{\partial t} \iiint_{c.v.} V\rho d\forall$

and for a fixed volume (as a bearing is assumed).

$$f = [\nabla.\, \rho VV] + \frac{\partial}{\partial t} \rho V \qquad (3\cdot8)$$

Expanding 3·8

$$f = \rho\, (V.\, \nabla)\, V + V\, (\nabla.\, \rho V) + V\, \frac{\partial \rho}{\partial t} + \rho \frac{\partial V}{\partial t}$$

$$(V.\, \nabla)\, V = u\frac{\partial V}{\partial x} + v\frac{\partial V}{\partial y} + w\frac{\partial V}{\partial z}$$

And because equation becomes $(\nabla.\, \rho V) + \frac{\partial \rho}{\partial t} = 0$ Laplace Equation

$$f = \rho\, (V.\, \nabla)\, V + \rho\frac{\partial V}{\partial t} = \rho\frac{DV}{Dt}$$

$$\therefore \quad \rho\frac{DV}{Dt} = \rho\, (u\frac{\partial V}{\partial x} + v\frac{\partial V}{\partial y} + w\frac{\partial V}{\partial t} + \frac{\partial V}{\partial t}) \qquad (3\cdot9)$$

Once again considering the equation

$$\rho \frac{DV}{Dt} = f$$

f consists of two types of forces - body forces and surface forces. In the absence of Electromagnetic forces gravity is the only body force encountered in fluid flow, the gravity force per unit volume is ρg, where g is the local gravitational acceleration.

The surface forces per unit area are:-

$$fT = \frac{\partial Tx}{\partial x} + \frac{\partial Ty}{\partial y} + \frac{\partial Tz}{\partial z}$$

Where Tx = i σxx + j τxy + kτxt and Ty and Tz have their respective components. Therefore T can also be written equal to fT = [∇.T] where T = Stress Tensor. Euler's Equation can now be written in terms of its stress components.

$$\rho \frac{DV}{Dt} = \rho g + [\nabla . T]$$

In cartesian co-ordinates Euler's Equation in terms of stress becomes:-

$$\rho \frac{Du}{Dt} = \rho \left(u \frac{\partial u}{\partial x} + V \frac{\partial V}{\partial y} + w \frac{\partial u}{\partial z} + \frac{\partial u}{\partial t}\right) = \rho gx + \left(\frac{\partial \sigma xx}{\partial x} + \frac{\partial \tau yx}{\partial y} + \frac{\partial \tau zx}{\partial z}\right)$$

$$\rho \frac{DV}{Dt} = \rho \left(u \frac{\partial V}{\partial x} + V \frac{\partial V}{\partial y} + w \frac{\partial V}{\partial z} + \frac{\partial V}{\partial t}\right) = \rho gy + \left(\frac{\partial \sigma xy}{\partial x} + \frac{\partial \sigma yy}{\partial y} + \frac{\partial \tau zy}{\partial z}\right) \quad 3\cdot10$$

$$\rho \frac{Dw}{Dt} = \rho \left(u \frac{\partial w}{\partial x} + V \frac{\partial w}{\partial y} + w \frac{\partial w}{\partial z} + \frac{\partial w}{\partial t}\right) = \rho gz + \left(\frac{\partial \tau xz}{\partial x} + \frac{\partial \tau yz}{\partial y} + \frac{\partial \sigma zz}{\partial z}\right)$$

3·1·4 STOKE'S LAW OF VISCOSITY

This derivation is based on the assumptions that the fluid has the following properties:-

(1) ISOTROPIC

(2) VISCOUS STRESSES ARE LINEARLY PROPORTIONAL TO RATES OF STRAIN

From the rates-of-strain at any point in a viscous flow field being Tensorial quantities, stress-and-rate-of-strain relationships can be established along the "principal" directions and then transformed to the desired Stoke's Law. On the principal axes all shear stresses vanish and the remaining stresses are the so-called principal

stresses. Likewise all the rates-of-shear-strain associated with the principal axes vanish and rates-of-principal-strain only remain. Since all the rates-of-shear-strain are zero on principal planes. The sums of the equation is an invarient.

$$\therefore \frac{\partial u}{\partial x} + \frac{\partial v}{\partial y} + \frac{\partial w}{\partial z} = \frac{\partial u'}{\partial x'} + \frac{\partial v'}{\partial y'} + \frac{\partial w'}{\partial z'} = \nabla . V$$

Where the local dilatation $\nabla . V$ is independent of the orientation of co-ordinate.

After considering relationships between stress and rates-of-strain one can arrive at the following equations:-

The full derivation is in Ref. (57).

$$\sigma xx = - P + 2 \eta \frac{\partial u}{\partial x} - 2/3 \eta \text{ div } V$$

$$\sigma yy = - P + 2 \eta \frac{\partial V}{\partial Y} - 2/3 \eta \text{ div } V$$

$$\sigma zz = - P + 2 \eta \frac{\partial w}{\partial z} - 2/3 \eta \text{ div } V$$

$$\tau yz = \tau zy = \eta \left(\frac{\partial V}{\partial z} + \frac{\partial w}{\partial y} \right) \qquad (3 \cdot 11)$$

$$\tau zx = \tau xz = \eta \left(\frac{\partial w}{\partial x} + \frac{\partial u}{\partial z} \right)$$

$$\tau xy = \tau yx = \eta \left(\frac{\partial u}{\partial y} + \frac{\partial v}{\partial x} \right)$$

$$\text{div } V = \frac{\partial u}{\partial x} + \frac{\partial v}{\partial y} + \frac{\partial w}{\partial z}$$

The above equations are termed Stoke's Law of Viscosity and relate stresses to rates-of-strain (viscous stress field to velocity field).

For incompressible fluids one dimensional Newton's Viscosity Law yields

$$\tau xy = \tau yz = \eta \frac{\partial u}{\partial Y} \qquad \eta = \text{Dynamic Viscosity}$$

3·1·5 NAVIER STOKE'S EQUATIONS OF MOTION

To arrive at the Navier Stokes Equations of Motion we substitute the Stokes Law of Viscosity into the Eulers Equation of Motion in stress components. This arrives at the Navier Stokes Equations.

$$\rho\frac{Du}{Dt} = \rho gx - \frac{\partial P}{\partial x} + \frac{\partial}{\partial x}\left[\eta\left(2\frac{\partial u}{\partial x} - 2/3 \text{ div } V\right)\right] + \frac{\partial}{\partial y}\left[\eta\left(\frac{\partial u}{\partial y} + \frac{\partial v}{\partial x}\right)\right] + \frac{\partial}{\partial z}\left[2\left(\frac{\partial w}{\partial x} + \frac{\partial u}{\partial z}\right)\right] \qquad 3\cdot12a$$

$$\rho\frac{Dv}{Dt} = \rho gy - \frac{\partial P}{\partial y} + \frac{\partial}{\partial y}\left[\eta\left(2\frac{\partial V}{\partial y} - 2/3 \text{ div } V\right)\right] + \frac{\partial}{\partial z}\left[\eta\left(\frac{\partial v}{\partial z} + \frac{\partial w}{\partial y}\right)\right] + \frac{\partial}{\partial x}\left[\eta\left(\frac{\partial u}{\partial y} + \frac{\partial v}{\partial x}\right)\right] \qquad 3\cdot12b$$

$$\rho\frac{Dw}{Dt} = \rho gz - \frac{\partial P}{\partial z} + \frac{\partial}{\partial z}\left[\eta\left(2\frac{\partial w}{\partial z} - 2/3 \text{ div } V\right)\right] + \frac{\partial}{\partial x}\left[\eta\left(\frac{\partial w}{\partial x} + \frac{\partial v}{\partial z}\right)\right] + \frac{\partial}{\partial y}\left[\eta\left(\frac{\partial v}{\partial z} + \frac{\partial w}{\partial y}\right)\right] \qquad 3\cdot12c$$

Equations 3·12 along with the Equation of Continuity $\nabla.\rho V + \frac{\partial \rho}{\partial t} = 0$,

the Energy Equation, the Equation of State $P = \rho(P.T)$ and the Empirical Viscosity Law $\eta = \eta(T)$, form a system of seven Equations to solve for the variables $u, v, w, P, \rho, T, \eta$ in most flow problems involving Newtonian fluids.

3·1·6 DERIVATION OF REYNOLD'S EQUATION FROM NAVIER STOKE'S EQUATIONS

The derivation of Reynold's Equation for gas lubrication is based on the following assumptions:-

(1) Height of Fluid Film (h) is very small compared with the other Dimensions x or z. (Length and Diameter).

(2) Variation of Pressure $\frac{\partial P}{\partial y}$ across the film → 0.

(3) The flow is Laminar and Irrotational (no vortex or turbulent flow present).

(4) No external body forces act on the Lubricating film hence $\rho gx = \rho gy = \rho gz = 0$.

(5) Fluid Inertia terms are assumed very small compared to the Viscous Shear terms. Inertia forces consist of the following:-

(i) Acceleration of the fluid.

(ii) Centrifugal forces of the fluid.

(iii) Fluid Gravity.

$$\therefore \quad \frac{Du}{Dt} = \frac{DV}{Dt} = \frac{Dw}{Dt} \rightarrow 0$$

(6) No slip occurs across the bearing surface.

(7) Compared to Velocity Gradients $\frac{\partial u}{\partial y}$ and $\frac{\partial w}{\partial y}$ all other Velocity Gradients are considered negligable.

Since u and to a lesser degree w are the predominant Velocities ∂y is a dimension much less than either x or z, the assumption is valid. Therefore $\partial u/\partial y$ and $\partial w/\partial y$ are assumed Shears while all other terms are Accelerations. Therefore any derivatives of terms other than $\partial u/\partial y$ and $\partial w/\partial y$ will be of much higher order, thus negligible.

Hence all derivatives except $\frac{\partial^2 u}{\partial y^2}$ and $\frac{\partial^2 w}{\partial y^2}$ are ommitted.

Assumptions 1 → 7 yield the following relationships

$$\frac{1}{\eta}\frac{\partial P}{\partial x} = \frac{\partial^2 u}{\partial y^2} \qquad (3\cdot13)$$

$$\frac{1}{\eta}\frac{\partial P}{\partial z} = \frac{\partial^2 w}{\partial y^2}$$

Upon integation and substitution into the Navier Stoke's Equations one arrives at the Reynold's Equation which includes Bush and Journal Velocities u_1 v_1 and u_2 v_2

$$\rho(v_2 - v_1) = I_1 + I_2 + I_3 + I_4$$

Where

$$I_1 = \frac{\partial}{\partial x}\left[\frac{\rho h^3}{12\eta}\frac{\partial P}{\partial x}\right],$$

$$I_2 = \frac{\partial}{\partial z}\left[\frac{\rho h^3}{12\eta}\frac{\partial P}{\partial z}\right]$$

$$I_3 = \left[\frac{u_2 - u_1}{2}\right]\frac{\partial \rho h}{\partial x} - \frac{\rho h}{2}\frac{\partial}{\partial x}[u_1 + u_2]$$

$$I_4 = -h\frac{\partial \rho}{\partial t}$$

Reynold's equation then becomes including Bush and Journal Velocities

$$\frac{\partial}{\partial x}\left[\frac{\rho}{\eta}h^3\frac{\partial P}{\partial x}\right]+\frac{\partial}{\partial z}\left[\frac{\rho h^3}{\eta}\frac{\partial P}{\partial z}\right] = 6\rho h\frac{\partial}{\partial x}[u_1+u_2]-6[u_2-u_1]\frac{\partial \rho h}{\partial x} \qquad (3\cdot14)$$

$$+12\rho(V_2-V_1)+12h\frac{\partial \rho}{\partial t}$$

Reynold's Equation can now be solved with the aid of the energy equation or because we assume an ideal gas one can use the Ideal gas relationship or Equation of State:-

$$\rho = \frac{P}{RT} \qquad (3\cdot15)$$

Substituting 3·15 into 3·14 and substituting for $x = R\theta$

$$\frac{\partial}{\partial\theta}\left[Ph^3\frac{\partial P}{\partial\theta}\right]+R^2\frac{\partial}{\partial z}\left[Ph^3\frac{\partial P}{\partial z}\right] = 6\eta RPh\frac{\partial}{\partial\theta}[u_1+u_2]-6\eta R[u_2-u_1]\frac{\partial Ph}{\partial\theta}$$
$$+12R^2\eta P(V_2-V_1)+12\eta R^2h\frac{\partial P}{\partial t} \qquad (3\cdot16)$$

If one neglects non-steady components Reynold's Equation becomes:

$$\frac{\partial}{\partial\theta}\left[Ph^3\frac{\partial P}{\partial\theta}\right]+R^2\frac{\partial}{\partial z}\left[Ph^3\frac{\partial P}{\partial z}\right] = 6\eta R\frac{\partial u_1 Ph}{\partial\theta}$$

Reynold's Equation becomes with $u_1 = \omega R$

$$\frac{\partial}{\partial\theta}\left[Ph^3\frac{\partial P}{\partial\theta}\right]+R^2\frac{\partial}{\partial z}\left[Ph^3\frac{\partial P}{\partial z}\right] = 6\eta\omega R^2\frac{\partial Ph}{\partial\theta} \qquad (3\cdot17)$$

3·1·7 NON-DIMENSIONALIZED REYNOLD'S EQUATION

$$\frac{\partial}{\partial\theta}\left[Ph^3\frac{\partial P}{\partial\theta}\right]+R^2\frac{\partial}{\partial z}\left[Ph^3\frac{\partial P}{\partial z}\right] = 6\eta\omega R^2\frac{\partial Ph}{\partial\theta}$$

Non-dimensionalizing

Let $\bar{P} = \frac{P}{Pa}$, $\bar{\theta} = \frac{\theta}{2\pi}$, $\bar{z} = \frac{z}{L}$, $H = \frac{h}{C}$, $h = HC$, $M-1 = m$, $N-1 = n$

Where $1 \geq i \geq M$ and $1 \geq j \geq N$

Rearranging the above Reynold's Equation becomes:-

$$\frac{\partial}{\partial\bar{\theta}}\left[\bar{P}H^3\frac{\partial\bar{P}}{\partial\bar{\theta}}\right]+\left(\frac{2\pi R}{L}\right)^2\frac{\partial}{\partial\bar{z}}\left[\bar{P}H^3\frac{\partial\bar{P}}{\partial\bar{z}}\right] = \frac{12\pi\eta\omega R^2}{PaC^2}\frac{\partial\bar{P}H}{\partial\bar{\theta}}$$

$$\frac{\partial}{\partial\bar{\theta}}\left[\bar{P}H^3\frac{\partial\bar{P}}{\partial\bar{\theta}}\right]+\left(\frac{\pi D}{L}\right)^2\frac{\partial}{\partial\bar{z}}\left[\bar{P}H^3\frac{\partial\bar{P}}{\partial\bar{z}}\right] = \frac{12\eta\pi\omega}{Pa}\left(\frac{R}{C}\right)^2\frac{\partial\bar{P}H}{\partial\bar{\theta}}$$

Letting $G = \left(\frac{2\pi R}{L}\right)^2$, $\Lambda = \frac{12\eta\pi\omega}{Pa}(R/C)^2$

$$\frac{\partial}{\partial\bar{\theta}}\left[\bar{P}H^3\frac{\partial\bar{P}}{\partial\bar{\theta}}\right]+G\frac{\partial}{\partial\bar{z}}\left[\bar{P}H^3\frac{\partial\bar{P}}{\partial\bar{z}}\right] = \Lambda\frac{\partial\bar{P}H}{\partial\bar{\theta}} \qquad (3\cdot18)$$

3·1·8 'Q' SUBSTITUTION METHOD

This method had been attempted reasonably successfully on Hybrid Gas Bearings by MacFarlane (15) and by Kaneko et al (16) to plane slider bearings.

Firstly differentiating Reynold's Equation (3·17) one obtains:-

$$3H^2 \frac{\partial H}{\partial \bar{\theta}} \cdot \frac{\partial \bar{P}^2}{\partial \bar{\theta}} + H^3 \frac{\partial^2 \bar{P}^2}{\partial \bar{\theta}^2} + GH^3 \frac{\partial^2 \bar{P}^2}{\partial \bar{z}^2} + 3GH^2 \frac{\partial H}{\partial \bar{\theta}} \cdot \frac{\partial \bar{P}^2}{\partial \bar{z}} = \Lambda \left[H \frac{\partial \bar{P}}{\partial \bar{\theta}} + \bar{P} \frac{\partial H}{\partial \bar{\theta}} \right] \quad (3·19)$$

Using the substitution $Q = \bar{P}^2$
Equation (3·19) becomes:-

$$3H^2 \frac{\partial H}{\partial \bar{\theta}} \cdot \frac{\partial Q}{\partial \bar{\theta}} + H^3 \frac{\partial^2 Q}{\partial \bar{\theta}^2} + GH^3 \frac{\partial^2 Q}{\partial \bar{z}^2} + 3GH^2 \frac{\partial H}{\partial \bar{z}} \cdot \frac{\partial Q}{\partial \bar{z}} = \frac{\Lambda}{\sqrt{Q}} \left[\frac{H}{2} \frac{\partial Q}{\partial \bar{\theta}} + Q \frac{\partial H}{\partial \bar{\theta}} \right] \quad (3·20)$$

This is Reynold's Equation with the Q Substitution.

3·1·9 FINITE DIFFERENCE FORMULATION OF 'Q' METHOD USING GAUSS SEIDEL ITERATION WITH S.O.R.

The Steady State Equation (3·20) can have its derivatives formulated as follows:-

$$\left(\frac{\partial Q}{\partial \bar{\theta}}\right)_{i,j} = (Q_{i+1,j} - Q_{i-1,j}) \cdot \frac{m}{2}$$

$$\left(\frac{\partial^2 Q}{\partial \bar{\theta}^2}\right)_{i,j} = (Q_{i+1,j} - 2Q_{i,j} + Q_{i-1,j}) \cdot m^2$$

$$\left(\frac{\partial Q}{\partial \bar{z}}\right)_{i,j} = (Q_{i,j+1} - Q_{i,j-1}) \frac{n}{2}$$

$$\left(\frac{\partial^2 Q}{\partial \bar{z}^2}\right)_{i,j} = (Q_{i,j+1} - 2Q_{i,j} + Q_{i,j-1}) \cdot n^2$$

Figure (3·1) shows Finite Difference Grid.

Substituting into Equation (3·20) and rearranging gives the Linearized Derivatives :-

$$Q_{i,j} = A_{i,j} \cdot Q(i+1,j) + B_{i,j} \cdot Q(i-1,j) + C_{i,j} \cdot Q(i,j+1) + C_{i,j} \cdot Q(i,j-1) \quad (3·21)$$

Where

$$A_{i,j} = \left[\frac{3}{2}\frac{m}{H}\frac{\partial H}{\partial \theta} + m^2 - \frac{\Lambda n}{4H^2\sqrt{Q}}\right]/E_{i,j}, \quad B_{i,j} = \left[-\frac{3}{2}\frac{m}{H}\frac{\partial H}{\partial \theta} + m^2 + \frac{\Lambda n}{4H^2\sqrt{Q}}\right]/E_{i,j}$$

$$C_{i,j} = \left[\frac{3}{2}\frac{Gn}{H}\frac{\partial H}{\partial z} + Gn^2\right]/E_{i,j}, \quad D_{i,j} = \left[-\frac{3}{2}\frac{Gn}{H}\frac{\partial H}{\partial z} + Gn^2\right]/E_{ij}$$

$$E_{i,j}\left[2m^2 + 2Gn^2 + \frac{\Lambda}{\sqrt{Q}\cdot H^3}\cdot\frac{\partial H}{\partial \theta}\right]$$

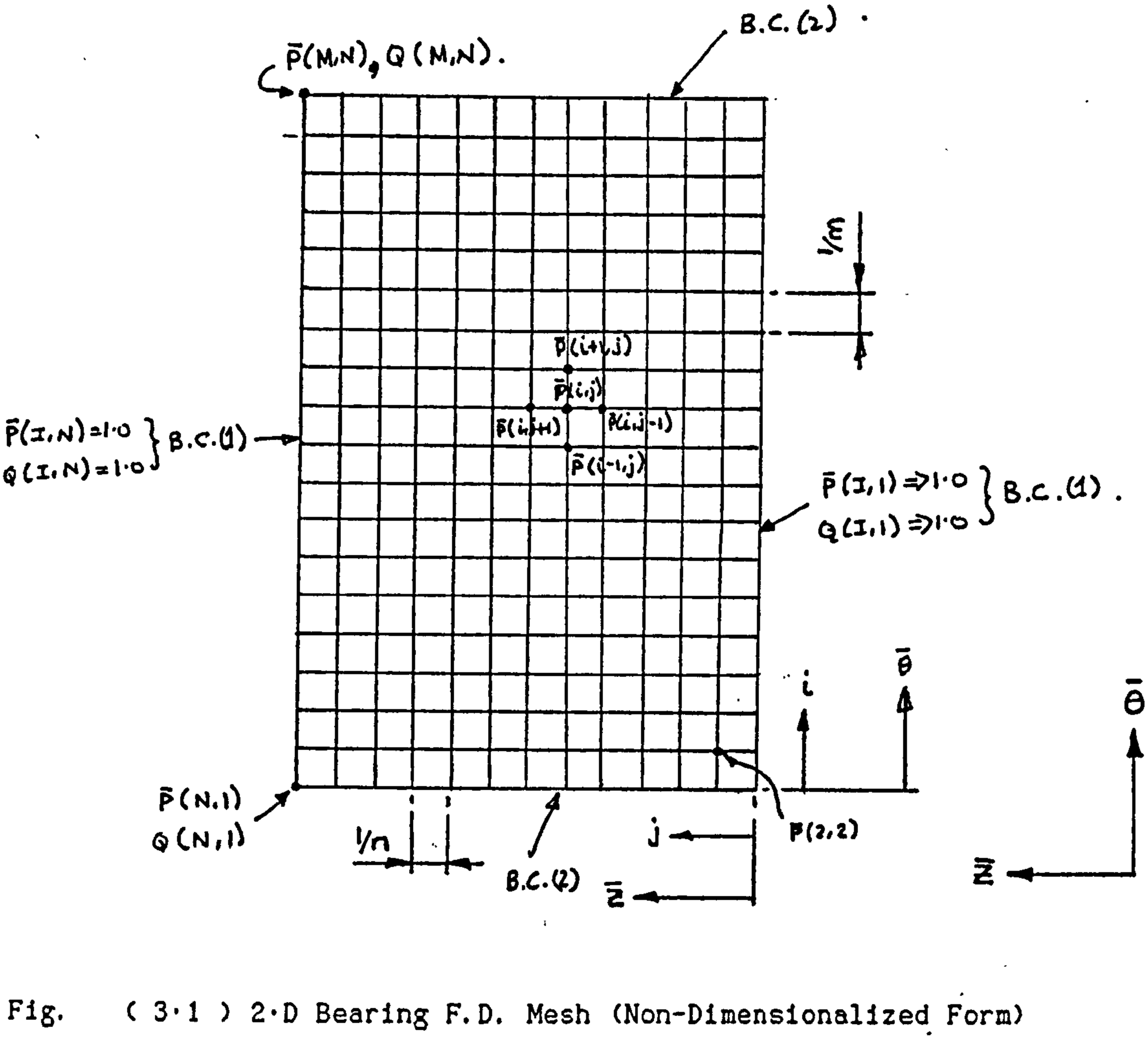

Fig. (3·1) 2·D Bearing F.D. Mesh (Non-Dimensionalized Form)

Boundary Conditions

Q Method	$\bar{P}$ Method
(1) $Q(I,1) = 1.0$	$\bar{P}(I,1) = 1.0$
$Q(I,N) = 1.0$	$\bar{P}(I,N) = 1.0$
(2) $Q(1,J) = Q(M,J)$	$\bar{P}(1,J) = \bar{P}(M,J)$

To increase the rate of convergence the equation invoked Gauss-Seidel iteration with successive over-relaxation, transferring the equation into the following format:

$$Q_{i,j}^{k+1} = Q_{i,j}^{k} + \omega[A_{ij}.Q(i+1,j) + B_{ij}.Q(i-1,j) + C_{ij}.Q(i,j+1) + D_{ij}.Q(i,j-1) - Q_{i,j}^{k}] \quad (3\cdot22)$$

Where ω = Over/Under relaxation factor.

The optimum over-relaxation Factor for oil bearings can be calculated (Lloyd & McCallion (17)) from the following relationship but was found unreliable and better convergence seemed apparent with under relaxed equations as observed by Raimondi (13). However Raimondi had found under relaxation to a certain degree unreliable especially at large eccentricity, L/D ratios and compressibility numbers.

$$\omega \text{ opt} = 2\left[\frac{1-(1-\lambda^2)^{1/2}}{\lambda^2}\right] \quad (3\cdot23a)$$

$$\text{Where } \lambda \simeq \frac{1-\pi^2\left[4+(\pi D/4)^2\right]}{2\left[m^2+(\pi Dn/L)^2\right]} \quad (3\cdot23b)$$

Where $\frac{1}{[m^2+(\pi Dn/L)^2]}$ is termed the Truncation Error and as m & n $\Rightarrow \infty$ the error reduces.

The convegence criterion for the above equations was:-

$$Q_{i,j}^{k+1} - Q_{i,j}^{k} \leq \rho_c\, Q_{i,j}^{k+1} \quad (3\cdot24)$$

Where ρ_c = 0·0001

A solution could only be considered when this condition was satisfied at each nodal position.

Due to the nature of the equations, on each iteration step the equation was divided by Q^{k+1} but convergence did not take place.

This at first was not easily understood, but upon further investigations one can see that the equations are non-linear with respect to Q.

These findings tended to agree with those of MacFarlane, Ref. (15) he also could not arrive at convergence with this substitution technique for solving the Aerodynamic Equations. He had however limited success with Hybrid Equations.

3·1·10 'Q' SUBSTITUTION WITH THE NEWTON RAPHSEN METHOD

Having been unable to achieve convergence with the S.O.R. technique, the Newton Raphsen method was investigated.

If one recalls the form of the Newton Raphsen Formulae:-

$$Q_{K+1} = Q_K - f(Q_K)/f'(Q_K) \qquad (3\cdot25)$$

Where $f(Q_K) = 0$ and rewriting Reynold's Equation in Finite Difference form and rearranging one arrives at:-

$$f(Q_K) = A(i,j).Q(i+1,j)+B(i,j).Q(i-1,j)+C(i,j).Q(i,j+1) +D(i,j).Q(i,j-1)-Q(i,j) \qquad (3\cdot26)$$

$$f'(Q_K) = A'(i,j).Q(i+1,j)+B'(i,j).Q(i-1,j)+C'(i,j).Q(i,j+1) +D'(i,j).Q(i,j-1)-1\cdot0 \qquad (3\cdot27)$$

Where A(i,j), B(i,j), C(i,j) and D(i,j) all contain $(Qi,j)^n$
So therefore these too require differentiation with respect to Qi,j.
This leads to a rather complex system of equations as can be seen below, and can be written thus:-

$$\left.\begin{aligned}
A(i,j)&=[0\cdot5+CODHA(i)-CODHB(i)/Q(i,j)^n].CONA-[CODHC(i).Q(i,j)^n]\\
&\quad .[1\cdot0+2\cdot0.CODHA(i)+2\cdot0.CODHB(i)/Q(i,j)^n]\\
B(i,j)&=[0\cdot5-CODHA(i)+CODHB(i)/Q(i,j)^n].CONA+[CODHC(i).Q(i,j)^n]\\
&\quad .[1\cdot0-2\cdot0.CODHA(i)+2\cdot0.CODHB(i)/Q(i,j)^n]\\
C(i,j)&=CONB.[CODHZ(i,j)+1\cdot0].CONA+[CODHD(i).Q(i,j)^n]\\
&\quad .[1\cdot0+2\cdot0.CODHZ(i,j)]\\
D(i,j)&=CONB.[CODHZ(i,j)+1\cdot0].CONA+[CODHD(i).Q(i,j)^n]\\
&\quad .[1\cdot0-2\cdot0.CODHZ(i,j)]
\end{aligned}\right\} \qquad (3\cdot28)$$

Their derivatives are:-

$$A'(i,j)=[0\cdot5.CODHB(i)/Q(i,j)^{3/2}].CONA-[CODHC(i)/Q(i,j)^{n}]$$
$$.[0\cdot5+CODHA(i)]$$

$$B'(i,j)=[CODHC(i)/Q(i,j)^{n}].[0\cdot5-CODHA(i)]$$
$$-[0\cdot5.CODHB(i)/Q(i,j)3/2].CONA \qquad (3\cdot29)$$

$$C'(i,j)=[CODHD(i)/Q(i,j)^{n}].[0\cdot5+CODHZ(i,j)]$$

$$D'(i,j)=[CODHD(i)/Q(i,j)^{n}].[0\cdot5-CODHZ(i,j)]$$

and the following constants are as follows:-

$$CONA = 1\cdot0 + \frac{m^2}{Gn^2}$$

$$CONB = \frac{G\cdot n^2}{2\cdot0.\,m^2}$$

Constants dependent upon θ, H & Z

$$CODHA(i) = 0\cdot75.HDASH(i)/(H(i).m)$$
$$CODHB(i) = (ALAMDA.n)/(8\cdot0.m^2.H(i)^2)$$
$$CODHC(i) = H(i)^3\cdot m^2/(ALAMDA.HDASH(i)) \qquad (3\cdot30)$$
$$CODHD(i) = H(i)^3.G.n^2/(ALAMDA.HDASH(i))$$
$$CODHZ(i) = 0\cdot75.HDASH(j)/(H(i).n)$$

HDASH(i) = Differential of H(i)

ALAMDA = Λ

Having thoroughly investigated this Newton Raphsen technique it was still not possible to arrive at well conditioned equations that converged at the required convergence criterion. As one will agree it is possible to arrive at an answer for any set of equations but the accuracy of the answer must be within set limits or one destroys one's objectives in using a refined technique.

3·1·11 NON-LINEAR OVER RELAXATION

It has been shown in section 3·1·10 that when Finite Difference approximations are applied to a non-linear Elliptic equation - non-linear algebraic equations result.

Several methods have been proposed to solve these systems, the earliest and best known being the Extended Leibmann method. This is a direct generalization of the Linear Gauss Seidel method. Berrs (18) and Schecter (19), discuss a number of iteration schemes for non-linear problems. While the Extended Leibmenn method has a sound theoretical basis , the following method of non-linear over-relaxation has only numerical experiments and semi theoretical arguments to justify it to this present day.

In all previous techniques the solution of large non-linear algebraic systems were obtained by an outer iteration, say Newton Raphsen, which linearizes, followed by some iterative techniques, say S.O.R. The process being repeated, thus constructing a cascade of out Newton iterations alternated with a large sequence of inner Linear iterations. This technique has obviously been attempted and did not arrive with a convergent answer.

The N.L.O.R. technique is a direct and simple method particularly suited to Non-Linear Elliptic Equations and owes much of its creation to Lieberstein (20).It is also known as an extension of the Yang-Frankel Linear S.O.R. method.

Consider a system of k algebraic equations, each have continuous first derivatives:-

$$f\rho\ (Q_1,\ Q_2,\ Q_3\ \ldots\ldots\ Q_k) = 0 \qquad \rho = 1, 2, \ldots .k$$

Let $$f_{pq} = \frac{\partial f\rho'}{\partial Q_q} \qquad (3\cdot31)$$

The basic idea is that N, L, O, R, is a different use of the Newton process from that carried out by Bellman, Juncosa and Kalaba. (21)

Where an over-relaxation factor ω is introduced thus the equations are as follows:-

$$\left.\begin{aligned}
x_1^{n+1} &= x_1^n - \omega f_1(x_1^n, x_2^n \ldots\ldots x_k^n) \\
&\quad\; f_{11}(x_1^n, \ldots\ldots\ldots\ldots x_k^n) \\
x_2^{n+1} &= x_2^n - \omega f_2(x_1^{n+1}, x_2^n, \ldots . x_k^n) \\
&\quad\; f_{22}(x_1^{n+1}, x_2^n \ldots . . x_k^n) \\
x_3^{n+1} &= x_3^n - \omega f_3(x_1^{n+1}, x_2^{n+1}, x_3^n \ldots . x_k^n) \\
&\quad\; f_{33}(x_1^{n+1}, x_2^{n+1}, x_3^n \ldots x_k^n)
\end{aligned}\right\} \quad (3\cdot32)$$

And so on.....

This method has the feature of the Gauss-Seidel method in that it uses corrected results immediately upon becoming available. In addition if the fp are linear functions of x this method reduces to S.O.R.

The convergence criteria for N.L.O.R. according to Ames (22) can be shown to be the same as that for S. O. R. with the Coefficient Matrix [A] being replaced by the Jacobian of the equation.

$$fp(x_1, x_2, x_3 \ldots\ldots\ldots x_k) = 0 \qquad (3\cdot33)$$

The proof of which can be seen in Appendix (3).

For convergence, the Jacobian J (f_{pq}^k), at each stage of the iteration, must have properties required for (A) in the S.O.R. method, see (22).To make the process most efficient an optimum value of ω should be calculated minimising the spectral norm of $L_{\omega n}$ at each iteration k. Ames states that this could be expensive and not rewarding since in his experience one does better to over estimate ω opt than to under estimate. Further, Ames suggests that for small systems one usually runs with $\omega = 1$ and for large systems $\omega \Rightarrow 2\cdot0$.

3·1·12 'Q' METHOD WITH N.L.O.R.

Section 3·1·11 explained that for the system of equations to converge the Jacobian Matrix of the Function of Q must have the same property as that of the A Matrix in the Linear Successive Over-relaxation method.

On closer inspection one can see that all First derivatives still contain Non-Linear values of Q. Therefore this Jacobian does not possess the A matrix property. It would be then prudent to assume that this would be the major factor restricting the convergence. It would also suggest why the S.O.R. method failed and to some degree also explain MacFarlane's (15) findings in this respect.

It would therefore seem that for convergence the First derivative or Jacobian of the Non-Linear function must itself become a Linear function for convergence. Armed with this Hypothesis a new technique was investigated, not however intil the Q method had been tried again for convergence. The system of equations for the N.L.O.R. method and Q substitution was as follows:-

$$Q^{k+1} = Q^{k} - \omega \frac{f(Q^{k})}{f'(Q^{k})}$$

The N.L.O.R. method with Q substitution did not converge so it somewhat agreed with the findings of Lieberstein and myself.

It was the objective, having obtained a solution for values of Q, to then reduce this back to values of P. Having then obtained values of P to arrive at Load carried by the bearing the Actual pressure differential was P which was:-

$P' = Pa\,(\bar{P} - 1)$, $\therefore (Q^{n} - 1).Pa = P'$

Since $\bar{P}^{2} = Q$

Integration of P' over the whole bearing surface gives the Load carrying capacity for any Eccentricity value and set of Parameters L/D, Λ, etc.

3·1·13 $\bar{P}$ METHOD WITH N.L.O.R.

In section 3·1·11 and 3·1·12 one saw that the equations were unable to yield convergence. The problem highlighted in N.L.O.R. was that the Jacobian of the function did not have a Linear Differential with respect to the substitution Q. To this end that approach was abandoned and an alternative approach looked at.

This new approach was the P method.

If one refers to equation (3·19) of section 3·1·8 the Steady State Equation then is as follows upon differentiating:-

$$H^3\left(\frac{\partial\bar{P}}{\partial\bar{\theta}}\right)^2+3H^2\bar{P}\frac{\partial H}{\partial\bar{\theta}}.\frac{\partial\bar{P}}{\partial\bar{\theta}}+\bar{P}H^3\frac{\partial^2\bar{P}}{\partial\bar{\theta}^2}+G\bar{P}H^3\frac{\partial z\bar{P}}{\partial\bar{z}^2}+3\bar{P}GH^2\frac{\partial H}{\partial\bar{z}}.\frac{\partial\bar{P}^2}{\partial\bar{z}}+H^3\left(\frac{\partial\bar{P}}{\partial\bar{z}}\right)^2=\Lambda\left[H\frac{\partial\bar{P}}{\partial\bar{\theta}}+\bar{P}\frac{\partial H}{\partial\bar{\theta}}\right] \quad 3\cdot19$$

The Difference Format of each term is as follows:-

$$\left(\frac{\partial\bar{P}}{\partial\bar{\theta}}\right)1,j = [\bar{P}(i+1,j)-\bar{P}(i-1,j)]\ \frac{m}{2}$$

$$\left(\frac{\partial^2\bar{P}}{\partial\bar{\theta}^2}\right)1,j = [\bar{P}(i+1,j)-2\bar{P}(i,j)+\bar{P}(i-1,j)]\ m^2 \qquad (3\cdot34)$$

$$\left(\frac{\partial\bar{P}}{\partial\bar{z}}\right)1,j = [\bar{P}(1,j+1)-\bar{P}(i-j,1)]\ \frac{n}{2}$$

$$\left(\frac{\partial^2\bar{P}}{\partial\bar{z}^2}\right)1,j = [\bar{P}(i,j+1)-2\bar{P}(i,j)+\bar{P}(i,j-1)]\ n^2$$

Substituting equations (3·34) into (3·19) and on rearranging one arrives at, in difference form:-

$$\bar{P}(i,j)^2-2\bar{P}(i,j)\left[\left(1+\frac{m^2}{Gn^2}\right)\left\{\left[\left(1+\frac{1\cdot5}{mH}\frac{\partial H}{\partial\bar{\theta}}\right).\bar{P}(i+1,j)+\left(1-\frac{1\cdot5}{mH}\frac{\partial H}{\partial\bar{\theta}}\right).\bar{P}(i-1,j)\right]\right.\right.$$

$$\left.\left.+\frac{Gn^2}{m^2}\left[\left(1+\frac{1\cdot5}{mH}\frac{\partial H}{\partial\bar{z}}\right).\bar{P}(i,j+1)+\left(1-\frac{1\cdot5}{nH}\frac{\partial H}{\partial\bar{z}}\right).\bar{P}(i,j-1)\right]-\frac{\Lambda}{m^2H^2}.\frac{\partial H}{\partial\bar{\theta}}\right\}\right]$$

$$-\left(1+\frac{m^2}{Gn^2}\right)\left[0\cdot5.(\bar{P}(i+1,j)-\bar{P}(i-1,j)^2+\frac{Gn^2}{m^2}\left(0\cdot5.(\bar{P}(i,j+1)-\bar{P}(i,j-1)^2\right)\right]$$

$$+\left(1+\frac{m^2}{Gn^2}\right)\frac{\Lambda}{mH^2}\left[\bar{P}(i+1,j)-\bar{P}(i-1,j)\right]=0 \qquad (3\cdot35)$$

Equation (3·35) is written as $f(\bar{P}) = 0$ and is obviously Non-Linear in $\bar{P}i,j$.

Simplifying (3·35) by substituting for

$$CONA = [1\cdot0+m^2/Gn^2]$$

$$CONB = Gn^2/m^2$$

$$CODHA(i) = \frac{1\cdot5}{mH}\frac{\partial H}{\partial\bar{\theta}}$$

$$CODHB(i) = \frac{\Lambda}{m^2H^2}\frac{\partial H}{\partial\bar{\theta}} \qquad (3\cdot30)$$

See Section 3·1·10

$$CODHC(i) = \frac{\Lambda}{mH^2}$$

$$CODHZ(i,j) = \frac{1\cdot5}{nH}\frac{\partial H}{\partial\bar{z}}$$

Equation 3·35 becomes:-

$$\begin{aligned} f\bar{P}(i,j) = {} & \bar{P}(i,j)^2-2\bar{P}(i,j).[CONA.\{[(1\cdot0+CODHA(i)).\bar{P}(i+1,j) \\ & +(1\cdot0-CODHA(i)).\bar{P}(i-1,j)]+CONB.[(1\cdot0+CODHZ(i,j)) \\ & .\bar{P}(i,j+1)+(1\cdot0-CODHZ(i,j)).\bar{P}(i,j-1)]-CODHB(i)\}] \qquad (3\cdot36) \\ & -CONA.[0\cdot5.\{0\cdot5.(\bar{P}(i+1,j)-\bar{P}(i-1,j))^2+CONB.0\cdot5.(\bar{P}(i,j+1) \\ & -\bar{P}(i,j-1))^2]+CONA.CODHC(i).[\bar{P}(i+1,j)-\bar{P}(i-1,j)] \Rightarrow 0 \end{aligned}$$

Remembering that for the N.L.O.R. method that the solution technique is thus:-

$$\bar{P}(i,j) = \bar{P}(i,j)-\omega\frac{f(\bar{P}(i,j))}{f'(\bar{P}(i,j))} \qquad (3\cdot37)$$

The $f(P(i,j))$ and $f'P(i,j)$ contain updated values of $P(i,j)$ when available in the iteration and ω is the relaxation factor, and $f'\bar{P}(i,j)$ is the Jacobian of the $f(\bar{P}(i,j))$.

$$\begin{aligned} f'(\bar{P}(i,j)) = {} & 2.\bar{P}(i,j)-2.[CONA.\{[(1\cdot0+CODHA(i)).\bar{P}(i+1,j) \\ & +(1\cdot0-CODHA(i)).\bar{P}(i-1,j)]+CONB \\ & .[(1\cdot0+CODHZ(i,j).\bar{P}(i,j+1) \\ & +(1\cdot0-CODHZ(i,j)).\bar{P}(i,j-1)]-CODHB(i)] \qquad (3\cdot38) \end{aligned}$$

One can see that on rearranging the Jacobian to the following:-

$$\bar{P}(i,j)=[CONA.\{[(1\cdot0+CODHA(i)).\bar{P}(i+1,j)+(1\cdot0-CODHA(i)).\bar{P}(i-1,j)] +CONB.[(1\cdot0+CODHZ(i,j)).\bar{P}(i,j+1)+(1\cdot0-CODHZ(i,j)) .\bar{P}(i,j-1)]-CODHB(i)\}] \quad (3\cdot39)$$

The equation (3·39) is of the same form as the standard linear form of the Reynold's equation in difference form.

$$\bar{P}(i,j) = A(i,j).\bar{P}(i+1,j)+B(i,j).\bar{P}(i-1,j)+C(i,j).\bar{P}(i,j+1) +D(i,j).\bar{P}(i,j)+E(i,j) \quad (3\cdot40)$$

See Ref. (24)
This equation is the same form as the S.O.R. method and the same as Vogel - Pohl's method used by Siew (23) and Hyett (24), for the oil Journal bearing which is known to converge.

Thus the Jacobian form of the $f'(\bar{P}(i,j))$ is of the same form as the [A] in the S.O.R. Linear method.

If Lieberstein's findings are correct one should obtain convergence therefore as noted in section 3·1·12. Ref. (22) shows the N.L.O.R. method applied to a numerical example.

Using the same boundary conditions as Figure (3·1) and the Q method it was still not possible to obtain convergence after some considerable time and work. The problem remained a puzzle and very disappointing, having proved analytically that Lieberstein's observations were true for this particular condition of the incompressible steady state form of Reynold's equation.

The problem of convergence induced the Author to look very carefully at the fundamental construction to see if one has neglected a fundamental principal. Since Raimondi (13) had had restricted convergence with his analytical and numerical technique for the gas incompressible lubrication problem. However he had to use under-

relaxation and had isolated certain non-linear terms and introduced them into the iteration at a later date to obtain convergence.

This problem forced the Author to investigate and study the fundamental structure of the equations to find a simplified and more rigorous mathematical conclusion to the convergence problem.

Raimondi's work is commented on and observed later on in this chapter and compared with the experimental results for the Plain Gas Bearing in Chapter (5).

3·1·14 FUNDAMENTAL INVESTIGATIONS OF EQUATIONS

From section 3·1·13 the $fn(\bar{P}(i,j))$ can be seen as follows:-

$$fn(\bar{P}(i,j)) = \bar{P}(i,j)^2 - 2\bar{P}(i,j).[CONA.\{[(1+CODHA(i)).\bar{P}(i+1,j) + (1-CODHA(i)).\bar{P}(i-1,j)] + CONB.[(1+CODHZ(i,j)).\bar{P}(i,j+1) + (1-CODHZ(i,j).\bar{P}(i,j-1)] - CODHB(i)\}] - CONA \cdot [\tfrac{1}{2}.[\bar{P}(i-1,j)]^2 + \frac{CONB}{2}\cdot[\bar{P}(i,j+1) - \bar{P}(i,j-1)]^2] + CONA.CODHC(i).[\bar{P}(i+1,j)] = 0 \qquad (3\cdot40)$$

The above is the steady state Reynold's gas bearing equation. It also includes misalignment terms in z.

H is an fn of θ and z, it is the form of

$$f(\bar{P}) = a\bar{P}^2 - b\bar{P} + c = 0 \qquad (3\cdot41)$$

From the above one can see that the values of the constants are at any one iteration as follows:-

$$a = 1\cdot0$$

$$b = 2.[CONA.\{[(1+CODHA(i)).\bar{P}(i+1,j) + (1-CODHA(i)).\bar{P}(i-1,j)] + CONB.[(1+CODHZ(i,j)).\bar{P}(i,j+1) + (1-CODHZ(i,j)).\bar{P}(i,j-1)] - CODHB(i)\}]$$

$$c = -CONA\left[\tfrac{1}{2}\left[\bar{P}(i+1,j)-\bar{P}(i-1,j)\right]^2+\frac{CONA}{2}.\left[\bar{P}(i,j+1)-\bar{P}(i,j-1)\right]^2\right.$$

$$\left.+CONA.CODHC(i).\left[\bar{P}(i+1,j)-\bar{P}(i-1,j)\right]\right.$$

N.B. C contains non-linear terms in:-

$$\left[\bar{P}(i+1,j)-\bar{P}(i-1,j)\right]^2 \propto \left(\frac{\partial\bar{P}}{\partial\theta}\right)^2$$

$$\left[\bar{P}(i,j+1)-\bar{P}(i,j-1)\right]^2 \propto \left(\frac{\partial\bar{P}}{\partial z}\right)^2$$

and $$\left[\bar{P}(i,j+1)-\bar{P}(i,j-1)\right] \propto \left(\frac{\partial\bar{P}}{\partial z}\right)$$

Examining the form of equation (3·41) it is of Quadratic form the roots being solved as below:-

$$\bar{P}_{1,2} = \frac{b}{2} \pm \frac{b}{2}\left[1-\frac{4c}{b^2}\right]^{\frac{1}{2}} \qquad (3\cdot42)$$

Depending upon the discriminant $d = b^2-4ac$, there are three distinct forms of the root pair of the equation.

(i) If $d < 0$, there are two complex conjugate roots

$$\bar{P}_1 = \frac{+\,b\,+\,i\,\sqrt{d}}{2a}\,,\quad \bar{P}_2 = \frac{+\,b\,-\,i\,\sqrt{d}}{2a}$$

i.e. $4c > b^2$

(ii) If $d = 0$ there are two real and equal roots

$$\bar{P}_1 = \bar{P}_2 = +\frac{b}{2}$$

i.e. $4c = b^2$

(iii) If $d > 0$, there are two real unequal roots

$$\bar{P}_1 = \frac{+b+\sqrt{d}}{2a}\,,\quad \bar{P}_2 = \frac{+b-\sqrt{d}}{2a}$$

i.e. $4c < b^2$

One can see that during an iteration scheme all three conditions could avail themselves, depending upon starting condition or point.

However condition (ii) cannot on its own be used to determine the entire pressure distribution since there is an obvious dependence on the non-linear terms contained in c. Also since c is almost always going to be negative we can assume that complex roots will never be manifested, Since square root will be positive.

Therefore determining the roots to condition (iii) will be utilized and we will be searching for the principal root, ie. P_1 not P_2. Since P_2 will also be an alternative answer but not of the highest magnitude or prime root.

3·1·15 BINOMIAL EXPANSION METHOD

If one assumes that the principal root P_1 can be determined as follows:-

$$\overline{P}(i,j) = \frac{b}{2} + \frac{b}{2}\left[1-\frac{4c}{b^2}\right]^{\frac{1}{2}} \qquad (3\cdot42)$$

One can expand the bracketed terms using a Binomial series expansion of the form. Letting $x = 4c/b^2$

$$[1-x]^n = 1 - nx + n\left(\frac{n-1}{2!}\right).x^2 - n(n-1)\ (n-2).x^3 + \ldots\ldots\ldots\ldots$$

$$[1-x]^{\frac{1}{2}} = 1 - \tfrac{1}{2}x + \frac{\tfrac{1}{2}(\tfrac{1}{2}-1).x^2}{2!} - \frac{\tfrac{1}{2}(\tfrac{1}{2}-1)(\tfrac{1}{2}-2).x^3}{3!} + \ldots\ldots\ldots\ldots$$

But under the proviso that $x<1$ or $4c/b^2<1$ or $4c<b^2$ substituting for $x = 4c/b^2$

$$[1-x]^{\frac{1}{2}} = 1 - \tfrac{1}{2}.\left(\frac{4c}{b^2}\right) + \tfrac{1}{2}\left(\frac{\tfrac{1}{2}-1}{2!}\right).\left(\frac{4c}{b^2}\right)^2 - \tfrac{1}{2}\left(\frac{(\tfrac{1}{2}-1)(\tfrac{1}{2}-2)}{3!}\right)$$

$$.\left(\frac{4c}{b^2}\right)^3 + \tfrac{1}{2}\left(\frac{(\tfrac{1}{2}-1)(\tfrac{1}{2}-2)(\tfrac{1}{2}-3)}{4!}\right).\left(\frac{4c}{b^2}\right)^4 - \tfrac{1}{2}\left(\frac{(\tfrac{1}{2}-1)(\tfrac{1}{2}-2)(\tfrac{1}{2}-3)(\tfrac{1}{2}-4)}{5!}\right)\left(\frac{4c}{b^2}\right)^5$$

$$[1 - x]^{\frac{1}{2}} = 1 - \frac{2c}{b^2} - \frac{2c^2}{b^4} - \frac{4c^3}{b^6} - \frac{20c^4}{b^8} - \frac{28c^5}{b^{10}} + \ldots\ldots\ldots\ldots$$

One can see that the expansion is in the form of a Polynomial in

$$\left(\frac{4c}{b^2}\right)$$

Substituting for $[1-\frac{4c}{b^2}]^{\frac{1}{2}}$ back into Equation (3·42) one arrives at the following:-

$$\bar{P}(1,j) = \frac{b}{2} + \frac{b}{2}\left[1 - \frac{2c}{b^2} - \frac{2c^2}{b^4} - \frac{4c^3}{b^6} - \frac{20c^4}{b^8} - \frac{28c^5}{b^{10}} + \ldots\ldots\ldots\ldots\right]$$

$$\bar{P}(1,j) = \frac{b}{2} + \frac{b}{2} - \frac{c}{b} - \frac{c^2}{b^3} - \frac{2c^3}{b^5} - \frac{10c^4}{b^7} - \frac{14c^5}{b^9} + \ldots\ldots\ldots\ldots\ldots$$

$$\bar{P}(1,j) = b\left[1 - \frac{1}{b^1}\left(\frac{c}{b}\right)^1 - \frac{1}{b^2}\left(\frac{c}{b}\right)^2 - \frac{2}{b^3}\left(\frac{c}{b}\right)^3 - \frac{10}{b^4}\left(\frac{c}{b}\right)^4 - \frac{14}{b^5}\left(\frac{c}{b}\right)^5\right] + \ldots\ldots\ldots$$

Truncation error will be used as $\frac{14}{b^5}\left(\frac{c}{b}\right)^5$

Therefore series will be:-

$$\bar{P}(1,j) = b\left[1 - \frac{1}{b^1}\left(\frac{c}{b}\right) - \frac{1}{b^1}\left(\frac{c}{b}\right)^2 - \frac{2}{b^2}\left(\frac{c}{b}\right)^3 - \frac{10}{b^3}\left(\frac{c}{b}\right)^4 - \frac{10}{b^4}\left(\frac{c}{b}\right) \ldots\ldots\right] \quad (3\cdot43)$$

Limiting Values

$c < \frac{b^2}{4}$ is neccessary for convergence.

(1) As $\frac{c}{b} \to \frac{b}{4}$

$$\bar{P}(1,j) \to b\left[1 - \frac{1}{b^1}\cdot\frac{b}{4} - \frac{1}{b^2}\left(\frac{b}{4}\right)^2 - \frac{2}{b^3}\left(\frac{b}{4}\right)^3 - \frac{10}{b^4}\left(\frac{b}{4}\right)^4 \ldots\ldots\right]$$

$$\bar{P}(1,j) \to b\left[1 - \frac{1}{4} - \frac{1}{16} - \frac{2}{64} - \frac{10}{256} \ldots\ldots\right]$$

$$\bar{P}(1,j) \to \frac{158}{256}\,b \to \frac{79}{128}\,b$$

For an Infinite number of terms $\bar{P}(1,j) \to \frac{3}{4}\,b$

(2) As $c/b \to b/4 \to 0$

$$\therefore \bar{P}(1,j) \to b\left[1 - \frac{1}{b^1}(0)^1 - \frac{1}{b^2}(0)^2 - \frac{2}{b^3}(0)^3 - \frac{10}{b^4}(0)^4 \ldots\ldots\right] \quad (3\cdot44)$$

$\bar{P}$ (i, j) → b

∴ One has two limiting values:

(1) For the Truncated series the answer will converge to 79b/128

(2) For a starting value $\bar{P}(i, j)$ → b and the non-linear terms can be initially ignored.

Therefore for convergence the values of $\bar{P}(i, j)$ at each mesh point must lie between b and 79b/128 at that point, for a solution to converge and be guaranteed.

Therefore one can allow the answer to relax between the two limits and helps a considerable amount the convergence problem.

3·1·16 BINOMIAL SERIES, ITERATION AND CONVERGENCE SCHEME

Some series although in themselves normally divergent can be made to converge to a specified answer by applying relaxation techniques. This is ensuring that the iteration scheme satisfies D'Alembert's test.

That is that $\frac{\bar{P}n}{\bar{P}n-1} < 1$ converges $\frac{\bar{P}n}{\bar{P}n-1} > 1$ diverges.

The system of equations of the Hydrodynamic oil bearing are in themselves convergent under the following conditions: P(i, j) < 0 then P(i, j)= 0.

For eccentricity values less than 0·99 and L/D values which are far less than ∞ convergence is guaranteed. The truncation error

$$0\left[\frac{1}{m^2} + \frac{1}{n^2 L/D}\right]$$

is seen to become negligable for values of m & n → large numbers, which also aids convergence.

Vogel Poht Ref. (25) improved iteration and the convergence of the hydrodynamic bearings problem by introducing the $Ph^{3/2}$ method of

which effectively reduces the pressure profile and pressure slopes within the bearing; increasing convergence probability.

Raimondi (13) was the first successful worker to obtain a meaningful solution to the Aerodynamic Plane Journal Bearing. His work included both Adiabatic and Isothermal solutions and relied upon a Polytropic expansion of the pressure field, but has restricted use to values of $\lambda < 4$.

Raimondi's numerical results do not wholly agree with the experimental findings of the Author and to this end various numerical and iteration schemes were investigated. The Author's latest method highlights the non-linearity of the problem, and thus the linear and non-linear terms can be easily seen. The 2nd degree Polynomial in terms of the pressure (non-dimensional) gives rise to a two root solution the principal root being the answer required at each iteration step.

The roots can be easily seen and are the values required at each mesh point in the Finite Difference grid. The main problem is ensuring that the root to the mesh point is valid. The Author's previous iteration schemes have failed to converge and obvious problems have been encountered in arriving at suitable starting values for the iteration scheme without making the techniques unwielding and cumbersome.

If one assumes that the square root in the Root equation can be expanded as a Binomial with the proviso that $4c/b^2 < 1$ a second series can be obtained.

Studying this series one can derive limits of the convergence validity or starting and operating values. One can see that these limits lie between b and 79b/128 for a solution to be valid. The iteration scheme therefore consists of calculating b initially, then iterating a number of times with the non-linear terms being added into the scheme. The Author's approach is different to Raimondi's

since it uncovers more non-linear terms and the Author suggests that the accuracy of the answer is dependent upon the terms added into the iteration loop.

Thus the Author's hope is that by iterating linearly to b (Linear Steady State Equation) at each node point that this is a sufficiently good starting value to use when re-iterating with the non-linear terms until final convergence.

3·1·17 COMPARISON WITH RAIMONDI'S WORK AND CONCLUSION

Raimondi's work Ref. (13) is compared to the Author's theoretical work and will, in Chapter (5) be compared with the Author's experimental findings in greater detail.
Raimondi's derivation of the steady state gas Reynold's equation is shown below:

$$\frac{\partial}{\partial x}\left[\gamma h^3 \frac{\partial P}{\partial x}\right] + \frac{\partial}{\partial z}\left[\gamma h^3 \frac{\partial P}{\partial z}\right] = 6u \frac{\partial(\gamma h)}{\partial x} \qquad (3\cdot45)$$

with the following limiting conditions:

(a) η is constant.

(b) Perfect gas law holds, and gas behaves Polytropically.

(c) No journal misalignment.

Reynold's equation can then be written as:

$$\frac{\partial}{\partial x}\left[(1+\frac{P}{Pa})^{1/k} \frac{h^3}{\eta} \frac{\partial P}{\partial x}\right]+\frac{\partial}{\partial z}\left[(1+\frac{P}{Pa})^{1/k} \frac{h^3}{\eta} \frac{\partial P}{\partial z}\right] = 6u\frac{\partial}{\partial x}\left[(1+\frac{P}{Pa})^{1/k}h\right] \qquad (3\cdot46)$$

Boundary conditions used in the above equation are:

$$P(x, \pm L/2) = 0$$

$$P(0, z) = P(B, z)$$

Equation (3·46) is non-dimensionalized using the following relationships:

$$P = \frac{\eta u R P}{c^2}$$

$$\lambda = \frac{\eta u R}{c^2 Pa} \qquad (3\cdot47)$$

$$h = cH$$

Also $\xi = nx/B, \zeta = mz/L$

Substituting the following relationships into equation (3·46) one arrives at:

$$\frac{\partial}{\partial\xi}\left[(1+\lambda P)^{1/k}H^3\frac{\partial P}{\partial\xi}\right]+\left[\frac{m}{n}\frac{\beta}{2(uD)}\right]^2\cdot\frac{\partial}{\partial\zeta}\left[(1+\lambda P)^{1/k}H^3\frac{\partial P}{\partial\zeta}\right]$$

$$= \frac{6\beta}{n}\cdot\frac{\partial}{\partial\xi}\left[(1+\lambda P)^{1/k}H\right] \qquad (3\cdot48)$$

Non-dimensional Boundary conditions are:

$$P(\zeta, \pm m/2) = 0 \qquad (3\cdot49)$$
$$P(0, \xi) = P(n, \xi)$$

Raimondi further reduced equation (3·48) to make the non-linear terms more apparent before reducing to finite difference form.

Raimondi used the following relationships to reduce the Reynold's equation further:

$$a = \left[\frac{m}{n}\frac{\beta}{2(L/D)}\right]^2 \qquad (3\cdot50)$$

$$b = \left[\frac{6\beta}{n}\right] \qquad (3\cdot51)$$

$$\varphi = (1+\lambda P)^{1/k} \qquad (3\cdot52)$$

The resulting equation being:

$$\frac{\partial}{\partial\xi}\left[H^3\frac{\partial P}{\partial\xi}\right]+a\frac{\partial}{\partial\zeta}\left[H^3\frac{\partial P}{\partial\zeta}\right]-b\frac{\partial H}{\partial\zeta} = -\frac{H^3}{\varphi}\left[\frac{\partial P}{\partial\xi}\cdot\frac{\partial\varphi}{\partial\xi}+a\frac{\partial P}{\partial\zeta}\cdot\frac{\partial\varphi}{\partial\zeta}\right]+\frac{bH}{\varphi}\cdot\frac{\partial\varphi}{\partial\xi} \qquad (3\cdot53)$$

He then expresses derivatives involving P in the non-linear terms by their φ equivalent expressions as below:

$$\frac{\partial P}{\partial\xi} = \frac{k}{\lambda\varphi^{1/k}}\cdot\frac{\partial\varphi}{\partial\xi} \qquad (3\cdot54a)$$

$$\frac{\partial P}{\partial\zeta} = \frac{k}{\lambda\varphi^{1/k}}\cdot\frac{\partial\varphi}{\partial\zeta} \qquad (3\cdot54b)$$

which are obtained by differentiating equation (3·52). Raimondi then lets the R.H.S. of equation (3·53)

$$P = 6\left(\frac{\beta}{n}\right)^2\cdot\varepsilon\cdot H^{-3/2}\cdot u \qquad (3\cdot55)$$

and proceeds as Carter Ref. (26) 1952 and transforms equation (3·53) by differentiation and manipulation to:

$$\frac{\partial^2 u}{\partial \xi^2} + a\frac{\partial^2 u}{\partial \zeta^2} - f(\xi).u + g(\zeta) = -I+J \qquad (3\cdot56)$$

$$\text{where } f(\xi) = \frac{3}{4}.\varepsilon.\left(\frac{\beta}{n}\right)^2\left[\frac{\varepsilon\sin 2\theta}{(1+\varepsilon\cos\theta)^2} - \frac{2\sin\theta}{(1+\varepsilon\cos\theta)}\right] \qquad (3\cdot57)$$

$$g(\xi) = \frac{\sin\theta}{(1+\varepsilon\cos\theta)^{3/2}} \qquad (3\cdot58)$$

Non-linear terms expressed by I and J are given by:

$$I = \frac{k}{6(\beta/n)^2\varepsilon.H^{-3/2}.\lambda.\varphi.\varphi^{1-k}}\left[\left(\frac{\partial\varphi}{\partial\xi}\right)^2 + a\left(\frac{\partial\varphi}{\partial\zeta}\right)^2\right] \qquad (3\cdot59)$$

I and J can be seen to contain the same form of non-linear terms as the Author's theoretical expressions.

Raimondi's Finite Difference Formation is as below:-

$$(u_1+u_2-2u_o) + a(u_3+u_4-2u_o) - f(\xi_o).u_o + g(\xi_o) = (-I+J)_o$$

Where

$$u_o = \frac{(u_1+u_2) + a(u_3+u_4) + g_o}{2(1+a)+f_o} + \frac{(I-J)_o}{2(1+a)+f_o}$$

First term contains linear relationships, second term contains the non-linear terms. Raimondi used linear relaxation techniques in the form of:

$u_k = u_{k-1} + \alpha\,(u_k - u_{k-1})$ where $\alpha < 1$ is the under relaxation factor. For full derivation see Ref. (13).

Raimondi states that he had certain instabilities in his calculations due to the increased contribution of the non-linear terms when using high values of λ, L/D or ε. This had also been reported by Michael Ref. (27). He overcame the problem by either increasing m or using under-relaxation techniques. At large values of λ (>4) he could not obtain convergence, but at small values of λ convergence

was accelerated by not calculating the N.L. terms at each pass through the mesh but at only specified passes. A convergence criterion of 0·0005 was used in his work.

From this statement it is clear that his work is not totally mathematically rigorous over a wide range of bearing operating parameter, (being restricted to a λ value of ≤ 4), since convergence stability was not entirely guaranteed. The Author to this end considered the use of non-linear relaxation techniques, as this method was considered far more mathematically rigorous. It was assumed initially that the non-convergence problem at high values of L/D, ε and λ could be mastered, however as previously mentioned these techniques proved very disappointing.

Raimondi's relaxation method was Quasi-linear, and because of the Author's experience with linear methods used to solve non-linear problems, it's validity is questionable in the light of the new experimental evidence.

However, his approach is analogous to using the first two terms of the Binomial expansion which iterates with one iteration step of the non-linear terms influence (pseudo non-linearity).

This approach may go a long way to explaining why Raimondi's theoretical results do not fully agree with the Author's experimental findings and those of Macfarlane Ref. (15) and the Author's in that, regions of stagnant flow can be detected. See results in Chapter (5).

Further explanation is that Raimondi's results do not fully describe this phenomenon because he has truncated the Author's Binomial expansion to only two terms both linear in terms of the non-linear influences, (B + C/B) and may have reduced the equations validity by his simplifying assumptions and relationships.

The Author's theoretical approach is proposed to try and explain the non-linearity of the flow regions within plain aerodynamic bearings, and to understand why the experimental results which were extremely repeatable vary so differently from the numerical results obtained by Raimondi. It is hoped that future workers could expand upon the thoughts and ideas expressed in this Chapter so that a more consistently, mathematically rigorous, solution can be derived.

CHAPTER 4

SINGLE GAS BEARING TEST RIG

4·1·1 INTRODUCTION AND HISTORY OF THE SINGLE GAS BEARING TEST RIG

In its original state the rig was designed by Pink (28) and later by Leppard (29). Leppard carried out tests on an Aerostatic bearing with four jets but due to shaft seizure only limited results were obtained for Hybrid running conditions.

Hustwick (30) carried out further modifications to the rig but also obtained limited results due to shaft seizure.

MacFarlane (15) completed the building of a new test bearing which included modifications to the surface treatment of shaft and bearing. Good correlation was found with theoretical results, but discrepancies were found with theoretical results. The discrepancies increased as feed pressure increased. Powell's design method was found to over-estimate the Aerodynamic influence of the Hybrid bearing. MacFarlane collected several Aerodynamic pressure profiles in his tests.

Crump (31) carried out work on the same test bearing and studied an additional influence of orifice diameter on bearing performance. Crump showed experimental evidence which indicated variations from theory. He discovered:-

(1) Powell's method over-estimated load carrying capacity at high speeds for Hybrid bearings.

(2) M.T.I. methods over-estimated the radial forces for large radial clearance bearings and under-estimated the forces for small radial clearance bearings.

El Gabari (32) carried out tests on capturing complete Hybrid pressure fields in the bearing. The rig was modified to introduce axial movement of the test bearing and slave bearing leaving the test shaft stationary. Pressure profiles of jet impingements and Aerostatic performance were obtained. Experimental results showed that theory generally under-estimated load carrying capacity in the Aerostatic mode.

Mellamed carried out work on the seizure properties of shaft and bearing material combinations and concluded that for all combinations tried, sulfiniz shaft and bearing treatments produced the best results.

The Author's use of the Test Rig is to ensure accurate data acquisition of the Aerodynamic performance of plain bearings operating over a wide range of conditions for L/D ratios of 1, 1½ and 2.

This Chapter deals with the problems, methods and Calibration results from Aerodynamic operation. The Test Rig is shown in Plate (4·1).

4·2·1 MOTOR CONTROLLER MODIFICATIONS

Initially after the Rig had been dismantled and thoroughly cleaned, it was reassembled to a condition where preliminary tests could be carried out upon it. The drive system consisted of a variable speed D.C. motor and controller. Initially the Rig was run up to speeds in excess of 20,000 Rpm, to ascertain if the system performed adequately. It was found that if the controller Pot, was not returned to its zero position, that, on re-starting the fuse of the controller failed. On another separate occasion when a moderate load was applied to the rotor system the control rectifier failed, and two Zener diodes were replaced.

To overcome these problems, firstly an interlock was devised. It consisted of replacing the V.S. Pot. with a larger unit, whose spindle had a large flat on. This was used as a cam, to actuate a microswitch. The microswitch disabled the start button of the controller if the Pot. had not been returned to its zero position. However, more significantly the problem of fuse failures continued. The fault was eventually traced to accelerating the Rotating Inertia of the Test Shaft and its effective drive components too quickly. The fuse was found to blow at transient currents in excess of 7 amps. An ammeter was connected across the fuse so that the current level could be monitored whilst accelerating to test speeds. Once full test speed was achieved, full load was then applied.

El Gabari had observed this problem during his tests but had not carried out remedial work. It took some time to completely understand and correct these phenomenon, but once corrected the variable speed drive performed very well for extended periods of time during testing and proved very reliable.

4·3·1 SPEED SENSING SYSTEM

The speed sensing system of the Rig originally consisted of a photo-electric pickup which drove an electronic Tachometer, purpose built by Cranfield.

On initial trials of the Rig the system was not found to operate at speeds above 20,000 Rpm. The speed sensor was calibrated via a Stroboscope and it was found that the Test Rig obtained speeds much in excess of of this cut off level. Remedial work was carried out but with no improvement.

A new sensing system was devised. A R.S. photo opto switch with an integial Schimit trigger was decided the best replacement. This required a minimum of 8 volt stabilized power supply, and out-put a square pulse wave linearly proportional to Rotational speed. If a

phase marker was placed on the shaft a single pulse per Rev. was obtained one cycle per revolution.

A six toothed aluminium 7075TE target disc was used and produced very successful results. A feasability study was carried out with a 9V battery but it was decided to devise a 9V stabilized power supply. A frequency to voltage converter chip was also considered so that if required a voltage output proportional to speed could be obtained. If one required a pulsed output this could then also be connected to a frequency counter which read out directly in Rpm/10. Help with the design and construction of the circuit was given by David Hammond, a collegue at the time of this study.

Upon testing of the Unit it was found extremely linear at speeds or frequency inputs of 200,000 Rpm, and gave a maximum output of up to 325mv/KHz full scale, with less than 0·1% deviation full scale. Fig. (4·1) shows the circuit diagram of the Unit and Fig. (4·2) shows the Unit itself. Plate (4·2) shows the Speed Sensor pick up.

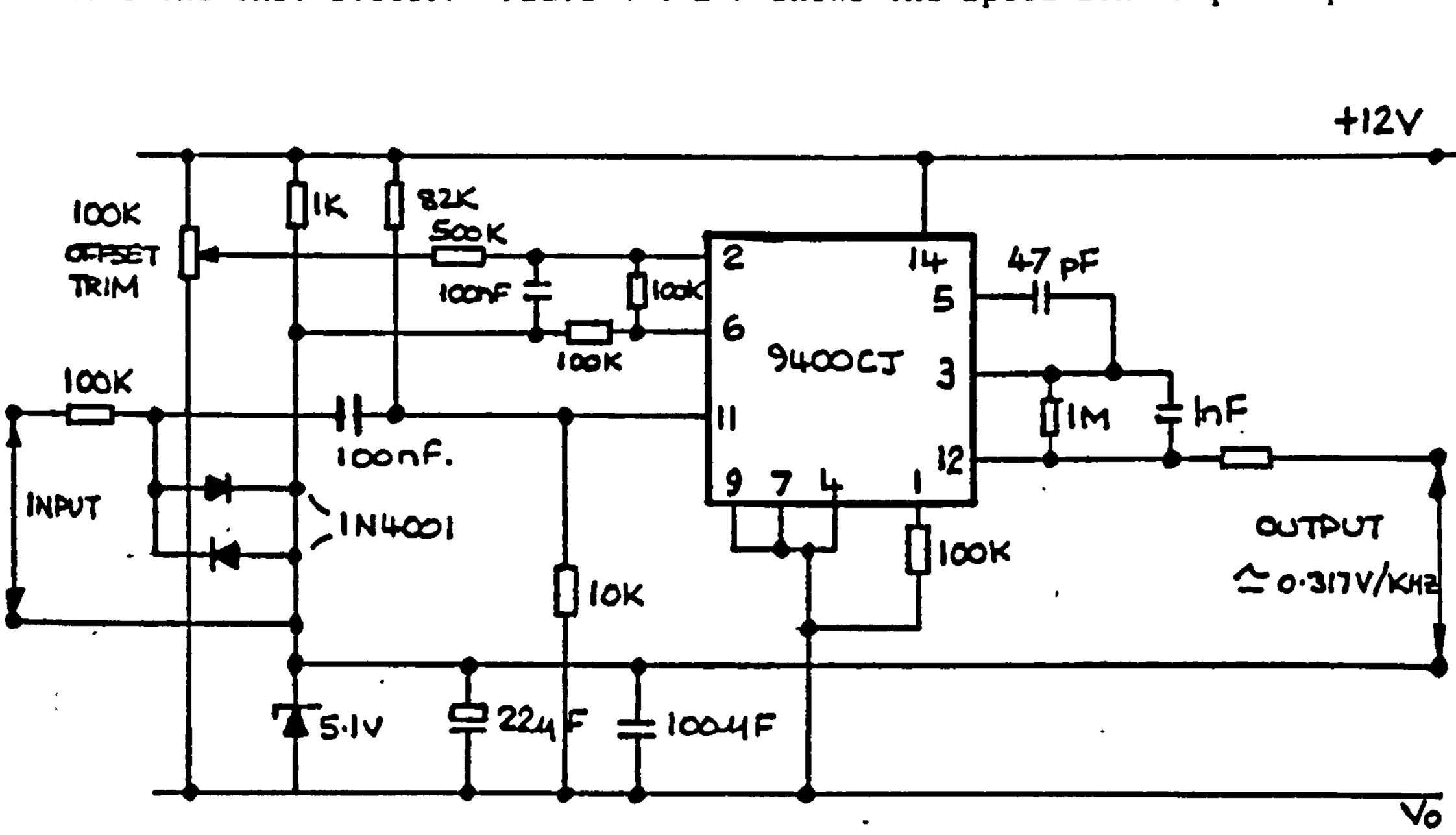

Figure (4·1) Frequency to Voltage Converter Using Proprietory Integrated Circuit Type Teledyne - 9400CJ.

Preliminary Calibration Via Frequency Counter Gain and Pulse Gen.

325 mv/KHz @ 10 KHz 326 mv/KHz @ 2 KHz

319 mv/KHz @ 20 KHz (1·8% down and the limit of linearity).

Linear range 1 - 18 Khz 325 mv/Khz < + 0·5% deviation

corresponding to 1·2 million rev./min = 200,000 Rpm using a disc number of pulses/rev.

giving 6 pulses per revolution.

The slotted opto switch type was energised via a 12 volt max. - 9 volt min. regulated power supply also housed in the same unit as the Frequency to Voltage Converter.

The internal logic of the opto switch (which contained a Schmit trigger) gave a clean square wave form for each pulse recorded, as shown in circuits below.

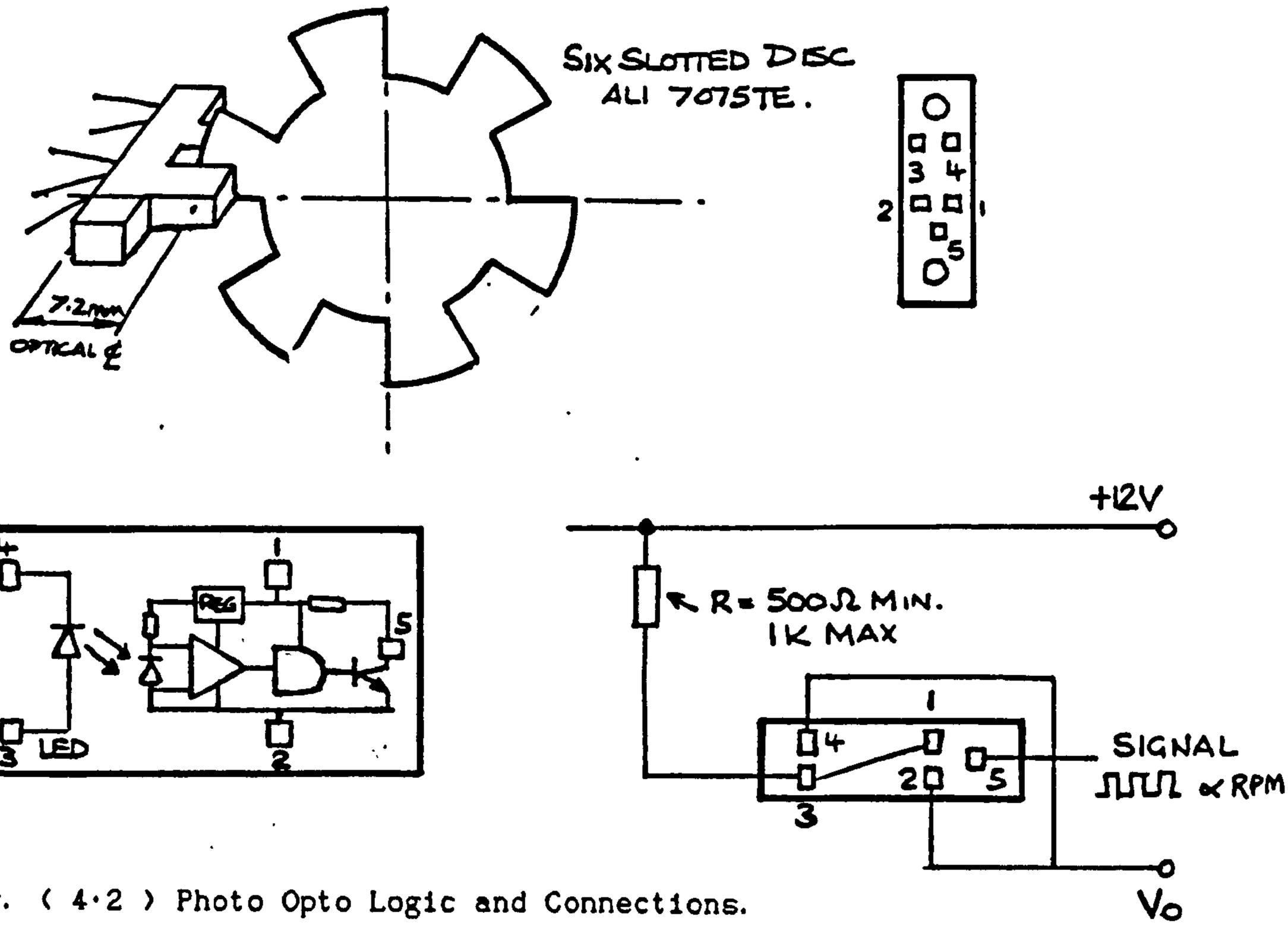

Fig. (4·2) Photo Opto Logic and Connections.

The frequency Sensor system worked very well and ran on the Phase I Rig as well as the preliminary seal tests on the Phase II test Rig. It is very successful and solved the cut off problems. I once again acknowledge the assistance of David Hammond in the advice and help given in the design and construction of the system.

4·4·1 DRIVE COUPLING DESIGN

Problems of connecting two shafts together without inducing either misalignment or translation are well known to shaft manufacturers.

However, for high speed machinery the problem is generally little investigated beyond the limiting burst capacity of shaft and or coupling materials. Before embarking on a coupling design one should immediately ascertain the problem statement which can be summarised below with coupling requirements. In Test Rig Design one must ensure that Tests do not embark away from what is envisaged happening in the real system.

(1) Allow test shaft to translate and misalign without undue restoring forces or moments being induced by the coupling system.

(2) Allow torque to be transmitted from the final layshaft to the Test Shaft.

(3) Operate away from any self resonance.

(4) Easily maintained and allow easy Test Shaft removal.

(5) Be structurally sound and have reasonable fatique life.
(Greater than Test period).

4·4·2 ORIGINAL COUPLING DESIGN

The original coupling design consisted of an aluminium drive adaptor with a female spigot which fitted onto the layshaft and a male spigot

which fitted into the Test Shaft. The female spigot was a sliding fit onto the layshaft and locked via hollow set screws. The male spigot carried a drive dowel of hypodermic stainless steel locked into the test shaft by two opposed screws. Damping of the coupling was obtained in the male spigot via silicon setting material and a silicon rubber sleeve fitted over the hypodermic stainless steel drive dowel.

Initially this set up was quite effective but with time the silicon rubber began to break down and the coupling engendered forcing into the Test shaft (noise began to increase) and results of tests were affected.

4·4·3 'O'-RING SUPPORTED DESIGN

The second coupling design tried consisted of the same coupling shaft but two Viton 'O'-Rings were added to dampen any vibrations and to allow angular misalignment between coupling and the Test shaft.

This coupling improved matters a little but the stainless steel dowels still presented a problem since only two degrees of freedom were present in this design. A moment being applied to the Test Rotor.

4·4·4 QUILL SHAFT COUPLING DESIGN

The final design consisted of a flexible quill system of stainless steel hypodermic, used mainly due to its ease of access. (Berylinium copper may have been better but tube sizes limited and expensive).

A drive plug was attached at both ends of the quill to aid connection into the layshaft and the Test shaft.

Transition fits were chosen so that good runout values could be obtained. The small plug end was connected into the layshaft and locked via a pair of hollow set screws. The large plug connected the quill into the Test shaft and was also locked by two opposed hollow set screws.

The quill was 'Loctited' into the plugs so that fracture of bonded joint would occur at any sign of touchdown thus protecting the Test shaft from excessive damage.

The quill can be seen in Fig. (4·3) below and Plate (4·2). It lasted the full set of tests and proved very reliable.

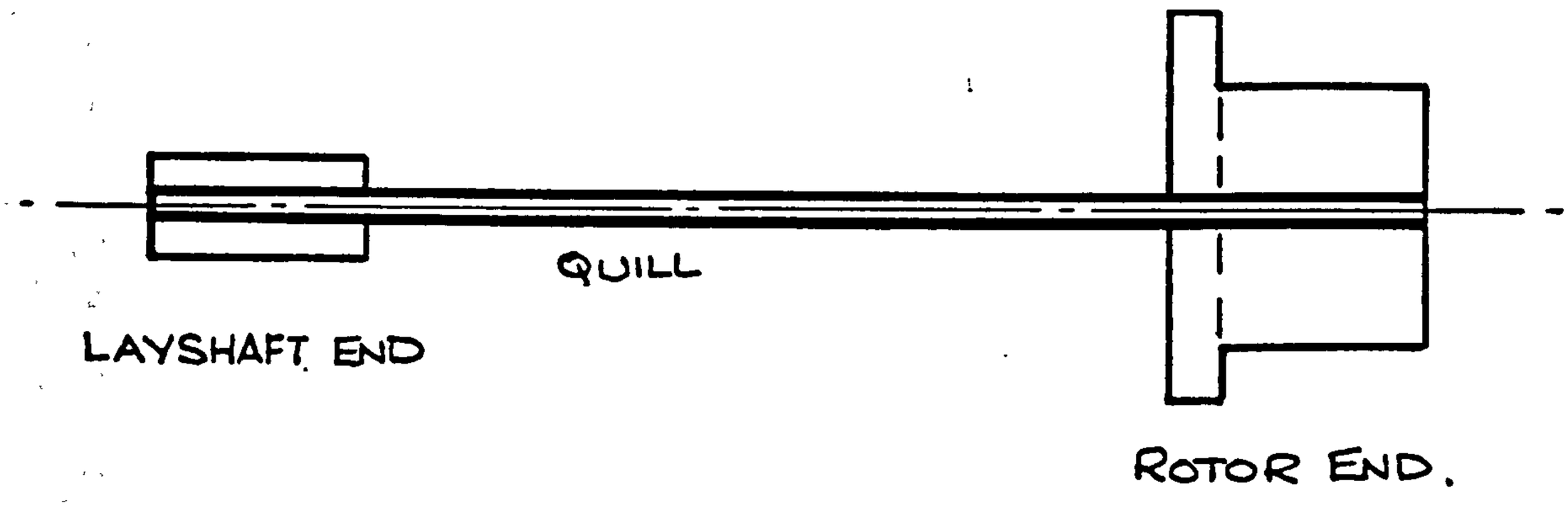

Fig. (4·3) Quill Drive Coupling

Before the implementation of the quill system the layshaft to Test module alignment was tested with a Dial Test indicator and a misalignment of 20 thousanths of an inch was detected. The layshaft housing was re-aligned and dowelled into position. This problem had also happened with the experiments of Al Gabari, found out at a later date.

With dowelling and the quill coupling design, misalignment and movements due to misalignment, were reduced to a minimum and the superior quill arrangement also decoupled the bending moments due to the quill's flexibility. Plate (4·2) shows the quill shaft mounted in the Rig. Fatique life was very high as a great deal of tests were carried out.

4·5·1 HYDROSTATIC LOADING SYSTEM

The original concept of the dished Hydrostatic loading system was devised by Dyer (33) for tests carried out on plain Hydrodynamic bearings. The original design as implemented by Pink (28) and Leppard (29) and used by MacFarlane, Crump and El Gabari suffered from the problem of lack of adjustment in the Pre-tensioning of the Tie bar and Jacking dish. The Author overcame this problem by modifying the Housing Well so that the correct attitude of Dish was obtained and the right Pre-tension put into the Tie Rod Assembly. Fig. (4·4) shows the loading system design and modifications.

To give an extra source of adjustment for alignment purposes, it was thought that a double pocketed spherical dish was required. This with the use of needle control valves enabled fine tuning of the lift so to reduce misalignment to a second order effect. With the aid of the Pre-tensioning nut it was possible to set the capacity of the lift, so that shimming, as used by other workers on the Rig was negated totally. At 3,000 PSI the lift gave full scale readings of the Tie Rod Sensing device of 600 mv+. Plate (4·3) shows the Tiebar Arrangement.

4·6·1 TIE BAR LOAD SENSING DEVICE

The original Tie bar loading sensing cell consisted of a solid brass bar of 6·3 mm (¼") diameter with a full poisson type bridge mounted upon it. See Fig. (4·5a) and Plate (4·3). The initial bar was damaged during the previous workers experiment so it was decided to replace it and at the same time greatly increase the overall sensibility of the system, since Aerodynamic bearings inherently have less load capacity than Aerostatic/Hybrid bearing for same L/D, speed etc. A 3 mm (⅛") diameter hole was bored into the bar making it into a tube in the section adjacent to the gauge fixing position.

Firstly an aluminium bar was constructed but gauge bonding was a problem due to surface layer oxidation and creepage was suspected and results were far from repeatable. A Berylinium copper Tie Rod was finally decided upon, as it has good Hysteresis properties and also good mechanical properties comparable with that of mild steel. The BeCu Tie bar was heat treated after machining to precipatation harden it and prevent creepage. This was carried out at 400°C for one hour and then allowed to cool in the furnace. 350 ohm resistance strain gauges were used in preference to the 120 ohm gauges of the original brass Tie bar, and were arranged in a Full Bridge (Poisson type).

The 350 ohm gauges enable higher excitation voltages to be implemented hence further increasing the sensitivity of the Bridge output.

It was found that upon calibration the Tie bars sensitivity had been increased by many orders of magnitude. The new arrangement gave an output of 158 mv @ 25 Kg Fig. (4·5a) compared to 2·75 mv at 25 Kg full scale of the original Tie bar arrangement.

When finally carrying out tests it was discovered that due to the oil temperature increasing whilst going through the loading system that this affected the zero setting of the Bridge during testing. Also the Tie bar was put on a long term drift test (100 hours) and it was

seen that temperature affected the zero of the Tie bar output voltage quite drastically.

The Tie bar was put into a small oven and thermally cycled up to temperatures of 158 - 159°C. It was found that the voltage output of the Tie bar under no load conditions was approximately 1 mv/°C (ie. for a °C change in temperature). See Fig. (4·6). PTFE leads did improve this effect by 33% See Fig. (4·6).

- Further research found that work had been carried out by Welwyn Strain Measurements of Basingstoke, Strain gauge manufacturers, and also prior to that the effect had first been discovered by Frank Hines (34) in 1960. He also derived an approximate relationship for what was called apparent strain with temperature increase or rise. Due to the Tie Bar's small radius, when using a full Poisson bridge, curvature induced apparent strain is due to the fact that the strain sensitive grid of the gauge is above the surface of the test speciman by the thickness of the gauge backing and the adhesive layer. Flat surfaces are not prone to this phenomenon and with Radii greater than 13 mm (½") this effect becomes negligible.

Welwyn Strain Measurements have carried out extensive work in this area and have derived expressions more accurate than Hines which embodies more gauge backing/adhesive and component material combinations.

One can then estimate, using a graph provided, the apparent strain one would expect to encounter in practice. Comparing results with the gauge backing/adhesive and Tie bar material the Author's results agreed with those of Welwyn Strain Measurements. At first to overcome this effect it was decided to further calibrate for temperature, so that a correction could be made for temperature effects . Therefore a type E thermocouple was bonded adjacent to the gauge bridge so that corrections could be made under testing. This was soon abandoned since temperature drifting occurred due to the oil

temperature in the bath varying during the tests, causing temperature Drift in the Tie bar.

A new alternative was therefore sought which would reduce this temperature/strain effect. The Author therefore decided upon a Proving ring loading cell which had a full bridge which was inherently temperature insensitive. It was also discovered that upon designing and testing that the Proving ring output was almost some 20 times more sensitive than the BeCu plain Tie bar. The proving ring was also made from BeCu 250 and heat treated in the same manner as the BeCu Tie bar. Upon testing it was found that the bridge output was 600 mv for a load of 5·1 Kg and a drift test of 100 hours found that the percentage full scale variation of voltage shift was less than 1·0% which compares very favourably with commercially available transducers. See Fig. (4·7) for drift test results, Fig. (4·5b) and Plate (4·3) shows Tie bar construction and Fig. (4·5c) shows the bridge circuit.

Some tests were carried out with the Tubular Tie bar but the vast majority were carried out with the Proof Ring Tie bar which gave very stable results.

4·7·1 PROXIMITY PROBE SYSTEMS AND EVALUATION

Due to the envisaged high speed operation of the single bearing test rig and the dual bearing rig, a number of proprietary made proximity probes were investigated, prior to the systems final purchase.

Bentley Nevada and Scientific Atlanta type Eddy current probes as used by Preece Ref. (73) proved reliable and produced repeatable results for the purposes of the Modal Analysis of 'O'-Ring and Bearing steel mounting.

Their size and sensitivity however, eliminated them from final selection since the probe was required to fit into the very confined space of the test bearing and also be used with the second test rig

where Bush and Journal relationships were to be studied, a proximity probe whose external diameter was no more than 4 mm was ideally suited. The small size of the probes would enable the test bearing to function without unduly inhibiting the bearing's natural performance characteristics.

After much searching, two systems bearing these attributes were found. One system was that marketed by BIRAL and manufactured by με of Germany, which was an Eddy current system. The second was an Inductance system manufactured by HBM, also of Germany.

The με system was much like the standard Scientific Atlanta or Bentley Nevada systems except it was in a much reduced size, the outside diameter of the probe being 4 mm diameter with a sensing diameter close to 2 mm. με kindly loaned a system including four probes and the driving Amplifiers to the Author, for evaluation. At least eight probes were initially required for the Dual Bearing Test Rig. Fig. (4·8a) shows a sketch of the test arrangement with two probes set at 90° for each slave bearing housing. The units were user friendly and lent to easy calibration, if one also purchased a calibration device.

It was found that it was not possible to DC couple the probes (ref. to 0 DC @ zero displacement). However the matching boards in the Amplifiers allowed easy linearization of the probes and leads. The probes were initially offset 0·05 mm then calibrated as below:-

0·05 mm offset 0 displacement = 0·00 volts DC

0·25 mm displacement = 5·00 volts DC

0·50 mm displacement = 10·00 volts DC

The output of each probe had to be re-adjusted and re-itterated until a minimum error was achieved. The displacement against voltage output was in fact of the form of a lazy S. See Fig. (4·8b).

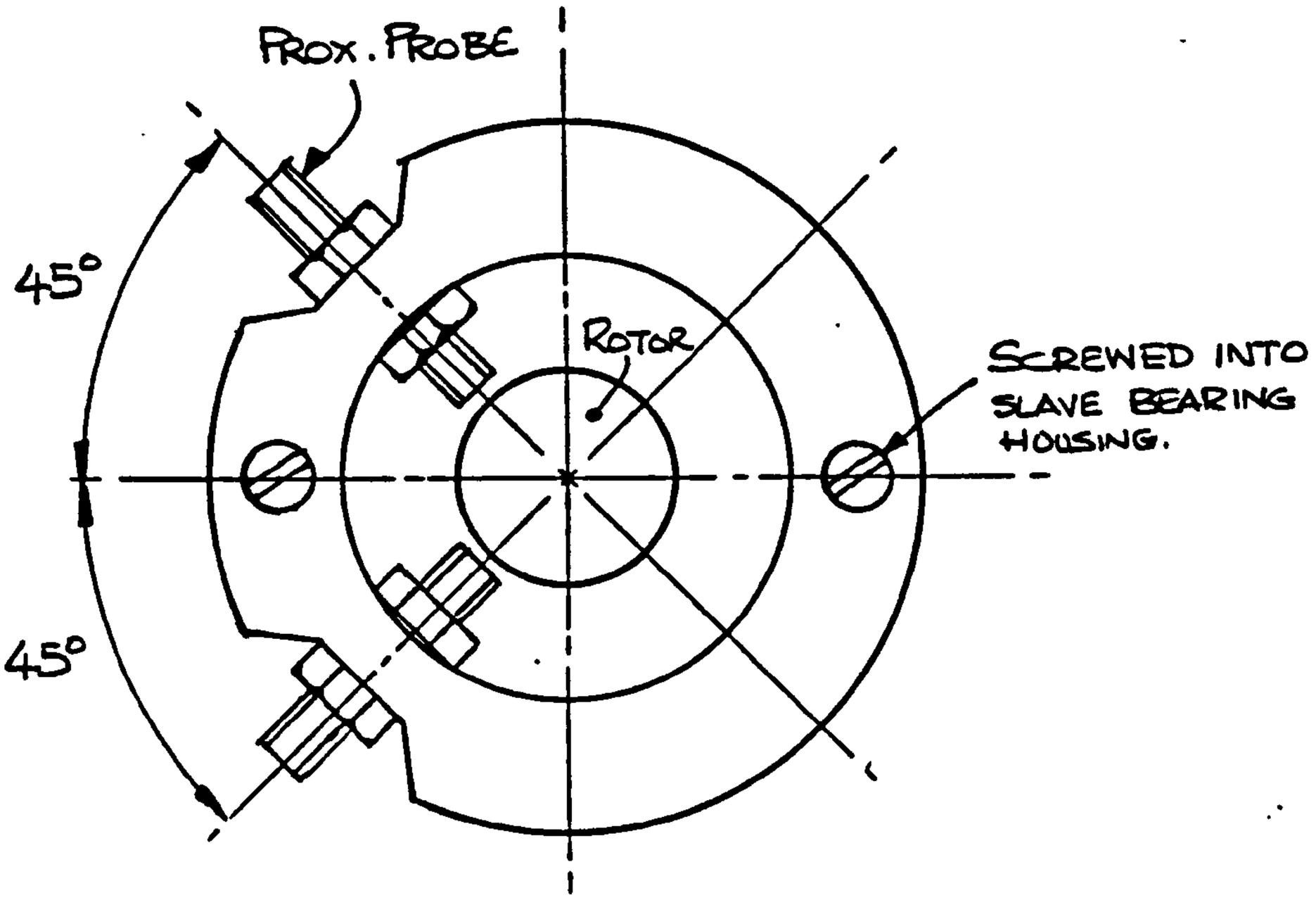

Fig. (4·8a) Mounting Method of με Probes

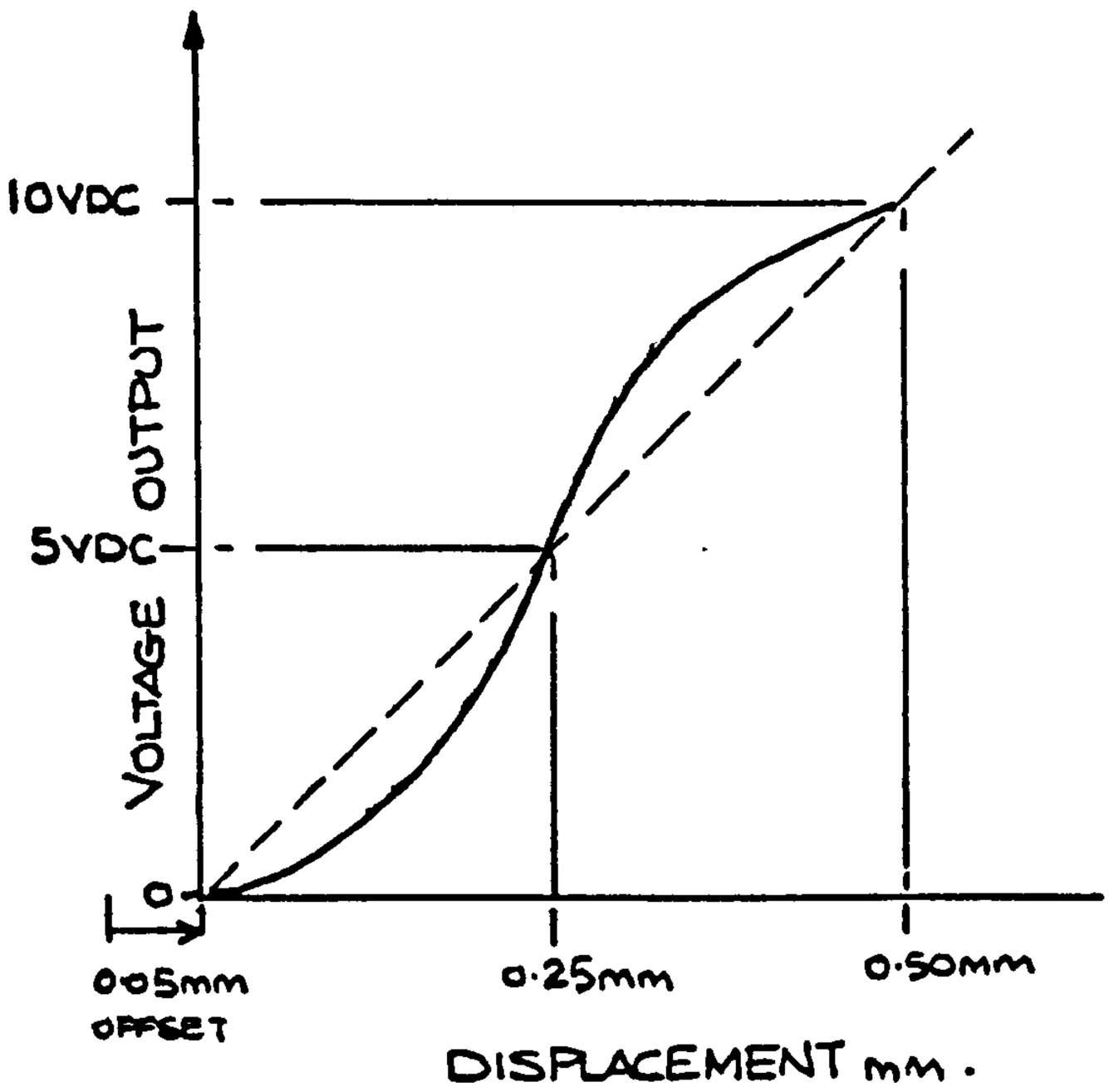

Fig. (4·8b) Calibration Curve με Probes

As previously mentioned the system required an additional Calibration Rig, the one supplied by με could only calibrate against flat plates. με also claim that the target material being calibrated should be identical to that being used in the actual test (material and geometry). Due to calibration against the platten a small error may be present. One advantage of Eddy current probes is that they can be used for non-ferrous materials, but at a reduced sensitivity, and a special board is required for each material to guarantee reasonable linearity. The probes were also calibrated against the anvil of a Depth Micrometer and obtained similar results to the Calibration Rig.

The Lissajous figures of the probes tested can be seen in Fig. (4·9a) to (4·9f). The figure of eight response of the rear probe set corresponded to shaft misalignement. The shaft coupling interface was later measured with a shaft mounted Dial Test indicator and 0·020" misalignement was detected. The layshaft was adjusted and dowelled into position.

The maximum displacement at the front pair of proximity probes corresponds to a displacement of $\frac{0{\cdot}58}{10} \times 0{\cdot}5 = 0{\cdot}029$ mm (0·0012")

this corresponds to a touchdown at approximately 30,000 Rpm, ie. Bearing instability also detected by MacFarlane in his tests.

The output signal of the probes was very noisy and any slight movement of the lead and connectors disturbed the output. Due to the limited period available a long term Drift and Stability Test was unobtained.

THe HBM system comprised a micro-miniature inductance probe 1·5 mm outside diameter which is driven by a 50 KHz Oscillator Amplifier Unit. For each measurement plane, using the HBM system, two probes are required diagonally opposite each other. Thus the output is half an inductance bridge the other half being produced by the instrument. The bridge inductance is made up of capacitance and resistance balancing in the instrument. The output however, is only the average

of the displacement so if one requires the absolute displacement one probe alone must be used with a pre-set gap of a dummy probe being the other ¼ bridge. The system is similar in many ways to the original AE amplifier sets used on the original Test Rig set up by MacFarlane and others.

One major disadvantage with the use of this probe type is that the outside case of the probes constitutes the zero connection. For the tests it was decided to clamp the probe into a brass collet with a lead soldered to the collet. The collet was clamped in a plastic non-conducting housing, one being bolted at each slave bearing position as the με tests. Calibration of the probes was carried out by wrapping PTFE tape round the collet and clamping in a steel ring. The ring had a Micrometer assembly clamped in position which could be adjusted in 0·0001" increments. Two such clamps were required for this test. One clamp set with a static displacement of 0·001", the other probe, being the moving probe had a range of 0·010" to 0·001" displacement calibration. Also a temperature variation test was carried out with the probe set at 0·010" and 0·001" (for 20 hours). Long term drift tests were also carried out (70 hours), and the HBM amplifier system produced marked variations of probe zero output against time.

Lissajous's figures can be seen in Fig. (4·10a) → (4·10c) where the rig ran to speeds of 57,000 Rpm. One can also see that the misalignment problem is much improved. Each pair of probes had been previously calibrated in Germany. HBM suggested an initial offset of 0·25 mm (0·010") and a linear range of 0·1 mm (0·004") be used. Four pairs of probes were supplied by HBM. Two pairs were mounted in each probe housing as previously mentioned. Having carried out the tests with the HBM system, it was decided to test the AE Amplifier Units which also had 50 HKz oscillators and the probes mounted in a ½ bridge configuration. The long term drift tests proved very promising as the temperature/time effect was far less than that produced by the standard HBM Amplifier set up. Plate (4·9) shows Proximity Probe in the Calibration Rig.

Modifications of the AE units were carried out to enable the use of a ½ bridge layout. The probes used on the original bearing tests had a ¼ bridge. Since the resistance and capacitance change of those probes pretty well cancelled each other out, temperature compensation was not required.

Since this last discovery would save the cost of the expensive purchase of the HBM amp units, it was decided to use the ½ bridge configuration set up for the bearing and therefore only purchase the probes.

4·8·1 TEMPERATURE SENSING DEVICES

The original thermocouples were of chrome aluminal type and housed in a Dummy Brass Test Holder. See Fig. (4·11). The original lead had fractured and was replaced with a type "E" which was encased in a ceramic insulated sleeve and fixed and sealed inside the holder with Epoxy Resin, (keeps good bond strength up to 200°C).

The temperature calibration curve can be seen in Fig. (4·13) and suggests good linearity up to 80°C. Fig. (4·12) shows the calibration procedure. Plate (4·8) shows the Dummy Thermocouple Holder Calibration Methods.

An additional thermocouple was fixed midway along the axial length of the bearing to ensure correlation of the assumptions used in gas bearing analysis. That is, it follows closely, an Isothermal process.

The variation of the two thermocouple readings for the tests concludes that indeed isothermal conditions can be safely assumed for a good degree of accuracy. These findings also agree with those of Smalley et Al, Marsh and the theoretical work of Raimondi.

4·9·1 OIL MIST SCAVENGING SYSTEM

The original scheme of things was to allow the oil mist to escape into the confined space of the Laboratory collecting in a scavenging well and contaminating the leather surface drive belt's material. Other than the obvious health hazard, the oil mist also degraded the drive system's performance as slipping took place between the belt and pulley tractive interface. The labyrinth sealing system did not adequately seal the oil mist (vapour) and this was found to be the major contribution to the slipping phenomenon. Chapter (8) describes fully the modifications carried out to the Phase II Rig but the alterations were not carried out on the Phase I Rig, since this effect was drastically reduced when the output of the inner chamber was taken through a baffle system. These alterations were successful such that slipping was reduced considerably and consistent results obtainable.

4·10·1 DRIVE BELT PROBLEMS

The original drive belt system was designed by Pink (28) in conjunction with Engineers of the Stephens' Belting Company. The 3,000 Rpm (max) motor output drove through a 20: 1 speed increasing double pulley ratio giving theoretically a maximum output layshaft spindle speed of 60,000 Rpm.

Work by others, MacFarlane and El Gabari claim that this performance was never obtainable in their work. The reason why the limiting speed was in the region of 35,000 → 40,000 Rpm was due to the final pulley being only 12·7 mm in diameter and slave bearing restrictions. When the belt was pretensioned to 2½% of the belt length, as recommended by the manufacturer, due to the small radius of the pulley, a permanent set was generated in the belt and led to premature fatigue failure of the Polymid outer layer.

A superior belt type, Extremulus, was investigated and used in the tests as it was better suited to high speed operation (up to 200 m/s)

over the leather/polymid belt material. The new belt type was also incorporated into the Phase II Rig where pulleys of the Manufacturers minimum diameter were utilised. The new belts ran at speeds in excess of 50,000 Rpm on the Phase II Rig on a 38 mm minimum diameter pulley.

4·11·1 SHAFT MODIFICATIONS

To enable variable L/D Ratios testing to be carried out it was at first suggested that different L/D Ratio test bearings be used, but further investigation showed that not only would this be a costly excercise, but also lead to complications regarding sealing methods and compatibility of recorded results. To this end it was decided to vary the L/D Ratio on the shaft. This was a far simpler method but had the limitation of reduced mapping sensitivity of pressure field with reduced L/D Ratio. It is however far easier to control shaft diameter than bore diameter. Plate (4·4 and 4·5) shows the test shafts.

Excellent repeatable results were obtained which proved the technique to be successful.

4·12·1 FLOW VISUALISATION TESTS

It was decided that a suitable method of recording flow patterns would prove extremely useful, especially if this technique allowed the study of Flow patterns and Boundary condition build up within a plain Air bearing.

An apparatus which had been used by previous workers was modified and incorporated into the Rig prior to Pressure Profile testing.

The apparatus comprised of a fluidised bed of dust particles which were contained in a perspex tank, mounted on a spring steel leaf spring. A small electric motor 240 V AC was also mounted on the underside of the perspex tank and had an eccentric mass, which

ensured that the dust particles were shaken free from collecting electrostatically to the sides of the tank.

Air was passed through the dust and an outlet pipe in the roof of the tank enabled the dust particles to pass along pipes and enter the Clear Flow Plastic Bearing. The bearing was loaded moderately such that the bearing would operate at a slight eccentricity ratio. The bearing had a circumferential groove either end of it which enabled the dust to penetrate the bearing. The "perspex" bearing had an L/D of 1·0.

From the tests carried out it was possible to see the dust particle movement through the bearing but the bearing was prone to instability, due to low loading and had a prepensity to wipe easily and the tests were eventually abandoned due to this phenomenon.

4·13·1 SCANNING VALVE AND BEARING OBSERVATIONS

The test bearing was found in remarkably good condition and as such was used for the Aerodynamic tests. It was however, reconditioned, which involved dismantling, cleaning and rebuilding with replacement parts where required. Plate (4·6) shows the Test Bearing and Pitot Tappings.

The inductance proximity probes were replaced with HBM type as already mentioned and new thermocouples were installed. Fittings of the pitot tappings were replaced and the sealing of the tubes were checked for leakage by placing the shaft in the bearing and pressurizing the bearing Aerostatically. Each reading of the scanning valve was then checked to ensure that the tappings were reading correctly at each tapping point. Plate (4·7) shows the Scanning Valve and Pressure Transducer.

The scanning valve was also reconditioned by replacing all 'O' Ring seals and refitting all new pitot tubing. "Helleman Oil" was used as the lubricant for the 'O' Rings and proved very successful. It

was found that occasionally touchdown debris did however, sometimes block a jet and if an occurence manifested itself the bearing was re-tested and unblocked upon each occasion. This was thankfully a rare occurrence.

The existing Pressure Transducer, as used by MacFarlane, Leppard and others was still in very good condition and gave excellent trouble free service.

Fig. (4·7) shows the Scanning Valve Arrangement.

4·14·1 CALIBRATION OF SINGLE GAS BEARING TEST RIG

The following describes the methods used to calibrate the major components of the Test Rig.

4·14·2 SCANNING VALVE

The scanning valve comprised two main components:-

(i) The Bottom plate - which contained 84 + Pressure Tappings.

(ii) The Top plate - which housed the Pressure Transducer.

Fig. (4·14) outlines the principle of the scanning valve. The pressure tapping tubes were secured to the valve with Epoxy Resin and were checked for leakage at the beginning of each bearing test. The number of each tapping position on the valve coincided with the number of the tapping position on the test bearing. 'O' Ring seals located in counter bored holes at each tapping point in the valve were lubricated to enable easy movement of the top plate from one tapping position to the next. Locking the handnut ensured that the tapping did not leak. The 'O' Ring lubricant used was a cable sleeve lubricant and proved very reliable. Plate (4·7) shows Transducer in the Scanning Valve. Fig. (4·5c) shows the Strain Gauge Bridge Circuit of the Transducer.

4·14·3 PRESSURE TRANSDUCER

The pressure transducer located as Fig. (4·14) in the valves top plate was a Bell and Howell type. The pressure range being 0 - 50 psi, 10 VDC excitation and 5 KHz resonant frequency of the diaphragm. The transducer was traversed to each tapping point, by revolving the top plate of the scanning valve, to ascertain each tapping pressure during each set of Bearing Tests (94 in total).

Prior to fitting into the scanning valve the pressure transducer was calibrated to obtain a relationship between Voltage output and operating pressure.

The calibration was carried out by the use of a Mercury Mamometer (0 - 20 psi) in 1 psi steps and also a Buden Berge Deadweight tester (10 - 50 psi) in 5 psi steps.

The transducer was energised via a 10 VDC stabilizer power supply which also amplified the output signal of the transducer (approximately 100 x). The signal was recorded via a Fluke D. V. M. Test procedure was repeated for decreasing pressure and was carried out three times to ensure repeatability of results.

Fig. (4·15) shows the calibration graph.

A long term (100 hour) zero drift test was recorded. The output of the transducer under zero (atmospheric) pressure was recorded against time. Fig. (4·16) shows maximum deviation, as a percentage of full scale readings.

4·14·4 TIEBAR (POISSON BRIDGE) CALIBRATION

The Tiebar loading arrangement as used by MacFarlane, Pink and Leppard gave unreliable results. As previously discussed, Section (4·6·1), the tiebar was bored out, see Fig. (4·5a), to the form of a tube to increase output response but due to curvature effects of the strain gauges bonded to the tiebar, the zero position was affected by temperature rise.

An apparent strain equivalent to 1 mv/°C made the load sensing procedure unreliable. Temperature calibrations were carried out such that at any operating temperature the bridge output could be corrected for this effect. Fig. (4·6) shows a calibration graph for temperature against apparent strain (mv). Fig. (4·17) shows the tiebar response to load. The calibration procedures were as the

Proof Ring type Tiebar. See Fig. (4·18). Due to this unpredictability the Poisson Tiebar was abandoned and a new type sought.

4·14·5 TIEBAR (PROOF RING) CALIBRATION

After the unpredictable results due to tiebar curvature effects a new design of tiebar was sought. A Proof Ring system was decided on, and devised. Fig. (4·19) shows this type of Tiebar construction. The central BeCu ring carries a full (bending) strain gauge bridge. The bridge circuit is shown in Fig. (4·5c). The bridge circuit was excited via a DC amplifier/power supply designed by the Instrumentation Department at Cranfield.

Fig. (4·18) shows the calibration arrangement. The output of the bridge was amplified and recorded on a Fluke D.V.M.

The calibration curves of load against Tiebar bridge output voltage can be seen in Fig. (4·20) for loads up to 5 Kg giving a maximum reading of 600 mv output. As mentioned in Section (4·6·1) this bridge circuit output is over 20 times more sensitive than the Poisson type Tiebar.

A 35 hour drift test of the system was carried out and the maximum % full scale variation was less than 1%. This rivals commercially available load cells.

4·14·6 SPEED SENSING CALIBRATION

The calibration of the speed sensing system on the Rig, consisted of marking the output shaft and comparing the accuracy of the stroboscope readings against those of the speed counting device. Table (4·3) shows the results of the calibration and the maximum percentage errors recorded, see S.M.E. Report TR/90/7.

The speed sensing system had already been Bench checked electronically so this calibration was more or less testing the accuracy of the stroboscope. The maximum % error in readings was 2·42% but this can be put down to error in reading the dial of the stroboscope rather than the error in the speed sensing device.

4·14·7 THERMOCOUPLE CALIBRATION

A type 'E' thermocouple was mounted in one of the Dummy jet holders. This holder was calibrated to ensure that the fixing of the device in the holder did not adversely affect the thermocouples performance.

Two calibration methods were carried out:-

(1) Oil bath (temperature up to 100 °C)

(2) Hot air oven (temperature up to 150°C)

Table (4·2) Ref. S.M.E. Report TR/90/7, compares the voltage output of the thermocouple in the oil bath and oven. One can see that an almost constant variation of 5% was recorded between the oil bath heating and oven heating cycles. The bearings heating environment was to be air so oil bath temperature outputs were neglected. The variation was assumed to be due to phase lag in heating cycle or variations in datum thermocouple positioning. Plate (4·8) shows the Calibration Apparatus.

4·14·8 PROXIMITY PROBE CALIBRATION

Two types of Inductance proximity probes were used in the single gas bearing tests:-

(1) AEI Inductance probes (temperature compensated)

(2) HBM Inductance probes (TR 1·5)

Both probes were however excited via a 50 KHz carrier frequency.

Two calibration procedures were carried out. The first method as used by MacFarlane and others proved to be unreliable and produced unrepeatability so this method was abandoned, see Ref. (15). To this end an alternative method of probe calibration was devised. Figs. (4·21) and (4·22) and Plate (4·9) indicate the calibration techniques. One drawback of this method over the former is that probes are calibrated outside the test bearing. Very repeatable results were obtained so this limitation was thought negligible. Initially it was decided that any eccentricity or 'run out' due to the micrometers rotation should be investigated, to ensure repeatability of calibration results.

An Inductance probe was therefore mounted in a steel ring and fixed in position. A micrometer was then positioned directly opposite and adjusted to give calibration curves of comparison to the probe calibration rig. Variation can be seen to be minimal. The effects of the micrometer run out due to rotation was therefore assumed negligible.

The Inductive probe circuit consisted of a Cranfield built 50 KHz Amplifier set. The inductance probe formed (in an anologous manner to a strain gauge) a ¼ of a bridge circuit, the internals of the amplifiers were modified such that a ½ bridge circuit could be used for the Dual Bearing Rig. The inductance circuit is produced by resistance and capacitance components. The resistance forming the real component and the capacitance forming the imaginary or quadrature component. The proximity probes were balanced by adjustments to resistance, capacitance and phase angle. Fig. (4·23) shows a well balanced signal output of bridge and demodulator output at (1) zero displacement, (2) bellow zero displacement and (3) above zero displacement. Plate (4·1) shows the AE Amplifiers and other Data Aquisition Instrumentation.

It was found that for some inductance probes calibrated that a false zero position could be obtained. However this can be discovered when displacing the probe to its full range, the resulting demodulator signal becomes saturated and response no longer is at its optimum ie. signals are not amplified as calibrated. It is important to note that this effect cannot be discovered by observing the amplifier output, one must observe the Demodulator and Bridge outputs. If calibration is not carried out to reasonable pains response will fall with time. One may not observe this and results will become meaningless.

Figs. (4·24) → (4·28) are calibration curves to enable the location of most linear and highest sloped section response of graph. Once this had been obtained fine calibrations were carried out in 0·0002" steps, see Tables (4·5) → (4·11), S.M.E. Report TR/90/7.

Altogether nine proximity probes were used in the Single Bearing Tests, two AEI and seven HBM. Some were rendered unserviceable due to bearing touchdowns, others were rendered unreliable due to the fixing methods of their connecting leads. The first tests of the bearing were carried out with AEI probes but No.2 probe began to give unreliable/unrepeatable results and could not hold its balance. The bearing probes were therefore replaced with HBM probes but the probe holder was modified, see Fig. (4·29) to accept this type of probe.

The earth or zero side of the HBM probe was through the probe's outer case, see Fig. (4·30). Discussions with HBM suggested that silver loaded epoxy would enable a positive connection between case and earth lead , since the probe was not to go beyond 100°C due to its construction. This method required curing the probe and holder in an oven for 20 hours at 100°C. Tests before and after curing suggested that only an increase of 2-3 ohms resistance was incured. However bearing tests revealed that after some time the probes moved in the adhesive and resistance gradually increased tending ⇒ ∞ and balance could not be held.

The Author decided to 'Loctite' the probe in its holder and solder the connection between the lead and the probe outer casing and holder and lead. Only one probe was damaged. Phosphoric acid was used to etch the stainless steel holder and casing and the problem thereon afterwards resolved itself. Fig. (4·31) shows the Inductance Transducer Schematic Test Circuit Diagram.

Calibration curve fits for all nine inductance probes can be seen in Tables (4·5) → (4·13), S.M.E. Report TR/90/7. Due to slight temperature effects since operating as a ¼ bridge, (HBM recommend as ½ bridge circuits), each bearing test involved taking a temperature/probe voltage curve fit so that the calibration temperature datum and hence displacement could be extrapolated. Figs. (4·32) → (4·43), S.M.E. Report TR/90/7, show the curves of some of the tests. Graphs were not plotted for each test but curve fit regression was carried out which proved successful. See Tables (4·14) → (4·100) for results, S.M.E. Report TR/90/7. Table (4·77a) and (4·77b) show the Eccentricity and Phase Angle Calculation Procedure for L/D = 1·0 (Test 71).

CHAPTER 5

EXPERIMENTAL RESULTS OF SINGLE BEARING RIG

5·1·1 EXPERIMENTAL STUDY OF PLAIN AIR JOURNAL BEARINGS

The first aim of this study was to investigate in greater detail the effects of variations in, load, speed and L/D ratio, and thereby ascertain their influence upon boundary conditions, pressure profile, temperature, compressibility number and bearing operating parameters.

Work carried out by MacFarlane and others, (18), whilst investigating hybrid bearings highlighted a trend in Aerodynamic bearings that were not wholly explained by Raimondi's (13) numerical analysis technique. Certain areas of stagnant flow were found that are symmetrical and occur on L/D ratios from 1 → 1½ → 2, and are not to be an effect of bearing test rig manifestation.

To this end the Author also investigated the theoretical influence and his findings are seen in Chapter (3).

Many previous workers in this area of experimentation have not investigated whole bearing pressure maps and have restricted themselves to central pressure profile mapping. See Chapter (3).

Therefore when Raimondi proposed his theoretical examination, this stagnated flow phenomena had not at the time been observed. His experimental varification was therefore restricted to L/D ratios of)

2. Pressure mappings being restricted to the circumferential central pressure profile. It is further noted that Cole and Kerr (7) found that assuming a parabolic axial pressure distribution, resulted in a lower load carrying capacity than recorded in their experimental work.

The second aim of this study was to verify the pressure profile at the onset of Instability, and the limitations of Steady State Bearing operation. This will be examined in the Dynamic Studies. The pressure profile was captured at speeds upto 40,000 Rpm where temperature increased in the bearing considerably and this is thought as the onset of Instability. This will be discussed in greater detail in Chapter (11). Temperature recording was a good indication of the friction produced in the bearing, and the onset of touchdown both at high speeds with low loading and at low speeds with high loading. Thus the study has highlighted a band of true Aerodynamic operation and obviously the limitations of assuming full Aerodynamic operation without consideration on one hand, low speed high load touchdown and high speed low load touchdown. The first consideration is one of a Boundary/Mixed Lubrication problem, the second consideration is that of Dynamic Instability.

Both conditions can be avoided if limiting factors are put upon load carrying capacity. For low speeds the limitation must be one of maximum applied load, at high speeds it must be of minimum applied load.

Obviously more work is required in this area, but from a Designer's point of view this area of thought must be further expanded. To this end Fig. (5·1) indicates the safe region of operation. Fig. (5·1) are curves of the slope of safe Aerodynamic operation for L/D ratios of 1, 1½, & 2. This Figure shows that the curves are ∝ to Instability or Safe operational speed N′. The curves indicate that increased specific load Pnom increases this condition until an asymptote is arrived at. Thus Fig. (5·1) shows the stable region of operation and the onset of Instability for this Bearing arrangement. This type of curve closely agrees with findings of Powell (103).

More results would be able to extend the curves to the right of the Figure. It is therefore obvious more work is still required to fully understand Aerodynamic phenomenon.

5·2·1 ECCENTRICITY RATIO AND ATTITUDE ANGLE

Eccentricity ratio and Attitude angle were determined experimentally from relative bearing to journal displacements in the horizontal and vertical directions.

Since eccentricity ratio and attitude angle cannot be directly measured and reliance has to be made upon the accuracy of the horizontal and vertical Displacements measured in the bearing. The accuracy of the eccentricity ratio and attitude angle are totally dependent upon the accuracy of measurements recorded and their translations from probe output voltage to physical displacements.

The translation of voltage to displacement is related from calibration curve fits. Calibration curves were carried out for each probe used in the Tests. When using the HBM proximity probes Tables (4·5) → (4·11), S.M.E. Report TR/90/7, slight temperature effects caused a requirement for a curve fit of Temperature/Probe voltage for each bearing test. This temperature curve fit was then extrapolated back to obtain a voltage output at the Calibration curve fit datum temperature.

Having obtained the probe displacement measurements in the horizontal and vertical directions, eccentricity ratio and attitude angle can be dertermined by the relationships in Equation (1), Equation (2) of Fig. (5·2) and Fig. (5·3).

Two relationships exist, one for clockwise rotation and one for anti-clockwise rotation of the Journal. All the bearing tests were carried out with the Journal rotating in the anti-clockwise direction.

Probe displacements in the horizontal and vertical directions were recorded as δx and δy respectively. However the x and y components of the bearing eccentricity e are determined as follows for anti-clockwise rotation. See Fig. (5·3).

$\Delta x = C - \delta x$ Where C = Bearing radial clearance.

$\Delta y = C - \delta y$

$e \cong (\Delta x^2 + \Delta y^2)^{1/2}$

Hence $\varepsilon_o \cong \frac{e}{C} \cong \frac{1}{C} (\Delta x^2 + \Delta y^2)^{1/2} = \frac{1}{C} [(C - \delta x)^2 + (C - \delta y)^2]^{1/2}$

And Attitude angle can be found from:-

$$\varphi_o = \text{Tan}^{-1} \left(\frac{\Delta x}{\Delta y}\right) = \text{Tan}^{-1} \left(\frac{C - \delta x}{C - \delta y}\right)$$

Tables (5·1) → (5·4) show the Eccentricity Ratio and Attitude angle calculations for all bearing tests. The results accuracy are largely dependent upon the accuracy and stability of the proximity probe output. ε_o and φ_o tend to follow the expected trends, that is for a fixed load and variation in speed one would expect to see a reduction in eccentricity ratio and an increase in attitude angle. This can be seen from Tables (5·1) → (5·4) to be largely the case but in some instances eccentricity ratio has increased along with an increase or decrease in attitude angle. This is mainly due to one of the components Δx or Δy being inaccurate. Since although the trend in eccentricity ratio may be correct, attitude angle is more sensitive to inaccuracies in positional measurement. One can also see that for tests 22 → 27 that instability has taken place since eccentricity has increased and phase angle sign has changed, after running through its onset. Since whirling is taking place during this instance results would therefore be unpredictable, since operating far away from steady state conditions.

One can therefore conclude that overall the trends of eccentricity and attitude angle are as one would expect but the absolute values are less accurate than anticipated. Accuracy of results could be improved by employing a proximity probe system less sensitive to temperature rise or by mounting them outside the bearing.

Eccentricity results overall are slightly disappointing, due to the care and time taken to calibrate the system. This leads one to believe that attitude angle and eccentricity ratio are probably the least easiest parameters to record accurately.

5·3·1 TEMPERATURE VISCOSITY EFFECTS

The temperature distribution in an Aerodynamic bearing has been found experimentally by Whitley and Betts, to closely follow the Isothermal process. During bearing tests with thermocouples positioned at opposite ends of the bearing only a variation of one to two degrees were observed. Due to this observation Air Viscosity was calculated from, the Absolute bearing temperature recorded and its temperature viscosity relationships, based upon air being at atmospheric pressure. The assumption is valid since the pressure viscosity effect of air does not become marked until pressures exceed 100 psi.

For all the tests carried out the maximum pressure recorded was approximately one third this figure hence the pressure viscosity effect was assumed negligible, and viscosity assumed a function of temperature only.

The results of Figs. (5·4) → (5·7) show curves of constant nominal specific pressure. Whilst Absolute temperature increase is plotted against bearing parameter $\eta N^1/P$. The curves are plotted to indicate the types of regime of bearing operation. It is thought that temperature/viscosity increase is a good indication of friction losses in the bearing, Viscosity $\propto$ Friction.

The type of Lubrication regime for any fixed L/D ratio is dependent upon journal speed and applied load. However a further function R/C ratio also shows signs of being a particular parameter which effects bearing performance, in particular bearing temperature rise for any fixed load rate.

5·3·2 TEMPERATURE/VISCOSITY OBSERVATIONS

For the L/D ratio of 2, two sets of tests were carried out. The first set 1 - 21 being for the Poisson Tiebar load cell and the second set 22 - 48 being for the Proof Ring Tiebar load cell. Figure (5·4) curves refer to test results 1 - 21 and Figure (5·5) refer to tests 22 - 46.

Referring to Fig. (5·4) it can be seen that for any given constant load temperature increases linearly with increase in speed until a non-linear region is manifested. The linear region of the curves indicates Aerodynamic lubrication the third stage of the classical lubrication regimes. The non-linear regime on the right hand side of the curves will be discussed in greater detail later. It can however be seen that with increase in specific load or pressure that the slope of the curves increases, that is the rate of change of temperature increases, with increase in specific load.

The curve of Pnom = 3·25 indicates that only two points were plotted, the reason being that if one refers to Plate (4·4) shaft one can be seen to have a considerable amount of surface scuffing caused by touchdown damage. This damage occured in tests 1-19 at high speed operation, at speeds > 30000 Rpm. This can be seen on Fig. (5·4) as the point at which the curves depart from a linear to a non-linear temperature/speed relationship. This non-linear effect however sees a marked reduction when specific pressure is increased.

The three classical regimes of lubrication can be observed clearly in Fig. (5·5). For the specific load of 2·05, the non-linear effects of tests 1 - 21 are seen quite clearly. On this particular curve can be seen two further regions of lubrication not normally associated with steady state bearing behaviour. For speeds up to 15000 Rpm the curve is linear, beyond this however up to 25000 Rpm the region as observed in Fig. (5·4) non-linear. This region is parabolic in nature. Beyond 25000 tending to 30000 Rpm the temperature gradient is again seen to be linear. What could explain this? One train of

thought is that, at 15000 Rpm with a low specific pressure 2·05 lbf/in^2 the instability threshold is reached, whereby the temperature rise is no longer linear. Since temperature viscosity effects are linear, and steady pressures monitored are no where greater than one third of the pressure viscosity effect, the non-linearity is thought due to a non-linear Force increase.

Unbalance Force effects are non-linear $m\omega^2C\varepsilon$. C(e) in this case is increasing beyond the onset of Instability with increasing Angular velocity. The constant gradient above 25000 Rpm is likely manifest by bearing and journal metallic asperity contact. Since surface velocity increase is linear this would correspond to a dynamic Friction coefficient. This gradient is approximately equal but of opposite sign to the boundary lubrication gradient.

If one refers to the Eccentricity ratio values calculated in Table (5·2) test 22 - 27, that at 15000 Rpm the eccentricity value has increased and phase angle sign has changed, consistant with having run through a critical speed. This effect is not detectable from the results of curves plotted of load ratio against compressibility number for various Eccentricity ratios, see Fig. (5·9 ⇒ 5·11), from Raimondi's theoretical work. Comparing the surface finish of shaft 2 for tests 22 - 46 surface scuffing can be seen. Referring again to Fig. (5·5) the curve of Pnom = 6·74 one observes that at 30100 Rpm the non-linear temperature rise is again manifested.

One can also observe that increasing the specific pressure increases the instability threshold. This has also been observed by other workers. Increasing diameter to clearance ratio increases the temperature rise gradient at lower specific pressures but decreases the gradients at higher specific pressures.

The curves plotted for L/D ratio of 1·5, tests 47 - 70 were carried out on shaft number 4. The three classical regimes of lubrication, boundary, mixed and fully Aerodynamic can be seen clearly. As the results of tests 1 - 48, when Pnom was increased the temperature rise

gradient increased. Due to damage incurred in the previous tests it was thought prudent to ensure bearing touchdown did not take place, since specific loads were higher and damage may have been far more catastrophic.

Therefore as specific pressure is increased one can observe that temperature rise gradient increases, but unlike tests 1 - 48 the non-linear region is not manifested. The bearing is operating in the Fully Aerodynamic region. An interesting observation is that for the same specific pressures, the temperature rise gradient is lower in the Aerodynamic region. Also for the same loading rates see Tables (5·1) → (5·4) the mixed region of lubrication is reached at a higher journal speed than tests 1 - 48. This suggests that reducing L/D ratio increases the point (speed) at which fully developed Aerodynamic lubrication is observed.

However for the same loading rates L/D of 1·5 increases (threshold of Instability over L/D ratio of 2), or the linear Aerodynamic range of operation at high speeds. This can be seen by the increased linearity of the curves of Fig. (5·6) over those of Figs. (5·4) and (5·5). Referring to Plate (4·5) shaft 4, one can see that little surface damage has occurred on the journal surface, being consistent with the observations of Fig. (5·6).

Figure (5·7) refers to tests 71 - 94 carried out on shaft 5 with an L/D ratio of 1·0. Two regimes of lubrication are observed, Mixed and Fully Aerodynamic. As the previous tests, increase in specific pressure increases the temperature rise gradient. Comparing the gradients to the previous tests; for the same load rate the L/D ratio of 1·0 at the highest specific load rate produces the lowest. Thus for low load rates the temperature rise gradient is the best, but for high load rates an L/D ratio 1·5 is best since this has a greater Instability threshold than L/D of 2·0.

It can be seen from Plate (4·5) that the shaft damage is minimal during tests 71 - 94 which is consistent again with the observations of Fig. (5·7) curves.

From all the tests it can be concluded that Boundary/Mixed lubrication causes less damage than that sustained due to reaching the Instability threshold and beyond. It is furthermore interesting to conclude that although high speed touchdown did occur in tests 1 - 48, that seizure had not occurred, was mainly due to the sulfinuzing surface treatment of shaft and bearing.

Concluding this set of results, Fig. (5·1) shows curves for varying L/D ratio, of Pnom against 1/m inverse of temperature rise. This gives an indication that there seems to be an assymptotic value of slope or temperature rise indicating that there is a finite value of load for any particular bearing geometry, this agrees with observations of other workers.

5·4·1 LOAD VARIATION EFFECTS

Load was applied via a Hydrostatic jacking system and monitored via a Tiebar load cell device. Two types were used. For tests 1 - 21 a Poisson type of tiebar was used. This was replaced with a more sensitive type, thus tests 22 - 94 were carried out with the Proof Ring Tiebar load cell. For all tests load was set to a nominal value and speed varied. One can see that generally temperature increased if speed was kept constant and the load varied, and also that eccentricity ratio increased, the converse of increasing speed for a given loading rate.

This can be seen clearly in Tables (5·1) → (5·4) where trends are as expected. However referring to Fig. (5·9) ⇒ (5·11) curves of constant eccentricity ratio. Load ratio P/Pa is plotted against compressibility number λ. Raimondi's curves for test results 22 - 27 suggest that all results should be operating Aerodynamically Fig. (5·10). From temperature rise plots against $\eta N'/P$ one can see that

there are obvious limitations, therefore to Raimondi's theoretical approach in as much as it overestimates eccentricity ratio at low load rates, for the L/D ratio of 2, however for L/D ratio of 1 the results are more encouraging.

Figure (5·1) shows curves plotted at L/D ratios of 1, 1½ and 2 for values of specific nominal pressure Pnom against 1/m, inverse temperature rise with increased speed. There can be seen three distinct curves, which seem to agree with other workers that there is a definite ultimate load capacity for any bearing geometry which refers to the fully Aerodynamic regime of lubrication. This form of curve may be of interest as it seems tp suggest safe limits with respect to speed and load and efficiency, or temperature rise as a function of journal friction, the safe limit of Instability.

5·5·1 L/D RATIO EFFECTS

Four test shafts were used in the experiments. Shaft 1 (tests 1 - 21) and shaft 2 (tests 22 - 48) had L/D ratios of 2. Shaft 4 (tests 49 - 70) had an L/D ratio of 1·5 and shaft 5 (tests 71 - 94) was an L/D ratio of 1·0.

As L/D ratio is reduced, the speed at which fully developed Aerodynamic lubrication is observed, increases. If one observes Figure (5·4) → (5·7) it can be seen that the temperature rise gradients of the L/D ratios of 1 (tests 71 - 94) and 2 (tests 22 - 48) are very similar at a load rate of 4·1 lbf. At the 13·5 lbf load rate the slope of L/D ratio of 1 is three times that of the L/D of 2, (tests 22 - 48). For the L/D ratio of 1·5 the slope at 4·1 lbf is greater than both the L/D ratio of 1 and 2 (tests 22 - 48). The gradient at 13·5 lbf is less than that of the L/D ratios of 1 and 2.

Therefore it can be assumed that the bearing journal which has a larger clearance than the L/D journals of 1 and 2 has greater frictional resistance at lower bearing loads but at higher bearing loads has less resistance than the other bearings. The bearing with

a large R/C ratio has greater load capacity at high speed before Instability is manifest.

5·6·1 COMPRESSIBILITY NUMBER λ

The compressibility number is calculated directly from bearing parameters and viscosity from the temperatures measured in the bearing. It enables an indication of amount of compressibility present and it enables results to be compared with Raimondi's theoretical work. As the clearance ratios (R/C) are relatively low the resulting calculated compressibility numbers are all less than one, the bearing is assumed almost to be incompressible since $\lambda = 0$ is incompressible and $\lambda \to \infty$ is totally compressible, so for a totally incompressible bearing the viscosity has to be large which is normally not the case, the speed is to be high or R/C ratio very large. Tables (5·1) → (5·4) show results of calculated compressibility number, the largest value being 0·389, the smallest being 0·0531.

As λ is proportional to viscosity and speed for any loading value λ increases with speed, which is shown to be true in the results calculated, and varies at each L/D ratio for the same load and speed conditions only by the R/C value or any temperature difference manifested.

5·7·1 SOMMERFELD NUMBER S $S = (R/C)^2 \mu N/P$

The Sommerfeld number was an indication of the bearings loading and is a secondary function of the bearing clearance ratio, viscosity, speed and specific pressure. These parameters have already been discussed in detail. However for a fixed S and speed increasing bearing temperature also increases, which is indicative of results arising from a constant specific pressure loading.

5·8·1 SPEED (N)

Each test was carried out with a fixed load increment and speed variation in approximately equal 5000 Rpm intervals (6000 → 40000 Rpm). If one refers to Figs (5·4) → (5·7) (L/D ratios 2, 1·5 and 1), as speed is increased (under constant loading) temperature values also increase linearly in the fully Aerodynamic region. The converse is also true. This linear region indicates true steady state bearing operation. Tables (5·1) → (5·4) show that increasing speed with constant load reduces the eccentricity ratio and increases attitude angle.

Compressibility number λ is plotted in Figs (5·9) → (5·11) against load ratio (L/D 1 and 2) and disturbing discrepancies in Raimondi's theoretical predictions are highlighted. Raimondi's results predict stable bearing operation when in practice the Instability threshold has been reached. This is indicated by the onset of non-linear bearing temperature rise. This is discussed in greater detail in Chapter (11).

5·9·1 CLEARANCE RATIO (R/C)

The clearance ratio (R/C) varied for each shaft and bearing combination. Shaft 1 (tests 1 - 21) L/D = 2 had an R/C ratio of 1427·14 however shaft 2 (test 22 - 48) L/D = 2 had an R/C ratio of 1331·87. Shaft 4 (tests 49 - 70) L/D = 1·5 had an R/C ratio of 1024·05 and finally shaft 5 (tests 71 - 94) L/D = 1·0 had an R/C ratio of 1480·08.

Referring to Fig. (5·4) L/D = 2·0, R/C = 1427·14 one can see that the temperature rise gradient m at Pnom of 3·25 is very much less than the gradient m of Fig. (5·5) L/D = 2·0, R/C = 1331·87 at Pnom of 2·99. However m at Pnom 6·91 of Fig. (5·4) is greater than m of Fig.(5·5) with Pnom of 6·74. From the results of Figs (5·4) → (5·7) one can conclude that a bearing with a large R/C ratio

under low specific pressures operates more efficiently than a bearing with a low R/C ratio operating with the same specific pressure.

Also one can see and conclude that a bearing with a large R/C ratio under high specific pressures operates less efficiently than a bearing with a lower R/C ratio. Therefore for any given L/D ratio and fixed specific pressure operating under variable speed conditions an optimum R/C ratio exists and is dependent upon whether operating under high or low specific pressures.

5·10·1 FRICTION EFFECTS

Friction was not monitored, however a relationship used by Summers Smith in Hydrodynamic bearing operation was used to calculate a friction relationship for the results.

What this parameter actually does is linearise the non-linear effects observed in temperature rise, see Fig. (5·8), both at the boundary and mixed regimes of lubrication and also at the non-linear instability threshold. It does however show that a reduction in R/C or D/C reduces the slope of the curves plotted. It should therefore not be used to estimate lubrication regimes for Aerodynamic bearings.

5·11·1 LIMITATION OF THE SELF-ENERGISED BEARING

For steady state operations in general two problem areas were encountered with the system, namely:

(1) Low-speed high-load touchdown.

(2) High-speed low-load touchdown.

For a given load (1) infers a minimum speed operating condition in the mixed or boundary lubrication regime, whilst (2) infers a maximum speed operating condition due to half frequency whirl or Test Rig limitation. See Table (5·1) → (5·4). Tests 1 - 94. Touchdown

in case (2) is more catastrophic than in case (1) as can be seen from shaft damage, Plates (4·4) ⇒ (4·5).

5·11·2 BEARING TEMPERATURE

Since bearing temperature could be measured and incipient touchdown always manifest itself by an escalating temperature response. This parameter gave an early warning as to any excursion into a touchdown situation and an indication of operating lubrication regime. Highest temperature recorded during testing was 64·3°C.

5·11·3 BANDED TEST REGION

From the preceeding, it is seen that steady state Aerodynamic operation test results are confined to a banded region whose demarcation, under constant load is defined by the upper and lower limits of speeds referred to above and a departure from linear temperature increase with increased speed.

5·11·4 LOW SPEED LIMIT

The lowest speed recorded during testing was 6000 Rpm. This restriction was due to two factors:

(1) Low synchronous speed limitation of the D/C drive motor. Below 6000 Rpm speed hunting was manifest.

(2) Touchdown of the journal arising from its inability to maintain Aerodynamic wedge action.

5·11·5 HIGH SPEED LIMIT

The highest steady state speed attained was 40200 Test 13. The lowest instability speed was 15000 Rpm recorded in Test 24, for an L/D of 2·0. However instability speed increased with an increase in

applied load. These steady state results are limited to linear temperature rise with increased speed, see Figs (5·3) → (5·7).

High speed investigations are referred to Chapter (11) where instability is studied in greater detail.

5·12·1 PHASE I TEST RESULTS PRESSURE PROFILES

It was initially considered that tests should be confined to steady state modes since the preliminary requirement was to study the effect of the two-dimensional pressure field and establish defination of the operating boundary conditions of the bearing system. However Fig. (5·12) tests (22) ⇒ (27) indicate a pressure field at or near the onset of half frequency whirl, see also Chapter (11).

Testing was initiated on the basis of variable L/D ratio, load and speed. Three L/Ds (2·0, 1·5 and 1·0) were employed for each set condition of load and speed, two dimensional pressure fields consisting of 84 points, being obtained for each condition.

The series of tests were repeated for loads of 18·1 N (4·1 lbf), 25·4 N (5·7 lbf), 34·8 N (7·82 lbf), 42·3 N (9·5 lbf), 51·2 N (11·5 lbf) and 59.8 N (13·44 lbf) and speed variations of approximately 6000, 10000, 15000, 20000, 25000, 30000, and for some tests also 35000 and 40000 Rpm. To obtain a picture of the general form of pressure profiles see Tables (5·5) ⇒ (5·10). Tests (1 - 6). The complete set of results can be seen in S.M.E. Report No. TR/90/7 Tables (5·5) → (5·98) Tests (1 → 94).

5·12·2 PRESSURE PROFILE RESULTS

Considering the results in general, they were found to agree reasonably with Raimondi but serious limitations can be seen in Fig. (5·12) → (5·24). However (and most importantly) the sub-ambient peak pressures recorded were higher than those predicted by Raimondi's theory.

The in depth study of the pressure profiles however, revealed several completely new features of an importance sufficient to instigate a full investigation.

5·12·3 L/D RATIO EFFECT ON PRESSURE CURVES

The following is discussed for load variations of 18·1 N (4·1 lbf), 15500 Rpm in order to obtain a picture of the general form of the pressure profiles with varying L/D ratio.

5·12·4 EFFECT OF L/D 2·0 → 1·5 (LOAD 4·1 lbf)

Since the load carried is the same for both L/Ds the effect of reducing the L/D ratio from 2·0 to 1·5 will be to increase the operating eccentricity ratio 'ε'. Considering Fig. (5·12) and Fig. (5·15) it is seen that the increase of eccentricity is manifest by an increase in the central peak pressure from 5 lb/in² to 8·8 lb/in², this peak moving forward (clockwise) by 60°, (from station '4' to station '6'). Whilst the maximum negative pressure remains relatively unaltered (-3·6 lb/in² to -3·4 lb/in²), its peak also moves forward (clockwise) by 30° from station ('2' to station '3').

Study of the pressure in the sub-ambient region reveals an unusual phenomenon, namely the existence of a 'double gradient' where the initial negative gradient changes to a positive one as the axial central plane of the bearing is approached. Since this infers an inward axial flow from the bearing extremities, wiping or an outward axial flow from the bearing centre line, there will clearly, be two stagnant filaments of air on either side of the bearing centre, approximately ⅓ of the axial half-length away from this point, (for the L/D = 2·0 case).

For L/D = 1·5 this region changes markedly, the stagnation filaments moving outward towards the bearing extremities whilst the whole region moves forward 30° (from station '3' to station '4').

As the L/D ratio decreases, it is further seen that the central plane pressure for this area increases out of the sub-ambient region at -11 lb/in^2 and enters the positive pressure area at a magnitude of 4 lb/in^2 (at station '4').

For station '3' however, the double gradient disappears, the peak pressure in the sub-ambient region increasing from -2 lb/in^2 to -3·4 lb/in^2, this now being the highest negative value of sub-ambient pressure.

In general, from a study of the two figures, the decreasing L/D (increasing eccentricity) tends to increase all positive pressures and decrease all negative, particularly as already described, around station '3'.

5·12·5 EFFECT OF L/D 1·5 → 1·0 (LOAD 4·1 lbf)

At L/D = 1·0 Fig. (5·18) the eccentricity has reached a maximum the most obvious effect of this being an increase in the central plane pressure from 8·8 lb/in^2 to 16·7 lb/in^2, although this occurs in the same plane (station '6').

A further manifestation of the increased specific pressure is the disappearance of the two stagnant air filaments implying a dramatic change of the pressure profile in the sub-ambient region, all pressure gradients (at station '4' in the axial direction) now being negative. In spite of the higher eccentricity ratio, the maximum value of negative pressure remains relatively unaltered (-3·4 lb/in^2 to -3·6 lb/in^2) and corresponds with a similar situation previously discussed for the L/D 2·0 to 1·5 case.

It is noted, however, that although the order of the circumferential station remains unaltered the magnitude of pressure at station '2' has increased from 2·5 lb/in^2 to 3·4 lb/in^2.

Thus since pressure magnitudes at stations '3' and '2' are now almost equal, the circumferential gradient itself is now almost zero between these stations on the bearing centre line, in marked contrast to the L/D = 2·0 case. In general, most changes occur around stations '3', '4', '5' and '6' with those around '3' and '4' being particularly marked.

5·12·6 EFFECT OF L/D 2·0 ⇒ 1·5 (LOAD 7·82 lbf)

Fig. (5·13) and (5·16) indicate the change of L/D from 2·0 to 1·5 for a higher load condition 7·82 lbf.

As before, it is clear that there has been an increase of eccentricity ratio as the L/D ratio is reduced.

Surprisingly, the change of 'ε' has virtually no effect on the maximum value of the positive peak pressure for this case, this being 11·00 lb/in^2 at station '4' for L/D = 2·0. The maximum does however, move forward 30° from station '4' to station '5' for the L/D = 1·5 case ie. more under the load line. Station '6' shows a more pronounced increase of pressure from 7 lb/in^2 for L/D = 2·0 to 10 lb/in^2 for L/D = 1·5. Thus there is a general enlargement of the circumferential pressure envelope in the loaded area as 'ε' itself increases, this enlargement moving forward towards the load line to give an enhanced pressure reaction to the applied load.

The most dramatic effect however, is at station '4'. This exhibits the double gradient effect previously mentioned, implying two filaments of stagnant air in the axial coordinate towards the bearing extremities, for the L/D = 2·0 case. For L/D = 1·5 however, there is a sudden reduction in the peak pressure at station '4' from 11 lb/in^2 (the maximum) to only 1·8 lb/in^2. The sub-ambient pressure at this station also shows a marked change, approximately 1·5 lb/in^2 for L/D = 2·0 to approximately 3·5 lb/in^2 for L/D = 1·5. Clearly there is a sudden fall in pressure once the peak has been passed and the sub-

ambient region is entered. This occurs within 30° for L/D = 2·0 (+11 lb/in² at station '4' to -3·6 lb/in² at station '3').

It is seen therefore, that an exceedingly steep pressure gradient exists at the central plane once the peak pressure is passed. This is consistent with findings for the oil journal bearing when operating at higher eccentricity ratios.

It has been seen that a reduced value of L/D ratio increases the value of 'ε' and sweeps the positive pressure forward towards the load line, this also has the effect of moving the sub-ambient region in the same direction and, since the gradient is steep around this point, this forward movement sweeps the sub-ambient pressure into what had been, previously, a region occupied by high pressure.

5·12·7 EFFECT OF L/D 1·5 → 1·0 (LOAD 7·82 lbf)

As with the lower load condition (4·1 lbf) the most marked change, for decreasing L/D, is in the value of the maximum central plane pressure, this increasing from 11 lb/in² to 28·4 lb/in², Fig. (5·19). This is accompanied by a positional change of pressure (station '5' to station '6') ie. a 30° movement clockwise towards the load line.

Unlike the lower load condition the two stagnant filaments, whilst moving axially outward, do not disappear, the maximum for station '4' increasing from 1·8 lb/in² (L/D = 1·5) to 6·0 lb/in² (L/D = 1·0). Whilst the minimum decreases from approximately -3·5 lb/in² (L/D = 1·5) to approximately -2·0 lb/in² (L/D = 1·0). Thus the stagnant filament remain throughout for all three L/D ratios.

5·12·8 EFFECT OF L/D 2·0 ⇒ 1·5 (LOAD 13·44 lbf)

The most surprising result from these graphs is that the maximum peak central pressure occurs at station '5' for the <u>larger</u> L/D 17·7 lb/in² station '5' Fig. (5·14) (L/D = 2·0) C.F. 15·4 lb/in² stations '6'

Fig. (5·17) (L/D = 1·5), even though the eccentricity ratio is higher for the smaller value of L/D. In fact, the general slope of the positive sides of the pressure profile are similar for the two L/D ratios. The peak pressure has, however, swept forward 30° towards the load line (from station '5' to '6') giving potentially, higher load carrying capacity. A study at station '4' shows an extensive modification of the axial profile, from a double gradient wholly negative distribution, both profiles producing the twin stagnant filaments previously discussed.

The marked difference is in the magnitudes of the pressure peaks at station '4', +4·8 lb/in^2 to approximately -3·2 lb/in^2 for the L/D = 2·0 case whilst being -1·5 lb/in^2 to -5·0 lb/in^2 for the L/D = 1·5 case. Again, station '4' appears to be the critical position, where large perturbations of pressure profile are taking place.

5·12·9 EFFECT OF L/D 1·5 → 1·0 (LOAD 13·44 lbf)

As with the two previous load conditions, the most obvious change is in the magnitude of the peak central pressure. This changes from a maximum of 15·4 lb/in^2 (station '6', L/D = 1·5) to 34·6 lb/in^2 (L/D = 1·0) at the same station Fig. (5·20). As with the 7·82 lbf load conditions the twin stagnant filaments do not vanish when the minimum L/D condition is reached. However, station '4' has now returned to a similar profile as that produced by the L/D = 2·0 condition ie. having both positive and sub-ambient components in the axial direction.

5·12·10 DISCUSSION OF PRESSURE PROFILES OBTAINED

From an examination of the pressure profiles obtained from the experiments on the Test Rig, it is not immediately apparent why the pressure envelopes/fields should be so complex in their distribution.

If however, we examine the geometry of the self-energised gas bearing at any given operating eccentricity it becomes apparent that, on the

basis of flow continuity, certain considerations begin to arise which give credence to the results obtained. Using this basis of continuity of flow, therefore, we can proceed to erect a preliminary hypothesis which would appear is capable of going some way towards both the complexity of the pressure envelope and the existence of the filaments of stagnant air already observed. Fig. (5·25) shows the Positions of the Pitot Tappings for L/D 2·0, 1·5 and 1·0.

Considering Fig. (5·26) it is seen that at any given eccentricity ratio, the attitude line of the bearing ie. the line through the centres of the shaft and bush, divides the clearance space into distinct halves which are, in fact, mirror images of each other about this attitude line.

Now since there is no external supply of air to the bearing radially through the bearing wall, the nett axial outflow of air arising from the pressurised zone must be by continuity of flow, be equal to the nett inflow of air into the sub-ambient region. Considering the loaded side of the bearing, it is apparent that the magnitudes of pressure existing in this sector must in general, be greater than those existing in the sub-ambient sector and, where this is so, particularly around the central region of the bearing, the axial gradients of pressure will be correspondingly greater than in the sub-ambient region.

For the oil bearing the difference in pressure gradient gives a nett outflow from the pressurised region greater than the nett inflow to the sub-ambient region. This creates a discrepancy of flow which can only be accommodated by supplying the bearing externally with lubricant.

In the case of the self-energised bearing, however, the outflow of air must equal the nett inflow, at least at the bearing extremities. This implies that at this point there must, in general, be similar pressure gradients for both the outflow from the pressurised region and the inflow feed into the sub-ambient region.

Examination of the axial pressure curves shows this to be so for all the pressure profiles examined (except for Fig. (5·12) (found to be at onset of Instability) ie. there is a symmetrical arrangement of pressure gradients around the bearing extremities. This supports the hypothesis of symmetry of pressure gradients at the bearing extremities, based on the flow continuity considerations previously mentioned, and implies the possibility of producing entirely new boundary conditions for the self-acting Aerodynamic gas bearing. Fig. (5·24) illustrates a typical set of pressure curves which, as has already been postulated, show the magnitude of the gradients for the loaded side of the bearing (shown as a dotted line) at a point, in board, towards the central plane (Z ≃ .L/4 in this case). In the present instance, they also exceed them in number (+7 against -5). This implies at this point, there must be a nett axial outflow from the central plane towards the bearing extremities. If therefore, flow continuity is to be maintained at the bearing extremities (enabling the bearing to maintain a constant eccentricity ratio) at least one of these gradients must reverse itself before the end of the bearing is reached, in order to give general gradient symmetry.

Examination of Fig. (5·24) shows that this has occurred at station '4' slightly inboard of the last row of pressure tappings. It is seen that, at this point the gradient suddenly decreases, passes through zero and reverses direction to give a 'web' of symmetrical pressure gradients at the bearing extremities. Clearly, around the point of gradient inflexion, there will be a filament of stagnant flow in the axial direction. This does not infer, however, that there will be stagnation of flow in the circumferential direction. Indeed, circumferential flow is the most likely mechanism for reducing the inbalance of pressure gradients occurring in this area. The term 'stagnation of flow' therefore, refers only to the axial co-ordinate at this point, and implies a 'finger' of air moving circumferentially around this local area.

Fig. (5·12), among all pressure profiles obtained, is curious in that it does not show a symmetrical distribution of pressure

gradients at the bearing extremities. Moreover, the gradients are all negative which indicates a continuous inflow of air to the bearing system. Although this is clearly impossible in a closed volume system, it was initially thought that a leakage of air was the cause from one or two tapping points. However, this pressure profile indicates a pressure profile at the onset of half frequency whirl. Fig. (5·7a) and (5·7b) show that from the temperature rise against $\eta N'/P$ plots that the rate of change of bearing temperature rise with rise in speed departs from a straight line, thus indicating the onset of instability. Also of extreme importance and great interest is that the central pressure profile Fig. (5·12) indicates that the Sommerfeld pressure distribution is approached, tending towards zero load carrying capacity. It is also to be noted that slight discrepancy of only ±0·5 psi from instrument drift would be all that is required to produce a symmetrical profile for the bearing extremities. For the same load and L/D at increasing speed the pressure profile is broken down completely, this will be discussed in greater detail in the Dynamic Studies of Chapter (11).

5·13·1 CONCLUSION TO STEADY STATE PLAIN BEARING RIG

The fact that two dimensional pressure profiles have been measured for self-energised gas bearings (Aerodynamic), for a range of L/D ratios loads and speeds are clearly important.

Firstly, since these results are unique they give a valuable insight, for the first time , into the complex behaviour of the gas film and enable any established theoretical model erected, to predict bearing behaviour, to be checked against the experimental results.

Secondly, the Rig has been shown to be capable of accurate pressure measurements (compare the symmetry of the pressure profiles obtained about the central plane of the bearing. This is particularly important as the physical extent of the pressure field can now be

established conclusively, enabling an accurate defination of boundary conditions to be incorporated into the Analytical model.

This, it is felt is one of the chief stumbling blocks in previous attempts at producing theoretical models for the self-energised gas bearing. This can be seen to be the case of Raimondi's theoretical pressure profile, see Ref. (13), which does not explain the complex changes of pressure gradient in the vicinity of station '4', leading to the newly discovered 'stagnation' sites, being an example of an event occurring in practice which could not be envisaged in theory.

A third consideration refers to the correct establishment of the two dimensional gas flow pattern during the bearing's operation. Clearly, since the magnitudes of the nodal pressures within the gas field have been determined it becomes possible to delineate, with good accuracy, the operating pressure gradients within the field. Since it is precisely these gradients which determine the characteristics of the local gas flows (and their interactions within the two coordinate axes) this leads, in general, to a better understanding of the gas dynamics, together with a better appreciation of the operating conditions producing these effects.

As previously suggested, this enhanced understanding can initiate a reconsideration of any analytical approach, in terms of the reality (or otherwise) of any assumptions made before such an understanding was available. New boundary conditions would require that summation of flow at axial boundaries should be zero. The solution scheme should now also require flow continuity at the boundaries. The veracity of any new analytical model incorporating modifications based on such results, can now be immediately correlated with the experimental findings, a situation which was not possible prior to the initiation of this experimental programme.

The results obtained have given valuable insight into Aerodynamic bearing operation. The comprehensive test programme concluded that

an Aerodynamic bearing can only operate in a limited speed region for any fixed loading condition. An important point discovered is that there exists an optimum R/C ratio which would give the greatest extension of this Aerodynamic lubrication region. From the results recorded it can be seen that for lightly loaded rotors a high R/C ratio is required (or a small radial clearance). For highly loaded rotors a low R/C ratio is required.

As already mentioned briefly, Raimondi's theoretical results seriously overestimate the extent of full Aerodynamic lubrication, as can be seen from Fig. (5·10) and (5·11) L/D of 2·0. His results however, for the L/D ratio 1·0 are more accurate, regarding this respect. Raimondi's results also do not explain the strange phenomenon discovered (stagnated axial flow) and to this end the Author's theoretical approach has tried more fully to explain and consider this phenomenon. Raimondi states that his results were restricted to compressibility ratios of ≯ 4, however, if one compares the experimental results recorded this could be further restricted with regard to Aerodynamic bearing operation, perhaps to compressibility numbers less than 1·0.

Another and perhaps one of the most important points is that the full pressure profile of a bearing at the onset of half frequency whirl has been captured for the first time (L/D = 2·0). This will be further discussed in the Dynamic Tests following. It further propounds that high L/D ratio bearings are more prone to instability than low L/D ratios.

Finally to conclude, the temperature relationships of the tests have been most interesting. It enables an alternative parameter which can be used to ensure Aerodynamic operation is always manifest. The limiting Aerodynamic operational speed range would obviously show that plain self-energised gas bearings are not suitable for conditions requiring wide high speed variations (0-100,000 Rpm +).

CHAPTER 6

HIGH SPEED SEALING METHODS

6·1·1 TEST RIG SEALING PROBLEM

Problems caused in the sealing arrangement of the Single Steady State Bearing Rig necessitated an alternative design to be investigated, for the Phase 11 Rig. (Dynamic Rotor Test Rig). The existing Labyrinth sealing system leaked oil mist at shaft standstill and also at high speed operation. This leakage caused oil ingress into the leather friction surface of the final stage drive belt and limited the Theoretical 60,000 Rpm due to slippage to approximately 35,000 Rpm. Other factors also affected this theoretical speed and will be touched upon in the Dual Bearing Test Rig Design. A secondary perhaps more important problem caused by the oil mist leakage was that oil mists are carcinogenic,to this end a baffle system was implemented in the final design.

A literature review revealed many types of sealing systems available. However, they can be normally categorised into two main types for Rotary shaft systems:-

(1) Rubbing or contact seals.
(11) Non-contacting seals.
(1) Contacting Seals
This type require surface contact between the Rotational part of the assembly and the stationary part. Contact seals can impart high surface pressures which cause high friction Torque and secondly increased wear characteristics. They generally have limited speed requirements due to excessive friction torque at elevated speeds. More commonly used types include single or dual lipped seals and vee seals. They have a finite sealing efficiency due to wearing of contacting surfaces. Other elaborate systems which have combinations of Rubbing and Labyrinth systems can also be found.
(11) Non-Contacting Seals

Generally fall into two main categories:-

(1) Externally pressurised (Hydrostatic/Aerostatic).

(2) Self energised (Hydrodynamic/Aerodynamic).

Both types tend not to cause surface rubbing and therefore can be utilized to much higher Rotational speeds, where heat generated by surface contact would be very high (and cause high energy loss in sealing system due to surface friction).

After an extensive study it was decided that the latter category would be investigated as a sophisticated sealing system would not be required.

6·2·1 HYDRO/AERODYNAMIC DISC SEALING

Literature seems to suggest that the Hydrodynamic disc seal which initially consisted of a wetted disc with a smooth/rough surface Interface developed later to be called the Vaned/smooth faced Hydrodynamic Disc Seal.

The efficiency of the Hydrodynamic disc seal has proven to be very high, efficiency increasing with increasing Rotational speed. The Hydrodynamic type seal has had many names but Baske (36) is thought the first researcher to have published data on this type, calling it the Hydrodynamic Seal.

Kelly, Wood and Marman (37) used the terminology dynamic seal. However, Wood, Manfredi and Cygner (38) used the term Centrifugal dynamic seal. Thew and Saunders (39) who has carried out with others by far the most extensive experimental work on this type agrees with Baske's terminology and use Hydrodynamic Disc Seal. He has with others developed the seal to a stage where it is capable of sealing particle laden fluids.

Fig. (6·1) shows the Disc Seal Model and Fig. (6·14) shows the Author's Design.

6·3·1 FORCED VORTEX MODEL (THEORETICAL MODEL AFTER THEW)

Basic Assumptions of Model as proposed by Thew.

(i) No axial pressure gradient at the periphey of the seal housing.

(ii) Fluid on both sides of the seal disc rotates at steady state conditions with uniform angular Velocities. ksω on the smooth side and kvω on the vaned side.

(iii) Fluid density is uniform (ρ).

(iv) Gravitational effects are neglected.

(v) Pressure on Gas side of Interface is uniform.

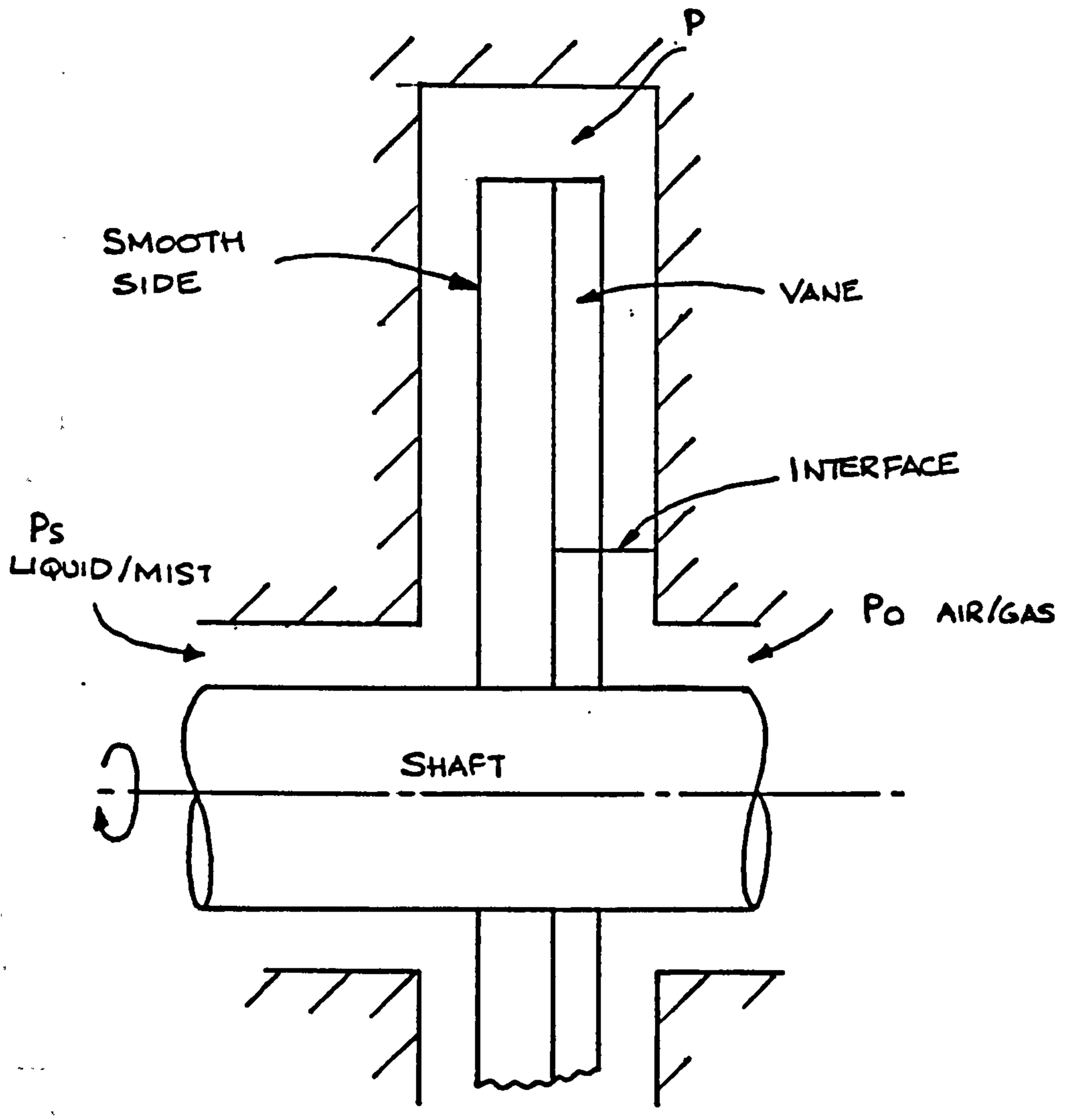

Fig. (6·1)

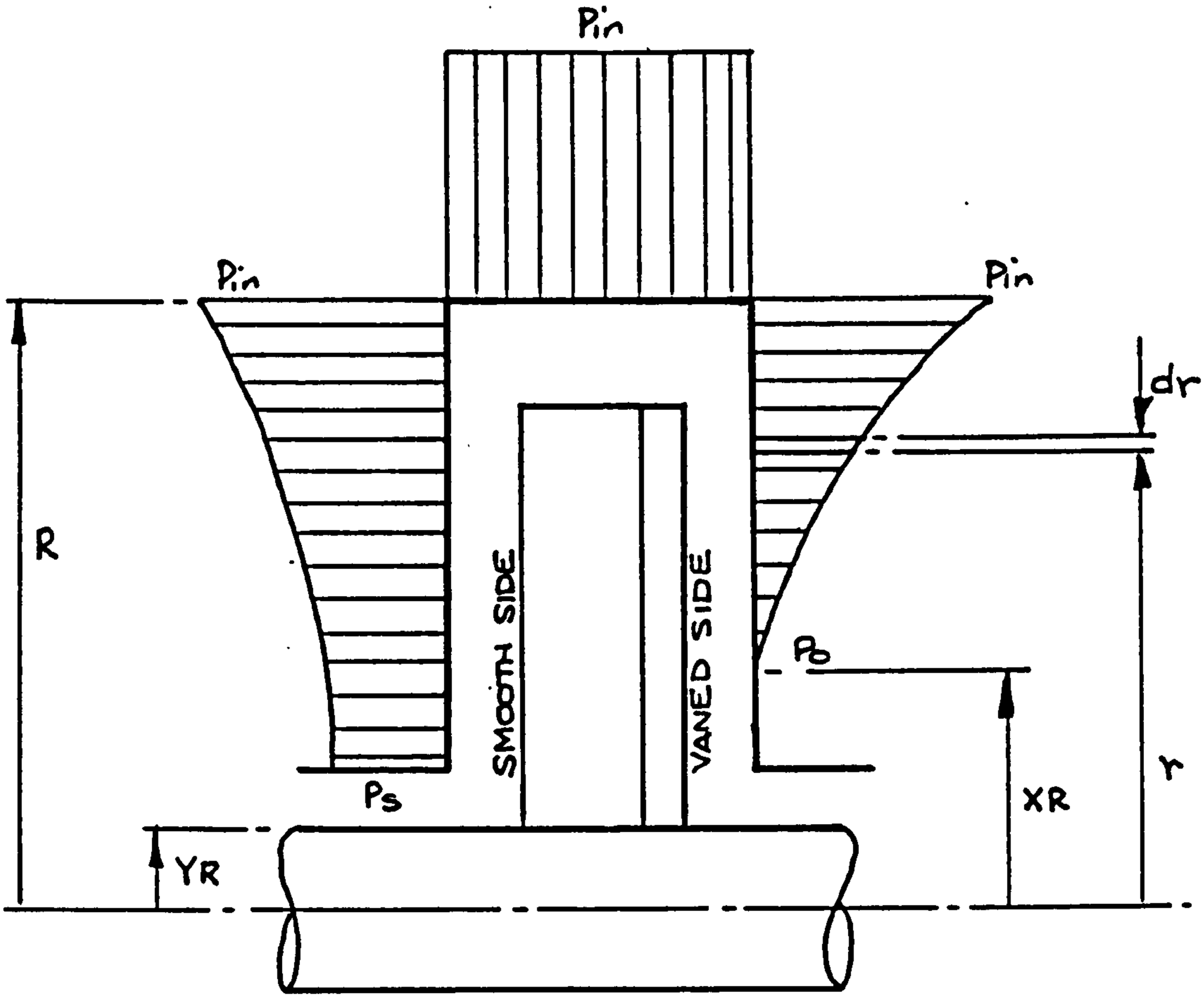

Fig. (6·2) Theoretical Pressure Profile

Figure (6·2) shows the Theoretical Pressure Profile Model developed by Thew et al (39)for the Hydrodynamic Disc Seal. It is used in the generation of a suitable model for the oil mist system and its applicability can be seen further on in this Chapter.

6·3·2 PRESSURE COEFFICIENT

(i) Considering pressure at disc tip. See Fig. (6·2).

$$P_s + \frac{\rho}{2}(k_s\omega)^2 [R^2 - Y^2 R^2] = P_o + \frac{\rho}{2}(k_v\omega)^2 [R^2 - X^2 R^2] \qquad (6\cdot1)$$

if one knows Ps, Po and ρ one can find unknowns k_v and ks with reference to tip clearance.

$$\therefore \quad \frac{P_s - P_o}{\frac{1}{2}\rho\omega^2R^2} = k_v^2 (1-X^2) - k_s^2 (1-Y^2)$$

But $\frac{P - P_o}{\frac{1}{2}\rho\omega^2R^2}$ = Cp = Pressure Coefficient

$$\therefore \quad Cp = k_v^2 (1-X^2) - k_s^2 (1-Y^2) \qquad (6\cdot2)$$

For a max Cp, X = Y and

$$Cp_{max} = (k_v^2 - k_s^2)(1-Y^2)$$

However

Smooth tip pressure = $P_s + \frac{\rho}{2}(k_s\omega)^2 [R^2 - Y^2 R^2]$ (6·1a)

Vaned tip pressure = $P_o + \frac{\rho}{2}(k_v\omega)^2 [R^2 - X^2 R^2]$ (6·1b)

which are both known from experimental work carried out on disc system.

6·3·3 END LOAD COEFFICIENT

Since the Radial pressure gradient on the vaned side of the disc is steeper than that of the smooth side. kv > ks there is a net end load.

However, as will be shown the Design has two opposed discs that will to all intents and purposes cancel each other.

$$Pr\ (smooth) = Ps + \frac{\rho}{2} (ks\omega)^2\ (r-Y^2\ R^2)$$

Intergrating above over smooth side gives smooth side end load contribution.

$$E_1\ (smooth) = \int_{YR}^{R} [Ps + \frac{\rho}{2} (ks\omega)^2\ (r^2-Y^2\ R^2)]\ 2\pi r dr$$

$$E_1\ (smooth) = 2\pi\ [\frac{PsR^2}{2}\ (1-Y^2) + \frac{\rho R^4}{8} (ksw)^2\ (1-Y^2\ )^2]$$

Substituting into (1).

$$E_1\ (smooth) = \pi\rho\omega^2\ R^4\ \{\frac{1}{2}\ (1-Y^2)[k_v^2(1-X^2)-ks^2(1-Y^2]+\frac{ks^2}{4}(1-Y^2)^2\}\quad (6\cdot3)$$

Also :-

$$E_1\ (vaned) = \int_{XR}^{R} [\frac{\rho}{2} (k_v\omega)^2\ (r^2-X^2\ R^2)]\ 2\pi r dr$$

$$E_1\ (vaned) = \pi\rho\omega^2R^4\ [\frac{k_v^2}{4}\ (1-X^2)]\quad (6\cdot4)$$

by inspection it can be seen that the end load acting on the smooth side is greater than that acting on the vane side.

$\therefore E_1\ (net) = E_1\ (smooth) - E_1\ (vaned)$

Substituting and defining C_{E1} as $\frac{E_1}{\frac{1}{2}\rho\omega^2R^4}$

$$C_{E1} = \frac{\pi}{2}(1-Y^2)\left\{k_v^2(1-X^2)\left[2-\frac{(1-X^2)}{(1-Y^2)}\right] - k_s^2(1-Y^2)\right\} \qquad (6\cdot5)$$

$\therefore$

$$C_{E1}\ (max) = \frac{\pi}{2}(1-Y^2)^2(k_v^2-k_s^2) = \frac{\pi}{2}(1-Y^2)\ C\rho\ max.$$

$\therefore$ If the above is a reasonable model the max end load can be determined from an experimental value of $C\rho$ (max).

Conditions when Ps = 0

From equation (6·2) when $Ps \to 0$ the value of X is given by the relationship

$$1-X^2 = \frac{k_s^2}{k_v} \qquad (6\cdot6)$$
$$1-Y^2$$

The end load when Ps = 0 is still finite as can be seen by substituting from equation (6·4) in equation (6·5).

$$C_{E1} = \frac{\pi}{2}(1-Y^2)^2 k_s^2\left[1-\frac{k_s^2}{k_v}\right] \qquad (6\cdot7)$$

If ks is reduced to zero by adding vanes to the housing then for Ps = 0, $X^2 = 1$ and $C_{E1} = 0$. If Ps < Po then for ks = 0 the seal will break down and gas will flow past the disc.

Therefore if the Ps < Po case is likely to arise, it is not desirable to reduce ks to zero.

6·4·1 EXPERIMENTAL FINDINGS AND COMPARISON WITH THEORETICAL MODEL

The Disc Seal arrangement can be seen on the High Speed Housing Assembly Fig. (6·3) and (6·14).

The Housing assembly forms the final layshaft, for connection to the Test Bearing Assembly, via a flexible quill shaft coupling system.

The housing assembly comprises a spindle supported in two pairs of Angular Contact Bearings. The Angular Contact Bearings are, due to the high speeds invisaged, lubricated via an oil mist system. It is this oil mist system therefore that the Disc Seal is envisaged to seal and improve the Single Bearing Rig Sealing Arrangement.

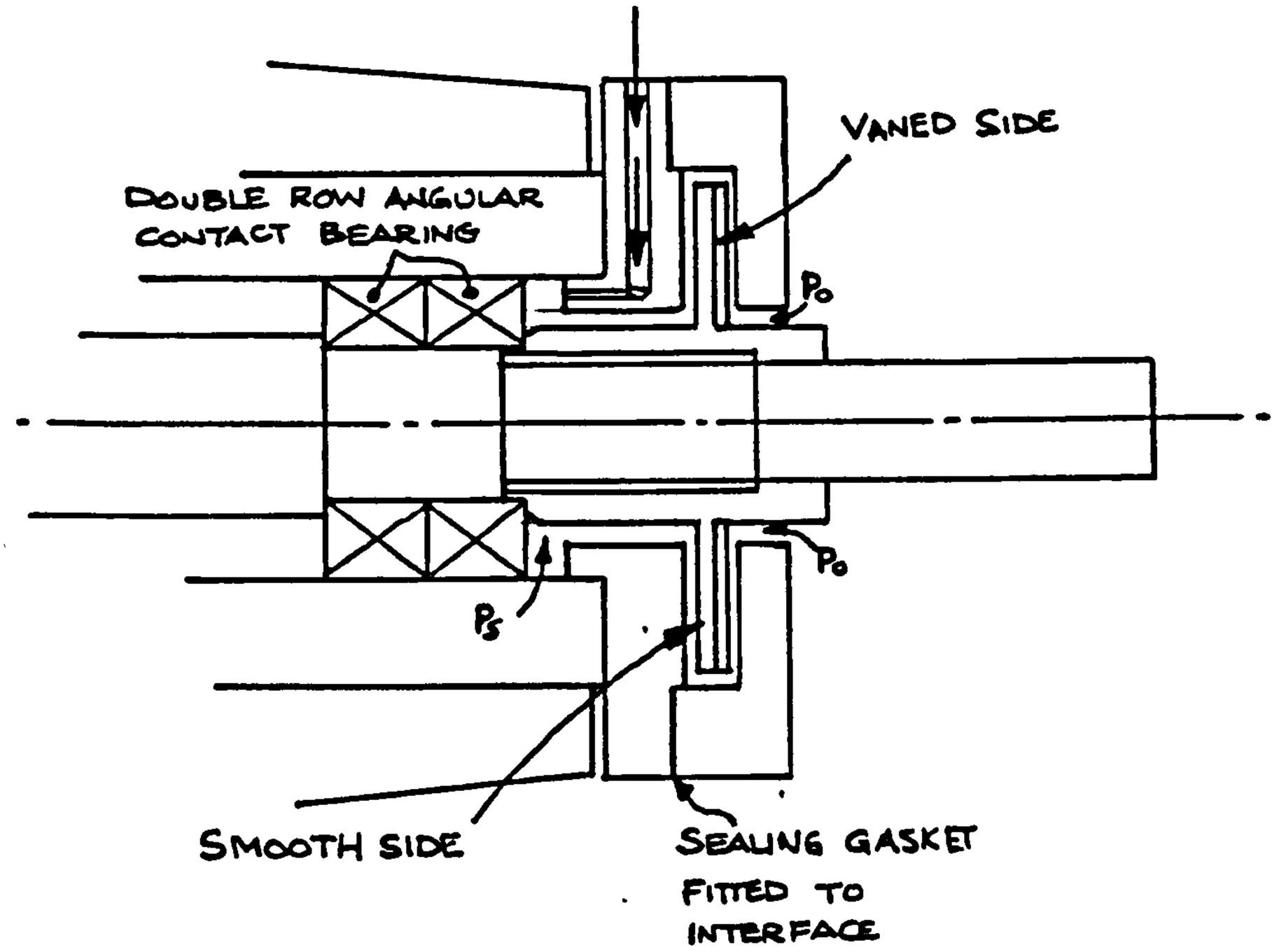

Fig. (6·3) Hydrodynamic Seal System (Oil Mist Sealing)

6·4·2 PRESSURE TAPPINGS AND PROFILE

The pressure profile of the Disc seal was monitored via a scanning - pressure valve, through tappings in the Endplate and Endcover. For all pressures recorded a fixed supply pressure Ps was kept at 10 psi (N/mm^2), monitored at the flow mixture and regulating valve. This supply pressure was thought to be the optimum for a high speed oil mist system.

The tapping positions can be seen in Fig. (6·4) and Pressure Profile Variations can be seen in Figs. (6·5 & 6·6). The pressure profile did not readily become apparent until ≃ 10,000 Rpm. and varied little with the values of hs and hv smooth and vaned side clearances respectively in the experimental tests carried out.

Ten pressure tappings were made P_1 - P_5 in the inner End plate and P_6 - P_{10} in the End cover.

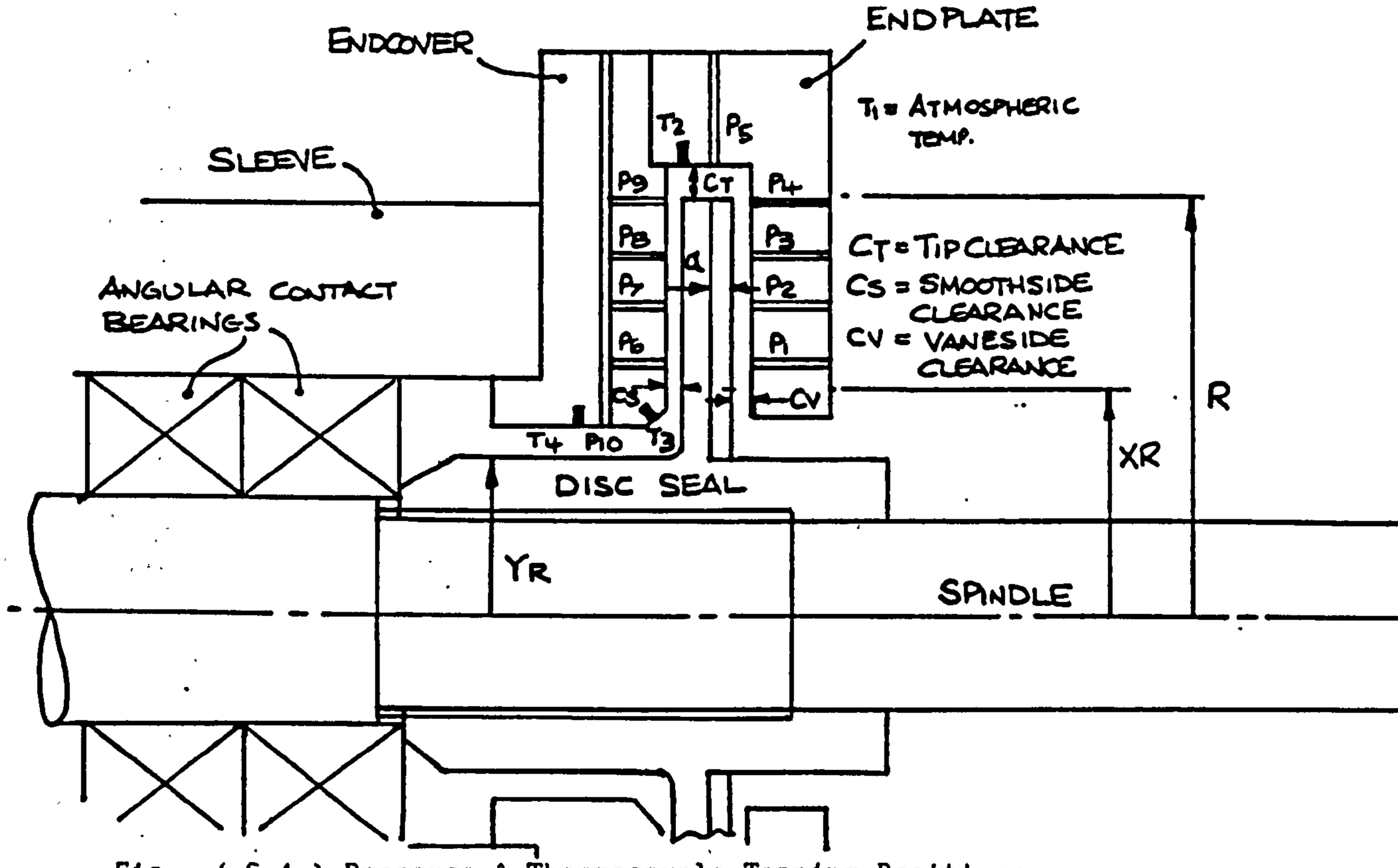

Fig. (6·4) Pressure & Thermocouple Tapping Positions

6·4·3 TEMPERATURE TAPPINGS AND DISTRIBUTION

Initially a single thermocouple was positioned in the endplate as an isothermal temperature distribution in the air film was postulated. (Tests 1-10). T_1 and T_2.

However for later tests further thermocouples were added to the Endplate and Endcover (Tests 11 - 16). T_3 and T_4 added. Four thermocouples were used T_1 (ambient) in the main frame, T_2 in the Endplate, T_3 and T_4 were located in the Endcover. T_4 trailing on the disc seal shoulder. See Tables (6·1 → 6·17). See S.M.E. Report TR/90/7. Fig. (6·4) shows location of the thermocouples T_2 → T_4. T_1 was located on main frame assembly. All Thermocouples were type 'E'.

As can be seen from tabulated results Thermocouples T_2 and T_3 show little variation and therefore one could then assume an isothermal temperature distribution through the oil mist film. (This also agrees with other work carried out on gas film lubrication).

This isothermal variation gives a good indication of the increase in Friction torque with increase in Rotational speed. It could therefore be said that the Friction torque varies in proportion to ω and independent of Cp.

One can see that the initial postulation was reasonably accurate. Temperature did however seem highly dependent upon Disc speed. See Fig. (6·7) → (6·8). Fig. (6·7) and (6·8) show that at speeds above 30000 Rpm the temperature rise begins to follow a Parabolic temperature variation consistent with ω^2. That is Temperature $\propto \omega^2$. The Flow of Air/Oil Mist in the Disc.

6·4·4 VARIATION OF hs AND hv

The initial starting clearances were those that Thew found to be optimum for his Hydraulic System. The tip clearance ht was at all times kept constant at ht = 2·0 mm (0·080"). Initial starting values for hs and hv were 0·84 mm (0·033") and 1·2 mm (0·047") respectively. Fig. (6·14) shows the Initial Starting Values and the Assembly of the Sealing System of the High Speed Housing.

A total of 16 groups of tests were carried out with clearance variations in hs and hv until the minimum clearances thought practical were arrived at.

[hs 0·06 mm (0·0015") & hv 0·08 mm (0·002")].

The method of varying hs and hv was by grinding accurately both the Endcover and the Disc seal.

The unusual result found was that the clearance variation did not increase the pressure profile.

It is quite probable that at clearance less than hs (0·06 mm) and hv (0·08) that a significant increase may well be detected but it was thought prudent not to " push one's luck " and destroy the system with a high speed touchdown.

hs clearance was checked with the aid of Feeler gauges, but the vane clearance was checked by the use of an inspection hole drilled and tapped with a flush fitting plug. Thus the clearance could be checked with a depth micrometer. This proved a very successful feature designed in at the initial onset.

6·4·5 SPEED VARIATION

The speed of the tests were varied from barring over at minimum speed of Variable Frequency Disc of 1,500 Rpm to a safe maximum speed of 45,000 Rpm.

The speed for each set of tests were varied by 5,000 Rpm steps, and it was not until approximately 30,000 Rpm that a significant pressure distribution could be seen.

Another significant variation brought about by increased speed was the increase in Oil Mist Film temperature. A typical distribution can be seen in Fig. (6·7) → (6·8). This temperature variation did not vary significantly with increase in clearance.

6·4·6 FLOW RATE AND EFFICIENCY FINDINGS

As previously mentioned the Disc seal was tested for speeds of 1,500 → 45,000 Rpm. However, for the purposes of the efficiency tests the tests were carried out for speeds varied at 30,000 → 45,000 Rpm and supply pressure variations of 5 → 60 psi. The pressure distribution was not recorded during these tests but was seen to increase slightly. Further investigation into pressure distributions would prove interesting for the future. Comparison of Oil Mist to Air Properties

Initially the flow rates of the oil mist were compared with those of clean air and are shown in Table (6·28) below at various supply pressures and calibration readings on a ⅛" Fischer Porter Flow Meter. Tables (6·19) → (6·23) and Fig. (6·9) show the flow meter characteristics and calibration for the efficiency tests.

Supply Pressure (psi)	Fischer Porter Flow Meter Scale Readings	
	Clean Air	Oil Mist
60	25·00	25·00
50	21·60	21·40
40	18·40	18·20
30	15·05	15·00
20	11·75	11·70
10	7·80	7·65
5	5·20	5·20

Table (6·28)

As can be seen both sets of readings are extremely close and to all intents and purposes can be taken as equivalent.

That is ρ Oil Mist $\simeq$ ρ Air
STP STP

To define the effectiveness of the Disc Oil Mist seal it was decided to carry out the following:-

(i) Calibrate the flow from the oil mist lubrication system with a fixed oil/air mixture but varying supply pressures, by use of a Fischer/Porter Flow Meter.

(ii) Running the Rig under varying supply pressures (Ps) and rotational speeds and recording the mass flow rate through the outlet of the high speed housing assembly.

The Figures of both tests were compared to arrive at sealing efficiency. The above tests were only carried out for speeds of 30,000 → 45,000 Rpm, since pressure profiles did not seem to become significant until the lower running speed of 30,000 Rpm was achieved. Tables (6·24) → (6·27) are for variations of Ps with speed and the resulting output mass flow rate through the flow meter and can be seen in the Appendix. Fig. (6·10) shows lines of constant pressure with variation of speed against efficiency. Fig. (6·11) shows lines of constant speed with variation of supply pressure against efficiency. Fig. (6·10) indicates the point of 100% effective sealing speed against supply pressure Ps. Fig. (6·12) and Fig. (6·13) show the schematic of the experimental tests.

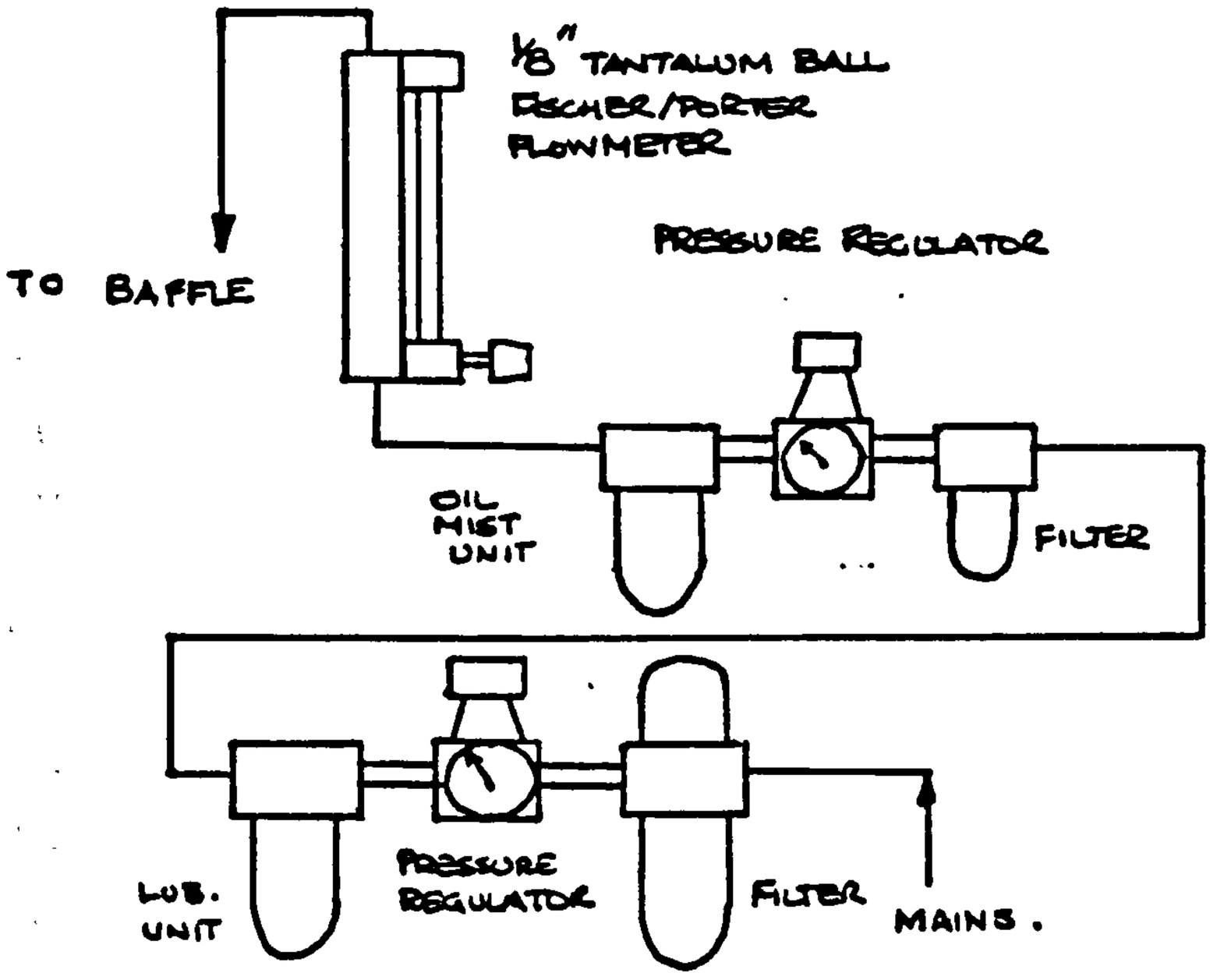

Fig. (6·12) Test Calibration

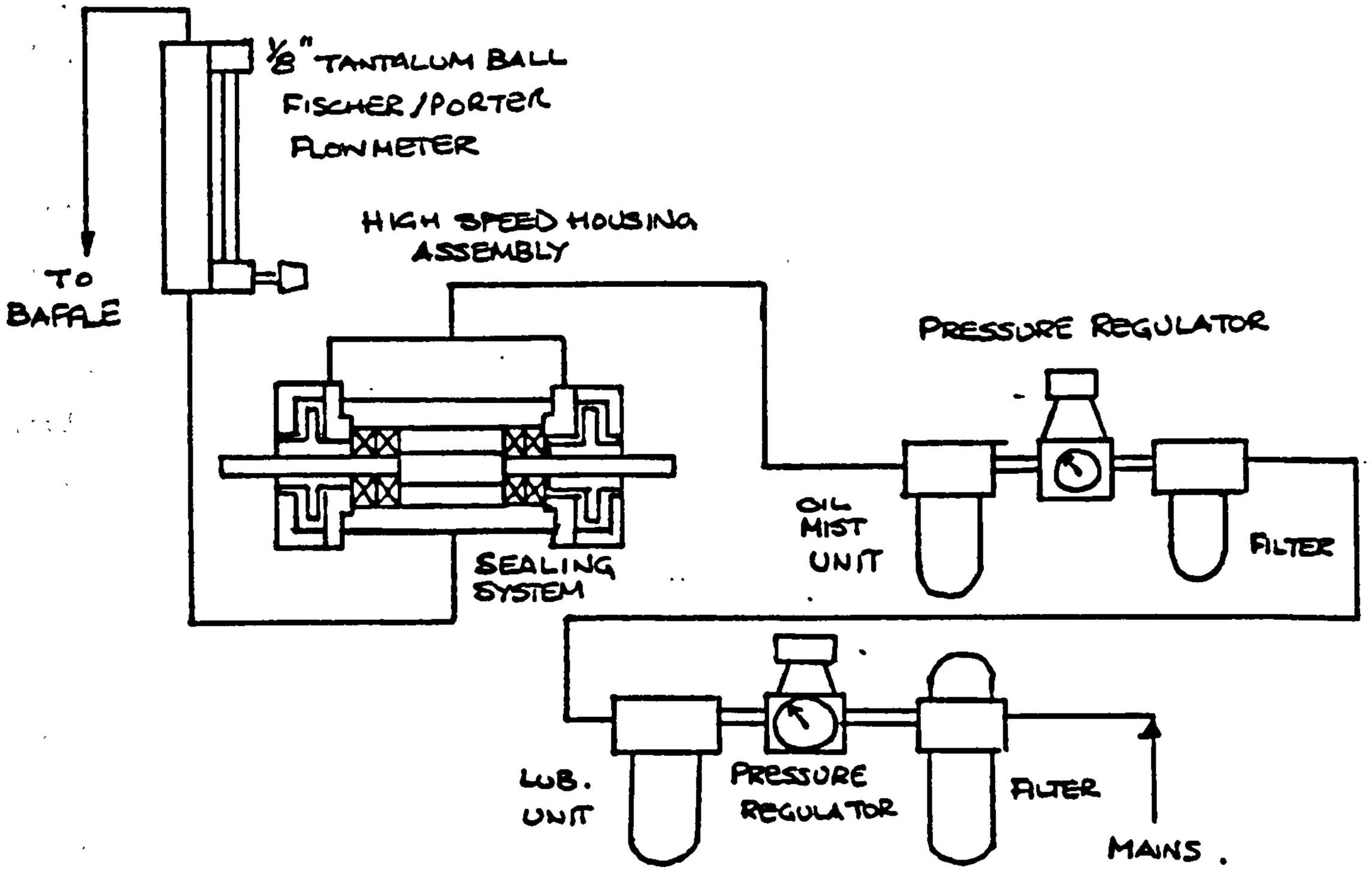

Fig. (6·13) Seal Efficiency Test

The results of efficiency further verify what was observed by the pressure profiles at various speeds. This is, that up to 30,000 Rpm the seal is not acting efficiently as a seal but has leakage to atmosphere.

However, at speeds above 30,000 Rpm the efficiency increases dramatically. At 45,000 Rpm the efficiency reaches as much as 2554%, that is, there is Air being drawn into the seal and pushing the Oil Mist through the bearing.

It can be seen from the Fig. (6·10) → (6·11) and Tables (6·24) → (6·27) that the efficiency at each speed reduces with increase in supply pressure Ps. However, at speeds above 30,000 Rpm particularly 35,000 Rpm all pressures up to 60 psi are sealed greater than 100%. Also from Fig. (6·10) one can depict the point of ≈ 100% sealing efficiency occurring at each Test supply pressure.

The efficiency of the seal agrees with Thew's findings, that is, an increase in sealing efficiency was detected with increase in speed, (also recorded was an increase in film temperature).

However, one must obviously guard against ingression of foreign particles into the bearings, but considering the hazards of the oil mist to one's health this would be of a secondary priority.

Another method of checking the seal effectiveness but not giving an indication of the seal's efficiency would be to have used a smoke detection method.

6·5·1 CONCLUDING REMARKS ON THE PRESSURE PROFILE AND EVALUATION OF ks AND kv

The pressure profiles for the smooth side and vaned side of the Disc seal agree well with Thew's findings even though they are of many magnitudes less since density of air is many times less than water approximately 1/800.

One can see the greater slope on the vaned side of Disc which becomes more apparent above speeds of 5,000 Rpm, however, the pressure profile of the smooth side of Disc does not become greatly apparent until after 30,000 Rpm. Fig. (6·5) → (6·6). This agrees with seal mass flow efficiency results. Fig. (6·10) → (6·11). The value of X does not change since Po stays unchanged where Po cuts zero axis.

Having carried out all the above tests for pressure temperature profiles it was then possible to duplicate the second seal to the optimised working clearances. After this modification to the seal the mass flow rate efficiency comparisons were made. The flow rate of each seal must then be assumed to be half the total flow rate recorded in the efficiency tests.

6·5·2 CALCULATION OF ks AND kv

The values of ks and kv can be determined experimentally in the following manner and from the following formulae:-

$$P_{max} = P_s + \frac{\rho_{opt}}{2} (k_s \omega)^2 [R^2 - Y^2 R^2] \qquad \text{to obtain ks}$$

$$P_{max} = P_o + \frac{\rho_{opt}}{2} (k_v \omega)^2 [R^2 - X^2 R^2] \qquad \text{to obtain kv}$$

Rearranging

$$ks = \frac{2.(Pmax-Ps)}{\rho_{opt}\cdot\omega^2[R^2-Y^2R^2]} \quad \text{in}$$

$$R = 1\cdot965"/2 = 0\cdot9825$$
$$YR = 0\cdot433$$
$$\therefore Y = 0\cdot4407$$

$$kv = \frac{2\cdot(Pmax-Po)}{\rho_{opt}\cdot\omega^2[R^2-X^2R^2]} \quad \text{in}$$

$$kv = \frac{2\cdot(Pmax-Po)}{\rho_{opt}\cdot\omega^2[R^2-X^2R^2]} \quad \text{in}$$

$$Re = \frac{\rho\ opt \times \omega\ R^2}{\mu_{opt}}$$

Take X as edge of End cover.

Take full sealing as inside diameter of End cover.

$$[R^2-X^2\ R^2] = 0\cdot71551$$

$$XR = 0\cdot4997$$

$$\therefore X = \frac{0\cdot4997}{0\cdot9825} = 0\cdot5087$$

SPEED RPM	Re	TEMP °C	TEMP °F	lb/sec²/in⁴ ρ_{opt} E-7	PRESSURE (Psi) Pmin (Ps)	Pmax	ω	ks	kv
1500	6453	23·2	73·76	1·1419	0·02	0·01	157·08	→ 0	→ 0
5000	21510	24·8	76·64	1·1360	0·02	0·01	523·60	→ 0	0·947
10000	43020	28·3	82·94	1·1220	0·05	0·05	1047·20	→ 0	1·060
15000	64530	30·9	87·62	1·1130	0·08	0·09	1570·80	0·623	0·957
20000	86040	34·0	93·20	1·1020	0·14	0·16	2094·40	0·664	0·962
25000	107550	35·0	95·00	1·0980	0·20	0·25	2618·00	0·842	0·964
30000	129059	36·0	97·88	1·0930	0·29	0·35	3141·60	0·770	0·952
35000	150569	39·1	102·38	1·0840	0·40	0·49	3665·20	0·812	0·969
40000	172079	43·5	110·30	1·0690	0·50	0·62	4188·80	0·826	0·961
45000	193589	44·5	112·10	1·0650	0·61	0·78	4712·40	0·876	0·960

Table (6·29)

Perhaps by reducing ks a better seal would be generated? $Re = \frac{\rho\omega R^2}{\mu}$

ks average = 0·770

kv average = 0·970 } Answers agree somewhat with those of Thew approach 0·95 average.

For the results of ks and kv the mathematical approach does seem to model reasonably well the dynamic behaviour of the seal with an oil mist / air mixing medium. However, the value of mix pressure at 10,000 Rpm should be about 0·04 psig this would render a value of kv → 0·95, less than unity closer to other results calculated.

The pressure profile generated by the seal seems wholly due to the value in the rough side of the disc, since no difference due to reduction in hs or hv was detected. However, if hs and hv were

reduced further it may prove that the seal is much more efficient at lower speeds where perhaps touchdown would not be as catastrophic as at high operational speeds.

It may be that clearances below (0·001") 0·025 mm would produce better results, however it was deemed prudent to keep the operational clearances of hs → 0·0015" hv = 0·002" so that any angular motion of the disc would not prove disastrous due to shaft whirl induced by relatively large discs overhung from each end of shaft.

A better seal may have been produced by reducing value of ks although the smooth side of the disc had a ground finish. Perhaps a lapped finish may well be required. Further investigations along these lines would prove very interesting.

Better values of ks may also have been obtained by omitting the counter bored holes in the endcover to the sleeve. (4 socket cap head). Thew (36) mentions that he carried out tests with vanes on the smooth side housing (perhaps inducing a similar effect), and found this deteriorated sealing properties, this may have occurred with the present system with 4 counter bored holes.

The values of ks_{av} and kv_{av} agree quite well with Thew's (36) work, his values for liquids gave ks 0·24 → 0·31 and kv 0·91 → 0·95. Re = $3·4\times10^{5}$ → 6×10^{5}; The test results gave values of ks_{av} = 0·77 and kv_{av} = 0·97. Re = $6·453\times10^{3}$ → 1.936×10^{5}. The values of Reynold number is much more varied but the results of ks and kv tend to arrive at the conclusion that the theory fits this system quite well.

6·5·3 CALCULATION OF Cp

Since it was seen that X and Y did not noticably vary for the system only one value of Cp can readily be calculated that is :-

$$Cp_{av} = kv_{av}^{2}\ (1-X^{2})-ks_{av}^{2}\ (1-Y^{2})$$

$\therefore Cp_{av} = 0{\cdot}97^2\ (1-0{\cdot}51^2)-0{\cdot}77^2\ (1-0{\cdot}44^2)$

$Cp_{av} = 0{\cdot}218$ for α speed ranges $10 \rightarrow 45 \times 10^3$ Rpm.

6·4·4 CALCULATION OF END LOAD El_{net} AND C_{El}

The maximum end load will be calculated and occurs at 45,000 Rpm.

$$El_{(smooth)}\ \max = \pi\rho_{opt}\omega^2 R^4 \left\{\tfrac{1}{2}(1-Y^2)\left[kv^2_{av}\ (1-X^2)-ks^2\ (1-Y^2)\right] + \frac{ks^2}{4}\ (1-Y^2)^2\right\}$$

$$= \pi .\ 1{\cdot}065 \times 10^{-7} .\ (4712{\cdot}4)^2 .\ 0{\cdot}9825^4\ [\tfrac{1}{2} .\ (1-0{\cdot}44^2)[0{\cdot}97^2\ (1-0{\cdot}51^2)-0{\cdot}77^2\ (1-0{\cdot}44^2)+\frac{0{\cdot}77^2}{4}(1-0{\cdot}44^2)]$$

$El_{(smooth)} = 0{\cdot}94$ lbf max (4·18 N)

$$El_{(vaned)}\ \max = \pi\rho_{opt}\omega^2 R^4\ \left[\frac{kv^2\ av}{4}\ [1-X^2]\right]$$

$$= \pi .\ 1{\cdot}065\times10^{-7} .\ (4712{\cdot}4)^2 .\ 0{\cdot}9825^4\ \left[\frac{0{\cdot}97^2}{4}\ [1-0{\cdot}51^2]\right]$$

$= 1{\cdot}21$ lbf max (5·38 N)

$\therefore El_{net} = El_{(smooth)} - El_{(vaned)}$

$= 0{\cdot}94 - 1{\cdot}21$

$= -\ 0{\cdot}27$ lbf (1·21 N)

$\therefore$ Maximum end load is negligible on bearings and is due to two sets of bearings (one each end of housing assembly) being opposed counteracted by each set.

$$CEl_{av} = \pi\ (1-Y^2)\left[kv_{av}^2\ (1-X^2)\left[2-\frac{(1-X^2)}{(1-Y^2)}1\right]-ks_{av}^2(1-Y^2)\right]$$

$$= \pi \cdot\ (1-0{\cdot}44^2)\ \left[0{\cdot}97^2\ (1-0{\cdot}51^2)\ \left[2-\frac{(1-0{\cdot}51^2)}{(1-0{\cdot}44^2)}\right]\ -\ 0{\cdot}77^2\ (1-0{\cdot}44^2)\right]$$

$CEl_{av} = 0{\cdot}349$

max

CHAPTER 7

INSTABILITY AND DYNAMIC CHARACTERISTICS

7·1·1 LITERATURE REVIEW

Montgomery and Sterry in 1955 (54) carried out tests on a Rotor (3/4" diameter) which was capable of 250,000 Rpm driven by an air turbine. The rotor was mounted on Bearings which were sintered bronze bushes, (with oil extracted). For the purposes of sealing and flexibility the bearings were mounted on Rubber 'O'-Rings. The thrust bearing was a single jet 0·020" diameter in the middle of a flat surface. The Rotor was a plain ground shaft with serrations machined in one end to provide a crude turbine wheel.

They carried out tests at bearing supply pressures of 15 - 90 Psi and diametral clearances of 0·0020" - 0·0035", and obtained speeds of 190000 - 258000 Rpm without bearing instability being detected. With a diametral clearance of 0·0035" the best arrangement was obtained. They did not unfortunately monitor journal or bush movement or bearing temperature.

Brix in 1956 (55) proposed an Analysis for determining the instability of a gas bearing rotor system, and carried out an experimental investigation on a bearing system at speeds up to approximately 26,000 Rpm. He proposed that the conical whirl of a system would describe a cone from a fixed point in space for an asymmetrical rotor. The L/D Ratios of the bearing were 3 and the bearings were flexibly mounted in diaphragms. His Experimental findings agreed reasonably well with his analytical proposals.

In 1957 Ford, Harris and Pantall (56) whilst carrying out experiments with gas bearings briefly mentioned the influence of half frequency whirl on bearing performance. They also found that the load carrying capacity of gas bearings wre in some instances greater than those theoretically predicted by Katto and Soda.

Whitley and Betts (14) published a paper in 1959 on the load capacity and half frequency whirl of gas bearings. The range of gases studied were Hydrogen, Nitrogen and Neon, giving a large viscosity variation. Argon and Carbon Dioxide were investigated for the effect of the ratio of specific heats. The Rotor used in their experiments was an assymetrical single bearing type with diameters of 50·80 mm, 101·60 mm, and 177·80 mm respectively. Speeds were varied between 3,000 - 20,000 Rpm with L/D ratios from 2 - 5 for plane bearings and an L/D ratio of 1 for a slotted bearing. They found that slotted bearings with axial slots cut half way along their length increased the half frequency whirl onset speed, however they had slightly reduced load capacity.

They concluded that experimental findings correlated well with isothermal conditions for an infinite bearing. Also noted was that all modes were conical. One would expect this from a system of their design, Assymetrical single bearing type.

Following this work Whitley, Bowhill and McEwan (58) in 1960 studied the whirling characteristics of an assymetric shaft in a single bearing. They predicted that a single end shaft posses 4 modes of whirl which depend upon the following:-

(1) The mass and tranverse Inertia of the Bearing.

(2) The mass and tranverse Inertia of the Rotor (shaft)

(3) The gas film dynamic stiffness.

They also observed improvements in whirl properties due to the following:-

(1) Axial slots cut into the top of the bearing.

(2) Circumferential slots cut into the bearing.

(3) Introducing ovality into the bearing.

The modifications above reduced slightly the load carrying capacity, circumferential growing being the more serious.

Reynolds and Gross (59) in 1962 carried out investigations on a range of plain gas bearings with L/D ratios varying from 1/4 - 1. They observed that the whirl ratio φ / ω was approximately equal to one half. $(0.485 < \chi < 0{\cdot}5)$, $\chi = \varphi / \omega$, where φ is the precession velocity and ω is the rotational velocity.

In general they found that whirl is composed of both synchronous and self excited components, each with cylindrical and conical modes. (obviously due to amount of residual balance also present).

Cheng and Trumpler (60) 1962 used Galerkins method to obtain an approximate solution to the steady state Equation. They arrived at three main conclusions when the Journal was arbitrarily displaced from the equilibrium running position:-

(1) At speeds above the threshold of instability a spiral with increasing amplitude was obtained.

(2) At speeds below the threshold of instability the Journal returned to the equilibrium position.

(3) At speeds near to the threshold speed the Journal trajectory formed an orbit. The shape of the orbit varying from a circle to an ellipse to highly irregular curves.

McCann in 1962 (61) produced a paper for the stability of an unloaded gas bearing (vertical rotor). He concluded that the threshold for such systems, such as a vertical rotor, was very much lower than the same Rotor mounted horizontally.

Sternlicht and Winn (62) in 1962 carried out a very extensive experimental study of a symmetric rotor system with a steady applied load. They varied the following bearing geometry, span between bearings, load mass and inertia. They concluded that there was good agreement between theory and experiment for static loading (steady state solution), they found four main characteristics:-

(1) An optimum clearance exists giving minimum onset of instability.

(2) Onset of half frequency whirl increases with increase in rotor mass, and increases almost linearly with load.

(3) For the same P/pa ratio the higher the L/D ratio the lower the onset of instability.
(4) External vibrations could sometimes excite the rotor into instability at speeds as low as 500 Rpm below the actual instability speed.

They also observed that for low specific loads 1 - 2 lbf/in^2 assymetry of a rotor system could lower the onset of instability by as much as 50%.

Marsh (63 & 64) in 1963 published a Ph.D thesis on the instability of gas bearings. He studied plain, slotted and lobed types. The apparatus consisted of an air impulse driven rotor mounted in a single bearing, and extrapolated his results for a dual symmetric bearing system. He also studied variables of L/D = 2,3 and α, eccentricity ratios of 0 - 0·6 and H (bearing number) of 0 - 1·6.

Marsh observed the following factors influence on the onset of half frequency whirl:-
(1) An optimum bearing length existed for both conical and cylindrical stability. Increasing bearing length increased the conical stability, but reduced the translational whirlspeed . (This resulted because the translational inertia is increased which will reduce conical whirl effects but this increase in mass reduces cylindrical whirl speed.) Also noted is that reducing the bearing radius increased both the translational and conical whirl speeds along with reducing the optimum bearing length.
(2) A region of clearance exists where the whirl speed becomes independent of clearance. When the clearance is reduced then the whirl speed increases rapidly and the opposite effect also occurs, at large clearances a reduction can worsen stability.
(3) Increasing head at onset of instability increased the stability threshold.
(4) An increase in ambient pressure seemed to reduce the whirl onset speed.
(5) At small clearances and low eccentricity, an increase in

viscosity improved stability, whilst at high eccentricities and large clearances this effect is reversed.

(6) For small bearing centres Marsh found that the conical mode was dominant and for large centres that cylindrical whirl was dominant. Conical whirl onset speed increased with bearing centre increase, but cylindrical mode showed no change.

(7) Slotted bearing instability speeds were higher than plain bearings which agreed with Whitley and Betts and Whitley, Bowhill and McEwan.

(8) He observed that for a flexible mounted bearing system there existed two half frequency whirl speeds, one of which could be advanced through to a stable region beyond if damping is present. However the second instability could not be passed through.

(9) At low compressibility numbers the stiffness of the shaft is far greater than that of the gas film. The system then behaves as if the shaft were rigid. Conversely at high compressibility numbers the shaft acts as a simply suported beam.

Marsh concludes that his approach is based upon a linearization of the pressure field for small motions of the journal centre ($\varepsilon_{max} \Rightarrow 0{\cdot}6$). He claims that his approach is for rigid and flexibility mounted systems, flexibility being examined via a spring anology. He extrapolates a single bearing approach to dual bearings neglecting assymetry. Dynamic loadings and forced vibrations are not examined.

Kerr (65) in 1966 in an N.E.L. report carried out tests on a symmetric rotor mounted in glass bushes flexibly mounted in 'O'-Rings. He noted that when bush / journal rubbing or touchdown occured displacements were measured at up to three times the level of clearance of the bush.

Kerr carried out tests for an unbalanced rotor and found that a greater stiffness is required for the cessation of whirl than that of a well balanced rotor. Kerr further noted that although 'O'- Ring damping coefficients varied by a ratio of 5:1 over a range of frequencies experimental whirl results appeared to depend mainly upon

stiffness. Finally he concludes that it was possible to proceed through the first instability to a region of stability beyond, and that the onset speed of half frequency whirl was not affected by stiffness, unlike Marsh's observations.

Lund (66) in 1968 presented a paper on the stability of a symmetrical flexible rotor supported in journal bearings. The bearings being mounted in flexible damped supports. His analysis is based upon the assumption that the bearing can be represented by frequency dependent spring and damping coefficients.

The conclusions he formulated were:-

(1) Rotor and support flexibilities by themselves lower the speed at onset of instability.

(2) When the bearing support possesses damping in addition to flexibility the speed at onset of instability can be raised significantly above the threshold of a rotor in rigidly mounted bearings. His results were in the form of curves.

Elrod, McCabe and Chu (67) in 1967 presented an approach based upon Duhammels Integual Theorum and determined the stability of the rotor bearings by its response to a step - jump and using a growth factor. Results were restricted to the infinitely long bearing and a idealized symmetric rotor, two bearing system. The bearing centres being placed far enough apart to neglect conical misalignment effects on forces and torque. Support flexibility is not considered therefore the method is restrictive in its use. They reduced the C.P.U. time over methods using complex variables.

Powell and Tempest (68) in 1968 carried out an extensive study of high speed machines with rubber stabalized air bearings. The gas bearings were of the Aerostatic or Hybrid type.

In their paper it was stated that Montgomery and Sterry were the first to use flexibly mounted bearings in an air turbine in 1955. The turbine was for rotating a mirror at high speeds. The bearings

were porous aerostatic sintered bronze. They successfully operated at speeds up to 258,000 Rpm.

Also mentioned was Powell and Tempest's work on a dental drill turbine in 1962 which had flexibly mounted aerostatic bearings. Two 'O'- Rings being used per bearing (acting as an air chamber). The normal operating speed of the drill was 450,000 - 500,000 Rpm with experimental units running as fast as 750,000 Rpm.

Powell and Tempest stated that Engineers at this time were sceptical of using rubber for damping purposes for two main reasons:-

(1) Many Engineers regard rubber moulded components as not sufficiently consistant in dimensional accuracy for use in precision Engineering.

(2) Lack of Engineering information from rubber 'O'- Ring manufacturers concerning their dynamic properties and the difficulty in obtaining them at that present time.

As Kerr, they noticed that unbalance, when running at speeds approaching the onset of instability could excite ½ frequency whirl when not running at the critical frequency. Also observed was that static unbalance excited cylindrical or translational whirl and dynamic unbalance excited conical whirl. Both these onset frequencies could be passed through if unbalance was within appropriate limits, however they did not quantify this statement. A mathematical model representing the 'O'- Ring was shown to be made up as complex stiffness with real and imaginary components. Damping not considered some useful points regarding dynamic properties of rubbers were discussed, with five major factors affecting the complex stiffness of rubber 'O'- Rings:-

(1) Type of rubber compound.

(2) Share hardness number.

(3) Filler - percentage.

(4) Temperature.

(5) Frequency of induced vibration.

From this study they produced a simplified model highlighting two important factors to be considered for 'O'- Ring systems:-

(1) To be effective in absorbing energy of the whirl, 'O'- Rings must have a high loss angle and a low modulus. The criterion being Sin δ (ω) / A (ω) should tend to a large number. δ (ω) = loss angle (argument) A (ω) = stiffness modulus.

(2) A high gas stiffness assisted energy absorption. Butyle rubber from their study had the highest loss angle 9° - 26° at room temperature 20° but deteriorated to 4 - 6° at 70°C.

Silicone rubber had more consistent loss angles for Temps 20 - 70°C being 5·1° and 4·6° respectively.

Viton (Fluronated Hydrocarbon) had good temperature properties but loss angle was not recorded.

Butyl would therefore be suitable for machines operating at room temperatures and for machines operating over a wide temperature range Silicon or Viton would be more suitable, since each has more consistent properties. With an increase in temperature was noted that Sin δ (ω) / A (ω) decreased so that a position could be found where for certain temperature conditions whirl may not be contained with the use of Butyl.

From this can be deduced that Silicon and Viton whose parameters vary least with temperature would be better suited and it was also varified in the tests.

Powell and Tempest concluded that:-

(1) At ambient temperatures for all of the rubbers tested, low shore hardness values are better employed below 60°.

(2) At elevated temperatures 80 → 160°C Viton and Silicon 'O'- Rings can only be used.

(3) The effectiveness of all rubbers tested decreased with increase in shore hardness.

(4) The effectiveness of all rubbers tested tended to decrease with increase in temperature but only slightly for Viton 'O'- Rings.

(5) A high loss angle is desirable and of all rubbers tested Butyl performed best, at room temperature though.

(6) Increase in gas film stiffness increases the energy absorbed by the 'O'- Rings.

(7) Harder rubbers can be used in larger machines and softer ones in small machines.

(8) Mass and inertia of the bearing shell must be minimised as a high mass or inertia can give rise to destructive bearing whirl.

(9) A reduction in bearing clearance can increase bearing stiffness.

(10) 2 - 12% precompression (squeeze) was found to have no significant effect upon the whirl stabilization.

Smalley, Tessanik and Badgley (69) in 1975 produced a paper on the testing of dynamic properties of materials dealing with elastomers in particular.

Elastomer deformation properties were investigated and found to be governed by a process of relaxation. Displacement for a given load relaxes with time reaching an assymtotic value. For very short periods of time the displacement for a particular load will be much lower than this assymtotic value. Thus for repeated loading hysterssis occured. The area under this loop is the energy loss per cycle. They mention that this characteristic will dissipate vibration energy and thereby dampen vibrational motion.

For such a system the material behaviour is linear (stiffness) but the damping is unique to any one particular vibration frequency. Also found was that the damping in the system was equal to the area of the Hystereris loop divided by the square of the peak amplitude and π. Also stiffness is equal to the force at maximum displacement divided by the peak amplitude or displacement. Dynamic stiffness was observed as being higher than the static value and increases with increase in frequency.

Three regions were found present in the Dynamic behaviour of elastomers:-

(1) Rubbery.

(2) Transition.

(3) Glass.

In the rubbery region damping was in the order of 10 - 30% of the stiffness, the Hysteresis loop being a narrow ellipse growing larger with increasing frequency. For a limited frequency range damping became higher than stiffness and the loss coefficient became greater than unity.

Therefore the Authors best test parameter suggested is dissipation. To measure dissipation the displacement signal must be constantly differentiated and multiplied by the force signal to give an instantaneous rate of doing work. The D.C. level being the average rate of work.

Smalley, Darlow and Mehta (70) in 1977 produced a paper concerning the testing of Viton 70° and 90° 'O'- Rings as a means of damping amplitudes of Aerodynamic bearings.

They investigated the following parameters:-

(1) 'O'- Ring material.
(2) 'O'- Ring cross-section.
(3) Temperature.
(4) Amplitude.
(5) Squeeze.
(6) Stretch.
(7) Groove width.

Smalley et al made measurements of dynamic stiffness and damping by means of a vibrating table with an acceleameter mounted on the table and one on the 'O'- Ring mass system, resulting in phase being measured, a phase shift of 90° inferring damping. With further increase in frequency they observed stiffness increased more than damping, levelling off at loss values of 0·3 or less.

Difficulties of maintaining controlled tests with the three major requirements were encountered:-

(1) Uniform stress.

(2) Uniform temperature.

(3) Low amplitude.

The Authors mentioned the problem of maintaining uniform stress and strain, since difficulties and contraints upon geometry were imposed. This limited ideal testing to shore tests only.

For uniform temperature tests since the elastomers were very sensitive to increase in temperature lack of uniformity resulted in variations in material and element properties throughout test specimens.

Low test amplitudes were found under dynamic loading to be important in establishing material properties because of the effects of dissipation when amplitudes are high. For low temperature rise dissipation had to be kept low at all frequencies. Therefore, amplitude was a poor test criterion since costant amplitude implies a wide variation in dissipation.

They carried out tests at temperatures up to 232°C. Their results with Viton 70 'O'- Rings showed that for a pair of 'O'- Rings:-

(a) Stiffness at $100H_z$ was 5×10^{6} N/m.

(b) Stiffness at $1,000H_z$ was 12×10^{6} N/m.

(c) Values of loss coefficient damping/stiffness were 0·7 → 1·0.

These results indicated that Viton 70 was a good damping material at room temperature and showed that it was a material in the transition region.

An interesting aside is that Viton 70 stiffness at 1KHz is over nine times its static stiffness ($1\cdot315\times10^{6}$ N/m).

Under temperature variation tests it was found that stiffness fell by a factor of over two for a temperature range between 25 → 66°C and the loss coefficient by a factor of 4. Above 66°C effect of temperature were found less pronounced and no change in stiffness was observed above 149°C. The Authors also studied the influence of

squeeze and stretch upon stiffness and damping properties. An optimum value of 15% squeeze was found to be the least sensitive value to stiffness properties, with squeeze as low as 5%, stiffness falls off sharply and contact between ring and steel is sometimes not maintained. When squeeze and stretch were contained the effective squeeze was not maintained since the cross-sectioned area was reduced.

At values of 5% squeeze the loss coefficient fell by 0·25 however for 15% they found that little effect was made. Finally, the Authors found the following effects:-

(1) Material and squeeze are the parameters which may offer the most direct control over the dynamic characteristics of 'O'- Rings.

(2) Large variations have not been observed the effects of stretch, cross- sectional area and groove width upon the dynamic characteristics of Viton "O" rings.

(3) Temperature and vibration amplitude have a major effect on 'O'- Ring characteristics.

(4) The high loss coefficient of Viton 70 'O'- Rings falls off sharply with temperature increase, stiffness also has a similar effect.

(5) Increasing amplitude decreases the effective stiffness and loss coefficient of Viton 70 'O'- Rings.

In 1979 Marsh and Simmons (71) (72) presented a pair of papers on an experimental method of determining Journal Bearing Stability Parameters. The first paper deals with the theoretical approach, devised by Marsh in his Ph.D. For a flexibly mounted bearing system experiments have shown a region of stable operation at low speed, a first whirl onset, a region of Instability, a whirl cessation speed, a bigger region of stable operation and a second whirl onset speed. Marsh and Simmons claim that if some damping was present in the mounting, then with a low value of mounting stiffness the first whirl onset and the first region of Instability may be suppressed. The system is then stable at all speeds less than the upper whirl onset speed. Marsh and Simmons state that for small damping, cessation

appears to correspond with the condition S = $K_{c1}^2 \gamma_{1m}$. By varying the stiffness of the Bearing Mount Marsh and Simmons suggest that design data for Rotor operation at speeds far in excess of whirl onset for a Rigidly Mounted Bearing System can be obtained. The Authors claim the principles to be general and the analysis relates to any Bearing System and Lubricant.

Simmons 1979 (72) presented the second paper. The design of an apparatus for the experimental determination of Journal Bearing Stability Parameters. The Test apparatus consisted of a Bearing (Rotor) fixed on two thin canti-levers bars which were supported in adjustable clamps fixed to a massive base. The clamps were adjusted (re-positioned) to change the bending stiffness of the bearings and hence vary the support stiffness of the bearing. The rotating member or bearing was a hollow steel shell, machined such that further disc weights could be attached to vary Inertia/Mass and also unbalance characteristics.

The support system was vibrated to determine the modal characteristics of the support. The stiffness value So was used to determine the Cessation speed ωo. The experimental work enabled a relationship for the test apparatus such that: $\omega_1 = \omega_o (M_B / (M_B + M_R))^{1/2}$ was derived for the first whirl onset.

Simmons also found that whirl cessation took place at a running speed which is twice the natural frequency of bearing alone upon its supports. ($\omega = 2\omega o$). Simmons claimed that ω_1 appeared < $(So / M_B + M_R)^{1/2}$ and $\omega_2 > (So / M_B)^{1/2}$.

Preece (73) in 1986 investigated the dynamic stiffness and damping characteristics of a bearing shell mounted in 'O'- Rings. He used Modal Analysis techniques to determine stiffness and damping characteristics. The test apparatus consisted of a vibrating loud speaker Cone forcing the bearing shell mounted in 'O'- Rings in an Aluminium block representing the geometry of the 'O'- Ring mounting

assembly. He vibrated the bearing assembly under constant force and varying the frequency (0-1,000 Hz).

Preece studied the effects of bearing mass and inertia, 'O'- Ring materials, temperature effects, Viton and Silicon 'O'- Ring materials and percentage squeeze on 'O'- Ring cross-section.

For percentage compression of 10% one saw an increase in damping and stiffness and hence resonant frequency. Above this one saw a drop in damping and the natural frequency was almost totally stiffness driven. Bearing mass variation saw a drop in resonant frequency with increase in mass.

The effect of 'O'-Ring compression seemed to be one area that may be exploited and required further investigation. This was to give interesting results as can be seen in Chapter (10).

CHAPTER 8

DUAL BEARING ROTOR (PHASE II) TEST RIG

8·1·1 DESIGN OF DUAL BEARING ROTOR TEST RIG

Having proven the proximity probe system on the Single Bearing Test Rig (Phase I), a new Test Rig was designed and constructed. The design was initiated and created to investigate the Dynamic behaviour of a C.A.U. rotor in bearings on elastomeric flexible mountings.

The design of the rig consists of three parts:

(1) The Drive Module.

(2) The Rotor Test Module.

(3) The Data Acquisition and Signal Processing System.

Plate (8·1) shows the general arrangement of the Test Rig and its associated Instrumentation. Plates (8·2), (8·19) and (8·5) show the Drive Module, Test Module and Rotor Bearing System respectively.

8·2·1 DRIVE MODULE

The feasibility of a new drive system was assayed after certain problems encountered with the single bearing test rig drive. An investigation of drive motors, pulley systems, high speed rolling contact bearing lubrication and sealing problems were undertaken.

The design consists of a high rigidity fabricated subframe, embracing an electrically controlled variable speed motor, driving a low inertia high speed belt, friction pulley system. The design

theoretical speed capability of the unit is 90,000 Rpm at Final Layshaft output.

The Final Drive Layshaft consists of a newly designed high speed preloaded rolling contact bearing arrangement, lubricated by a pressurised oil mist system which incorporates an oil mist Hydrodynamic disc seal arrangement (Thew Seal). See Chapter (6) for detailed investigation.

8·2·2 DRIVE MOTOR SYSTEM

Problems encountered with the single bearing Test Rig DC motor, encouraged an investigation into alternative types of Drive Unit. An electronic Drive System was chosen due to its instantaneous controllerbility through Dynamic braking etc. A survey of motor types was carried out to ascertain the optimum design and type of unit. Due to the non-availability of high speed motors, maximum speed was restricted to 3,000 Rpm. Variable speed motors can be categorised into two main groups:

(1) Variable Speed DC.

(2) Variable Speed AC.

The DC variable speed drives comprise two types of motor.

(1) Permanent Magnet type. (Variable Armature).
Maximum speed 5,000 Rpm at 2 hp (max), permanent field.

(2) Standard DC Motor. (Variable Armature and Field).

AC variable speed motors also formed two categories:

(1) Variable Frequency (two pole motor where the coil frequency is varied from 50 Hz @ maximum speed to 2·5 Hz @ minimum rated speed). (Closed or open loop systems available).

(2) Variable Voltage (brush gear of the motor is moved in and out of contact with the armature of the motor thus varying the speed of the motor), (open loop system).

Depending upon ones requirements the two types of variable speed motor AC/DC have the following merits.

If constant torque variable speed is required and a wide speed band (100/1) the DC Thyristor type should be used, however at the expense of drive compactness. If a moderate speed range is required (20/1) then an AC drive offers a more compact drive layout. However, torque calculations are critical and should be based on lowest speed range and referred to Manufacturers for their comments. (Since units are derated due to power factor dropping with reduction in excitation frequency). Due to the drive compactness a variable frequency AC unit was chosen with a 20:1 speed reduction or range. Fig. (8·1) and Plate (8·1) show the motor mounted on the Drive Subframe. An advantage of motorised drive system over an air impulse type is that due to dynamic braking of motor inertia control at onset of instability is guaranteed, not so for air impulse driven rotors. ie. not easy to slow since no inertia in air flow.

8·2·3 PULLEY RATIO SYSTEM

This consisted of a double increase pulley system. Pulley material was Aluminium Alloy 7075TE. This material has a high proof stress of 380 Mpa, the pulleys had a correspondingly low inertia approximately a third that of steel. The two step increases were 20:1 giving 60,000 theoretical top speed and 30:1 giving 90,000 Rpm the top speed. Each speed increase was the square root of the total speed increase ie. √20 and √30. Aluminium is not a particularly good traction surface for pulleys due to the oxide layer depositing onto the drive belt which reduces tractionability.

There are two ways of overcoming this:

(1) Deep Anodise the Pulley.

(2) Coat the Traction Surface.

Method (2) was chosen since it is relatively inexpensive compared to (1) and one can also apply a suitable wear resistant material to optimise tractionability and wear. The coated pulleys can be seen in Plate (8·2). The surface coating finally chosen was Metco 447 which consists of Molybdenum - Nickel - Aluminium composite. It is a general purpose "tough coating" and is self-bonding, tough, internally strong and has good wear resistance even in applications with a degree of impact wear. Resistance to abrasive wear is better than 18-8 stainless steel and slightly less than a high chrome stainless and Molybdenum. Hardness is Rb 75-80 and in the sprayed condition a surface roughness of 450-550 (micro inches aa).

The coating is applied by plasma torch which does not heat the surface more than 100°C. Therefore precipitation heat treatment of 7075TE is undisturbed. The crowned drive surface of the pulleys was initially shot blasted to enable strong metallic bond between pulley and coating. The Belt Manufacturers stated that a Pulley length approaching 4" (100 mm) was required to run at 60,000 Rpm. Due to the surface roughness pulleys were manufactured to 30 mm long and in the tests no significant wear was found on the pulleys, or did the belts track sideways and leave the pulleys, standard crowning values being used.

It can therefore be concluded that this type of application is very successful since many millions of cycles would have been acccumulated during testing and no surface damage could be seen anywhere.

The belt chosen for the Pulley system was a Stephens Miraculas Extremulus type and could withstand surface velocities up to 200 m/s. Plate (8·1) and Fig. (8·1) shows the system of belts, pulleys and shafts, (note the plasma sprayed traction surfaces) on the Drive Module Assembly.

8·2·4 LAYSHAFT SYSTEMS

The Intermediate Layshaft system consisted of a 25 mm diameter shaft supported by rolling contact ball bearings in oil bath lubrication (SAE20 oil). Fafinir Bearing Block DRN1. The pulley ratio at this stage was either ⁄20:1 or ⁄30:1. This can clearly be seen in Fig. (8·1) and Plate (8·1).

8·2·5 FINAL LAYSHAFT (HIGH SPEED HOUSING ASSEMBLY)

The final layshaft system consisted of a Fafnir DRN1 Bearing Block bored to carry a steel sleeve. Inside the sleeve were two pairs of Fafnir (2 mm-202W1CR DUL) Angular Contact Bearings, which supported the layshaft spindle. One pair at the driver end were fully located, whilst at the other, a pair loaded to 20 lbf by a spindle sliding sleeve arrangement. At each end seals of the arrangement were 'Thew' seals, designed and developed to run with an oil mist environment, see Chapter (6).

The oil mist was supplied at 10 psi through an oil mist regulator unit. At the driver end was attached a 38 mm diameter crowned Alloy Drive Pulley (fixed by 'Loctite' and located by the end screw). The high speed housing assembly was bolted to the subframe and located by dowels. Fig. (6·14) and (8·2) and Plates (8·1) and (8·2) show the design and construction of the Assembly.

8·2·6 DRIVE TENSIONING

Belt tensioning was carried out by the adjustment of the motor and intermediate layshaft sub-assembly. Both were mounted on separate baseplates key located in the fabricated subframe and locked in position by bolts. See Fig. (8·1) and Plate (8·1).

8·3·1 ROTOR TEST MODULE

The drive unit is coupled to the test rotor via a low inertia drive coupling and a diaphragm/quill shaft assembly. Plate (8·3) Coupled to the opposite end of the rotor via another diaphragm/quill shaft arrangement is a Telemetry sub rotor or alternately a slip ring assembly. Excitation and output wires for the rotor mounted pressure transducer are carried through the hollow quill as shown in Fig. (8·2) (air bearing rotor assembly). The Telemetry system is housed in a small rotor mounted on a Hybrid air bearing sub assembly, see Fig. (8·3), coupled to the test rotor by a diaphragm/quill shaft arrangement.

Connected via another diaphragm/quill arrangement is the voltage excitation system for the Telemetry Transmitter and Pressure Transducer. This is a high speed (gold plated contacts) slip ring system mounted on a support bracket. The Telemetry and slip ring assembly form the Data Acquisition System.

8·3·2 TEST ROTOR CAPABILITIES

The Test Rotor is capable of modelling a Cool Air Unit or any Turbo Machine type device, but has additionally the following variable parameter capabilities:

(1) 'O'-Ring Stiffness (via Material, Geometry and Pressurization).

(2) 'O'-Ring Mounting Centres in Bearings.

(3) Variable Gyroscopic Properties.

(4) Variable Mass.

(5) Rotor Perturbation Monitoring.

(6) Bearing Perturbation Monitoring.

(7) Central Dynamic Pressure Profile Capture.

(8) Variable Unbalance Forces.

(9) Variable Speed.

(10) Variable Bearing Air Flow / Stiffness

8·3·3 ROTOR SYSTEM

The rotor was manufactured from EN24T (817M40) and basically a bored tube of inside diameter 20·00/20·02 and outside diameter (Journal) of 29·997/29·974. At each end of the Rotor were an external shoulder and fine thread (M28x1·0p). This was used to mount the disc of variable Gyroscopic properties by their locking rings via the M28x1·0p threads. See Plate (8·4).

At the centre of the rotor can be seen a 32 mm diameter shoulder and M32x1·0 pitch thread. This was used to mount a central disc and locking ring to simulate the C.A.U.s Thrust Bearing Disc. See Plate (8·4).

The discs at each rotor end were to model Gyroscopic, mass and unbalance properties of a Turbine, Compressor or Impellor. The disc material was EN24 (817M40), hardened and tempered to conditions U (70 TON/in^{2}UTS, and 50 TON/in^2 yield minimum).

The disc pairs diameters varied from 40-90 in 10 mm steps. One additional pair were 90 diameter and had provision for balancing weights to be added. The mass of the disc varied from 0·1 Kg → 0·3 Kg with a variation of mass moment of inertia from $0{\cdot}285 \times 10^{-4}$ Kgm^2 → $2{\cdot}60 \times 10^{-4}$ Kgm^2 respectively. Disc design and construction can be seen in Fig. (8·2) and Plate (8·4).

The rotor and discs were manufactured to exacting Tolerances. Talyrond roundness and concentricity plots were taken for each

rotating component. An aluminium rotor and discs were also manufactured to the same design, the journals were however produced by plasma spraying a journal surface from Metco 447. Plate (8·4) shows rotor and disc construction. Plate (8·5) shows rotors manufacture, two steel EN24T and one aluminium 7075TE, in foreground.

8·3·4 BEARING SHELLS

The bearing L/D ratio was fixed at 1·0 so as to simulate the dynamic behaviour of the C.A.U. bearing bush. Initially six bearing pairs were designed and manufactured with varying 'O'-Ring centres (5·0 → 25 mm) and can be seen in Fig. (8·2) and Plates (8·6) and (8·8). Bearing material was EN3A and following turning and grinding they were sulfinized. Bearing nominal inside diameters were 30·005/30·002 and nominal outside diameter was 36·00 ± 0·05 prior to sulfinizing. After sulfinizing no significant bearing movement was detectable due to stress relaxation following the machining process.

Following initial tests a central plane of 8 jets, of 0·0015" diameter, were drilled into the bearing bushes to aid the start up condition. The motor controller had difficulty at low speed start up because, the motor torque drops off to next to nothing at low revs below the 20:1 speed reduction. The rotor was then able to start satisfactorily with the bearings operating in a Hybrid manner.

However, it does mean that the bearings tested were not strictly plain bearings. However Marsh used the same type in his experimental work. It was thought that the size of hole would not diverte the performance much away from Aerodynamic behaviour. Results do however indicate that the plain bearings instability is manifest at a lower speed than Hybrid Air Bearings.

Three pairs of porous bearings were designed (modified from oilite BM5 30ID × 38OD × 40 long). (25,20 & 15 mm 'O' Ring centres). These were used as a comparison to Montgomery and Sterry's (54) findings

with the Rotating Mirror. Hence the test programme proper was a comparison of flexibly mounted Plain, Hybrid and Hybrid Porous Bearings operating with an L/D ratio of 1·0 and a bearing nominal bore of 30 mm. Plate (8·6) indicates the plain modified bearings. Plate (8·8) shows modified porous bearing of 20 mm 'O'-Ring centres. The 20 mm porous bearings were damaged whilst initially testing and a set of results was not obtained for this size. The process of removing the impregnated oil and etching the porous bearings is mentioned in more depth in the Telemetry Rotor System Design, in Section (8·5·9).

8·3·5 DIAPHRAGM QUILL SHAFT ASSEMBLY

A major problem of connecting the test rotor to the Drive Module was the design of a suitable coupling device. A survey carried out regarding the state of the present Art Proceedings of the International Conference on Flexible Couplings for High Speed and Powers, suggested that for high speeds only a quill shaft was appropriate. See Plate (8·7). However, the major difficulty with this type of device is that they generally have to be slender flexibility manifested by loose fitting splines or end fixings. Slenderness of quill enables a certain degree of bending flexibility.

For the test rotor the major drawbacks of this type are:

(1) End fixing complexity.

(2) Critical speed of quill.

(3) Due to quills mass and slenderness an interference of rotor systems natural characteristics.

It was decided that what was sought had to satisfy the following criteria:

(1) Decouple the test rotor from drive in both the Translational and Conical modes of Vibration (Flexibility).

(2) Ability to allow electrical leads to pass through centre.

(4) High stiffness.

(5) Withstand Rotational Stresses.

(6) Reasonable Fatigue Strength.

(7) Transmit Torque.

The final design of device consisted of a hypodermic stainless steel central tube, with, fixed at both ends Be.Cu. diaphragms. Due to the Mechanical Integrity required, three constructional methods were considered:

(1) The design consisted of separate coupling diaphragm components silver soldered together.

(2) The second consisted of a fully machined from solid diaphragm coupling, however putting restrictions upon diaphragm thickness.

Testing of the above two devices proved that their flexibility was inadequate and buckling of the couplings soldered diaphragm occurred.

(3) The final design consisted of placing the diaphragm at the extreme end of each coupling. This enabled the coupling diaphragm to be fully turned to desired tolerances. The coupling was then placed face down in a jig and the end face ground until a 0·003" diaphragm thickness was accomplished.

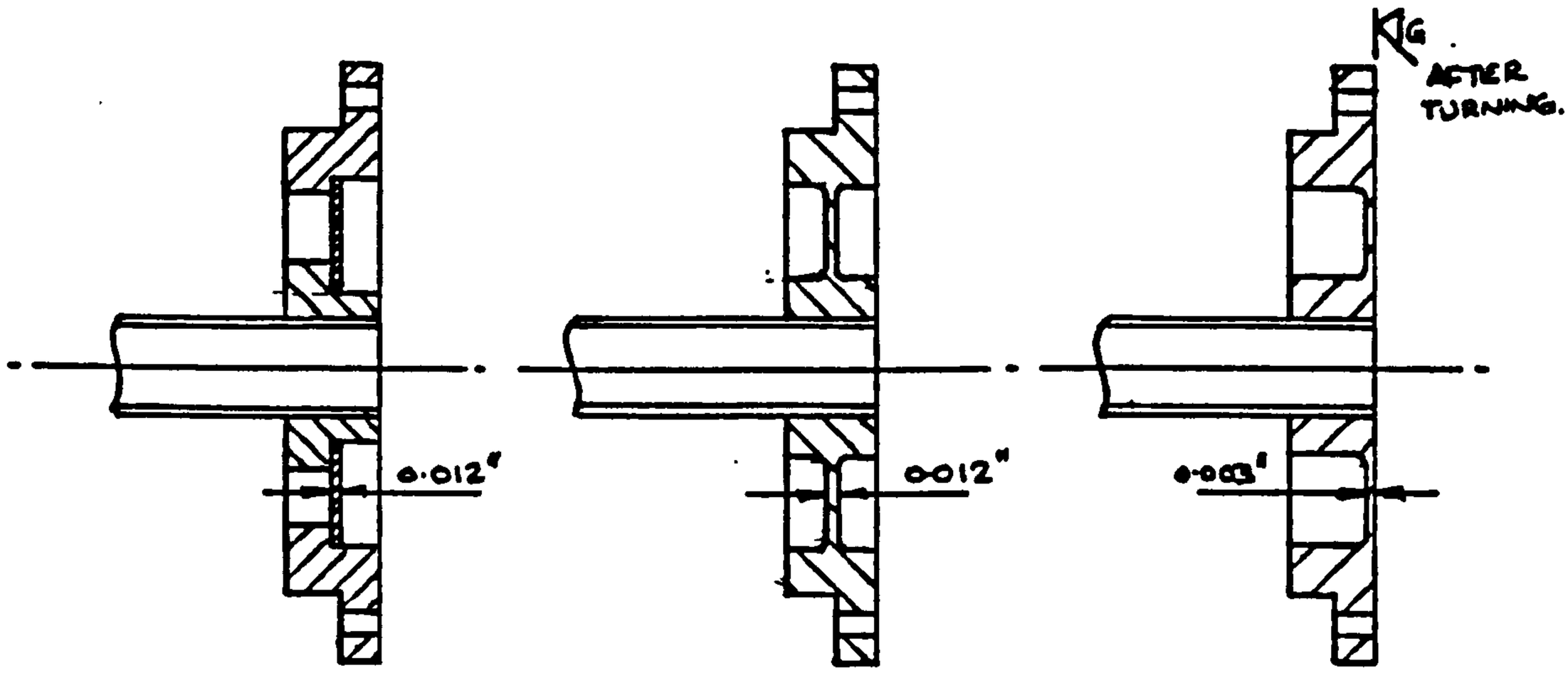

Type (1) Soldered Type

Type (2) Solid Fully Machined

Type (3)

Fig. (8·4) Diaphragm Designs

The Diaphragms were heat treated for one hour @ 400°C.

Types 1 & 2 had restricted diaphragm thickness due to the requirement of stability whilst turning. Type 3 had the stability requirement then was finally ground to the diaphragm finished thickness (0·003").

Plate (8·7) shows the type 3. Plate (8·8) shows failed type 3 caused by fatigue of diaphragm at the point of the maximum bending stress.

8·3·6 BEARING BRACKET ASSEMBLY

The bearing bracket was designed as an easily dismantled bolted and dowelled structure with a high degree of rigidity. The bracket is located on the concrete baseplate by dowels, its position being pre-determined by the Drive Module. Centre height and axes alignment precedes final dowelling. An inordinate amount of time was spent ensuring the bracket was aligned as exactly as humanly possible.

However, some setbacks arose due to machining errors of outside sub-contractors which our University workshops kindly rectified.

The bearing bracket has the following parameter capabilities:

(1) Variable 'O'-Ring stiffness (via material and geometry).

(2) Variable 'O'-Ring mounting centres.

(3) Rotor perturbation monitoring.

(4) Bearing perturbation monitoring.

(5) Variable bearing air flow / stiffness

Fig. (8·2) shows the Air Bearing Rotor Assembly. Fig. (8·2) and Plate (8·1) show the Bearing Bracket Assembly.

8·3·7 'O'-RING STIFFNESS VARIATION

Initially 5 types of 'O'-Ring material (Silicon, Polyurethane, Nytrile, E.P. and Viton) were considered. However, the final testing was restricted to only Nytrile, Silicon and Viton types due to limited availability from manufacturers. The 'O'-Rings were of type BS 220 cross-sectioned diameter 0·139" and internal diameter of 1·359". All 'O'-Ring shore hardness were nominally 70. Although the 'O'-Ring materials had nominally the same shore hardness it is true to say this is not the case with Dynamic stiffness. This is discussed in greater detail in Chapter (10). 'O'-Ring stiffness was further varied during testing by pressurising the chamber between the 'O'-Rings with air, (up to 120 psi).

8·3·8 'O'-RING MOUNTING CENTRES

Two types of Bearing Flange were designed to enable the six bearing 'O'-Ring centre variations to be tested (5, 7·5, 10, 15, 20 & 25). One Flange accommodated 5-15 mm centre variations whilst the other 20-25 mm . Plate (8·9) shows both Bearing Flange types and a Flange Insert. The insert enabled the bearing Flange to satisfy a variation of centre distance. The bearing Flanges were accurately located in the End Plates of the Bearing Bracket and securely bolted and dowelled. Therefore locking in position the bearing in its 'O'-Ring mountings. Fig. (8·2) shows the 'O'-Ring centre variation clearly and indicate the application of the Flange Inserts. One can also see the Plenum Chamber formed by the 'O'-Rings. This was used to carry out stiffness variation (due to pinch) by air pressurization. Plate (8·10) shows the location of the Flanges in the Bearing Bracket.

8·3·9 ROTOR AND BEARING PERTURBATION MONITORING

Another particular reason why two types of bearing Flange were designed was to accommodate proximity probe location. Fig. (8·2) shows clearly the condition arising when using 'O'-Ring centre bearings greater than 15 mm. Thus the bearing proximity probe is then able to monitor the bearing movement by being positioned in board of the 'O'-Ring. However, this requires the proximity probes to be completely leakproof. For centres ‹ 15 the proximity probes are monitored outside the 'O'-Rings as indicated in Fig. (8·2) and Plate (8·10). Fig. (8·2) shows the location of the probes in the Bearing Bracket with 'O'-Ring centres ‹ 15 mm.

Rotor perturbations are monitored by proximity probes mounted on the extreme of the bearing Flanges. One can also see in Fig. (8·2) and Plate (8·10) that micrometers are mounted in the Horizontal and Vertical planes of the Assembly. This is to aid insitu probe calibration without the requirement of Rotor removal from the bearings. A light load is applied to the Rotor to ensure that the micrometer is always in contact, via its anvil, during calibration.

It also means that all probes in a single plane can be calibrated in one set of micrometer movements. This greatly speeds calibration, several calibrations can be carried out during a set of tests if required.

8·3·10 VARIABLE BEARING AIR FLOW

At the onset of the Air Bearing Rotor Assembly design a provision for bearing pressurization was incorporated. This as it turned out proved to be an invaluable asset. Due to problems associated with low motor torque at initial starting, it enabled Aerostatic starting to be incorporated. This eleviated wear and high motor starting torque where fully developed Aerodynamic lubrication was not present.

Bearing Feed Air Pressure was registered on the Filter Regulator Unit and the flow rate monitored via a Fisher Porter meter (¼" steel ball Tri Flat). Hybrid and Porous bearings were able to be compared with plain bearings during testing.

An investigation into 'O'-Ring squeeze was carried out. This was prior to the plain bearings being modified. The bearing Plenum Chamber was pressurized at 0, 60 and 120 psi. Stiffness parameters were measured for the three different types of 'O'-Ring material at each test pressure. Plate (8·1) shows the pressurised air system and flow meters used in the tests mentioned previously.

8·4·1 DATA ACQUISITION/PROCESSING SYSTEM

The system consists of the following: a Telemetry and Slip Ring Assembly (to monitor Dynamic Central Pressure Profile), a Rotor and Bearing perturbations Monitoring System and a Speed Sensing Device. An Entran pressure transducer mounted in the Rotor is excited via a Telemetry Transmitter, itself initially excited via a high speed slip ring assembly.

The output signal is received in the transmitter and sent to the receiver which can output either a Digital or Analogue signal. Rotor and bearing perturbations are monitored by 8 active and 8 dummy inductance probes. They are excited by CIT Amplifiers and the probes output are captured on a Digital Storage Oscilloscope. The Digital information can therefore be either sent along an IEEE Interface to a computer, or on to an XY plotter for a hard copy of the screen information. Speed was monitored and recorded on a Phillips Digital Frequency Counter with storage facility. The sensor also produced a phase marker for the whirl Trajectories and Lissajous figures.

8·5·1 TELEMETRY SYSTEM

The use of the Telemetry system is to transmit central pressure profile data from the rotating shaft system, at invisaged speeds up to 60,000 Rpm. A literature survey revealed four main methods of Telemetry Transmission (transmissions of data over a distance).

8·5·2 FREQUENCY MODULATION

Carrier frequency is varied in direct proportion to the variations ocurring in the measured parameter (strain from pressure transducer). At the receiver these variations are converted to a correspondingly varying voltage, the size of which is directly proportional to the measured parameter. FM systems have the widest frequency response and lowest cost per single channel. Measurement systems. Not applicable where the measured parameters change slowly - less than ten times per second. Noise immunity is less than most other systems except amplitude modulated (AM) systems. Can be used in hazardous conditions up to 50,000 g acceleration and temperatures of 175°C.

8·5·3 FREQUENCY MODULATED SUB-CARRIER SYSTEMS

Uses a double FM (FM/FM) method, where variation in the measured parameter vary the frequency of an Audio-Frequency Sub-Carrier in the transmitter. The sub-carrier then frequency modulates the

transmitters RF carrier. At the receiver two conversions take place. The first extracts the sub-carrier from the received signal, yielding an audio frequency (AF) signal whose frequency is Analogous to the size of the measured parameter (suitable for direct recording onto magnetic tape). The sub-carrier audio frequency signal is then "discriminated" to a voltage which corresponds to the measured parameter. FM/FM offers superior noise immunity, reliable measurement of static and slowly changing parameters as well as those changing at moderate rates. Frequency response is limited to 20% of the sub-carrier frequency (measurement frequency is 2000 Hz for a sub-carrier of 10 KHz), temperatures up to 175°C.

8·5·4 PULSE CODE MODULATION

Input data is converted to a digital code, then transmitted as a series of pulses comprising shifts in carrier and sub-carrier frequency. The pulses can be binary, binary coded - decimal or other standard digital codes.

Receiver demodulates the transmission, extracting the pulse code as logic level shifts and presenting the data in either digital form, or after digital to analogue conversion as a voltage analogue of the input signal (pressure change). PCM has the greatest potential accuracy since effects of analogue drift are limited to circuitry before the analogue - to - digital converter in the transmitter and after the digital - to - analogue conversion in the receiver whilst in use.

Adaptable to high speed time division multiplexing for several parameters in one radio link. Noise immunity is excellent and cost is reasonably low.

Due to (general) unbolted constructions of Electronics restricted to less arduous operating conditions (vehicles operating on test tracks where data is transmitted to stationary receiver).

8·5·5 PULSE AMPLITUDE MODULATION

PAM transmits multiple measurements over a single radio link by sending a series of pulses. The amplitude of each pulse being the analogue of one measurement point. Standard PAM transmits the pulses as a frequency modulation of a sub-carrier in a FM/FM transmitter. In principle, PAM operates as the FM/FM equipment except that the measurement input to the transmitter is multiplexed.

Excellent stability and noise immunity. Available in extreme environment package up to 30,000 g, 125°C. Lowest cost per channel for multi-channel applications. Frequency response is limited by the sample interval.

8·5·6 ANTENNAE

Transmitters may or may not require an antenna depending on the distances involved. However receivers almost always require an antenna. In machinery applications, the distance between the transmitter and receiver antenna is generally within three feet (≃ 900 mm). This typically requires no external transmitter antenna. The distance for the Test Rig Telemetry System is restricted however to 150 mm (6") operating without antenna on the transmitter.

8·5·7 POWER SUPPLY

Normal power supply to the transmitters is by batteries. However batteries cannot withstand high g loadings, or high temperatures. Some batteries can however withstand up to 10,000 g, but not very high temperatures. Some can withstand high temperatures up to 150°C but tolerate only light loads. Thus some thought must be given to battery location.

For situations where batteries are not used since a continuous power supply is required or loadings or temperatures too high Inductive

Systems have been used. A relatively easy solution if shaft end is free.

However, for the Rotor Test Module Data Acquisition solution, high speed slip rings were used.

Of the four Telemetry methods FM is the most suitable to dynamic applications due to its high frequency response and its large frequency range. There are however slight drawbacks against it, as it is not as easy to calibrate or zero as the FM/FM system as this enables static calibration and zeroing to take place. Another slight drawback is the noise immunity problem but this is thought to be secondary to the importance of dynamic pressure profile capture.

8·5·8 TRANSMITTER ROTOR HOUSING ASSEMBLY

Wessex Electronics, agents for PMD (Physical Measurement Devices, USA) supplied the Telemetry equipment for the Transmitter Rotor Housing Assembly. Of the aforementioned Telemetry systems they market FM and FM/FM systems. As a dynamic central pressure profile was investigated only one FM system could be considered.

However due to high g loading a transmitter was specially designed and manufactured for the tests by PMD. The device was fully incapsulated (plotted in Epoxy) in a 0·625" diameter stainless steel tube, 3·25" long, to withstand up to 32,000 g, rated at 60,000 Rpm. This enabled easy installation into the 30 mm diameter rotor.

Transmitter excitation voltage was 9V DC, the transmitter supplied a regulated 5V DC to the pressure transducer which had a bridge resistance matching of 350 ≃. The peak to peak signal output of the unit was 75 mv suitable for the pressure transducer. The two transmitter excitation input pins (square) can be seen close to the vee location mark. The two round pins are high and low antennae connections. The four square pins below the antennae pins are: outer

most bridge excitation and innermost signal input to transmitter from transducer.

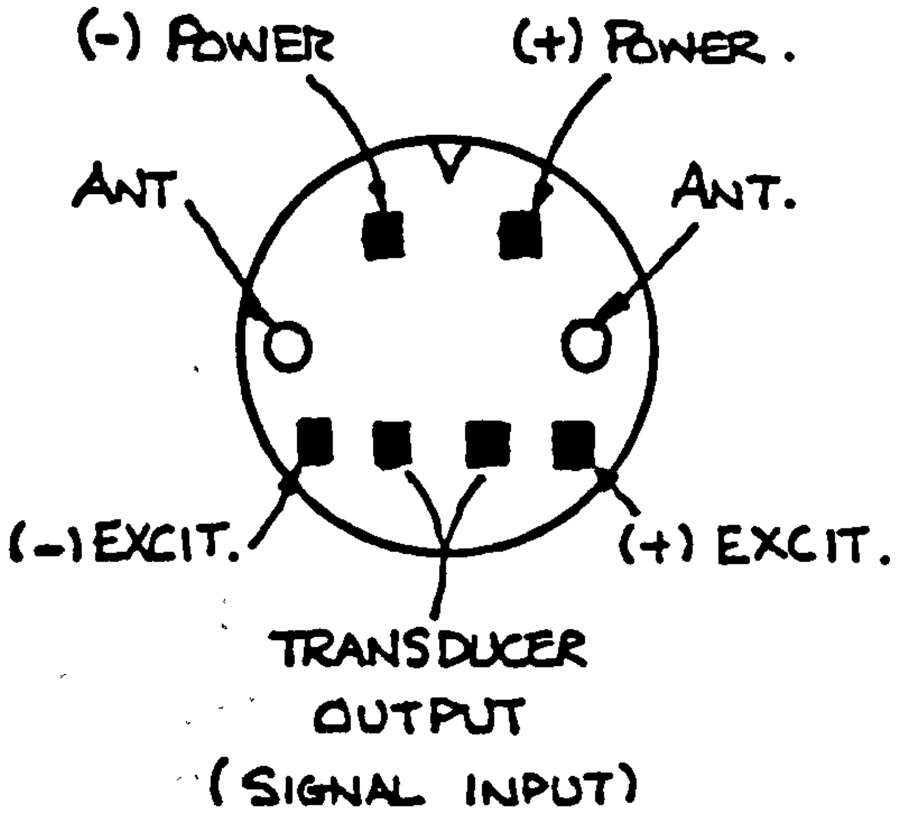

Fig. (8·5)

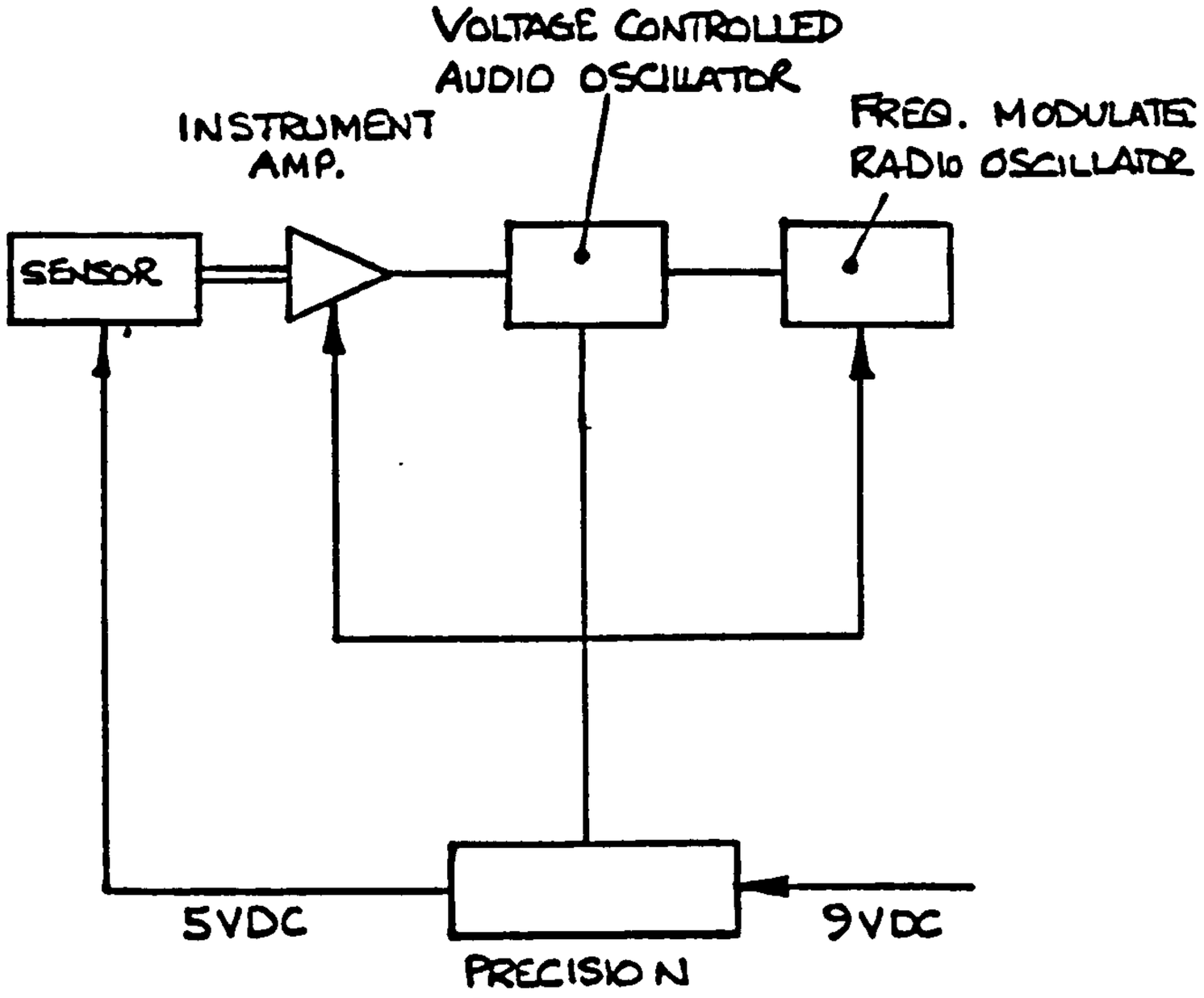

Fig. (8·6)

Plate (8·11) shows the transmitter T - 20/HM (T764). Plate (8·1) shows the R - 102B receiver. Fig. (8·5) and Fig. (8·6) show the wireless link transmitter functional diagram and the transmitter connections respectively.

8·5·9 TELEMETRY ROTOR ASSEMBLY

The Rotor System was designed to carry the transmitter and enable interface between the test shaft mounted pressure transducer and the slip ring assembly excitation voltage.

The rotor itself was a 30 mm diameter EN16T Alloy shaft × 120 mm bored to accept the transmitter. To pass electrical leads around the

transmitter and through the shaft, four holes were drilled along the axis of the rotor. On final boring 3 moon shaped clearance holes were left. This allowed the excitation and transducer output leads to pass away to the transducer and back from the transmitter. (Hence the requirement for a hollow quill shaft). A mild "Loctite" (screw lock) was used finally to secure the transmitter. To lock the transmitter into position and enable centralization of the C of G two threaded locking rings were secured at each end of the transmitter. Fig. (8·3) shows the Rotor Design clearly and Plate (8·11) shows the exploded Assembly of the Jetted/Porous Rotors clearly.

8·5·10 TELEMETRY ROTOR BEARING SUPPORT

The Rotor was designed with Hybrid bearing support in mind. Two separate Flexible Mounted 'O' Ring systems were devised:

(1) Hybrid Sulfinized Steel Bearing, comprising a single central plane of compensated Orifice (Ruby Jewels) in each bearing.

(2) Hybrid Sintered Phospher Bronze Porous Bearings.

(1) Compensated Jetted Bearing

The design incorporated a pair of EN 3A steel Sulfinized bearings ground to a very rigid tolerance envelope. (30 mm inside diameter × 38 mm outside diameter × 40 mm long with L/D = 1·33). Eight compensated orifices were arranged on the central plane of the bearing. The orifices were Ruby Jewels 2 mm OD and 0·18 mm ID mounted in a brass holder. The holders were fixed into the bearing with "Loctite" on final assembly. The Ruby Jewels are, as used in clocks and wrist watches, by watchmakers. Plate (8·12) shows the watchmakers press, used for the following:

(a) To ream brass holder with the correct interference hole for the jewel to be fitted without damage.

(b) To press jewel to right depth into the reamed hole with the minimum risk of jewel damage. (No adhesive used).

Plate (8·13) shows a jewel recessed into the brass Jet holder. This recessing produces a pocket some 0·010" deep. A micrometer device on the top of the press when using the fitting pin enables any depth to be achieved. This also enables the brass holder to be set flush with the bore of the Bearing Bush.

(2) Porous Bearing

Montgomery and Sterry (37) first used porous gas bearings on the design of a high speed Rotating Mirror and Powell and Tempest (51) used them in the design of a high speed electric motor and Dental Turbine. During their tests with the mirror, running at speeds greater than 200,000 Rpm, no instability problems were recorded or manifest. It was therefore thought not unreasonable that porous bearings might prove a successful means of supporting the Telemetry Rotor.

Oilite (Sintered Phospher Bronze) porous bearings were obtained and 'O'-Ring grooves added to flexibly mount the bearings in rotor assembly housing. The bearing type was BM5 (30 mm ID × 38 mm OD × 40 long). To ensure the correct bore fit a fitting pin and housing was manufactured so the bore could be sized. Past workers with Porous Gas Bearings state two main disadvantages:

(1) Difficulty of manufacture (unless using standard sizes).

(2) Variable permeability.

Tolerable results can be obtained (regarding permeability) by impregnating the bearing with oxalic acid after oil has been removed. Oxalic acid etches the Phospher Bronze spheres and produces a more consistent permeability through the bearing.

Following machining the sintered bearings were fitted into the housing. The air inlet connections were fitted to pipework which were in turn connected to a gear pump system with a pressure gauge attached. "Gramasol" (Tetrachloride) was then pumped into the housing through the bearings at a pressure 45-50 psi and recirculated for 5 minutes. Fig. (8·7) shows the configuration. The bearings were allowed to dry in air and placed in a dilute solution of Oxalic acid overnight (12 hours). Having removed all oil and having supposedly improved permeability the bearings were tested for real and proved very efficient and successful.

The geometry of both bearing types was designed for interchangeability. As already stated the bearings were supported at 30 mm 'O'-Ring centres with Silicon 'O'-Rings and located in the housing bore with the endcovers. The whole assembly was aligned with the rotor module and finally dowelled into position.

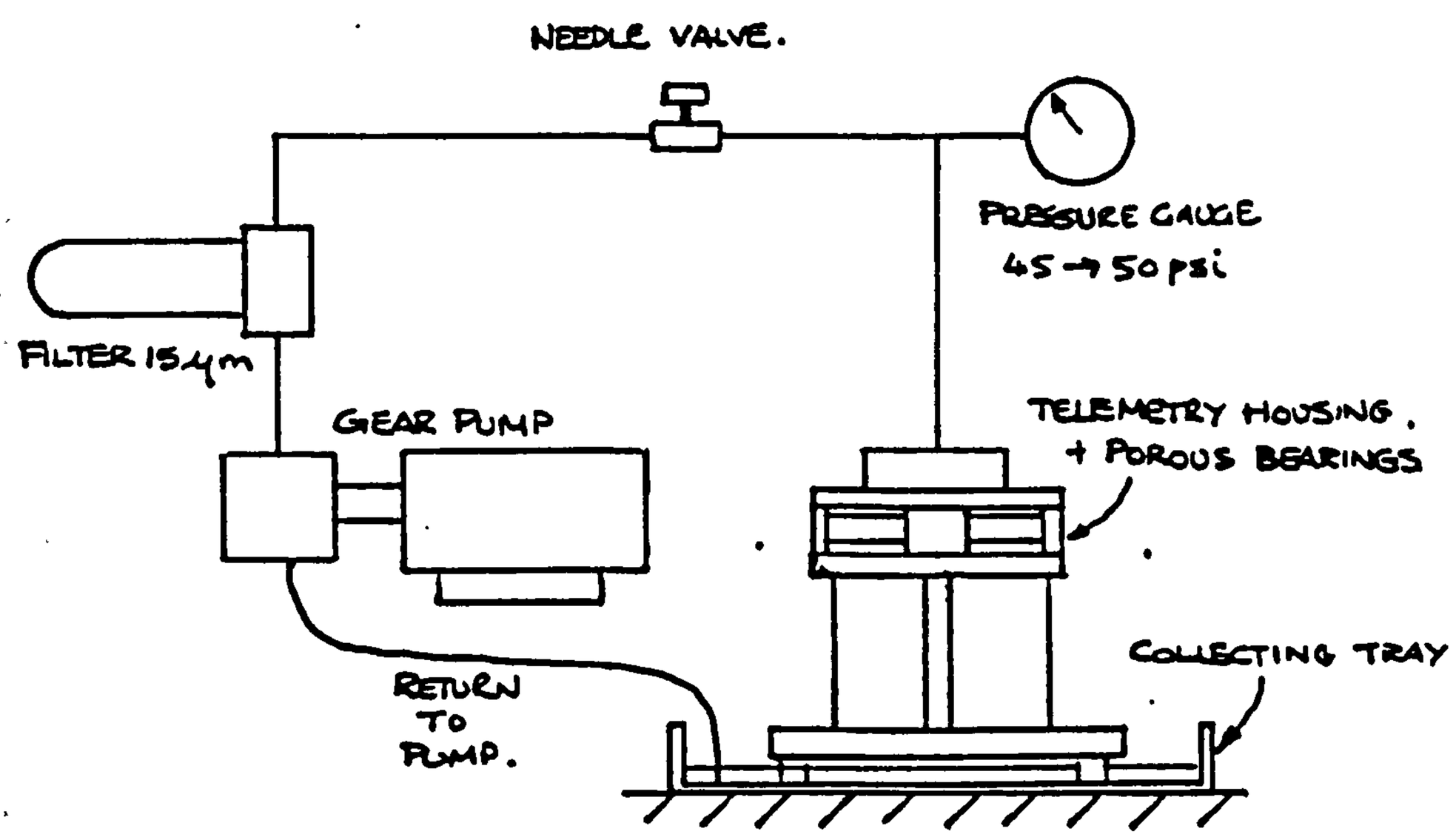

Fig. (8·7) Porous Bearing De-Greasing Rig Configuration

8·6·1 TEST ROTOR AND BEARING DATA ACQUISITION AND PROCESSING

The Test Rotor Data Acquisition consisted of two main functions:

(1) Rotor and Bearing Perturbation Monitoring.

(2) Central Dynamic Pressure Profile Delineation.

Both data signal responses were able to be displayed and stored on four Hameg (20 MHz sampling) digital storage oscilloscopes.

The above functions were to be recorded under the remaining variation of the test module variable parameters.

8·6·2 PROXIMITY PROBE DESIGN (ROTOR AND BEARING PERTURBATION MONITORING).

The HBM test TR 1·5 proximity probes were proven on the Single Bearing Test Rig. However for the Dual Bearing Rig tests they were used in pairs (ie. one half of an inductive bridge circuit). The Instrumentation Department (SME) modified the AEI amplifier units to accept a half bridge circuit. One of the proximity probes was the active and the other the dummy probe. Thus the changes in inductance will be proportional to the displaced physical measurement. HBM recommend that both probes be used to monitor displacement on the same axis opposite each other. However this gives displacements as a function of the mean shaft measured displacement. This can prove catastrophic if monitoring critical shaft displacements.

The proximity probes were mounted in stainless steel carriers as the Single Gas Bearing Rig. The probe carriers were mounted in stainless steel threaded holders. The probes were mounted in such a fashion for the following reasons:

(1) To hold the probe insert and HB TR 1·5 probe.

(2) To inhibit corrosion of probe holder material.

(3) To present a more acceptable physical size of unit.

(4) For probe positioning and location.

(5) To enable easy probe removal from holder for repair and/or replacement.

During the Dynamic tests 16 Inductive Probes were mounted on the Rotor Test Module. (8 active and 8 dummy). Plate (8·14) shows the Probe Construction. The active probes detected movements where the dummy probes were set with a constant 0·010" displacement. Fig. (8·9) shows the location of the active probes, for various tests. Four active probes monitored journal perturbations, 2 at each end of the bearing, one in each horizontal (x) and vertical (y) plane. Four active proximity probes also monitored bearings perturbations in exactly the same configuration. All displacements were absolute (ie. relative to a fixed co-ordinate system, namely the bearing bracket, hence the ground). Relative displacements could be obtained by differencing the Rotor and Bearing absolute displacements. Plate (8·29) shows the differencing units designed for the rig by the Instrumentation Laboratory. Fig. (8·8) shows the Circuit Layout of this unit. Plate (8·10) shows the Proximity Probes in their locations and also indicates the Dummy Probes with their fixed displacements. The Signal Amplifiers can be seen in Plate (8·1). The setting procedures are as for the Single Gas Bearing Rig.

8·6·3 CENTRAL PRESSURE PROFILE DELINEATION

In order to verify theoretical predictions of pressure profile at Instability Onset a Pressure Transducer was decided to be mounted (in the Rotor) to capture the Central Pressure Profile.

To this end a survey was carried out to find a suitable device. Eventually an Entran EPI-050-200 pressure transducer was selected for the following reasons:

(1) High Diaphragm Natural Frequency (1·4 MHz). Maximum operating frequency response recommended at 20% of Natural Frequency (u 280 KHz).

(2) Low Pressure Range 0 - 200 Psi.

(3) Small Physical Size - 1·27 mm diameter × 12 mm long (incuding stand off tube).

(4) Temperature Compensated.

The maximum fullscale transducer output was 75 MV @ 200 Psi. Excitation voltage was 5V DC, bridge resistance of 350 . Plate (8·5) shows the Pressure Transducer Mounted in the Shaft. Plate (8·5) also shows the Transducer mounted in its Holder. Initially the shaft mounted system was to be fully fixed in position in the test shafts. It was later decided prudent to fix the transducer into a screwed holder which could be easily removed if damage arose, enabling the transducer to be used in other applications. Due to the high centripetal accelerations present the diaphragm would deflect outwards at speeds up to 60,000 Rpm. This would show itself as a negative pressure operating with no exciting pressure. A DC shift.

From information given by Entran of USA this effect could be catered for. The Calibration Section shows the g effect upon diaphragm compensation.

8·7·1 SLIP RING ASSEMBLY

An in depth literature search was carried out to ascertain the state of the art. A high speed Slip Ring Assembly was kindly donated by Rotech. This device contained Gold Plated Rings and Brushes. It was

decided therefore to utilise this assembly into the Rig design. Further information was collated regarding Gold Plated contact wear and slip ring noise.

Also found was that Boeing had investigated a high speed slip ring assembly. The assembly was water (distilled) cooled and lubricated. The casing was plastic and the rings and brushes brass. Reasonably successful results were obtained and improved performance over Silver Oxide brushes. The brushes were made from the brass wires of a clothes brush and soldered into a brass threaded connector. The device ran for speeds up to 50,000 Rpm on a Fan unit and good results were obtained.

To this end water and air lubrication were investigated. Air was finally considered since large modifications to the slip rings would be required to use distilled water such as plastic housing (insulation) etc.

A housing was designed to enable compressed air to be fed into the assembly. The initial thoughts of exciting and receiving the pressure transducer signal was later abandoned. A Hybrid system was devised where the slip ring was used to excite the Telemetry transmitter. This however had the disadvantage of only having one channel available for Data Acquisition. Plate (8·15) shows the Slip Ring Assembly. The housing with baffle, the slip ring mounting bracket and the slip ring device coupling can all be easily recognised.

8·8·1 SPEED SENSING

Speed Sensing was carried out by a photo-optic reflective device. The pulse was fed to a circuit containing a Schmitt trigger. This changed the signal into a square pulse. The pulse was then fed either straight into a digital counter or through a digital-to-analogue converter which outputs voltage ∝ to frequency. This signal

was used as a phase marker for the signals of the Rotor and Bearing Perturbations captured by Oscilloscope.

Plate (8·10) shows the Speed Sensing Device located below the coupling. The coupling was sprayed black, with a single reflective band for an once per rev. square pulse.

CHAPTER 9

9·1·1 CALIBRATION OF DUAL BEARING TEST RIG

The following Chapter concerns the Calibration of some of the more important components of the Test Rig. The Entran pressure transducers proved terribly unreliable and therefore were returned to the manufacturers for further investigations. The inductance proximity probes were used to capture perturbations of the Journal and Bearing movements. The Telemetry Transmitter/Receiver slip ring was used as part of the pressure Transducers excitation and signal capture equipment.

9·2·1 PRESSURE TRANSDUCER CALIBRATION

Having decided upon a Pressure Transducer type, meetings with Entran Technical staff were held.

High speed rotation up to 60,000 Rpm imposed high centripetal accelerations on the transducer diaphragm. The effect is to induce a negative strain (pressure) upon the strain gauge circuit. The actual reading at any particular pressure would be lower by this centripetal error. It must therefore be added back on to the signal as a steady DC offset voltage. Errors approaching 3·6% (7·1 psi) being apparent at 60,000 Rpm. Information regarding mass/g of the diaphragm enabled a correction curve to be calculated. It would be more accurate to carry out a calibration of induced strain against speed, however this would require a Rig of almost as much sophistication as the Test Rig itself. Fig. (9·1) shows the theoretical g loading effects of the Transducer Diaphragm.

From Entrans information the g loading at 60,000 Rpm is 59443 g. A custom made transducer was finally chosen with a 0 - 200 psi pressure range and temperature compensation from -40 → 150°C. This latter factor would allow high temperature investigation to take place at a

later date. (To compliment tests carried out by Preece (73)). The 200 psi range would also enable Hybrid Bearing pressure investigations to take place, and had an increased Resonant Frequency 1·4 (20%) - 280 Hz, ie. signal response for a 1/280 th of the circumference of the journal. The temperature compensation device was also moved to six inches to enable mounting inside the rotor.

A pressure housing sub-assembly was designed. This housing was slipped over the journal surface and locked into position by compression of the 'O' ring seals onto the rotor. The housing offered a plenum chamber into which air or oil could be pumped under pressure.

Two methods of pressurising the chamber were the Mercury Mamometer and the Budenburge Dead Weight tester.

The transducer was excited via a 5V DC stabilised power supply through the slip ring assembly. The Telemetry transmitter was not connected since only dynamic signals could be transmitted and received. Plate (9·1) shows the Test Shaft with Transducer insitu, also can be seen the Pressure Housing, Endplates and 'O' Rings. The Endplates enable satisfactory sealing by 'O' Ring compression. Plate (9·2) shows the Mercury Manometer Pressure Calibration Method.

Pressure is applied in steady increments and the output of the transducer recorded on a DVM. An initial drift test was carried out to check for transducer stablility. Both transducers were found to be faulty. One transducer made a step jump in zero offset. To this end they were both returned to Entran for investigations. The initial sensitivity of the transducers as calibrated by Entran were 0·583 mv/psig # 87H87F29-W01 and 0·427 mv/psig 87G00007-007.

Entran repaired 87H87F29-W01 as the transducer was damaged inside the unit. Entran changed it to a half bridge device. 87G00007-007 was however said to be undamaged. Since 87H87F29-W01 was mounted inside the shaft it was calibrated as a half bridge unit, however its

sensitivity had dropped to 0·225 mv/psig due to the addition of a 680 ohm resister in each arm of the damaged bridge. 87H87F29-W01 was calibrated and can be seen in Fig. (9·2). 87G00007-007 however failed to respond to treatment. No change in signal at all could be registered under stimulation. This unit was sent back to Entran who changed it again to a half bridge unit. On its return it again failed to respond.

Both units were treated with the utmost care and consideration. If they malfunctioned in the calibration process it is unlikely that a dynamic signal would have been obtainable. They were obviously not robust enough. The probable cause of the malfunction is that they were made incorrectly as Entran knew the application and suggested that they would work. As one EPI-050 had been placed in a cannon shell and had worked successfully, they claim. This proved very disappointing as a lot of time and effort had been taken up in this exercise, and to have got so near is depressing. This meant that the Slip Ring assembly and the Telemetry system could not be utilised. A ten week delivery was needed for a replacement unit.

Table (9·2), See S.M.E. Report TR/90/7, shows the Transducer specification and Fig. (9·3) the Circuit Schematic of the Transducer. It was however a useful exercise in thinking and should have worked extremely well. One looks forward to the day when a robust micro-pressure transducer is available on the market.

9·3·1 PROXIMITY PROBE SYSTEM CALIBRATION

The proximity probes were mounted on the Bearing Bracket to enable monitoring of bearing brush and journal displacements. Four pairs of active probes were used to monitor both journal and bearing movements. Two pairs monitored the bearing and two pairs the journal in the horizontal (x) and vertical (y) directions. Their mounting principle can be seen below in Fig. (9·4) and in Plate (9·3). Each Active Probe had a Dummy Probe connected to it in one half of the Inductance arm of the bridge to form a half active bridge.

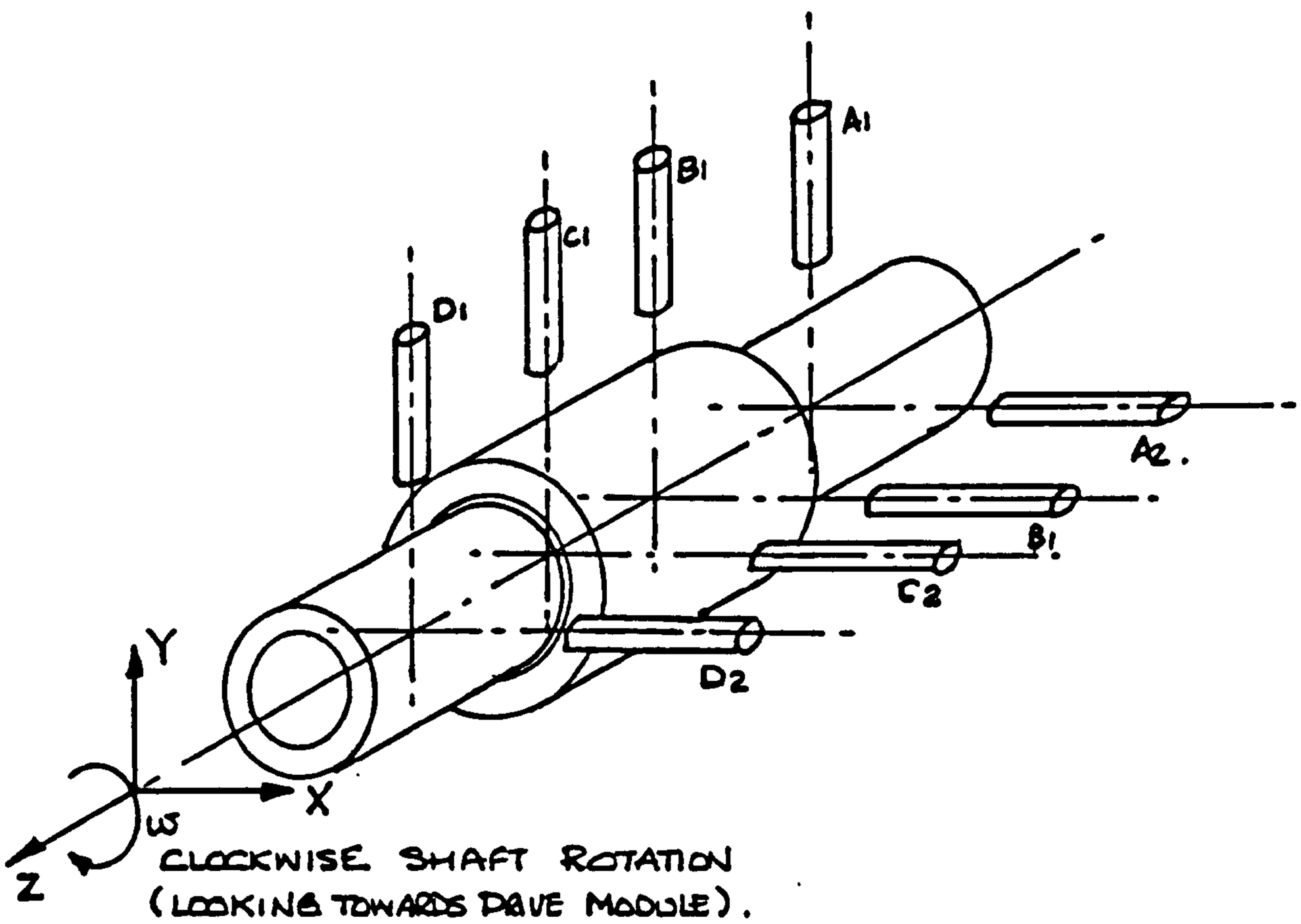

Clockwise Shaft Rotation (looking towards Drive Module).

Fig. (9·4) Active Proximity Probe Layout

The dummy probes were set against a steel plate target, with a fixed displacement of 0·010". They can be clearly seen in Plate (8·10). Plate (9·3) indicates the calibration method. The test rotor was lightly loaded against the micrometers by a pulley and weight system to ensure contact with the micrometer at all times. Rollers were suspended between the micrometer anvils and test shaft to offer a point (ellipse actually), contact and obviate corner contact of the micrometer anvil. The micrometers were screwed inwards towards the proximity probes until the bearing had bottomed on the probe safety shoulder. In doing so the 'O'-Ring supports had then been compressed. This was the zero starting point for calibration purposes. The micrometer pressure was then released in 0·001" increments until no signal change could be recorded for the bearing probes. This gave a total movement of 0·011" displacement.

The probe response was non-linear but for calibration purposes the last 0·005" was only used for curve fit purposes. It is unlikely that the total peak/peak displacement would exceed 0·003", as recorded from British Aerospace findings on the CAU.

The principle of calibration was carried out in both the horizontal and vertical planes. The process being repeated three times and the average reading taken for each increment of displacement. Figs. (9·5) → (9·8) show that the curves of displacement to probe output voltage follow an experimental form. However over the last 0·005" range chosen a very good linear approximation can be taken, and can be seen by the values of correlation coefficient obtained (lowest being 0·946).

The reason for this assumption was to enable absolute journal displacements to be subtracted from bearing displacements and obtain relative journal to bearing displacements if required. The idea being that the slope being the rate of change of voltage with displacement, that if this were linear each proximity probes curve fit slope could be made the same by the addition of a suitable electronic circuit. To this end Mean and Difference devices

(calibrations) were deleloped by the Instrumentation Laboratory by Mr Brian Moffat. Fig. (8·8).

One can perform the curves that for displacements up to 0·002" or 0·003" that the displacement response is not far removed from a linear relationship. (Actual maximum peak/peak of British Aerospace). However perhaps 0·005" is perhaps stretching it a little far. Initial testing of the devices proved reasonably satisfactory but a lot of noise pick up was superimposed onto the output signal making it almost impossible to distinguish between synchronous signal and actual noise. The device was removed from the circuit and a much clearer signal was manifest.

Filtering was not considered as this would deter from real time analysis (ie. damping applies a phase shift to the signal and rejects some high frequency content which may be part of the real signal). Table (9·6) shows the Displacement Response of the Proximity Probes. Tables (9·7) → (9·14), see S.M.E. Report TR/90/7, and Figs. (9·5) → (9·8) show the Curve Fits for each Proximity Probe.

9·4·1 CALIBRATION OF SPEED SENSOR

The Speed Sensor device was calibrated with a hand held optical Tachometer. The accuracy of the Tacho was up to 20,000 ± 3 Rpm, and had a variable sensitivity of 0 - 5 seconds duration (averaging time). For the calibration 1 second was used. Sensing distance was 50 - 300 mm and angular displacement ± 30°. The speed sensor (photo-opto switch) is set at 5 mm away from coupling, recommended by manufacturers. For calibration a reflective aluminium strip was attached to the drive coupling. The coupling was sprayed matt black with an aluminium reflective strip left for the photo-opto switch. The calibration range was carried out only over a range of 2,000 - 20,000 Rpm the limitation of the Tachometer. The sensing device (black box) had been previously calibrated in the Instrumentation Laboratory.

The speed was increased from 2,000 - 20,000 Rpm in 2,000 Rpm steps. At each speed increment the Tachometer was held against the reflective strip and the reading (Rpm) recorded.

Table (9·1) shows the results of Tacho reading against those of the speed sensing device. The output of the photo-opto device after travelling through the Schmitt trigger (which clears up the pulse signal) and returns to a Phillips digital counter. The scale being set on the counter in Rpm. The results in Table (9·1) show that over the range 2,000 - 20,000 Rpm that the deviation between systems is a 3 Rpm max in 20,000 Rpm a negligable figure.

Plate (8·10) shows the speed sensor in position. The device also outputs a single pulse which is used to trigger the four different storage scopes recording journal and bearing perturbations.

READING (NOM SPEED)	SPEED SENSOR Rpm	OPTO TACHO Rpm	ERROR Rpm	%ERROR
1(2000)	1940	1942	2	0·1
2(4000)	4017	4017	0	0·0
3(6000)	6184	6184	0	0·0
4(8000)	8067	8065	-2	-0·03
5(10000)	10282	10283	+1	0·01
6(12000)	12118	12118	0	0·0
7(14000)	13978	13979	+1	0·01
8(16000)	16020	16023	+3	0·02
9(18000)	18149	18150	+1	0·01
10(20000)	19899	19902	+3	0·02

Table (9·1) Calibration of Speed Sensor

Specification of Optical Tachometer

Accuracy

60 - 4000 Rpm ± 1 Rpm

4000 - 12000 Rpm ± 2 Rpm

12000 - 20000 Rpm ± 3 Rpm

Sample 0 → 5 seconds

Sensing distance 50 → 300 mm

Target = Reflective Aluminiumised Strip (10×10).

9·5·1 TELEMETRY SYSTEM CALIBRATION

Information from PMD's dynamic (FM) transmitter is transmitted as a direct frequency modulation of radio frequency carrier. When used with such a transmitter (FM mode) the receiver performs a single discrimination, recording the audio frequency signal which is a direct analogue of the measured parameter.

R102B receivers can operate with another FM or FM/FM mode by virtue of their mode select switching capability. Receiver configuration is also independent of the sensing parameter. The standard unit will accept signals representing strain (pressure), temperature, voltage or any other measurement for which a transmitter is available.

9·5·2 TRANSMITTER CONNECTION

For a most reliable operation it is advisable to solder all transmitter connections into place. PMD also recommend for good operating technique the use of shielded lead wires for both sensor and power connections to the transmitter. Failure to adequately shield all connections can lead to both excessive noise in acquired data and zero (offset) errors. Figs. (8·5) and (8·6) show the Transmitter Connections.

With an FM transmitter, in the absence of a dynamic stimulus at the sensor, no tone is present. Reception of the unmodulated carrier may be recognised by the occurance of "quietening" the elimination of background (static) noise from the receiver. While tuning through the carrier signal, the tuning meter will deflect first to one side, track through zero then deflect in the opposite direction.

On some occasions the transmitter is operating (as shipped) at a frequency where local radio or police can be intercepted. Return the transmitter to a "clear" frequency. This can be done by resetting the "carrier tune" core with a non-metallic screwdriver. Tune the receiver by selecting a frequency at which no transmissions can be heard, then tune the transmitter until its sub-carrier tone occurs at the receiver and the tuning meter in near nil ("0"). Using the receiver time control, zero the meter and place the AFC switch "ON". When clear reception has been obtained, free from interference the receiver will be delivering analogue voltage measurement data at the audio data connectors in the FM mode. More indepth information can be obtained from the User Manual.

9·5·3 FM SYSTEM INSTRUCTIONS

The following applies when the model R102B is used with a direct FM dynamic data transmitter T-20/HM.

(1) Place mode select switch to "FM".

(2) Turn system on in accordance with "general instructions".

(3) Turn AFC "ON".

(4) Connect an appropriate measurement or recording device to an audio data output on the receiver.

(5) Dynamically stimulate input sensor with a known calibration level at a frequency greater than 30 Hz (if possible).

(6) Adjust span control to obtain approximately scaled amplitude of received data.

In the event no dynamic calibration source is available, as marginally less acceptable calibration may be obtained as follows:

(1) Turn AFC "OFF".

(2) Adjust Tune control to obtain zero volts on audio data output.

(3) Statically stimulate sensor with a known calibration level and adjust span control for the corresponding DC voltage output.

(4) Turn AFC "ON".

The Transmitter and Receiver Specification and Calibrations can be seen in Tables (9·16) → (9·17).

CHAPTER 10

STUDY OF THE BEHAVIOUR OF BEARING 'O' RING SUPPORTS TO MATERIAL, CENTRE DISTANCE AND PRESSURE VARIATIONS

10·1·1 'O'-RING TESTING PROGRAMME

The significance of this investigation began when Preece (73) had undertaken a Dynamic Study of Bearings Mounted in Flexible 'O'-Ring Supports. His results indicated that variations in 'O'-Ring radial compression brought about marked changes in the stiffness and damping properties of the mounting system.

His curves show that a condition is present at 9 - 10% radial compression where damping is a maximum. Beyond this point however it falls sharply with increased compression. Stiffness continues to increase beyond this point with increased radial compression, there being no sign of a maximum. Other workers in this area had also observed this phenomenon but at compressions of 15% (Smalley et el).

Preece's was entirely restricted to the comparison of the dynamic properties of different 'O'-Ring materials under temperature and bearing mass variations. 'O'-Ring centres were fixed at one 'O'-Ring diameter. The 'O'-Rings were split (non-continuous). British Aerospace had observed more consistent results of material properties with this method. Inconsistency of material parameters (stiffness and damping) arises because of the following:

(1) Geometry (Diameter, Cross section, Ovality and Non-Linear Load Response).

(2) Material (Hardness, Batch Variations of Material).

Fig. (10·1) shows the results of Preece where variation in equivalent stiffness and damping can be clearly seen, plotted against radial compression. One can also see that Natural Frequency of the support system increases with increasing radial compression.

It was therefore decided that this area of Dynamic property variation may prove beneficial with a totally fixed Geometry. How could radial compression effects be manifested without changing bearing geometry of a wide speed range? Two methods were thought possible:

(1) Gross Unbalance.

(2) Pressurization of Space formed between the Bearing and Housing, by the 'O'-Ring Mounts.

British Aerospace had had some success with (1) Gross Unbalance, but the unbalance has a limited speed range applicability fixed maximum, and also cannot be varied independent of speed. Also increasing loads at high speeds induces high friction losses, displacements and the real possibility of unbalanced weights coming off completely, with obvious catastrophic consequences.

The second method was thought worthwhile considering. A simple test was undertaken. A single bearing was mounted in its 'O'-Rings and a load applied. The displacement was recorded. The bearing cavity was then pressurized and the displacement recorded once more. The second displacement was less than the unpressurized case. This led to a large scale testing programme, where three bearing types, three 'O'-Ring types and three pressure values were tested for comparison.

The maximum air pressure was restricted by the output of the Laboratory's compressor at 120 psig. If higher pressures were required, either compressed air or CO_2 was available.

The tests consisted of the following: Three bearings were tested with variable 'O' Ring centres of 7·5, 15 and 25 mm. Each bearing was almost the same mass to within 1·0%. The bearings were mounted on their 'O' Rings in the Bearing Bracket, such that the space between housing and bearing, formed by the 'O'-Ring was leakproof. The Aluminium Test Rotor was secured in the bearing under test, and a weight hanger (60 gm), placed along its length at a fixed distance.

Loading was varied and the displacements measured by Vernier height gauge and recorded. The test was repeated for pressures of 60 and 120 psig. For each bearing three 'O'-Ring materials were tested. (Nitrile, Viton and Silicon. All of 70° Shore Hardness).

For bearings (15 mm and 25 mm centres) loading varied from 0 - 70 gm in 100 gm increments with moment arms of 141·5 mm and 146·5 mm respectively. (See Fig. (10·2) and (10·3)). The loading for the 7·5 mm bearing however varied from 0 - 300 gm in 50 gm increments. (Due to its increased flexibility). 'O'-Ring Reactions, Displacements and Stiffness can be seen in Tables (10·1) → (10·10). See S.M.E. Report TR/90/7.

10·2·1 DISCUSSION OF RESULTS

The main aim was to derive Translational and Conical Stiffness values of the 'O'-Ring materials. (Nitrile, Viton and Silicon @ 70° shore hardness) operating under variable load, centre distance and pressure.

Pressure was used to induce radial compression in the 'O'-Rings. The tests carried out were to ascertain which 'O'-Ring material presented itself as the best (regarding stiffness) under radial compression, manifested by internal pressure variation.

It can be seen that stiffness values are dependent upon variations in load, pressure and 'O'-Ring centres, and by no means present themselves in well ordered Linear relationships. The discussion of results in each 'O' Ring centre distance is summed up in the Sections on 7·5, 15 and 25 mm 'O'-Ring centres, where variation of pressure, load and material properties are considered.

10·2·2 7·5 mm 'O'-RING CENTRES

Fig. (10·4) → (10·6) show the curves of pressure/displacement under constant load conditions. Load varying from 0 - 300 g at

pressures of 0, 60 and 120 psig. One can see immediately for Viton, Fig. (10·4) and Silicon, Fig. (10·5) that as load increases the sensitivity of the 'O'-Ring material to pressure stiffening increases (ie. displacement reduces). Nitrile on the other hand, Fig. (10·6) shows highly irregular behaviour, there being very little increase in stiffness with increasing pressure for any constant load. In fact at 200 g loading one can observe that displacement increases at 60 psig and returns to the initial value of zero psig at 120 psig. At 250 g however Nitrile sensitivity to pressure increases. See also Table (10·2), S.M.E. Report TR/90/7.

Nitrile's response to load variation/displacement constant pressure can be seen in Fig. (10·7). One can see that increasing load increases displacement in a non-linear manner for 0 psi and 120 psi pressure values, being almost linear for 60 psi. Table (10·11), S.M.E. Report TR/90/7, shows for Nitrile at 7·5 mm centres that at zero psig stiffness increases with increasing loading. At 60 psig Translational and Conical stiffness increases with increasing load and reaches a maximum at 150 g (25N) having passed a minimum at 100 g (16N). For a pressure of 120 psig stiffness actually reduces with increasing load.

Viton shows best characteristics regarding pressure/displacement over the range 0 - 300 g. One can see from Fig. (10·5) that between 60 and 150 g loading that non-linearity changes. A transition takes place, from a wholly concave curve to one of a convex nature. At 100 g the response approaches linearity and with increasing load beyond 100 g the non-linear effects reduce as can be seen.

Fig. (10·8) shows the Curves of Load/Displacement under constant pressure. For Viton one can again observe the non-linear load/displacement relationship and that increasing pressure reduces 'O'-Ring displacement. One can also see a change in the nature of the curve from one of concavity at zero psig to an almost linear relationship at 60 psig to a curve of convex nature at 120 psig. See also Table (10·3), S.M.E. Report TR/90/7.

Table (10·12), S.M.E. Report TR/90/7, shows that for Viton at 7·5 mm centres the following characteristics are present. At zero pressure Translational and Conical stiffness increases with increase of loading range, (0 → 33 N). One can see that at 100 g (16 N) a local minimum occurs. At 60 psig the stiffness increases with increasing load, with a maximum occurring at 150 g (25 N). For 120 psig stiffness decreases with increasing load.

Fig. (10·6) shows Silicon's pressure/displacement relationships under constant loading movement. Two transition conditions occur in Silicon. One between 100 - 150 g and the other between 150 - 250 g. At 300 g Silicon's pressure stiffening (reduction in displacement) relationship can be observed to be much greater than Viton or Nitrile. The trends can also be seen in Table (10·4), S.M.E. Report TR/90/7. Fig. (10·9) shows Curves of varying Load/Displacement under constant pressures of 0, 60 and 120 psig. The curves are grouped much closer together than Viton, but at 120 and 60 psig the displacements can be seen to reduce greatly with pressure increase.

Table (10·13), S.M.E. Report TR/90/7, indicates Silicon's Translational and Conical stiffness values at 7·5 mm 'O'-Ring centres. At zero pressure Translational/Conical stiffness reduces with increasing load. A minimum being presented at a load of 150 g (25 N). At 60 psig the same trend is seen but a minimum occurring at 100 g (16 N). For 120 psig stiffness values reduce with increasing load a minimum value occurring at 200 g (33 N).

10·2·3 15 mm 'O'-RING CENTRES

Fig. (10·10) → (10·12) highlights the Curves of Pressure/Displacement for a fixed load increment of 100 - 700 g. Nitrile shows the lowest pressure stiffening sensitivity but the lowest overall displacement. Nitrile's response shows more regularity than at the 7·5 mm centres.

Curves of load/displacement under constant pressure can be seen in Fig. (10·13). One can see that curves are more regular and that increasing pressure does not reduce displacement response greatly. Table (10·11), S.M.E Report TR/90/7, shows that for Nitrile at zero pressure stiffness values (Translational and Conical) increase for load up to 200 g (16 N) where it reaches a maximum, decreasing with increasing load thereafter. At 60 psig stiffness values initially reduce with increasing load until a minimum is reached at 100 g (10 N). The curve then increases to a maximum at 300 g (25 N), finally falling to a minimum at 400 g (33 N). At 120 psig stiffness reduces with increasing load, a maximum present at 200 g (16 N).

Viton shows rather parodoxical tendencies over that of Nitrile and Silicon regarding pressure/displacement under constant load, see Fig. (10·11). At 100 g, increasing pressure actually increases displacement at the 'O'-Ring. For 200 g loading displacement is reduced for pressure up to 60 psig increasing again at 120 psig. At 300 g the behaviour is more marked where between 0 - 60 psig a reduction in displacement is observed, increasing the pressure to 120 psig increases the displacement. Above 300 g loading the relationship is seen to increase steadily to a maximum sensitivity at 700 g.

Viton's Load/Displacement Curves under constant pressure 0, 60 and 120 psig can be seen in Fig. (10·14). One can also see that the relationships are non-linear. Generally increasing pressure tends to reduce displacements.

Table (10·12), S.M.E. Report TR/90/7, underlines that for zero pressure of 3 stiffness values reduce with increasing loading. A maximum being present between 100 g (10 N) and 200 g (16 N). Increasing pressure to 60 psig shows that stiffness increases with increasing load to a maximum at 300 g (25 N). At 120 psig increasing loading increases stiffness, a maximum present between 200 g (16 N) and 300 g (25 N).

Silicon shows the best sensitivity to pressure/displacement under constant load for all materials tested at 15 mm centres. Fig. (10·15). Between 100 g and 200 g one can detect a transition. For all load values Silicon shows a reduction in displacement with increasing pressure. At 700 g one can observe that displacements are reduced by 50% over that of 30% for Viton and 12% for Nitrile. Although Viton has a lower initial displacement than that of Silicon at 700 g loading, at 120 psig displacements are almost identical due to Silicon's increased pressure stiffening ability.

Fig. (10·12) shows curves of load against displacement under constant pressure. One can see the non-linearity clearly. This effect reducing with increasing pressure to an almost linear relationship at 120 psig.

From Table (10·13), S.M.E. Report TR/90/7, one can see stiffness values for Silicon under varying load and pressure. At zero pressure stiffness reduces with increasing load a minimum occurring at 300 g (25 N). Increasing pressure to 60 psig an overall reduction in stiffness with increasing load is seen. A maximum at 200 g (16 N) and a minimum at 300 g (25 N). At 120 psig an overall reduction in stiffness is manifest with a minimum occurring at 300 g (25 N).

10·2·4 25 mm 'O'-RING CENTRES

Curves of pressure/displacement are seen in Figs. (10·16) → (10·18). Nitrile shows the lowest displacements but has least sensitivity to pressure stiffening. At loads up to 200 g Nitrile's sensitivity to pressure is better than that of Viton. At 300 g and 400 g an appreciable reduction in displacement can be observed. Above 400 g displacement relationships show marked irregularities. At 500 g one observes a steady increase in displacement with increasing pressure. At 600 g and pressures up to 60 psig an obvious reduction in displacement is seen, displacement increases between 60 and 120 psig slightly reducing overall displacement reduction. At

700 g the pressure stiffening effects again fall to a region where little displacement is reduced with increased pressure.

Nitrile's Curves of Load against Displacement can be seen in Fig. (10·19). One can observe that the results are non-linear and that pressure increase has little effect upon reducing displacements. Table (10·11), S.M.E. Report TR/90/7, shows Nitrile's stiffness variation under varying load and pressure. At zero pressure stiffness reduces with load increase, a local minimum being present at 300 g (16 N).

For pressures of 60 and 120 psig one can observe that stiffness reduces with load increase.

The picture for Viton is much improved over that of Nitrile, regarding the pressure (displacement response). Referring to Fig. (10·17) one can see clearly a steady reduction in displacement with load increase (pressure stiffening). The greatest reduction in displacement being present at 700 g. One can observe clearly two transitions, one between 100 - 200 the other at 600 g.

Curves of Load/Displacement under constant pressure Fig. (10·20) show a non-linearity with displacements reducing with increasing pressure.

Table (10·12), S.M.E. Report TR/90/7, shows Stiffness Variations with loading and pressure. For 0, 60 and 120 psig stiffness values reduces as load values increase.

Silicon shows the best response to pressure stiffening and follows the trends observed on the 7·5 mm and 15 mm 'O'-Ring centres. In Fig. (10·18) a steady increase of pressure stiffening (reduction of displacements) with increasing loading is observed. The maximum value occurring at 700 g. Displacements reduce at 700 g by 14% compared to Viton's 12% and Nitrile's 3%. One can also observe from Fig. (10·18) that a constant slope is present between 300 → 700 g.

Fig. (10·21) shows Load/Displacement under constant pressure. One sees clearly the non-linearity and it can be seen that displacements reduce with increased pressure.

Table (10·13), S.M.E. Report TR/90/7, shows Silicon's Stiffness Variation under loading and pressure. At zero pressure stiffness can be seen to increase to a maximum at 300 g (16 N), where upon it falls with increasing load. For 60 and 120 psig stiffness decreases with increased load.

Procedure to Calculate Stiffness Parameters

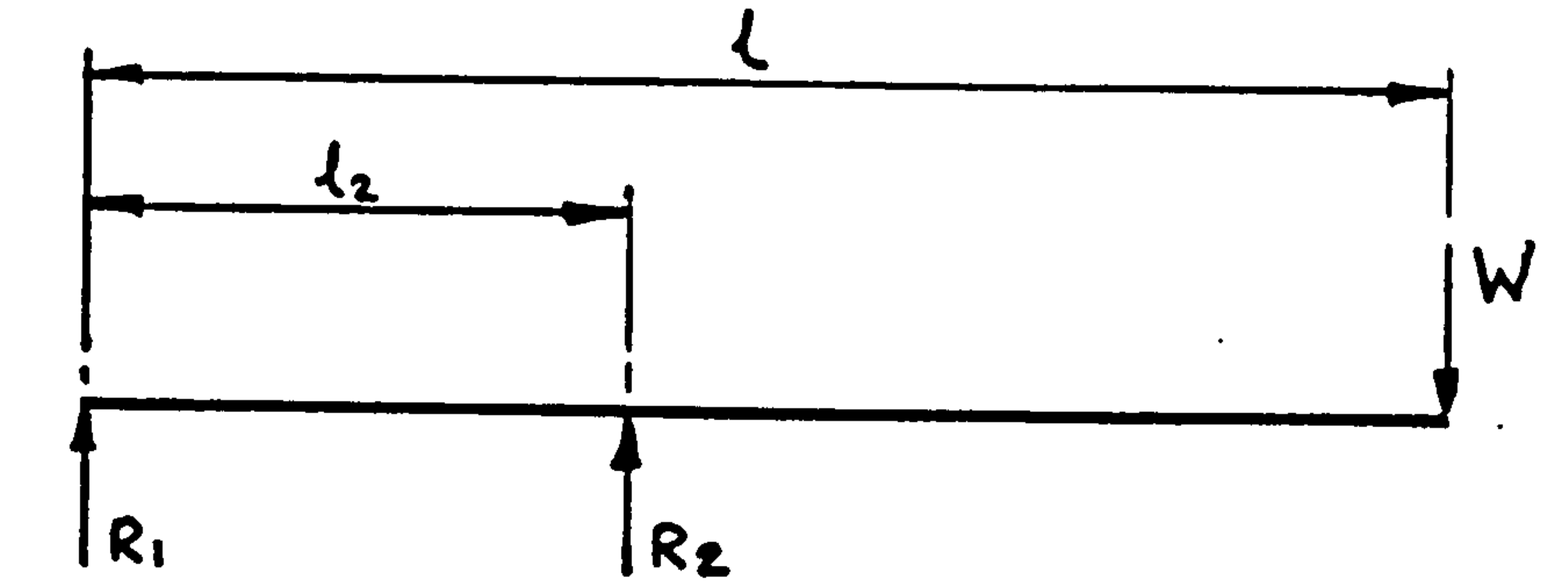

7·5 mm 'O' Ring Centres $l = 126·75$

$l_2 = 7·5$

15 mm 'O' Ring Centres $l = 141·5$

$l_2 = 15·0$

25 mm 'O' Ring Centres $l = 146·5$

$l_2 = 25·0$

Fig. (10·2) Lever Arm Acting on 'O'-Rings

'O'-Ring Reactions

Moments about R_1

$W \times l = R_2 \times l_2 \quad \therefore R_2 = W\, l/l_2 \quad \therefore R_1 = W(1 - l/l_2)$

7·5 mm Centres $R_1 = W(1 - 16·9)$, $R_2 = 16·9\ W$

15 mm Centres $R_1 = W(1 - 9·433)$, $R_2 = 9·433\ W$

25 mm Centres $R_1 = W(1 - 5·86)$, $R_2 = 5·86\ W$

'O'-Ring Displacements

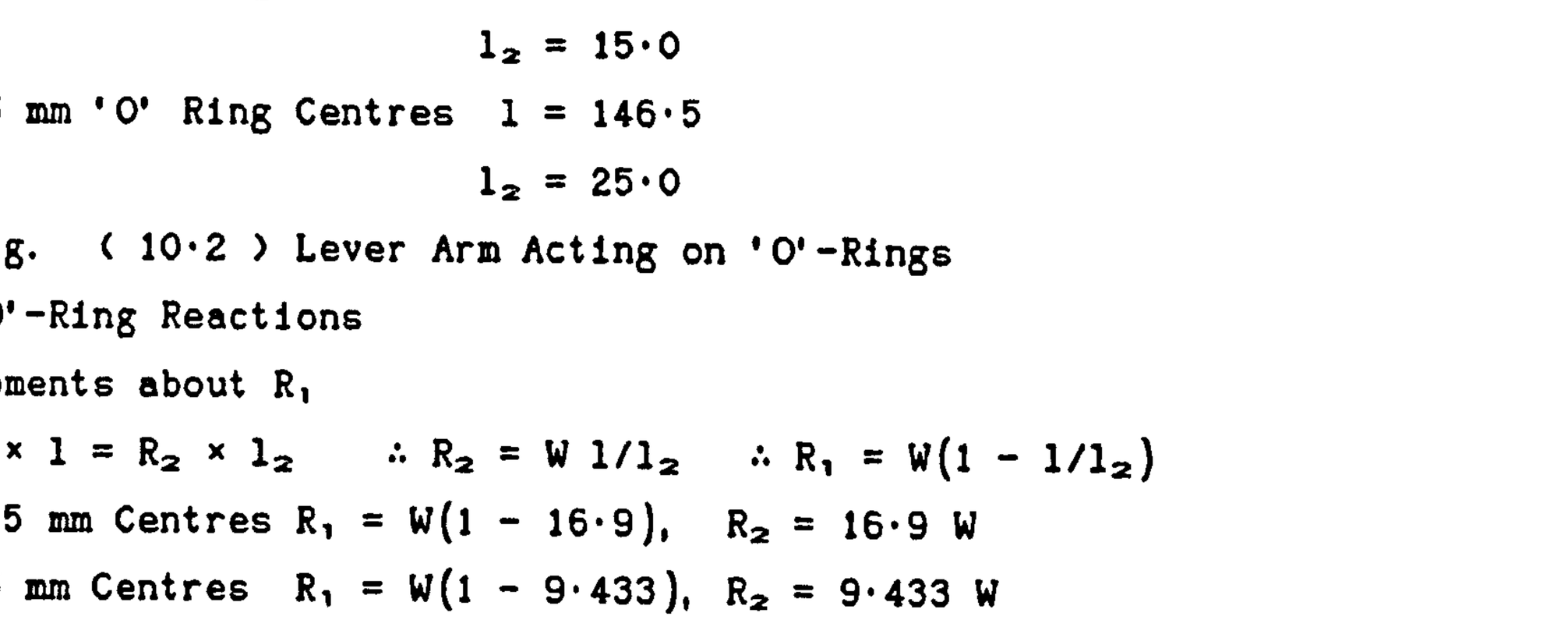

Fig. (10·3) Displacements at 'O'-Rings

$\therefore \theta_1 = \theta_2 = \theta_x = \theta$ Compatability & $\Delta_1/l_a = \Delta_2/l_b = \Delta_x/(1 - l_a) =$ Tan $\theta = \theta$ For small angles. But $\Delta_1 \neq \Delta_2 \neq \Delta_x$

Also $\Delta_1 = R_1/K_1$ & $\Delta_2 = R_2/K_2$ Where K_1 and K_2 are 'O' Ring Stiffness.

An assumption is that $K_1 = K_2 = K$

Also $l_2 = l_a + l_b$ $\therefore \Delta_1 = R_1/K$ and $\Delta_2 = R_2/K$

From similar Triangles $R_1/l_a = R_2/l_b$

$\therefore \Delta_1 = \Delta_2\ l_a/l_b$ and $\Delta_2 = \Delta_1\ l_b/l_a$

$\therefore l_2 = R_1 \cdot l_b/R_2 + l_b = (R_1/R_2 + 1)\ l_b$

and $l_b = \dfrac{l_2}{(R_1/R_2+1)}$ and $l_a = l_2 - l_b$

10·3·1 7·5 'O'-RING CENTRES TRANSLATIONAL AND CONICAL STIFFNESS

One can observe from Fig. (10·22) and (10·25) that Translational and Conical Stiffness vary greatly for the range of materials tested (Nitrile, Viton and Silicon). For low loading rates one can observe that at pressures of 120 psig stiffness is much more sensitive to load variation. At 120 psig a maximum stiffness value can be seen in each material at the 60 g load. Beyond this point however, the stiffness falls rapidly to a region where stiffness is little affected by load increase. Between 150 - 300 g for all materials and pressures little change is seen with increasing load.

Viton has the highest stiffness value at 120 psig of 15598 N/m. Viton at 60 psig shows a steady increase in stiffness to a maximum value at 150 g load, whereupon it follows almost a constant stiffness value with increased load.

At zero pressure Viton stiffness increases rapidly to 60 g whereupon a steady increase can be seen until a maximum is reached at 300 g. Tendencies are thus that stiffness values beyond 150 g increase very little with increasing load.

Silicon has its highest stiffness value at 120 psig of 3899 N/m at a load of 60 g. Silicon at 60 psig also has its maximum occurring at 60 g following by a decrease in stiffness at 100 g whereupon stiffness increases to a region where stiffness varies little with increasing load.

Silicon at zero pressure follows the trends of 60 psig where between 150 - 300 g stiffness varies little with load.

Nitrile can be seen also to have its maximum value at a pressure of 120 psig and a load of 60 g. Stiffness falls beyond this load to an almost constant value of stiffness. Nitrile at 60 psig rises rapidly to a stiffness at 60 g, where after stiffness is seen to vary very little with load increase.

At zero pressure Nitrile stiffness increases steadily to a maximum at 200 g.

10·3·2 15 mm 'O'-RING CENTRES TRANSLATIONAL AND CONICAL STIFFNESS

Fig. (10·23) and (10·26) shows the Translational and Conical Stiffness Variations of Materials under variable loading. For 15 mm centres one can observe that the maximum stiffness generally occurs between 100 and 200 g loading. Nitrile at 120 psig shows the greatest stiffness value at 100 - 200 g loading of 3930 N/m. Beyond this maximum stiffness falls rapidly to a point at 300 g loading where stiffness decreases at a steady rate with increased load.

At 60 psig a maximum stiffness is reached at 200 g whereupon a rapid reduction in stiffness is manifest between 200 and 300 g. Beyond 300 g stiffness falls off at a steady rate. At zero pressure the maximum stiffness occurs at 200 g and stiffness drops rapidly beyond this point. It can be observed that stiffness drops steadily with increasing load.

Silicon at 120 psig has a maximum stiffness at 100 g loading of 1570 N/m. Beyond this load rate stiffness falls with increasing load, until at 500 → 700 g an almost constant value of stiffness is observed. At 60 psig Silicon has its highest stiffness value at 200 g. The stiffness rate falls in a sinusoidal decaying manner, whereas at 500 - 700 g an almost constant stiffness is detected with increasing load.

Silicon at zero stiffness exhibits its maximum value at 100 g loading whereupon a sinusoidal fall in stiffness is observed until 500 g loading, whereupon any increase in load brings little change in stiffness values.

Viton at 120 psig increases steadily to an almost constant value of stiffness at 500 g. At 60 psig Viton increases steadily until a

maximum is reached at 300 g, whereupon stiffness falls steadily with little change in stiffness with increasing load.

At zero pressure a maximum stiffness value is apparent between 100 and 200 g loading, beyond which stiffness drops off with increased load.

10·3·3 25 mm 'O'-RING CENTRES TRANSLATIONAL AND CONICAL STIFFNESS

Variations in Material Translational and Conical Stiffness can be seen in Fig. (10·24) and (10·27).

Nitrile at 120 psig can be seen to have the highest stiffness value of 2800 N/m. Again stiffness values fall rapidly to a region at 300 g. Beyond 300 g stiffness falls slowly to a minimum value at 700 g, in a sinusoidal decaying manner.

At 60 psig the maximum value of stiffness occurs between 100 and 200 g, beyond this point it falls to a minimum value at 700 g.

At zero pressure stiffness steadily increases to a maximum at 200 g. Stiffness varies sinusoidally beyond this point falling to a minimum value at 700 g.

Viton at 120 psig has a maximum value of stiffness between 100 g and 200 g, whereupon stiffness falls with increasing value of load. At 60 psig stiffness increases rapidly to a maximum value 100 g. Stiffness again falls with increasing load to a minimum value at 700 g.

At zero pressure stiffness increases with increasing load to a maximum at 200 g. Beyond 200 g stiffness decreases with increasing load at 400 g. Beyond 400 g stiffness values remain constant with increasing load.

Silicon at 120 psig shows its maximum value at 100 g. Between 100 g and 300 g the stiffness values are constant with increasing load. Beyond 300 g the stiffness falls with increasing load to a minimum at 700 g.

Silicon at 60 psig has a maximum value of stiffness occurring at 200 g loading. Beyond this stiffness falls with increasing load to, at 600 g, a region of constant stiffness present with increasing load.

At zero pressure Silicon's stiffness can be seen to increase rapidly to 100 g where an almost constant stiffness region is present between 100 g and 700 g, ie. stiffness increases little with increasing load.

10·4·1 MATERIAL/'O'-RING CENTRE RELATIONSHIPS UNDER LOADING

Tables (10·11) → (10·13), S.M.E. Report TR/90/7, show Loading/Bearing Centre Distance for all the Three 'O'- Ring Materials. Some very interesting results can be seen.

Referring primarily to Nitrile, Table (10·11), S.M.E. Report TR/90/7. At zero pressure Translational Stiffness can be seen to increase by increasing centre distance for loadings of 10 and 16N, again at 25 mm centres. For all other pressures and loads Translational Stiffness falls with increasing centre distance and load, Conical Stiffness however, increases. One can clearly see that for each centre distance and constant load stiffness increases with increase in pressure.

One can also observe that increasing load reduces both Translational and Conical Stiffness values for 'O'-Ring Centres.

Table (10·12), S.M.E. Report TR/90/7, refers to the material Viton where Translational and Conical Stiffness relationships can be seen to vary with loading and centre distance.

Translational Stiffness for all loads and pressures can be seen to decrease with increasing 'O'- Ring Centre distance. In some instances a local minimum is observed at 15 mm centres as Translational Stiffness increases again at 25 mm 'O'-Ring Centres. Some interesting trends regarding increasing pressure can be observed under nominal constant load.

At 10 N and 'O'-Ring Centres of 15 mm one can see that Translational and Conical Stiffness actually decrease with increasing pressure. At 16 N for 15 mm centres stiffness increases at 60 psig, but at 120 psig stiffness values drop to those of zero psig. This again happens at a load of 25 N. However at 33 N the stiffness increases to a maximum at 60 psig and 120 psig.

Generally for all other loads and centres stiffness increases with increasing pressure. Conical Stiffness increases with increasing 'O'-Ring Centres, maximum occurs at 25 mm centres.

Of all the materials tested Silicon shows the most sensitivity to Pressure Stiffening and shows more consistent operational properties. Seen in Table (10·13), S.M.E. Report TR/90/7.

Silicon stiffness can be seen to decrease with load increase for each centre distance. Also for any fixed load increasing bearing centres can be seen to decrease Translational Stiffness but increase Conical Stiffness. Increasing pressure at each 'O'-Ring Centre can be seen to increase both Translational and Conical Stiffness.

At 15 mm centre bearings it can be seen at each load that by increasing pressure one can change the stiffness values from those of a 7·5 mm to almost those approaching that of a 25 mm bearing. To explain this more fully referring to Table (10·13), S.M.E. Report TR/90/7, one can see that for a 15 mm bearing Translational and Conical Stiffness approaching both 7·5 mm and 25 mm bearing can be achieved by pressurizing the 'O'-Ring cavity, such that variable dynamic characteristics of the bearing support can be achieved.

10·5·1 CONCLUSION

One can see from the complex nature of the response of the 'O'-Ring materials to Pressurization and Load that no clear relationship is derived for Load/Displacement at each pressure. However Silicon, of all the materials tested, responded best to pressurization stiffening, its relationship being more ordered. See Fig. (10·22) → (10·27) for comparison of Stiffness of all materials tested. Viton generally had greater stiffness values than Nitrile and Silicon at 7·5 mm Centres. However at 15 mm and 25 mm Centres Nitrile had greater stiffness values than both Viton and Silicon. Nitrile response to pressurization was not consistent. The trends can be seen clearly in Fig. (10·22) → (10·27).

Generally all materials initial stiffness increase with increasing load and reach a maximum value whereupon they fall towards an asymptotic value with increasing load. This trend is not general with elastomers and is manifest by the geometric nature of the displaced 'O'-Ring.

CHAPTER 11

INSTABILITY STUDIES OF THE SINGLE GAS BEARING TEST RIG

11·1·1 RESULTS OF INSTABILITY ONSET AND PRESSURE PROFILE DELINEATION

The Instability studies of the Single Gas Bearing Test Rig were isolated to the L/D ratio of 2 bearing tests since the other L/D ratios did not reach Instability. This bearing L/D had the lowest bearing specific pressures. Thus the propensity to whirl was more probable than that of the L/D Bearings of 1·5 and 1·0.

From Chapter (5) it can be seen that the transition point from linear to non-linear temperature rise with increasing speed indicates the instability onset in a Plain Aerodynamic Bearing.

This point can also be recognised by the half speed whirl onset. (Where the whirl trajectory precesses at half the rotational speed of the journal). Beyond this point the whirl onset grows with increasing speed, as does the temperature. Within the non-linear temperature rise Force increase is non-linear due to residual unbalance ($f = mw^2r$).

Once full metallic contact has taken place this Force vector is balanced by a reaction at the bearing surface. The temperature rise in the bearing from this point onwards is again linear. Consistent with a constant rubbing coefficient of friction. This gradient is almost identical to the gradient produced during boundary lubrication at rotor unit start up.

It can be seen from Figure (11·1) Tests 22 - 27 that at the onset of instability (Test 24) the central pressure profile tends towards a Somerfeld distribution. It is well known that integration of such a profile results in zero load carrying capacity. Between Test 22 (6400 Rpm) and Test 23 (10000 Rpm) one can see the build up of an

Aerodynamic pressure field, the maximum pressure occurring in Test 23 at station 5. At the onset of instability in Test 24 (15500 Rpm) the profiles maximum pressure magnitude falls and moves forward to station 4 indicating a change in phase angle. One can also observe the mirror image of the positive and negative pressure distribution.

This effect can also be observed in Fig. (11·2) Test 1 - 6, at Test 4 (25000 Rpm) and Fig. (11·3) Test 7 - 13 at Test 13 (40200 Rpm). The pressure distribution in Tests 4,5 and 6 dwells from 25000 - 35000 Rpm. This is thought an effect of the increased specific pressure.

The onset of Instability Of Test 4 and 13 are higher than Test 24 due to the increased specific pressure condition.

Fig. (11·4) shows a Curve of Specific Pressure against Speed of Instability Onset. One can observe an almost Linear relationship. This agrees with the findings of Whitley, Bowhill and McEwan, and Marsh's theory. Their results are however in terms of Rotor Mass not Specific Pressure.

Fig. (11·1) Test 23 - 27 show the various stages of pressure profile degradation. One can observe a considerable fall in maximum pressure magnitude at Test 25. Test 26 indicates the point at which full metallic contact takes place and the transition from the non-linear temperature rise with speed increase to that of a linear one. The pressure profile is almost zero in magnitude at this point all over the surface of the bearing.

From Test 26 to Test 27 the temperature rise can be seen from Chapter (5) to be again linear, and almost identical to the boundary lubrication temperature rise at start up.

This breakdown of the pressure field agrees with the findings of Whitley, Bowhill and McEwan (58), and the Hypothesis of Marsh (63) and (64).

At Test 27 Fig. (11·1) one can see two perturbations in pressure at station 4 and 6. This is consistent with pressure generation from Cardioidal motion of the Journal. This Cardioidal motion was more easily observed on the Dual Bearing Test Rig at the Onset/Touchdown condition.

Beyond Test 6 and 13 in Fig. (11·2) and Fig. (11·3) one would expect a similar condition to occur as above. For the L/D ratios of 1·5 and 1·0 there was little or no sign of instability, but care was taken to inhibit metallic journal and bearing contact. Very good steady state behaviour was observed however. · Touchdown was manifest at lower speeds due to boundary lubrication conditions where surface damage is far less catastrophic.

From the pressure profiles captured at the onset of Instability it is clear that monitoring the Central Pressure Profile is also, like Temperature, a good means of determining whirl onset. One can see that with a constant load and variation of speed that the central pressure profile builds to a maximum in the steady state condition, and then falls as the onset of Instability is approached. By monitoring pressure one could then determine the onset of whirl by this reduction in Maximum peak pressure. A theoretical approach that calculates pressure profile, with speed increase, could be adopted, when the Sommerfeld central profile is detected, Instability is then assumed to be manifest.

Thus for a given rotor load and speed, the peak pressure profile can be monitored until a maximum is reached. With any further increase in speed the peak pressure will decrease until the pressure field no longer can sustain the shaft load and touchdown takes place.

11·2·1 EFFECT OF SLAVE BEARINGS IN A THREE BEARING TEST APPARATUS

The two slave bearings introduce an additional element of flexibility into the system and this effects the onset of Instability as proven by Marsh. Marsh assumes the slave bearings as such to be modelled as axially symmetric springs.

If the flexibility of the slave bearings is to have little effect on the first whirl onset speed, then it is necessary to have:-

$$2S \gg K^2 ce\ (\gamma_{1B}+\gamma_{1R})$$

$$\text{or} \quad 2S_o \gg \omega_1^2\ (m_B+m_R) \simeq \omega^2\ (m_B+m_R)$$

$$g_o \qquad\qquad 4g_o$$

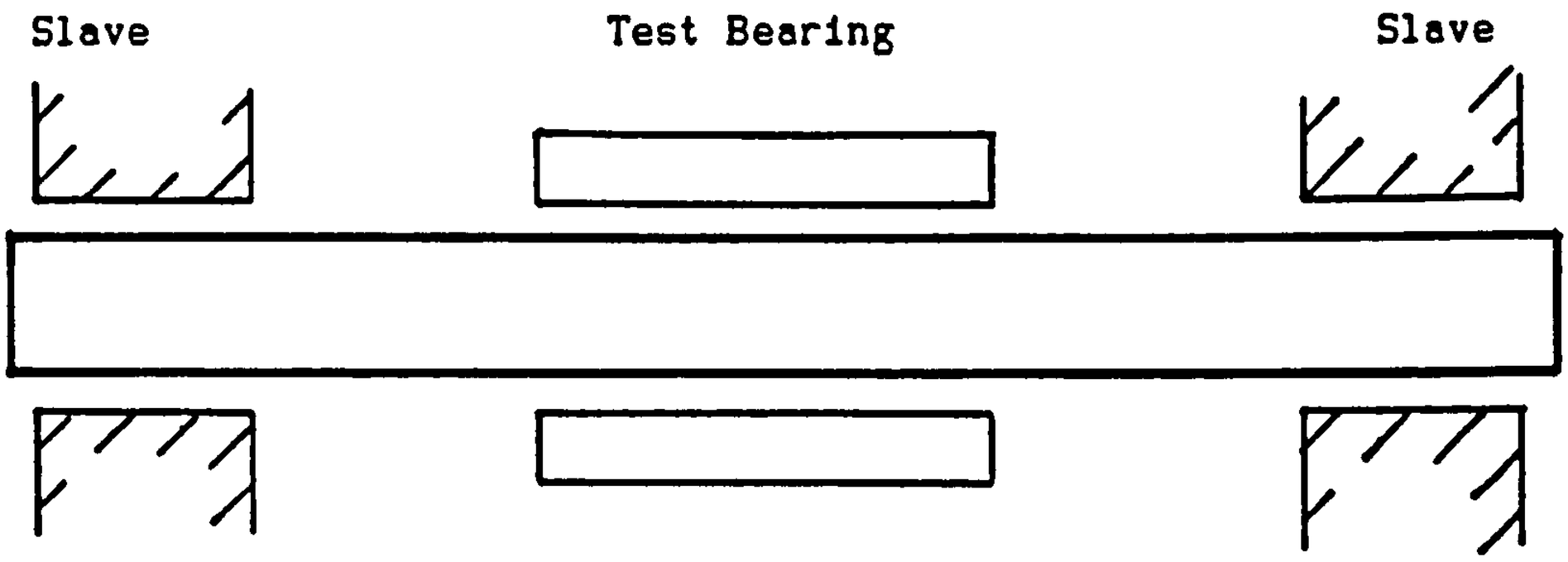

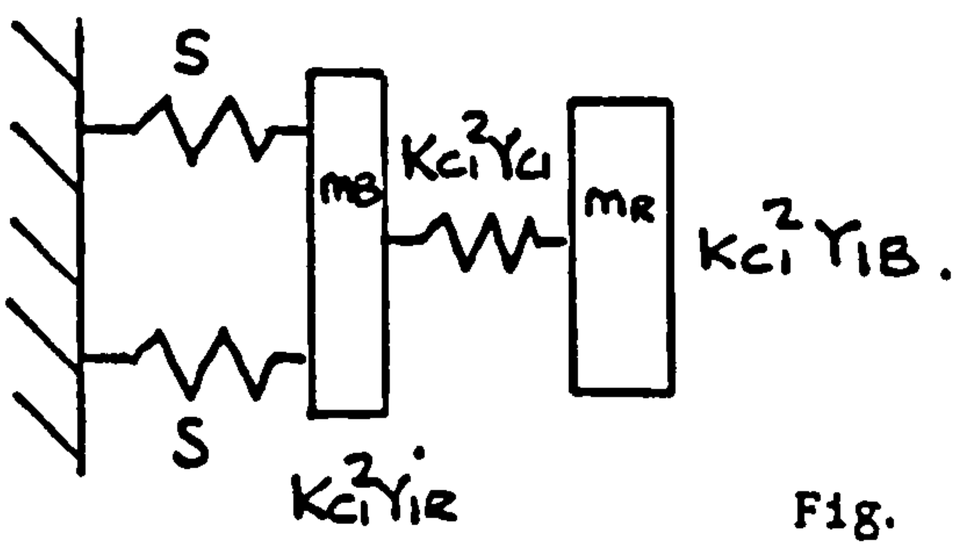

Fig. (11·5)

However the whirl onset speed may therefore be reduced by about 24% Similarly at the second Instability the effective mass of the Test Bearing is reduced by 71% and the second onset speed is increased by about 86% assuming that

$$N\omega \propto \frac{1}{\sqrt{m}}$$

as shown in Section 9·1 of Marsh's Thesis.
There is always an increase of mass in the effective mass at the first whirl onset speed, irrespective of the stiffness of the Bearing Static Loading. This serves to emphasise that the Instability is a Dynamic phenomenon. It is not sufficient to assimilate the Static Slave Bearing behaviour. Marsh's criterion overleaf must be adhered to.

From the above it is clear that the whirl onset speeds of the Single Bearing Test Rig would be greater for a bearing not mounted in slave bearings but this does not change the theoretical error condition in Raimondi's Steady State Theory for Aerodynamic Lubrication.

The results of this Chapter clearly shows for the first time the effects of the pressure field at HFW onset and corroborate Marsh's Hypothesis that the pressure field is disrupted at the Instability threshold. Marsh does not, as other workers, predict the pressure field shape and its Sommerfeld characteristics.

CHAPTER 12

DYNAMIC INSTABILITY EXPERIMENTAL STUDIES

12·1·1 INTRODUCTION

The aims of this experimental study were to gain greater fundamental understanding of Rubber Stabilized Whirl (RSW) and Half Frequency Whirl (HFW), associated with the operation of High Speed Rotors suspended in Self-energised and Hybrid Air Bearings. The Bearings are flexibly supported upon elastomeric 'O'-Rings.

Three types of bearings were investigated namely: Aerodynamic, Hybrid (single row of jets) and Hybrid Porous. Comparisons in their performance can be seen further on in this Chapter.

Other system parameters studied were Bearing Pressure, 'O'-Ring Material, 'O'-Ring Support Centres, Rotor Mass and Inertia, Unbalance and Speed.

Previous workers Montgomery & Sterry (54) and Powell & Tempest (68) had had success with specific types of Air Bearing Supported Designs. Their investigations however, were not extensive and therefore it was decided that a Test Facility that varied fundamental parameters, enabling both C.A.U. and other general Rotor Systems to be studied would be of great merit.

The Test Rig aided the understanding of limitations of the Self-Energised and Hybrid Suspensions, and the effect of varying system parameters upon overall performance, in particular RSW and HFW onset.

The experimental study also allowed the collation of a great deal of experimental data. Thus comparisons could be made and conclusions drawn on the general application of Aerodynamic and Hybrid Bearings as a means of High Speed Rotor Suspension. The C.A.U. application was a specific example of the trends recorded.

The following Chapter discusses the results recorded and offers Hybrid Air Bearings as an alternative means of C.A.U. Rotor Suspension over the present Aerodynamic Bearings.

12·1·2 PROCEDURE OF TESTING

The following series of Tests were carried out on a Test Rig designed to simulate a general High Speed Rotor System and the fundamental Cool Air Unit. Three Bearing types were studied notably: Aerodynamic, Hybrid (single central row of jets) and Hybrid Porous (Phospher Bronze). Initially three Symmetric Rotor masses and Inertias were tested - 0·596 kg (shaft), 0·984 kg (shaft + 60 dia discs) and 1·258 kg (shaft + 90 dia discs) for each bearing 'O'-Ring Centre and material variation. See also Table (12·1) → (12·16).

Bearing 'O'-Ring Centre were varied as follows:- 5 mm, 7·5 mm, 10 mm, 15 mm, 20 mm, and 25 mm. Two 'O'-Ring material types were selected, Silicon and Viton, both of 70 shore hardness and commercially available from major 'O'-Ring stockists. Both 'O'-Ring materials had been previously tested by Preece Ref. (75) and B.Ae, on Cool Air Unit Bearing Mount Tests. Both materials are said to keep almost constant loss angles (measurement of damping) even at elevated temperatures. Viton has however greater stiffness and damping properties than Silicon, which will be shown later in detail. Preece, whilst investigating Dynamic properties of the bearing mount via modal analysis, indicated in graph form that damping can be improved by increasing percentage 'O'-Ring pinch in its housing. Fig. (10·1). The Author carried out tests to ascertain whether pressurization of the plenum chamber increased stiffness properties and hence damping, of the 'O'-Ring mount. See Fig. (10·1). Results of Chapter (10) indicate that static stiffness is increased for Silicon and Viton with increasing plenum pressure (bearing supply pressure). It was decided therefore that pressurization of the plenum chamber would be an ideal manner of varying pinch and hence stiffness and damping properties of the 'O'-Rings. The 'O'-Ring is forced outwards against the housing and

bearing bush, effectively creating a change in geometry. The initial pinch at 0 psi can be seen in Tables (12.1) → (12·16) and was nominally 8 → 10%

Two bearing supply pressure variations were studied, 120 psi (Hybrid) and 0 psi (Aerodynamic), for each Test 'O'-Ring centre and mass variation. Two Porous bearing 'O'-Ring centres were also tested being 15 and 25 mm. The bearings were modified from standard Porous Phospher Bronze Oil Bearings (Oilite). The oil being washed out under pressure (45psi) using a degreasing agent. The bearings when dried, were then etched with a dilute solution of Oxalic Acid, said by Gross (98) to enhance the permeability homogeneity through the bearing. Initial investigations indicated that the flow rate varied from bearing to bearing. Closely matched pairs were selected for each Bearing Centre Variation, prior to machining 'O'-Ring centres.

Following the Symmetric Rotor Tests Asymmetric Rotor Configurations were investigated to discover the response of gross Asymmetry. Where the C. of G. moves away from the centre of the bearing span. Unbalance response was also investigated and broadly the findings agree with those of other workers.

12·2·1 INFLUENCE OF ROTOR MASS UPON RSW AND HFW

Generally for Silicon 'O'-Ring supports, as mass increased the threshold of ω_n falls. The relationship between Rotor mass m, and Instability speed ω_n varies with 'O'-Ring Centre distance. One observes at 5 mm 'O'-Ring centres Fig. (12·1) that at minimum Rotor mass (0·596 kg) a maximum onset speed is obtained for 120 psi bearing supply pressure. The relationship between ω_n and Rotor mass for 120 psi is $\omega_n \propto m^{-1/3}$ & 0 psi $\omega_n \propto m^{-1/4}$. However for Viton 'O'-Ring supports the RSW onset increases as mass increases such that $\omega n \propto m^{1/4}$.

For 7·5 mm 'O'-Ring Centres Fig. (12·3) the Instability speed against Rotor mass relationship changes to a condition where $\omega_n \propto m^{-}$

$^{1/2}$ for RSW at 120 psi and 0 psi bearing supply pressures, and HFW at 0 psi bearing supply pressures.

At 10 mm 'O'-Ring Centres Fig. (12·5) ω_n/m the relationship for RSW and HFW vary such that HFW $\omega_n \propto m^{-1/2}$ and for RSW $\omega_n \propto m^{-1/3}$. Also one can observe that HFW occurs in both 120 psi and 0 psi bearing supply pressures, as does RSW onset.

If one refers to 15 mm 'O'-Ring Centre results Fig. (12·7) the relationship between ω_n and Rotor mass can be seen to be almost linear for masses 0·596 → 1·258 kg. Where $\omega_n \propto m^{-0·4}$. RSW for both 120 psi and 0 psi have identical relationships.

One can see for 20 mm 'O'-Ring results Fig. (12·8) that ω_n against Rotor mass follows a more recognisable trend, $\omega_n \propto m^{-0·42}$ for both RSW modes at 120 psi and 0 psi supply pressure.

For 25 mm 'O'-Ring Centres Fig. (12·9) the relationship between ω_n and Rotor mass is as follows: $\omega_n \propto m^{-0·48}$ for both 120 psi and 0 psi supply pressures. HFW was not detectable on 'O'-Ring Centres greater than 10 mm.

For the Asymmetric Rotor Tests on the 15 mm 'O'-Ring Centres Fig. (12·10) ω_n/m relationship follows $\omega_n \propto m^{-1/3}$ beyond the maximum instability conditions which is for 120 psi 0·984 kg and 0 psi 0·596 kg. For the 120 psi condition for between mass 0·596 and 0·984 kg the RSW instability threshold can be seen to increase to a maximum detected at 0·984 kg. At this point of the curve $\omega_n \propto m^{+1/3}$. Beyond 0·984 kg RSW onset falls with increasing Rotor mass.

The response of Rotor mass to ω_n for Porous Bearings can be seen in Fig. (12·11) and Fig. (2·12). For 15 mm Centres Fig. (12·11) the relationship between ω_n and Rotor mass is $\omega_n \propto m^{-0·39}$ for Silicon 'O'-Rings and $\omega_n \propto m^{-2/3}$ for Viton. For both tests supply pressure was 120 psi.

However for 25 mm Centres Fig. (12·12) the relationship of ω_n to Rotor mass was $\omega_n \propto m^{-2/3}$ for Silicon 'O'-Rings, where the supply pressure was 120 psi.

Referring to Figures (12·1) → (12·12), that for Silicon 'O'-Ring supports as mass increases both RSW and HFW onset speeds reduce in each 'O'-Ring centre variation for Aerodynamic operation. The relationship of ω_n to mass of Rotor falls between $\omega_n \propto m^{-1/4}$ and $\omega_n \propto m^{-0.43}$, (as 'O'-Ring centre distance tends towards the bearing length), the average being $\omega_n \propto m^{-0.365}$. For large 'O'-Ring centres tending towards the length of the bearing $\omega_n \propto m^{-2/3}$ for Porous bearings. For Hybrid bearings RSW ⇒ $\omega_n \propto m^{-1/3}$ or $\omega_n \propto m^{-1/2}$ for short 'O'-Ring centres.

For Viton 'O'-Ring mounted bearings at 5 mm Centres Fig. (12·2) the RSW onset increase with increasing mass (0·596 → 1·258 kg Rotor masses). As 'O'-Ring centres increase one sees a complex trend where a maximum condition occurs at a mass of 0·984 kg and beyond that the RSW threshold reduces. For increasing mass the relationship for ω_n against Rotor mass for 5, 7·5 and 10 mm centres are as follows:- 5 mm centres Fig. (12·2) $\omega_n \propto m^{0.26}$, for 7·5 mm Fig. (12·4) $\omega_n \propto m^{1.0}$ and for 10 mm centres Fig. (12·6) $\omega_n \propto m^{\pm 1/3}$ as are observed.

Relationships for Viton at 15, 20 and 25 mm 'O'-Ring Centres of 120 psi and 0 psi supply pressures were not detected in excess of 40,000 Rpm and up to 55,000 Rpm.

For Porous Bearings as mass increased the whirl onset decreased for both Silicon and Viton. The relationships varied from $\omega_n \propto m^{-1/3}$ to $\omega_n \propto m^{-2/3}$. See Fig. (12·11) & (12·12).

12·3·1 EFFECT OF ROTOR INERTIA (I_T) UPON RSW AND HFW

The effect of increasing inertia (I_T) upon the RSW and HFW onset speeds are shown clearly in Figs. (12·13) → (12·26). For most Silicon 'O'-Ring supported bearing centres as I_T is increased ω_n threshold is reduced. At 5 mm Silicon 'O'-Ring Centres Fig. (12·13) RSW (120 psi) and HFW (Opsi) onset $\omega_n \propto I_T^{-0.2}$, but for Viton supported 'O'-Rings $\omega_n \propto I_T^{0.2}$ RSW (Opsi). For Viton at 5 mm Centres Fig. (12·14) ω_n increases with increasing Rotor mass.

For 7·5 mm Silicon 'O'-Ring Centres Fig. (12·15) $\omega_n \propto I_T^{-0.32}$ at RSW (120 psi) and HFW (0 psi) $\omega_n \propto I_T^{-0.346}$, for 7·5 mm Viton 'O'-Rings Fig. (12·16) $\omega_n \propto I_T^{-0.32}$ for RSW (0 psi).

At 10 mm Silicon 'O'-Ring Centres Fig. (12·17) both RSW and HFW onset occur in 120 psi and 0 psi bearing supply pressures. For HFW $\omega_n \propto I_T^{-0.348}$ (120 psi and 0 psi). At RSW $\omega_n \propto I_T^{-0.23}$ (120 psi and 0 psi) for Viton Fig. (12·18) one observes that the variation of I_T causes a maximum whirl onset to be present. A maximum whirl onset occurred at $I_T^{-3.651}$ E-3 kgm^2. For inertia greater than this $\omega_n \propto I_T^{-0.107}$.

For 15 mm Centres Fig. (12·19) Silicon 'O'-Ring supports both onset modes are RSW and $\omega_n \propto I_T^{-0.266}$ (at 120 psi and 0 psi). One can see for 20 mm 'O'-Ring Centres Fig. (12·20) the relationship between ω_n and I_T is $\omega_n \propto I_T^{-0.254}$. However for 25 mm 'O'-Ring Centres Fig. (12·21) the relationship between ω_n and I_T is $\omega_n \propto I_T^{-0.31}$. For 15, 20 and 25 mm 'O'-Ring Centre bearings Viton 'O'-Rings did not exhibit RSW or HFW onsets for speeds in excess of 40,000 and up to 55,000 Rpm.

Two Porous bearings were tested with 15 and 25 mm 'O'-Ring Centres Fig. (12·23) & (12·24). At 15 mm 'O'-Ring Centres and Silicon 'O'-Ring supports $\omega_n \propto I_T^{-0.595}$ for Viton 'O'-Ring supports $\omega_n \propto I_T^{-0.43}$.

It can be seen that generally the relationships of ω_n to I_T is very similar to that of ω_n to Rotor mass. For Silicon increasing I_T simply reduces ω_n onset speed, but with Viton increasing I_T effects ω_n in another more complex manner, dependant upon 'O'-Ring Centres as can be seen for 5, 7·5 and 10 mm 'O'-Ring Centres. For 'O'-Ring Centres 15, 20 and 25 mm Viton 'O'-Rings did not exhibit RSW or HFW characteristics.

12·4·1 EFFECT OF RSW AND HFW WITH VARYING 'O'-RING CENTRES

As one can see Fig. (12·27) → Fig. (12·31) shows the variation of bearing centre upon whirl onset speeds for both RSW and HFW modes. Referring to Figure (12·27) with mass of 0·596 kg (I_T = 2·221 E-3 kgm^2) the variation of bearing centre upon RSW and HFW can be seen. Three curves are plotted. One curve shows that for a bearing supply pressure of 120 psi that only RSW was detected. However for a bearing supply pressure of 0 psi (Aerodynamic) both RSW and HFW were present. Increasing 'O'-Ring Centres has a dramatic effect upon HFW onset. HFW was not detected at 15 mm 'O'-Ring Centres at 0 psi (Aerodynamic) operation, for speeds up to 55,000 Rpm and in excess of 40,000 Rpm. 55,000 Rpm was used as the safe working limit of the Test Rig. For RSW modes, the variation in bearing supply pressure increases the onset speed by an average of 15 %. The influence being by the increased Airfilm Stiffness, Damping and increased 'O'-Ring Support Stiffness/Damping.

For increasing bearing centres at RSW onset one sees a slight increase in onset speed for 'O'-Ring Centres of 15 mm and greater. Thus as the 'O'-Ring centres tend towards the length of the bearing, the HFW onset speeds dramatically increase along with a slight increase in RSW threshold.

From Fig. (12·27) a maximum RSW onset occurs for bearing centres of 7·5 at 120 psi. However for Aerodynamic operation HFW occurs at 31,000 Rpm. For Hybrid (120 psi) operation it can be seen that HFW does not occur below 40,000 Rpm and was not detected up to 55,000

Rpm. This shows an enhanced performance over Aerodynamic operation for all bearing 'O'-Ring Centres in this series of tests.

Fig. (12·28) shows identical trends to Fig. (12·27). Rotor mass of 0·984 kg tends to decrease all whirl onset speeds except at 5 mm centres where the HFW onset remains close to the same for Aerodynamic operation. At 7·5 mm Centres the HFW onset falls from 31,000 Rpm to 24,400 Rpm a reduction of 21 % for Aerodynamic (0 psi) operation. The distance/span between RSW and HFW onset is also reduced, for the 0·596 kg Rotor at 10 mm 'O'-Ring Centres from 11,700 Rpm to 6,100 Rpm. Hence the overall effect of increasing Rotor mass and or Inertia being the reduction of whirl onset speed and to shift RSW and HFW onsets closer together. For Hybrid (120 psi) operation HFW is seen for the first time and occurs at 10 mm 'O'-Ring centres. For both RSW onset speeds the difference between Hybrid and Aerodynamic operation falls to an average of 2,000 Rpm. Aerodynamic RSW onset falls from 20,000 Rpm to 15,000 Rpm and Hybrid RSW from 25,000 to 20,000 Rpm.

Fig. (12·29) shows the effect of increasing mass to 1·258 kg. The effect is far less dramatic than the increase of mass from 0·596 → 0·984 kg in Fig. (12·28). HFW for bearing supply pressure of 0 psi (Aerodynamic) falls at 7·5 and 10 mm centres from approximately 25,000 Rpm to 20,000 Rpm. The RSW onset for all bearing 'O'-Ring centres compress closer together, suggesting that at 1·258 kg Rotor mass very little improvement is seen between Hybrid RSW and Aerodynamic RSW. The average difference between Hybrid and Aerodynamic RSW remains approximately 2,000 Rpm, however at 15 mm 'O'-Ring Centres hardly any improvement can be observed. One can also see at 10 mm centres that HFW at 120 psi has only dropped from 32,000 Rpm to 30,900 Rpm, a variation of only 3·5% for Rotor Masses of 1·258 → 0·984.

It is clear that for Silicon 'O'-Ring supports that best results are obtained with light weight Rotors for short 'O'-Ring Centre mounted bearings, (5, 7·5 and 10 mm). Fig. (12·29) shows the influence of

bearing 'O'-Ring centres against whirl onset with the variation of Rotor mass for Viton 'O'-Ring material. RSW onset was only detected for 0 psi bearing supply pressure. No instability was detected whilst operating with a bearing supply pressure of 120 psi. The curves plotted show similar trends to those obtained for Silicon 'O'-Ring material operating at HFW onset. This seems to suggest that the HFW Instabilities obtained with Silicon 'O'-Rings are changed to that of RSW mode with Viton and at an increased onset speed, consistent with a heavily damped system where ω_n is increased and amplitude decreased (critically damped). One notes that for the 1·258 kg mass that an increase in RSW onset is arrived at for 5 mm and 7·5 mm 'O'-Ring Centres. Silicon induces light damping See Fig. (12·32a) & (12·32b).

One can clearly detect overall that as mass is increased Viton's RSW onset increases which is the reverse characteristic of Silicon, which reduces with increasing Rotor mass. One sees that HFW is not present for all the Tests up to 55,000 Rpm with Viton 'O'-Rings. Also RSW onset was only present at 0 psi (Aerodynamic) operations. At Bearing 'O'-Ring Centres greater than 10 mm, RSW was not detected at speeds in excess of 40,000 Rpm and up to 55,000 Rpm.

From Fig. (12·31) one can see that the influence of 'O'-Ring Centres upon the whirl onset of Porous Phospher Bronze Bearings at 15 and 25 mm 'O'-Ring Centres. As mass is increased whirl onset speed decreases. For 25 mm Centres the effect of mass is not as marked, (due mainly to increased bearing pressurized load supporting area).

As Rotor mass increases towards 1·258 kg the advantage of Viton 'O'-Ring mounts is more apparent. With Viton at 0·596 kg there is an improvement in whirl onset speed with increased 'O'-Ring centres.

With Silicon there is no real improvement in whirl onset speed until 1·258 kg load is reached. Generally Porous bearings had higher whirl onset than that of Hybrid and Aerodynamic bearings at low Rotor mass (0·596 kg). As mass was increased the Hybrid and Aerodynamic

bearings performed better with higher whirl onsets than the Porous bearing. This effect of load capacity limitation of Porous Bearings is seen in the use of Hydrodynamic Porous Bearings. The Porous bearings were more susceptible to metallic touchdown damage (smearing of the Porous media took place) than the Hybrid or Aerodynamic bearing. Once metallic contact had taken place, the permeability was seriously affected hence load carrying capacity, since a drop in mass flowrate usually ensued.

A major disadvantage of Porous bearings is the much higher mass flowrates required, to support the same load, over that of the Jetted Hybrid. For the 15 mm 'O'-Ring Centres Porous bearing the mass flowrate was 61·4 gm/min until touchdown whereupon this reduced to 41·9 gm/min at a constant supply pressure of 120 psi. This compares with 15·56 gm/min for the 15 mm 'O'-Ring Centres Hybrid bearing also at 120 psi supply pressure. One can see that the Porous bearing requires four times the mass flow of the Hybrid bearing. See Tables (12·1) → (12·16).

For 25 mm 'O'-Ring Centres Porous Bearing the mass flowrate is 87·5 gm/min at 120 psi constant supply pressure. This compares to 17·0 gm/min for the Hybrid bearing at 120 psi and 0 psi for the Aerodynamic bearing. For 25 mm 'O'-Ring Centres it is observed that the Porous bearing has five times more mass flowrate than the Hybrid, for the same supply pressure and more or less the same load carrying capacity at low Rotor masses.

Referring to Fig. (12·26) for 25 mm 'O'-Ring Centres bearing one can see that at low Rotor masses the Porous bearing behaves much the same as a Hybrid bearing, as load is increased however the Dynamic characteristics of the bearing tend to those of the Aerodynamic bearing.

For 15 mm Centre bearings referring to Fig. (12·25) one observes that the Silicon mounted Porous bearing performs slightly better than the Hybrid bearing at low Rotor mass and Inertia. With increasing

Rotor mass the Instability onset falls to a much lower speed than that of the Hybrid bearing at 1·258 kg Rotor mass.

The 15 mm 'O'-Ring Centres Porous bearing supported in Viton 'O'-Rings at low Rotor masses has a greater RSW onset than both the Hybrid and Aerodynamic. However with increasing mass the performance follows that of the Aerodynamic bearing mounted in Silicon 'O'-Rings.

Referring to Fig. (12·25) one can see the influence of Assymmetry upon whirl onset. For Hybrid (120 psi supply pressure) bearings mounted in 15 mm 'O'-Ring Centres an increased RSW curve is present, but for the Aerodynamic (0 psi supply pressure) performance follows the trends of the Porous bearing. At low mass and Inertia values the Aerodynamic (0 psi) RSW onset speed for the Assymmetric Rotor is greater than that of the corresponding Symmetric mass or Inertia. However as mass increases the Aerodynamic RSW onset speed falls more sharply than that of the corresponding Symmetric Rotor as can be seen by Fig. (12·25). It could be suggested that Assymmetry of low Inertia Rotors can be a means to increase RSW onset in Aerodynamic bearing systems. For Hybrid operation it can be seen that whirl onset Assymmetry can be beneficial at higher Inertias and masses but detrimental at low Inertias and masses as whirl onset speed falls sharply with decreasing Inertia and mass. A maximum for Hybrid operation occurs at 0·984 kg mass, but as Mass and Inertia increases beyond this point the whirl onset falls again. However, whirl onset speeds are still greater than that of the Symmetric Rotor Case. During this set of Assymmetric tests the Rotor speed was not taken beyond 40,000 Rpm to ensure Rig damage did not occur.

12·5·1 ROTOR AND BUSH RESPONSE

One can see that from Fig. (12·36) RSW Test (1) & (12·37) HFW (Test 26a) for Test 1 & 26a that Bearing displacement is generally seen to vary in two manners. See also Test 1 → 100 Fig. (12·34 → 12·114) S.M.E. Report TR/90/7.

Firstly, that at RSW (Test 1) onset the Bearing whirls in phase with the Displacement of the Rotor. Secondly, that at the onset of HFW (Test 26a) the Bearing whirl amplitude is far less than that of the journal until at touchdown where a Cardioid or Re-entrant loop can be seen to be manifest. This is because Air film Stiffness is much lower than 'O'-Ring support at HFW onset and whirl orbits of Journal are large. Whirl amplitude at HFW is also dependent upon Steady State Eccentricity, a high Eccentricity resulting in a low whirl orbit before metallic contact. If the airfilm contains damping then the unbalance force from the Rotor can be tolerated to a greater level. Also because the Rotor airfilm has greater stiffness self excited half frequency whirl will take place at a higher frequency and be damped such that touchdown may not occur. Damping in the airfilm also reduces the forces transmitted to the bearing .

A Rotor mounted in Aerodynamic bearings mounted on flexible 'O'-Ring supports has two whirl onset speeds. If the 'O'-Ring stiffness is less than the bearing stiffness at whirl onset, touchdown can occur. If enough damping is present in the 'O'-Ring support, then touchdown does not take place but a region of stable whirl orbit can be passed into. For Aerodynamic behaviour, the second whirl onset, if reached, generally results with catastrophic consequences, and the Rotor will normally touchdown and or seize. However if the second region is reached with a Hybrid bearing airfilm which has sufficient damping, the second onset may also be passed through again to a stable whirl region. This postulation could be investigated with a Rig of higher speed capabilities.

12·6·1 FREQUENCY RATIO HFW/RSW

The frequency ratio HFW/RSW shows a measure of the damping present in the Rotor support system whilst varying 'O'-Ring materials and Rotor mass/inertias.

For a pure spring mass system HFW/RSW may tend to 2·0. However for 'O'-Ring mounted systems this can vary dramatically dependent upon

stiffness and damping present in the 'O'-Ring support, the frequency of vibration and the 'O'-Ring centre distance of the bearing.

For 7·5 mm 'O'-Ring Centre Tests it was seen that Rotor mass at 0 psi (Aerodynamic) operation strongly influences 'O'-Ring support response. For a Rotor mass of 0·596 kg the damping present increases the onset of RSW such that HFW/RSW = 1·724. However as Rotor mass is further increased to 0·984 kg the frequency ratio increases to 2·0. Increasing the mass from 0·984 kg to 1·258 kg slightly reduces the frequency ratio HFW/RSW ⇒ 1·96.

At the 10 mm Tests one can observe that RSW and HFW occur at both 120 psi (Hybrid) and 0 psi (Aerodynamic) operation, with Silicon 'O'-Ring supports. For these tests with 0 psi (Aerodynamic) as mass was increased the frequency ratio HFW/RSW reduces. At 0·596 kg HFW/RSW ⇒ 1·623, at 0·984 kg HFW/RSW ⇒ 1·383 and at 1·258 kg HFW/RSW ⇒ 1·322. This paradoxically is the reverse trend of the 7·5 mm centres bearing. One sees that as mass increases the RSW ⇒ HFW. For increased centres damping takes place with HFW.

For Hybrid operation (120 psi) as Rotor mass was increased the frequency ratio HFW/RSW increased following the same trends as those for 0 psi bearing supply tests for the 7·5 mm centre bearing. As Rotor mass was increased (see Fig. (12·1)) in the above tests a commensurate fall in RSW and HFW whirl onset was observed. However for all 'O'-Ring centres and for each Rotor mass the RSW onset varied little (± 5% as can be seen in Fig. (12·27) → (12·31)).

HFW at 120 psi showed little change in onset speed with increasing mass from 0·984 → 1·258 kg. One observes that supply pressure and orifice geometry play a more predominant part in airfilm stiffness than eccentricity value. Since ε changes and P_s ⇒ constant, hence HFW (120 psi) ⇒ constant.

Above 10 mm Centres RSW and HFW were not detected between 40,000 → 55,000 Rpm for Silicon 'O'-Rings. Whilst operating the Rotor mounted

on Viton 'O'-Rings HFW was not detected at all, indicating its strong suitability as a damping material and Bush 'O'-Ring support material.

For 5 → 10 mm 'O'-Ring Centres one can see that Viton damps the HFW mode such that RSW onset takes place and also increases the onset speed, which shows its excellent room temperature characteristics.

12·7·1 OBSERVATIONS OF RSW AND HFW

As previously mentioned two major whirl modes were observed: those being RSW and HFW.

RSW or Rubber Stabilized Whirl is that brought about by 'O'-Ring support stiffness being excited by the rotating unbalance..

RSW is excited by residual unbalance at the point where load carrying capacity is Rotor Inertia Force - upward restoring forces = 0. Hence a point tending toward zero relative Displacement between Journal and Bearing is observed. Residual unbalance forces in the Rotor bearing are $\propto m\omega^2 X_u$ so as speed increases the whirl orbit grows until at RSW, inversion takes place and the orbit reduces again. However if damping is present in the 'O'-Ring support and its stiffness is less than the airfilm, the damping of the support prevents metallic contact between Journal and Bearing. If the airfilm stiffness is not greater than the 'O'-Ring support stiffness then the Bush is not excited by the rotating unbalance in the Rotor and metallic contact is inevitable. Aerodynamic film stiffness can be increased in a number of ways by changing bearing geometry. However this serves to reduce load carrying capacity of the bearing and increases the threshold of instability and does not control whirl amplitude at its onset. For RSW ω_n/ω ratio was in all cases 1·0, that is the Rotor precessed at the same frequency of vibration as the Rotors Rotational speed. HFW half frequency whirl is that point at which the load carrying capacity of the airfilm reduces to zero. It generally takes place for a Rigidly mounted Rotor and for a Rotor mounted in a Spring mass system at ω_n/ω = 0·5 that is the Rotor

precesses synchronously at half the speed of the Rotors Rotational speed. A Rotor which has zero unbalance can operate at such a condition but any disturbance can cause touchdown to occur since there are no restoring forces left in the airfilm. Usually Rotors contain residual unbalance and thence any increase in speed at this point results in metallic contact between Journal and Bearing and can result in seizure.

HFW in a flexibly mounted Rotor system is the upper limit for Aerodynamic bearings. However for Hybrid bearings with sufficient airfilm damping this need not be the case, and much further investigation is required for Hybrid operation.

From all the tests carried out it can be seen that HFW onset normally occurred with a commensurate metallic contact condition. Some results however were recorded just prior to or preceding HFW. This HFW condition required split second timing for a Lissjous to be recorded properly. Due to the damping present in the 'O'-Ring support the whirl ratio ω_{r_1}/ω varied from 0·492 → 0·58. This frequency ratio being subject to instrumentation errors etc. It did however indicate the presence of the phenomenon and the catastrophic nature of this mode of vibration. For HFW with 0 psi (Aerodynamic) the frequency ratio ω_n/ω reduced with increased Rotor mass. However for HFW at 120 psi (Hybrid) the frequency ratio increased with increasing Rotor mass.

Those bearing Bushes exposed to this mode of vibration received scuffing damage as can be seen in Plates (8·6) and (8·8). Due to the sulfinizing Bush treatment complete seizure did not occur, but for the Porous Phospher Bronze bearings the bearing surfaces were seriously damaged impairing Dynamic performance. Metallic contact of the Porous Bushes resulted in transfer of Phospher Bronze material onto the steel Rotor, causing intermittent pickup and increased probability of complete seizure. Complete seizure occurred on the 25 mm Porous Bearing and Lissajous plots were unobtainable.

12·7·2 ROTOR, BEARING MASS AND % PINCH EFFECT UPON RSW

Figure (12·33) shows the relationship between Bearing Mass and 'O'-Ring Centre distance for Bearing A and B of all Tests with Silicon 'O'-Rings. Referring to Figs. (12·27) → (12·29) depicting RSW onset against 'O'-Ring Centres the trends of (12·33) are strikingly similar. This implies that variation of Bearing mass directly influences a change in RSW onset speed, and that the variation of 'O'-Ring pinch, approximately 1%, did not influence RSW significantly.

RSW is also dependent upon Rotor Mass, 'O'-Ring Support Stiffness, where 'O'-Ring Support Stiffness is a function of Rotor plus Bearing Mass, % nominal Pinch and Bearing Supply Pressure for Hybrid operation. The relationship between 'O'-Ring Support Stiffness, Rotor plus Bearing Mass and Supply Pressure can be seen in Chapter 10, where 'O'-Ring Stiffness reduces with increasing mass, and increases with increase of supply pressure. (A load of low stiffness increases with increase in load). The increase in 'O'-Ring support stiffness is due to the 'O'-Ring being forced further into the 'O'-Ring groove which simulates a geometry change and increases the % Pinch. Rotor and bearing mass increase reduces the 'O'-Ring stiffness of the support.

Both of these effects can be seen in RSW where Hybrid Bearing operation (120 psi supply pressure) has a greater RSW onset speed than Aerodynamic operation (0 psi supply pressure). Also as the mass of the Rotor is increased, Rotor and Bearing mass increases, and the RSW onset reduces. This is seen for both Hybrid and Aerodynamic operation in Figs. (12·27) → (12·31).

RSW for Viton 'O'-Ring supports followed the trends of HFW onset and the onset speeds reduced with increased Rotor Mass.

It can be concluded that RSW is more sensitive to variations of Bearing Mass, Rotor Mass (a reduction in either, increases onset

speed of RSW) and Supply Pressure, than the variation of Nominal % Pinch of the Tests. This is further substantiated since the RSW variations do not follow trends of % Pinch variation of any of the Tests. Viton's RSW response behaves similar to the HFW onset of Silicon 'O'-Rings.

12·8·1 WHIRL ORBIT RESPONSE AT VARYING 'O'-RING CENTRES

Proximity probes were mounted at Bearing A and Bearing B such that Rotor and Bush Perturbations could be monitored. The resulting Lissajous Figures were captured at the Instability onset of RSW and HFW and recorded on a Digital Storage Oscilloscope (DSO). The resultant whirl orbits were then plotted via a Philips dual pen plotter to give the curves shown in Fig. (12·36) → (12·114), Test 1 → 100, see S.M.E. Report TR/90/7. Phase and frequency were calculated approximately by scaling from the plots and gave a rough indication of frequency ratio ω_n/ω at Instability onset. For RSW $\omega_n/\omega \Rightarrow 1{\cdot}0$ for HFW $\omega_n/\omega \Rightarrow 0{\cdot}493 \rightarrow 0{\cdot}58$, indicating the existence of half or fractional speed whirl. HFW and RSW plots are seen in Figs. (12·36) & (12·37) for Tests 1 & 26a. For a complete record of the tests see S.M.E. Report TR/90/7.

Broadly speaking the whirl orbit responses can be categorized into 'O'-Ring Centre distances, operating at 120 psi (Hybrid) and 0 psi (Aerodynamic) bearing supply pressures.

The following results refer to variations of 'O'-Ring Centres.

12·8·2 15 mm - 'O'-RING CENTRES - SILICON MATERIAL (TESTS 1 - 6)

As mass was increased, the amplitude of whirl at RSW reduced, (Tests 1 → 6) together with a reduction in RSW whirl onset speed. This indicates that damping improves with increased Rotor mass and increased Air film Stiffness.

The accuracy of the phase angle calculation, scaling from frequency plots, can not be assumed to show the absolute phase angle. However the figures do show accurately, that passing through RSW is accompanied by a phase angle change, and most importantly that the phase angle increases beyond RSW, a condition of resonnance.

Figure (12·32a) and Figure (12·32b) show whirl amplitude against ω/ω_n and phase angle (φ) against ω/ω_n respectively. One can see that for Tests 1-3 results were recorded for three ω/ω_n ratios, (1) $\omega/\omega_n<1\cdot0$, (2) $\omega/\omega_n\Rightarrow1\cdot0$ and (3) $\omega/\omega_n>1\cdot0$. For $\omega/\omega_n<1\cdot0$ at speeds below RSW phase angle is between 0 and 90° dependent upon damping present in the Bearing Airfilm and 'O'-Ring support. At $\omega/\omega_n\Rightarrow1\cdot0$ at RSW phase angle is 90° and is present in all tests where RSW occurred. When $\omega/\omega_n>1\cdot0$ at speeds above RSW phase angle ⇒ 180°. These trends can be seen in Figs. (12·32) & (12·36). Fig. (12·32) shows the relationship of ω/ω_n with respect to whirl amplitude. At $\omega/\omega_n<1\cdot0$ a small stable whirl orbit is observed. However, as $\omega/\omega_n\Rightarrow1\cdot0$ the whirl orbit grows, to a maximum at $\omega/\omega_n=1\cdot0$.

Beyond $\omega/\omega_n=1\cdot0$ ($\omega/\omega_n>1\cdot0$) the whirl orbit reduces once more to a stable orbit slightly larger than that captured below $\omega/\omega_n\Rightarrow1\cdot0$ as in Figure (12·36). This Rotor whirl amplitude response can be seen to be mirrored in the bearing bush amplitude response abeit at a lower magnitude.

For all the Tests 1-6 the whirl amplitude at 120 psi supply pressure (Hybrid) and at 0 psi (Aerodynamic) were to all intents and purposes identical, recorded by the proximity probes. Both RSW modes could be driven though to a far more stable region of reduced whirl amplitude. RSW for 0 psi (Aerodynamic) cases occurs at a lower speed and is assumed due to the air films reduced dynamic stiffness. The nominal percentage pinch of the 'O'-Rings was 8·71% in both bearings. See also S.M.E. Report TR/90/7, Figs. (12·34) → (12·39).

12·8·3 15 mm 'O'-RING CENTRES - VITON MATERIAL (TESTS 7 - 12)

As mass was increased no discernable increase in whirl amplitude was detected, for speeds in excess of 40,000 Rpm and up to 55,000 Rpm the safe limitation of the Test Rig arrangement.

One can observe that both the bush and journal amplitudes remained small and one therefore assumes very good damping and stiffness

properties are present in the 'O'-Ring material. The percentage pinch of the Viton 'O'-Rings was nominally 9·38% in both bearings.

During all the tests carried out (7-12) no HSW onset was recorded. See S.M.E. Report TR/90/7, Figs. (12·40) → (12·45).

12·8·4 5 mm 'O'-RING CENTRES - SILICON MATERIAL (TESTS 13 - 18)

The general observation of Tests 13-18 was that as Rotor mass is increased the whirl orbit amplitude decreases. If one closely observes Tests 13 and 14 as an initial example. It can be seen for Test 13 Rotor mass of 0·596 kg and bearing supply pressure of 120 psi that at RSW onset the Journal whirl amplitude is of a similar magnitude to the Bushes whirl amplitude. However if one regards Test 14 at HFW with the same Rotor characteristics except 0 psi supply pressure (Aerodynamic). The Journal whirl amplitude is far greater than the Bush whirl amplitude and at HFW there will be Journal/Bush metallic contact. The bearing clearance being fully taken up. This is due to the Air film being unable to excite the Bush 'O'-Ring support. That is the Dynamic Stiffness of the Air film is less than the 'O'-Ring Stiffness.

This trend can also be seen in Tests 15-18. The maximum whirl amplitude occurring at Test 14 at HFW onset. For all cases of HFW the onset speed is lower than that recorded for RSW, and HFW was only recorded for 0 psi (Aerodynamic) conditions in that series of tests.

For all HFW onsets the point of incipient metallic contact was not recorded and $\omega/\omega_n \Rightarrow 1{\cdot}0$ not 0·5, (just prior to or above HFW onset). One can discern that as Rotor mass was increased that the x component of whirl decreased, and the whirl orbit tends towards an ellipse, moving away from a circular orbit. 'O'-Ring percentage pinch was 9·3% Bearing A and 8·93% Bearing B. See S.M.E. Report TR/90/7, for Figs. (12·46) → (12·51).

12·8·5 5 mm 'O'-RING CENTRES - VITON MATERIAL (TESTS 19 - 24)

For Test 19, 0·596 kg mass and bearing supply pressure of 120 psi, there was no instability detected beyond 40,000 Rpm and up to 55,000 Rpm. However, for Test 20 with the same Rotor mass as Test 19 but at 0 psi (Aerodynamic) RSW onset was observed, no other instabilities were detected up to 55,000 in this test. For Test 21 the mass was increased to 0·984 kg and a supply pressure of 120 psi, again no instabilities were detected with a small whirl orbit beyond 40,000 Rpm and up to 55,000 Rpm. RSW onset was detected in Test 22 with the same Rotor characteristics as Test 21 but 0 psi (Aerodynamic). The whirl amplitude is slightly increased over Test 20. At Test 23 1·258 kg and 120 psi bearing supply pressure, RSW onset is observed.

Whirl amplitude decreased for Test 24 at 0 psi (Aerodynamic) 1·258 kg mass, over Tests 20 and 22 to an extent that bush perturbations are only just detectable. For all Aerodynamic Tests in this series as mass increased from 0·596 kg ⇒ 0·984 kg a slight increase in whirl amplitude could be seen. Rotor mass was further increased to 1·258 kg and a decrease in whirl amplitude was seen. This indicates a complex variation of damping with respect to Rotor mass as the minimum damping does not occur at the minimum Rotor mass. The percentage pinch for the two Viton 'O'-Rings was 9·96 for Bearing A and 9·60 for Bearing B. See S.M.E. Report TR/90/7, for Figs. (12·52) → (12·57).

12·8·6 7·5 mm 'O'-RING CENTRES - SILICON MATERIAL (TESTS 25 - 30)

The relationships for Silicon in Tests 25-30 follow those of the previous tests, such that, as Rotor mass increases from 0·596 kg ⇒ 1·258 kg whirl amplitude reduces. A minimum whirl amplitude occurs at 0·984 kg mass for bearing supply pressure of 120 psi indicating a maximum condition of damping at this point.

For Test 25, with a mass of 0·596 kg and a bearing supply pressure of 120 psi, RSW onset is seen with a large amplitude of whirl.

Interesting trends appear in Test 26, where both RSW and HFW onsets are present at 0 psi (Aerodynamic) operation. The whirl amplitude for Test 26A at RSW is greater than that for Test 25 and shows also large bush whirl amplitudes. Test 26B shows HFW onset at a lower amplitude, bush whirl amplitude is also much lower and traces a Cardioid (re-entrant loop) Lissajous. This orbit shape depicts Journal/Bush metallic contact and upon later inspections scuffing was seen to have taken place. See Plate (8·6) & (8·8). The RSW/HFW Frequency Ratio = 0·58.

For Test 27 with a Rotor mass of 0·984 kg and bearing supply pressure of 120 psi the whirl amplitude was of lower magnitude than that of Test 25.

For Test 28 with a Rotor mass as Test 27 but with 0 psi (Aerodynamic) operations both RSW and HFW are present. Test 28A shows the RSW onset at 0 psi with a lower amplitude than Test 26A. However, for Test 28B HFW onset the whirl amplitude is slightly increased over Test 26B and again a Cardioid is traced in the whirl orbit. The RSW/HFW Frequency Ratio is 0·5.

In Test 29 with a Rotor mass of 1·258 kg and a bearing supply pressure of 120 psi the RSW onset occurs with a smaller whirl amplitude than Tests 25 and 27. No HFW was detected for Tests 25, 27 and 28 for speeds beyond 40,000 Rpm and up to 55,000 Rpm.

Finally Test 30, with the same Rotor mass as Test 29 but with 0 psi (Aerodynamic) operations show both RSW and HFW as Tests 26 and 28. Test 30A shows RSW onset again with a lower amplitude of whirl than Test 26A and slightly increased over 28A. For Test 30B HFW occurs with a smaller amplitude of whirl than at RSW (Test 30A). The amplitude of HFW is less than for Tests 26B and 28B, again a Cardioid is traced by the whirl orbit and the RSW/HFW Frequency Ratio is 0·51.

The variation of the RSW/HFW Frequency Ratio indicates that Rotor mass strongly influences 'O'-Ring support damping. For a Rotor mass

of 0·596 kg the damping present increases the onset of RSW such that RSW/HFW ⇒ 0·58. As Rotor mass increases the frequency ratio reduces to 0·5 at 0·984 kg and rises slightly to 0·51 for 1·258 kg mass. The percentage 'O'-Ring pinch for all Tests was 8·79 Bearing A and 8·57 for Bearing B. See S.M.E. Report TR/90/7, for Figs. (12·58) → (12·63).

12·8·7 7·5 mm 'O'-RING CENTRES - VITON MATERIAL (TESTS 31 - 36)

It can be observed from Test 31 (Rotor mass of 0·596 kg), Test 32 (Rotor mass of 0·984 kg) and Test 33 (Rotor mass 1·258 kg) with bearing supply pressure of 120 psi that no instability was detected at speeds greater than 40,000 Rpm and up to 55,000 Rpm. Both the Journal and Bush whirl amplitudes were very small stable orbits.

However, for Test 32 (0·596 kg Rotor mass), Test 34 (0·984 kg Rotor mass) and Test 36 (1·258 kg Rotor mass) and at 0 psi (Aerodynamic) operation, as mass was increased the RSW onset speed increased and the amplitude of whirl reduced, thus the greatest whirl amplitude occurred in Test 32. One can comment that this is the reverse observation of Silicon 'O'-Ring Support behaviour. The percentage pinch for all Tests of the Viton 'O'-Rings was 9·45 for Bearing A and 9·23 for Bearing B. See S.M.E. Report TR/90/7, for Figs. (12·64) → (12·69).

12·8·8 10 mm 'O'-RING CENTRES - SILICON MATERIAL (TESTS 37 - 42)

The trends for Silicon 'O'-Ring supports in Tests 37-42 follow broadly those of previous tests. Such that, for increasing mass (0·596 → 1·258 kg) the whirl amplitude reduces. At Rotor mass of 0·984 kg, as for the 7·5 mm 'O'-Ring Centre Tests, a minimum whirl orbit amplitude occurs signifying a maximum damping condition at that point.

One observes for Test 37 with Rotor mass of 0·596 kg and bearing supply pressure of 120 psi that RSW onset is seen with a large whirl

amplitude. One can see in Test 38 with Rotor mass of 0·596 kg and bearing supply pressure of 0 psi (Aerodynamic) that both RSW and HFW onsets are detected. For Test 38A at RSW onset the whirl amplitudes were greater than for Test 37. The amplitude of whirl for Test 38B at HFW whirl onset was less than at RSW of Test 37 and 38A. The whirl orbit traced out a Cardioid, signifying metallic Journal and Bush contact. The RSW/HFW Frequency Ratio was 0·616. RSW occurred at a lower frequency than HFW, and Bush amplitudes are also much lower in the HFW mode of vibration.

In Test 39 with a Rotor mass of 0·984 kg and a bearing pressure supply of 120 psi both RSW and HFW onsets are present. For Test 39A at RSW the whirl amplitude was less than for Test 37 and occurred at a frequency less than that at HFW. For Test 39B at HFW onset the whirl amplitude was less than Test 39A. The Frequency Ratio RSW/HFW was 0·638.

For Test 40 with Rotor mass of 0·984 kg and 0 psi bearing supply pressure RSW and HFW onsets were present. The whirl amplitude of Test 40A was less than for Test 38A and less than HFW. For Test 40B at HFW onset the whirl amplitude is greater than for Test 40A RSW but less than for Test 38B. RSW again occurred at a lower frequency than HFW, and the RSW/HFW Frequency Ratio ⇒ 0·723.

Test 41 with Rotor mass of 1·258 kg and 120 psi bearing supply pressure has RSW and HFW whirl modes. Test 41A at RSW onset shows the whirl onset is slightly greater than Test 39A. Test 41B at HFW onset has whirl amplitude less than Test 39B. RSW occurs at a lower frequency than HFW. The Frquency Ratio RSW/HFW ⇒ 0·596.

For Test 42 with Rotor mass of 1·258 kg and 0 psi (Aerodynamic) operation both RSW and HFW vibration modes are present. In Test 42A at RSW onset the whirl amplitude is less than that of 42B HFW and less than 38A and 40A. HFW onset of Test 42B whirl amplitude was greater than RSW amplitude of Test 42A and traced out a Cardioid. The RSW/HFW Frequency Ratio ⇒ 0·756. The percentage Silicon 'O'-Ring

pinch is 8·71 for Bearing A and 8·57 for Bearing B. See S.M.E. Report TR/90/7, for Figs. (12·70) → (12·75).

12·8·9 10 mm 'O'-RING CENTRES - VITON MATERIAL (TESTS 43 - 48)

For Test 43 (0·596 kg mass), Test 45 (0·984 kg mass) and Test 47 (1·258 kg mass) at bearing supply pressure of 120 psi no instability was detected above 40,000 Rpm and up to 55,000 Rpm.

The largest whirl amplitude detected was at Test 44 at 0 psi bearing pressure (Aerodynamic). For Test 44 (mass 0·596 kg), Test 46 (0·984 kg) and Test 48 (1·258 kg) at 0 psi bearing pressure RSW was detected but HFW was not for speeds in excess of 40,000 Rpm and up to 55,000 Rpm. The whirl amplitude at 120 psi was much greater than that at 0 psi (Aerodynamic) operations. Percentage 'O'-Ring pinch was 9·38 for Bearing A and 9·23 for Bearing B. See S.M.E. Report TR/90/7, for Figs. (12·76) → (12·81).

12·8·10 20 mm 'O'-RING CENTRES - SILICON MATERIAL (TESTS 49 - 54)

All modes of whirl at RSW had a stable orbit. One can observe that for Test 49 (0·596 kg mass), Test 51 (0·984 kg mass) and Test 53 (1·258 kg mass) at 120 psi that as Rotor mass was increased the amplitude of RSW onset reduced. For Test 50 (0·596 kg mass), Test 52 (0·984 kg mass) and Test 54 (1·258 kg mass) at 0 psi that the same trend can be seen. The whirl amplitudes of RSW at 0 psi and 120 psi at each mass are almost identical. HFW was not detected at speeds in excess of 40,000 Rpm and up to 55,000 Rpm the safe limitations of the Test Rig. The percentage Silicon 'O'-Ring pinch was 8·57 for Bearing A and 9·00 for Bearing B. See S.M.E. Report TR/90/7, for Figs. (12·82) → (12·87).

12·8·11 20 mm 'O'-RING CENTRES - VITON MATERIAL (TESTS 55 - 60)

No instability was detected at speeds in excess of 40,000 Rpm and up to 55,000 Rpm. Whirl orbits were not recorded but were of a small amplitude stable nature. The results were of an exploratory nature. The percentage Viton 'O'-Ring pinch was 9·16 for Bearing A and 9·65 for Bearing B.

12·8·12 25 mm 'O'-RING CENTRES - SILICON MATERIAL (TESTS 61 - 66)

All modes of vibration are RSW for speeds in excess of 40,000 Rpm and up to 55,000 Rpm. No HFW onset was detected. For Test 61 (0·596 kg mass) and at 120 psi RSW can be observed. The whirl amplitude is of the form of a small stable orbit. One can see for Test 62 (0·596 kg mass) and at 0 psi (Aerodynamic) operation, RSW onset but at a slightly larger whirl amplitude.

In Test 63 (0·984 kg mass) and at 120 psi bearing supply pressure, the whirl amplitude is greater than for Test 61. For Test 64 (0·984 kg mass) and at 0 psi (Aerodynamic) operation, the whirl amplitude is the largest of this series of tests. One observes that for Test 65 with Rotor mass of 1·258 kg and bearing supply pressure of 120 psi that the whirl amplitude is lower than Test 61 and 63.

Test 66 with Rotor mass as Test 65 and bearing supply pressure of 0 psi (Aerodynamic) operation, the whirl amplitude is lower than both Test 62 and 64. The percentage 'O'-Ring pinch was 8·71 for Bearing A and 8·80 for Bearing B. See S.M.E. Report TR/90/7, for Figs. (12·88) → (12·93).

12·8·13 25 mm 'O'-RING CENTRES - VITON MATERIAL (TESTS 67 - 72)

No RSW or HFW was detected at speeds in excess of 40,000 Rpm and up to 55,000 Rpm. Whirl amplitudes were not recorded but were of a small stable orbit. The results were therefore of an exploratory

nature. The percentage 'O'-Ring pinch was 9·30 for Bearing A and 9·45 for Bearing B.

12·8·14 15 mm 'O'-RING CENTRES (POROUS) - SILICON MATERIAL (TESTS 73 - 75)

Generally as mass is increased whirl orbit amplitude is seen to increase. For Test 73 with 0·596 kg Rotor Mass and bearing supply pressure of 120 psi, a small stable orbit is observed. However, for Test 74 with 0·596 kg Rotor mass and 120 psi bearing supply pressure both RSW and HFW can be seen. Test 74A at RSW onset shows a whirl amplitude of greater amplitude than Test 73 and occurs at a lower frequency than HFW. For Test 74B at HFW onset the whirl amplitude is greater than that of the RSW onset. The frequency ratio RSW/HFW ⇒ 0·727. The orbit traced for HFW is a Cardioid which depicts metallic Journal and Bearing Bush contact.

Test 75 with a mass of 1·258 kg and 120 psi bearing supply pressure depicts RSW with an increased whirl amplitude over Tests 73 and 74. Touchdown also occurred at this speed due to metallic contact which took place in Test 74. The percentage 'O'-Ring pinch was 7·9 for Bearing A and 7·17 for Bearing B. See S.M.E. Report TR/90/7, for Figs. (12·94) → (12·96).

12·8·15 15 mm 'O'-RING CENTRES (POROUS) - VITON MATERIAL (TESTS 76 - 78)

One again observes that for Test 76, with a Rotor mass of 0·596 kg and a bearing pressure of 120 psi, operates with RSW at a small stable whirl orbit. As Rotor mass is increased to 0·984 kg for Test 77 with a bearing supply pressure of 120 psi the whirl orbit amplitude can be seen to increase at onset of RSW over that of Test 76. However, as mass is further increased to 1·258 kg for Test 78 with bearing pressure of 120 psi the whirl orbit amplitude can be seen to reduce to a value lower than that of Test 76 and 77 at onset of RSW. The percentage 'O'-Ring pinch was 8·58 for Bearing A and

7·85 for Bearing B. See S.M.E. Report TR/90/7, for Figs. (12·97) → (12·99).

12·8·16 25 mm 'O'-RING CENTRES (POROUS) - SILICON MATERIAL (TESTS 79 - 81)

One observes that the trends are very much the same for those of the 15 mm 'O'-Ring centre tests. One can detect that for Test 79 with 0·596 kg mass and bearing supply pressure of 120 psi that at RSW onset a small stable whirl amplitude is present. By increasing the Rotor mass to 0·984 kg in Test 80 with bearing supply pressure of 120 psi the whirl amplitude at RSW onset increases to a greater value than that of Test 79. As the mass is further increased to 1·258 kg for Test 81 with 120 psi bearing supply pressure the whirl orbit amplitude reduces to a further smaller value of whirl. It is observed that the amplitude of Test 80 is the maximum amplitude for the Test series. The percentage Silicon 'O'-Ring pinch was 5·63 for Bearing A and 6·95 for Bearing B. See S.M.E. Report TR/90/7, for Figs. (12·100) → (12·102).

12·8·17 25 mm 'O'-RING CENTRES (POROUS) - VITON MATERIAL (TESTS 82 - 84)

For Test 82 with a Rotor mass of 0·596 kg and a bearing supply pressure of 120 psi at the onset of RSW a stable whirl orbit can be observed. The further increase of Rotor mass to 0·984 kg in Test 83 caused touchdown and the increase of Rotor mass to 1·258 kg caused final seizure, with the Viton 'O'-Ring seeing a very high temperature and fumes given off. The percentage 'O'-Ring pinch was 6·31 for Bearing A and 7·63 for Bearing B. See S.M.E. Report TR/90/7, for Fig. (12·103).

12·8·18 15 mm'O'-RING CENTRES (ASYMMETRIC ROTOR)-SILICON MATERIAL (TESTS 85-96)

One can observe for Test 85 with an Asymmetric Rotor mass of 0·932 kg and 120 psi bearing supply pressure that at RSW onset a large amplitude of whirl was present at the end of the Rotor opposite to that where the 90° diameter disc was mounted. At the (90 dia.) disc end of the Rotor the whirl amplitude was many times smaller in magnitude, because the eccentricity value and hence load is lower at the opposite end to the 90 diameter disc.

For Test 86 with an Asymmetric Rotor mass of 0·932 kg and 0 psi supply pressure (Aerodynamic) the whirl amplitude is reduced over Test 85. In Test 87 two RSW onset speeds were detected, one for each bearing. Test 87A refers to Bearing A and Test 87B refers to Bearing B. The RSW onset for Bearing B appears at 1,600 Rpm less than Bearing A. The whirl amplitudes are reduced over Tests 85 and 86.

Test 88 with Asymmetric Rotor mass of 1·1213 kg and 0 psi bearing supply pressure at HFW onset shows a low amplitude of whirl but traces a Cardioid whirl orbit indicating metallic contact between Bush and Journal. However, $\omega_n/\omega \Rightarrow 1{\cdot}0$ not 0·5 and the amplitude is lower than for Test 87A or 87B.

One can see in the case of Test 93, with an Asymmetric Rotor mass of 0·795 kg, that there are also two RSW onset speeds, one for each bearing. Test 93A refers to Bearing A and Test 93B refers to Bearing B. Bearing A RSW onset speed occurs at 1,000 Rpm lower than Bearing B. The whirl orbits are almost identical and the amplitude is generally less than for Tests 85, 86, 87 but not Test 88.

Test 94, with an Asymmetric Rotor mass of 0·795 kg and 0 psi, also indicates two RSW onset speeds. Bearing A refers to Test 94A and Bearing B refers to Test 94B. Test 94B RSW onset speed occurs at 500 Rpm greater than Bearing A. The whirl amplitude is greater than that

of Test 93. For Tests 93 and 94 bearing whirl amplitudes are also very large in comparison to HFW cases.

The percentage 'O'-Ring pinch was 8·71 for Bearing A and Bearing B. For all Tests due to the Asymmetry the Rotor was not accelerated past 40,000 Rpm in this series of Tests (85-96). See S.M.E. Report TR/90/7, for Figs. (12·104) → (12·110).

12·8·19 20 mm 'O'-RING CENTRES (UNBALANCE RESPONSE) SILICON MATERIAL (TESTS 97 - 100)

One can see for Test 97 with Rotor mass of 1·258 kg and 120 psi bearing supply pressure that the couple unbalance shown in Fig. (12·111) induces conical whirl in the Rotor system, a, and d, being approximately 90° out of phase with each other. Fig. (12·35) shows the Unbalance Vectors for Test 97 → 100.

The phase offset of the whirl orbits scales approximately equal to the Angular Displacement between the two unbalance masses. The whirl amplitude is much greater and occurs at only 63·6% of the Symmetric Rotor RSW of Test 53.

For Test 98 the Rotor characteristics are as Test 97 but bearing supply pressure is 0 psi (Aerodynamic). RSW occurs at a lower speed than that of Test 97 which follows relationships of the Symmetric Rotor Tests (1-96). One can observe the increase in whirl amplitude over Test 97. Phase offset of whirl orbit response curve approximates to the Angular Displacement of the two unbalance masses. The RSW onset speed occurs at 69·2% of the Symmetric Rotor RSW speed of Test 54.

In Test 99 Rotor characteristics are as Test 97 and 98 with 120 psi bearing supply pressure but the unbalance masses are moved so that only 22° Angular Displacement is between them. (Almost static unbalance). One can see that this unbalance couple induces a higher amplitude of whirl than the Symmetric Rotor of Test 53: an estimate

of 2 or 3 times greater displacement. The phase offset scales approximately 20-22°. The RSW onset speed occurs at 75·9% of the Symmetric Rotor Test 53.

Test 100 has Rotor characteristics of Test 99 but with 0 psi bearing supply pressure. The phase offset scale is 20-22°. Once again the whirl amplitude can be seen to be of a much greater amplitude than the Symmetric Rotor and the RSW onset occurs at 64·1% of the Symmetric Rotor Test 54.

One can see that generally unbalance is detremental to the operation of Rotor Systems mounted in Flexibly Supported Air Bearings. Not only are whirl amplitudes of a higher magnitude but the RSW onset speed is much lower than that for Symmetric Rotors (63·6% ⇒ 75%). This does not mean that all unbalance is detremental, since for wholly Aerodynamic operation gross unbalance increases the HFW threshold and ensures that Bearing Air Film Stiffness and Damping is sufficient to induce Damping in the 'O'-Ring support, and give safe passage through the RSW region at the lower Instability speed. Since some residual unbalance is always likely in these Rigid Rotor Systems, then for safe operation one must ensure that Support Flexibility not only includes Stiffness but enough Damping for safe Rotor operation.

This short series of Unbalance Response Tests was to highlight that some levels of unbalance are detremental. Certainly Dynamic Unbalance is a more serious problem than Static Unbalance. This would be especially catastrophic for bearings with low conical stiffness where bearing wipe could easily take place. Conical whirl can also cause more catastrophic failures regarding seal touchdown and in the case of turbo machinery compressor, turbine or fan failure due to high speed metallic contact with stator or housing. Figs. (12·111) → (12·114). See also S.M.E. Report TR/90/7, for Figs. (12·34) → (12·116) and Figs. (12·111) → (12·114).

12·9·1 DYNAMIC INSTABILITY CONCLUSION

The work of Marsh (63) and (64) concerns Aerodynamic bearings flexibly mounted in diaphragms. This spring and mass analogy may also apply to a Rotor system with bearings mounted in 'O'-Rings with centres less than, or approaching one 'O'-Ring thickness (single spring). His analysis based upon the spring mass analogy of the Rotor, Airfilm, Bearing Bush and Support Structure, however does not consider the damping behaviour of the 'O'-Ring support at RSW onset.

This is an important ommittance since it is thought that the damping in the 'O'-Ring support that enables the whirl (due to unbalance) at RSW to be passed through. Support damping allows also the RSW onset to be run at without bearing damage. Without damping present the whirl excursion would seriously damage the Journal and Bearing surface. Damping allows a stable whirl orbit to be maintained at RSW onset. However in the spring mass system, this onset would be reached and touchdown would be manifest with large whirl excursions.

Two 'O'-Ring materials were tested, and Viton proved to have superior damping properties, over Silicon, for all the bearing 'O'-Ring Centres investigated.

Tests with Viton did not detect RSW at the larger 'O'-Ring Centres (15-25). The HFW trends observed in the Silicon 'O'-Rings were manifest as RSW, with Viton, and could be passed through as seen in Fig. (12·27) → (12·31). RSW in the Hybrid (120 psi) and Aerodynamic (0 psi) conditions for Viton could not be compared since in the Hybrid mode neither RSW or HFW was observed. However a small stable whirl orbit was manifest at speeds up to 55,000 Rpm. For Silicon however very interesting comparisons regarding RSW and HFW can be made.

Variation of 'O'-Ring mounting centres did not change much the onset of RSW for each mode, the variation of RSW was inversely proportional to bearing mass for HFW as 'O'-Ring centres increased the HFW onset

speed increased until at 15 mm 'O'-Ring centres HFW was not detectable below 40,000 Rpm and up to 55,000 Rpm.

The effect of the Hybrid (120 psi) and Aerodynamic (0 psi) modes of operation, was that Hybrid operation increased the speed of RSW onset. The explanation of this being, the increased % pinch of the 'O'-Ring due to pressurization and maybe some slight increase in the Airfilm stiffness. Increased pinch increases 'O'-Ring stiffness and damping. The increase in airfilm stiffness is of secondary importance since the overwhelming influence of RSW is from the 'O'-Ring support characteristics. However if the Airfilm Stiffness is less than the 'O'-Ring Stiffness touchdown is likely to occur at RSW onset, as damping is not afforded.

The advantage of this increased % pinch reduced with increased Rotor mass. (One may require softer 'O'-Ring materials for greater change in pinch for larger masses). Referring to the static stiffness values (under varying pressure and load) Fig. (10·22) → (10·27) it can be seen that beyond the loading of 10N (where a maximum stiffness takes place) as load increases a decrease in stiffness is seen and the variation of stiffness with pressurization is not so pronounced, at large loads. This implys that 'O'-Ring Stiffness reduces with load increase, and this trend can be seen in the results of HFW and RSW onset. When Rotor mass increased the onset speeds reduced. Thus the static trends of the 'O'-Rings agree well with the Dynamic trends.

Short 'O'-Ring centre bearings had a low HFW onset due to their low conical stiffness and low damping characteristics. Whirl with couple unbalance can induce the onset of a conical instability in the 'O'-Ring mount causing metallic contact of journal and bearing. As 'O'-Ring centres increase conical stiffness of the 'O'-Ring support increases and this propensity diminishes, such that increased damping is afforded by the 'O'-Rings and stable whirl results. It must be noted that conical whirl was not observed, and low HFW onset at short centres may be due entirely to lack of 'O'-Ring Damping.

The forcing of HFW at short 'O'-Ring centres is thought by the Author to be by the rotating fingers of the sub-ambient pressures, observed in the tests of the Single Gas Bearing Test Rig.

At short 'O'-Ring centres the location of these fingers of air will be outside the 'O'-Ring points of reaction, since the bearing L/D is constant.

Any asymmetry in the Bearing arrangement or Rotor system induces a rotating variation in these air fingers as whirl takes place. This variation is sufficient to excite the bearing and leads to metallic contact. It must be noted that very small variations in conical motion of the Bearing and Journal may be all that is required to destroy the load carry capacity at these short 'O'-Ring centres, resulting in metallic contact between Bearing and Journal. The 10 mm 'O'-Ring centred Hybrid Bearing had a HFW mode of Instability and this can be traced to the Aerodynamic Forcing condition. The bearing clearances are the smallest of all the tests and Aerodynamic operation may be more predominant than Hybrid at this small clearance.

This conclusion is consistent because as 'O'-Ring Centres increase the fingers of air fall inside the 'O'-Ring mounting positions, where increased bearing conical stiffness and damping will be present, and hence greater stability.

Hybrid operation induces HFW Instability at much higher speeds due to the increased Airfilm Stiffness of Hybrid bearings over Aerodynamic.

One can conclude that for operation in the Aerodynamic mode at low 'O'-Ring centres a light Rotor is of an advantage as HFW occurs at a much higher threshold. However HFW cannot be easily controlled by Aerodynamic means, and it is the upper limit of safe Rotor operation.

Marsh (63, 64) has used gross unbalance as a means to increase the threshold of HFW but it does not conclude that the upper limit HFW can be run at with non-catastrophic results.

RSW occurred at higher speeds for Hybrid operation due to the increased 'O'-Ring support stiffness produced by the bearing supply pressure. Test results of RSW onset argue with the findings of Chapter 10, that increasing bearing supply pressure to the 'O'-Rings increases the support stiffness and therefore RSW onset speed.

Powell (68) has carried out much work with shafts mounted in Aerostatic bearings in flexibly mounted 'O'-Rings. The clearance ratios being in the order of 0·002. Powell's bearings generally ran with 'O'-Ring centres tending towards the length of the bearing, thus offering very good conical stiffness to the bearing bush. Dental Turbines have operated up to 500,000 Rpm successfully in Aerostatic bearings mounted on 'O'-Rings, one wonders why Aerodynamic bearings were pursued for Cool Air Unit operation.

Kerr (65) carried out investigations of a Rotor with bearings mounted in 'O'-Rings which had their centres tending towards the length of the bearing. He observed that the first whirl onset (RSW) could be driven through to a much more stable region. He also observed that HFW could not be driven though since metallic contact took place.

Powell (68) suggests that Rotors mounted rigidly in Aerostatic bearings can pass through the onset of whirl (HFW) to a more stable whirl region. This is due to the damping present in the Aerostatic Airfilm. One could assume that this would be possible in a flexibly mounted 'O'-Ring system, where the first onset RSW is passed through because of damping in the supports and HFW can also be passed through due to the Aerostatic damping effects. HFW is fixed mainly by the Airfilm Stiffness and if damping is present such as in the case of Hybrid or Aerostatic operation. Hybrid operation is more complex, since it relies on both Aerodynamic and Aerostatic operation and runs

with smaller clearances than Aerostatic Bearings. HFW onset however need not be destructive and a more stable whirl region may be reached. However inversion at the first onset takes place and this may aid the Aerostatic operation, but much work is still required in this area.

The Author's Test Rigs Hybrid operation holds testimony to Powell's findings regarding Aerstatic operation. For Aerodynamic operation however, as 'O'-Ring centres were increased HFW was not detectable below 40,000 Rpm and up to 55,000 Rpm. This is not conclusive proof that HFW does not exist. It may well exist at 60,000 Rpm, but shows trends that increasing 'O'-Ring centres creates better damping and lifts the threshold of HFW.

Thus one can conclude that for 'O'-Ring centres tending towards the bearing length HFW has a nominally high value. As already discussed HFW was not detected whilst operating with Viton 'O'-Rings below 55,000 Rpm, and showed excellent whirl amplitude damping properties. At low 'O'-Ring centres Viton's whirl onset speed actually increases to a maximum at some Rotor masses, at higher 'O'-Ring centres the relationship for Rotor mass increase falls and follows that of the Silicon material. This is consistent with the load/stiffness or Rotor mass against support stiffness passing over the point of a maximum. This dynamic stiffness of the support follows similar trends to static stiffness. The RSW onsets for Viton generally occurred at much higher speeds than those for Silicon, generally 10,000 → 15,000 Rpm higher.

Porous bearing operation did not give as much advantage as one would have expected. At low Rotor masses there was little advantage of using Viton over Silicon, or that of, using Porous bearings over Aerodynamic. However, at larger Rotor masses the advantages were about a 25% increase in onset speed, (see Fig. (12·25) & (12·26)), for using Viton instead of Silicon.

The obvious disadvantages of using Porous bearings have already been commented on, such that 4 → 8 times more mass flow is required to support the same load at low Rotor masses. At large Rotor masses a drop in Instability onset speed is seen over Hybrid and Aerodynamic operation. Porous bearings are more susceptable to touchdown damage over the Sulfiniz Hybrid alternative, and as yet have an indeterminate permeability factor such that bearing design is very much a 'try it and see' approach.

The experimental evidence is obviously not exhaustive but shows that Hybrid bearings mounted in a suitably chosen 'O'-Ring support can afford good Dynamic behaviour over the tested speed range of 0 - 55,000 Rpm.

Evidence of Powell (68) would not disclaim that the Hybrid/Flexible arrangement could perform at speeds in excess of 100,000 Rpm without bearing HFW failure at large 'O'-Ring centres, and at perhaps elevated temperatures, where 'O'-Ring pinch variation can compensate for thermal effects of 'O'-Ring expansion etc.

Thus it is left to future workers to discover the latter trends, and the work carried out serves to understand the Instability phenomenon more fully and methods of controlling it for the operation of a Rotor over a wide speed range.

It can be seen from Fig. (12·20) and Table (12·16) that any unbalance, be it couple (Dynamic) or static, causes the onset of RSW to drop to as much as 60-75% of its original well balanced value. It is important then that the Rotors be either well balanced or grossly unbalanced.

Fig. (12·34) shows the Curves of HFW and RSW for ω/ω_n for all Bearing Centres, with Bearings operating in the Aerodynamic mode. The curves agree with the findings of Marsh and Simmons (71) and (72) such that the slope of HFW is twice that of RSW. One can see the definate advantages of Viton over Silicon regarding the RSW onset

values. Rotor Asymmetry causes the reactions in both bearings to be different such that two onset speeds will be present in both the RSW and HFW Instability modes. This was detected experimentally by a difference of RSW onset speed in Bearing A to Bearing B and varied by about 1,000 → 1,600 Rpm for the range of Asymmetry tests carried out. See Table (12·15). Gross Asymmetry therefore can reduce the speed of HFW onset considerably.

CHAPTER 13

DYNAMIC INSTABILITY THEORETICAL STUDIES

13·1·1 COOL AIR UNIT ROTOR DYNAMICS (SPRING MASS DAMPER SYSTEM)

Firstly consider the one dimensional model of the Rotor System in Fig. (13·1).

The Rotor System models mathematically in Spring mass, damper form the cool air unit, a Rotor mounted in two Aerodynamic/Hybrid bearings.

One observes three masses and three inertias and hence six degrees of freedom (Equations of Motion) resulting in six Eigen values and Eigen vectors are manifest.

Three Equations of Motion describing translational motion manifest translational whirl. Three Equations of Motion describing conical motion manifest conical whirl. If the coordinates are coupled (either Statically or Dynamically) mixed modal vibration can take place. If the bearing bush masses and inertias are identical then only four equations are required to describe the vibrational characteristics.

If the Rotor is symmetric about its bearing centres then the Equations of Motion can be further reduced to two, since the system does not have conical whirl characteristics which are manifest when the system of equations are dynamically coupled.

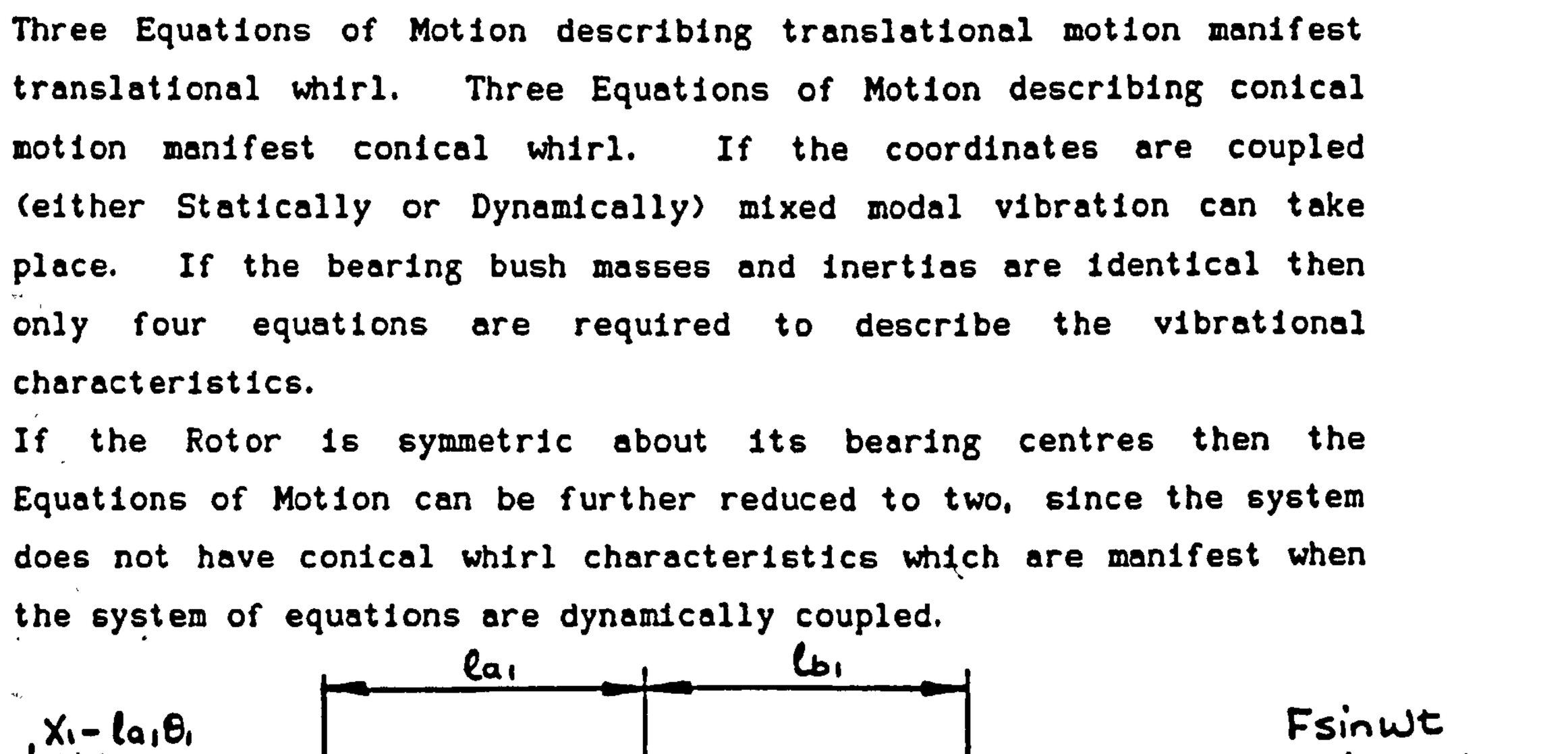

Fig. (13·1)

$$\sum FX = 0$$

$$1\ m_1X_1 + Kg_2(X_1-la_1\theta_1) + Kg_3(X_1+lb_1\theta_1) - Kg_2X_2 - Kg_3X_3 = Fsin\omega t \qquad 13\cdot1$$

$$2\ m_2X_2 + K_{21}(X_2-la_2\theta_2) + K_{22}(X_2+lb_2\theta_2) + Kg_2X_2 - Kg_2X_1 = 0 \qquad 13\cdot2$$

$$3\ m_3X_3 + K_{31}(X_3-la_3\theta_3) + K_{32}(X_3+lb_3\theta_3) + Kg_3X_3 - Kg_3X_1 = 0 \qquad 13\cdot3$$

$$\sum MX = 0$$

$$4\ I_1\theta_1 - Kg_2(X_1-X_2la_1\theta_1)la_1 + Kg_3(X_1-X_3+lb_1\theta_1)lb_1 = Tsin\omega t \qquad 13\cdot4$$

$$5\ I_2\theta_2 - K_{21}(X_2-la_2\theta_2)la_2 + K_{22}(X_2+lb_2\theta_2)lb_2 = 0 \qquad 13\cdot5$$

$$6\ I_3\theta_3 - K_{31}(X_3-la_3\theta_3)la_3 + K_{32}(X_3+lb_3\theta_3)lb_3 = 0 \qquad 13\cdot6$$

Assuming a solution of the form $X = Xe^{j\omega t}, \theta = \theta e^{j\omega t}$

$$X = -\omega^2Xe^{j\omega t}, \theta = -\omega^2\theta e^{j\omega t}$$

In matrix format the Equations of Motion reduce to

$$[K - \omega^2M]\ [X] = [F]$$

Without unbalance the Equations of Motion are Homogeneous and

$$[K - \omega^2M] = [0]$$

However the addition of damping in the structure makes the equations of motion non-orthogonal.

The equations of motion can be solved for the homogeneous condition by the sweeping matrix technique to reveal Eigen values and Eigen vectors, as Marsh's Spring Mass Analogy.

The unbalance case requires special consideration as the equations are non-homogeneous. One can obtain the frequency response by solving the equations of motion for a given speed sweep and compare the resulting amplitudes, where a maximum value would indicate the near presence of a resonant condition.

By plotting $\omega/\omega n$ against F/X_1, F/X_2 or F/X_{12} (receptance) one can detect the resonant conditions. The characteristic plot of receptance against frequency is shown in Fig. (13·2).

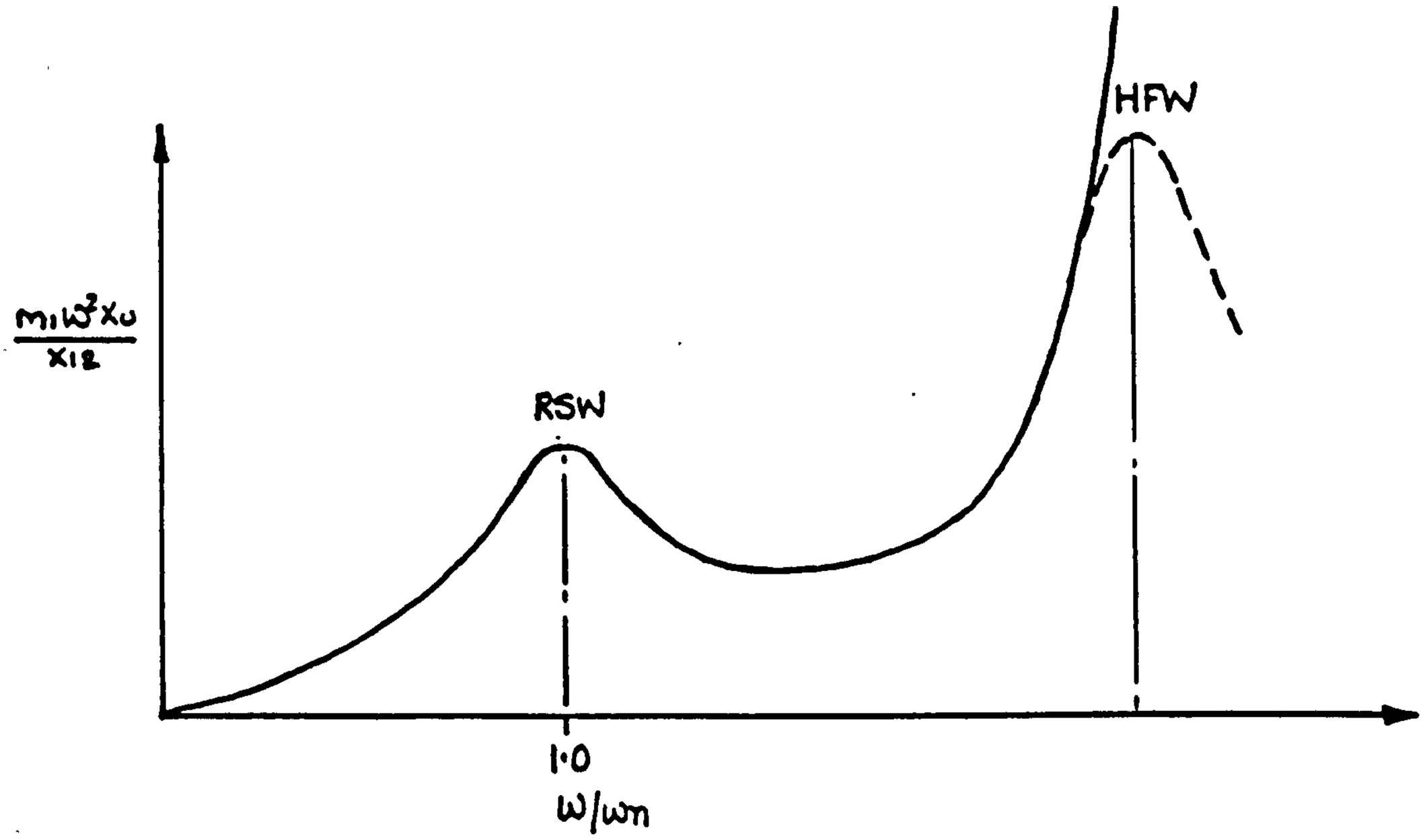

Fig. (13·2)

This frequency plot can then be determined for the Rotor, bearing bush and also the relative movement of Rotor to bush X_{12} as shown and the conical motion of the Rotor system also. Phase angle can also be plotted such that a Nyquist plot can be generated.

13·2·1 TWO DEGREE OF FREEDOM SYSTEM WITH UNBALANCE

If one now reduces the system of equations to that of a Symmetric Rotor mounted in a Symmetric bearing one has a Two Degree of Freedom System With Unbalance, as the Fig. (13·3) below. This being consistent for a Symmetric System.

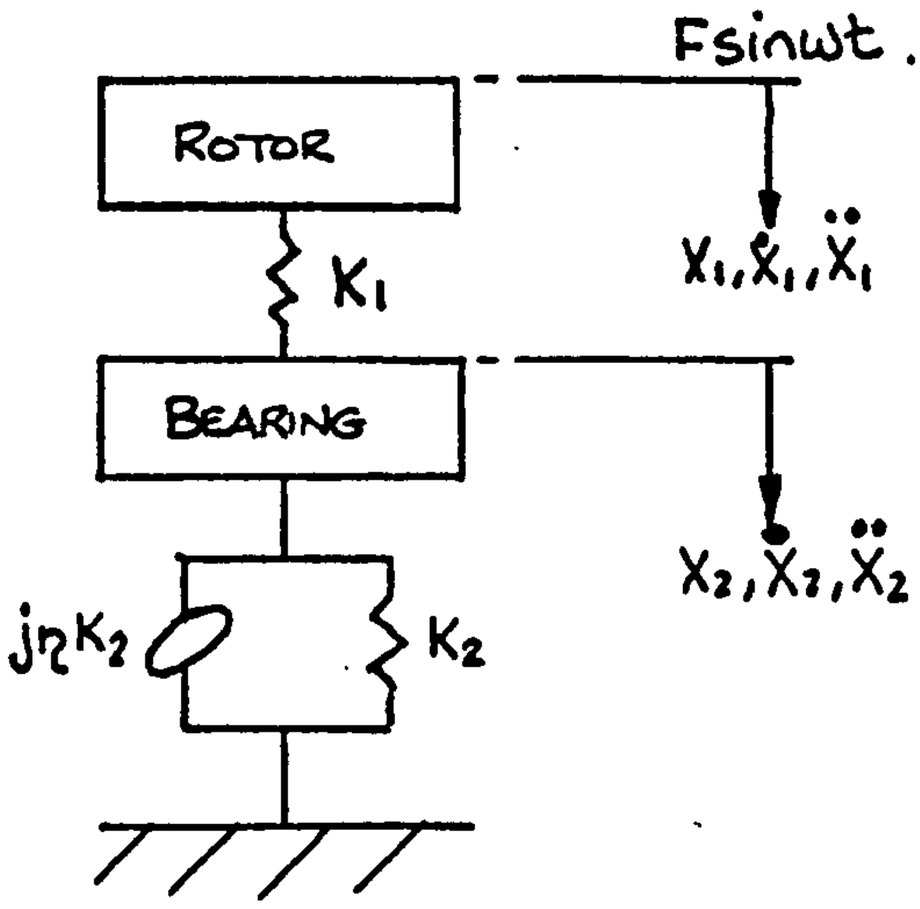

$F\sin\omega t \Rightarrow (m_1\omega^2 X_u \sin\omega t)$

m_1 = Rotor mass (Journal)

m_2 = Bearing mass (Bush)

$K_2^* = K_2(1+j\eta)$ = 'O' Ring Stiffness

η = Loss angle (Varies for Elastomeric Materials)

Fig. (13·3) Two Degree of Freedom System

Equations of Motion

$$m_1 X_1 + K_1(X_1 - X_2) \Rightarrow m_1\omega^2 X_u \sin\omega t \qquad (13\cdot7)$$

$$m_2 X_2 + K_2^* X_2 - K_1(X_1 - X_2) \Rightarrow 0 \qquad (13\cdot8)$$

Let $X_1 = X_1 \sin\omega t \quad X_2 = X_2 \sin\omega t$

Hence

$$-m_1\omega^2 X_1 + K_1(X_1 - X_2) = m_1\omega^2 X_u \qquad (13\cdot9)$$

$$-m_2\omega^2 X_2 + K_2^* X_2 - K_1(X_1 - X_2) \Rightarrow 0 \qquad (13\cdot10)$$

In Matrix Format

$$\begin{bmatrix} (K_1-m_1\omega^2) & , & -K_1 \\ -K_1 & , & (K_2^*+K_1-m_2\omega^2) \end{bmatrix} \begin{bmatrix} X_1 \\ X_2 \end{bmatrix} = \begin{bmatrix} m_1\omega^2 \\ 0 \end{bmatrix} \begin{bmatrix} X_u \\ 0 \end{bmatrix} \qquad (13\cdot11)$$

Rearranging Equations

$$X_2 = \frac{m_1\omega^2X_uK_1}{\Delta} \qquad (13\cdot12)$$

$$X_1 = \frac{m_1\omega^2X_u[K_2^*+K_1 - m_2\omega^2]}{\Delta} \qquad (13\cdot13)$$

From derivation $X_2 = \frac{m_1\omega^2X_uK_1}{\Delta}$

$$X_1 = \frac{m_1\omega^2X_u[K^*_2+K_1-m_2\omega^2]}{\Delta} \qquad \text{Where } K^*_2 = K_2(1+j\eta)$$

$$X_1-X_2 = X_{12}$$

$$* \therefore X_{12} = \frac{m_1\omega^2X_u[K_2^*-m_2\omega^2]}{\Delta}$$

But $X_1 = X_2+X_{12}$

$$X_1 = \frac{m_1\omega^2X_uK_1}{\Delta} + \frac{m_1\omega^2X_u\ [K_2^*-m_2\omega^2]}{\Delta}$$

$$X_1 = X_2 + \frac{m_1\omega^2X_u\ [K_2^*-m_2\omega^2]}{\Delta} \qquad (13\cdot14)$$

* X_{12} is referred to by Marsh (63, 64) as the relative displacement of the Bearing Journal to the Bush, but in terms of unbalance force, Critical Bearing relationship $[K_2^*-m_2\omega^2]$ and the Natural Frequency of

Unforced Vibrations Characteristic Equation Δ.

For $X_1 \Rightarrow X_2$ either $m_1\omega^2X_u \Rightarrow 0$ or $K_2^*-m_2\omega^2 \Rightarrow 0$

That is there is either no unbalance force $m_1\omega^2X_u$ or $K_2^*-m_2\omega^2 \Rightarrow 0$

13·2·2 CRITICAL FILM STIFFNESS (K_1c)

$$X_1 = \frac{FK_1}{\Delta} \qquad (13\cdot15)$$

$$X_2 = \frac{F(K_2^* + K_1 - m_2\omega^2)}{\Delta} \qquad (13\cdot16)$$

Rearranging these equations and subtracting the (13·16) equation from the (13·15) we have:-

$$X_{12} = \frac{-F(K_2^* - m_2\omega^2)}{\Delta} \qquad (13\cdot17)$$

$$\therefore \quad X_{12} = -\frac{m_1\omega^2X_u\ (K_2^* - m_2\omega^2)}{[K_1c(K_2^*-m_1\omega^2-m_2\omega^2)-m_1\omega^2(K_2^*-m_2\omega^2)]}$$

$$\frac{X_{12}}{X_u}[K_1c((K_2^*-m_2\omega^2)-m_1\omega^2)-m_1\omega^2(K_2^*-m_2\omega^2)] = -m_1\omega^2(K_2^*-m_2\omega^2)$$

$$\text{Hence} \quad K_1c \Rightarrow \frac{m_1\omega^2(K_2^*-m_2\omega^2)(1-X_uc/X_{12}c)}{[(K_2^*-m_2\omega^2)-m_1\omega^2)]} \qquad (13\cdot18)$$

One can see that if $X_u/X_{12} \Rightarrow 0$

$$K_1c \Rightarrow \frac{m_1\omega^2(K_2^*-m_2\omega^2)}{[K_2^*-m_2\omega^2]-m_1\omega^2}$$

This agrees with Marsh and Simmons (71) for the Critical Film Stiffness for Aerodynamic Bearings without unbalance.

.The above equation indicates that if unbalance is in phase k_1c is increased.

$$K_1c_B = \frac{A\ B}{B-A} \qquad \text{Where } A = m_1\omega^2 \text{ \& } B = (K_2^*-m_2\omega^2)$$

$$K_1 c_u = \frac{A\ B}{B-A} \cdot (1-c) \qquad \text{Where } c \Rightarrow X_u/X_{12}\ ,\ X_u = \frac{X_{12}\ \tan\varphi}{\tan\beta}$$

Where β is the angle between c of g and the resultant force. δ is the constant distance between the centre of mass and the centre of rotation of the shaft. See Fig. (13·4a) below.

Thus the Critical Film Stiffness is reduced with residual unbalance. If $X_u/X_{12} \Rightarrow 0$ $K_1 c$ is not affected. If $X_u/X_{12} < 1$, The Critical Stiffness is reduced and hence the frequency of Whirl onset. Also if $X_u/X_{12} \Rightarrow 1$ $K_1 c \Rightarrow 0$, and $X_u/X_{12} > 1$ for above RSW. This agrees with the findings of other workers and the Experimental work with Unbalance. Lastly if $X_u/X_{12} > 1$ $K_1 c$ is negative as in the case of gross unbalance.

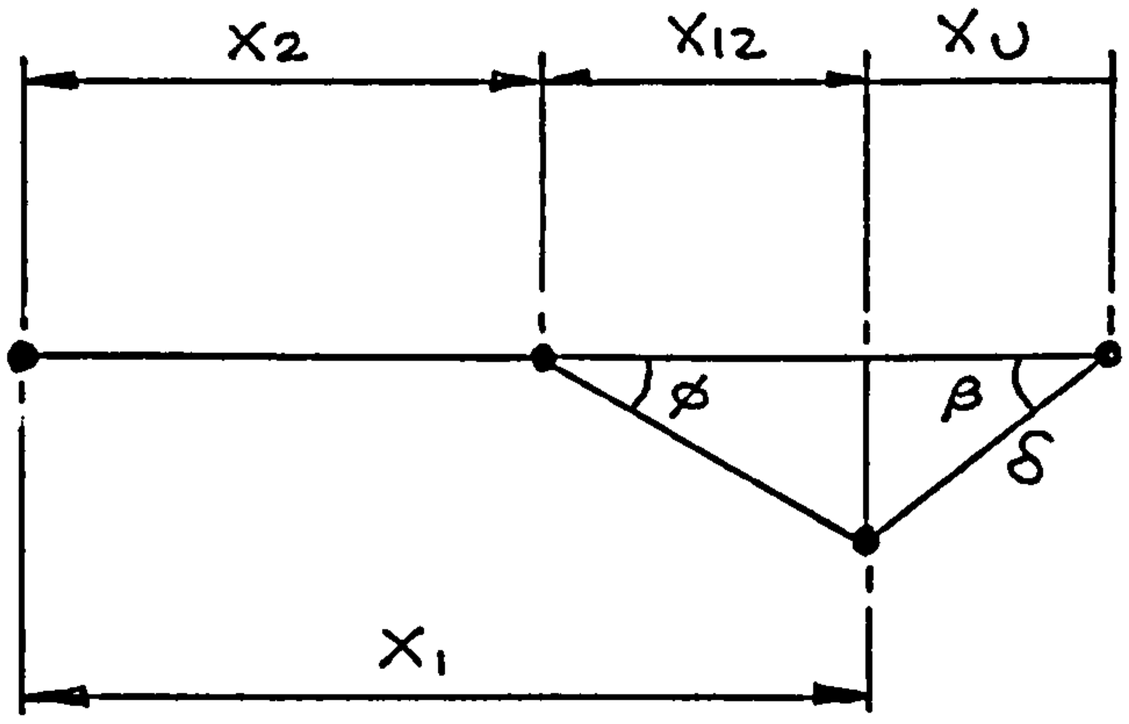

Figure (13·4a)

$$K_1 c = \frac{m_1 \omega^2\ \left[K_2^* - m_2\ \omega^2\right]\ \left[1 - \delta\cos\beta\ /\ c\varepsilon\cos\varphi\right]}{\left[\ (\ K_2^* - m_2\ \omega^2\ ) - m_1\ \omega^2\ \right]} \qquad (13\cdot19)$$

Where $\delta \cos\beta \Rightarrow c \Rightarrow X_u$ Above RSW $X_u > 1$

$\frac{}{c\varepsilon\ \cos\varphi}$ $\frac{}{X_{12}}$ $\frac{}{X_{12}}$

δ = Constant & β = Angle between c of g and Resultant Force

$\frac{X_{12}\tan\varphi}{X_{12}\tan\beta} = \frac{\tan\varphi}{\tan\beta}$ Can be seen from Fig. (13·4a)

And if $\beta \Rightarrow 0$ ie. $\beta \ll 90$

$$\therefore K_1c = \frac{m_1\omega^2 [K_2^* - m_2\omega^2]}{[(K_2^*-m_2\omega^2)-m_1\omega^2]} \cdot \left[1- \frac{\delta}{c\varepsilon\cos\varphi}\right] \qquad (13\cdot20)$$

If $\beta = > 90$

$$K_1c = \frac{m_1\omega^2 [K_2^* - m_2\omega^2]}{[(K_2^*-m_2\omega^2)-m_1\omega^2]} \quad \text{ie. @ RSW}$$

If $\beta > 90 \Rightarrow 180$

$$K_1c = \frac{m_1\omega^2 [K_2^* - m_2\omega^2]}{[(K_2^*-m_2\omega^2)-m_1\omega^2]} \cdot \left[1 + \frac{\delta}{c\varepsilon\cos\varphi}\right] \quad \text{ie. Inversion}$$

13·3·1 DYNAMIC ANALYSIS OF JOURNAL AND BEARING

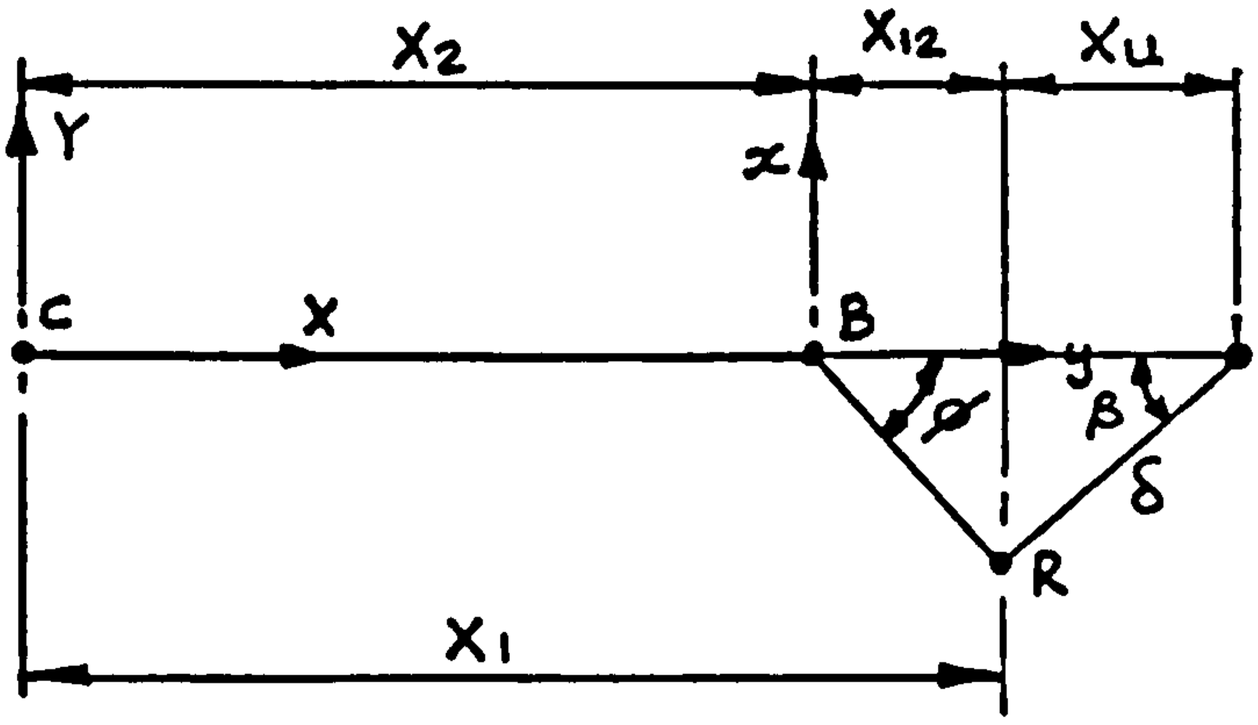

Fig. (13·4b) Vector Relationship of Bearing, Journal and Machine Centre. (Unbalance Vector Relationship shown above RSW).

Consider Fig. (13·4b) which shows an arbitrary Vectoral relationship between Machine, Bearing and Journal Centres, whilst the Journal is fixed relative to the Bearing and the Bearing and Journal rotate about the fixed machine centre at Rate ω. X_1 is the absolute position of the Journal centre, X_2 is the absolute position of the Bearing centre and X_{12} is the relative position of Journal to Bearing Bush.

Position X_1 consists of the following Vectoral Quantities.

$$X_1 = X_2 + X_{12} \qquad (13·21)$$

$$X_1 = X_2 + x_{12}i + y_{12}j + z_{12}k \qquad (13·22)$$

Differentiating w.r.t. time

$$\dot{X}_1 = \dot{X}_2 + \frac{d}{dt}(x_{12}i + y_{12}j + z_{12}k) \qquad (13·23)$$

$$\dot{X}_1 = \dot{X}_2 + (\dot{x}_{12}i + \dot{y}_{12}j + \dot{z}_{12}k) + (x_{12}\dot{i} + y_{12}\dot{j} + z_{12}\dot{k}) \qquad (13·24)$$

But $\dot{i} = \omega \times i$

$\dot{j} = \omega \times j$

$\dot{k} = \omega \times k$

Hence $\dot{X}_1 = \dot{X}_2 + \dot{X}_{12}r + \omega \times X_{12}$ (13·25)

$\dot{X}_{12}r$ is the velocity of the Rotor relative to the moving system xyz (Bush). Differentiating the velocity expression w.r.t. time one obtains:-

$\ddot{X}_1$ = Absolute Acceleration of the Journal (Rotor).

$$\ddot{X}_1 = \ddot{X}_2 + (\ddot{x}_{12}i + \ddot{y}_{12}j + \ddot{z}_{12}k) + (\dot{x}_{12}\dot{i} + \dot{y}_{12}\dot{j} + \dot{z}_{12}\dot{k})$$
$$+\dot{\omega}\times(x_{12}i + y_{12}j + z_{12}k) + \omega\times(\dot{x}_{12}i + \dot{y}_{12}j + \dot{z}_{12}k)$$
$$+\omega\times(x_{12}\dot{i} + y_{12}\dot{j} + z_{12}\dot{k}) \qquad (13\cdot26)$$

$$\ddot{X}_1 = \ddot{X}_2 + \omega\times\dot{X}_{12}r + \dot{\omega}\times X_{12} + \omega\times\dot{X}_{12}r + \omega\times(\omega\times X_{12}) + \ddot{X}_{12}r$$

$$\ddot{X}_1 = \ddot{X}_2 + \dot{\omega}\times X_{12} + \omega\times(\omega\times X_{12}) + 2\omega\times\dot{X}_{12}r + \ddot{X}_{12}r \qquad (13\cdot27)$$

Where X_1 = Absolute Acceleration of the Journal (Rotor).

The first three terms $\ddot{X}_2 + \dot{\omega}\times X_{12} + \omega\times(\omega\times X_{12})$ are the Absolute Accelerations of the Bearing Centre.

The last two terms $2\omega\times\dot{X}_{12}r + \ddot{X}_{12}r$ are the total Acceleration of the Journal relative to the Bearing.

$$\therefore \quad \ddot{X}_1 = \ddot{X}_2 + \dot{\omega}\times X_{12} + \omega\times(\omega\times X_{12}) + 2\omega\times\dot{X}_{12}r + \ddot{X}_{12}r$$

Absolute Acceleration = Absolute Acceleration + Relative Acceleration
of Journal of Bearing of Journal to Bearing

13·3·2 EQUATION ADMISSABILITY

$$\ddot{X}_1 - \ddot{X}_2 = \dot{\omega}\times X_{12} + \omega\times(\omega\times X_{12}) + 2\omega\times\dot{X}_{12}r + \ddot{X}_{12}r = 0$$

For a fixed radius circular orbit at constant Rotational speed.

$$\dot{\omega}\times X_{12} = \ddot{X}_{12}r = 0$$

$$\therefore \quad \omega\times(\omega\times X_{12}) + 2\omega\times\dot{X}_{12}r = 0$$

13·3·3 FIRST ONSET SPEED CONDITION

The first whirl onset condition is obtained by referring to the phase relationship of the Journal Bearing mass vibration in the first mode of vibration.

In phase components

$$\ddot{X}_1 - \ddot{X}_2 = \ddot{X}_{12} \Rightarrow 0$$

If $X_1 \Rightarrow X_2$

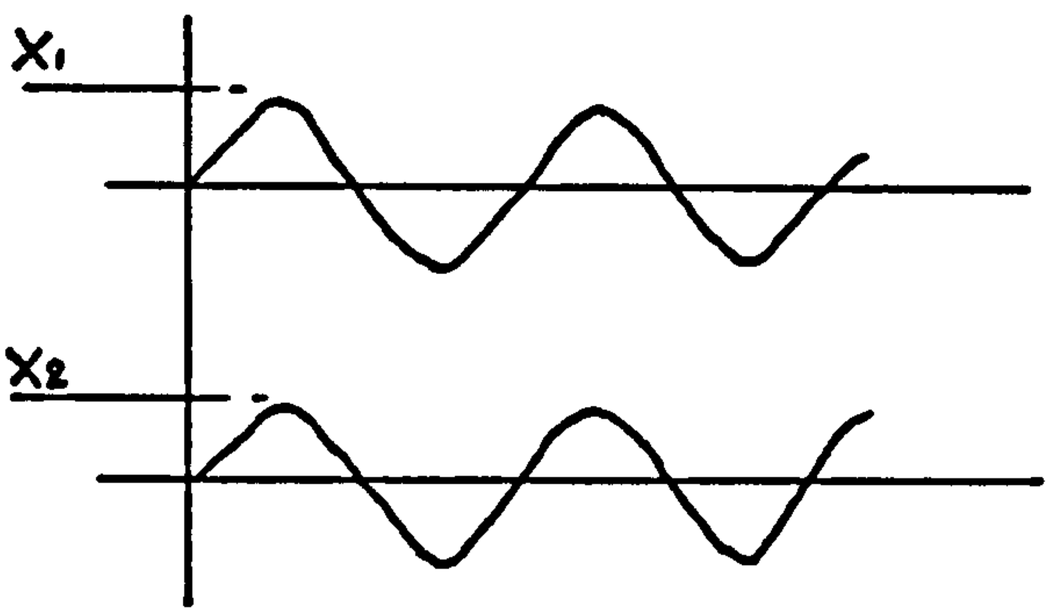

Fig. (13·5) First Instability Onset Amplitude/Phase Relationship

Hence Equation (13·27) becomes

CENTRIPETAL CORIOLIS

$$0 = \omega\times(\omega\times X_{12}) + 2\omega\times\dot{X}_{12}r \qquad (13\cdot28)$$

But $X_{12} \Rightarrow c\varepsilon$ & $\dot{X}_{12}r \Rightarrow c\varepsilon\dot{\varphi}$

$$\therefore \omega^2 c\varepsilon = -2\omega c\varepsilon\dot{\varphi}$$

$$\therefore 1+2\frac{\dot{\varphi}}{\omega} \Rightarrow 0 \qquad (13\cdot29)$$

and is obtained when $\dot{\varphi} = -\omega/2$ that is the Journal precesses backwards at half the forward Rotational speed of the Journal. The condition of Instability is manifest by the Centripetal and Coriolis Acceleration terms being equal to zero. The Bearing Bush and Journal

Accelerations are also equal and are vibrating in phase. The Force balance therefore being zero.

13·3·4 SECOND ONSET SPEED CONDITION

The second whirl onset condition is obtained also by referring to the phase and amplitude relationship of the Journal and Bush mass whilst vibrating in the second mode.

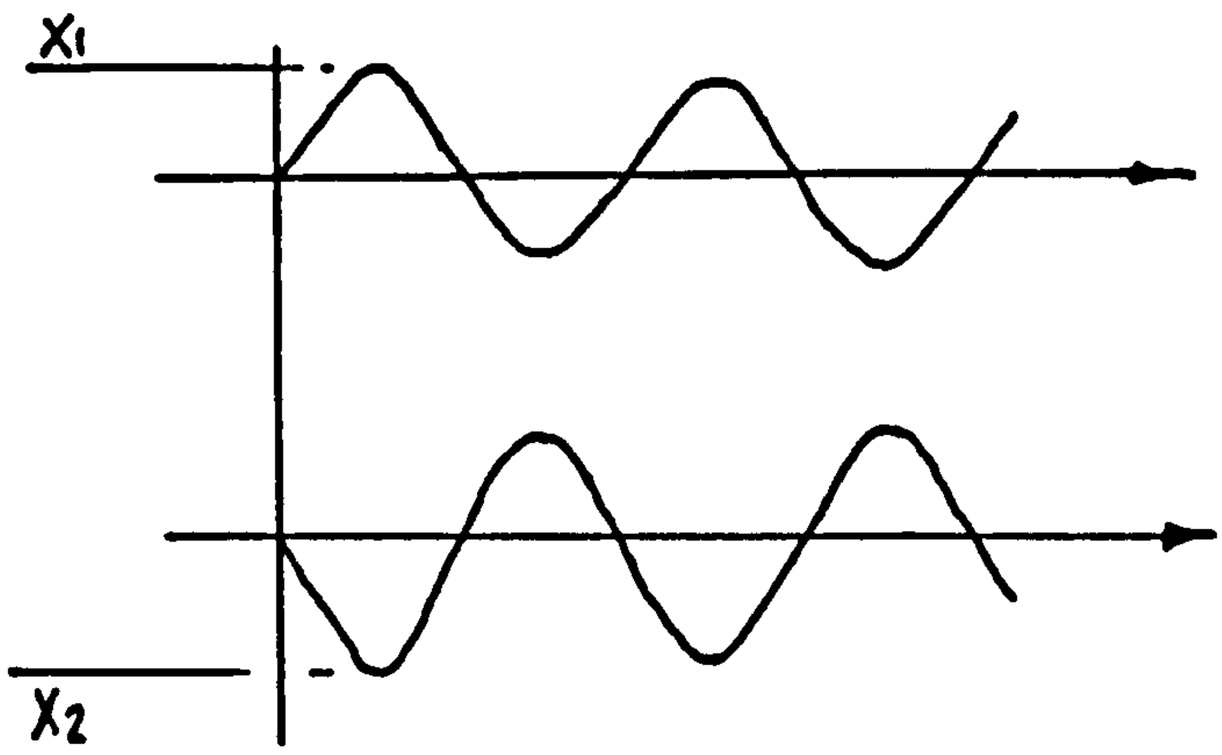

Out of phase components

$\ddot{X}_1 - (-\ddot{X}_2) \Rightarrow 0$

Fig. (13·6) Second Instability Onset Amplitude/Phase Relationship

$$\therefore \quad \ddot{X}_1 - (-\ddot{X}_2) \Rightarrow 0$$

CENTRIPETAL CORIOLIS

$$0 = \omega \times (\omega \times X_{12}) + 2\omega \times \dot{X}_{12}r \qquad (13\cdot28)$$

$$1 + 2\omega \times \dot{X}_{12}r \Rightarrow 0$$

$$\overline{\omega \times (\omega \times X_{12})}$$

Which becomes upon substituting components for X_{12}

$$1 + \frac{2\omega c\varepsilon\dot{\varphi}}{\omega^2 c\varepsilon} \Rightarrow 1 + \frac{2\dot{\varphi}}{\omega} \Rightarrow 0 \qquad (13\cdot29)$$

Hence $\dot{\varphi} = -\omega/2$

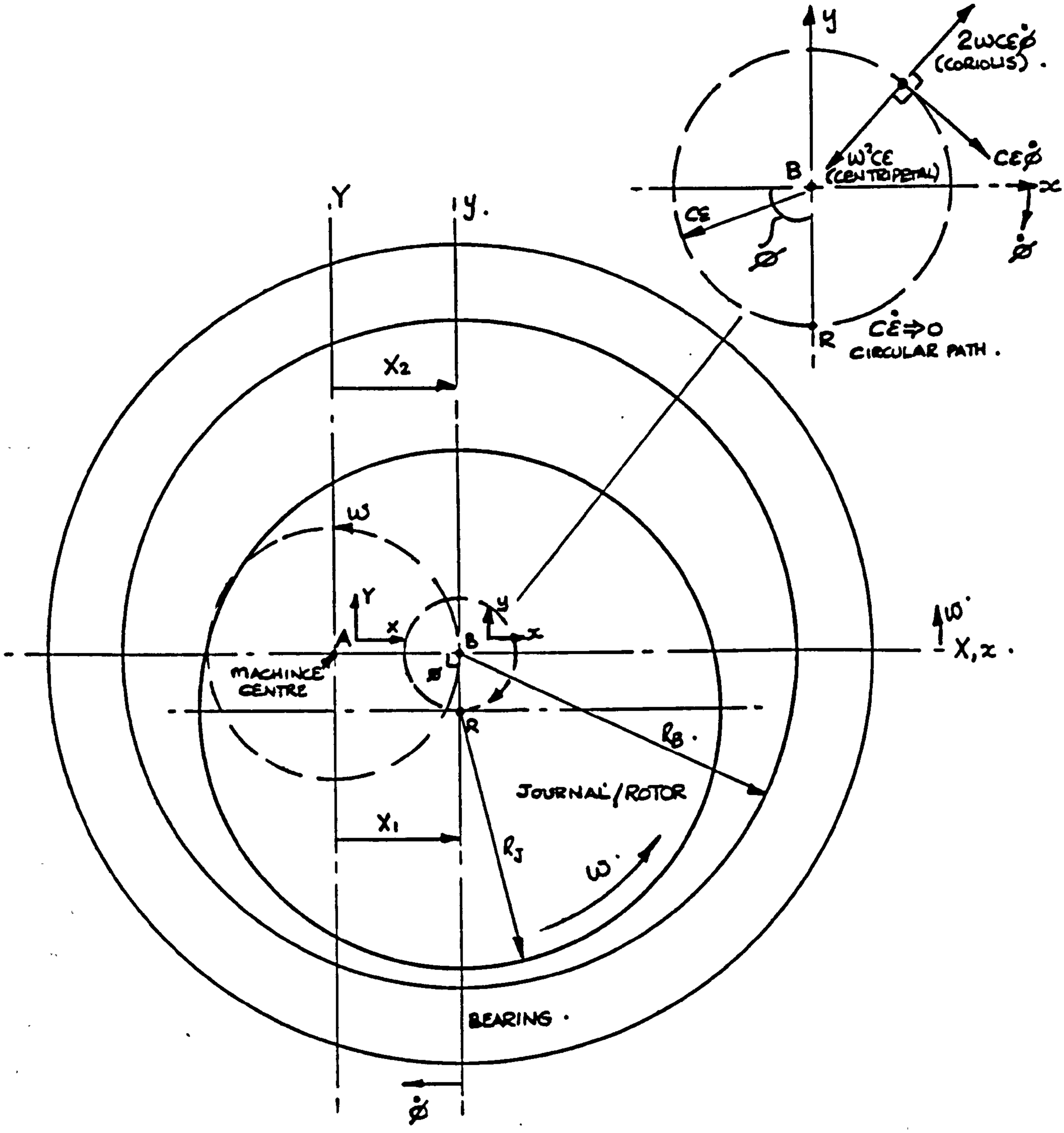

Fig. (13·7) BEARING AND JOURNAL CENTRE RELATIONSHIP (ωn_1)

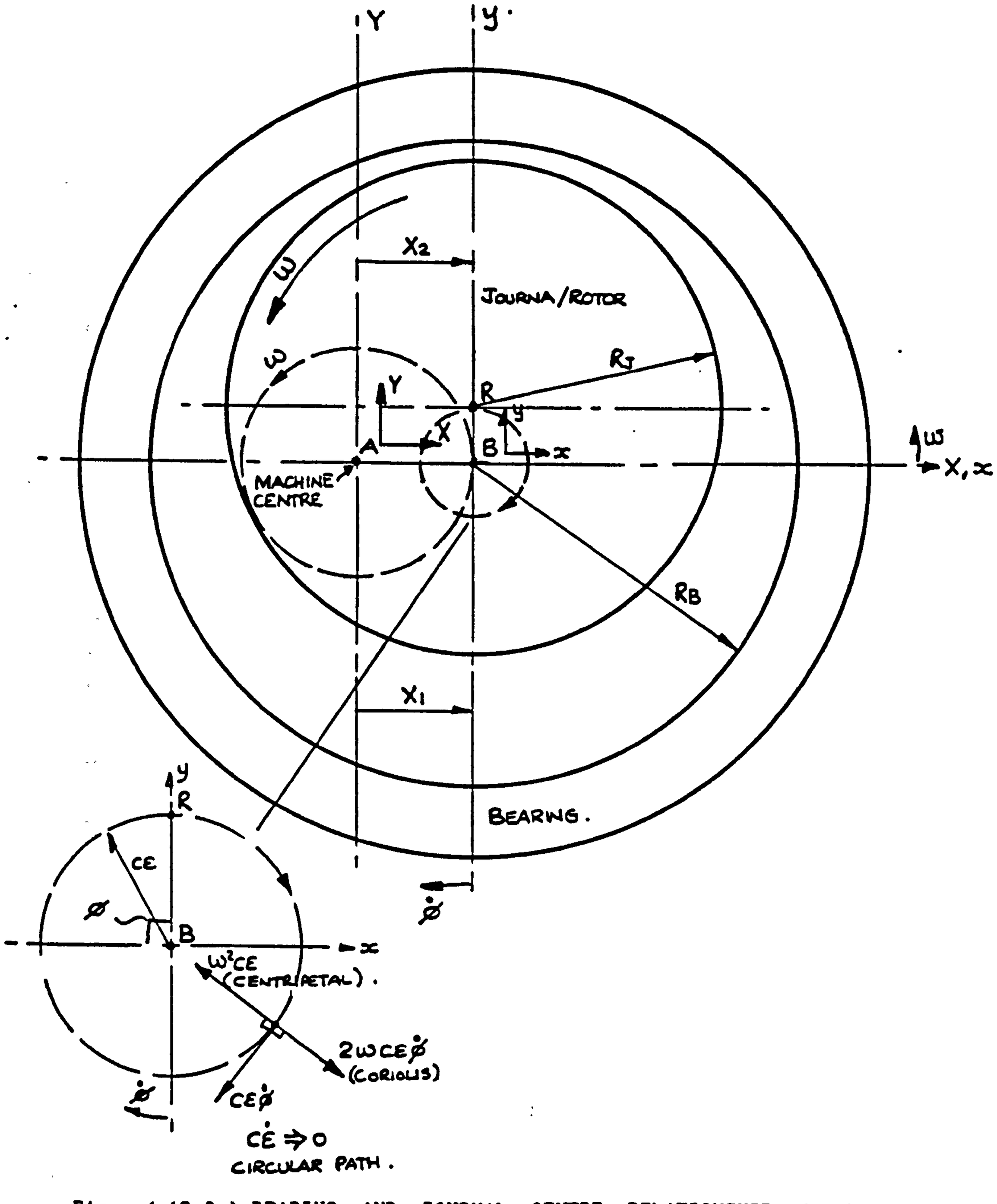

Fig. (13·8) BEARING AND JOURNAL CENTRE RELATIONSHIP (ωn_2)

The two modal onsets of Instability is Analogous to a spring mass system but if constant damping is present and a phase angle is present the same principle very much takes place.

The experimental HFW onset speeds were found to be very close to ½ even with damping present in the 'O'-Ring support. The worst condition being only 16% in error. The error could easily be accounted for by slight inaccuracies in measurement of speed or frequency, but is probably attributable to damping in support structure.

The phase relationship tends to agree favourably also with the findings of HFW and RSW onset. The phase angle tending to 90° at or near an Instability. However at RSW all frequency ratios measured were 1·0 not ½. One condition to account for this is that unbalance moment area X_u is of the same magnitude as the Rotor Displacement cε which results in a φ/ω ratio of 1·0 as described further on in the analysis.

13·3·5 RESIDUAL UNBALANCE

The preceding Acceleration Equation can be modified to accommodate unbalance.

$$\omega\times(\omega\times X_{12}) + \omega(\omega\times X_u) + 2\omega\times\dot{X}_{12r} = 0 \qquad (13\cdot30)$$

$$X_{12} = c\varepsilon$$

$$\dot{X}_{12r} = c\varepsilon\dot{\varphi}$$

$$X_u = X_{12}\,\frac{\delta\cos\beta}{c\varepsilon\cos\varphi} = \frac{c\varepsilon\delta\cos\beta}{c\varepsilon\cos\varphi}$$

$$\therefore \quad 0 = \omega^2\, c\varepsilon + \omega^2\, c\varepsilon\,\frac{\delta\cos\beta}{c\varepsilon\cos\varphi} + 2\omega c\varepsilon\dot{\varphi}$$

$$\omega \left(1 + \frac{\delta \cos\beta}{c\varepsilon\cos\varphi}\right) + 2\dot{\varphi} = 0$$

$$\therefore \frac{\dot{\varphi}}{\omega} \Rightarrow \frac{-1}{2}\left(1 + \frac{\delta\cos\beta}{c\varepsilon\cos\varphi}\right) \Rightarrow \frac{-1}{2}\frac{(X_{12}+X_u)}{X_{12}}$$

If X_u is negative and less than X_{12} $\dot{\varphi}/\omega < \frac{-1}{2}$

If X_u is negative and greater than X_{12} $\dot{\varphi}/\omega > \frac{-1}{2}$

One therefore observes that the frequency ratio $\dot{\varphi}/\omega$ is increased if $(X_{12} + X_u)/X_{12}$ is greater than 1·0 and reduced if $(X_{12} + X_u)/X_{12}$ is less than 1·0.

Also Marsh has discussed Ref. (117) that Inversion takes place with Rotors operating with residual unbalance, and does not take place with gross unbalance. However if the unbalance vector X_u is less than $c\varepsilon$ and occurs at 90° phase angle as in a resonant condition, the frequency ratio can be >½ or <½ for a residually unbalanced Rotor and has been monitored for the HFW condition.

13·4·1 CONCLUSION

At the onset of RSW the Absolute Bush Displacement tends to that of the Absolute Displacement of the Journal and therefore there is none or very little Relative Displacement $X_1 - X_2 = X_{12} \Rightarrow 0$.

At this point the Phase difference of the Unbalance Force and Restoring Force K_2X_2 is 90° which signifies a Resonant condition and can be seen for all the Tests carried out. For all tests RSW resulted with a Phase Angle of 90°.

Above RSW the phase angle increases towards 180° but is dependent upon the damping present in the supporting structure $j\eta K_2$. Tests 1→3

Chapter (12) indicate a small amount of damping present due to the phase and amplitude response to frequency, both before and after RSW.

Both Marsh Ref. (117) and Powell Ref. (103) have discussed the phenomena of inversion present in a system with small residual unbalance. This phenomenon enables the phase inversion of the Unbalance Force $m\omega^2X_2$ and the Restoring Force K_2X_2. With damping present in the structure $j\eta K_2$, it is postulated that this HFW onset at high speed with Aerostatic/Hybrid Air Bearings may be run through enabling high speed trouble free operation.

For a Spring Mass system the onset of Instability can be seen to be modelled as a mechanical resonance. For a Two Mass system there are two such resonances.

Simmons and Marsh (63) & (64) state that the first Instability speed in a Spring Mass system should lie below

$$\omega_{n1} < \left(\frac{K_2}{m_1+m_2} \right)^{1/2} \qquad (13\cdot33)$$

and the second onset speed should be greater than

$$\omega_{n2} > \frac{(K_2)}{m_2}^{1/2} \qquad (13\cdot34)$$

where $K_2 \Rightarrow S_o$, m_1 = mR and m_2 = mB from Simmons and Marsh's notation.

Simmons (72) has discussed that whirl cessation ocurred at $\omega_1 \Rightarrow 2\omega_o$ where

$$\omega_o = \frac{(K_2)^{1/2}}{m_2} \qquad (13\cdot35)$$

where K_2 and ωo are obtained by modal analysis techniques.

The Author's theoretical model considers the stiffness and damping present in a Bearing system, whereupon the one dimensional Equations of Motion for Translational and Conical motion are derived. Both equations contain damping terms and forcing imparted by residual unbalance (Synchronous Force). In a two degree of freedom system unbalance force being synchronous imparts a force that leads the line of centres by an angle φ. Up to the first onset of Instability the Unbalance Force is in phase with the restoring Force K_2X_2. Beyond

this onset due to phase inversion the unbalance force is then in phase with the Inertia forces.

Marsh claims that this phase angle φ is equal to the attitude angle of a steady state force of the same magnitude.

K_2 varies with supply pressure so that the 'O'-Ring stiffness at 0 psi is less than that at 120 psi. Also the Air film stiffness at 120 psi is greater than that at 0 psi.

We know from observations and the characteristics of a two degree of freedom system that at RSW $X_1-X_2 \Rightarrow 0$ so that $\ddot{X}_1-\ddot{X}_2 \Rightarrow 0$ with an in phase vibrational motion of Journal and Bush. However at HFW, $X_1-(-X_2) \Rightarrow 0$ so that $\ddot{X}_1-(-\ddot{X}_2) \Rightarrow 0$ with an out of phase vibrational motion of Journal and Bush.

Therefore one observes two convenient Boundary conditions:-

① At RSW $X_1-X_2 \Rightarrow 0$ $\quad (\ddot{X}_1-\ddot{X}_2 \Rightarrow 0)$

② At HFW $X_1-(X_2) \Rightarrow 0$ $\quad (\ddot{X}_1+\ddot{X}_2 \Rightarrow 0)$

Figure (13·9) → (13·11) show the conditions of Unbalance Force relative to Inertia, Damping and Restoring Forces.

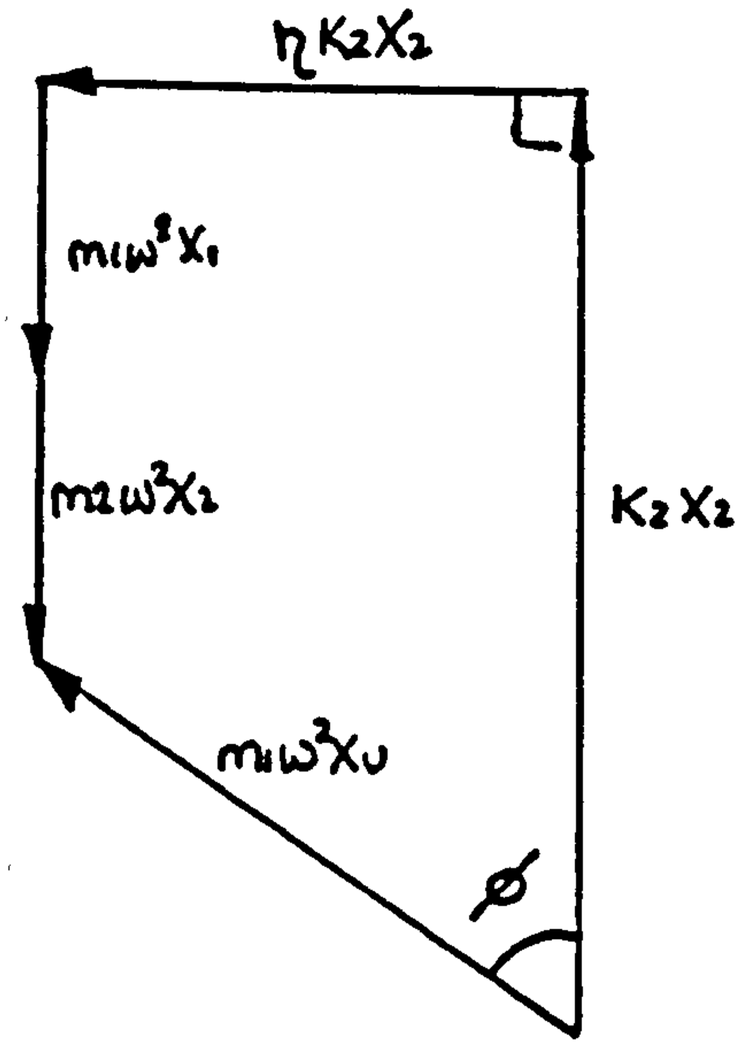

Fig. (13·9)
Below RSW φ < 90

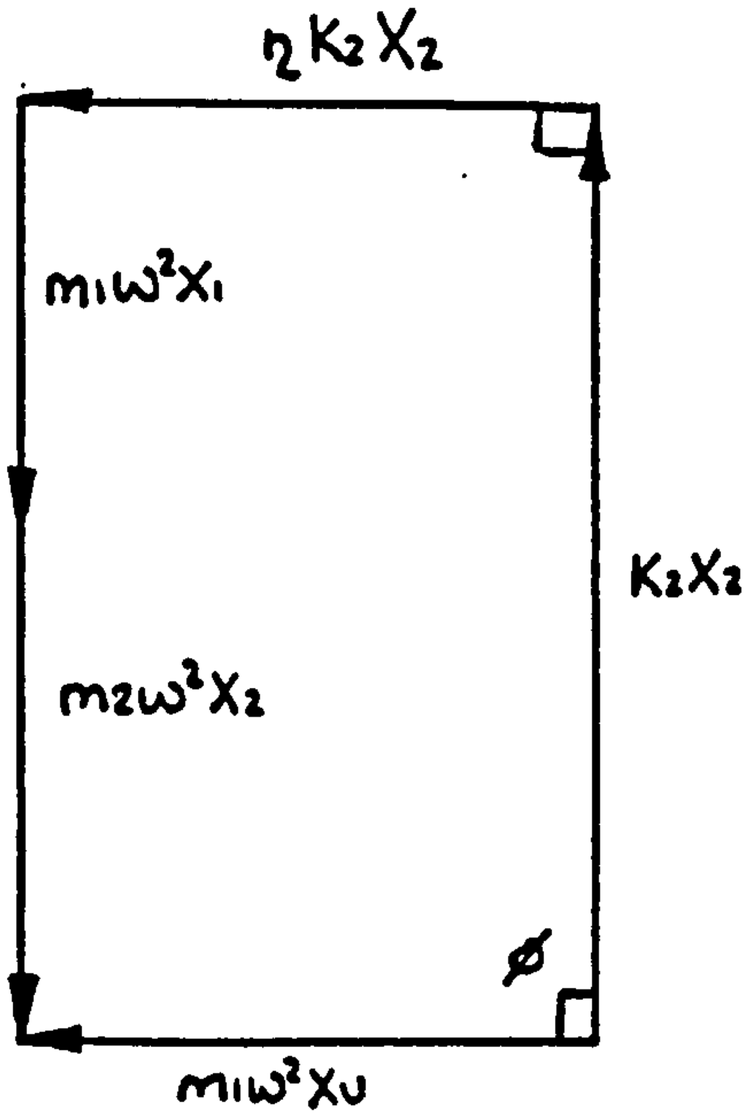

Fig. (13·10)
At RSW φ = 90

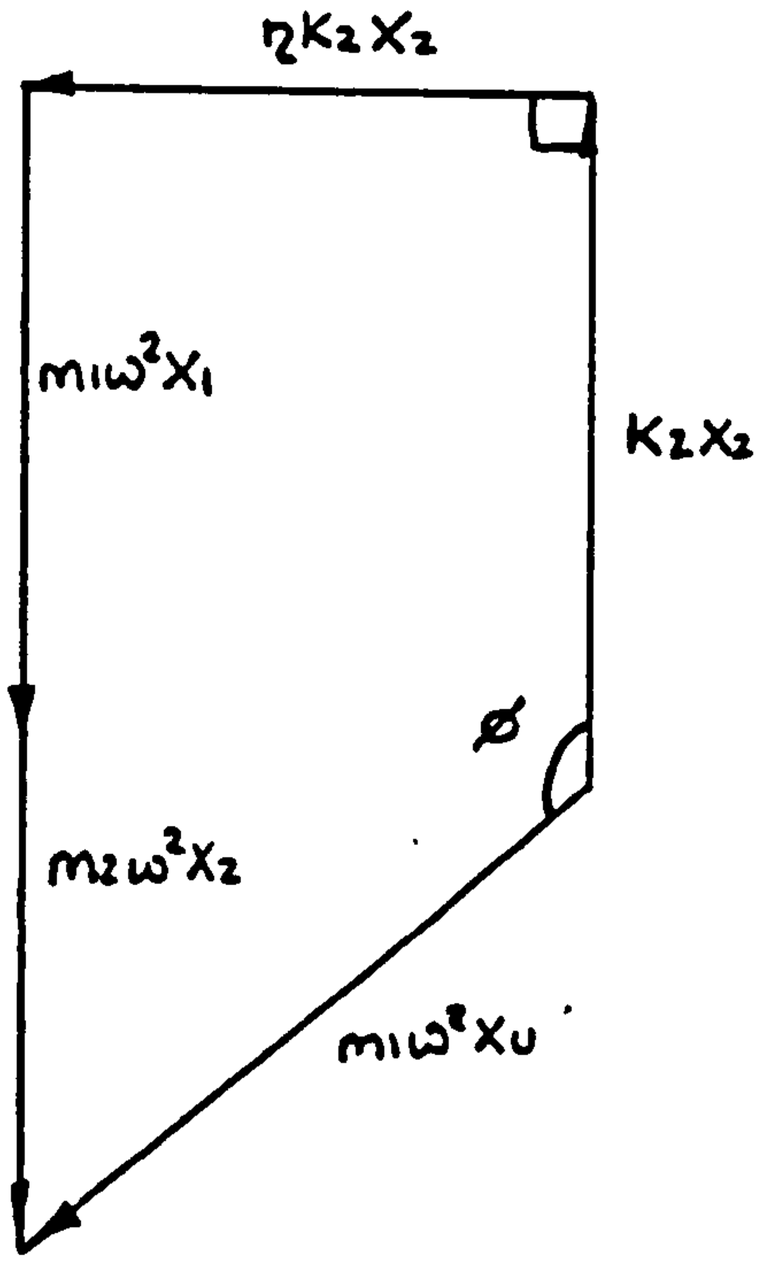

Fig. (13·11)
Above RSW φ > 90

If one observes the condition where at RSW the unbalance force vector is balanced by the damping present in the 'O'-Ring support as shown. At this condition the whirl onset speed is seen to be

$$m_1\omega^2X_1 + m_2\omega^2X_2 \Rightarrow K_2X_2$$

Hence $$\omega^2 \Rightarrow \frac{K_2X_2}{m_1X_1 + m_2X_2} \qquad (13.36)$$

But at RSW $X_1 \Rightarrow X_2$

Hence $$\omega^2 \Rightarrow \frac{K_2X_2}{m_1X_2 + m_2X_2} = \frac{K_2}{m_1 + m_2} \qquad (13\cdot37)$$

One observes that Ratio of Displacement Vector X_2/X_1 is an important parameter. Thus for a soft 'O'-Ring material K_2 will be low and a low RSW speed will be present. Variations of m_2 Bearing mass can be seen to vary RSW. Increased Rotor mass also reduces RSW and HFW onsets. The equation for whirl onset is therefore:-

$$\omega^2 = \frac{K_2}{(K_1m_1+K_2m_2)}\cdot\left[K_1\left(\frac{m_1+m_2}{m_2}\right) + K_2(1+j\eta)\right] \qquad (13\cdot38)$$

One observes that from Equation (13·38) that two coefficients within the square brackets, the mass ratio $(m_1+m_2)/m_2$ and Hysteristic damping factor $(1+j\eta)$ strongly influence the resonant condition at RSW onset. This agrees somewhat with Simmons and Marsh's observations that RSW $\propto [(m_1+m_2)/m_2]^{1/2}$. However with damping present the onset speed can be seen to be slightly higher because of the additional $K_2(1+j\eta)$ and agrees with findings for damped two degrees of freedom systems.

The value of η (the loss angle) is not likely to be very large in practice, and for Silicon is in the region of 5°. For Viton the loss angle has as yet not been measured at room temperature with the methods available to date. At room temperatures however, other materials have greater loss angles than Viton and Silicon. Viton behaved at room temperature in an overdamped manner. Silicon keeps an almost constant loss angle up to temperatures approaching 200°C. Therefore Viton and Silicon would show advantages at elevated temperatures, as B. Ae have investigated.

CHAPTER 14

14·1·1 CONCLUSION

Two main areas of investigation have been carried out. Firstly that of studying the Pressure distribution of a single gas (Air) bearing operating at steady state and at Instability conditions. Secondly the investigation of a Rotor mounted in flexibly supported Air bearings (C.A.U.). This apparatus was designed to model closely a C.A.U. and any high speed lightweight Rotor/bearing configurations (Turbo-charger or small turbines).

Steady state Air bearing investigations further substantiated the findings of MacFarlane (15) that there is indeed two areas of stagnant flow within the pressure field. This does however indicate that the Raimondi theory for Aerodynamic operation does not fully explain this phenomenon. The experimental tests also suggests that Raimondi's theory seriously over extends the steady state applicability of his Air bearing theory. In some instances the Journal would be running in an unstable region, which, according to his theory should be well within the steady state Aerodynamic operating region.

This discrepancy was found only for the L/D of 2·0 bearing condition. His theory for L/D of 1·0 is reasonably agreeable with experimental findings for load capacity, but not however for the pressure profile as can be seen in Chapter (5). Discrepancies in the pressure field and the maximum sub-ambient pressure were detected. Also discovered on the single gas (Air) bearing Test apparatus was the pressure field variation as the Instability threshold was approached and passed through. Having traversed the onset of Instability due to the lack of damping in the structure or Air film, metallic Journal/bearing contact was present. This was indicated by a steep linear temperature rise with linear speed increase.

The central pressure profile increased with increasing Journal speed until just prior to the Instability onset the central pressure profile begins to drop to a condition at the onset where the central profile tends to the Sommerfeld condition as seen in Chapter (11). Fig. (11·1) → (11·3).

As the Journal speed was further increased the whirl orbit tends towards a Cardioid and the pressure profile delineates this very well in Fig. (11·1) at 30000 Rpm where two small pressure peaks are seen with the rest of the pressure profile tending towards zero. These pressure peaks are thought to be due to the convergent nature of the Journal at the peaks of the resultant loops of the Cardioid.

The temperature distribution of the Journal/bearing operation can be seen to vary, depending on load and speed conditions and the tests carried out.

For the three L/D ratios tested the three classical lubrication regimes can be seen clearly. Also for the Instability condition it is seen that metallic contact causes the temperature rise to be of similar slope to the boundary lubrication regime but of opposite sense. This latter lubrication regime points towards an additional fourth condition manifest beyond HFW.

Having discovered the limitations of Raimondi's theoretical model a theoretical programme was embarked upon to further improve the mathematical rigority of the Reynold's equation. Several attempts and methods were made until a final approach based on the Reynold's equation with Binomial stepwise Linearization of the Non-Linearity of the Finite Difference equation was conceived. However the applicability of this theoretical model was not fully tested but the Author is convinced that the approach will prove more fruitful and will not rely on under-relaxation, which to date has no rigorous mathematical proof.

It is hoped that this experimental and theoretical work will help further understand the Aerodynamic lubrication process.

The second main area of study involved the Dual Bearing Test Rig (Phase II). The greatest exponent of HFW understanding to date is Marsh (63/64) who modelled the flexibly mounted Rotor in Air bearings with a Spring Mass Analogy. This does not however explain the condition when the first whirl onset is able to be run through. The Test Rig was conceived by the need to understand the phenomenon of half frequency whirl and its alleviation under certain operating conditions. Marsh goes on to state that damping in the bearing support can produce a condition of stable operation beyond the first HFW onset. To this end the experimental apparatus was designed such that a Cool Air Unit could be simulated with many Rotor and System variables.

Due to the problems of the Single Gas Bearing sealing at the final Layshaft, a study on high speed sealing methods was undertaken, based upon the Thew seal system. See Chapter (6). Reasonably successful results were obtained. However the seal did not become effective (100% sealing) until 30,000 Rpm. It is thought that if a second seal was placed in series with the first, or if the clearances were tighter, better results may have been manifest. However it was thought prudent to leave the clearances as they were, to alleviate any possibility of Seal Touchdown, which would have had catastrophic consequences whilst running at the high Rotational speed of the unit.

For all the tests carried out except the unbalance tests, the modes of Instability were Translational. Since there was no discernable phase difference between either ends of the Rotor. The findings suggest that as the 'O'-Ring mounting centres of the bearing tend towards the bearing length, that the Instability threshold is increased, especially the second onset speed of HFW. Half frequency whirl only occurred in the smaller 'O'-Ring mounting centres < 15 mm. One is therefore led to believe that this HFW is manifest by low Conical Stiffness and Damping in the bearing at low 'O'-Ring centres. Although no 90° phase angle of the Bearing and Bush Lissajous was detected Fig. (12·27) → (12·31) clearly show

that HFW probability is reduced with increased 'O'-Ring centres, such that HFW is not seen at speeds up to 55,000 Rpm. From static tests it was found that Conical stiffness increased with increased 'O'-Ring centres, therefore it is believed that this is the condition found. Also 'O'-Rings displaced at greater centres impart more damping than those at a reduced centre distance.

The bearing types tested on this Rotor Test Rig were Aerodynamic, Hybrid and Hybrid Porous.

Hybrid bearings operated better than the Aerodynamic and Hybrid porous bearings and showed that a vast increase in performance could be had at a small additional extravagance.

Generally the RSW onset speed of the Hybrid bearings was greater than the Aerodynamic RSW. This was due to the increased 'O'-Ring stiffness created by Air Pressurization. During tests with the Hybrid Sulfinized bearings HFW was only manifest at 10 mm 'O'-Ring centre bearings. This was probably due to the low mass flow rate of this bearing over the others tested, since the Air film stiffness may have been critically low, even at 120 psi. The clearance value was also the lowest value recorded of the Bearings tested.

Porous Hybrid bearings were investigated since good results had been obtained by Powell and Tempest (68) at speeds up to 100,000 Rpm in a high speed electric motor. The Author's findings were that the bearings did not perform as well as the Hybrid sulfiniz bearings and required 4-8 times the mass flow rate, to support the same Rotor mass. They were also susceptable to surface smearing due to metallic contact. This reduced the mass flow rate and caused eventual seizure due to surface pickup. The Sulfiniz Hybrid bearing did not suffer from this problem. The experimental findings in general tended to follow those of previous workers. Increasing the Rotor mass reduces the Instability onset speed, but in some instances also reduced the vibrational amplitude. This latter trend was not consistent due mainly to the non-linear nature of the support stiffness and damping

characteristics of the rubber 'O'-Rings. The Dynamic stiffness and damping characteristics did however follow closely the static results of Chapter (10). The vibrational mode was always Translational and may well be a characteristic of the Test Rig.

Of the two 'O'-Ring materials tested on this Test Rig 70° Viton out performed the 70° Silicon material. HFW was not detected in any of the tests carried out at room temperature with Viton. The RSW onset speeds for Viton occurred at a greater speed than those of Silicon. The variation of pinch was kept to a minimum, nominally 8% for Silicon and < 10% for Viton. The 'O'-Rings were off the shelf items and had no special geometry or material composition. The 70° Silicon material did however enable HFW to be observed, such that RSW and HFW could be studied and compared in greater detail. RSW varied little with change of 'O'-Ring centres, the variation being due to differences in bearing mass. RSW did however reduce with increased Rotor mass as did HFW.

RSW appeared with a frequency ratio $\omega/\omega n \Rightarrow 1{\cdot}0$ where as HFW appeared with a frequency ratio $0{\cdot}493 < \omega/\omega n < 0{\cdot}58$. The whirl orbit of HFW depicted a Cardioid with a single re-entrant loop. Not pure circular motion but a more complex orbit. RSW showed no re-entrant loop characteristics. For Dynamic Tests 1-3 Fig. (12·34) → (12·36) Lissajous and frequency amplitude plots were taken such that the amplitude and phase could be compared below RSW, at RSW and above RSW. The phase angle φ below RSW was less than 90°, at RSW $\varphi \Rightarrow$ 90° and above RSW tended towards 180°. This trend agrees with having passed through a condition of resonance.

It is thought that the existence of residual unbalance enables RSW to take place such that the unbalance induces damping in the 'O'-Ring support, which is enough to alleviate metallic contact between Journal and the Bearing Bush. Theoretical results seem also to suggest that the frequency ratio $\omega/\omega n$ varies with magnitude of residual unbalance.

Powell (103) and Marsh (117) have discussed the existence of phase inversion when residual unbalance is present in a Rotor system. Powell states for Aerostatic operation where c/R ≈ 0·002 that this phase inversion takes place in rigidly mounted Aerostatic Bearings. Marsh (117) has also carried out work with gross unbalance and has found interesting results. His results were carried out for bearings with 'O'-Ring centres tending towards one 'O'-Ring diameter. Hence it is thought that very little damping is afforded and his Spring Mass Analogy is valid for such a condition.

The experimental results show that Hybrid operation offers good performance for Rotors mounted in flexibly supported Air bearings. Such that when the Air film stiffness is greater than the 'O'-Ring support stiffness good damping is afforded from the 'O'-Ring support, as seen in the Lissajous plots obtained. Hybrid bearings mounted in 'O'-Rings offer greater potential in the long term and require study in greater detail.

The theoretical model of the C.A.U. is derived to understand the Dynamic principle of the flexibly mounted bearing based upon a Spring Mass Damper system. The damping being afforded by the 'O'-Ring as Hysteristic damping. The results show the model to be comparable to that of Marsh's (if damping is neglected). The theoretical model also considers unbalance force and its influence on Instability. A further model which derives the fundamental acceleration components indicates the condition for HFW and RSW and postulates the Instability conditions of both.

It is hoped that this work is useful in highlighting that HFW may be controlled if the conditions are favourable and good design policy is undertaken. (The conditions being simplicity and understanding).

It is shown that whirl amplitude can be drastically reduced if the right material is used and that HFW may be eliminated totally if Hybrid bearings are utilized in C.A.U. design instead of Aerodynamic, with 'O'-Rings placed at the extremities of the bearings.

It is thought by the Author that due to the stagnant flow areas in the Aerodynamic bearing that they are inherently unstable, so have a limited use in high speed Rotating machinery. Geometric changes such as lemoning and offsetting, do not alleviate, but simply raise HFW to a higher onset speed.

Plain Aerodynamic bearings are also inherently unstable when there is zero g acting on them. For use in an Aircraft system where the condition of zero g may take place signifies disastrous consequences. Since touchdown may take place and possible seizure leading to the unit failure and the breakdown of the Ventilation and Avionics systems.

There are alternatives to the Aerodynamic bearing and the Hybrid path looks the most favourable for C.A.U.'s. Hybrid bearings can enable the implementation of positive feedback systems such that whirl amplitude and Rotor dynamics can be optimized at each running speed condition. Also this may enable Resonance to be tuned out of a Rotors performance spectrum altogether. This will further increase the safety and reliability of the C.A.U. over an extended period of time.

CHAPTER 15

15·1·1 RECOMMENDATIONS FOR FURTHER WORK

The recommendations for further work can be put into two distinct parts. Part I; The Single Gas Bearing Rig recommendations and Part II; The Dual Bearing Rig (C.A.U. Simulation) recommendations.

The recommendations for the Single Gas Bearing Rig Study:

1) Make modifications to Rig to enable Torque monitoring.

2) Look at mounting Proximity Probe out board of the bearing to enable easier insitu Calibration.

3) Investigate, (from Dual Bearing Rig), the new and improved Sealing Method for the Layshaft System.

4) Incorporate improved Drive System of Dual Bearing Rig into Single Bearing Rig.

5) Look at improving Proximity Probe performance.

6) Fully Computerize Data capture to speed up Test procedure.

7) Investigate more fully the Mathematical model and develop further.

8) Capture Instability Pressure Profiles for L/D Ratios of 1 and 1·5.

9) Look at other Bearing types ie. Lemon, Lobed and Offset halves.

10) From (9) investigate their Theoretical Analysis.

The Dual Bearing Rig was designed and Developed to understand the fundamentals of the C.A.U. Obvious improvements can be made and are mentioned as the following recommendations:

1) Modify Bearings to enable Temperature distribution of bearing.

2) Carry on work to capture Dynamic Pressure Profile of Journal whilst whirling.

3) Investigate Hybrid Bearing Analysis and Experiments with influence of Unbalance.

4) From (2) develop the Telemetry System fully.

5) It was initially invisaged that the Rig could be turned through 90° to investigate zero g Loaded Rotors. This could be carried out to develop a greater understanding.

6) Look at adding a Thrust Bearing configuration on to the Rig. (Perhaps via the Bearing Shell in the easiest option ie. a Hybrid type).

7) Investigate increasing the Test Rig speed to 100,000 and this may find upper speed limitations of Silicon and Viton.

8) Look at other classical types of Bearing such as Offset halves, Lobed, Lemoned and Tilting Pad.

9) Investigate modal analysis (F.F.T.) on the Rig to further understand RSW and HFW.

10) Use more sophisticated methods to devise Phase Angle relationships and Acceleration, Velocity and Displacements.

11) Look at developing a Feedback System which could be implemented onto the C.A.U. System to control Whirl Orbit Excursion and hence Whirl Onset.

12) Investigate the High Speed Sealing, towards developing a System suitable for High Speed Turbines and Compressors.

13) Develop a Computerized System for Data capture.

14) Implement Computerization of the Theoretical Analysis.

BIBLIOGRAPHY

1 Hirn G — "Sur Le Principaux Phenomenes Qui Presentent Les Frottements Mediates, Soc. Ind. Mulliouse Bull, 26 (1854) pp. 188-277.

2 Kingsbury A — "Experiments with an Air Lubricated Journal" Transactions Am. Soc. Naval. Eng. Vol. 9 pp. 267. 1897.

3 Harrison W J — "The Aerodynamic Theory of Lubrication with Special Reference to Air as a Lubricant". Trans. Cambridge Philosophical Soc. 1913. V. 22 pp. 39-54.

4 Katto Y & Soda H — "Theory of Lubrication by Compressible Fluid with Special Reference to Air Bearings". Proc. of 2nd Japan Nat. Cong. For. App. Mech. 1952. pp 267-270.

5 Ausman J S — "Finite Gas Lubricated Journal Bearing." Inst. Mech. Eng. Proc. of Conference on Lubrication and Wear, 1957 pp. 39-45.

6 Osferle J F & Hughes W F — "High Speed Effects in Pneumodynamics Journal Bearing Lubrication". Appl. Sc. Rsc. Section A. Vol. 17. pp. 89-99. 1957

7 Cole J A & Kerr J — "Observations on the Performance of Air Lubricated Bearings". Proc. IME. London Confr. on Lub. and Wear. pp. 164-170. 1957

8 Burgdorfer A — "The Influence of the Molecular Mean Free Path on the Performance of Hydrodynamic Gas Lubricated bearings." Trans. ASME. March 1959 pp. 94-100.

9 Elrod H G & Burgdorfer A "Refinements of the Theory of the Infinately Long Self Acting Gas Lubricated Journal Bearing." Proc. of 1st Int. Symposium on Gas Lubricated Bearings, Oct 26-28, pp. 93-118 1959.

10 Michael W A "A Gas Film Lubrication Study Part II." Numerical Sol. of Reynold's Equation for Finite Slider Bearings, IBM J. Res. Dev.,3 pp. 256-259.

11 Gross W A "A Gas Film Lubrication Study Part I." Some Theoretical Analyses of Slider Bearings IBMJ. Res. Dev. 3: pp. 237-255. 1959.

12 Sternlicht B "Gas Lubricated Cylindrical Journal Bearings of Finite Length Part I Static Loading." Report prepared under an ONR Contract No. NON 122844 (00) (Aug 15 1960).

13 Raimondi A A "A Numerical Solution for the Gas Lubricated Full Journal Bearing of Finite Length." ASLE Paper 60. LC-14, ASLE (AM Soc. Lubr. Eng.) Trans. 4 (1961) pp. 131-155.

14 Whitley S & Botts C "Study of Gas Lubricated, Hydrodynamic Full Journal Bearings." Br. J. Appl. Phys. 10, pp. 445-465. 1959.

15 MacFarlane C W R Theoretical and Experimental Studies of Hybrid Gas Journal Bearings. MSc. Thesis School of Mech. Eng. C.I.T. 1978.

16 Kaneko R Matsuda R & Hara S "The Designing and Application of Floating Head Mechanics for Magnetic Recording." 6th Int. Gas Bearing Symp. Unv. Southampton 1974.

17 Lloyd T & McCallion H — "Recent Developments in Fluid Film Lubrication Theory." Proc. Inst. Mech. Eng. 1967-68 V182 N 3A pp. 36-50.

18 Bers L — J Res. Natn. Bur. Std.51. 229. 1953.

19 Schecter S — Trans. Am. Math. Soc. 106. 179. 1962.

20 Leiberstein H M — "Over-Relaxation for Non-Linear Elliptic Partial Differential Equations." Tech. Rept. No. MRC-TR-80. Unv. of Winsconsin. Mathematical Research Centre, Madison, Winsconsin. 1959.

21 Bellman R E, Juncosa M J & Kalaba R — "Some Numerical Experiments Using Newton's Method for Non-Linear Parabolic and Elliptic Boundary Value Problems." Report No. P2200. Rand. Corp. Santa Monica, California 1961.

22 Ames W F — "Numerical Methods for Partial Differential Equations." Nelson 1969. and "Non-Linear Partial Differential Equations in Engineering." Academic Rep. 1965.

23 Siew A H — A Computational Approach to the Design and Performance Optimisation of Solid and Porous Journal Bearings. Ph.D Thesis 1981. School of Mech. Eng. C.I.T.

24 Hyett P W — A Comparison between Theoretically Predicted Hydrodynamic Journal Bearing Performance and Experimental Findings. MSc Thesis. School of Mech. Eng. C.I.T. 1983.

25 Vogel Pohl G — Beitrage Zur Kenntnis Der Gleitlaherreibung Vdi- Forschungsheft 386, Berlin. 1937.

26 Carter D S "An Electrical Method for Determining Journal Bearing Characteristics." J April. Mech. 19, pp. 114-118 (1952).

27 Pao R H F "Fluid Dynamics." Charles Merril Book Inc. 1967. (Chapter 3).

28 Pink E Studies of High Speed Aerostatic Bearings. MSc Thesis (Unpublished) Dept. Mech. Eng. Cranfield Inst. of Tech. 1972

29 Leppard P P F Investigations of Aerostatic and Hybrid Bearings MSc Thesis Dept. Mech. Eng. C.I.T. 1973

30 Hustwick J M The Influence of Operating Parameters on the the Envelope of Hybrid Journal Air Bearing. MSc Thesis Dept. Mech. Eng. C.I.T. 1977.

31 Crump M J Experimental and Theoretical Investigation into Hybrid Gas Journal Bearings. MSc Thesis School of Mech. Eng. C.I.T. 1979.

32 Al-Gabari Y N G "Studies of Correlation between Experimental Performance and Theoretical Prediction for Hybrid Gas Journal Bearings. MSc Thesis School of Mech. Eng. C.I.T. 1980.

33 Dyer D Theoretical and Experimental Studies of the Effect of Clearance and Geometry in Hydro-Dynamic Journal Bearings. Ph.D Thesis 1973. School of Mech. Eng. C.I.T.

34 Hines F F Proc. Western Regional Strain Gauge Comm. Nov 9. 1960. pp. 39-44.

35 Anon — Strain Gauge Temp. Effects. Tech. Note. TN 504. Meas. Group. Inc. Raleigh, North Carolina 27611. USA. 1983.

36 Baske U M — Development of Some Innovational Centrifugal Pumps. Proc. I. Mech. E. 174 11 pp. 437-461. (1960). Especially pp. 444-445.

37 Kelly R W; Wood G M & Marman H V — Development of a High Temperature Liquid Metal Pump. ASME Paper 62-Hyd. 15 (1962).

38 Wood G M; Manfredi D V & Cygner J E — Centrifugal Types of Dynamic Shaft Seals. ASME Paper pp. 63-167 (1963).

39 Thew M T & Saunders M G — The Hydrodynamic Disc Seal. Proc. 3rd Int. Conf. on Fluid Sealing. Cambridge Paper No. H5, pp. H5-97 to H5-124. Organised by British Hydrodynamics Research Assc. (April 1967) pp. 382-395.

40 Thew M T — Further Experiments on the Hydrodynamic Disc Seal. Proc. 4th Int. Conf. Fluid Sealing. Philadelphia, USA. (May 1969).

41 Goddard S J & Thew M T — A Dynamic Shaft Seal for Particle Laden Liquid The Hydrodynamic Disc Seal. Proc. 7th Int. Conf. Fluid Sealing. Unv. Nottingham. Sept 1975. Pub. BHRA Cranfield.

42 Baske U M — Investigations on the Pumping Effect of Rotating Discs. Proc. Inst. Mech. Eng. Vol 189 36/75 pp. 341-349.

43 Ketola H N & McGrew J M — Theory of the Wetted Disc. Proc. 3rd Int. Conf. Fluid Sealing. Cambridge 1967. Paper H4-69

44 Muller H K — Externally Pressurized Shaft Seals. Proc. 4th Int. Conf. Fluid Sealing. Philadelphia, USA. (May 1969) pp. 361-371. Pub. BHRA Cranfield.

45 Adams M C & Colsher R J — An Analysis of Self Energised Hydrostatic Shaft Seals. Proc. 4th Int. Conf. Fluid Seal. Philad. USA. (May 1969). pp. 372-381. Pub. BHRA Cranfield.

46 Dailey K W & Nece R E — Chamber Dimensions Effects on Inducted Flow and Frictional Resistance of Enclosed Rotating Discs. Jnl. Basic Eng. Trans. ASME March 1960. pp. 217-232.

47 Dega R L — Zero Leakage: Results of an Advanced Lip Seal Technology. Proc. 3rd Int. Conf. Fluid Seal. Cambridge. April 1967. Paper D3-17.

48 Fern A G — Part 1- Recipricating Seals and Gaskets. Dowty Seals Ltd.

49 Nau B S — Part 2- Rotary Seals. Dowty Seals Ltd.

50 Morse W — Seals Handbook. Design Eng. Series. Morgan Grampion.

51 Anon — Aeroquip - Seals for Industrial Application Cat. No. 622 1978.

52 Wigram S B — Static Metallic Seals. Reprint from Pumps June 1977.

53 Anon — Fischer Porter Handbook. 10A9010 Ti-Flat Variable Area Flowmeters.

54 Montgomery A G & Sterry F — "A Simple Air Bearing Rotor for Very High Rotational Speeds." Report ED/R 1671, Atomic Energy Research Est. Harwell, Berks, Eng. 1955

55 Brix V H — Synchronous Whirling of Shafts in Plain (Gas) Bearings. Report IGR-R/CA 176. UKAEA.

56 Ford G W K Harris E N & Pantall K — Principles and Applications of Hydrodynamic Type Gas Bearings. Proc. Inst. Mech. Eng. 171:93-128.

57 Whitley S — A Review of Research on Gas Bearings in the UK Energy Authority. Proc. 1st Int. Symp. Gas Lubricated Bearings. Oct 26-28, pp. 30-70 Report ONR/ACR-49. Superintendent of Docs. US Gov. Party Office, Washington.

58 Whitley S Bowhill A J & McEwan P — Half Speed Whirl and Load Capacity of Hydro-Dynamics Gas Bearings. Proc. Inst. Mech. Eng. 1962, 176 pp. 554-565.

59 Reynolds D B & Gross W A — Experimental Investigation of Whirl in Self Acting Air Lubricated Journal Bearings. ASLE Trans. 5, 392-402 (1962).

60 Cheng H S & Trumpler P R — Stability of the High Speed Journal Bearing Under Steady Load to the Compressible Film. Trans. ASME Journ. Eng. For. Ind. Aug 1963. pp. 274-280.

61 McCann R A — Stability of Unloaded Gas Lubricated Bearings. Trans. ASME Journ. Basic Eng. Dec 1963. pp. 513-518.

62 Sternlicht B & Winn L W — On the Load Capacity and Stability of Rotors in Self Acting Gas Lubricated Plain Cylindrical Journal Bearings. Trans. ASME Jnl Basic Eng. Dec 1963 pp. 503-512.

63 Marsh H — The Stability of Aerodynamic Gas Bearings. Ph.D Dissertion, Cambridge Unv. 1963.

64 Marsh H — The Stability of Self Acting Gas Bearings with Non-Circular Members and Additional Elements of Flexibility. Jnl. Lubrication Tech. Trans. ASME Series F 1969 91 (No 1), 113-119.

65 Kerr J — The Onset and Cessation of Half Speed Whirl in Air Lubricated Self Pressurized Journal Bearings. NEL Report No. 237 July 1966.

66 Lund J W — Calculation of Stiffness and Damping Properties of Gas Bearings. Jnl. Lubr. Tech. 90 pp. 793-803.

67 Elrod H G McCabe J T & Chu T Y — Determinations of Gas Bearing Stability by Response to a Step Jump. Jnl. Lubr. Tech. No. 89 (4) pp. 493-498.

68 Powell J W & Tempest M C — A Study of High Speed Machines with Rubber Stabilized Air Bearings. Jnl. Lubr. Tech. Oct 1968 pp. 701-708.

69 Smalley A J Tessarik J M & Badgley R H — Testing for Material Dynamic Properties. ASME Pub. Vibration Testing Instr. and Data Analysis AMD Vol. 12. 1975 p117.

70	Smalley Dalow Mehta	The Dynamic Characteristics of 'O'-Rings. Jnl. Mech. Design Trans. ASME Paper No. 77-DET 27. pp. 1-7.
71	Marsh H & Simmons J E L	An Experimental Method for the Determination of Journal Bearing Stability Parameters Part I Theory. Jnl. Mech. Eng. Science. Vol. 21 No. 3 1979. pp. 179-185.
72	Simmons J E L	An Experimental Method for the Determination of Journal Bearing Stability Parameters. Part II Experiment. Jnl. of Mech. Eng. Science. Vol. 21 No. 3 1979. pp. 187-196.
73	Preece G	Dynamics of the Elastomeric Mounting of High Speed Self Acting Gas Journal Bearings. MSc Thesis 1986 C.I.T.
74	Morrant G A Powell J W & Hargreaves P	Air Bearings and their Application to Dental Turbine Handpieces. British Dental Journal. Vol. 116 No. 12
75	MacFarlane CWR & Reason B R	Experimental Studies in the Operational Performance of a Hybrid Air Journal Bearing with Particular Reference to Pressure Profile Measurement. Proc. 8th Int. Gas Bearing Symp. April 1981. Paper 20, pp.267-285. Leicester Polytech. Pub. BHRA Cranfield.
76	Gross W A	Gas Bearings a Survey Wear. Vol.6. (1963). pp.423-443.
77	Castelli V & Pervics J	Review of Numerical Methods in Gas Bearing Film Analysis. Jnl. Lubr. Tech. Oct 1968 pp. 777-791.

78 Ausman J — An Improved Analytical Solution for Self Acting Gas Lubricated Journal Bearings of Finite Length. Jnl. Basic Eng. Trans. ASME June 1961 pp. 188-194.

79 Osterle J F & Hughes W F — High Speed Effects in Pneumodynamic Journal Bearing Lubrication. Appl. Sci Res. Sect. A 7 pp. 89-99.

80 Cohen M J — A Non-Linear PH Method of Solution for Journal Gas Bearings. Jnl. Lub. Tech. Oct 1976. pp. 613-619.

81 Tao L N — On the Variational Principle and La Grange Equations in Studies of Gas Dynamic Lubrication. Jnl. Appl. Mech. March 1964 pp. 43-46.

82 Pan C H T Malonoski S B Broussard P H & Burch J L — Theory and Experiments of Squeeze Film Gas Bearings Part I Cylindrical Journal Bearing Jnl. Basic Eng. March 1966. pp. 191-198.

83 Laub J H — Externally Pressurized Journal Gas Bearings. ASLE Trans. Vol. 4 (1961) pp. 156-171.

84 Pink E G & Stout K J — Design Procedures for Orifice Compensated Gas Journal Bearings Based on Experimental Data. Trib. Int. Feb. 1978 pp. 63-75.

85 Pao N S & Majumdar B C — Dynamic Characteristics of Gas Lubricated Externally Pressurized Porous Bearings with Journal Rotation. Wear Vol. 50 (1978) pp. 201-210

86 Larson R H & Richardson H H — A Preliminary Study of Whirl Instability for Pressurized Gas Bearings. Jnl. Basic Eng. Dec 1962 pp. 511-520.

87 Ausman J S — Torque Produced by Misalignment of Hydrodynamic Gas Lubricated Journal Bearings Jnl. Basic Eng. June 1960 pp. 335-341.

88 Khrisanova L B — Analytical and Experimental Investigation of the Pressure in the Oil Film of a Journal Bearing with Axes of Journal and Bushing Skewed. Frict. Wear. Mach. 1959. Vol 13. pp. 192-208.

89 Smalley A J & McCallion H — The Effect of Journal Misalignment on the Performance of a Journal Bearing Under Steady Running Conditions. Proc. Inst. Mech. Eng. 1966-67. Vol. 181 Pt. 3B. Paper 5 pp. 45-54.

90 Stokley J R & Donaldson R R — Misalignment Effects in 180° Partial Journal Bearings ASLE. Trans. Vol. 12 (1969) pp. 216-226.

91 Singh D V Sinhasm R & Singh H N — Analysis of Hydrodynamic Journal Bearing with Axes Skew. Jnl. Mech. Eng. Sci. Vol 15 No 2. 1879 pp. 123-131.

92 Lund J W — The Stability of an Elastic Rotor in Journal Bearings with Flexible Damped Supports. Jnl. Appl. Mech. Dec. 1965 pp. 911-920.

93 Lund J W & Nielson H B — Instability Threshold of an Unbalanced, Rigid Rotor in Short Journal Bearings. Proc. IMechE. 1980. pp. 91-95. Paper (C263/80).

94 Bishop R E D — The Vibration of Rotating Shafts. Jnl.Mech. Eng. Sci. Vol.1 No. 1959 pp.50-65.

95 Gladwell G M L & Bishop R E D — The Vibration of Rotating Shafts Supported in Flexible Bearings. Jnl. Mech. Eng. Sci. Vol 1 No 3 (1959) pp. 195-206.

96 Murray M F — Material Combinations for Hydrodynamic Inert Gas Lubricated Bearings. Jnl. Lubr. Tech. Jan 1968 pp. 49-55.

97 Welveden L D & Harris T A — Rolling Element Bearings Operating at the Extremes. Mach. Design Aug. 1987. Appl. Tech. pp. 72-76.

98 Gross W A — Fluid Film Lubrication.1980 John Wiley & Sons.

99 Gross W A — Gas Film Lubrication 1962. John Wiley & Sons.

100 Ames W F — Non-Linear Partial Differential Equations in Engineering. 1965. Academic Press. N York.

101 Pinkus O & Sternlicht B — Theory of Hydrodynamic Lubrication 1961. McGraw-Hill. N York

102 Pao J S — Rotor Dynamics 1983. Wiley Eastern Ltd.

103 Powell J W — Design of Aerostatic Bearings. Machinery Publishing Co Ltd. 1970.

104 Pinkus O — Analysis of Non Circular Gas Journal Bearings Jnl. Lubr. tech. Oct 1975 pp. 616-623.

105 Smith G D — Numerical Solution of Partial Differential Equations. Oxford Unv. Press. 1965.

106 Payne A R & Scott J R — Eng. Design with Rubber. MacLaren & Sons.Ltd. 1960.

107 Torby B J — Advanced Dynamics for Engineers. Holt, Rinehart & Winston 1984.

108 MacMillan W D — Dynamics of Rigid Bodies. (Theoretical Mech.) Dover Pub. Inc. 1936.

109 Thompson W T — Theory of Vibration with Applications. George Allens & Unwin. 1981.

110 Fuller D D — Theory and Practice of Lubrication for Engineers. 2nd Ed. 1984.

111 Beards C F — Structural Vibration Analysis. Ellis Horwood Ltd. 1983

112 Walshaw A C — Mech. Vibrations with Applications. Ellis Horwood 1984.

113 Doebelin E O — Measurements Systems Application & Design. 3rd Ed. McGraw Hill 1983.

114 McCalla T R — Introduction to Numerical Methods & Fortran Programming. John Wiley & Sons. 1967.

115 Froberg C E — Introduction to Numerical Analysis. 2nd Ed. Addison Wesley Pub. Co. 1979.

116 Neale M J — The Comparative Performance of Coupling Types. Int. Conf. Flex. Couplings. June 1977 Paper E2-1

117 Marsh H — The Performance of CoolAir Units Supported on Gas Bearing. 1985. Report to B. Ae.

118 Bannister R H — Notes on Rotor Dynamics. MSc Course Notes (1985). C. I. T.

119 Reason B R — Air Bearings SME/BRR/1378 (1985) C. I. T.

120 Ewins D — Modal Testing : Theory and Practice John Wiley & Son Inc. 1984

121 Mcluckie I R W & Reason B R — Self Energised Gas Bearing Studies. British Aerospace Contract (MC47918ML/001) C I T Report No. 1 Nov 1986

122 Mcluckie I R W & Reason B R — Self Energised Gas Bearing Studies. British Aerospace Contract (MC47918ML/001) C I T Report No. 2 Dec. 1987.

123 Mcluckie I R W & Reason B R — Self Energised Gas Bearing Studies. British Aerospace Contract (MC47918ML/001) C I T Final Report No. 3 Dec. 1988.

124 McLuckie I R W — S. M. E. Report TR/90/7. Gas Bearing Studies. Oct. 1990.

APPENDIX 3

Jacobian of System of Equations N.L.O.R

J (f^k_{pq}) This is accomplished by one of the Taylors series so that the vector form for $x^{k+1}-x^k$ is

$$x^{k+1}-x^k \approx -\omega[D^{-1}_k\ L_k\ \varepsilon^{k+1}+(I+D^{-1}_k\ U_k)\varepsilon^k]$$

where ε^k stands for an Error Vector $\varepsilon^k = x^k-x$ and L_k, D_k, U_k are lower triangular, diagonal and upper triangular materials formed from:

$$J(f^k_{pq}) = L_k+D_k+U_k$$

From above it can be shown that :

$$\varepsilon^{k+1} \approx L^{\omega k}\ \varepsilon^k = -\left[\frac{1}{\omega} D_k + L_k\right].\left[\left(1-\frac{1}{\omega}\right) D_k + U_k\right].\varepsilon^k.$$

which is exactly the same as the Error matrix in the S.O.R. Method. See Ref. (23) for Derivation of S.O.R. Error Matrix.

APPENDIX 6A

OIL MIST LUBRICATION SYSTEM

Oil Mist Lubrication Systems are used in high-speed continuous operation applications. This system permits close control of the amount of lubricant reaching the bearings.

The oil may be metered, atomized by compressed air and mixed with air, or it may be picked up from a resevoir using a venturie effect. In either case, the air is filtered and supplied under sufficient pressure to assure adequate lubrication of the bearings. Control of this type of lubricating system is accomplished by monitoring the operating temperatures of the bearings being lubricated.

The continuous passage of the pressurized air and oil through the labyrinth seals used in the system prevents the entrance of contaminants from the atmosphere into the system.

The successful operation of this type of system is based upon the following factors:-
1) Proper location of the lubrication entry parts in relation to the bearings being lubricated.

2) Avoidance of excessive pressure drops across void spaces within the system.

3) The proper air pressure and oil quantity ratio to suit the particular application.

4) The adequate exhaust of the air-oil mist after lubrication has been accomplished.

To ensure "wetting" of the bearings and to prevent possible damage to balls and races, it is imperative that the oil-mist system be turned on for several minutes before the equipment is started. The importance of "wetting" the bearings before the starting cannot be overstressed and has particular significance for equipment that has been idle for extended periods of time.

APPENDIX 6B

CALIBRATION PROCEDURE FOR FISCHER AND PORTER FLOWMETERS

The Fischer and Porter Flowmeter utilized for air flow measurement was the tri-flat variable area type. The two sizes utilized for experimental testing were the 1/8" and 1/16" diameter tubes with taitulum flats, general details are presented in Table A.

Calibration of the Flowmeters requires the use of design information available from Ref. (13) and the procedure involves the evaluation of the viscous influence Number N and hence the Flowrate W, from graphical data.

From Ref. (13) the viscous influence Number is given by:-

$$N = \frac{A}{\mu OPT} \left[(\rho F - \rho\ OPT)\ \rho\ OPT \right]^{m} \quad \rightarrow \quad (1)$$

where

A = Size Factor
μOPT = Fluid Viscosity at Operating Conditions
ρF = Float Density
ρOPT = Fluid Density at Operating Conditions

and the Flow Rate by :-

$$W = CB \cdot \left[(\rho F - \rho\ OPT) \cdot \rho\ OPT \right]^{m} \quad \rightarrow \quad (2)$$

where C = Flow Coefficient

B = Size Factor

The values for the fluid viscosity and density can be obtained from the following equations :-

$$\mu OPT = \mu STP + (\text{Temp Coefficient}) (t - 70) \quad \rightarrow \quad (3)$$

where t = Ambient Temperature (°F)

μSTP = Fluid Viscosity at S.T.P. (Centipoises)

μSTP = 0·1812 C.P and the temperature coefficient is given as:- 0·000026 cps/deg. F.

Therefore μOPT = 0·01804 Centipoises

$$\rho OPT = \rho STP \times \rho / 14{\cdot}7 \times 530 / (460 ft)$$

where P = Supply Pressure (PSia)

ρSTP = Fluid Density at S.T.P. (g/cc)

Thus ρOPT = $8{\cdot}21 \times 10^{-5}$ ρg/cc.

Therefore for a specified supply pressure it is possible to obtain the value of the viscous influence number from equations (1), (3) and (4) and Table A shows these values for the required pressure range. Entering these values into the appropriate float characteristic curve of Ref (13). gives values for the flow coefficient C, dependent upon the flowmeter scale reading.

Utilizing the values of the flow coefficient in equations (2) enables the flowrates (g/min) to be evaluated. Tables 6 to 20 show the values of C, and the final flow presented in SC form units see Ref. (8).

The resulting calibration curves for the 1/8" and 1/16" diameter flow meters are shown in Figs. (18) and (19) respectively.

APPENDIX 6C

FLOWMETER CALIBRATION

Table A
1/8" Flowmeter

Supply (psig) Pressure	Viscous Influence Number (N).
10	4108·70
20	4870·60
30	5526·93
40	6119·93
50	6641·52
60	7142·50
Nominal Bore	1/8"
Float Type	Tantalum (Density = 16·6 g cc)
Max. Scale Reading	20
Size Factor	A - 404
	B - 76·8

APPENDIX 6D

1/16" Flowmeter

Supply (psig) Pressure	Viscous Influence Number (N)
1	1159·9
2	1207·32
4	1265·30
6	1331·50
8	1392·80
10	1454·30
12	1512·00
14	1567·60
16	1621·29
Nominal Bore	1/16"
Float Type	Tantulum (Density = 16·6 g/cc)
Max. Scale Reading	16
Size Factor Constants	A = 143
	B = 13·6

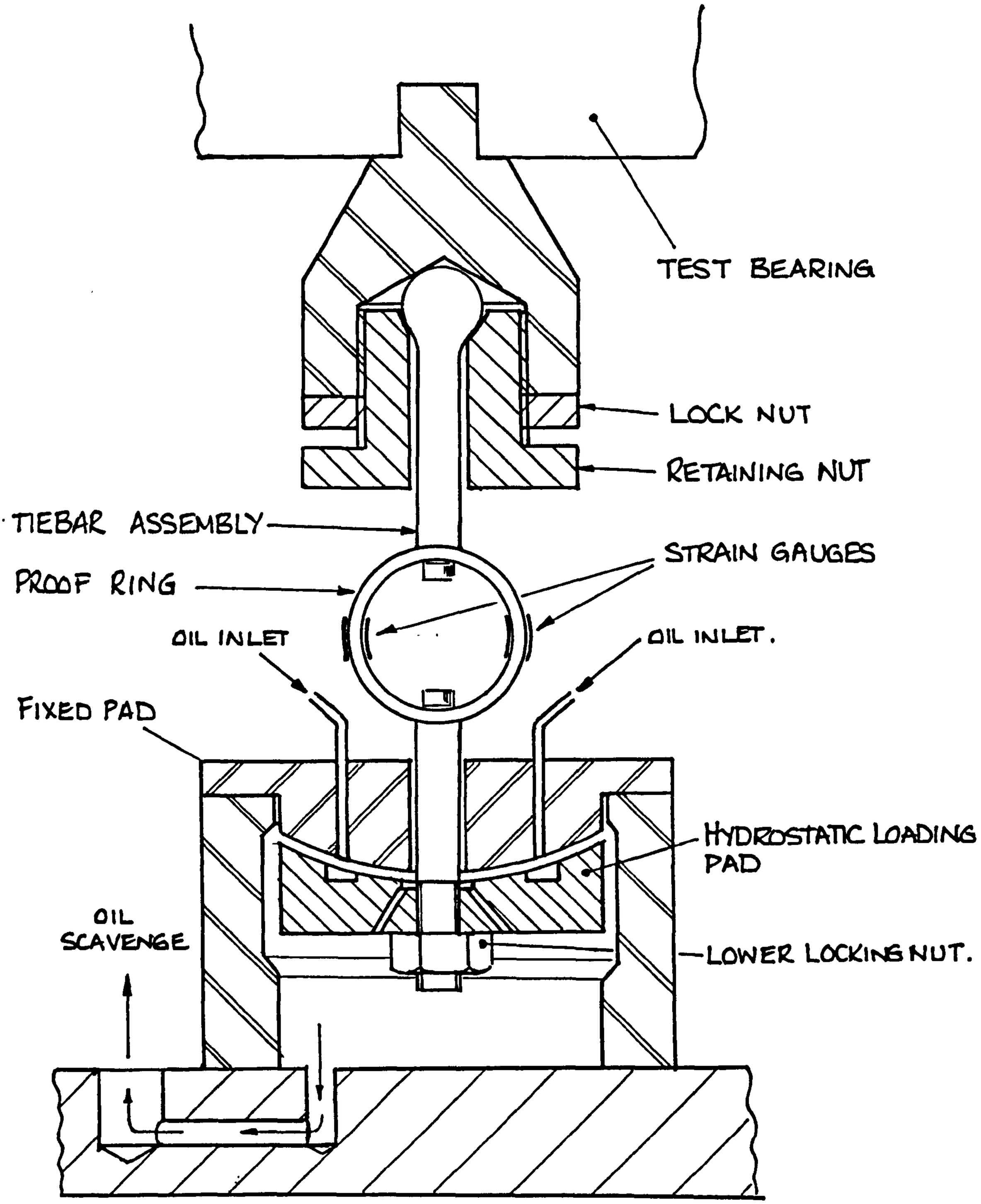

FIG. (4.4) LOADING PRINCIPLE OF SINGLE BEARING TEST RIG.

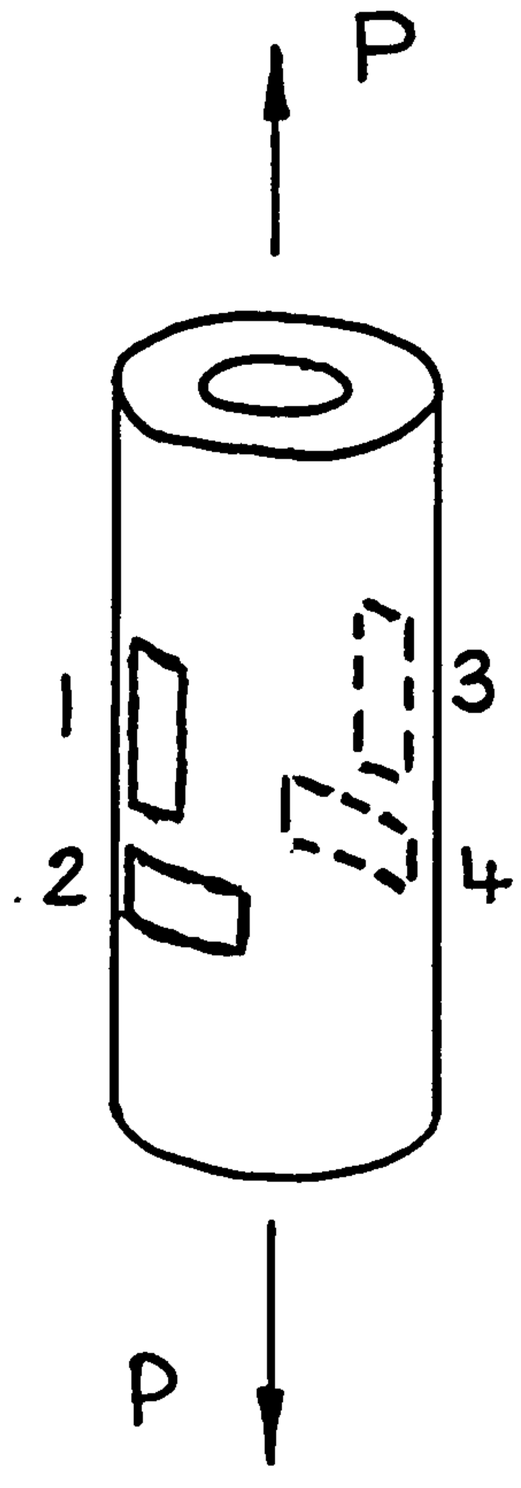

POISSON ARRANGEMENT

FIG. (4.5a)

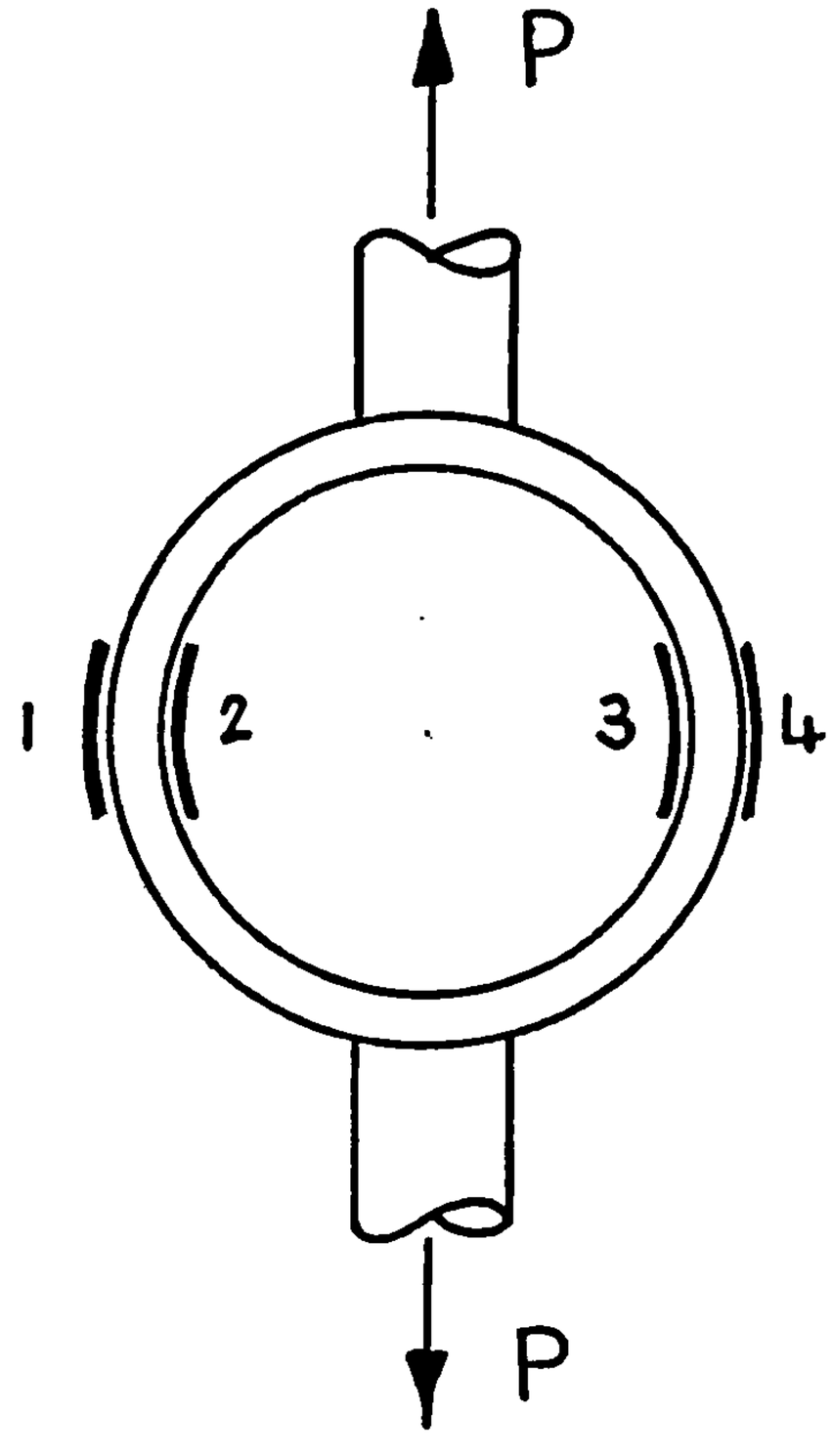

PRODF RING.

FIG. (4.5b)

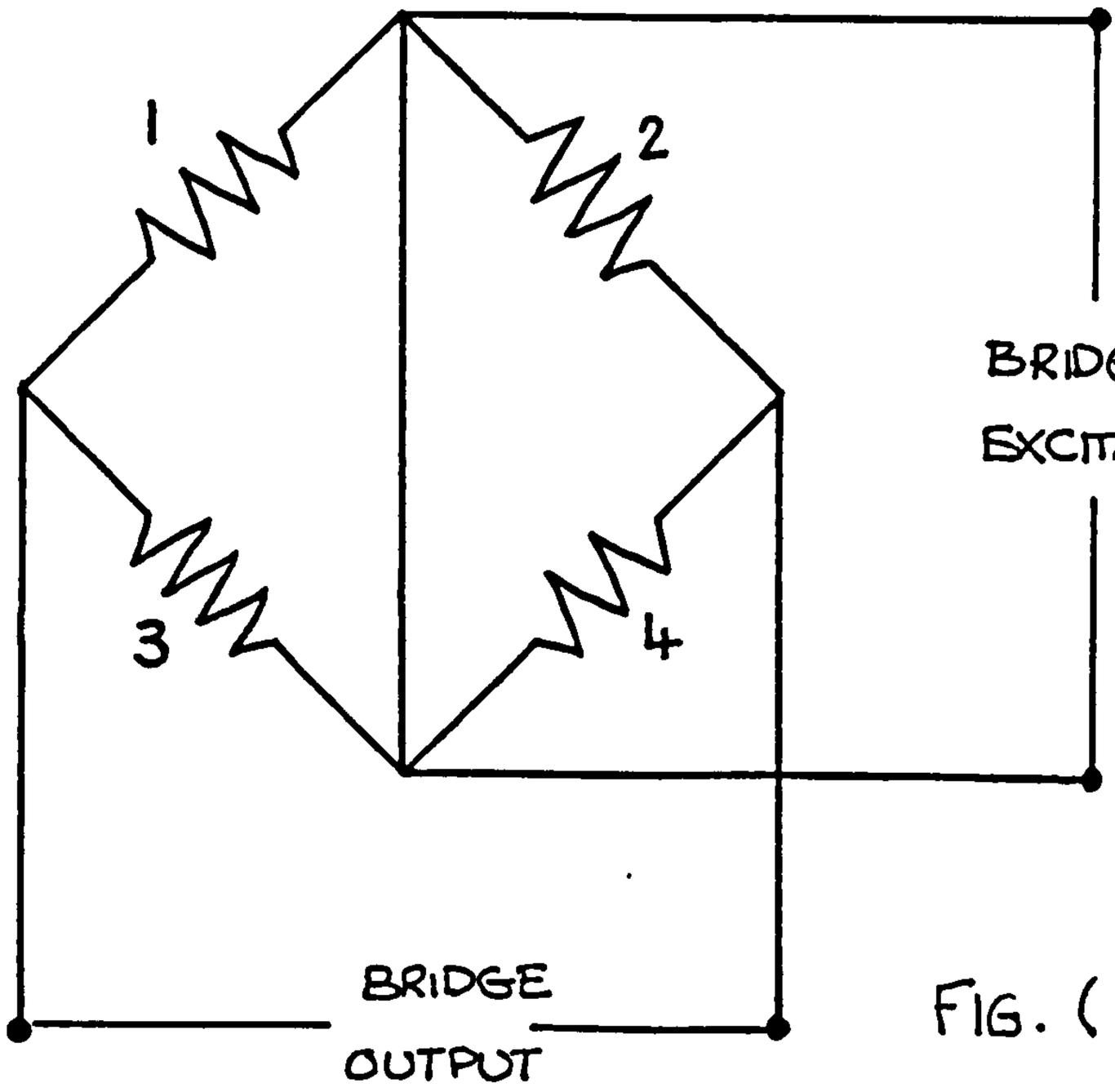

FIG. (4.5c).

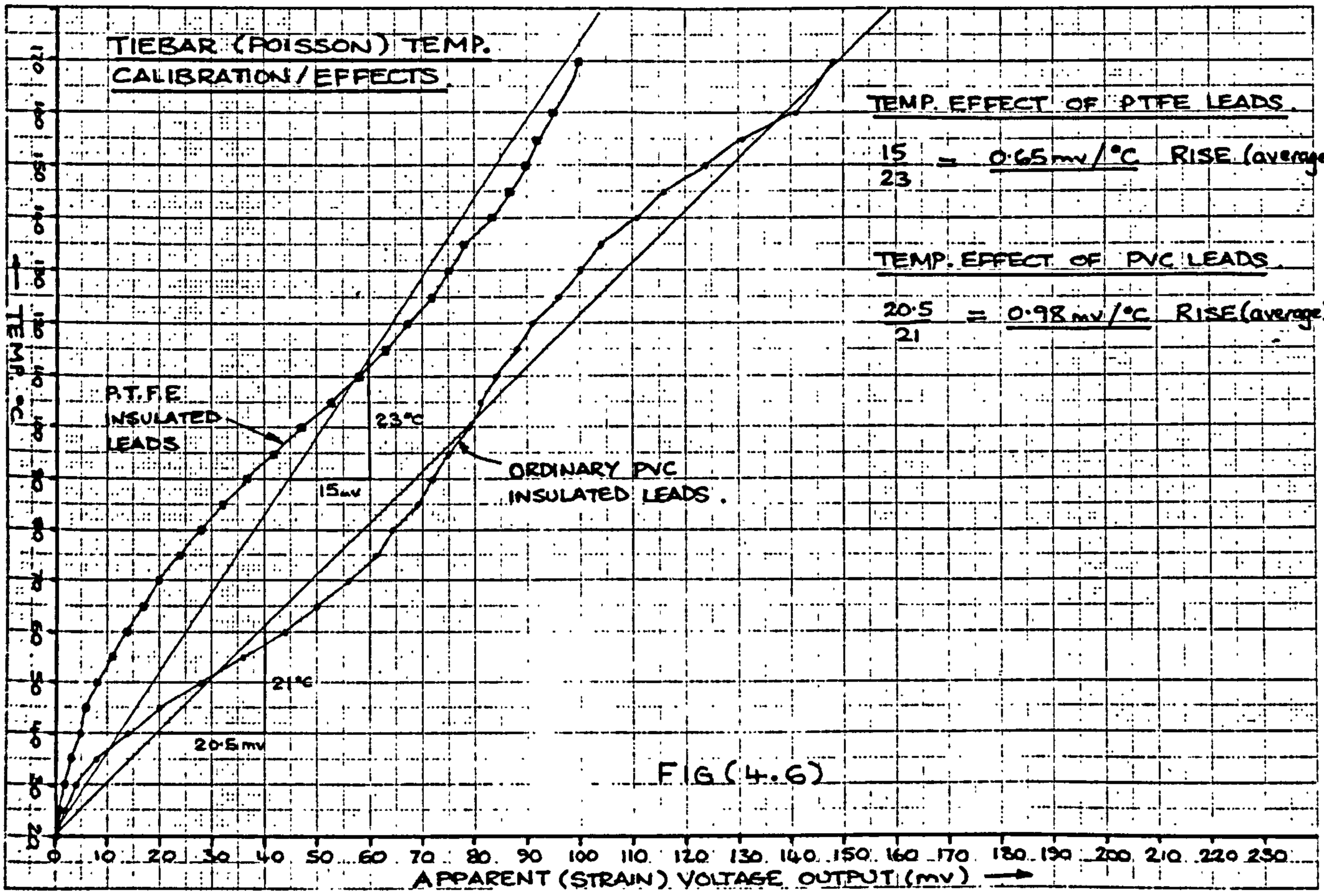
TIEBAR (POISSON) TEMP.
CALIBRATION / EFFECTS.
TEMP. EFFECT OF PTFE LEADS.
15/23 = 0·65 mv/°C RISE (average)
TEMP. EFFECT OF PVC LEADS.
20·5/21 = 0·98 mv/°C RISE (average).
P.T.F.E INSULATED LEADS
ORDINARY PVC INSULATED LEADS.
23°C
21°C
15 mv
20·5 mv
TEMP °C
APPARENT (STRAIN) VOLTAGE OUTPUT (mv)
0 10 20 30 40 50 60 70 80 90 100 110 120 130 140 150 160 170 180 190 200 210 220 230
20 30 40 50 60 70 80 90 100

FIG (4.6)

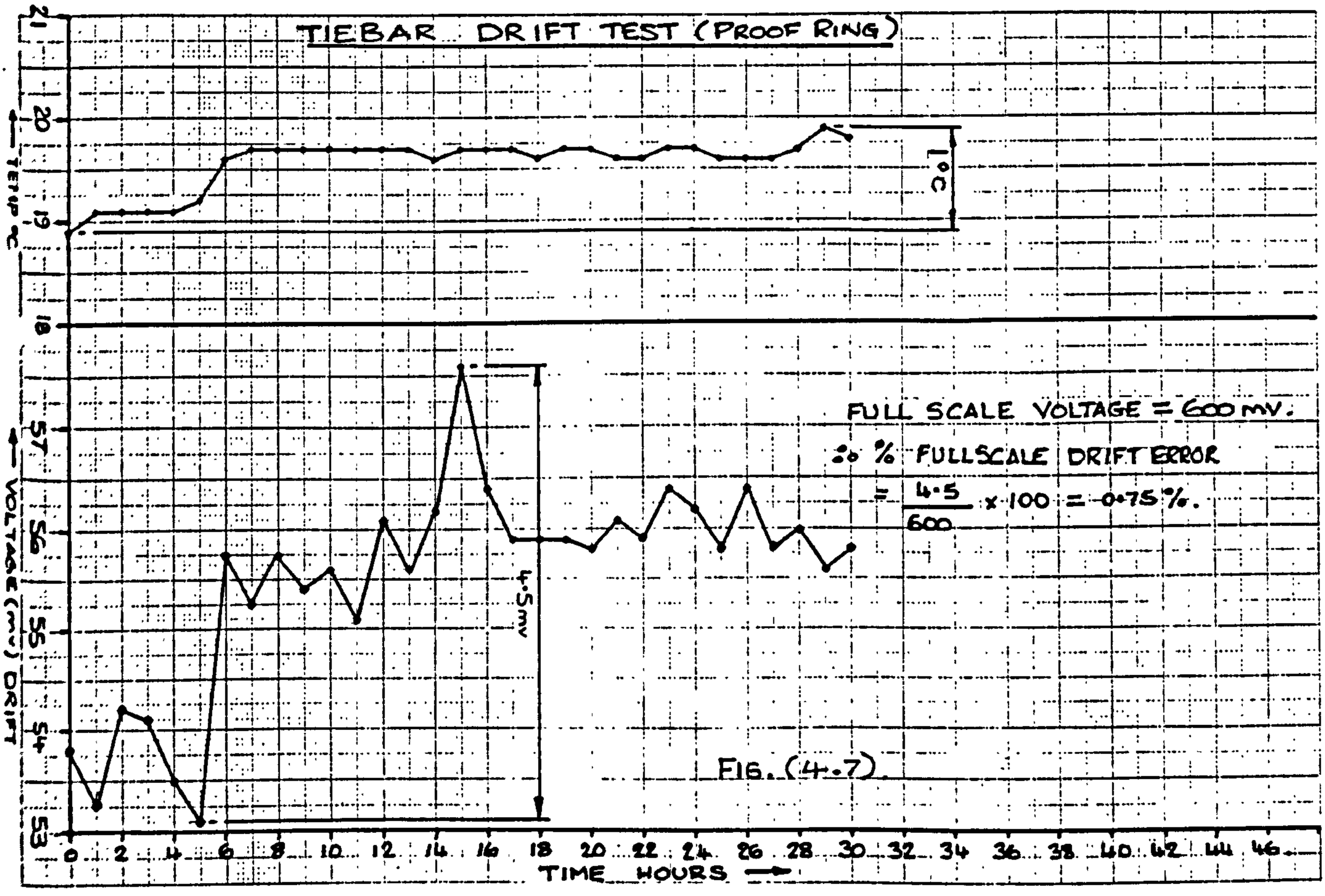
TIEBAR DRIFT TEST (PROOF RING)
TEMP °C
1°C
VOLTAGE (mv) DRIFT
4·5 mv
FULL SCALE VOLTAGE = 600 mv.
∴ % FULLSCALE DRIFT ERROR
= 4·5/600 x 100 = 0·75 %.
TIME HOURS
0 2 4 6 8 10 12 14 16 18 20 22 24 26 28 30 32 34 36 38 40 42 44 46
18 19 20 21
53 54 55 56 57

FIG. (4.7)

FRONT BACK.

FIG. (4.9a) 5930 RPM.

FIG. (4.9b) 10,012 RPM.

FIG. (4.9c) 15040 RPM.

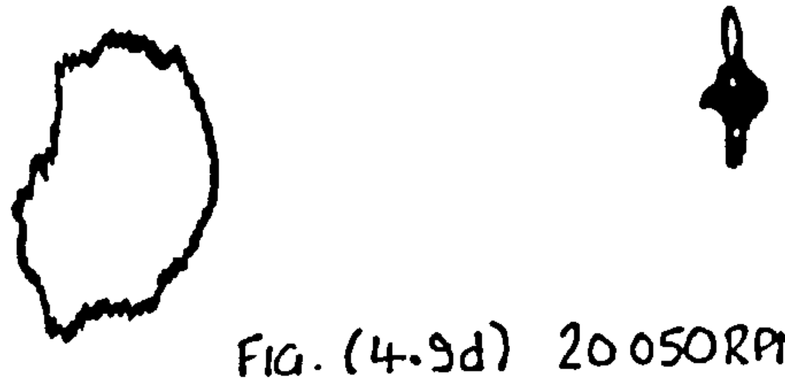

FIG. (4.9d) 20050RPM

FIG (4.9) TESTS ON M.E. PROXIMITY PROBES.

FRONT BACK.

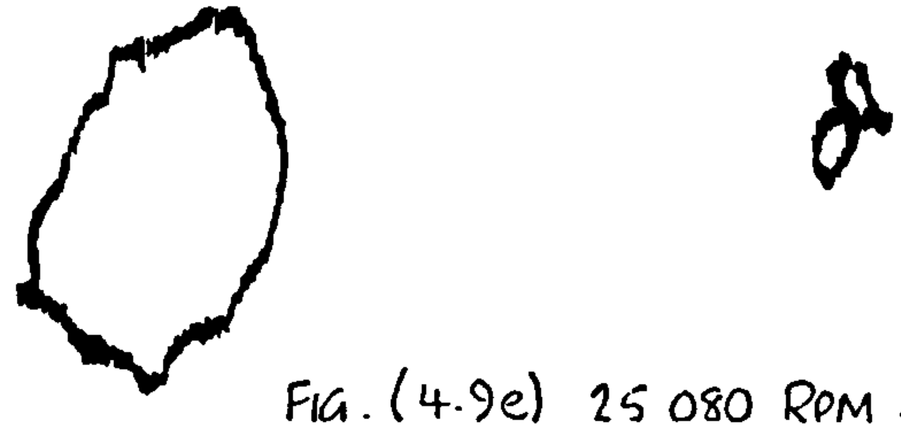

FIG. (4.9e) 25 080 RPM.

FIG. (4.9f) 29.110 RPM.

INSTABILITY OCCURED AT ≤ 30000 RPM.

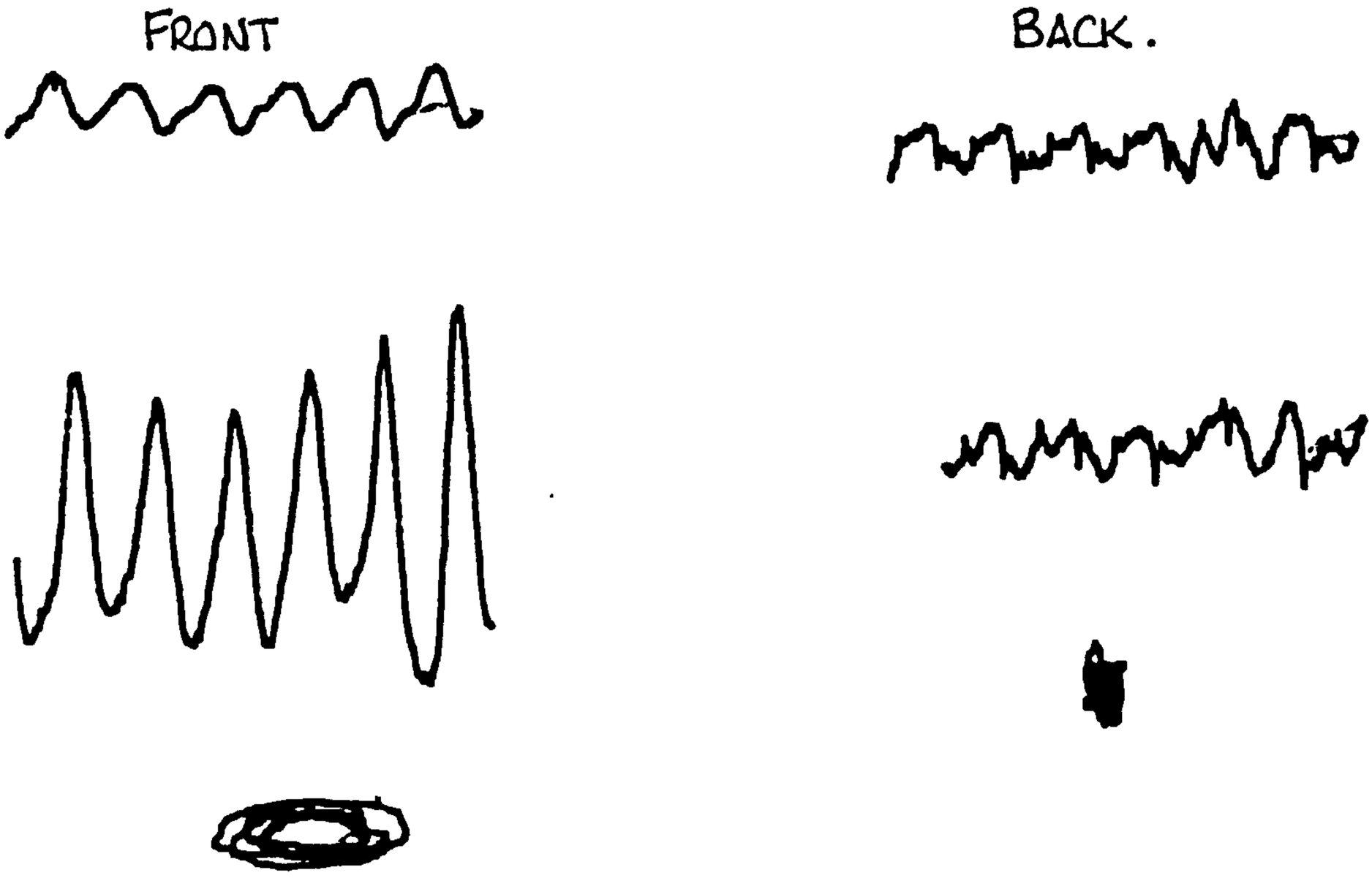

FIG. (4.10a) 17970 RPM.

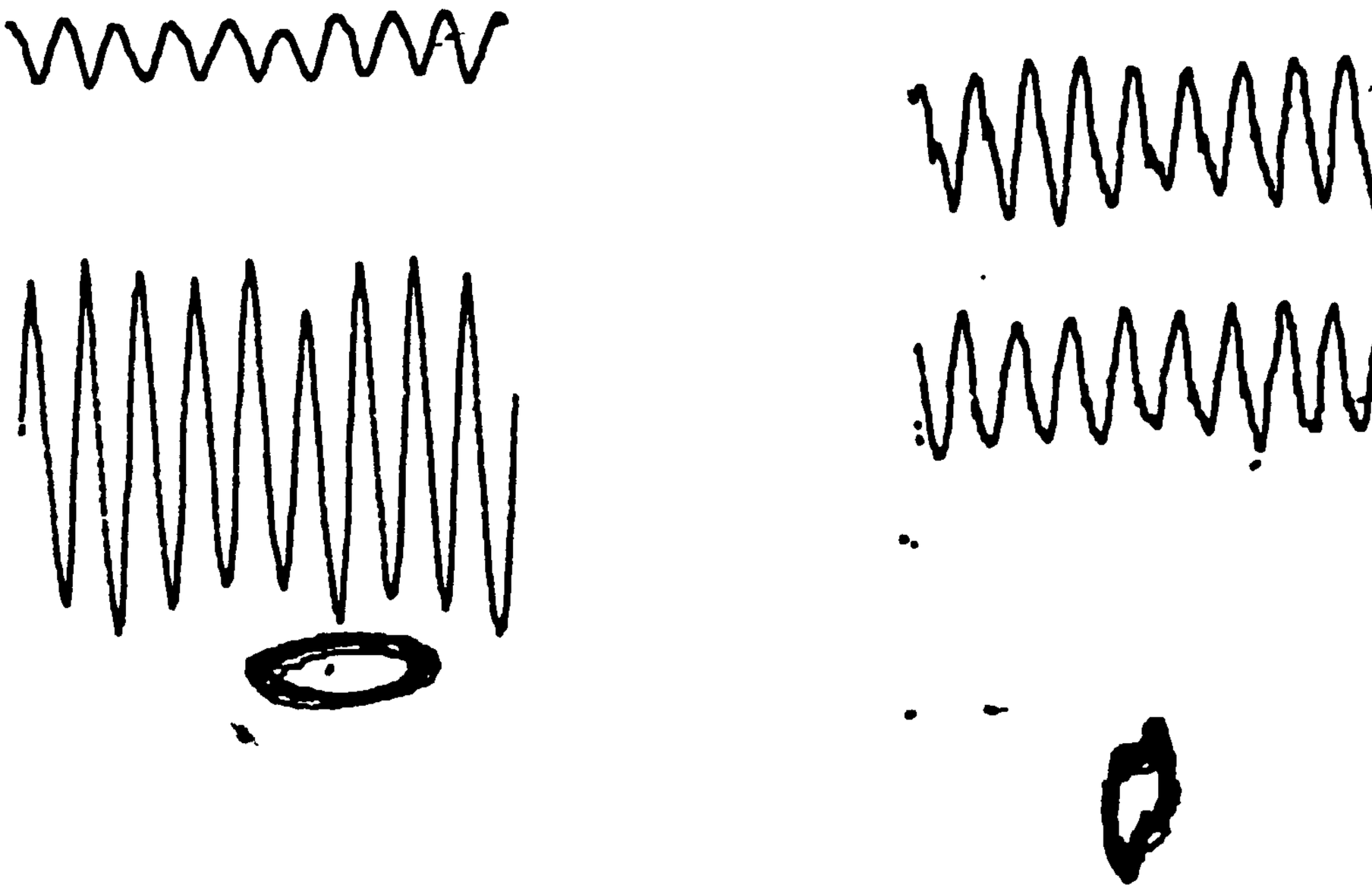

FIG. (4.10b) 26500 RPM

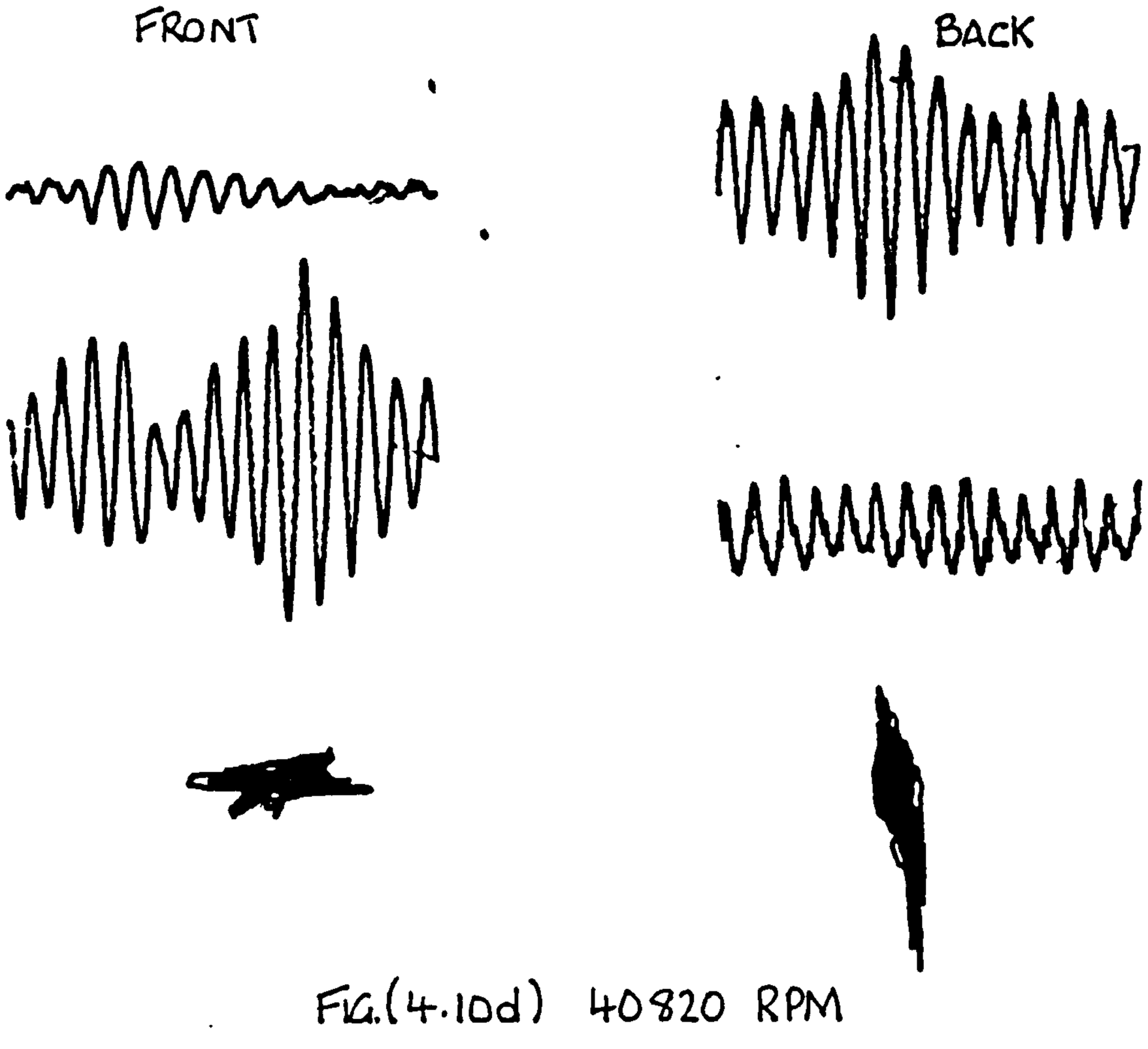

FIG.(4.10d) 40820 RPM

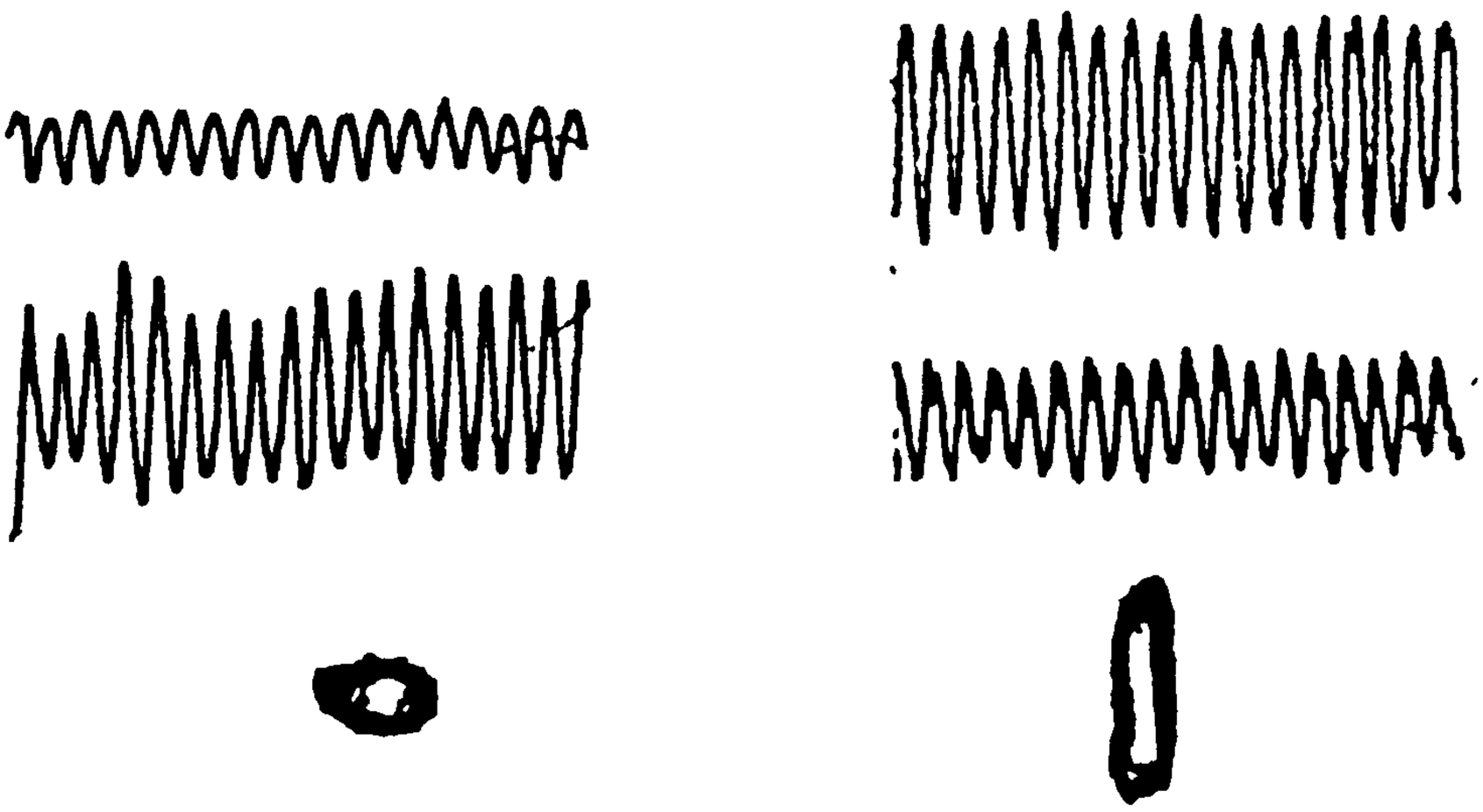

FIG.(4.10e) 51150 RPM.

FRONT

BACK.

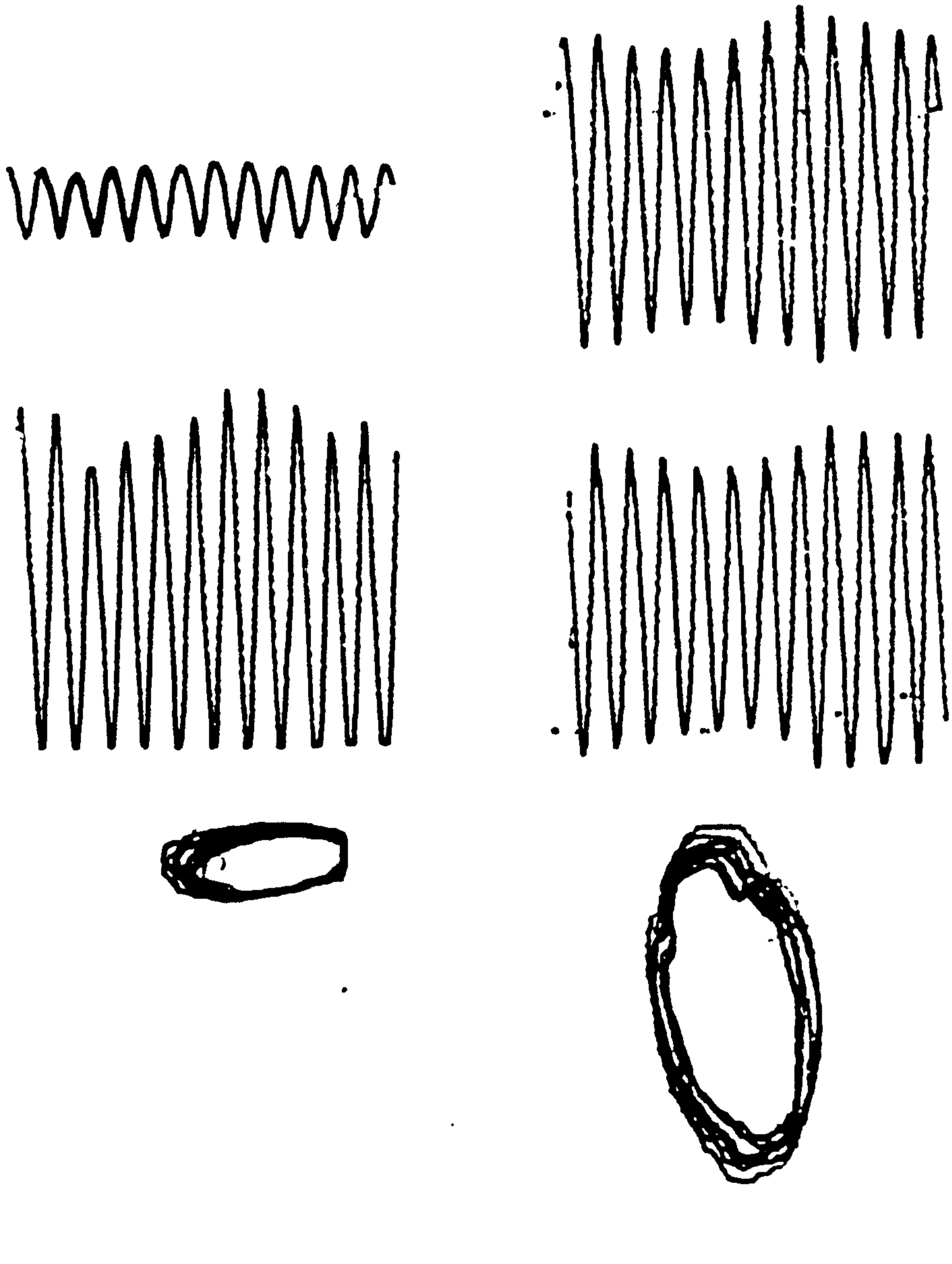

Fig. (4.10c) 32400 RPM.

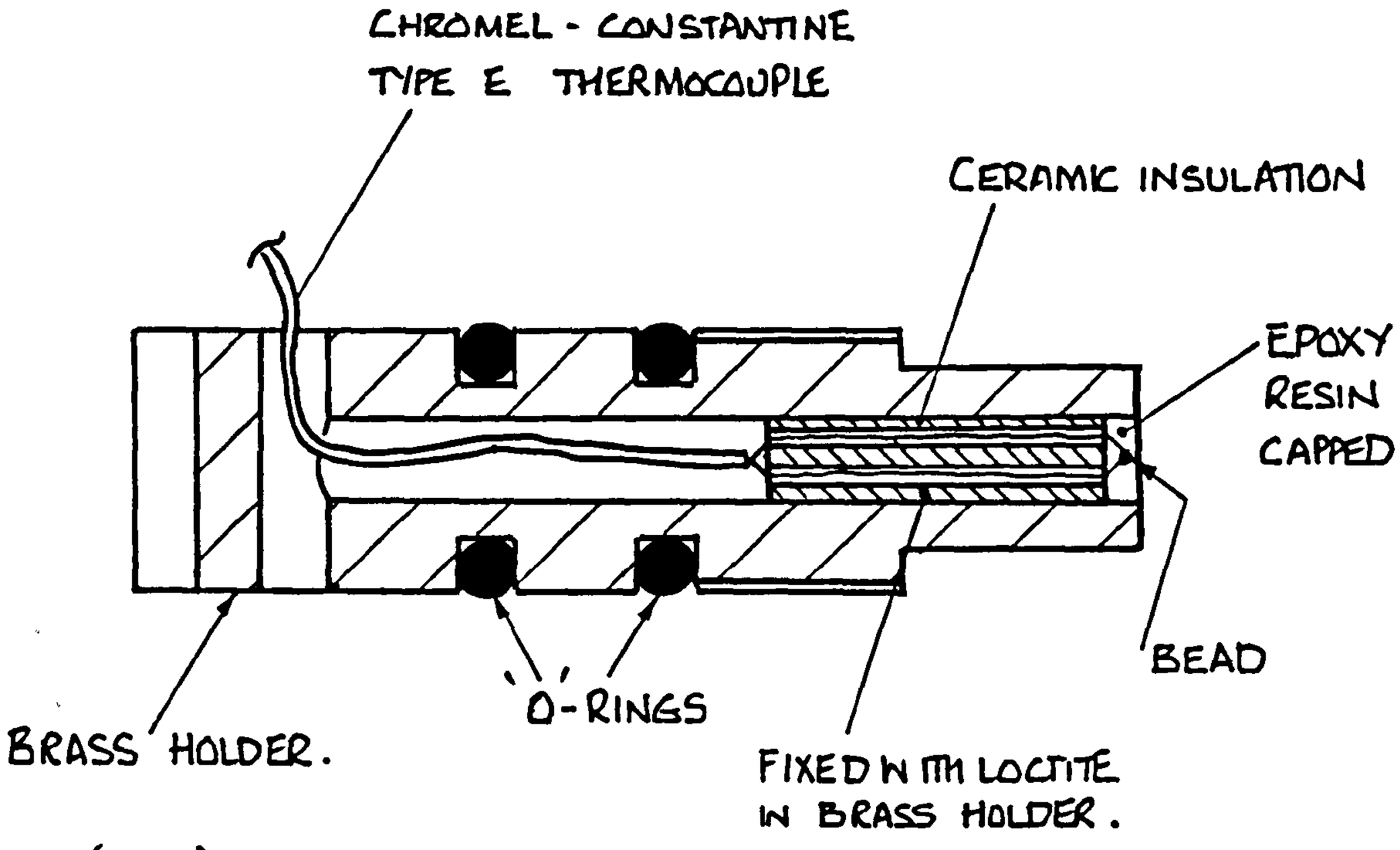

FIG.(4.11) THERMOCOUPLE MOUNTING TECHNIQUE

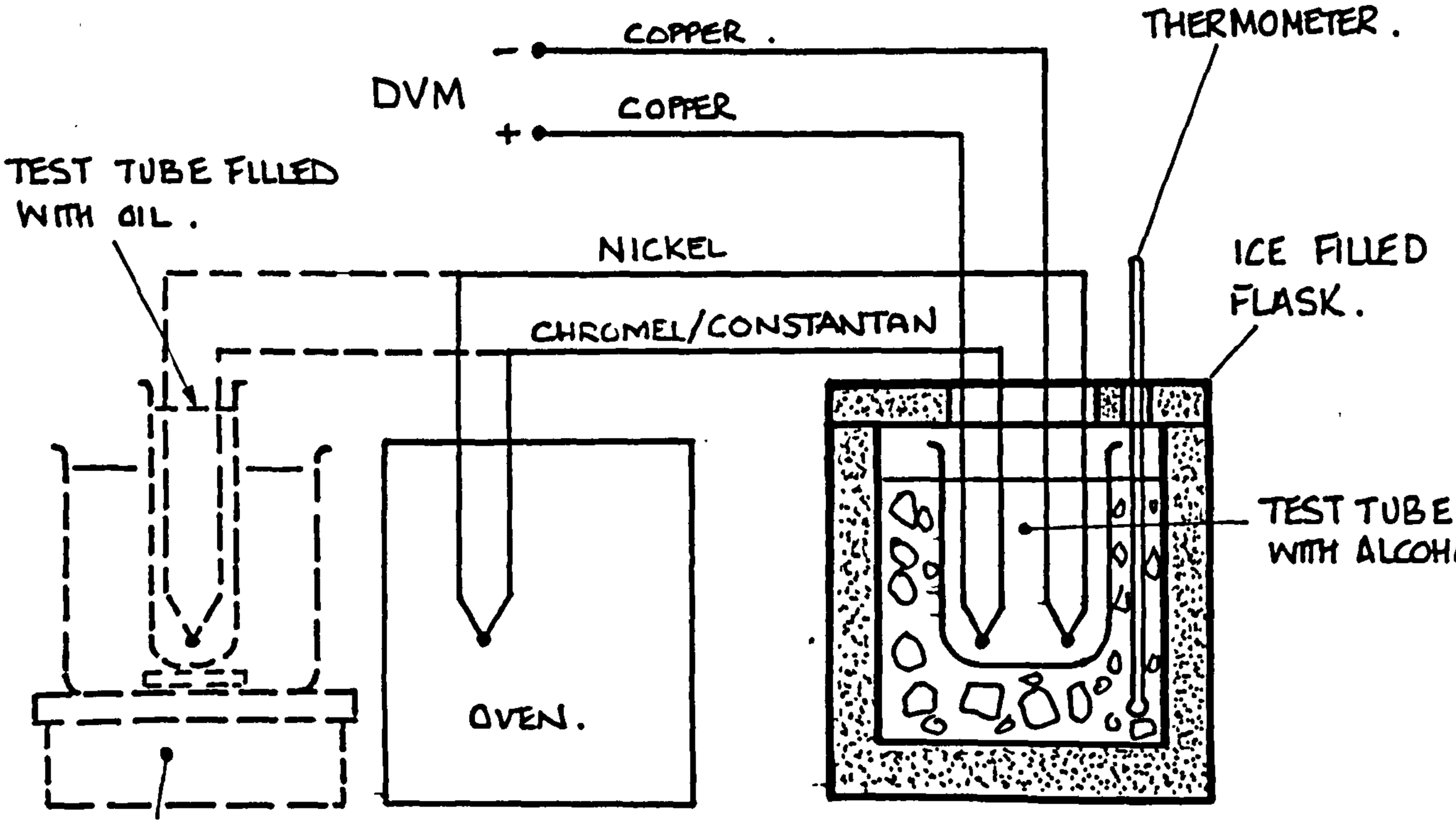

FIG. (4-12) THERMOCOUPLE CONNECTIONS.

OIL BATH & OVEN THERMOCOUPLE CALIBRATION

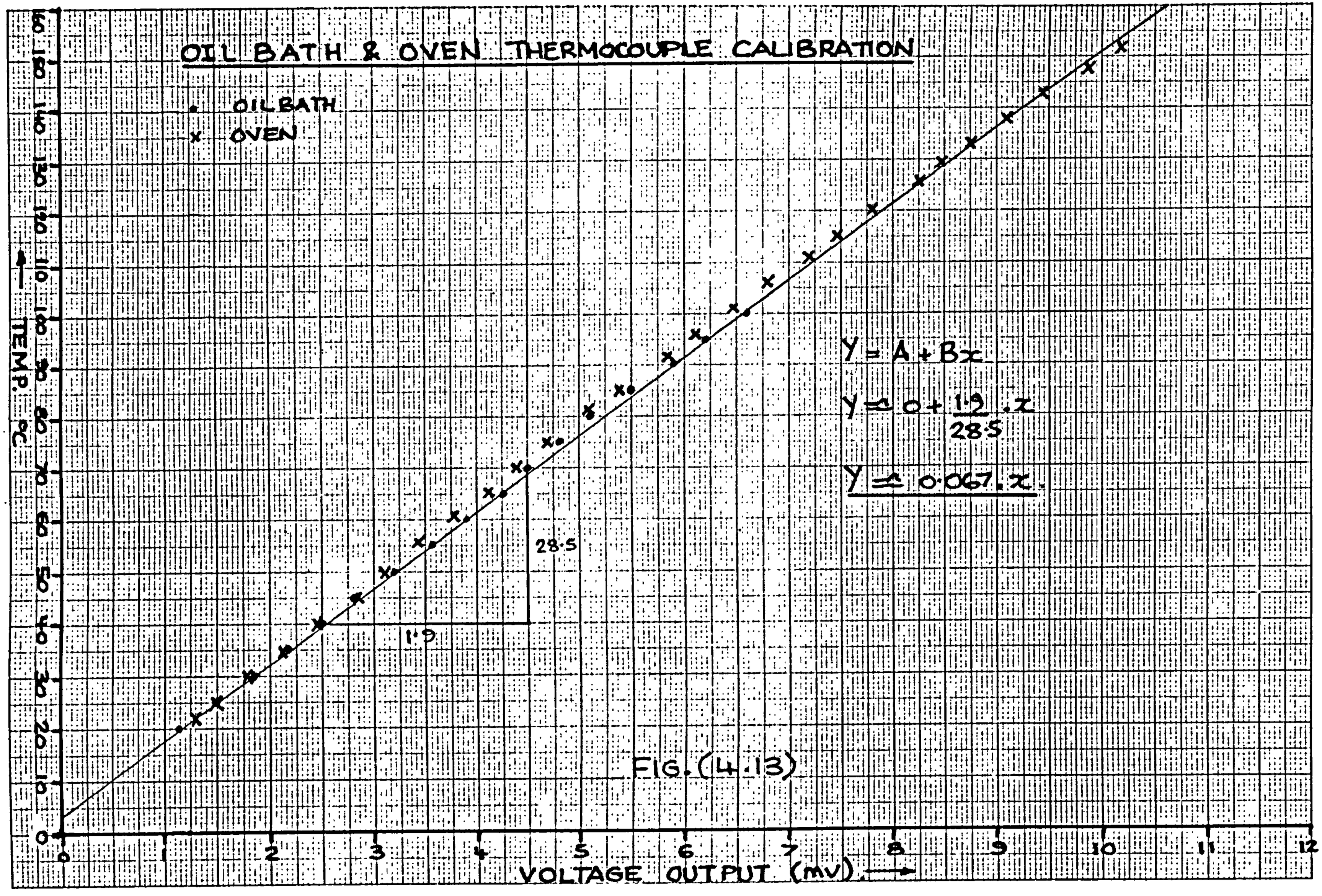

FIG. (4.13)

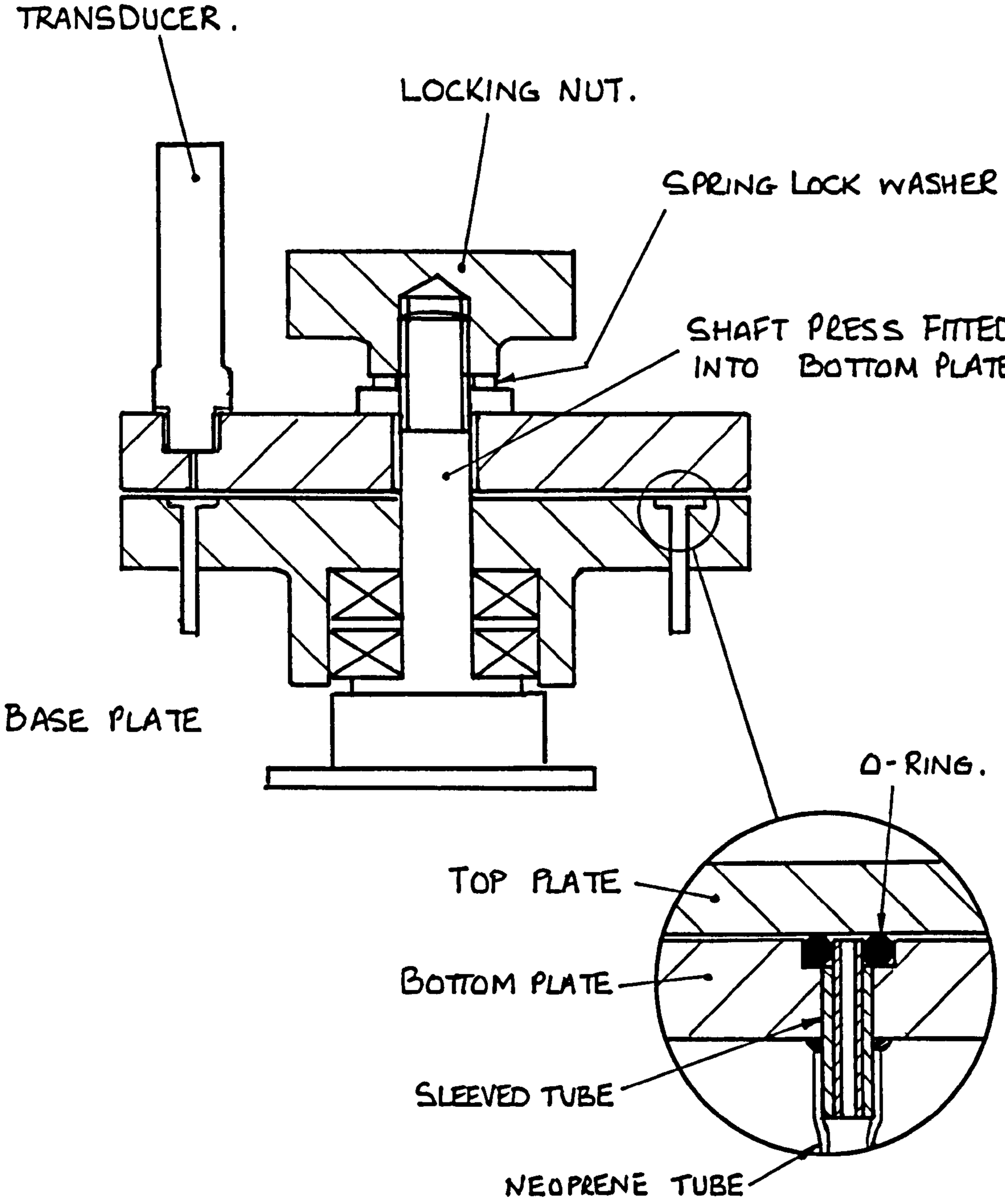

FIG.(4.14) SCANNING VALVE ASSEMBLY.

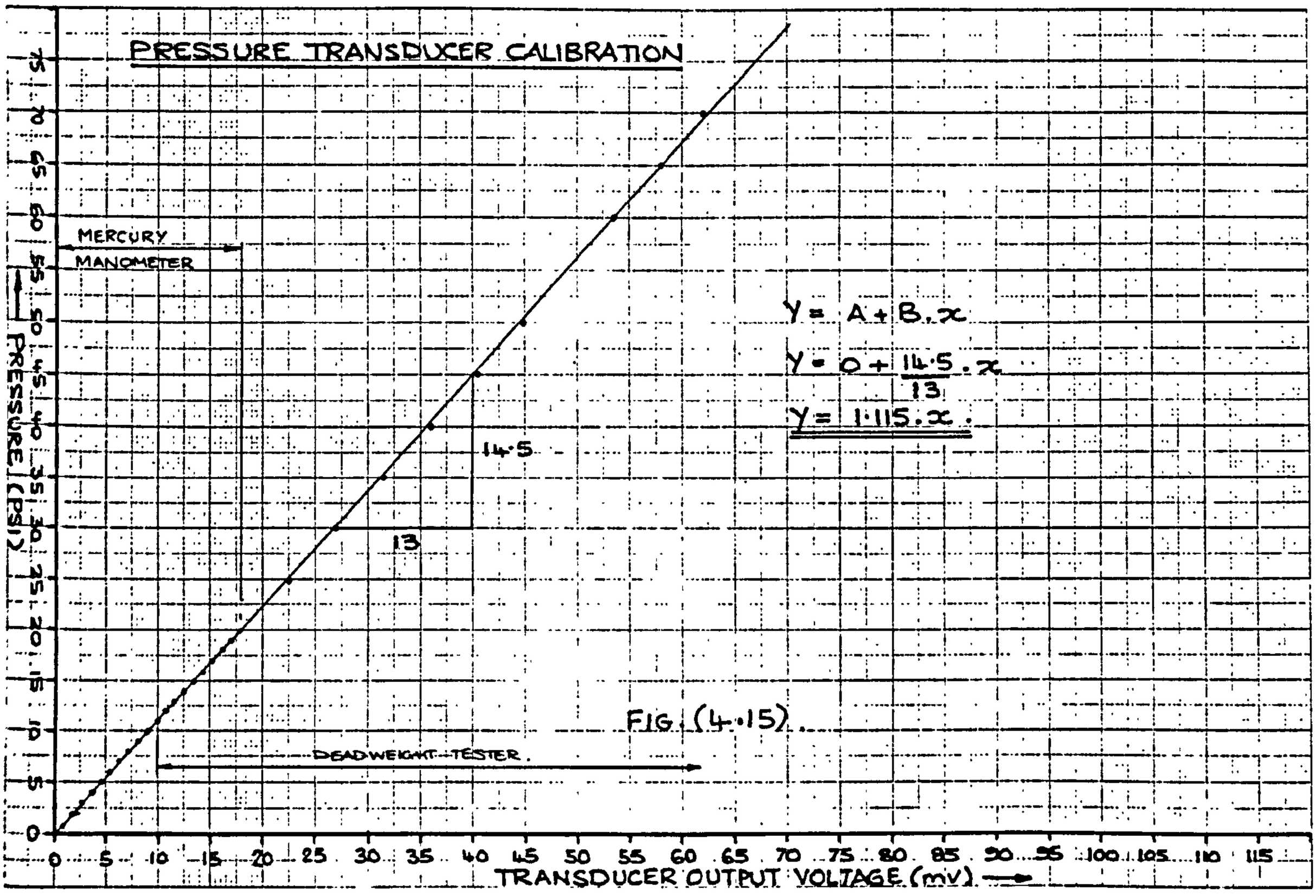

FIG. (4·15).

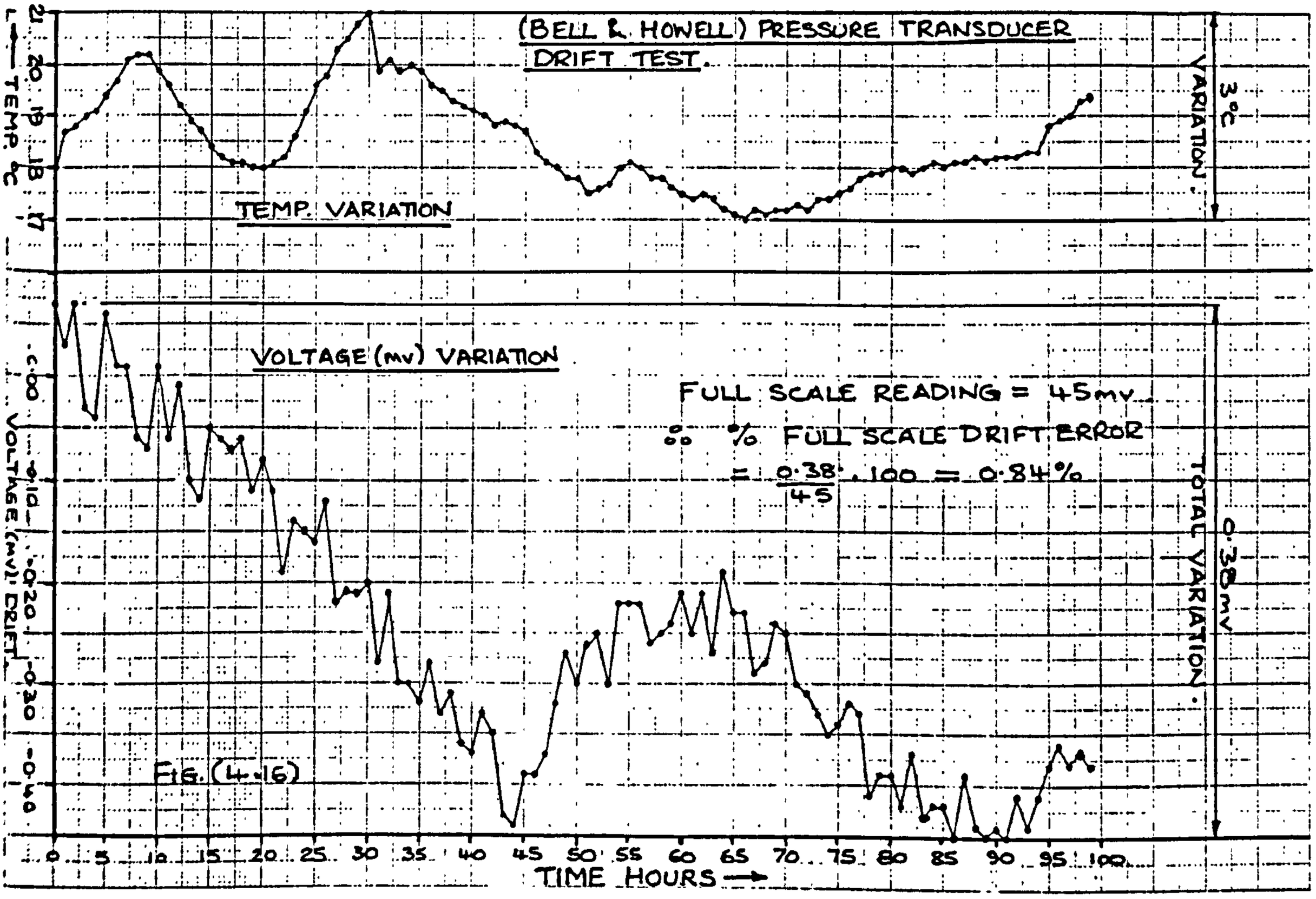

FIG. (4·16)

TIEBAR (POISSON) CALIBRATION

$Y = A + B \cdot x$

$Y = 0 + \frac{10}{63} \cdot x$

$Y = 0.159 \cdot x$

10 Kg

63

LOAD (Kg) ←

TIEBAR VOLTAGE OUTPUT (mV) →

FIG. (4.17)

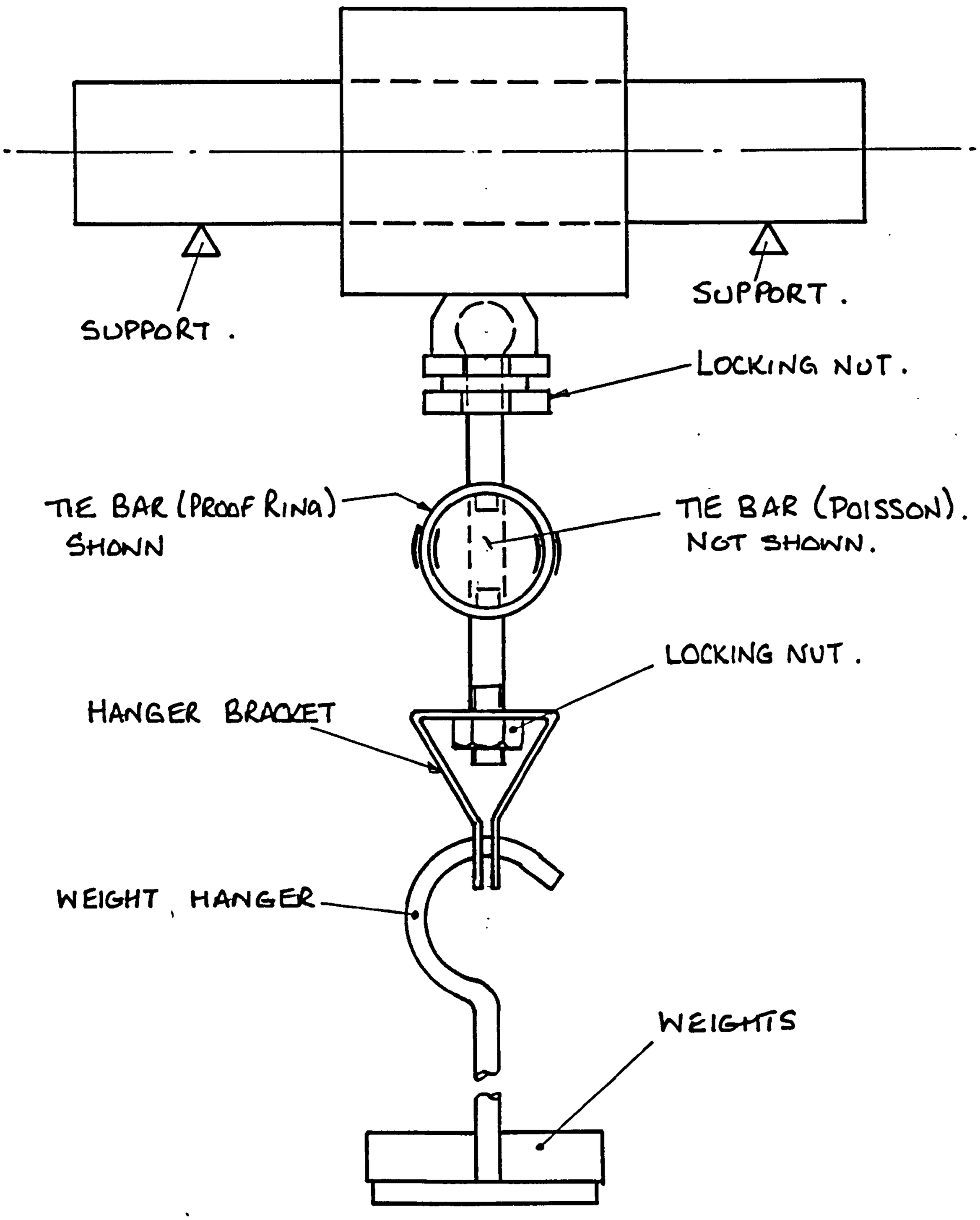

FIG.(4.18) TIEBAR CALIBRATION LOADING. SYSTEM.

DRAWING No. PD 19375	
ISSUE	MODIFICATION
A	—

ALL DIMENSIONS IN MILLIMETRES UNLESS OTHERWISE STATED.

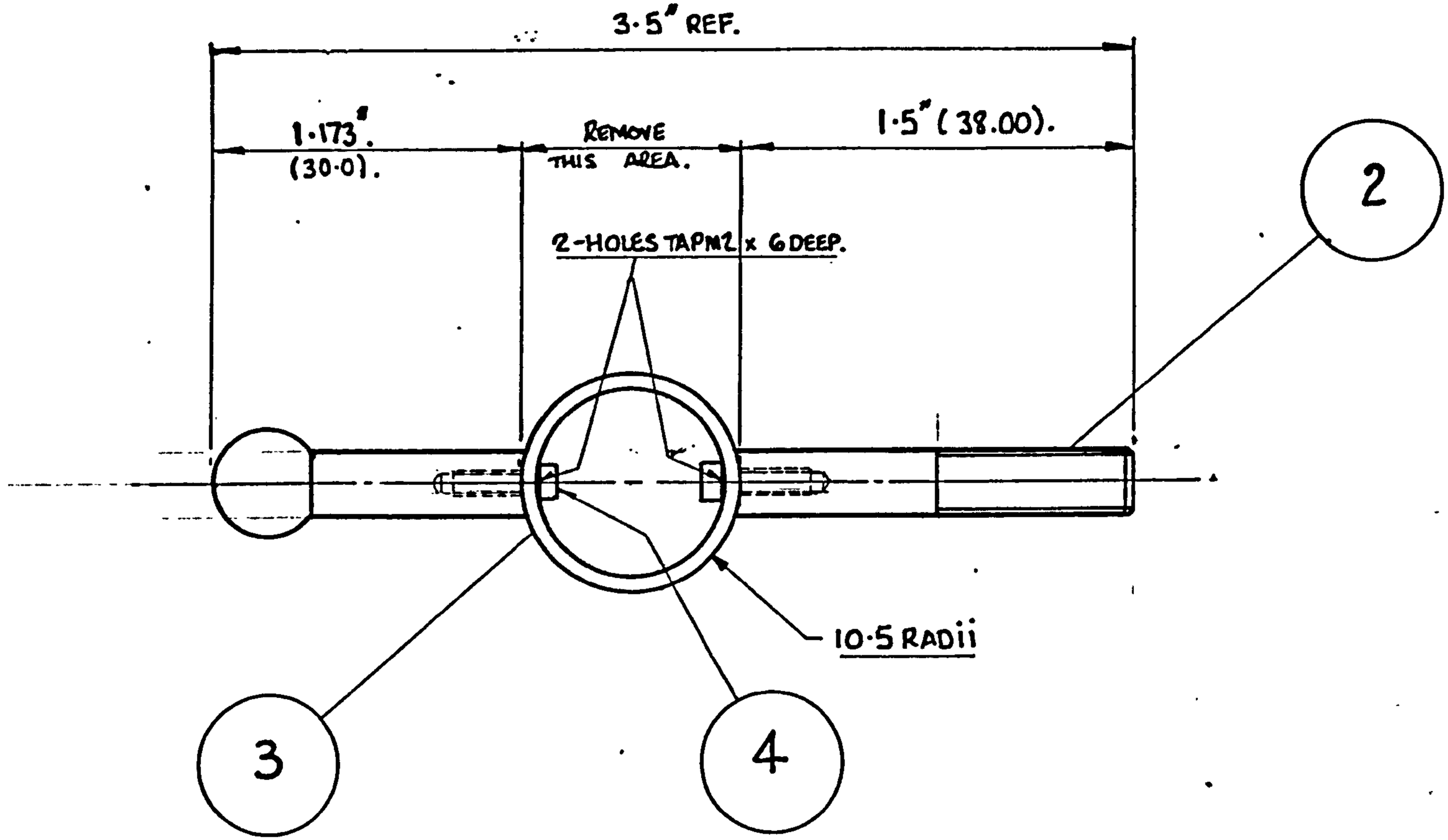

ITEM	PART No.	DESCRIPTION	No. OFF	MAT'L	SPEC.	REMARKS
4		CAP HEAD SCREWS	2			M2 x 6 LONG.
3		PROOF RING.	1			EXISTING.
2		TIE BAR	1			EXISTING
1	PD 19375	LOAD CELL TIE BAR.	1			

FIG. (4.19)

THIRD ANGLE PROJECTION

SHEET SIZE A 3

GENERAL TOLERANCE ON DIMENSIONS
MACHINED
UNMACHINED
OTHER DIMENSIONS AS STATED
WELD WHERE SHOWN THUS
MACHINE WHERE SHOWN THUS

JOB No.	No. OF SETS REQ'D
407.	1
USED ON DRG.	

SCALE 2:1

FINISH NAT.

DRAWN	CHK'D	APPV'D	STRESS APPVD.
IRW McCuckie 28/2/88.	RHD 29/2/88		

TITLE:- LOAD CELL TIE BAR

ISSUED BY SME

CRANFIELD INSTITUTE OF TECHNOLOGY
CRANFIELD.

DRAWING No. PD 19375

SHT 1 OF 1 SHEETS

TIE BAR (PROOF RING) CALIBRATION.

$$y = A + Bx \quad , \quad A = 0$$

$$y = 0 + \frac{1.7}{200} . x$$

$$y = 8.5\,E\text{-}3 . x \ (Kg).$$

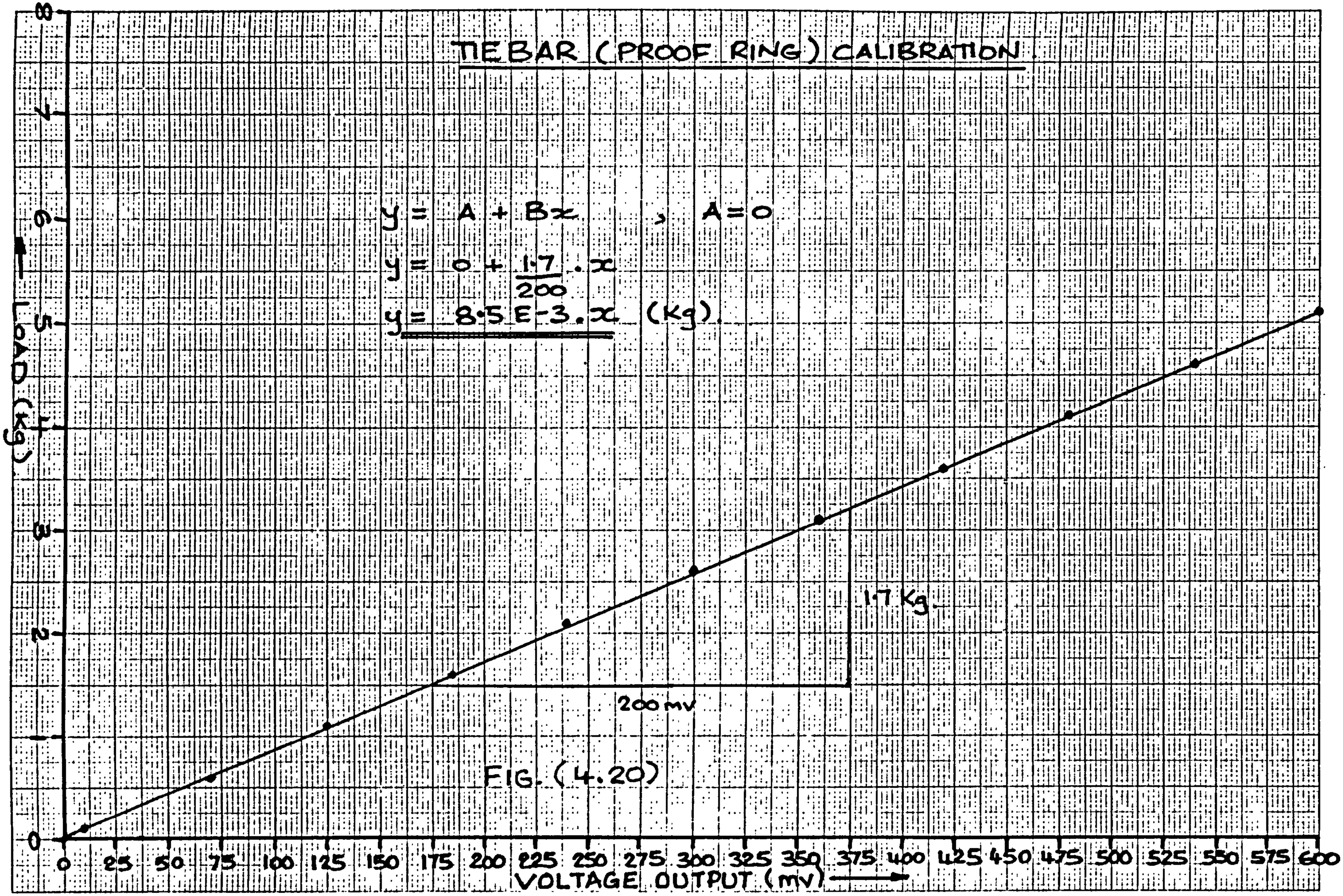

FIG. (4.20)

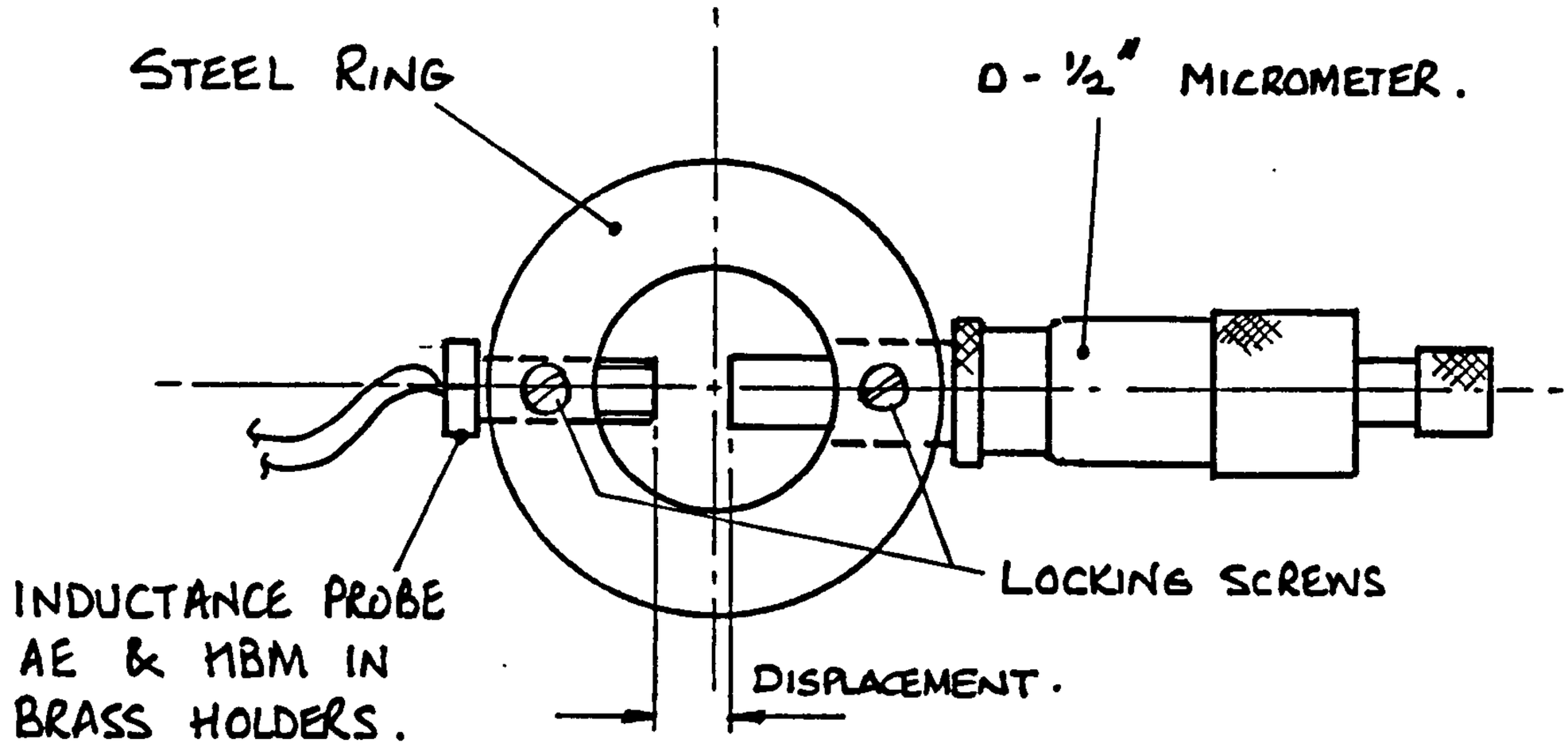

FIG.(4.21) FIXED PROBE CALIBRATION CHECK.

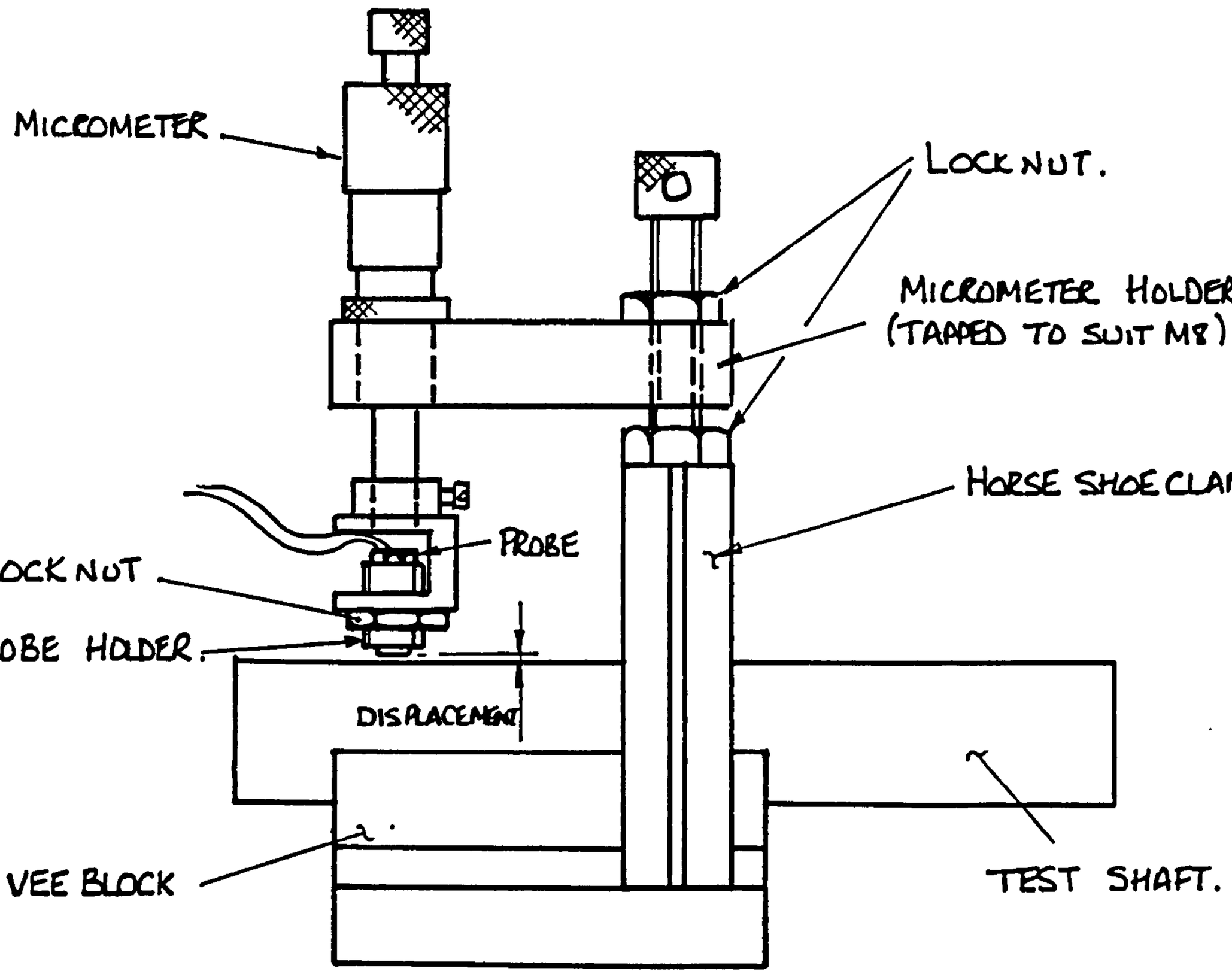

FIG.(4.22) PROBE CALIBRATION RIG.(SHAFT TARGET).

(i) AT ZERO DISPLACEMENT.

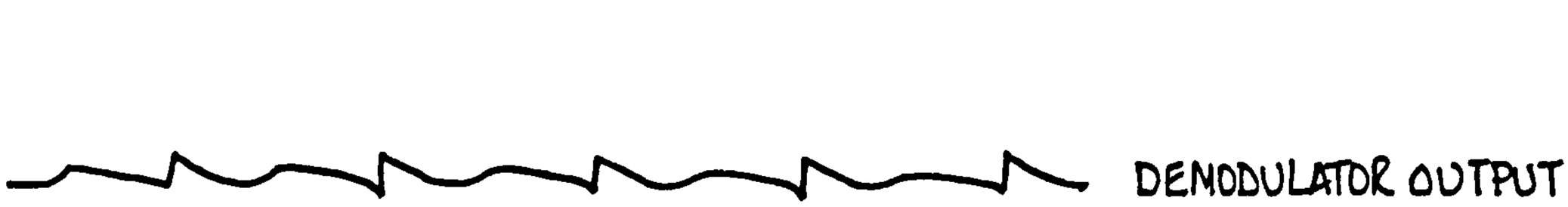

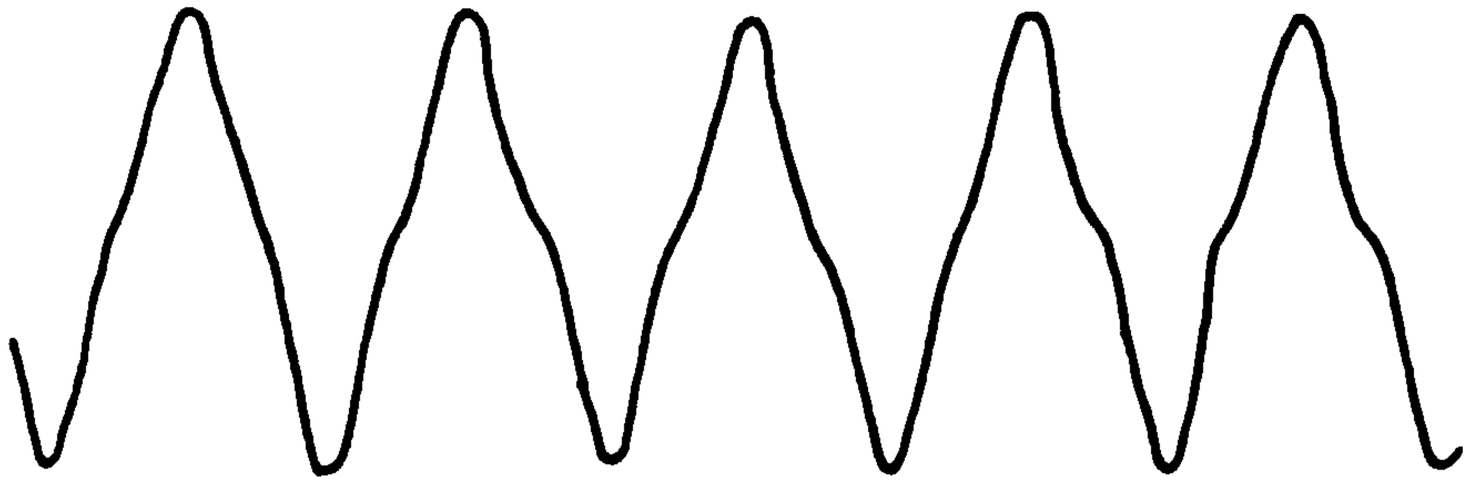

(ii) BELOW ZERO DISPLACEMENT.

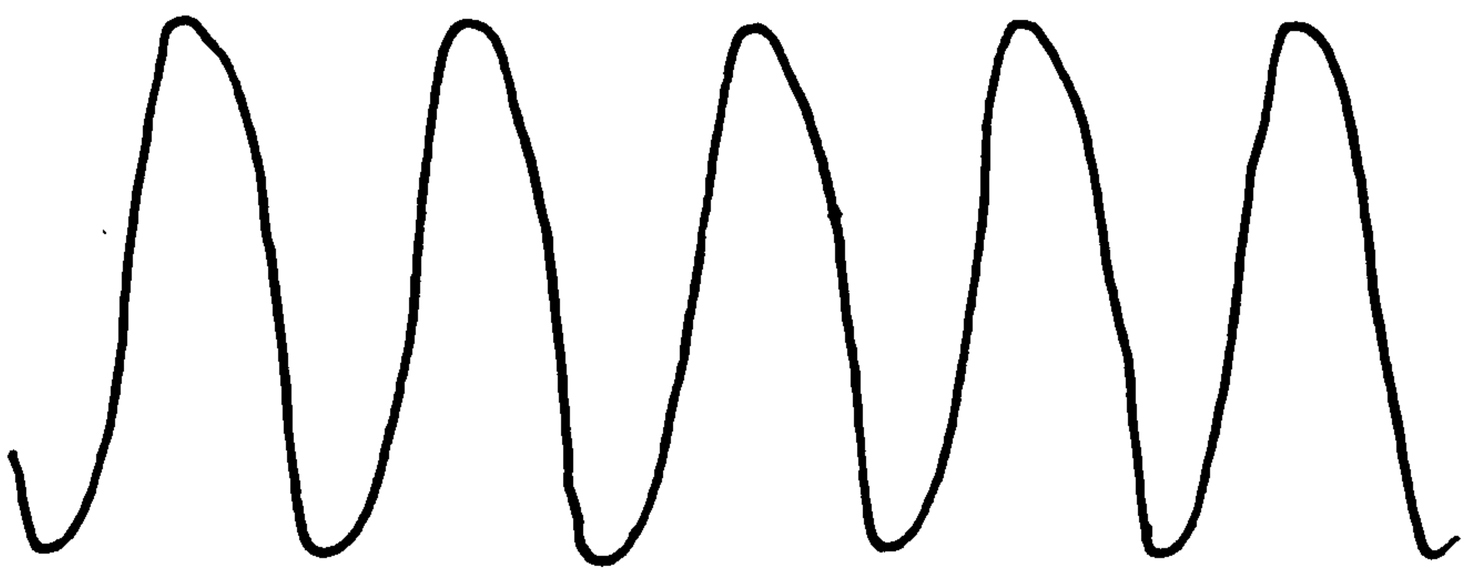

(iii) ABOVE ZERO DISPLACEMENT.

FIG.(4.23) WAVEFORMS OF BRIDGE OUTPUT AND DEMODULATOR OUTPUT AT VARIOUS DISPLACEMENTS (WELL BALANCED SIGNAL).

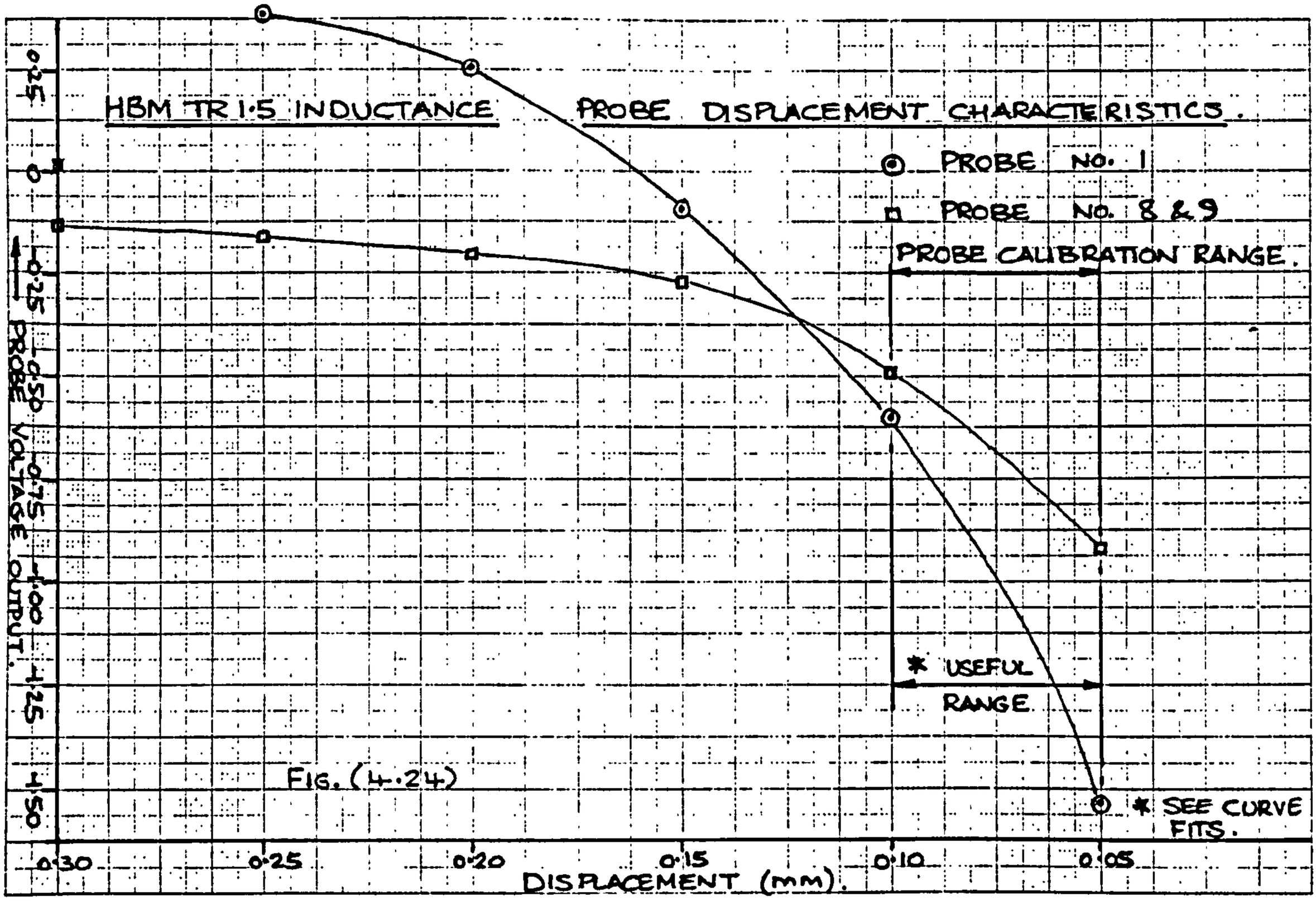

FIG. (4·24)

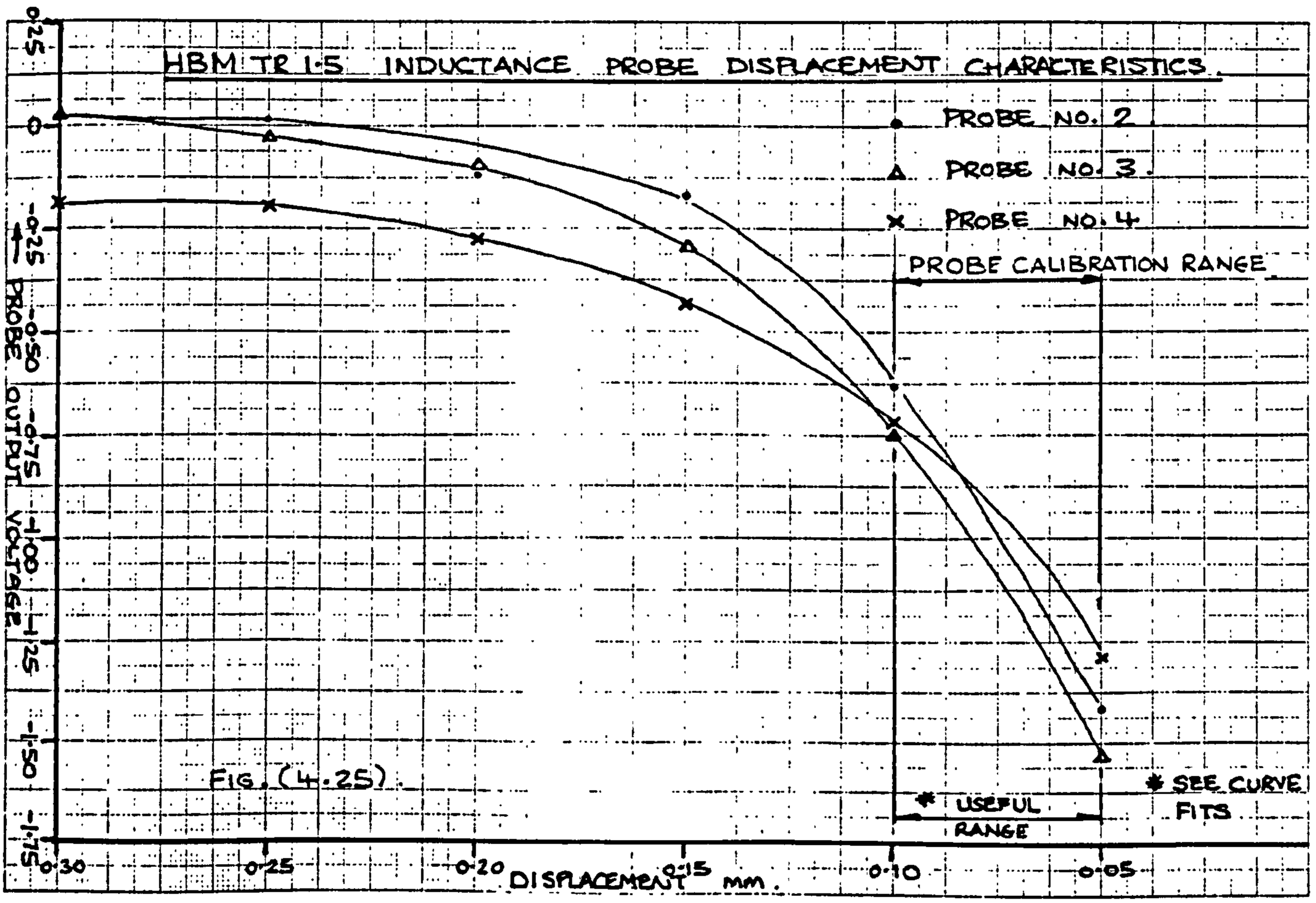

FIG. (4·25)

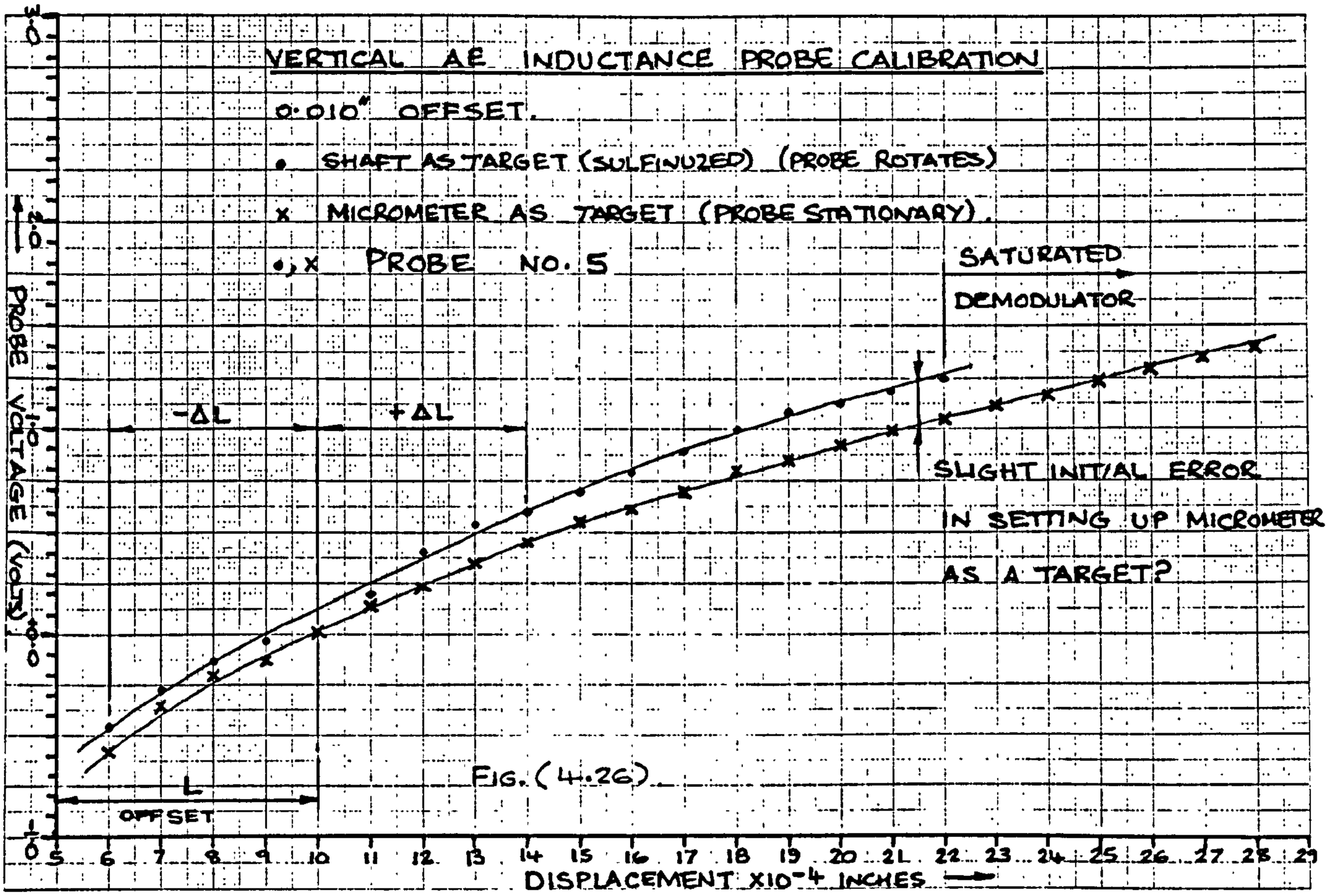

FIG. (4.26)

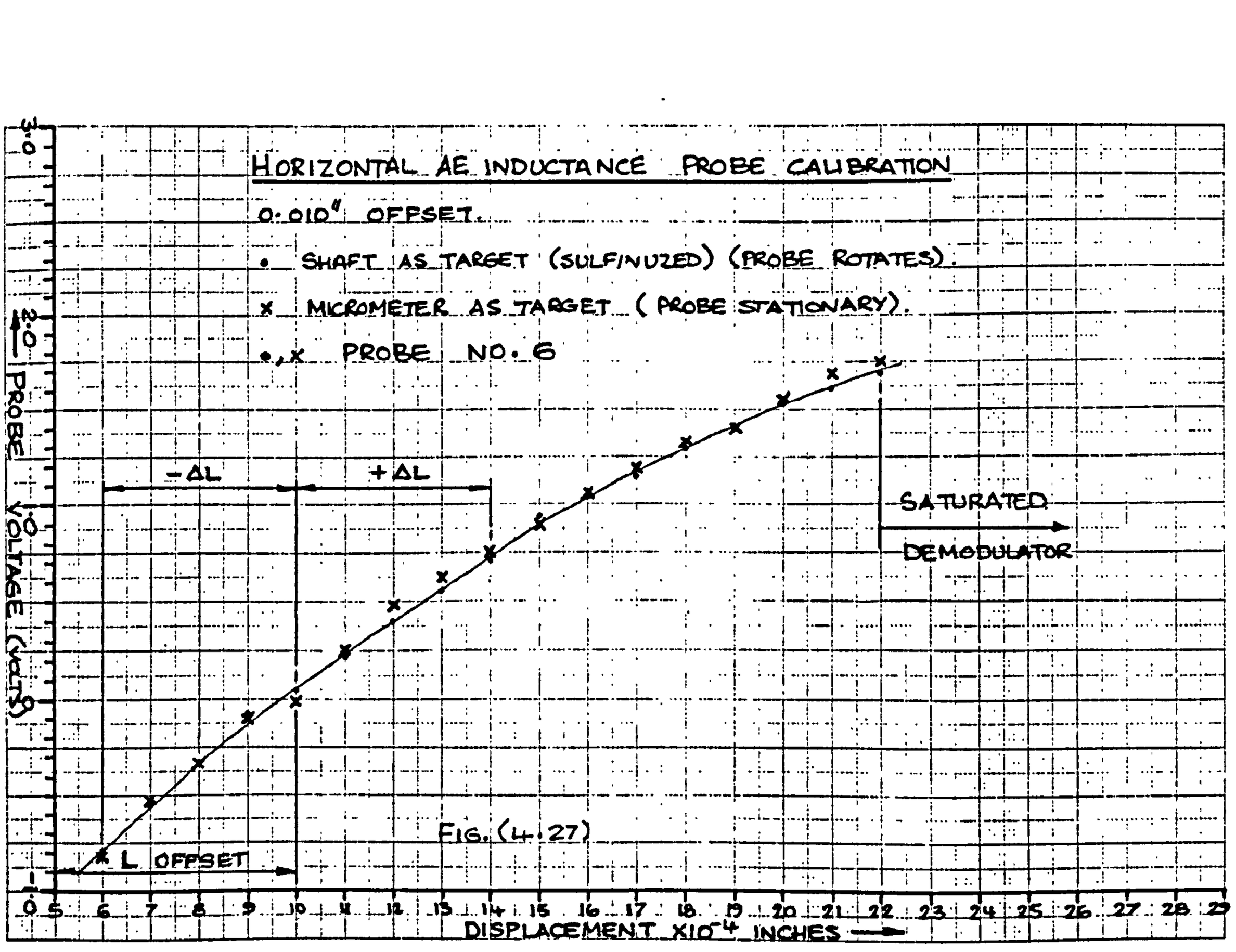

FIG. (4.27)

HBM TR 1-5 INDUCTANCE PROBE DISPLACENT CHARACTERISTICS

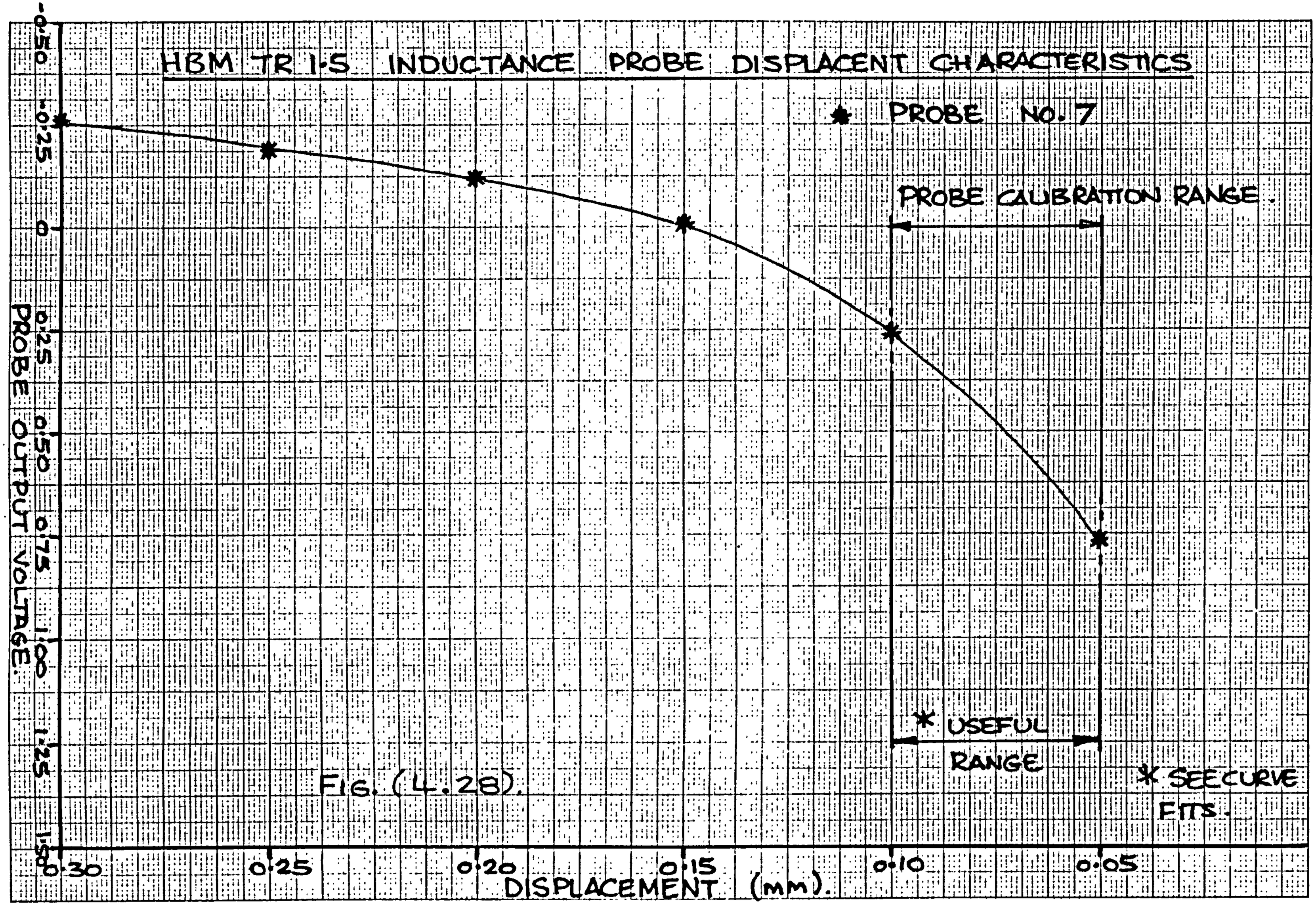

FIG. (4.28).

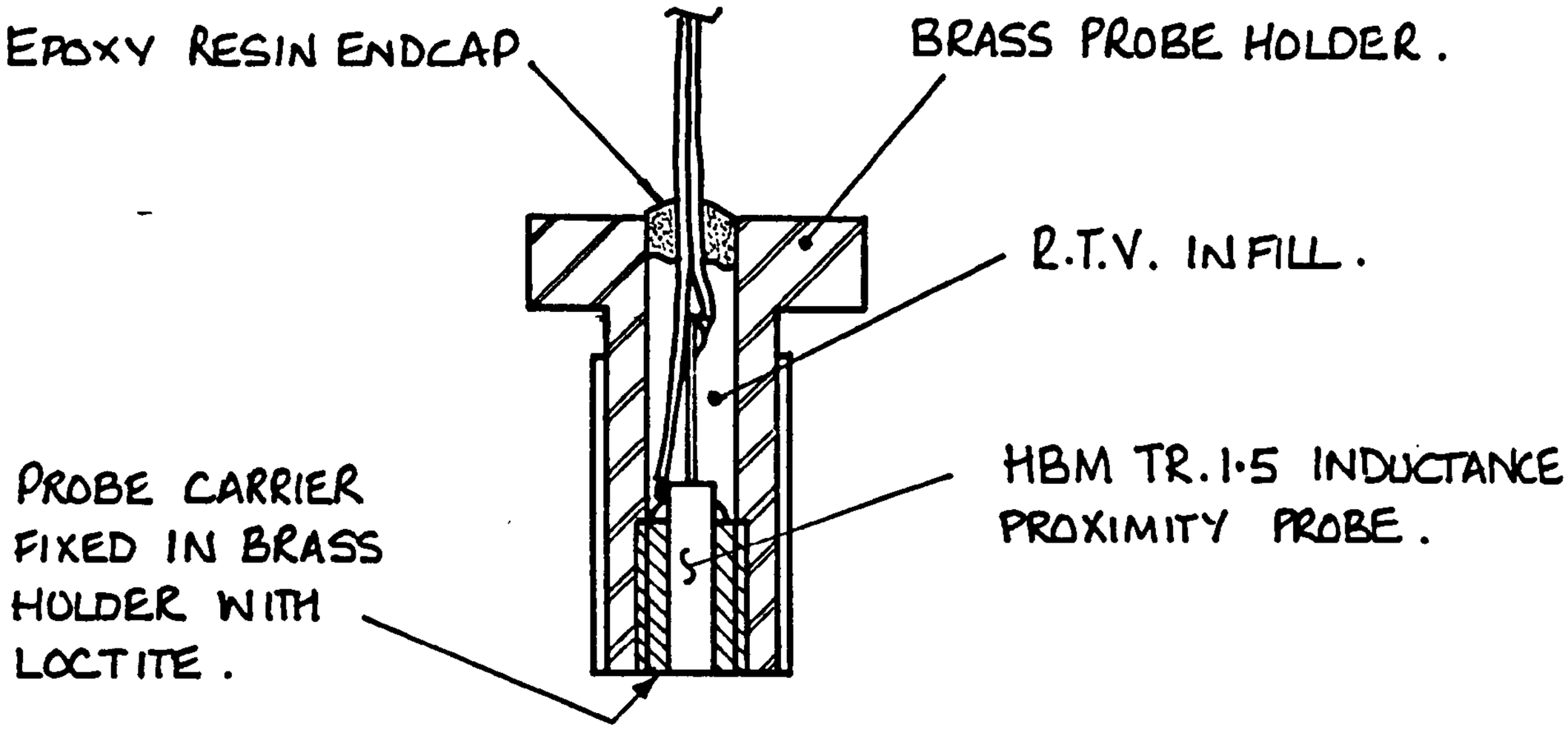

FIG. (4.29) INDUCTANCE PROBE ASSEMBLY.

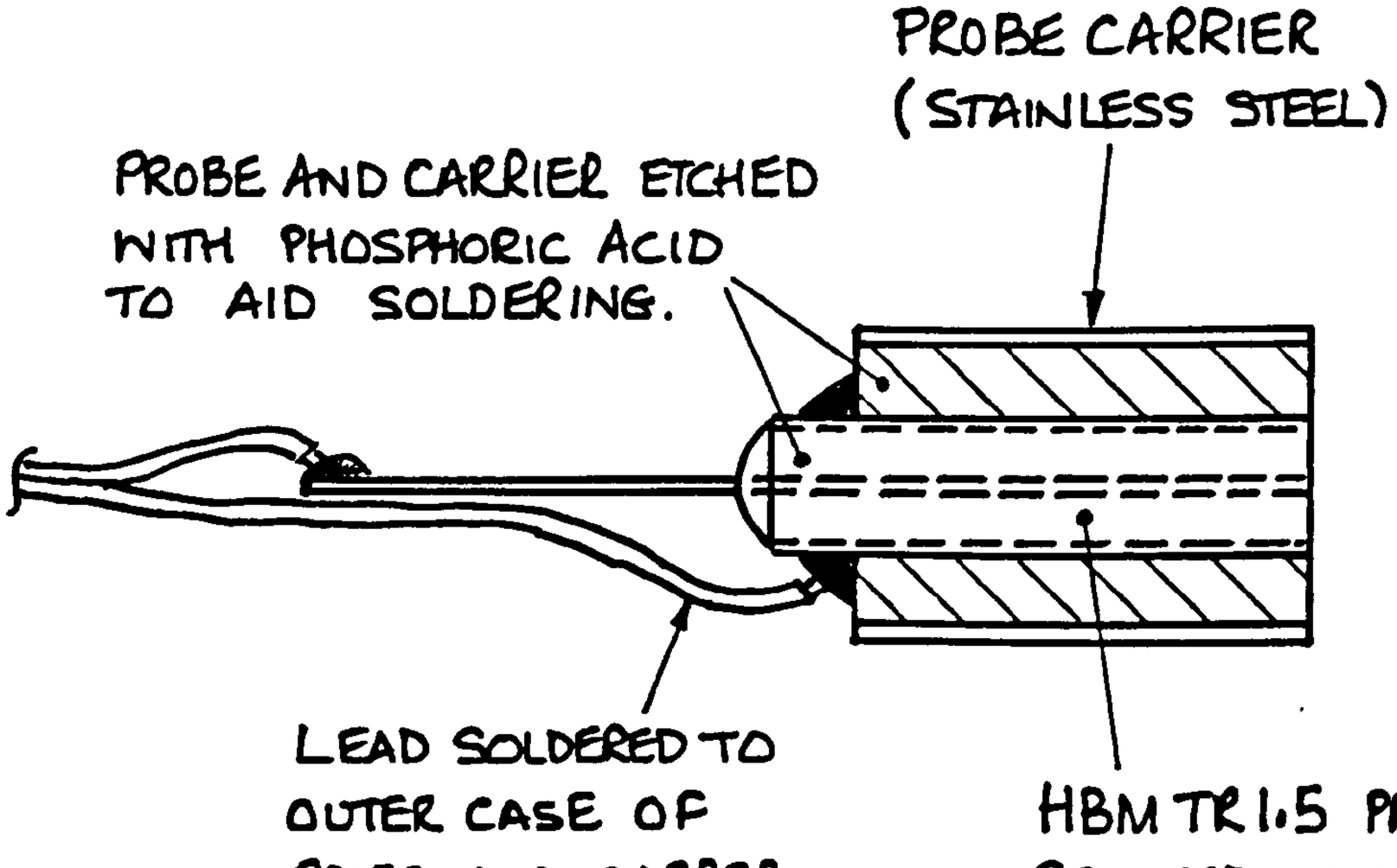

FIG. (4.30) HBM PROBE FIXING TECHNIQUE

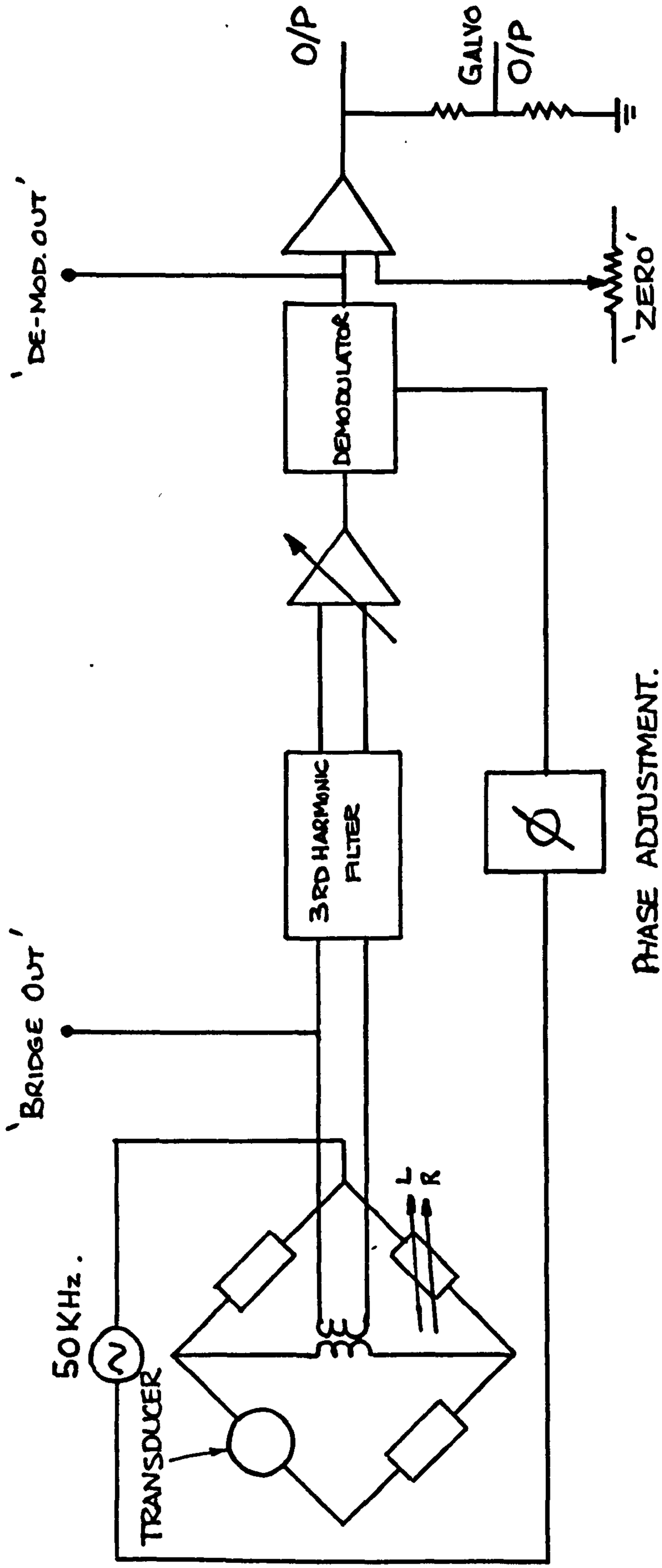

FIG. (4.31) INDUCTIVE TRANSDUCER SCHEMATIC CIRCUIT DIAGRAM

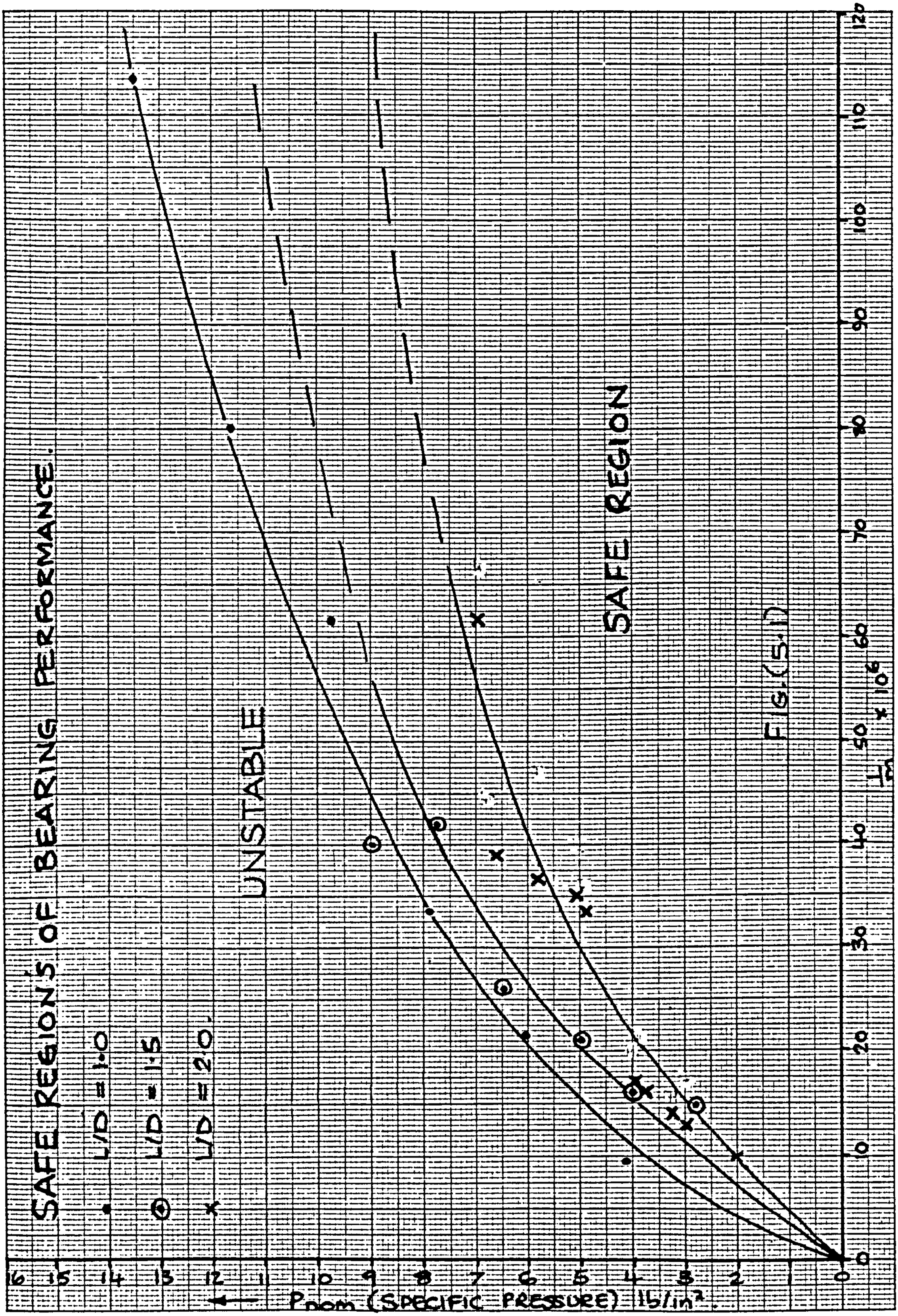
SAFE REGION
UNSTABLE
SAFE REGION
L/D = 1.0
L/D = 1.5
L/D = 2.0
PERFORMANCE
NO'S OF BEARING
E/C (S.I.)
P_{DOM} (SPECIFIC PRESSURE) lb/in²
120
110
100
90
80
70
60
50
40
30
20
10
0
16
15
14
13
12
11
10
9
8
7
6
5
4
3
2
0

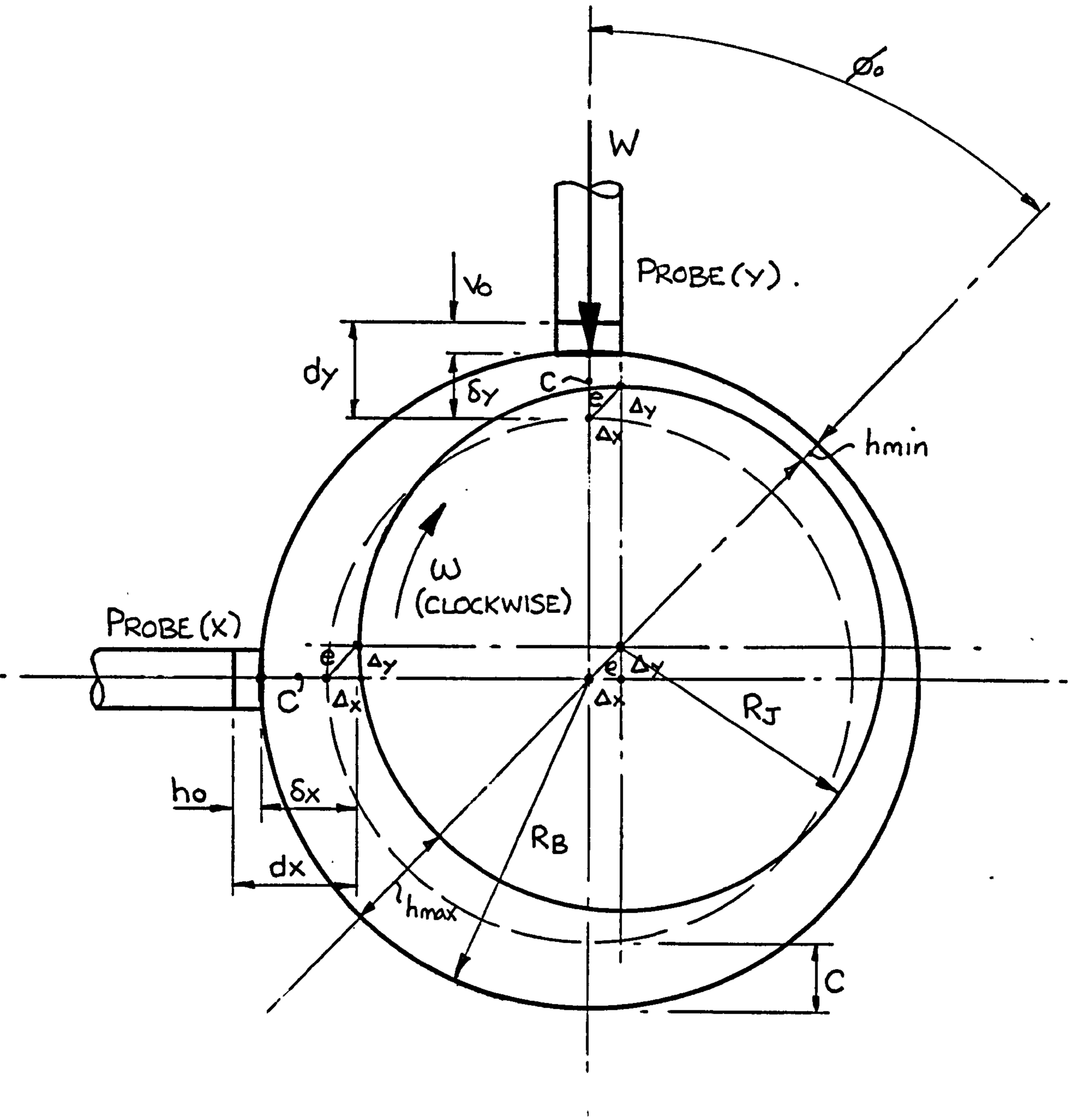

Fig. (5·2) Showing Eccentricity Condition of Test Bearing System

For small displacements and angles, C = Radial clearance.

ω = Clockwise

$\delta x \simeq \Delta x + C \qquad \therefore \Delta x = (\delta x - C)$

and $\delta y \simeq C - \Delta y \qquad \therefore \Delta y = (C - \delta y)$ } Clockwise Rotation

<u>To Calculate Eccentricity Ratio from Displacement Probes</u>

$\therefore e = (\Delta x^2 + \Delta y^2)^{1/2}$

But $\varepsilon_o = \frac{e}{C}$

$\therefore \varepsilon_o = (\Delta x^2 + \Delta y^2)^{1/2}/C$

Which for a clockwise rotation becomes

Remembering $\varepsilon_o = (\Delta x^2 + \Delta y^2)^{1/2}/C$

$$\varepsilon_o = \{(\delta x - C)^2 + (C - \delta y)^2\}^{1/2} \cdot \frac{1}{C}$$

<u>To Calculate Attitude Angle from Displacement Probes</u>

$$\text{Tan } \varphi_o = \frac{\Delta x}{\Delta y}$$

$$\therefore \varphi_o = \text{Tan}^{-1} \left(\frac{\Delta x}{\Delta y}\right)$$

$\therefore$ Remembering $\Delta x \simeq \delta x - C$

and $\Delta y \simeq C - \delta y$

and substituting into the above equation

$$\varphi_o = \text{Tan}^{-1} \left\{\left(\frac{\delta x - C}{C - \delta y}\right)\right\}$$

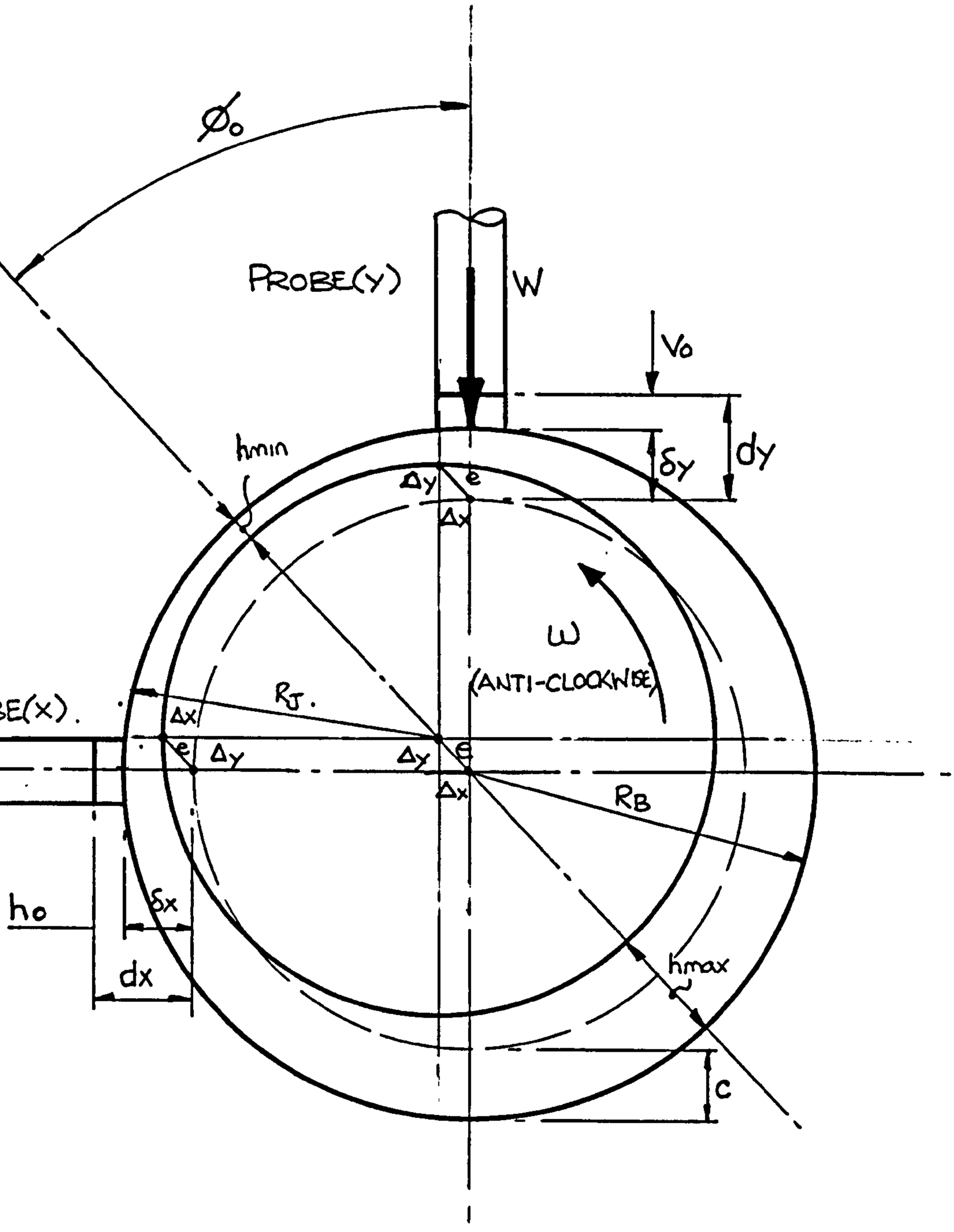

Fig. (5·3) Showing Eccentricity Condition for Test System

For small displacements and angles, C = Radial clearance

ω = Anti-clockwise

$\delta x \simeq C - \Delta x \qquad \therefore \Delta x = (C - \delta x)$

$\delta y \simeq C - \Delta y \qquad \therefore \Delta y = (C - \delta y)$ } Anti-clockwise Rotation

<u>To Calculate Eccentricity Ratios from Displacement Probes</u>

$\therefore e = (\Delta x^2 + \Delta y^2)^{1/2}$ But $\varepsilon_o = \frac{e}{C}$

$\therefore \varepsilon_o = \frac{e}{C} = \frac{(\Delta x^2 + \Delta y^2)^{1/2}}{C}$

Which becomes: $\varepsilon_o = \{(C - \delta x)^2 + (C - \delta y)^2\}^{1/2} \cdot \frac{1}{C}$

<u>To Calculate Attitude Angle from Displacement Probes</u>

$\text{Tan } \varphi_o = \frac{\Delta x}{\Delta y}$ $\therefore \varphi_o = \text{Tan}^{-1} \left(\frac{\Delta x}{\Delta y}\right)$

$\therefore$ Remembering $\Delta x \simeq C - \delta x$ and $\Delta x \simeq C - \delta y$

and substituting into the above equation

$\varphi_o \simeq \text{Tan}^{-1} \left\{\left(\frac{C - \delta x}{C - \delta y}\right)\right\}$

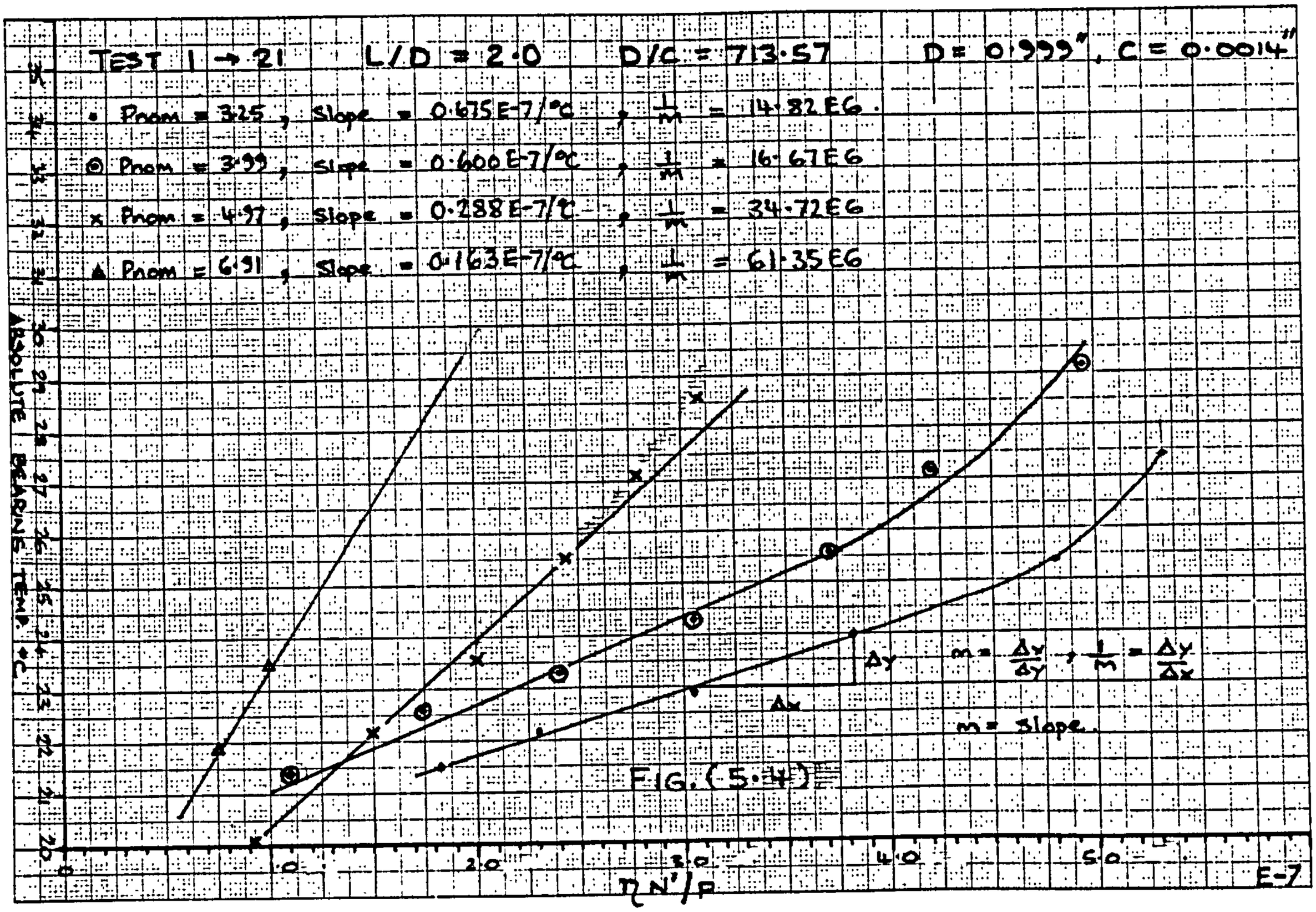
TEST 1 → 21 L/D = 2.0 D/C = 713.57 D = 0.999" , C = 0.0014"
• Pnom = 3.25 , Slope = 0.675E-7/°C , 1/m = 14.82E6
⊙ Pnom = 3.99 , Slope = 0.600E-7/°C , 1/m = 16.67E6
× Pnom = 4.97 , Slope = 0.288E-7/°C , 1/m = 34.72E6
▲ Pnom = 6.91 , Slope = 0.163E-7/°C , 1/m = 61.35E6
ABSOLUTE BEARING TEMP. °C
Δy
Δx
m = Δy/Δx , 1/m = Δy/Δx
m = Slope.
FIG. (5.4)
η N'/P
E-7

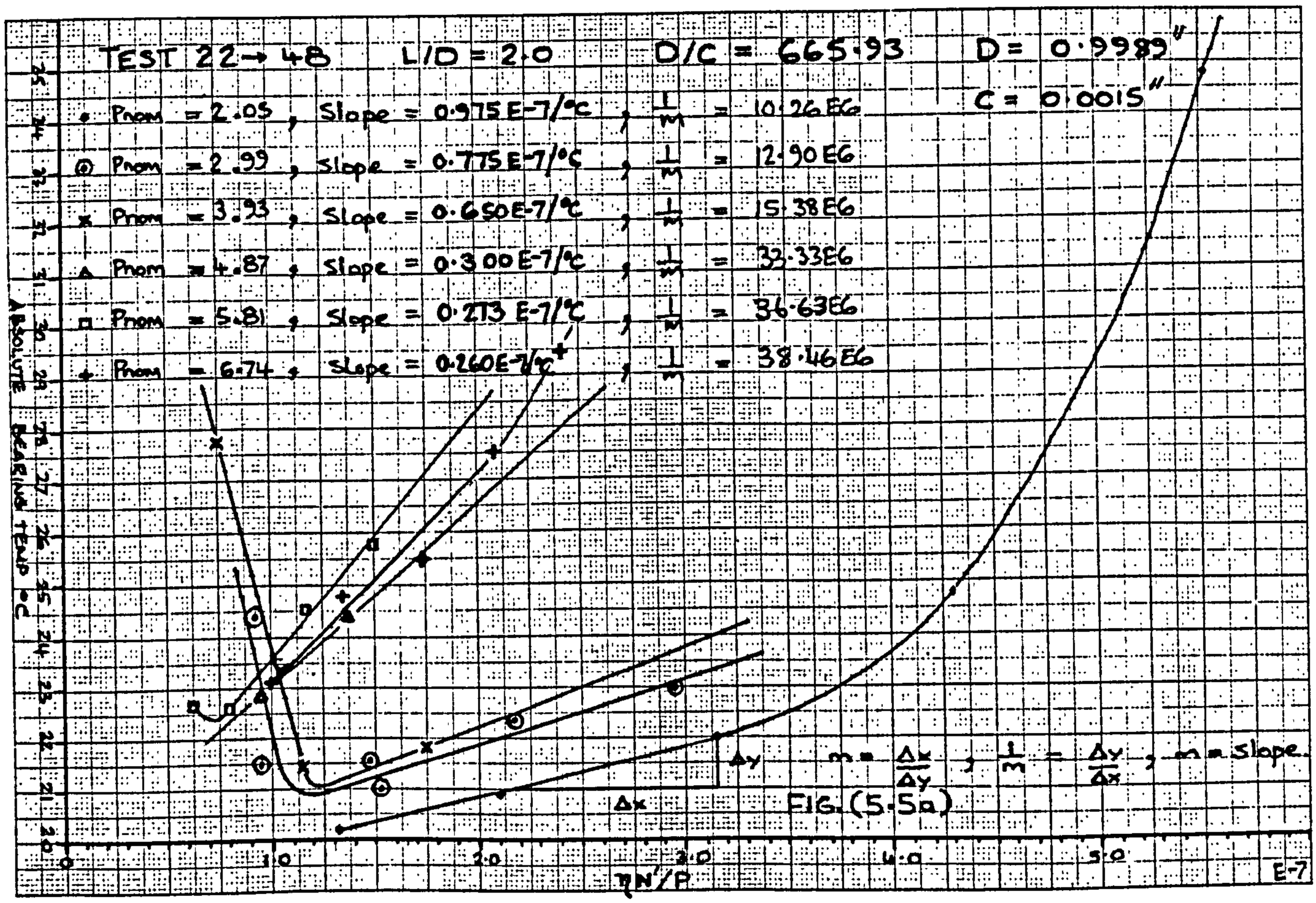
TEST 22 → 48 L/D = 2.0 D/C = 665.93 D = 0.9989"
C = 0.0015"
• Pnom = 2.05 , Slope = 0.975E-7/°C , 1/m = 10.26E6
⊙ Pnom = 2.99 , Slope = 0.775E-7/°C , 1/m = 12.90E6
× Pnom = 3.93 , Slope = 0.650E-7/°C , 1/m = 15.38E6
▲ Pnom = 4.87 , Slope = 0.300E-7/°C , 1/m = 33.33E6
□ Pnom = 5.81 , Slope = 0.273E-7/°C , 1/m = 36.63E6
+ Pnom = 6.74 , Slope = 0.260E-7/°C , 1/m = 38.46E6
ABSOLUTE BEARING TEMP °C
Δy
Δx
m = Δx/Δy , 1/m = Δy/Δx , m = Slope.
FIG. (5.5a)
η N'/P
E-7

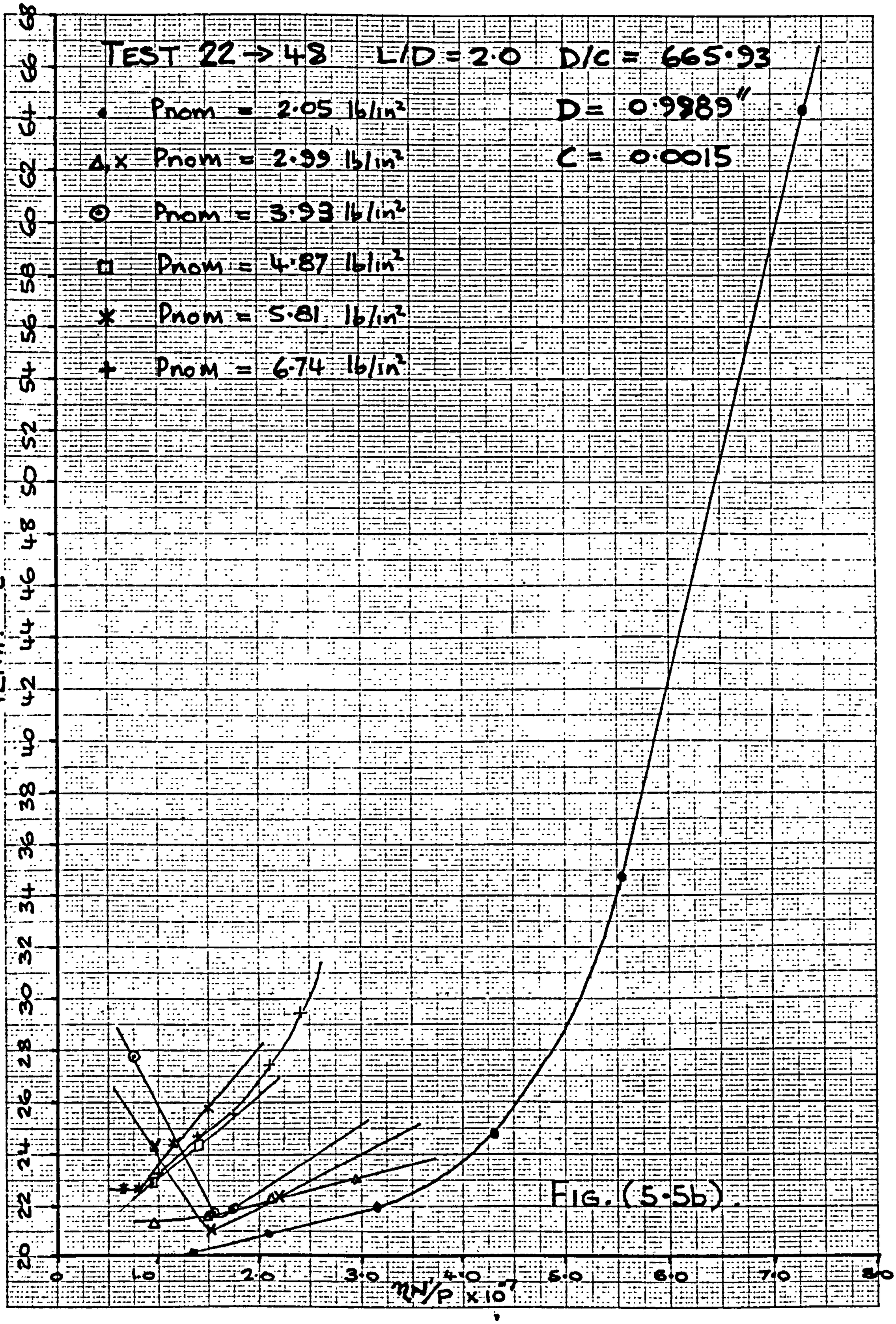
TEST 22 → 48 L/D = 2·0 D/C = 665·93
• Pnom = 2·05 lb/in²
Δ x Pnom = 2·99 lb/in²
⊙ Pnom = 3·93 lb/in²
□ Pnom = 4·87 lb/in²
* Pnom = 5·81 lb/in²
+ Pnom = 6·74 lb/in²
D = 0·9989"
C = 0·0015
TEMP. °C
ηN'/P x 10⁻⁷

FIG. (5-5b).

TEST 71→94 L/D = 1.0 D/C = 740.04 D = 0.9905" C = 0.00135".

- • Pnom = 4.10, Slope = 1.075E-7/°C, $\frac{1}{m}$ = 9.30E6
- ⊕ Pnom = 5.98, Slope = 0.463E-7/°C, $\frac{1}{m}$ = 21.60E6
- × Pnom = 7.86, Slope = 0.300E-7/°C, $\frac{1}{m}$ = 33.33E6
- △ Pnom = 9.73, Slope = 0.163E-7/°C, $\frac{1}{m}$ = 61.35E6
- □ Pnom = 11.61, Slope = 0.125E-7/°C, $\frac{1}{m}$ = 80.00E6
- + Pnom = 13.49, Slope = 0.088E-7/°C, $\frac{1}{m}$ = 113.64E6

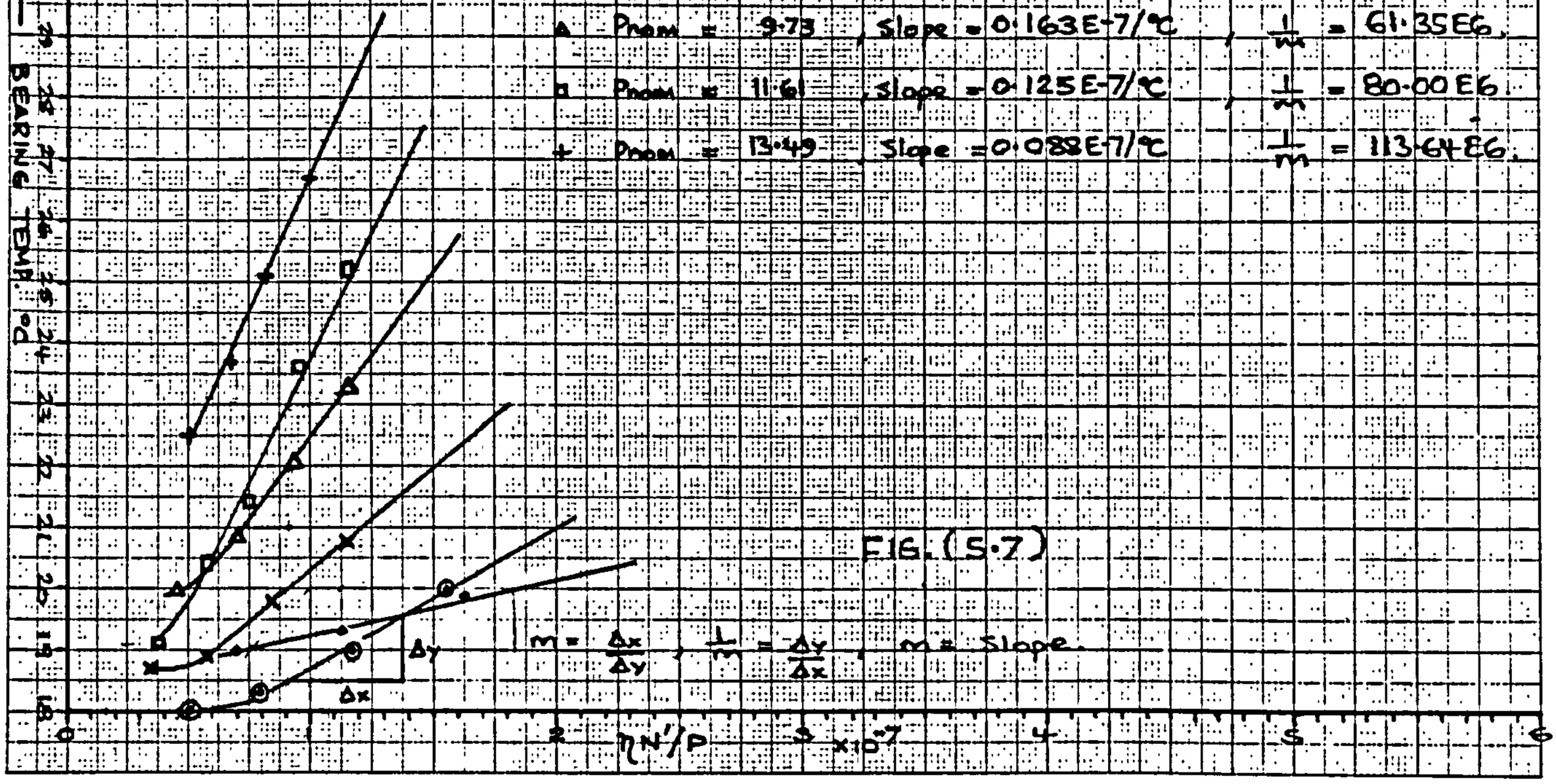

FIG. (5.7)

$m = \frac{\Delta x}{\Delta y}$, $\frac{1}{m} = \frac{\Delta y}{\Delta x}$, m = Slope.

TEST 49→70 L/D = 1.5 D = 0.99845" D/C = 512.03 C = 0.00195"

- • Pnom = 2.74, Slope = 0.675E-7/°C, $\frac{1}{m}$ = 14.82E6
- ● Pnom = 3.99, Slope = 0.625E-7/°C, $\frac{1}{m}$ = 16.00E6
- × Pnom = 5.24, Slope = 0.475E-7/°C, $\frac{1}{m}$ = 21.05E6
- △ Pnom = 6.49, Slope = 0.388E-7/°C, $\frac{1}{m}$ = 25.77E6
- □ Pnom = 7.74, Slope = 0.238E-7/°C, $\frac{1}{m}$ = 42.02E6
- + Pnom = 8.99, Slope = 0.250E-7/°C, $\frac{1}{m}$ = 40.00E6

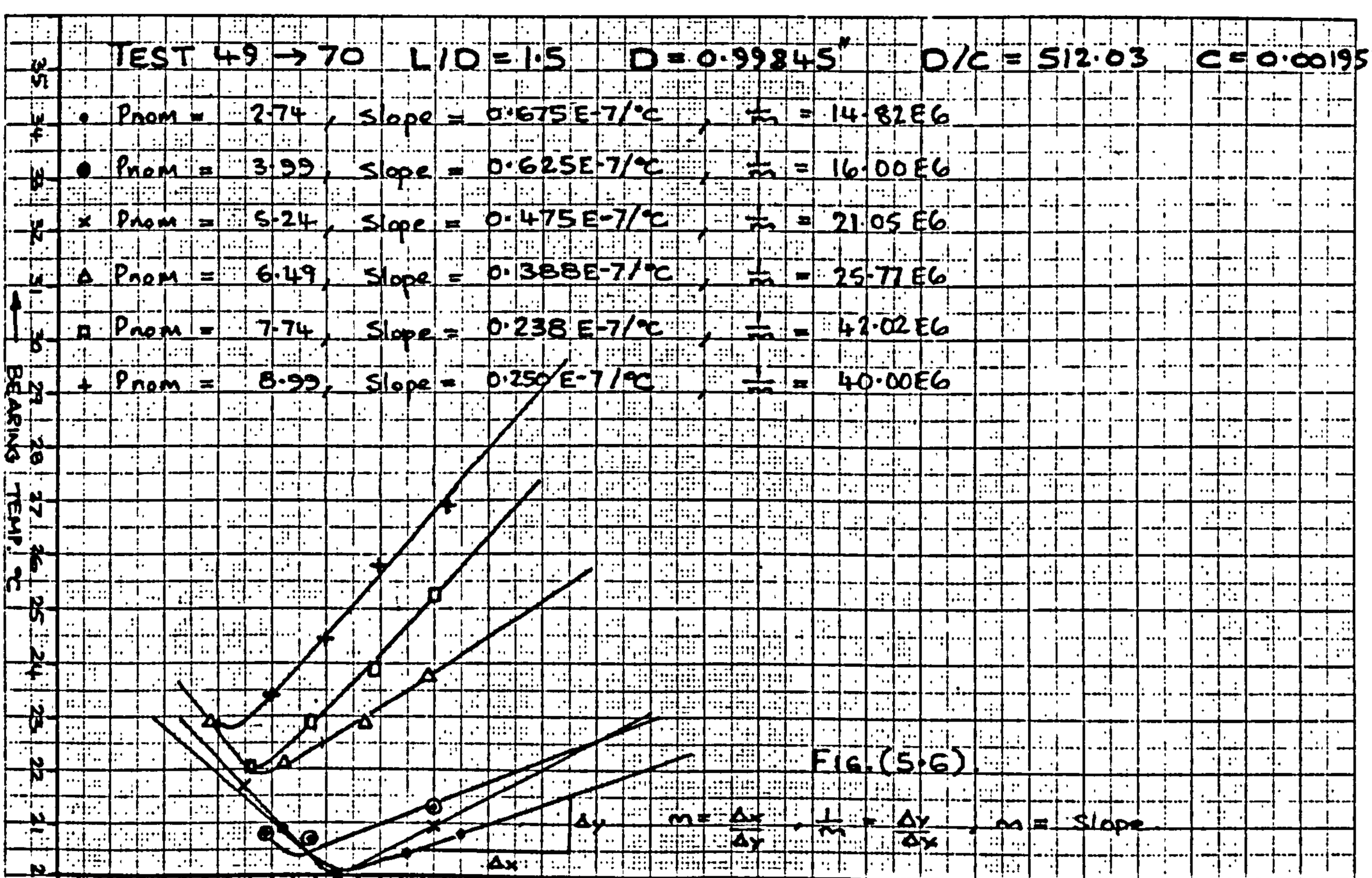

FIG. (5.6)

$m = \frac{\Delta x}{\Delta y}$, $\frac{1}{m} = \frac{\Delta y}{\Delta x}$, m = Slope

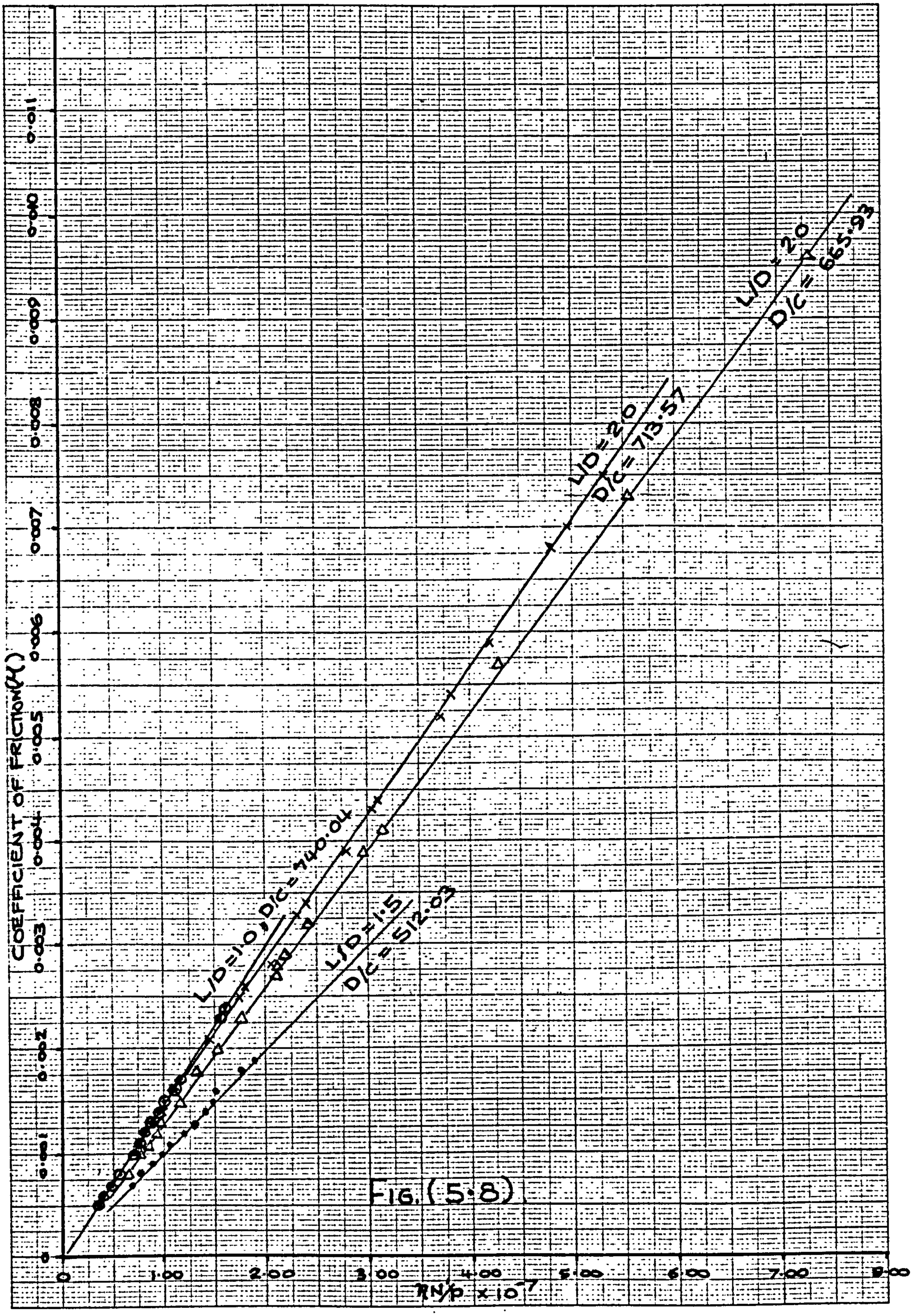
L/D = 2.0
D/c = 65.93
L/D = 2.0
D/c = 713.57
L/D = 1.0, D/c = 140.04
L/D = 1.5
D/c = 512.03
COEFFICIENT OF FRICTION(λ)
0.003
0.004
0.005
0.002
0.001
0
1.00
2.00
3.00
4.00
5.00
6.00
7.00
8.00
πN/p x 10⁻⁷

FIG. (5.8)

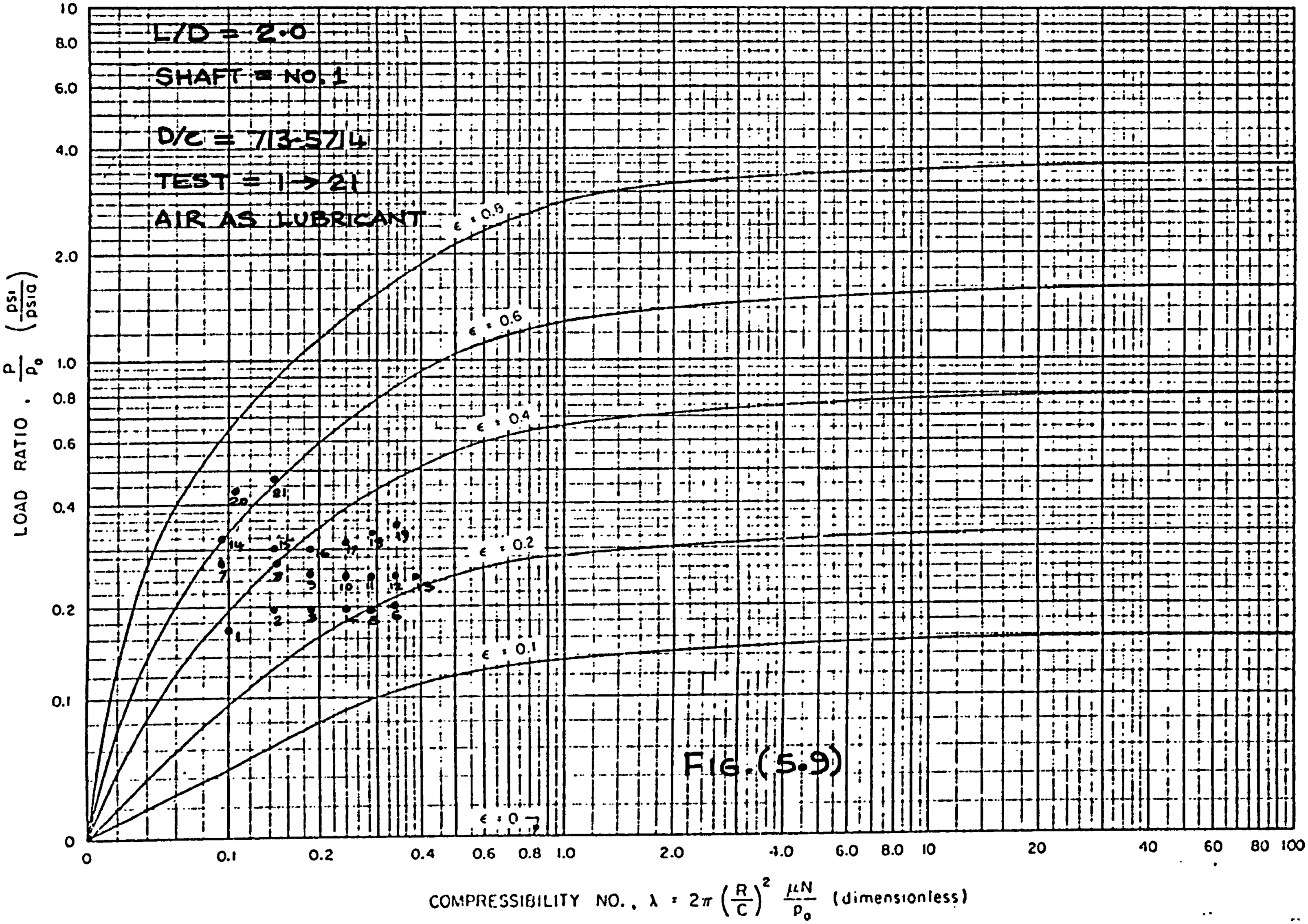
L/D = 2.0
SHAFT = NO. 1
D/C = 7/3-57/4
TEST = 1 → 21
AIR AS LUBRICANT
ε = 0.8
ε = 0.6
ε = 0.4
ε = 0.2
ε = 0.1
ε = 0
LOAD RATIO . P/P0 (psi/psia)
COMPRESSIBILITY NO., λ = 2π (R/C)² μN/P0 (dimensionless)
0
0.1
0.2
0.4
0.6
0.8
1.0
2.0
4.0
6.0
8.0
10
20
40
60
80
100

FIG. (5.9)

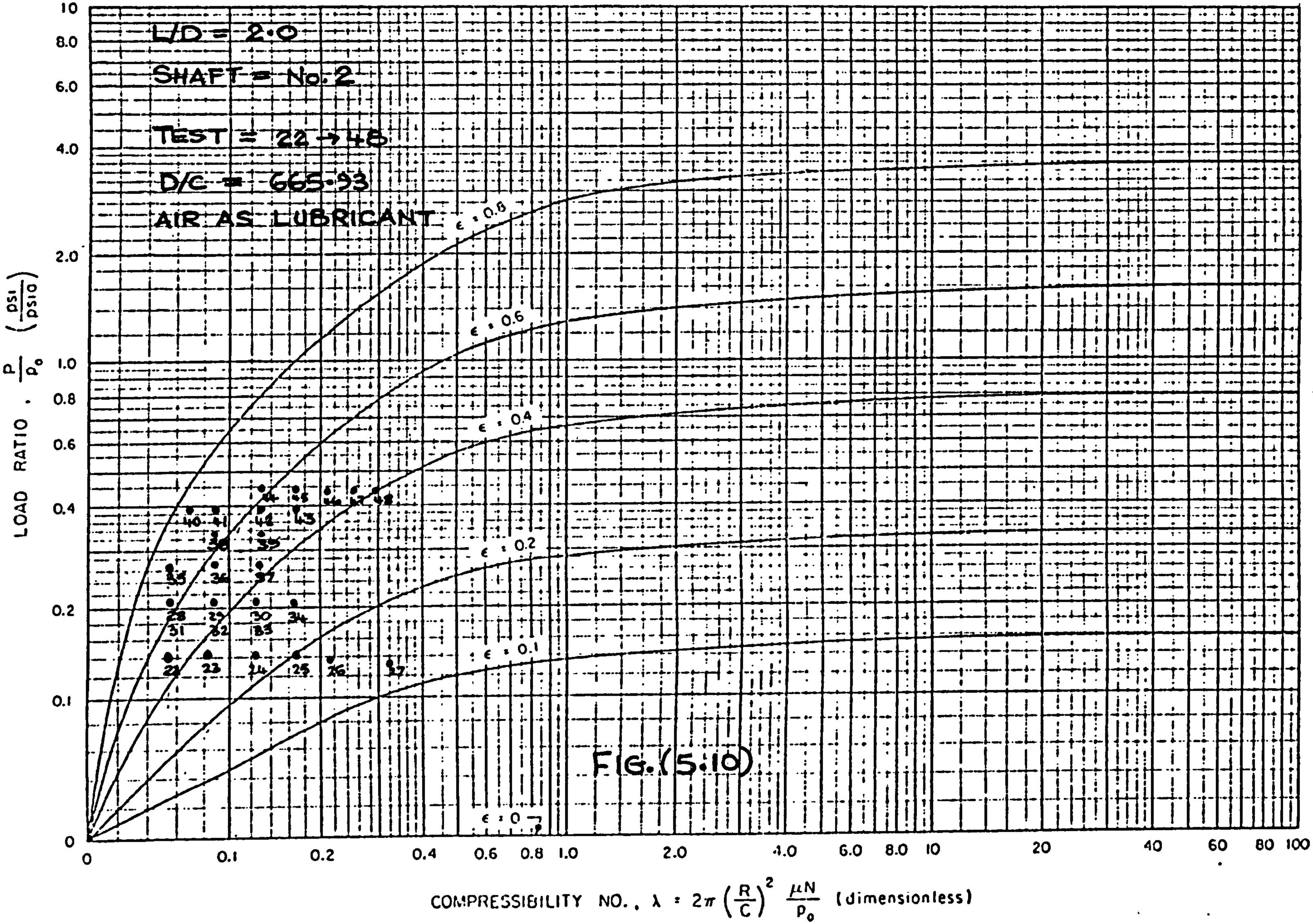
L/D = 2.0
SHAFT = No. 2
TEST = 22 → 48
D/C = 665-93
AIR AS LUBRICANT
ε = 0.8
ε = 0.6
ε = 0.4
ε = 0.2
ε = 0.1
ε = 0
LOAD RATIO . $\frac{P}{P_0}$ $\left(\frac{psi}{psi0}\right)$
10
8.0
6.0
4.0
2.0
1.0
0.8
0.6
0.4
0.2
0.1
0
0
0.1
0.2
0.4
0.6
0.8
1.0
2.0
4.0
6.0
8.0
10
20
40
60
80
100
COMPRESSIBILITY NO., $\lambda = 2\pi\left(\frac{R}{C}\right)^2 \frac{\mu N}{P_0}$ (dimensionless)

FIG. (5.10)

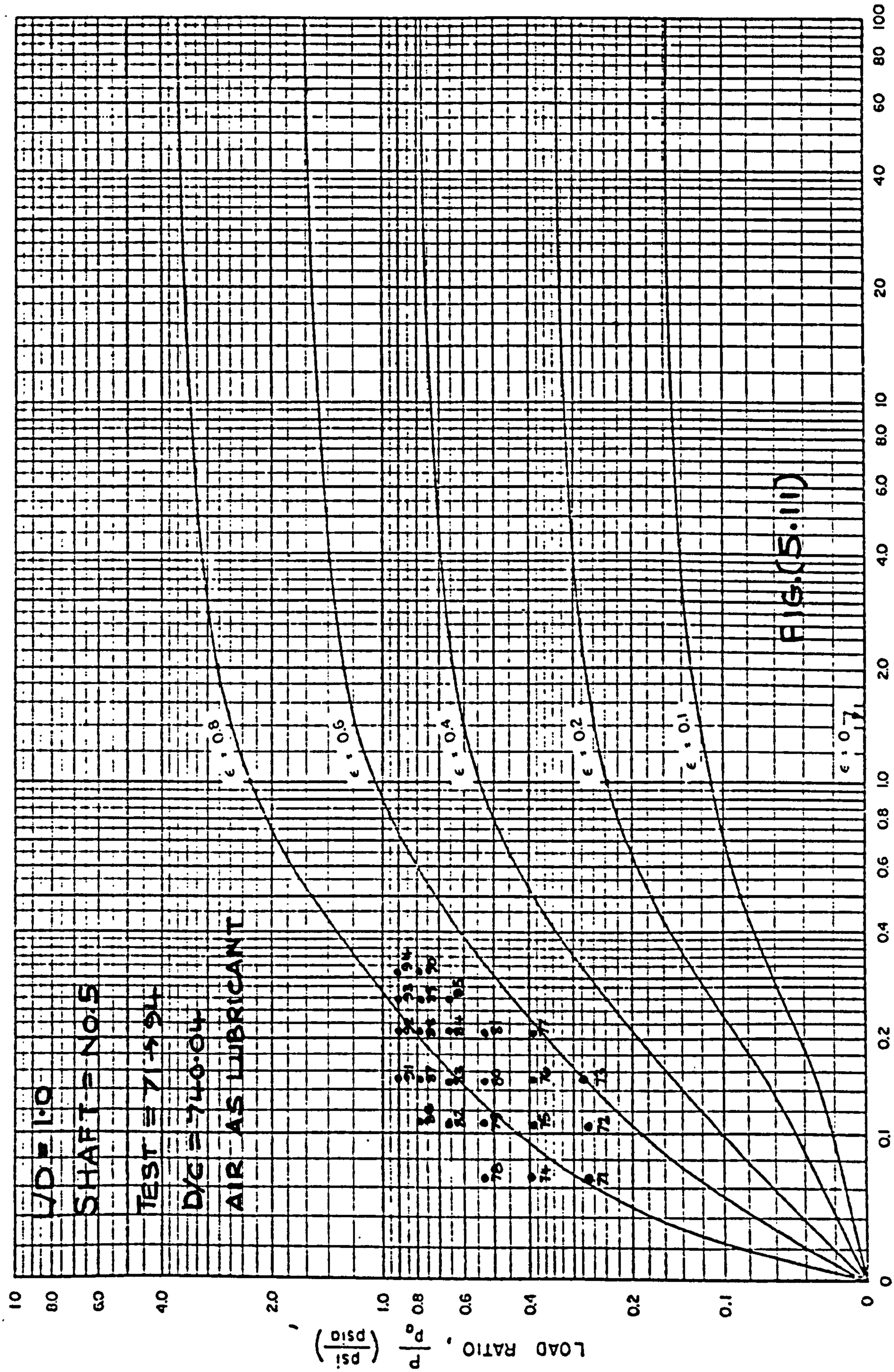
FIG. 13.11D
SHAFT = NO. 45
L/D = 1.0
TEST = 7-4-64
D/C = 7140.04
AIR AS LUBRICANT
ε = 0.8
ε = 0.6
ε = 0.4
ε = 0.2
ε = 0.1
ε = 0
LOAD RATIO, $\frac{P}{P_o}$ $\left(\frac{psi}{psia}\right)$
COMPRESSIBILITY NO., $\lambda = 2\pi \left(\frac{R}{C}\right)^2 \frac{\mu N}{P_o}$ (dimensionless)
0
0.1
0.2
0.4
0.6
0.8
1.0
2.0
4.0
6.0
8.0
10
20
40
60
80
100

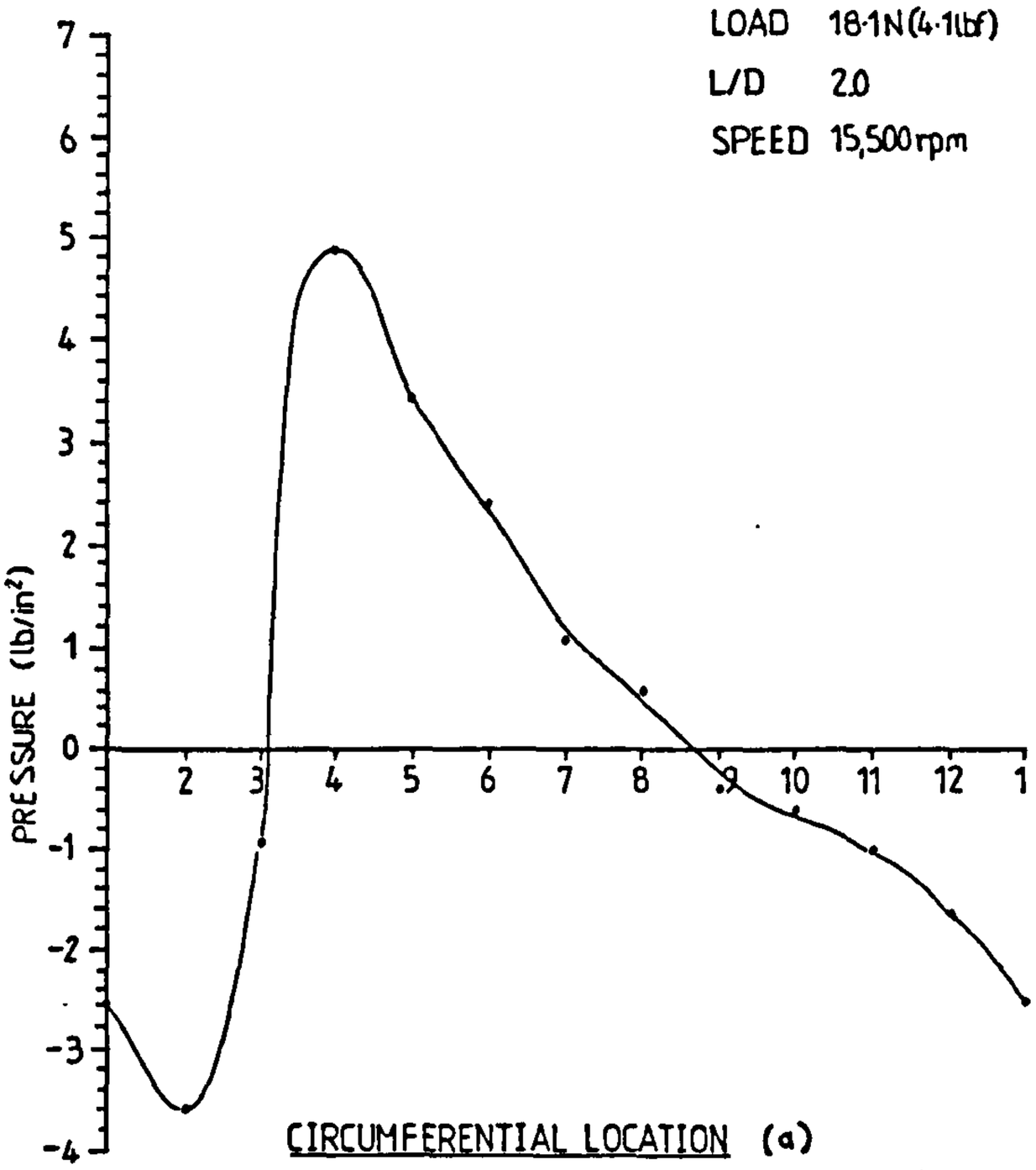

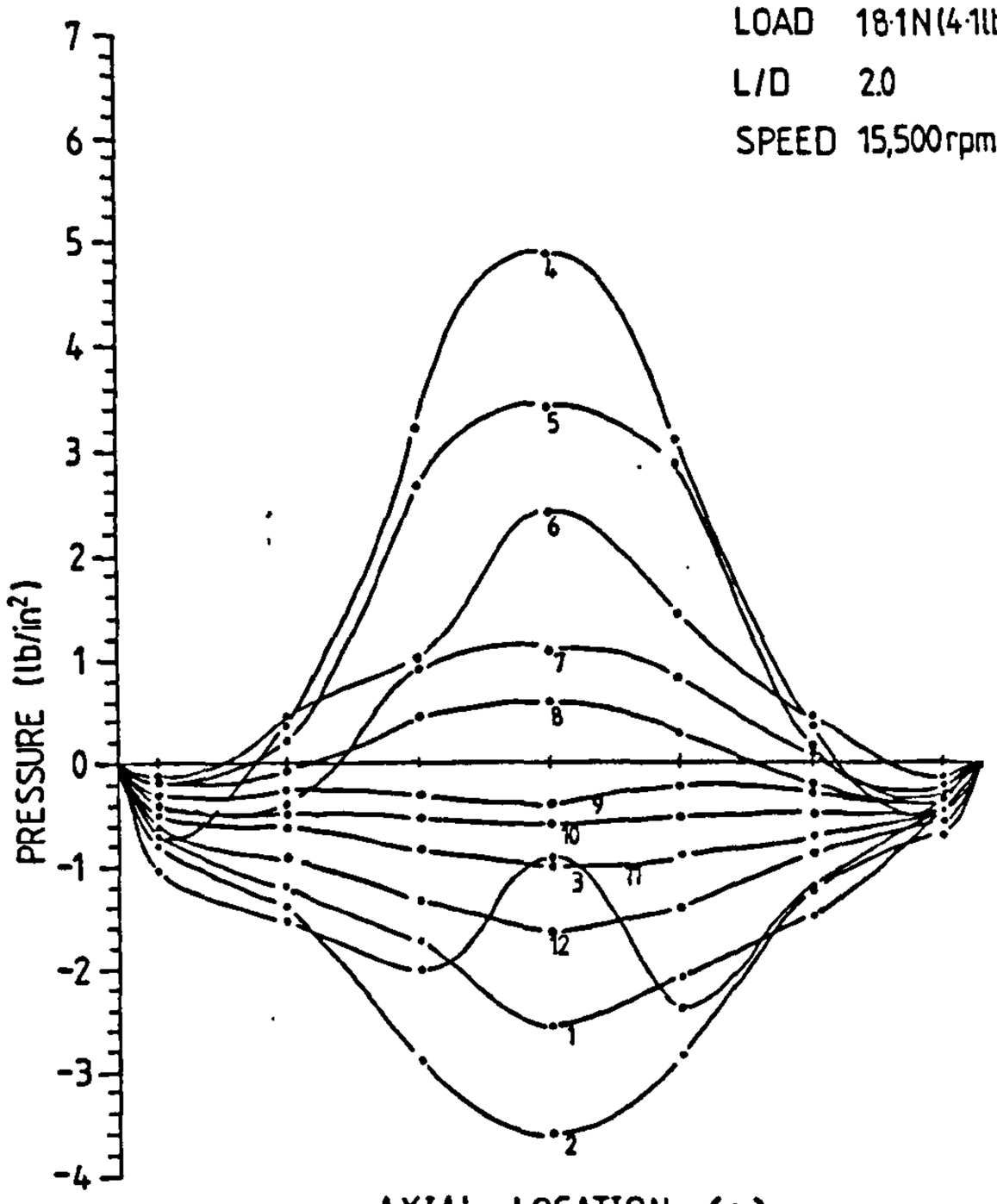

FIG.(5.12) TEST 24.

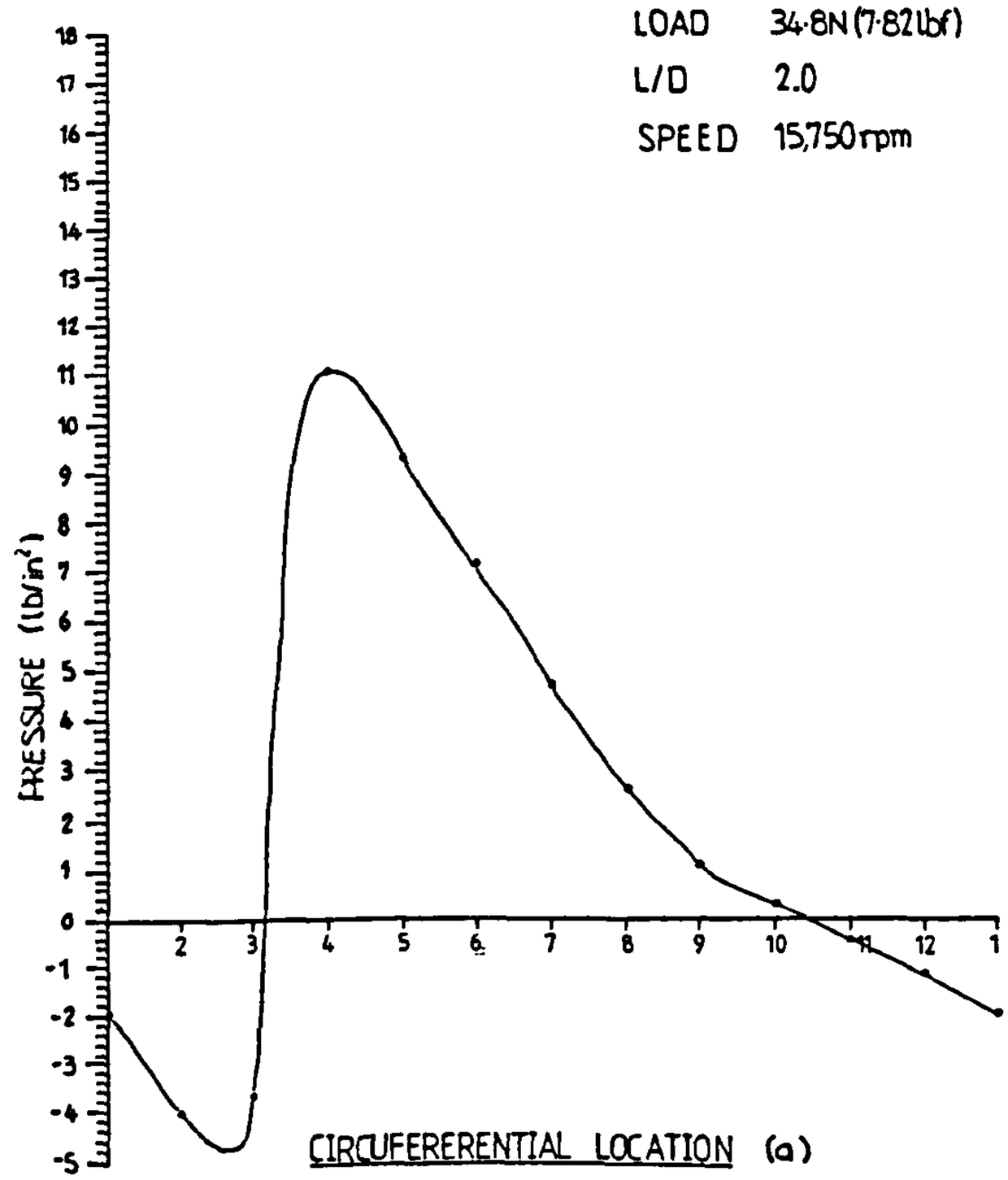

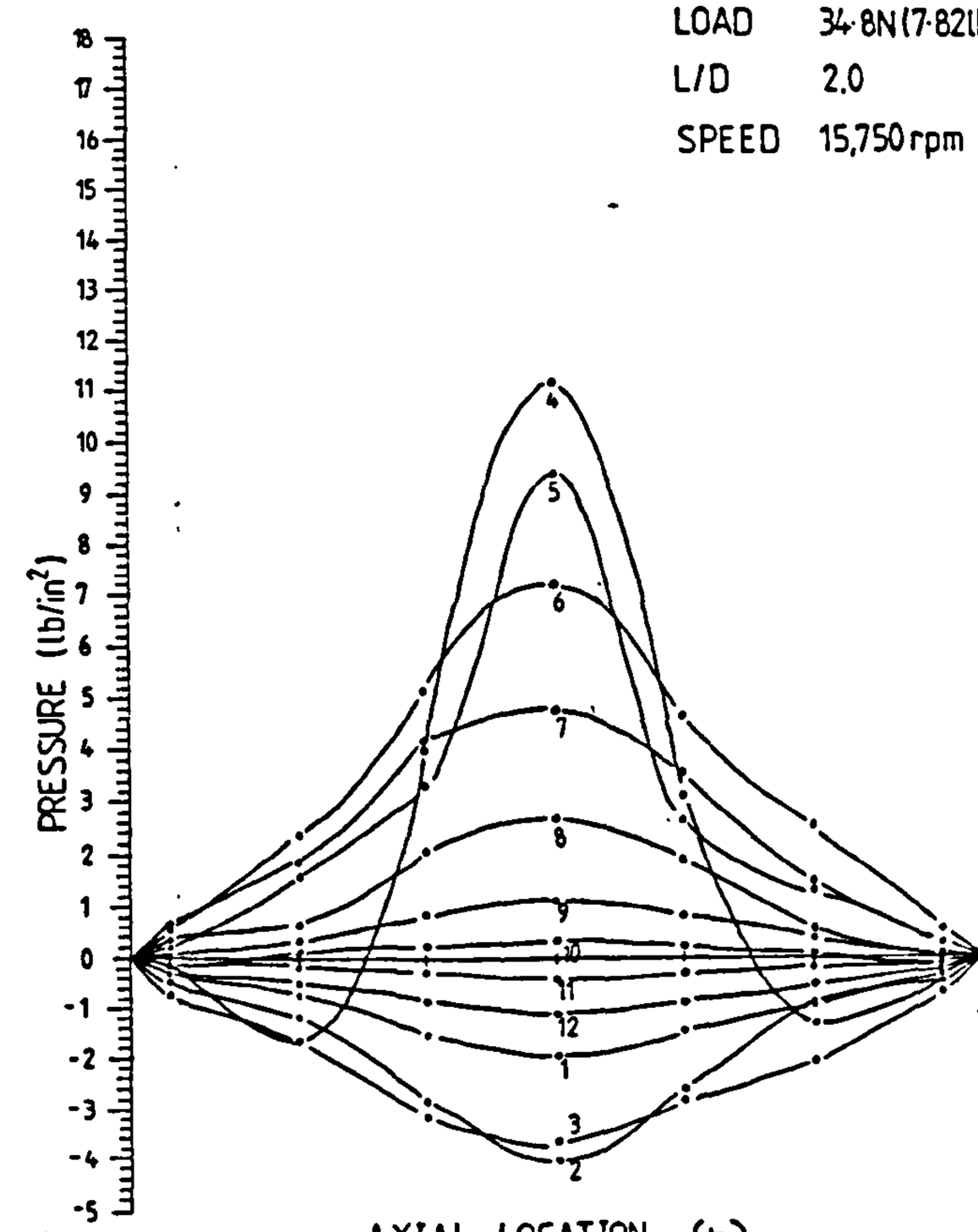

FIG. (5.13) TEST 37

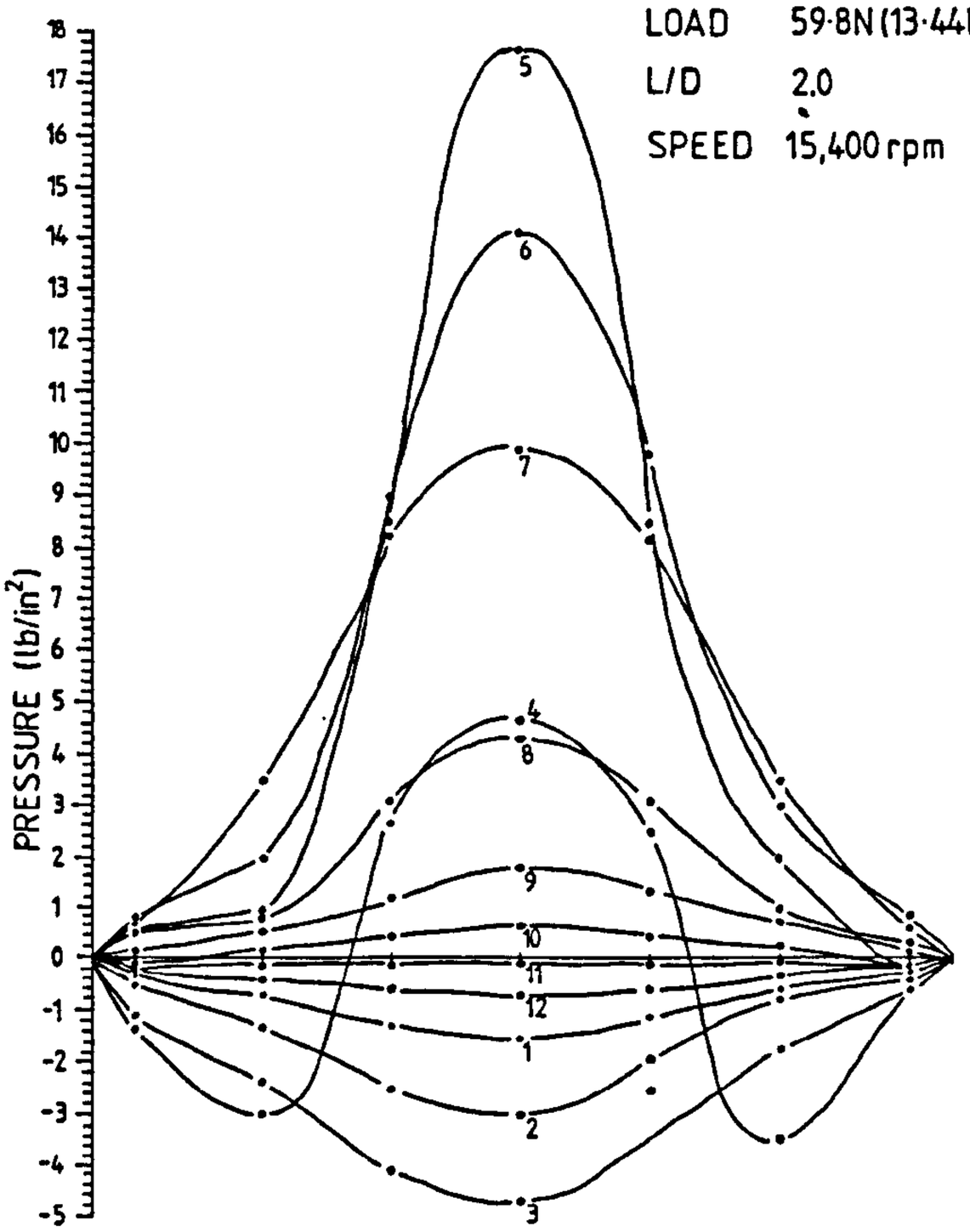

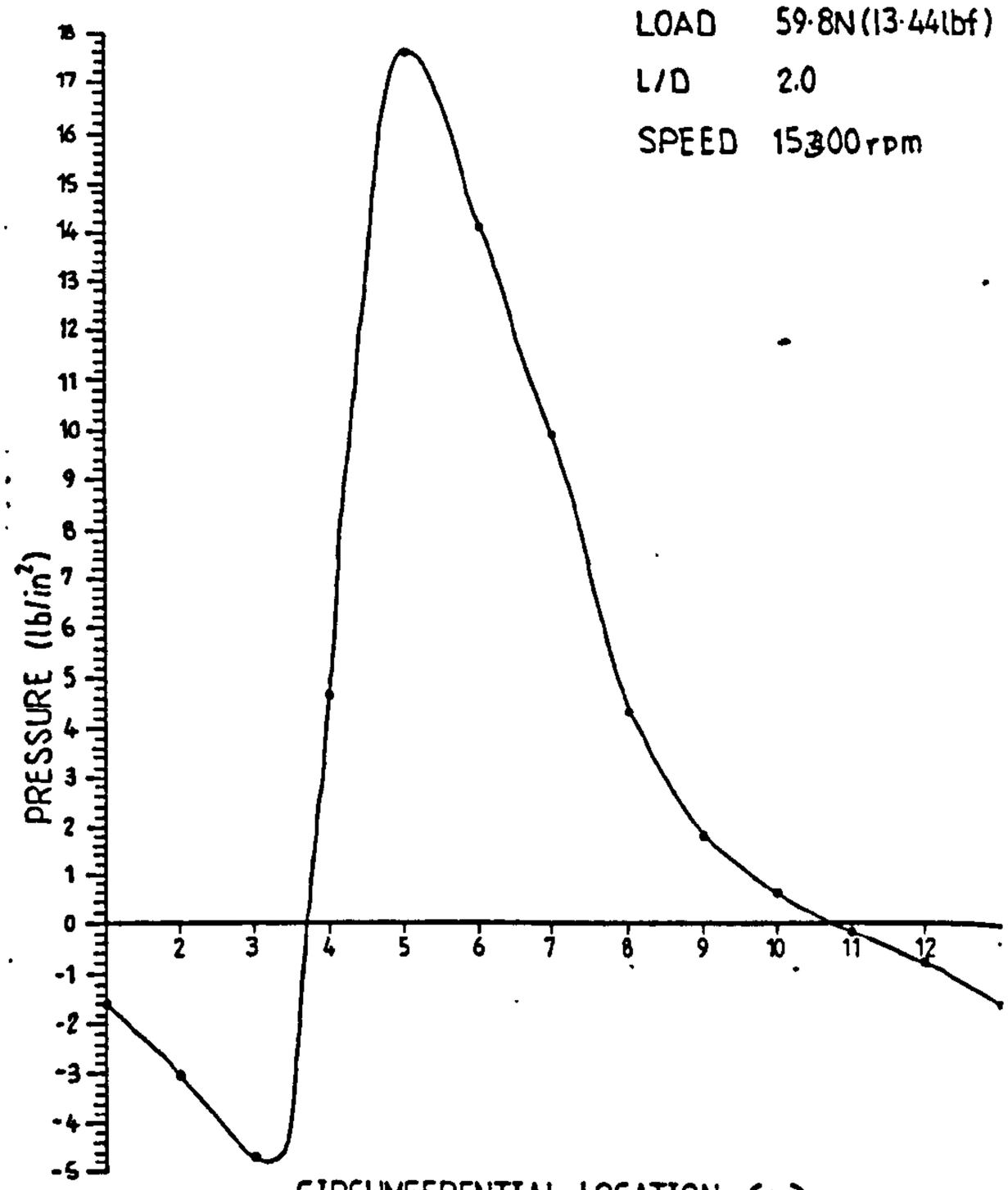

FIG. (5.14) TEST 44

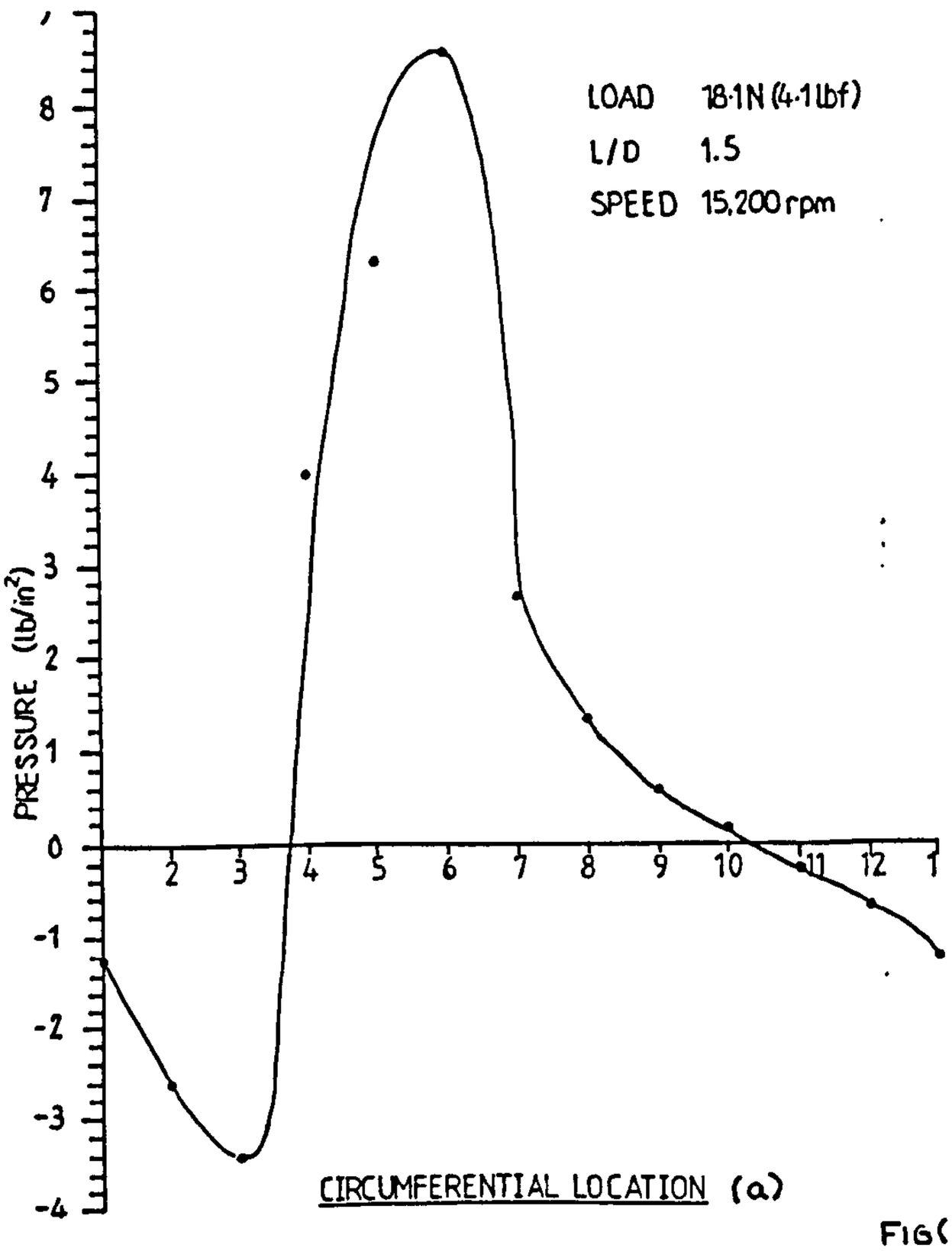

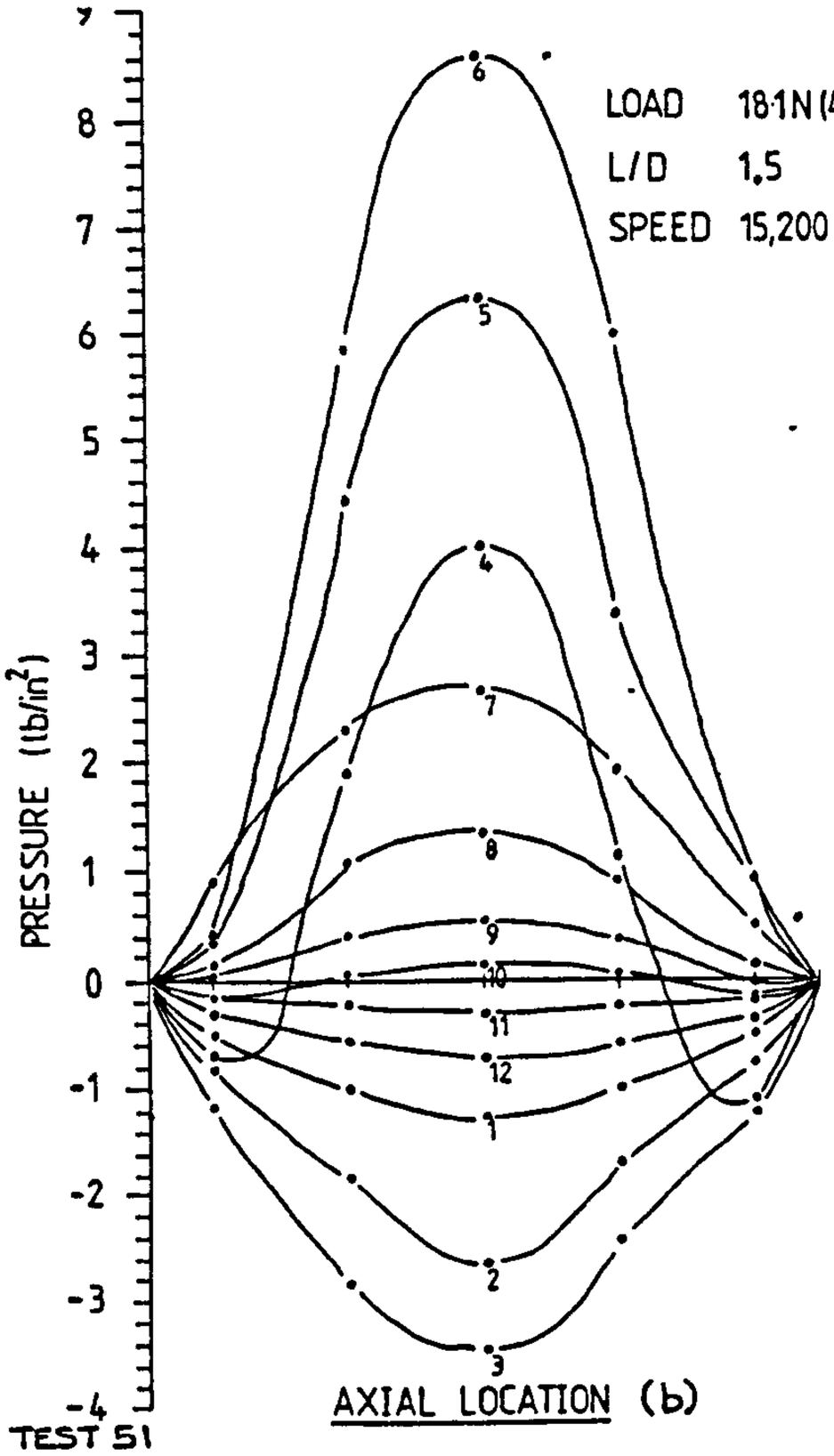

FIG(5.15) TEST 51

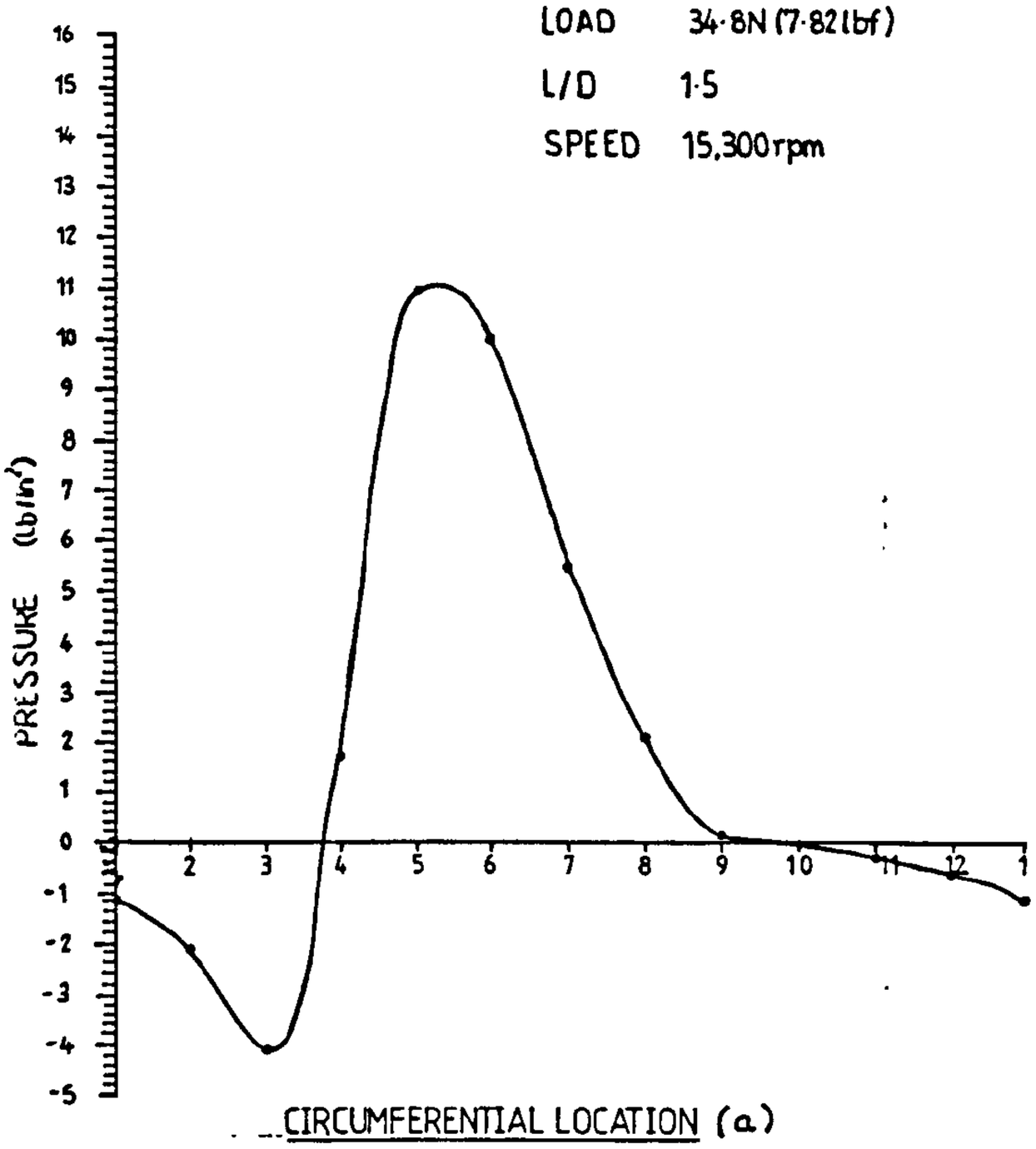

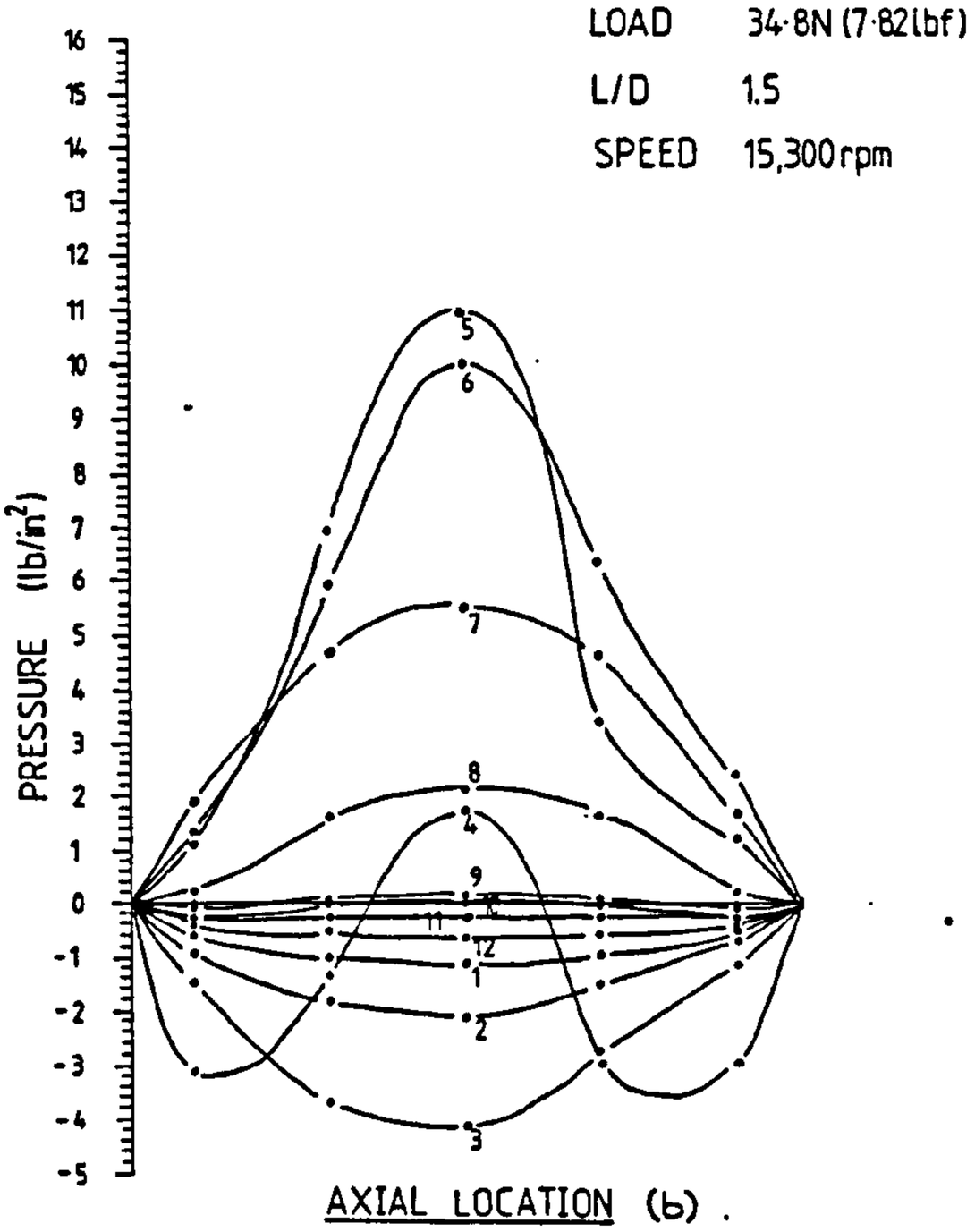

FIG. (5.16) TEST 56.

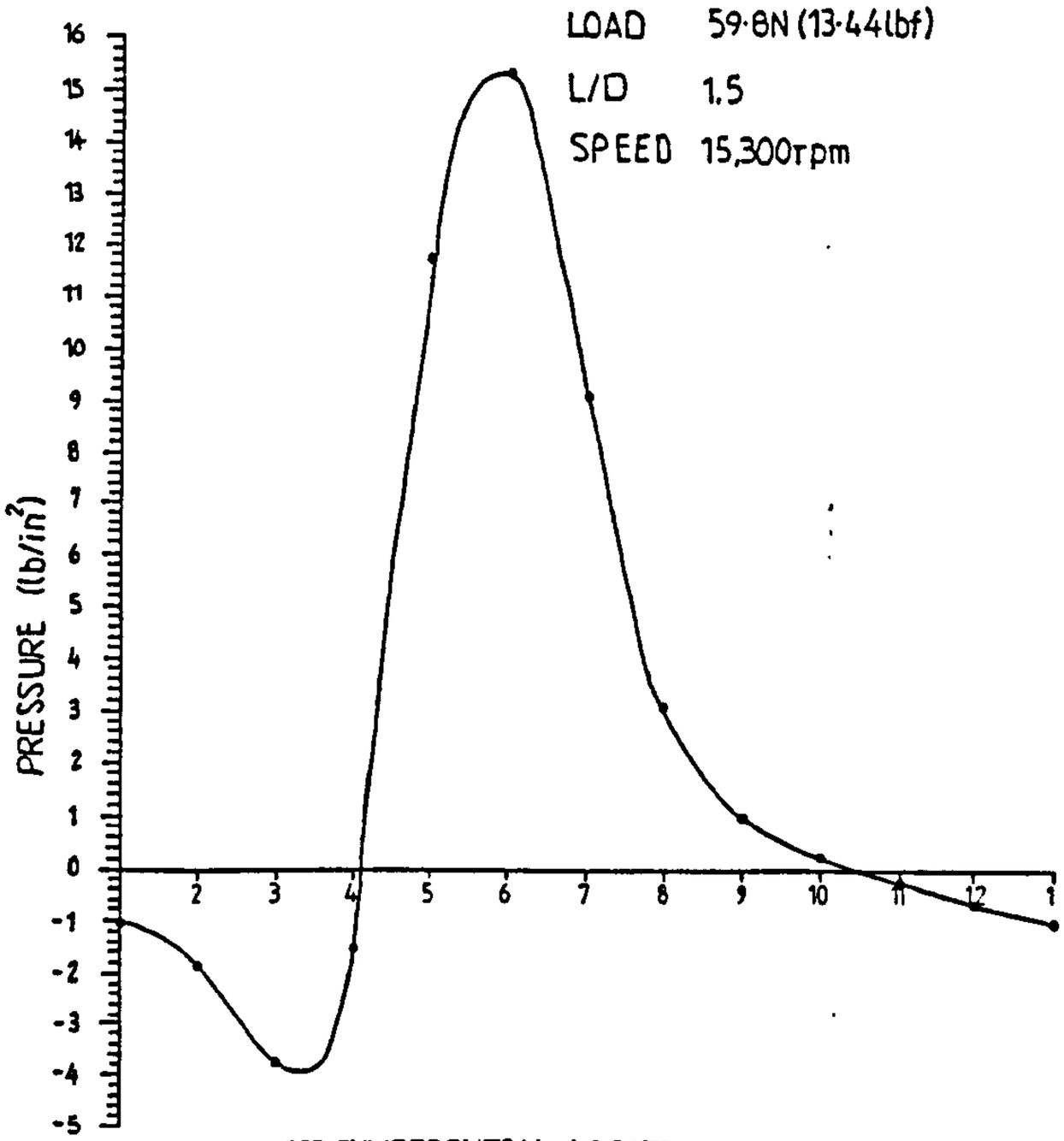

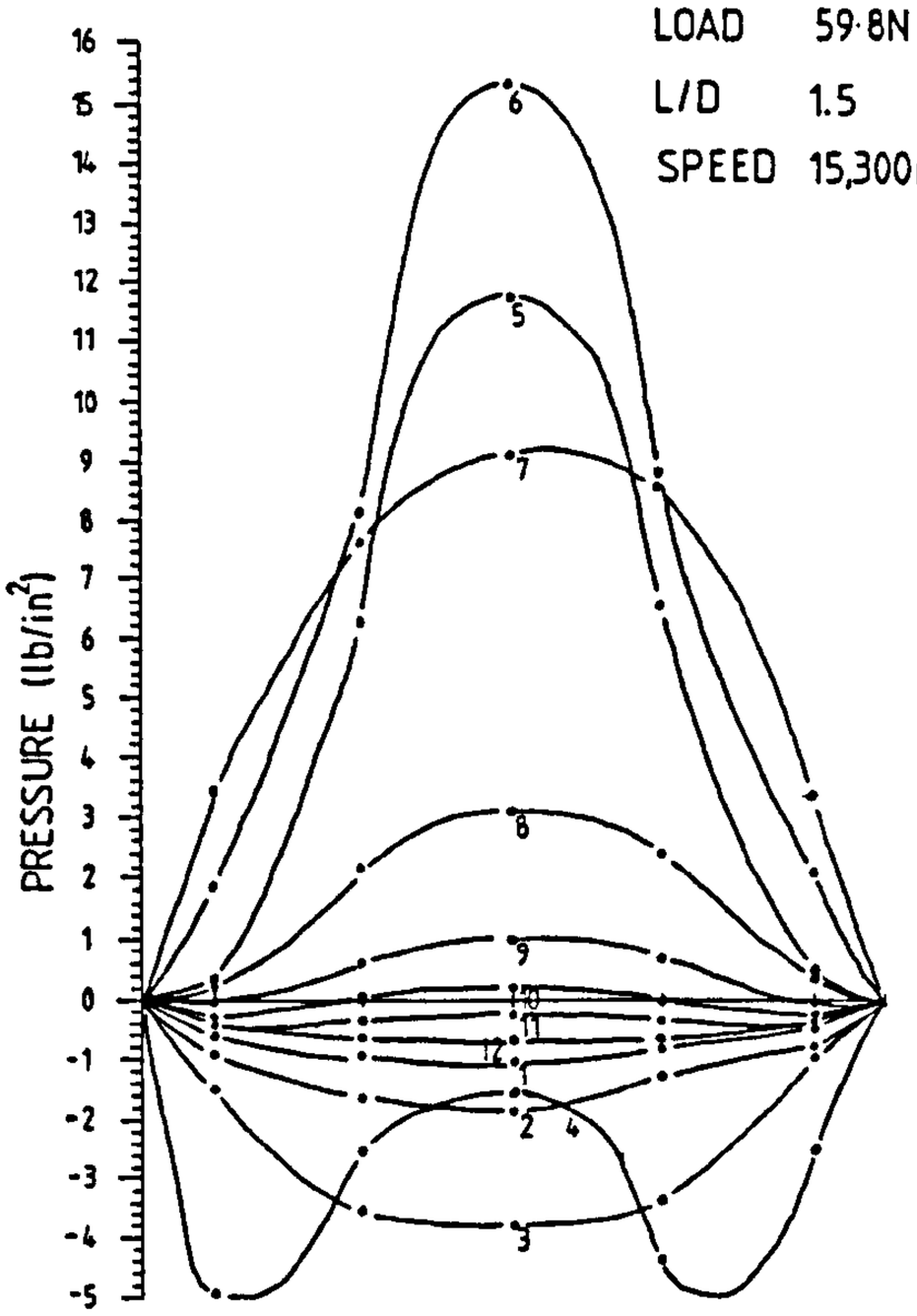

FIG. (5·17) TEST 66

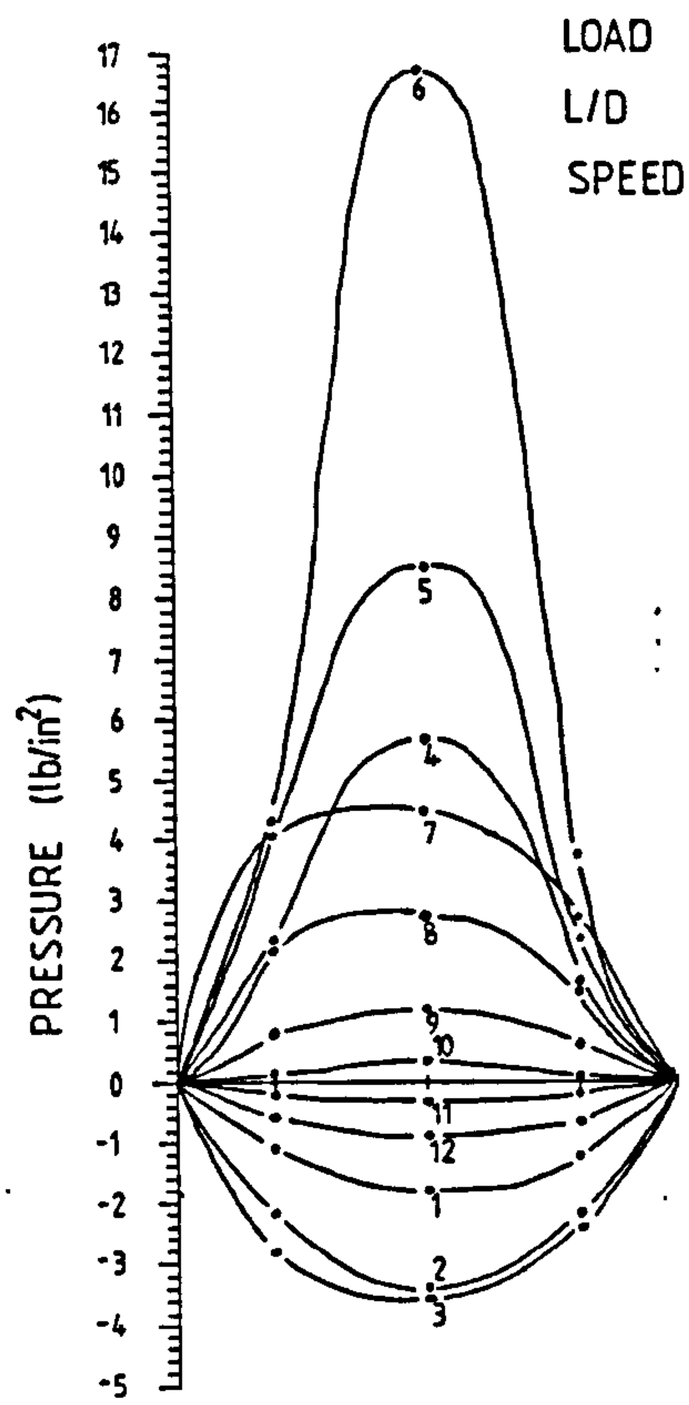

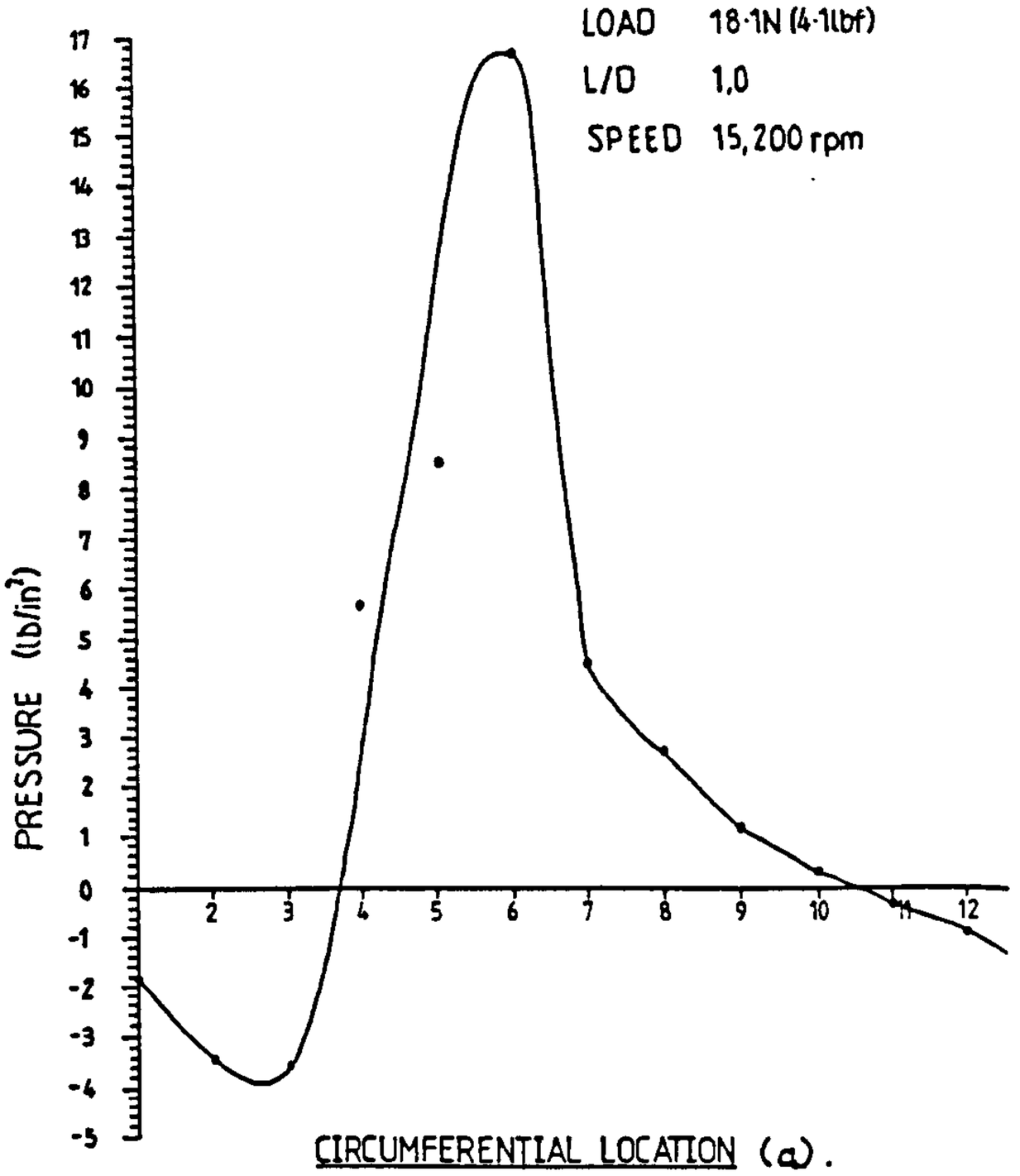

FIG. (5·18) TEST 73

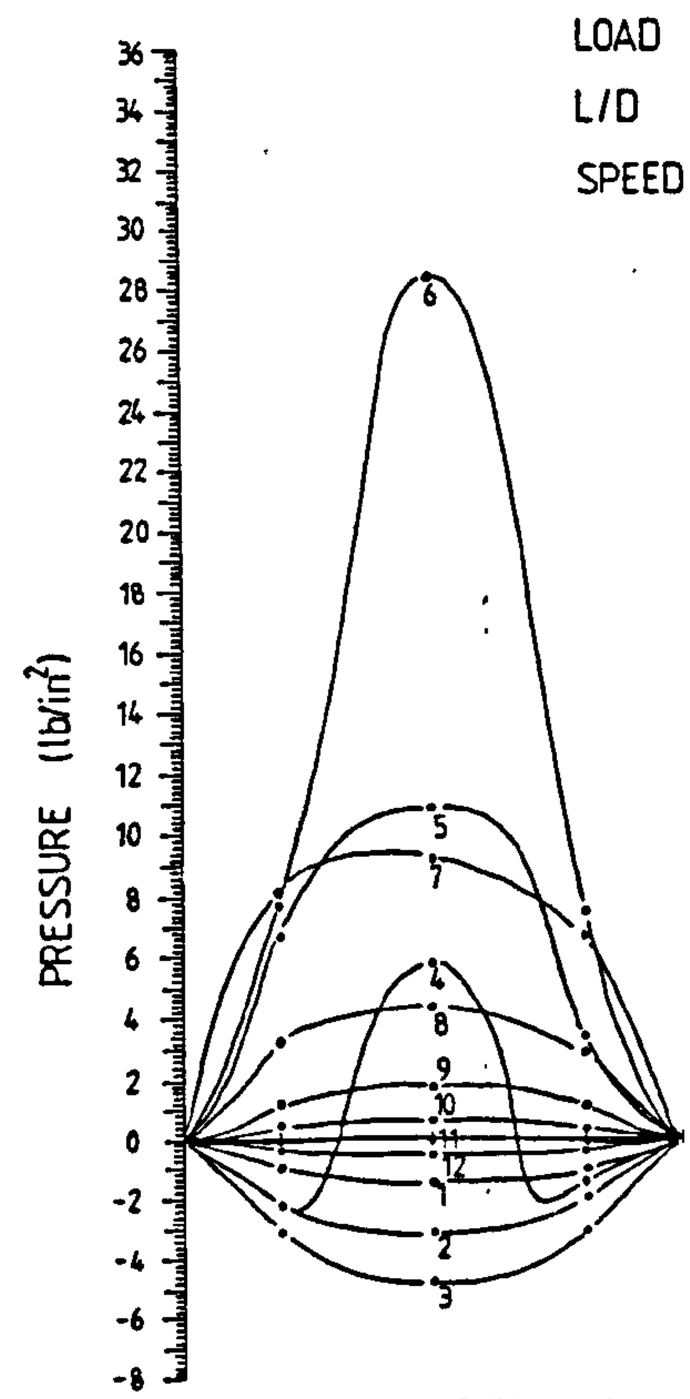

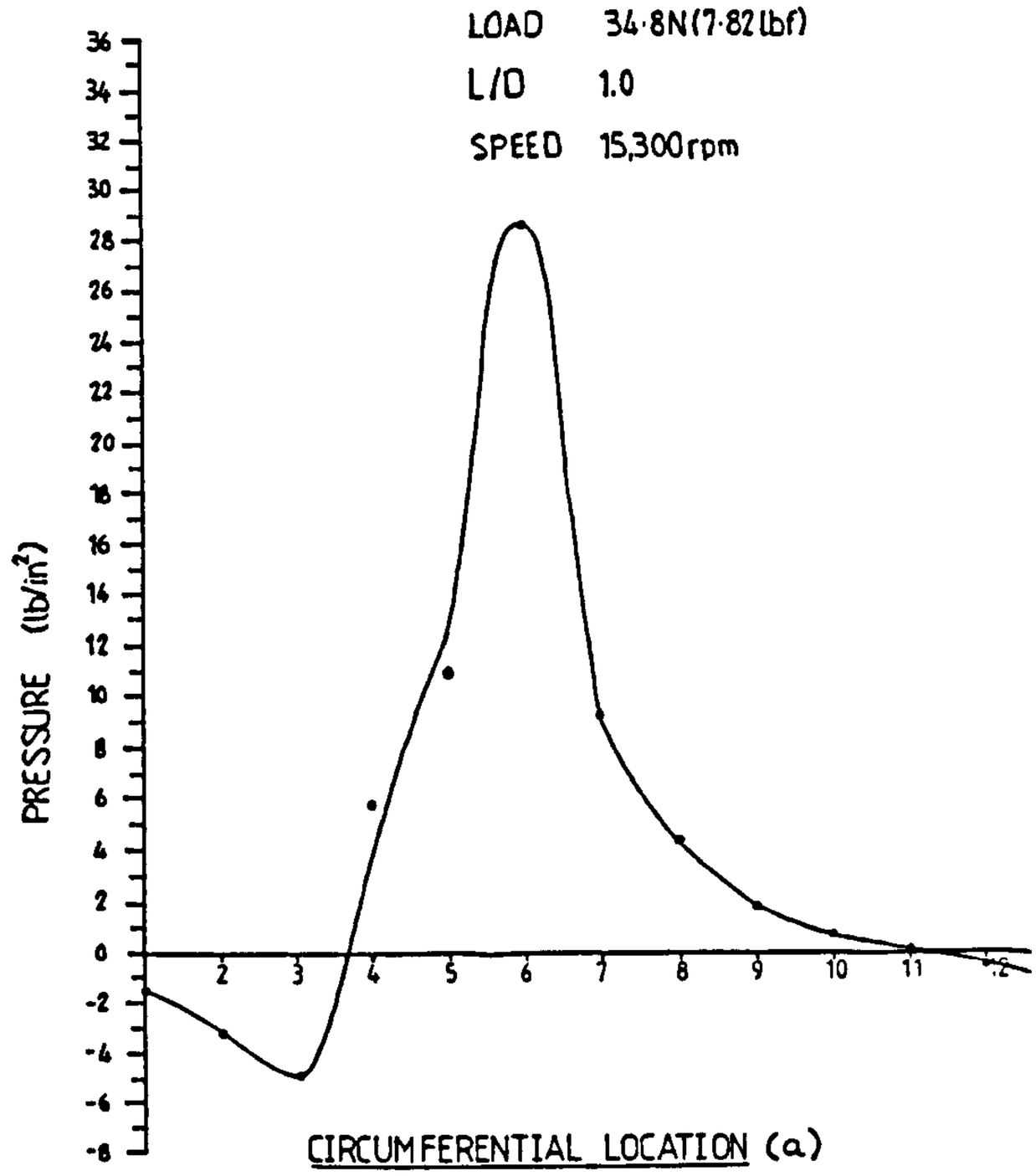

FIG. (5·19) TEST 80

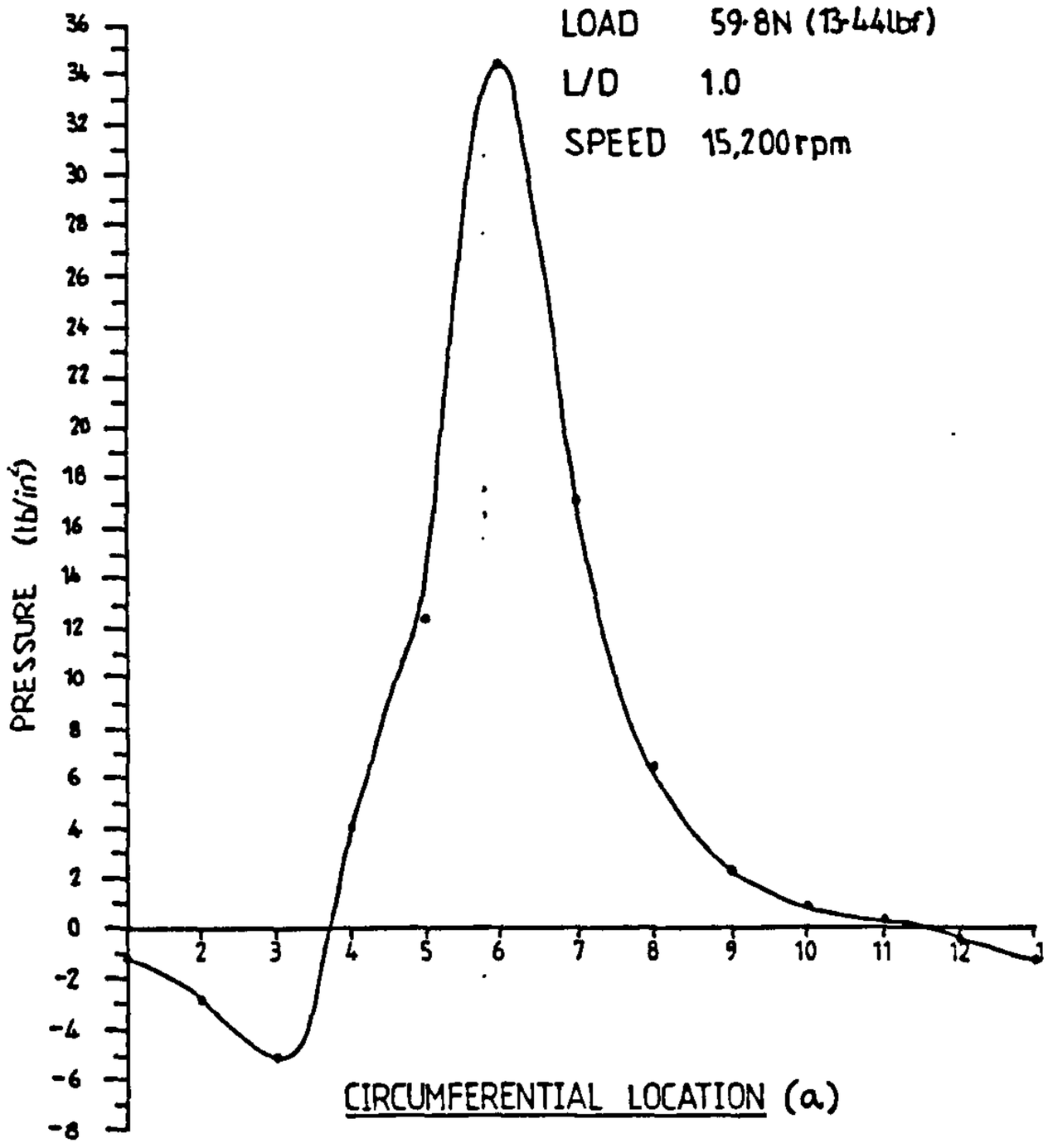

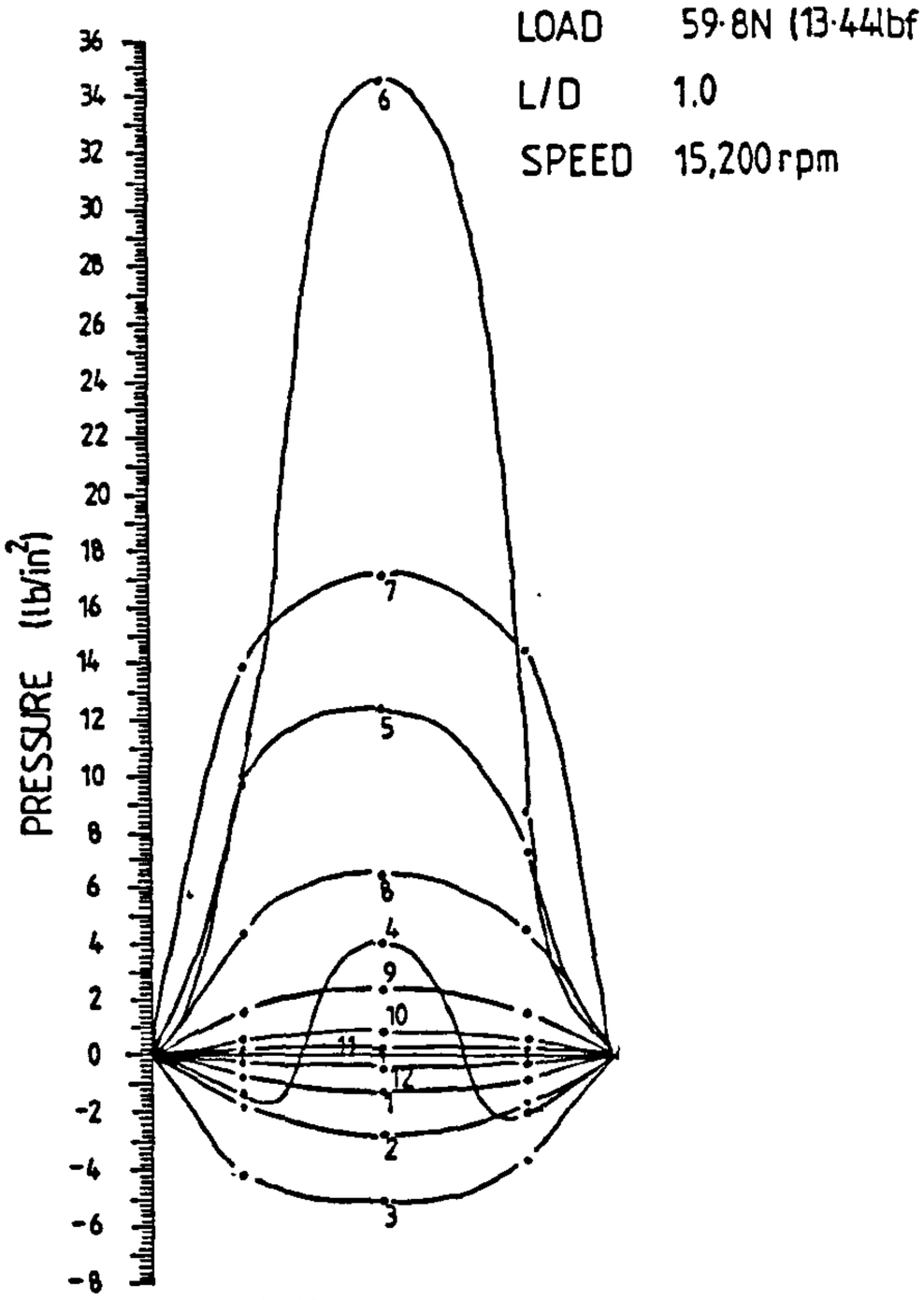

FIG.(5.20) TEST 91

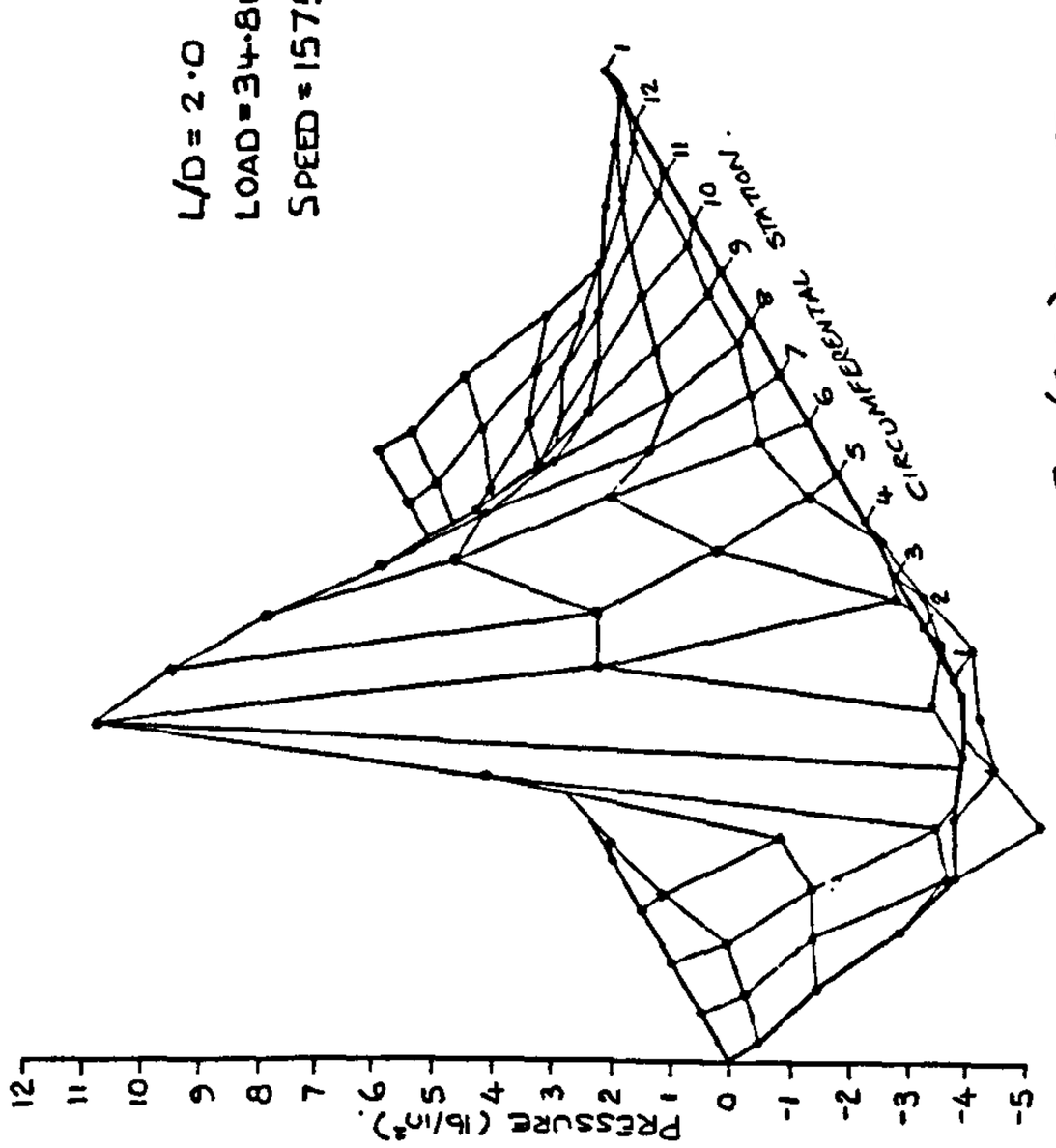

FIG. (5,21) TEST 37

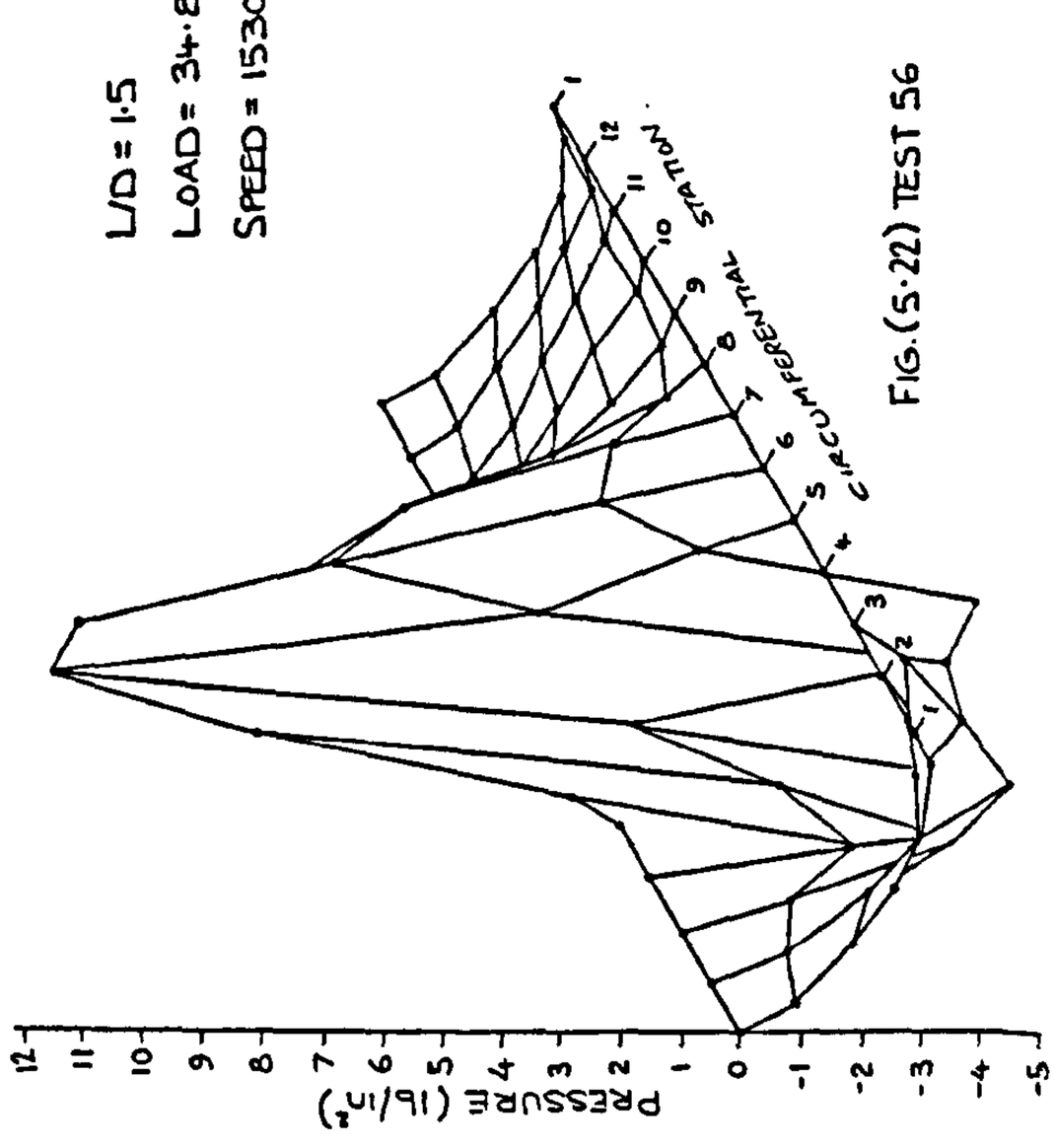

FIG.(5·22) TEST 56

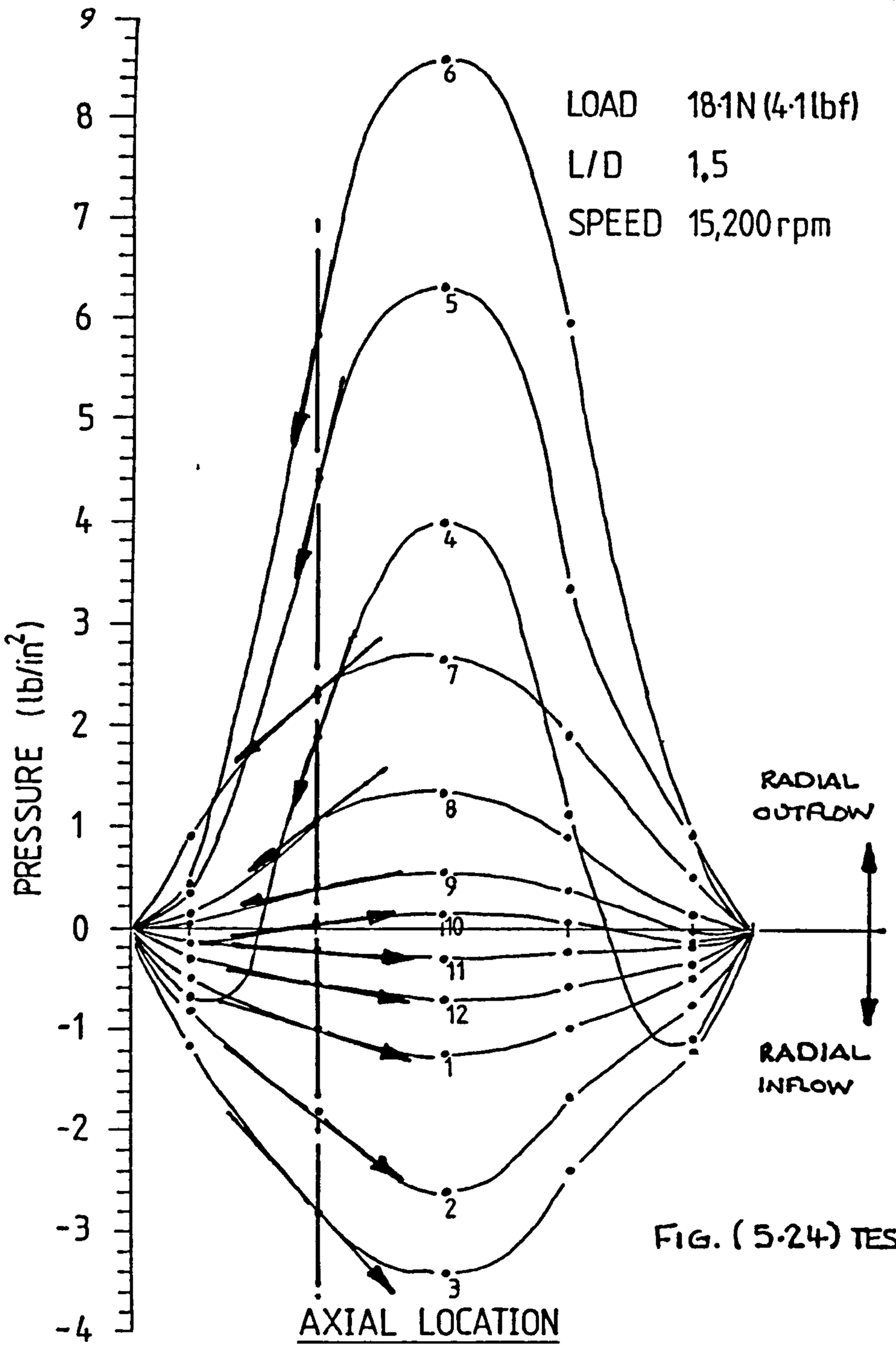

FIG. (5·24) TEST 51

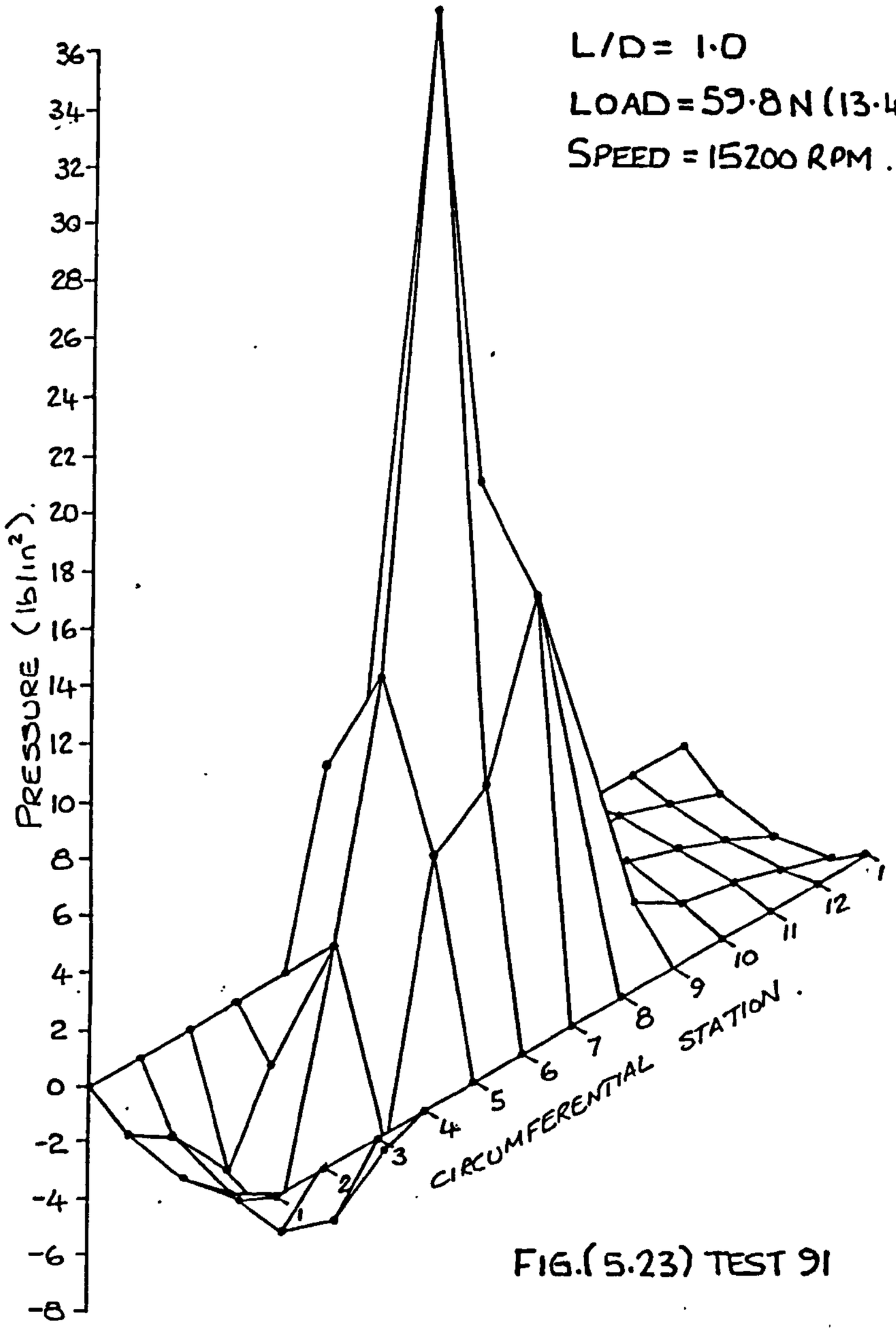

FIG.(5.23) TEST 91

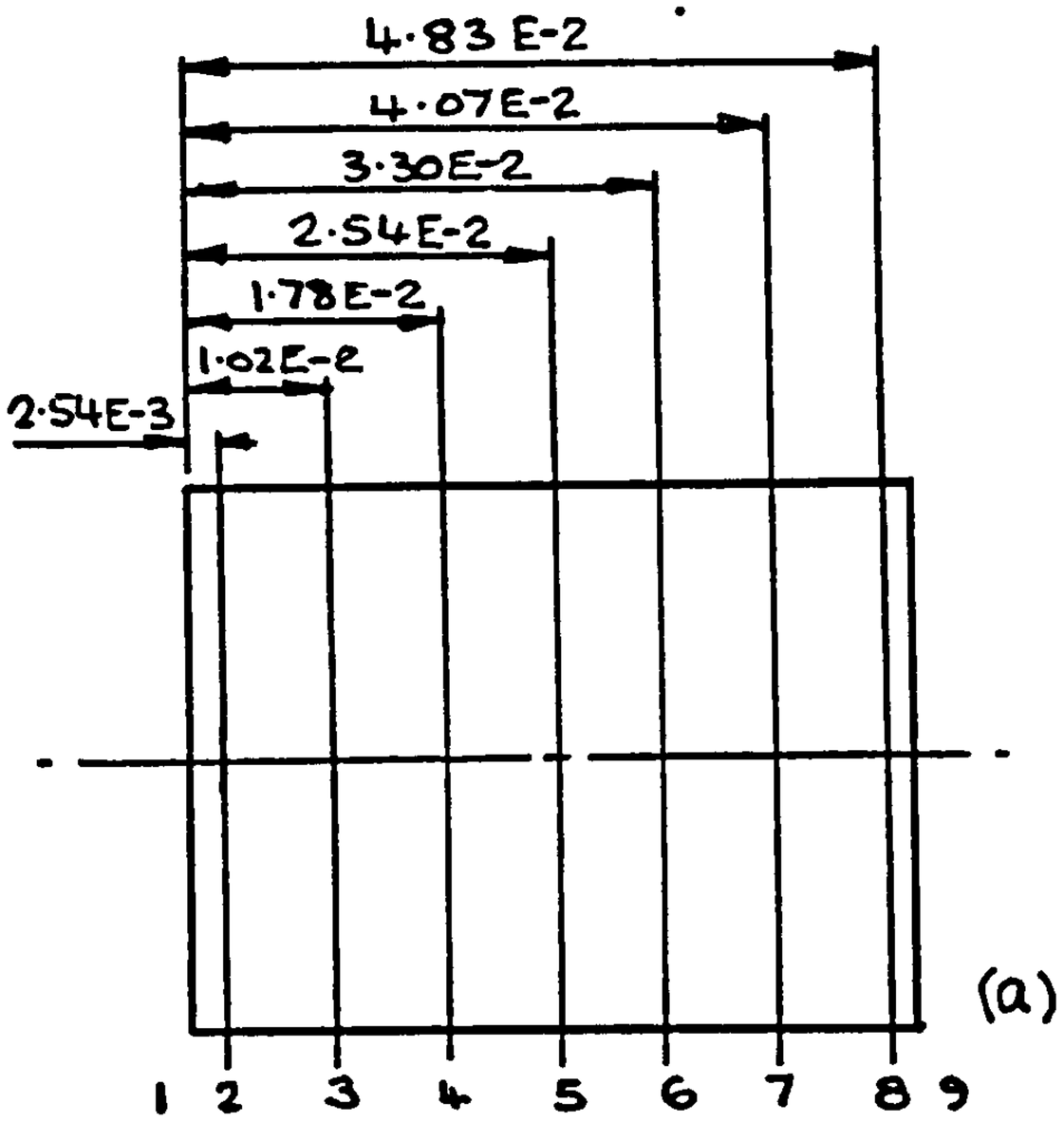

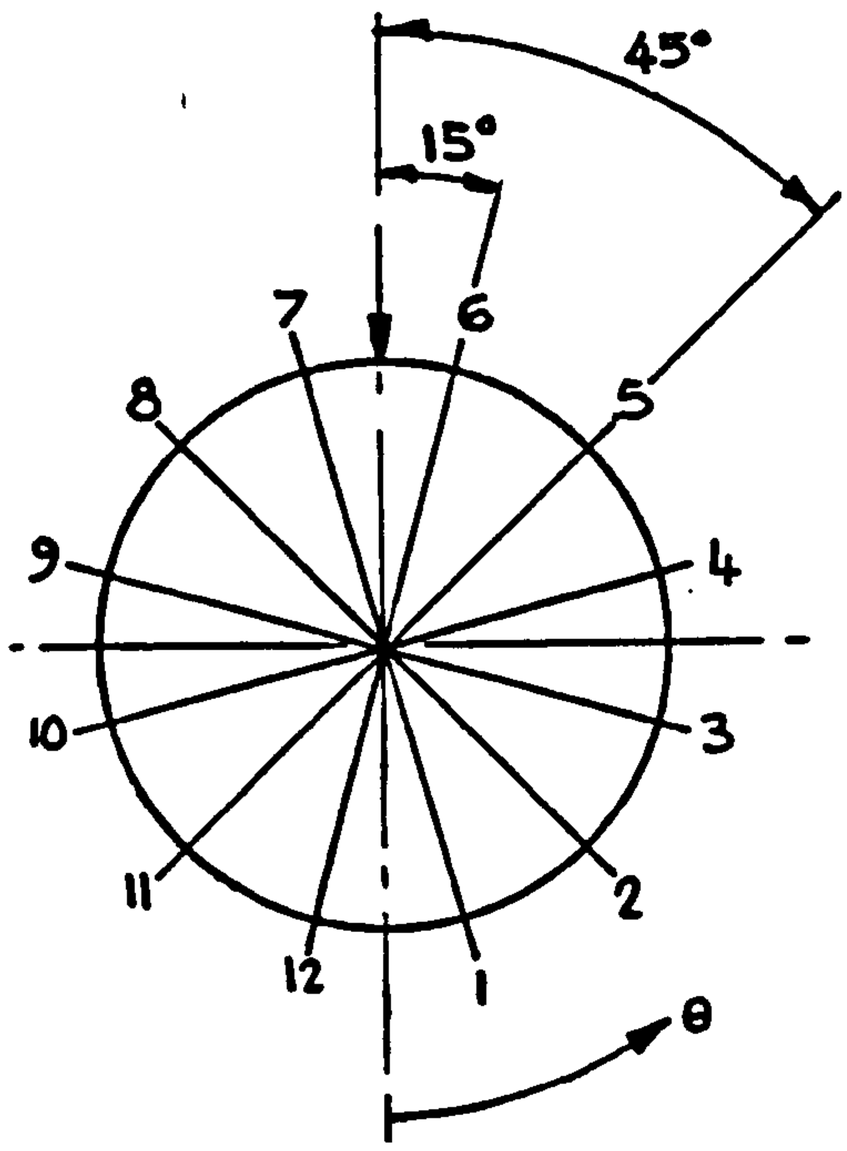

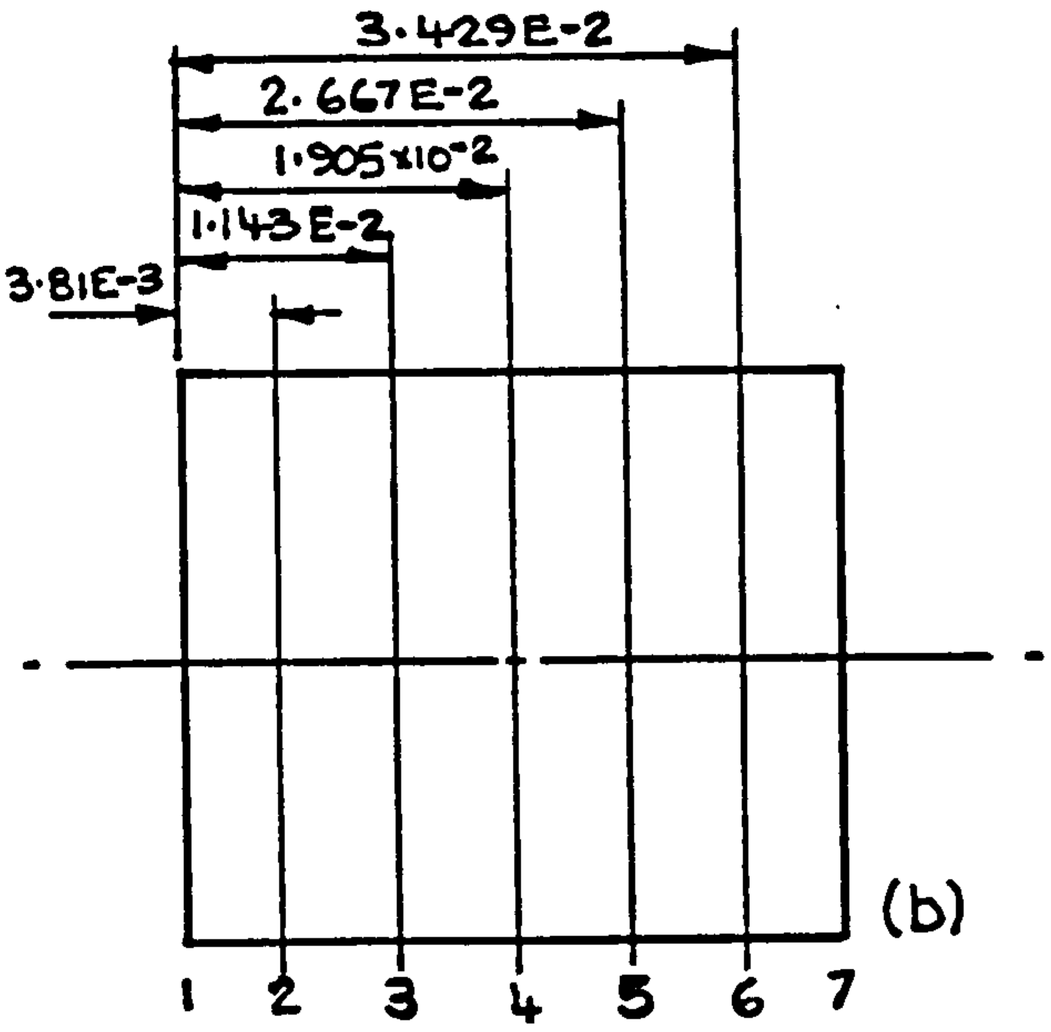

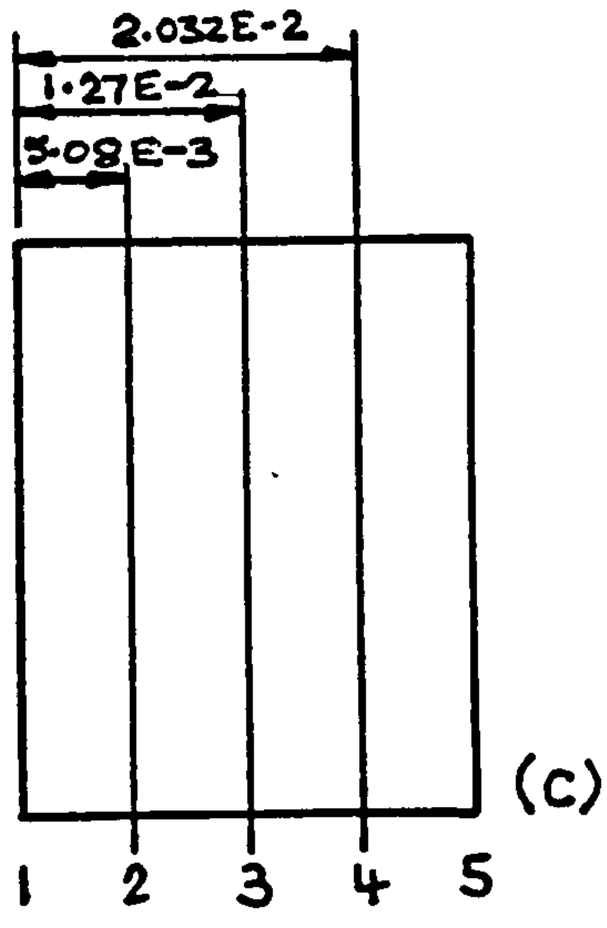

FIG. (5.25) PRESSURE TAPPING CONFIGURATION

(a) L/D = 2·0, (b) L/D = 1·5, (c) L/D = 1·0.
(DIMENSIONED IN m)

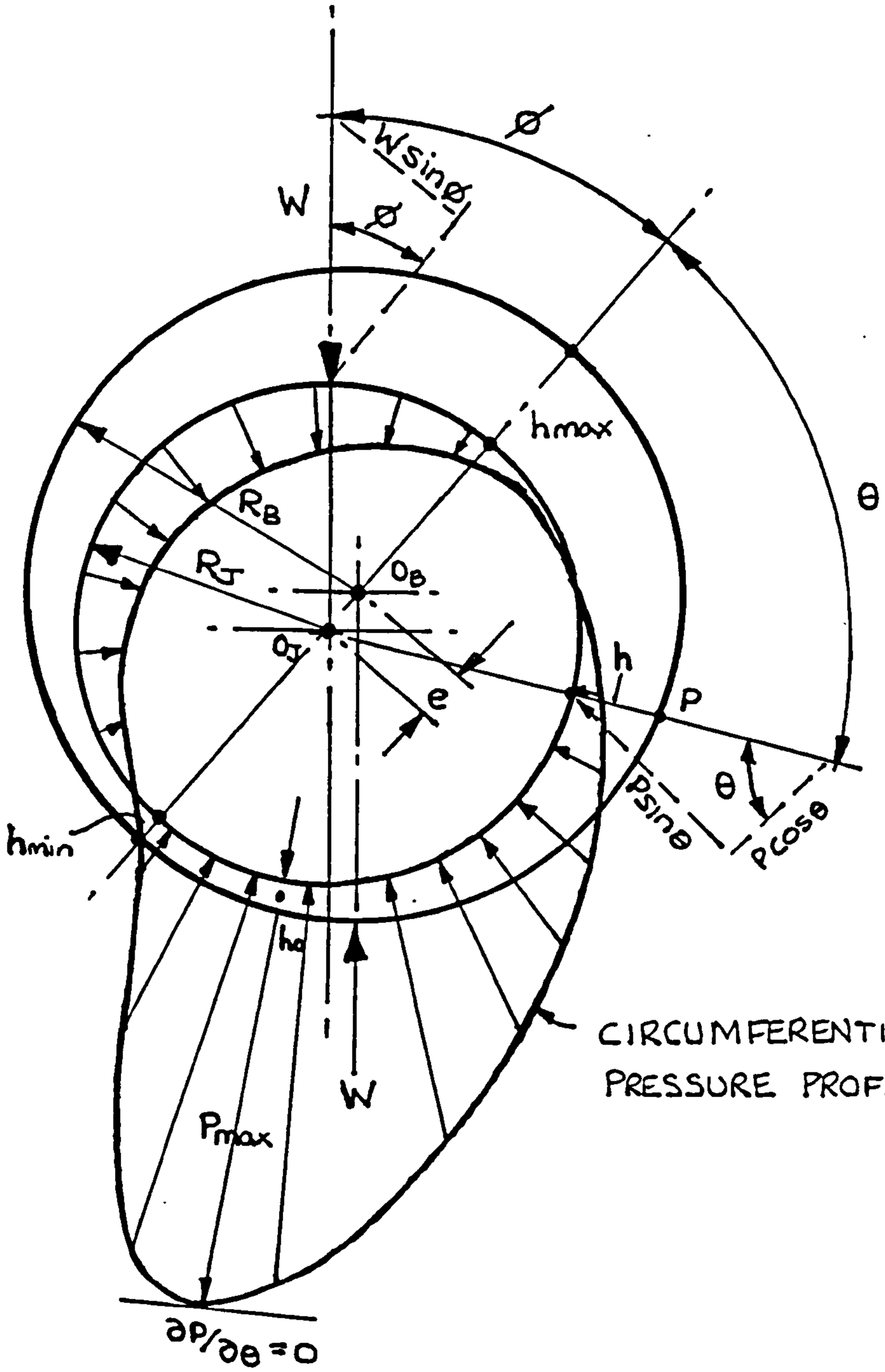

$R_B - R_J = C$

$\varepsilon = e/C$

FIG. (5.26) BEARING NOMENCLATURE

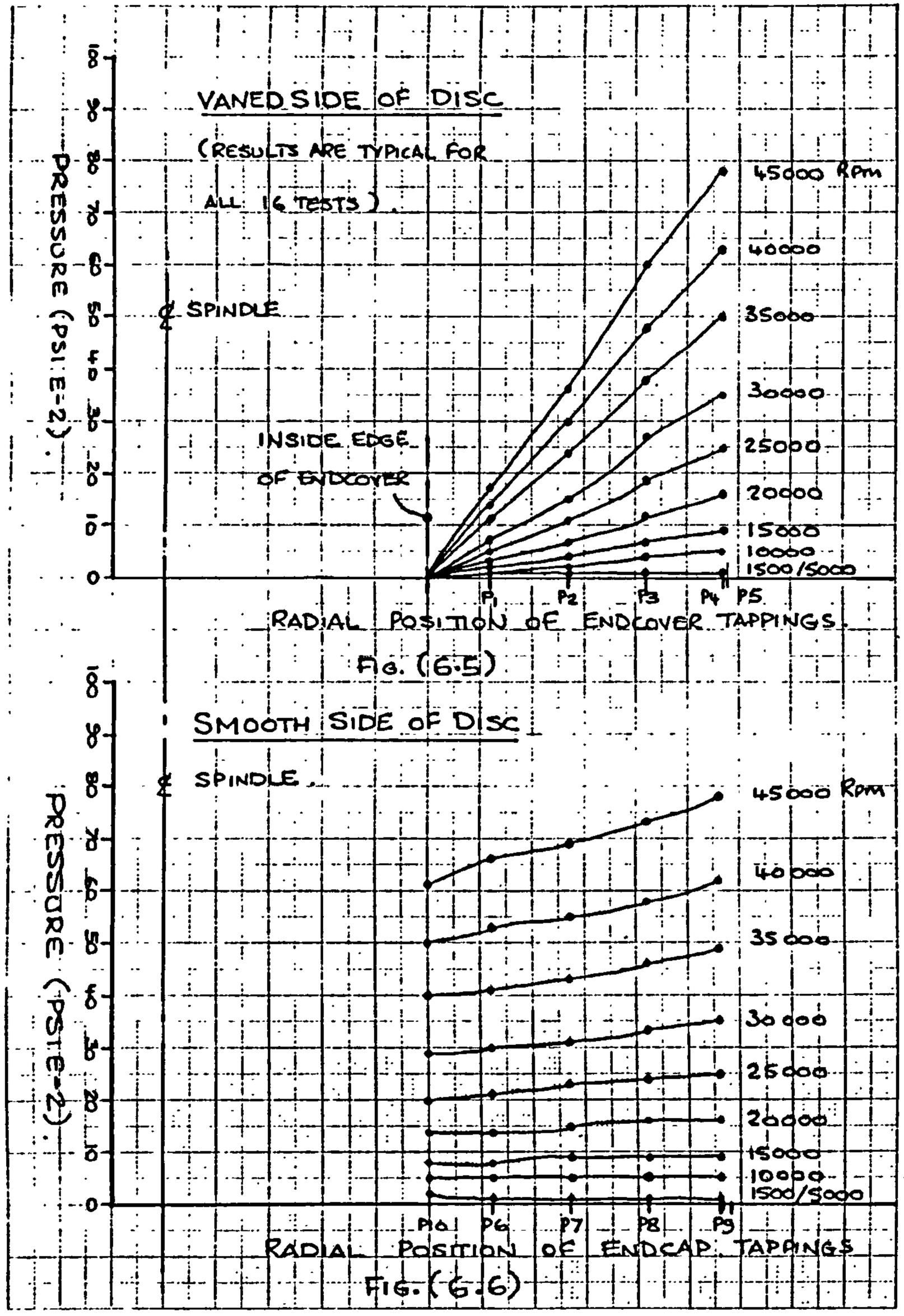

Fig. (6.5)

FIG. (6.6)

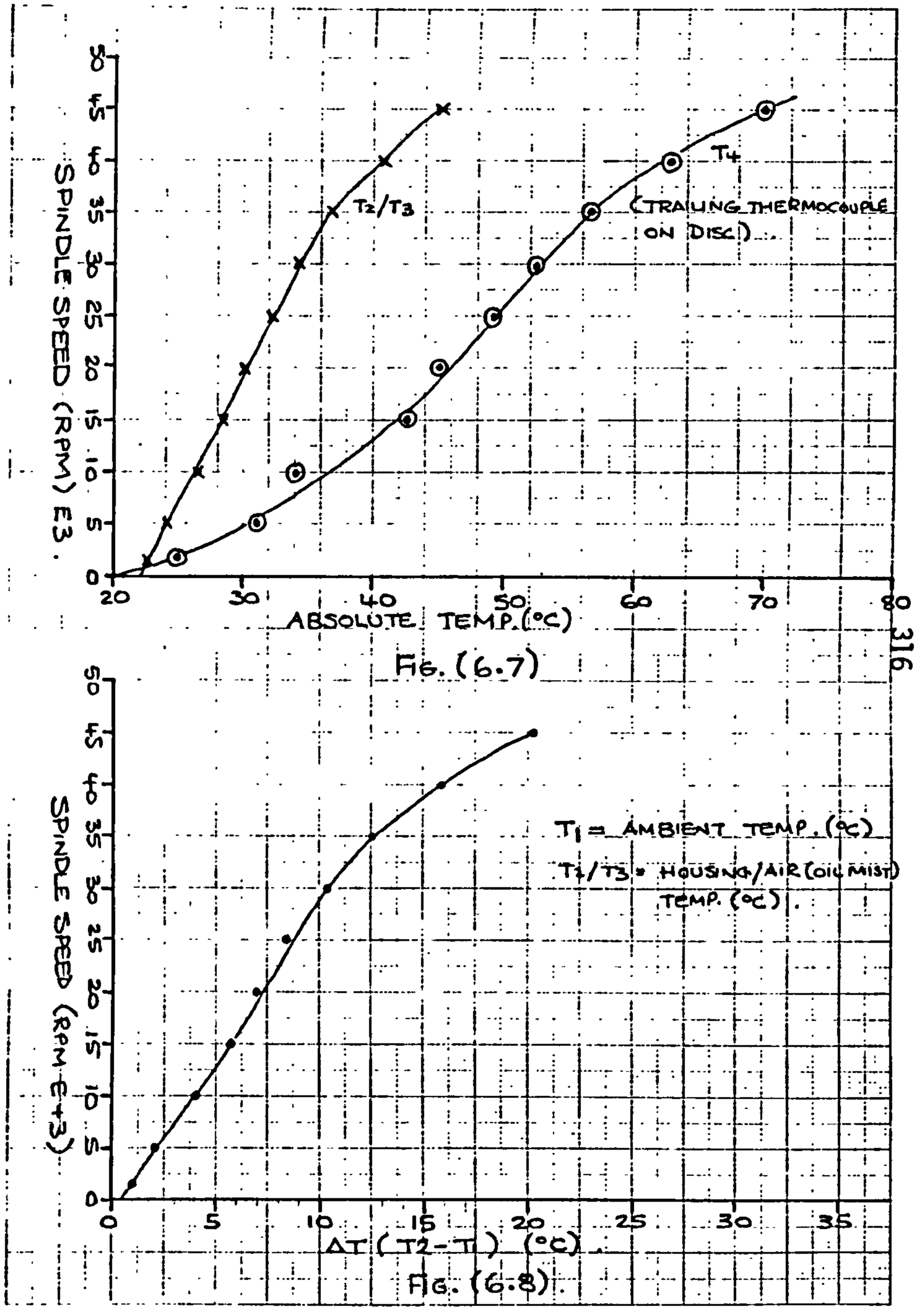

Fig. (6.7)

Fig. (6.8).

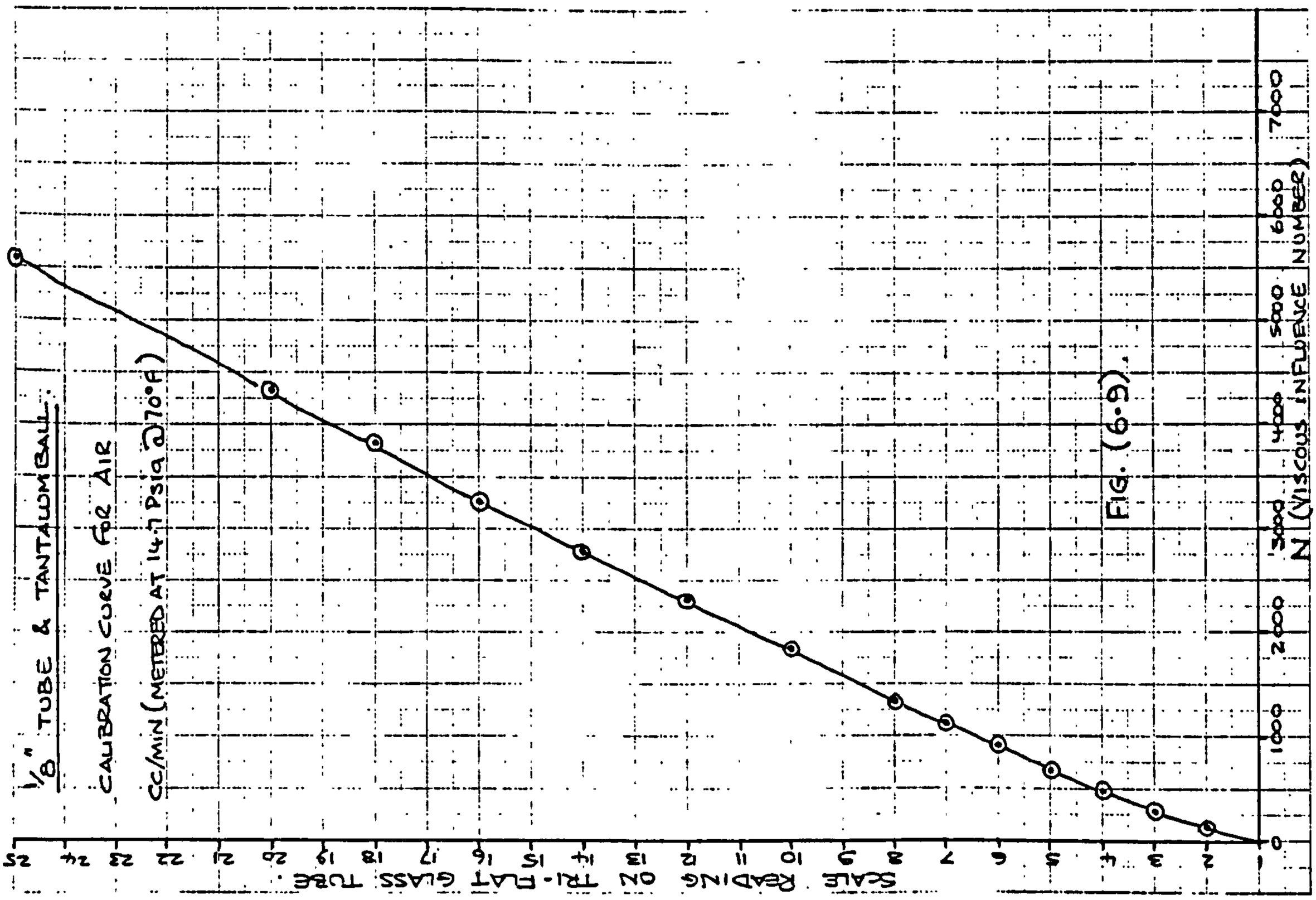

FIG. (6.9).

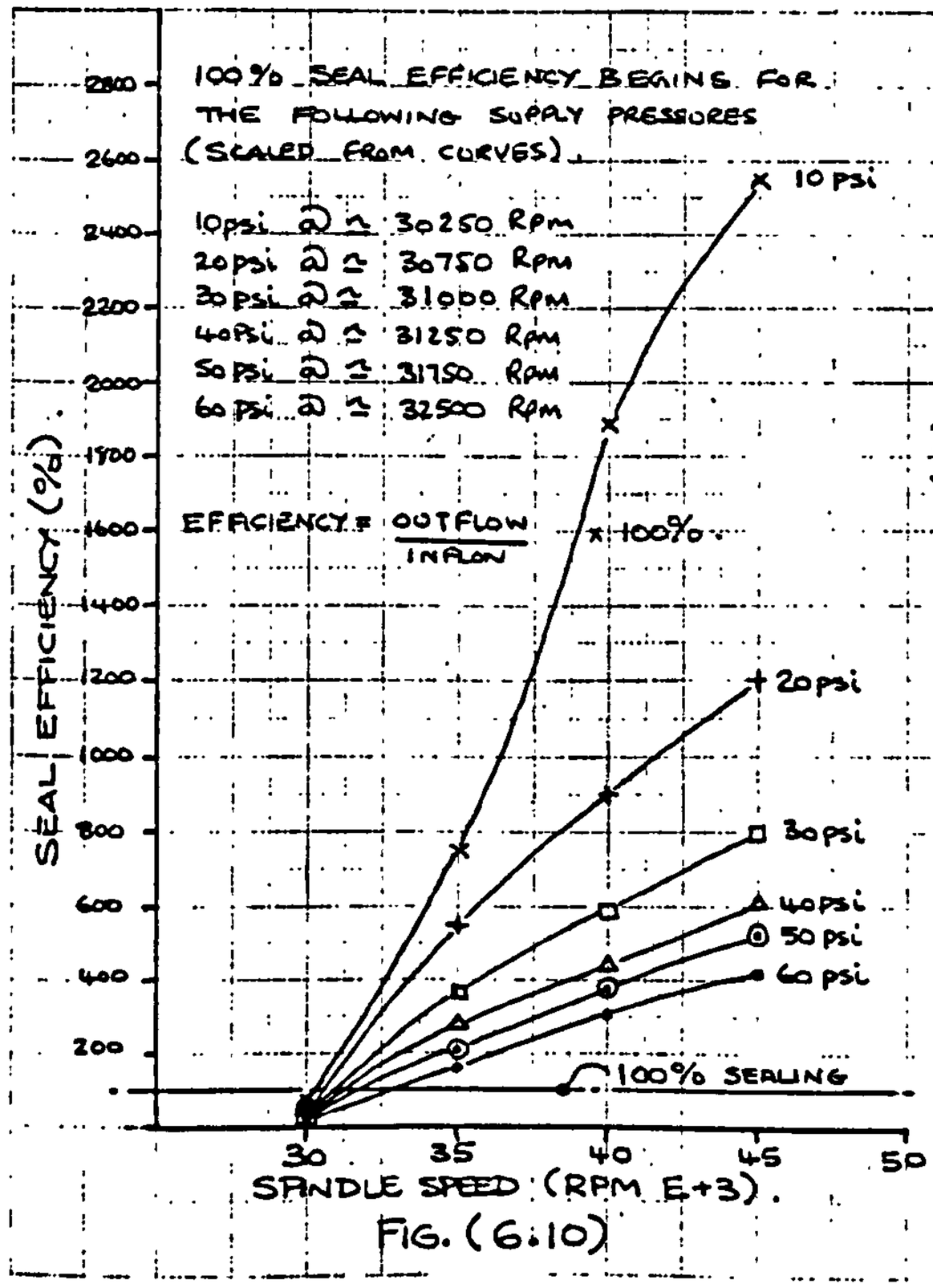

FIG. (6.10)

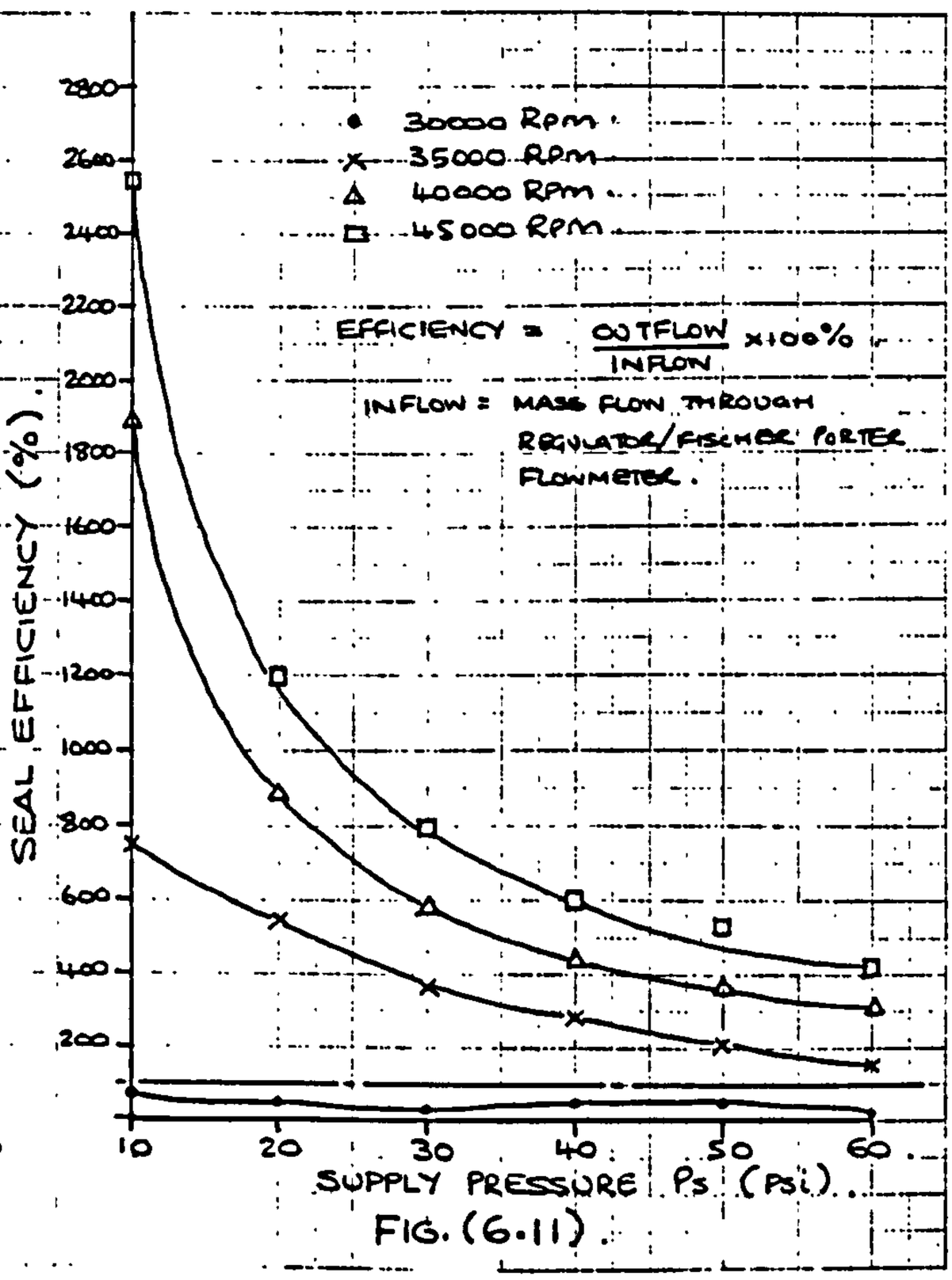

FIG. (6.11).

PB18058

ISSUE — ALTERATION

A — —

B — SPINDLE NOD. SEE DETAIL DWGS. 6/5/87 SRNM.

L

ISSUE — NEW

221 SCREWLOCK.

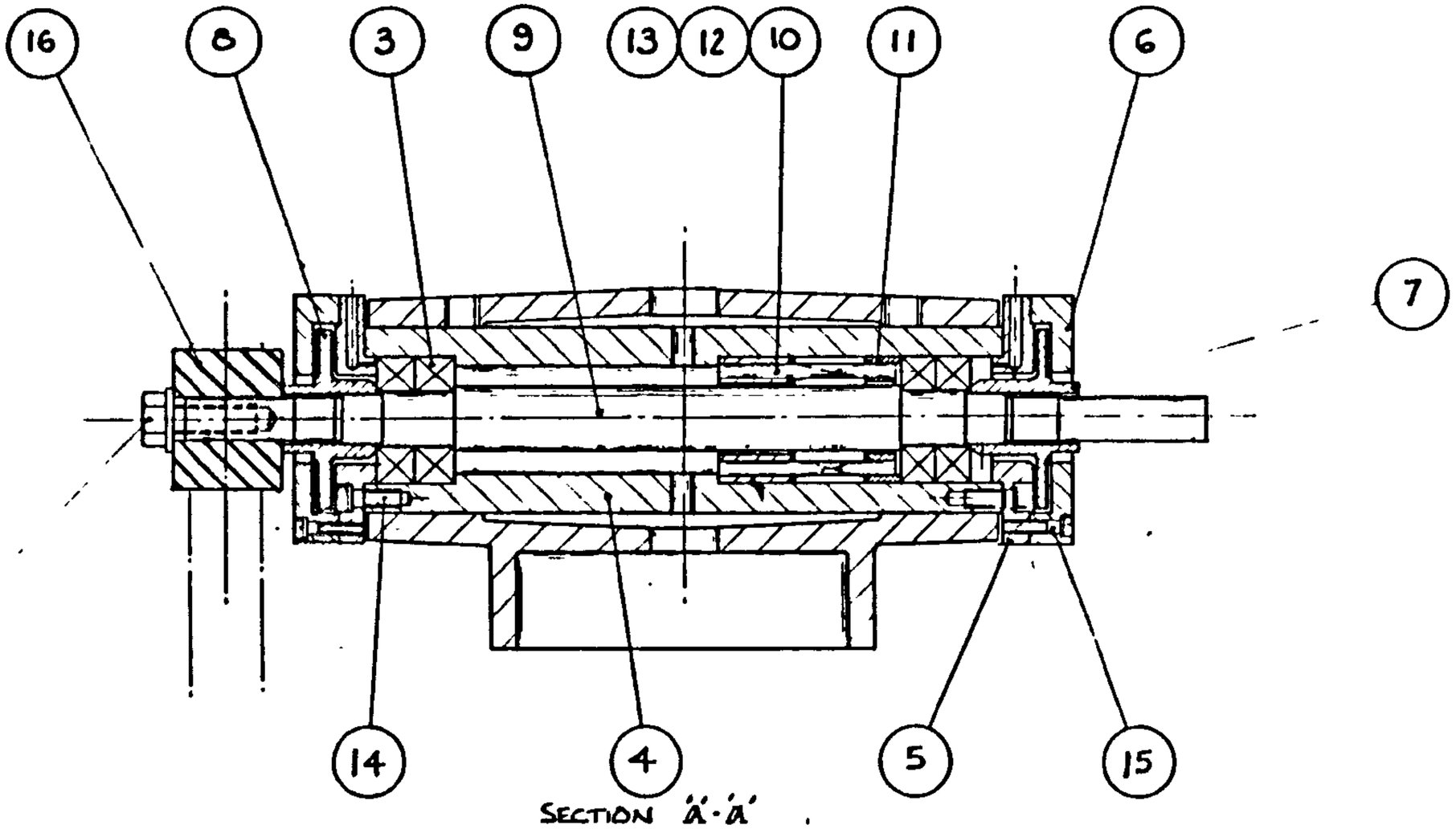

LOCTITE BOLT WITH 241 NUTLOCK

SECTION 'A'-'A'

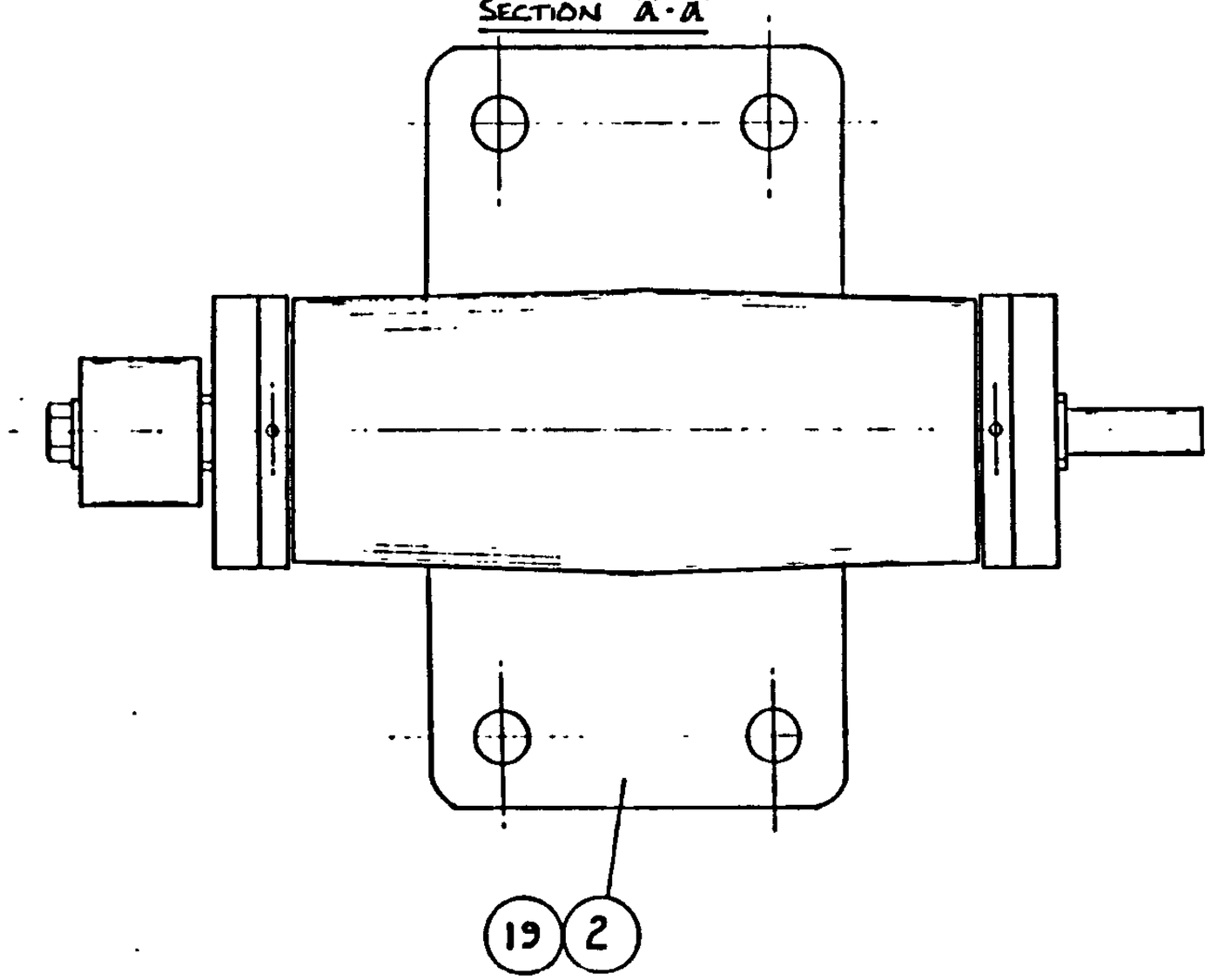

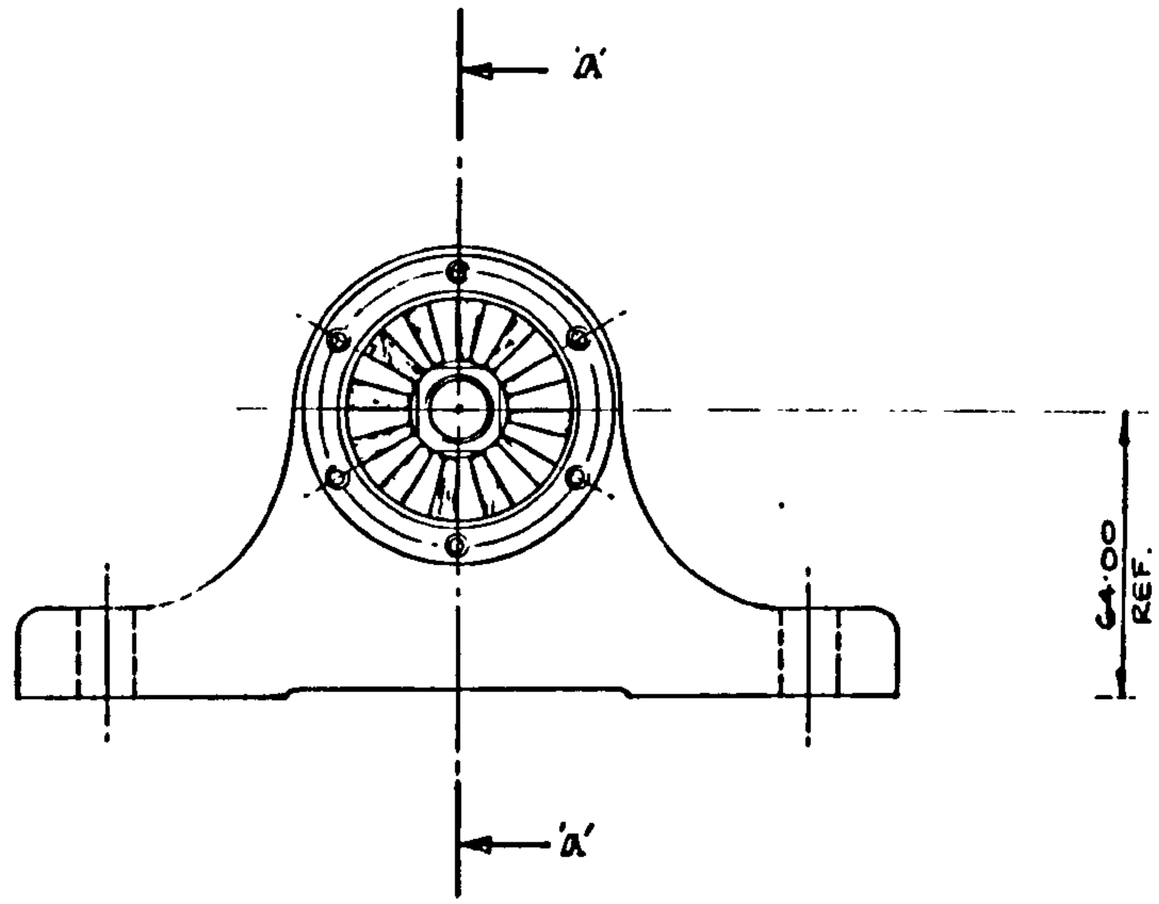

END VIEW WITH ITEM 6 REMOVED.

S_N = 0·5mm.
S_S = 1·25 – 2·5
S_T = 1·25 – 10·0.
V_{max} = 13·
θ = 1·5 – 20.

ITEM	PART No	DESCRIPTION	No. OFF	MAT'L	SPEC	REMARKS
20						
19		SOCKET SETSCREW	2.			3/8" BSF x 3/8" LONG
18		HEX. SETSCREW	1			M8 x 25 LONG.
17		PLAIN WASHER	1			A I DIA.
16	PD18063	PULLEY 36T	1			SURFACE COATED ALUMINIUM.
15		—"—	12			4BA x 5/8" LONG
14		SOC CAP HEAD SCREW	12			10A x 3/4" LONG
13		SPRING GUIDE	2	M.S		5/8" DIA x 1 3/4" LONG
12		SPRING	2	STEEL		LEWIS L.S 800/19.
11	PD9829	THRUST RING	1			
10	PD9828	STATIONARY RING	1			
9	PC 9804A	SPINDLE	1			
8	PD18062	DISC SEAL - L.H	1			
7	PD18061	DISC SEAL - R.H	1			
6	PC18060	END PLATE SUB. ASSY.	2			
5	PC18059	END COVER	2			
4	PC9823	SLEEVE	1			
3		BEARINGS	4			ARMIN 2MM-302 WIDE DBL. FAFNIR DRNI
2	PC9800B	HOUSING MACHINING	1			
1	PC9445	HIGH SPEED HOUSING	1			

EXISTING. EXISTING. EXISTING EXISTING. EXISTING. EXISTING. EXISTING. EXISTING.

THIRD ANGLE PROJECTION

SHEET SIZE A1

GENERAL TOLERANCE ON DIMENSIONS
MACHINED
UNMACHINED
OTHER DIMENSIONS AS STATED
WELD WHERE SHOWN THUS
MACHINE WHERE SHOWN THUS

JOB No. 407 — No OF SETS REQ'D 1 — USED ON DRG. PA18051

SCALE 1:1 — FINISH ~

DRAWN SRNM Turner 20/1/87. — CHK'D — APP'D — STRESS APPVD.

ISSUED BY SME.

CRANFIELD INSTITUTE OF TECHNOLOGY CRANFIELD.

TITLE:- HIGH SPEED HOUSING ASSY.

DRAWING No. PB18058

SHT 1 OF 1 SHEETS

FIG. (6.14).

318

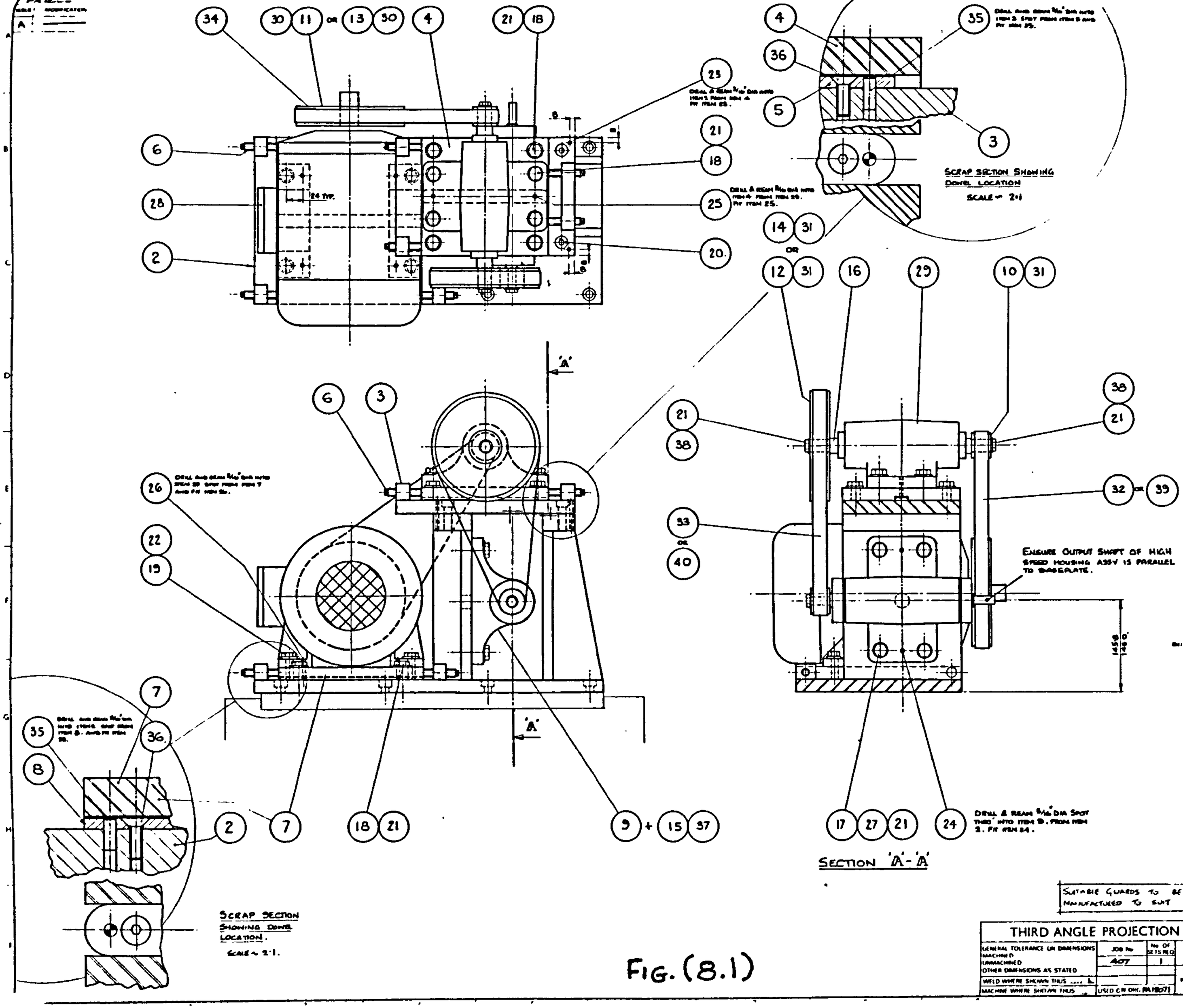

ITEM	PART No	DESCRIPTION	No OFF	MAT	SPEC	REMARKS
40		MOTOR DRIVE BELT	1			STEPPING 300 LONG
39		MOTOR DRIVE BELT	1			STEPPING 300 LONG
38		HEX SETSCREW	2			M12 x 20 LONG
37		SOC CAP HEAD SCREW	4			M5 x 20 LONG
36		SOCKET CSK SCREW	6			M5 x 16 LONG
35		DOWEL PIN	4			5/16" DIA x 3/4" LONG
34		HOUSH SETSCREW	2			M6 x 10 LONG
33		MOTOR DRIVE BELT	1			STEPPING 347 LONG
32		MOTOR DRIVE BELT	1			STEPPING 823 LONG
31		WOODRUFF KEYS	4			No 306
30		KEY	1			8-7 M10 KEY STEEL
29		PULLEY BLOCK	1			FAPHIC DEN 1"
28		HOUSE (GAS BEARING)	1			VACUUM PUMP & PULLEY BLOCK
27		HEX NUT	4			M12
26		DOWEL PIN	2			5/16" DIA x 1" LONG
25		DOWEL PIN	2			5/16" DIA x 1 1/4" LONG
24		DOWEL PIN	2			5/16" DIA x 1 1/2" LONG
23		DOWEL PIN	4			5/16" DIA x 1 3/4" LONG
22		PLAIN WASHER	4			10 I DIA
21		PLAIN WASHER	18			12 I DIA
20		SOC CAP HEAD SCREW	4			M12 x 30 LONG
19		HEX SETSCREW	4			M10 x 25 LONG
18		HEX SETSCREW	12			M12 x 40 LONG
17		HEX SETSCREW	4			M12 x 50 LONG
16	PC 18070	SLAVE SHAFT	1			
15	PD 18069	PULLEY SEPARATOR	1			
14	PC 18068	340 DRIVE PULLEY	1			
13	PC 18067	360 DRIVE PULLEY	1			
12	PC 18066	170 DRIVE PULLEY	1			
11	PC 18065	170 DRIVE PULLEY	1			
10	PD 18064	IDLER PULLEY	1			
9	PA 18063	HOUSING ASSY	1			
8	PD 18062	MOTOR PLATE SLIDE HSG	1			
7	PD 18061	MOTOR MOUNTING PLATE	1			
6	PD 18060	JACKING SCREW	2			
5	PD 18059	BEARING HSG MOUNT PLT	1			
4	PC 18058	BEARING HSG MOUNT PLT	1			
3	PB 18057	JACKING PLT WELD ASSY	1			
2	PB 18056	BRACKET WELD ASSY	1			
1	PA 18055	GAS BEARING DRIVE ASSY	1			

SUITABLE GUARDS TO BE MANUFACTURED TO SUIT

THIRD ANGLE PROJECTION

GENERAL TOLERANCE ON DIMENSIONS MACHINED / UNMACHINED
OTHER DIMENSIONS AS STATED
WELD WHERE SHOWN THUS .....
MACHINE WHERE SHOWN THUS .....

JOB No 407 | No OF SETS REQ 1 | SCALE 1:2 | FINISH MMT

USED ON DRG. PA 18071

DRAWN CMF 3-87 | CHK | APPV | DATE | ISSUED BY SME

TITLE: GAS BEARING DRIVE ASSEMBLY.

CRANFIELD INSTITUTE OF TECHNOLOGY CRANFIELD

DRAWING No PA 18051 SHT 1 OF 1

FIG. (8.1)

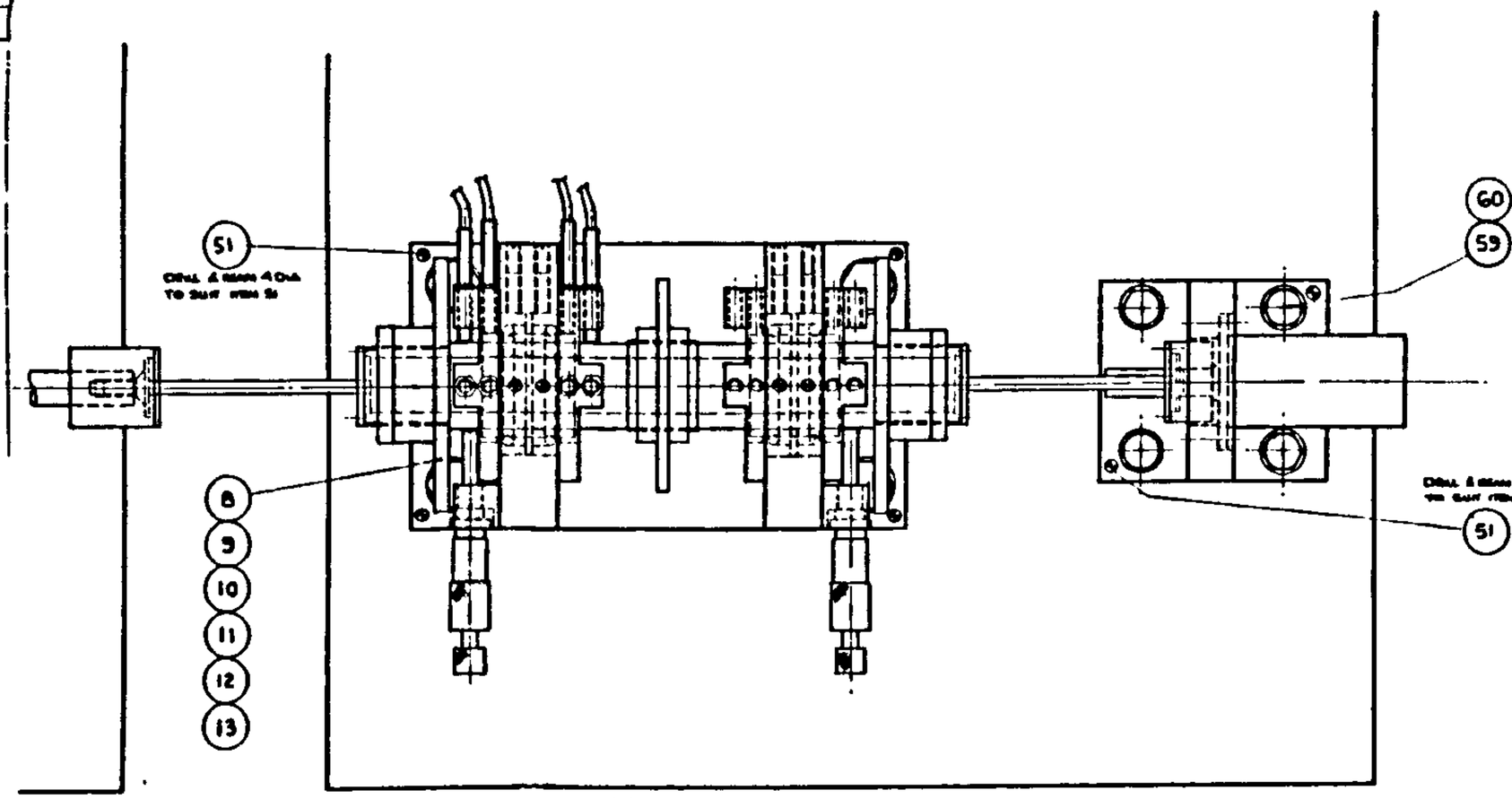

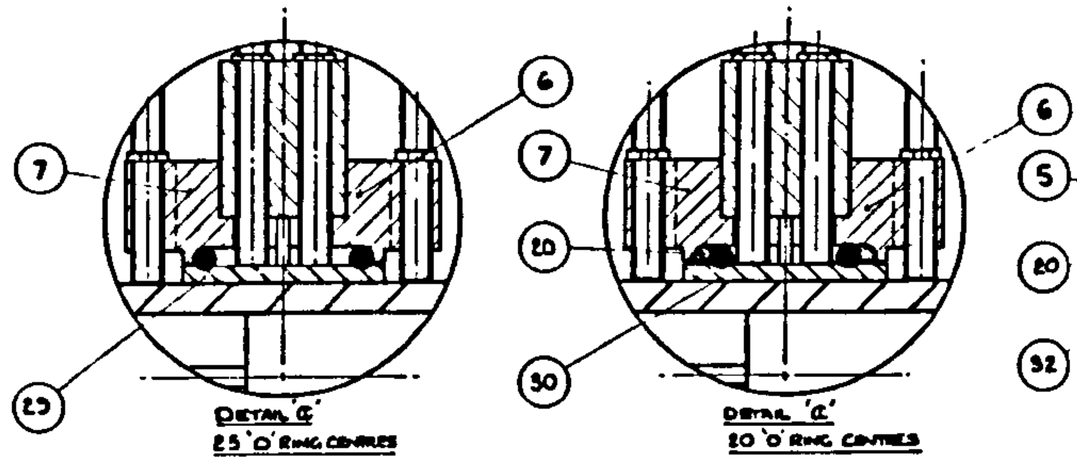

4

320

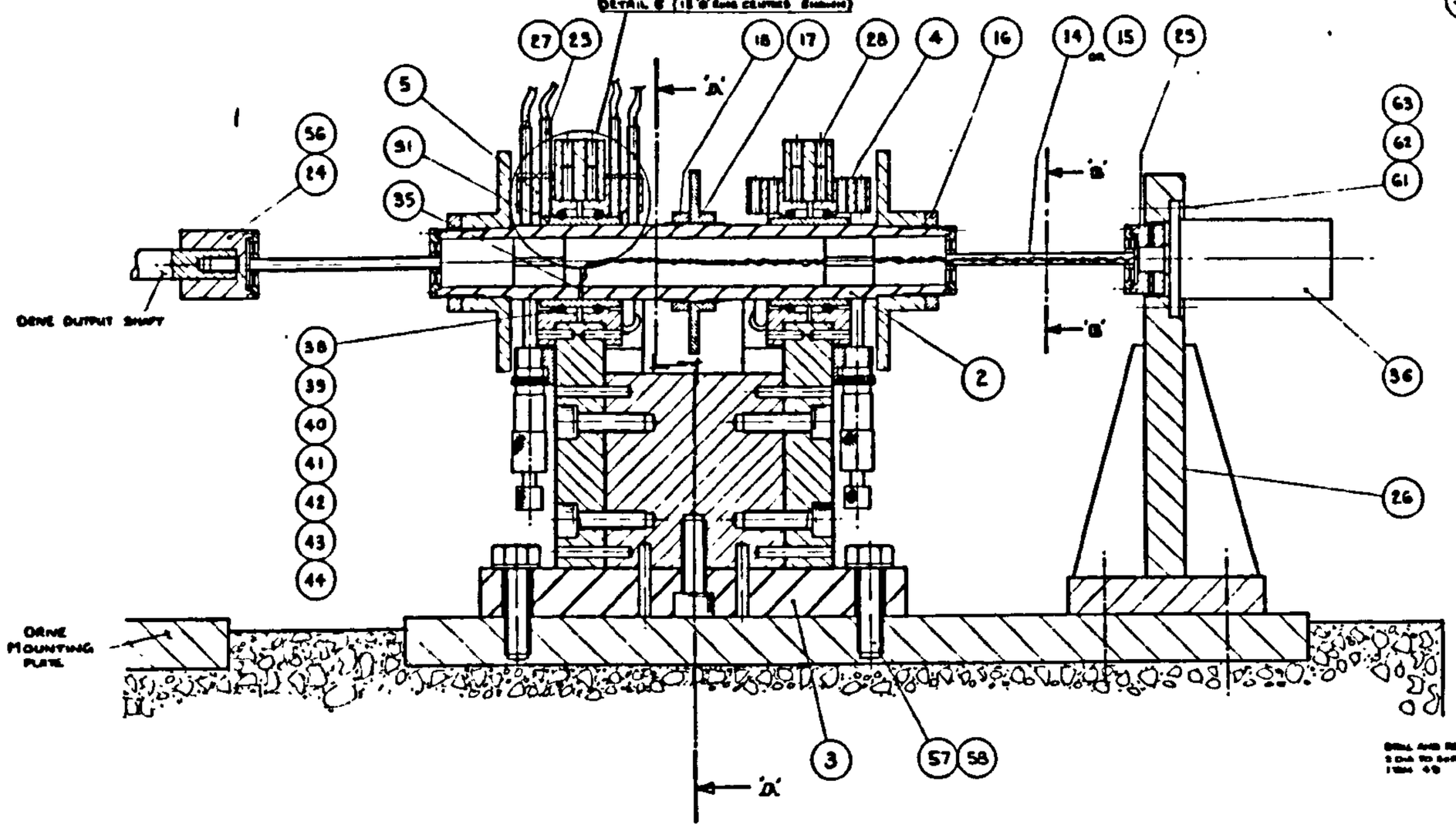

SECTION ON ℄ (SHOWING 15 'O'RING CENTRES)

NOTE!! ROTOR ASSY IS TO BE BALANCED

SUITABLE GUARDS ARE TO BE MANUFACTURED

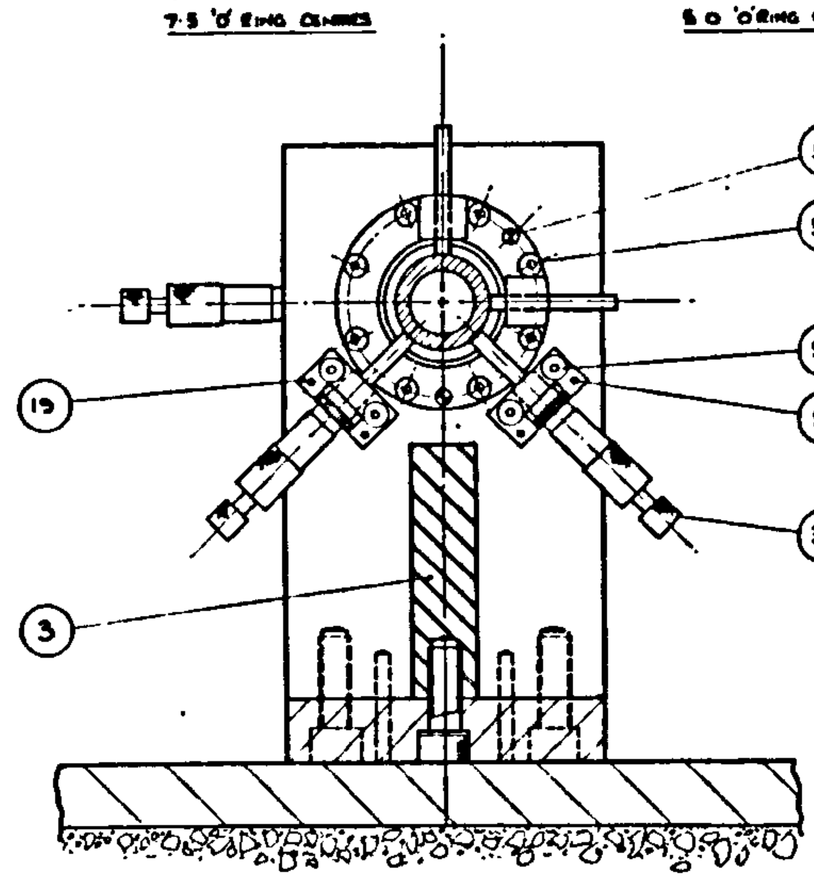

SECTION 'A'-'A'

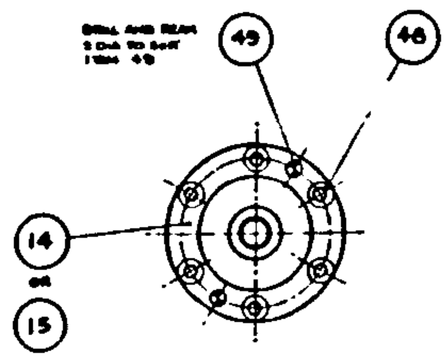

SECTION 'B'-'B'

ITEM	PART No	DESCRIPTION	No OFF	MAT'	SPEC	REMARKS
65						
64						
63		PLAIN WASHER	3			3 DIA
62		DOWEL PIN	1			3DIA x HOLDING
61		SOC. CAP HEAD SCREW	5			M3 x 12 LONG
60		PLAIN WASHER	4			8 DIA.
59		HEX. SETSCREW	4			M8 x 30 LONG.
58		PLAIN WASHER	4			10 DIA.
57		HEX. SETSCREW	4			M10 x 35 LONG.
56		SOC. CSK HEAD SCREW	1			M6 x 15 LONG
55		DOWEL PIN	16			5 DIA x 60 LONG
54		SOC. CSK HEAD SCREW	16			M5 x 25 LONG.
53		DOWEL PIN	5			4 DIA x 15 LONG.
52		SOC CAP HEAD SCREW	22			M4 x 15 LONG
51		DOWEL PIN	4			4 DIA x 25 LONG.
50						
49		PLAIN WASHER	24			6 DIA.
48		SOC CAP HEAD SCREW	24			M6 x 8 LONG.
47						
46						
45						
44		'O' RING	4	FVMQ	MOULD	83.82 MM INSIDE DIA 5.33 MM THK SHORE A 70
43		d RING	4	E P	MOULD	48.36 MM INSIDE DIA 3.53 MM THK SHORE A 70
42		'O' RING	4		MOULD	48.36 MM INSIDE DIA 5.33 MM THK SHORE A 70
41		'O' RING	4	SILICONE	MOULD	86.36 MM INSIDE DIA 5.33 MM THK SHORE A 70
40		'O' RING	4	VITON	MOULD	86.36 MM INSIDE DIA 5.33 MM THK SHORE A 70
39		'O' RING	4	NITRILE	MOULD	86.36 MM INSIDE DIA 5.33 MM THK SHORE A 70
38		'O' RING	4	NITRILE	MOULD	86.36 MM INSIDE DIA 5.33 MM THK SHORE A 70
37		MACHINED HOUSE	1			
36		BALL BEARING SLAD RACE ASSY.	1		BEARING	
35		MACHD PRESSURE TRANSDUCER	1			
34	PC 19473	5 · PLAIN WASHER	2			
33	PC 19471	M5 PLAIN WASHER	2			
32	PC 19470	M8 PLAIN WASHER	2			
31	PC 19469	M6 PLAIN WASHER	2			
30	PC 12442	M4 PLAIN WASHER	2			
29	PC 19468	M5 PLAIN WASHER	2			
28	PD 19466	BEARING SPACER	2			
27	PD 19465	PISTON ROD with VENT	2			
26	PA 19464	SHAFT & PISTON ASSY	1			
25	PD 19463	SHAFT COUPLING	1			
24	PD 19462	DRIVE COUPLING	1			
23	PC 19461	PRESSURE PLATE ASSY	1			
22	PD 19460	END PLATE ASSY	1			
21	PD 19459	7·5 PLATE ASSY	1			
20	PD 19458	20 & 30 PLATE ASSY	1			
19	PC 19394	MACHINED MOUNTING	1			
18	PD 19456	CENTRE DISC WITH VENTS	1			
17	PC 19396	CENTRE DISC	1			
16	PD 19455	DISC WITH VENTS	1			
15	PC 19398	CENTRE SHAFT ASSY (MALE)	1			
14	PC 19396	CENTRE SHAFT ASSY	1			
13	PC 19400	40 DIA DISC				
12	PC 19402	50 DIA DISC	2			
11	PC 19403	60 DIA DISC	2			
10	PC 19401	70 DIA DISC	2			
9	PC 19400	80 DIA DISC	2			
8	PC 19398	90 DIA DISC	2			
7	PC 19397	L.H. BEARING FLANGE	1			
6	PC 19396	R.H. BEARING FLANGE	1			
5	PC 19395	L.H. BEARING FLANGE	1			
4	PC 19394	R.H. BEARING FLANGE	1			
3	PA 19392	BEARING HOUSING ASSY	1			
2	PC 19391	ROTOR SHAFT	1			
1	PA 18475	AIR BEARING ROTOR ASSY	1			

THIRD ANGLE PROJECTION

GENERAL TOLERANCE ON DIMENSIONS
MACHINED
UNMACHINED
OTHER DIMENSIONS AS STATED
WELD WHERE SHOWN THUS
MACHINE WHERE SHOWN THUS

JOB No A07 | No OF SETS REQ 1 | USED ON DRG

SCALE 1·1 & 2·1 FINISH

DRAWN | CHK'D | APP'D | DATE | TITLE
26/8/87
ISSUED BY

TITLE AIR BEARING ROTOR ASSY.

CRANFIELD INSTITUTE OF TECHNOLOGY
CRANFIELD

DRAWING No PA 18475

SHT 1 OF

FIG.(8.2)

ISSUE	MODIFICATION
A	———

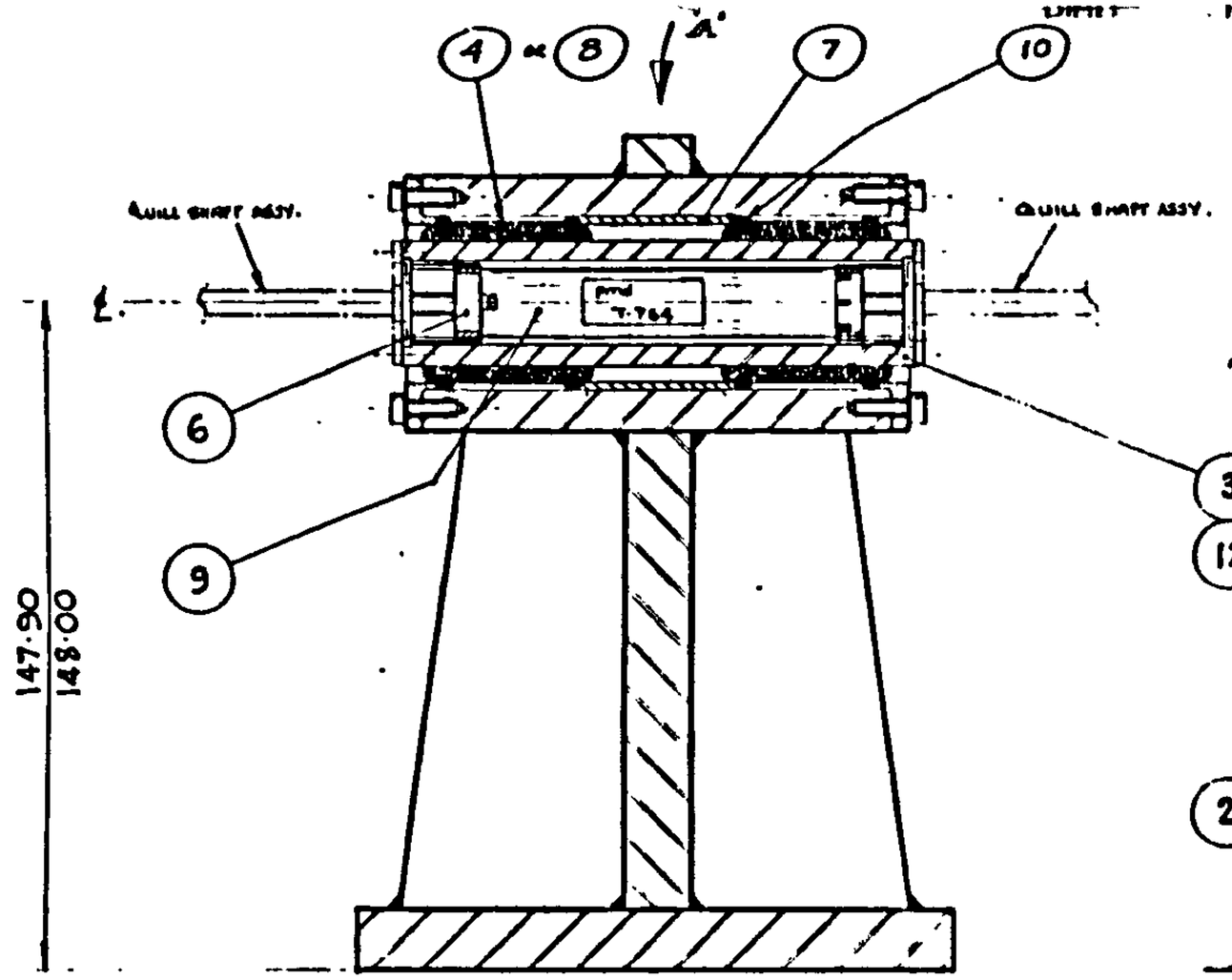

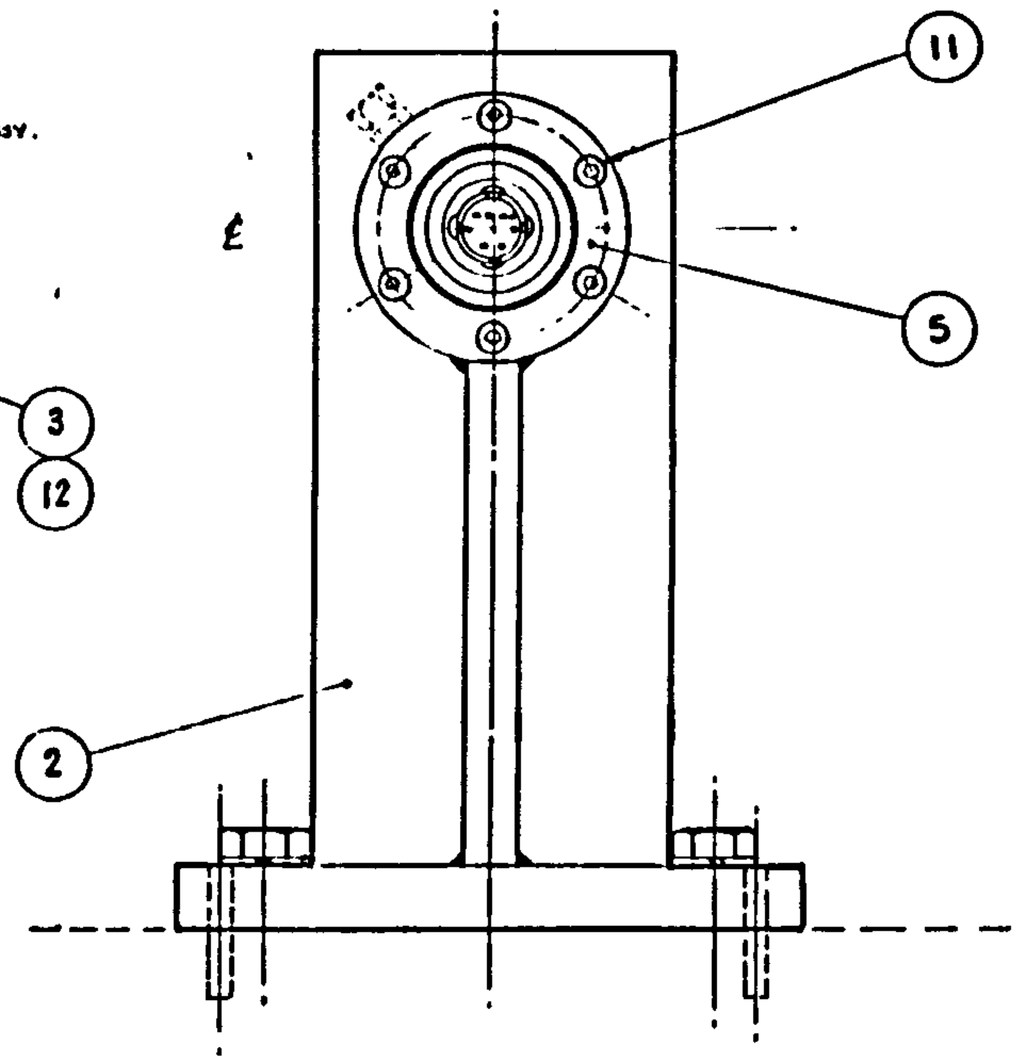

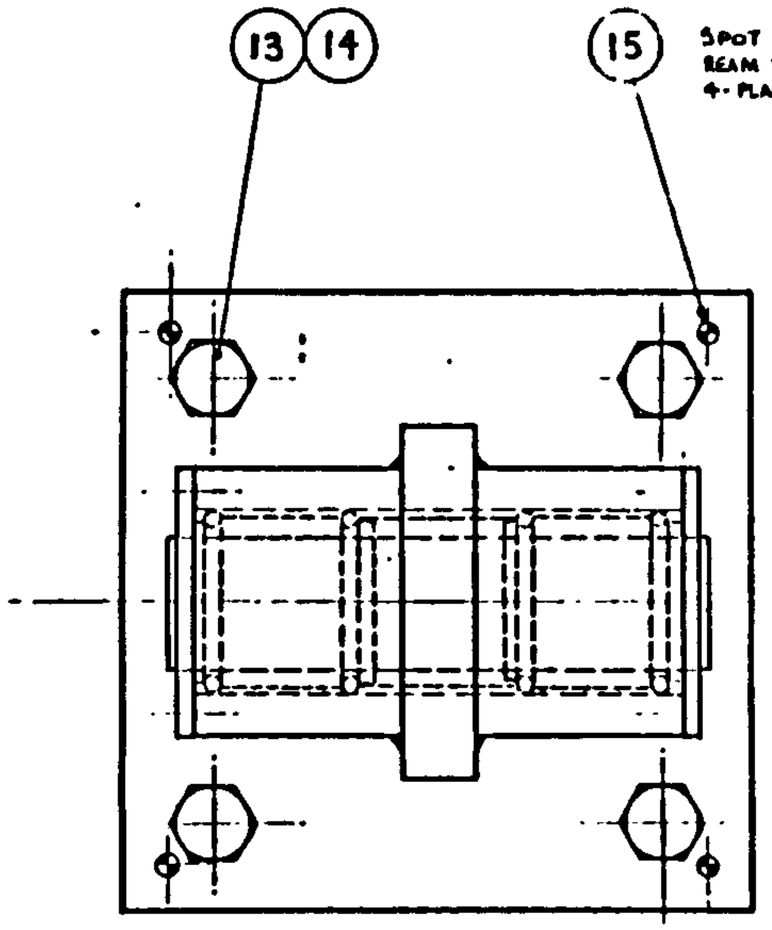

VIEW ON ARROW 'A'

FIG. (8.3).

ROTOR ASSY (WITH TRANSMITTER) IS TO BE BALANCED.

ITEM	PART No	DESCRIPTION	No OFF	MAT'L	SPEC	REMARKS
16.						
15		DOWEL PINS	4			5 DIA x 30 LONG.
14		SINGLE COIL LOCK WASHER	4			12 DIA.
13		HEX SETSCREWS	4			M12 x 35 LONG.
12		SOCKET CAP HEAD SCREWS	12			M2 x 5 LONG.
11		SOCKET CAP HEAD SCREWS	12			M4 x 12 LONG.
10		O-RINGS	4	VITON	HALLITE	BS 220 70° SHORE HARDNESS
9		TELEMETRY TRANSMITTER	1	SPECIAL	T-764	WELSH INSTRUMENTS. (PMD). 50,000g CAPACITY
8	PC19370	JETTED BEARING	2			
7	PC19069/3	SPACING RING	1			
6	PC19069/2	SECURING RING	2			
5	PC19069/1	CLAMPING FLANGE	2			
4	PC19068	POROUS BEARING	2			
3	PC19067	TRANSMITTER ROTOR	1			
2	PB19066	BEARING HOUSING SUB ASSY	1			
1		TRANS ROTOR HOUSING ASSY	1			

THIRD ANGLE PROJECTION

GENERAL TOLERANCE ON DIMENSIONS
MACHINED
UNMACHINED
OTHER DIMENSIONS AS STATED
WELD WHERE SHOWN THUS ⁴⁴⁴
MACHINE WHERE SHOWN THUS ✓

JOB No. 407.
No OF SETS REQ'D
USED ON (NG

SHEET SIZE A1
SCALE 1:1
FINISH NAT.

DRAWN	CHK'D	APP'D	STR'S APP'D
[illegible] 16-1-89.			

TITLE:- TRANSMITTER ROTOR HOUSING ASSEMBLY.

ISSUED BY SME.

CRANFIELD INSTITUTE OF TECHNOLOGY CRANFIELD.

DRAWING No PB 19065

SHT | OF | SHEETS

321

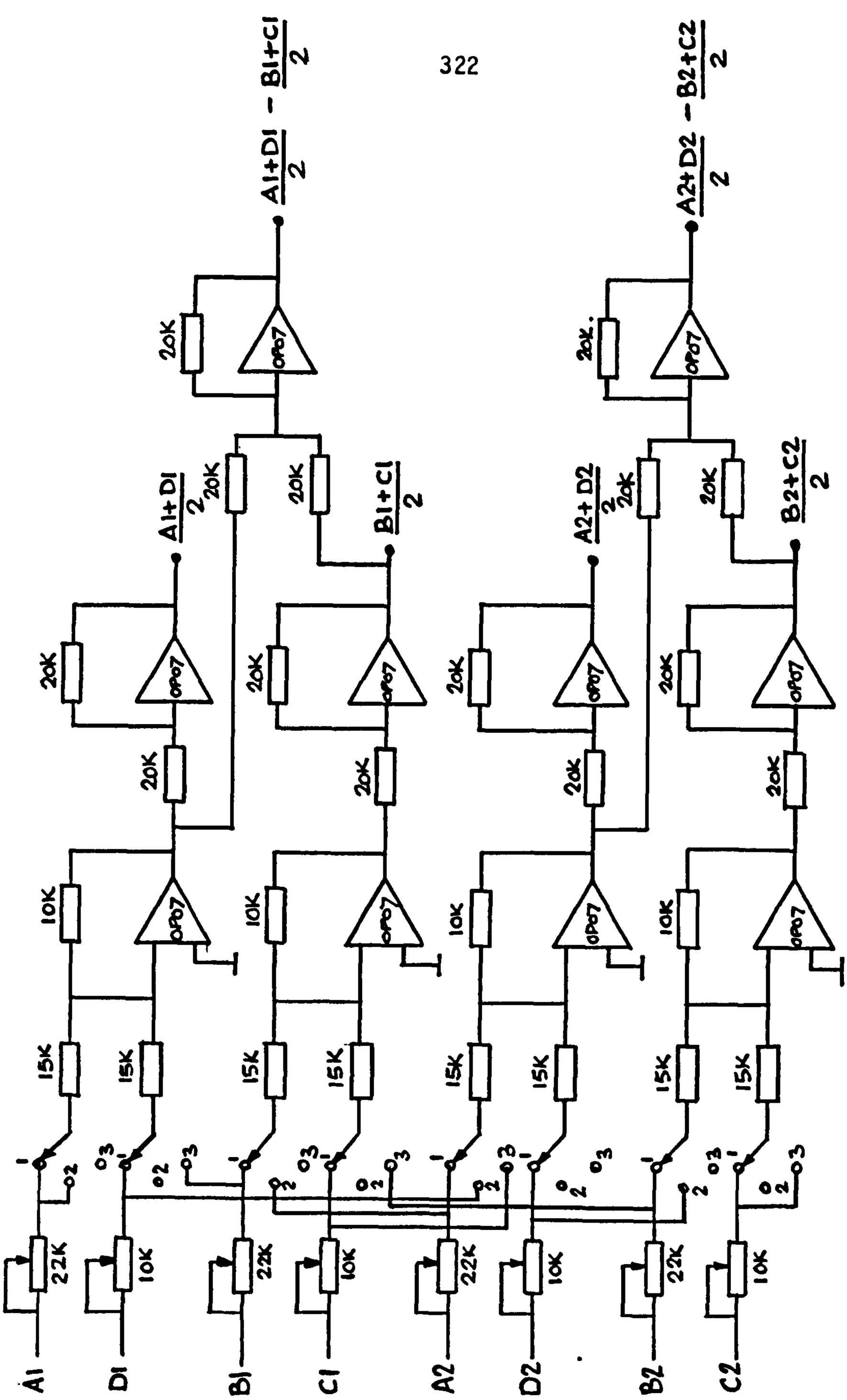

FIG.(8.8) MEAN AND DIFFERENCE CALCULATOR.

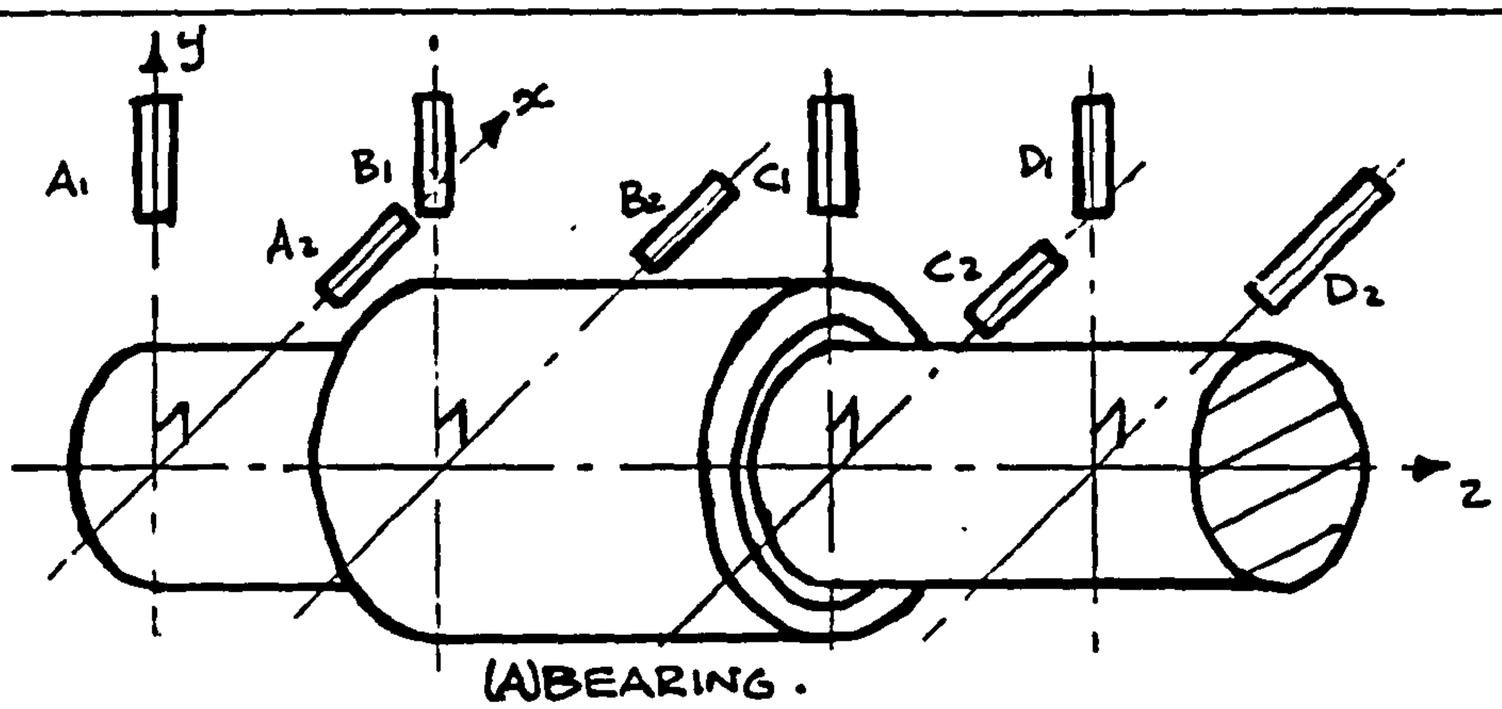

(A) BEARING.

(a) CONFIGURATION I (PROX. PROBES)

O·RING CENTRES 15

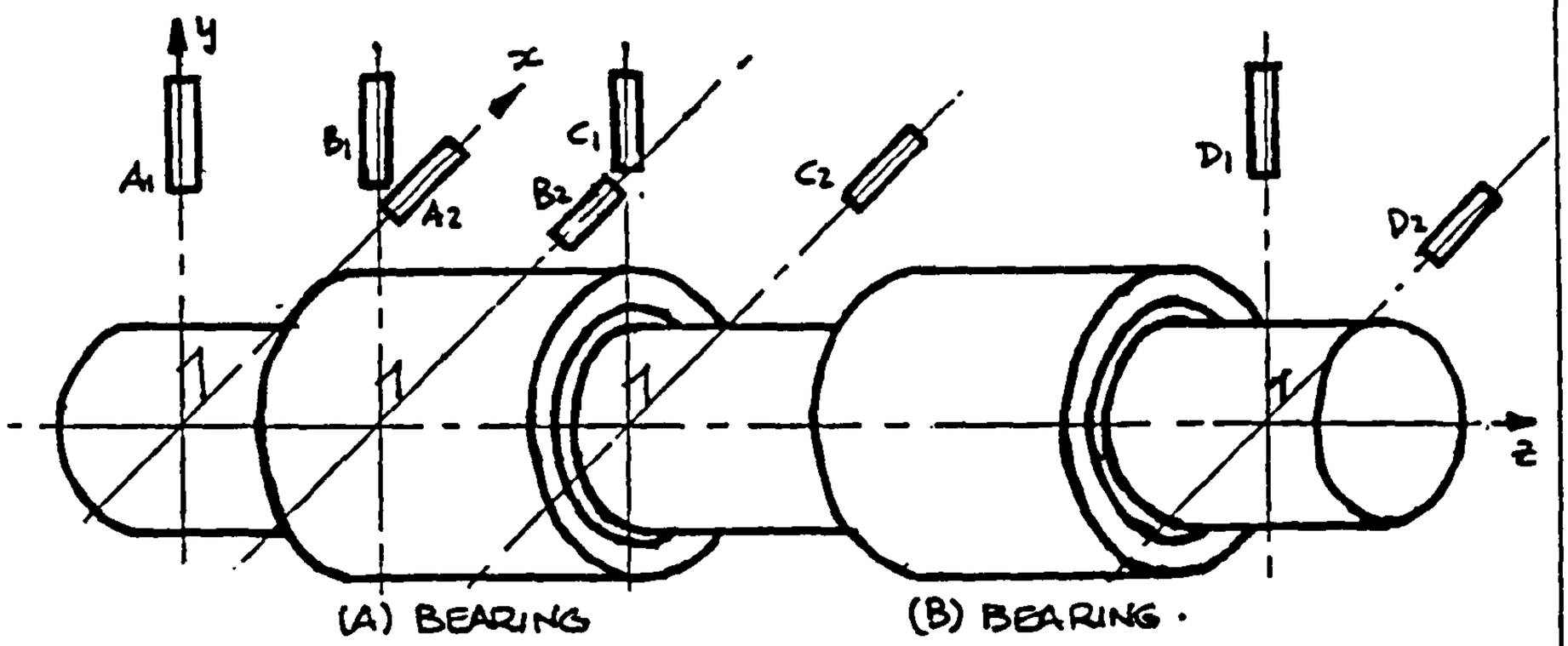

(A) BEARING (B) BEARING.

(b) CONFIGURATION II (PROX. PROBES)

O-RING CENTRES. 5. 7.5. 10 & 15 (POROUS)

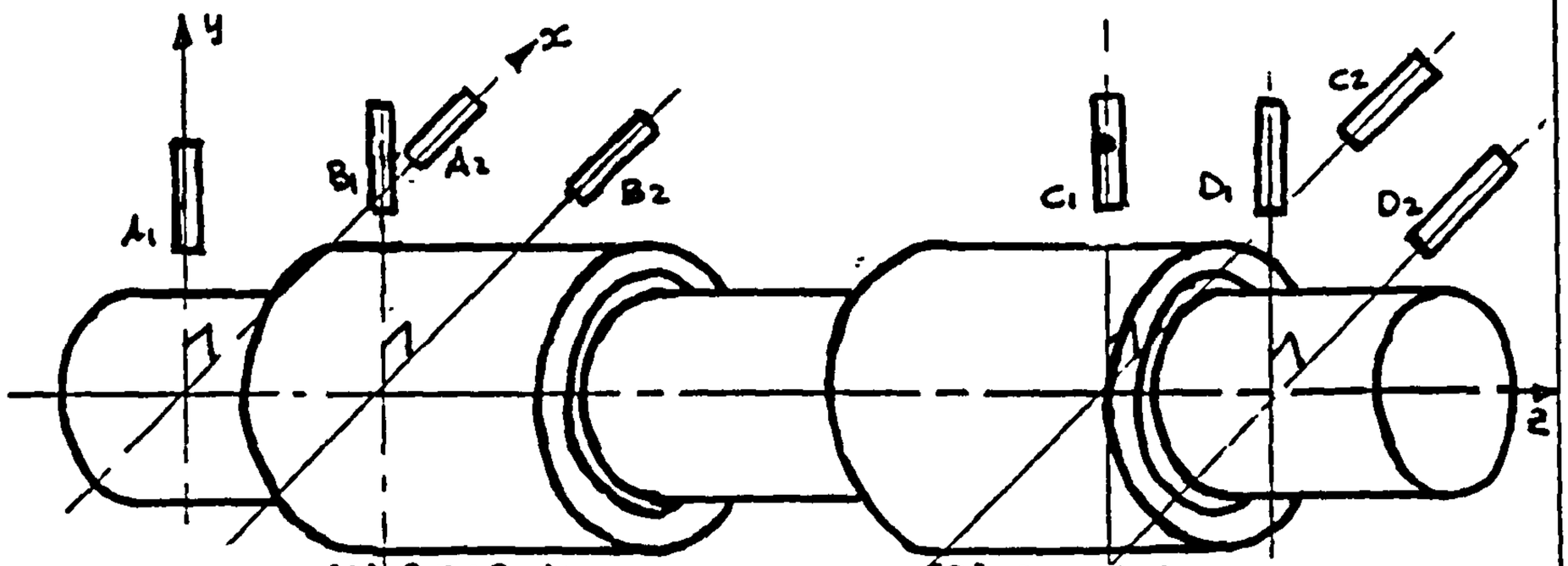

(A) BEARING (B) BEARING.

(C) CONFIGURATION III (PROX. PROBES).

O-RING CENTRES 20, 25 & 25 (POROUS).

FIG. (8.9)

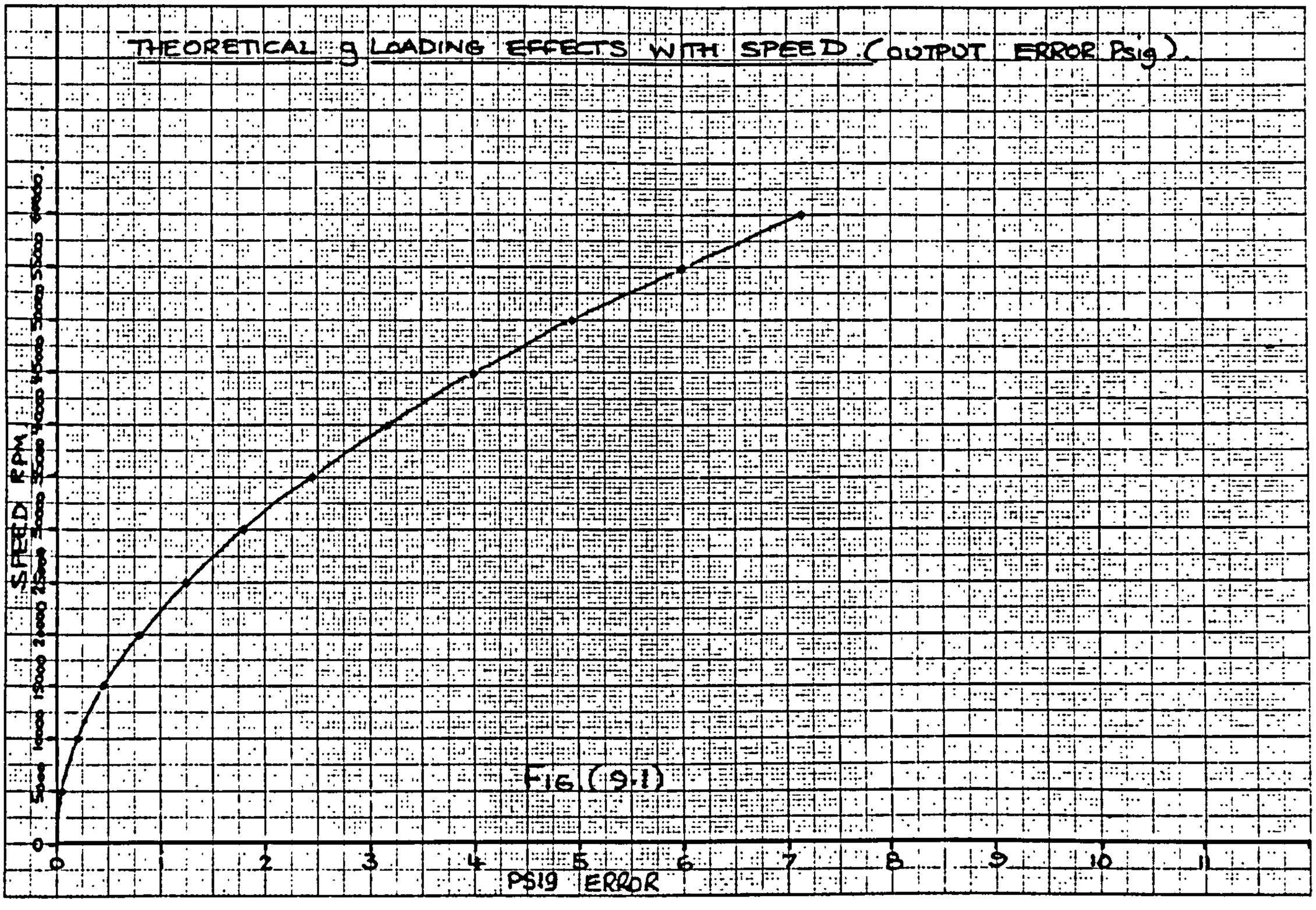

FIG (9.1)

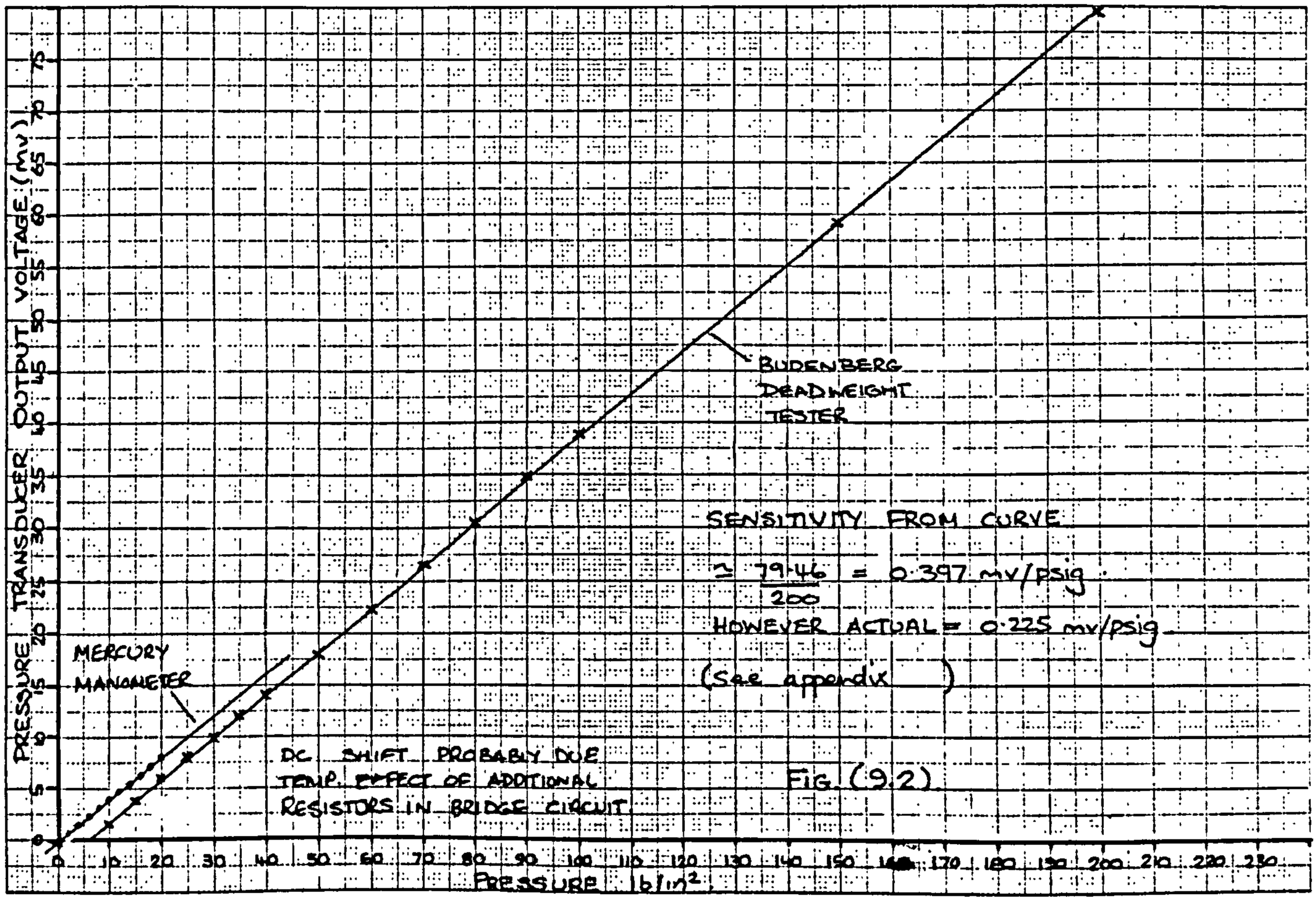

SENSITIVITY FROM CURVE

$\simeq \frac{79.46}{200} = 0.397$ mv/psig

HOWEVER ACTUAL = 0.225 mv/psig

(See appendix)

FIG (9.2)

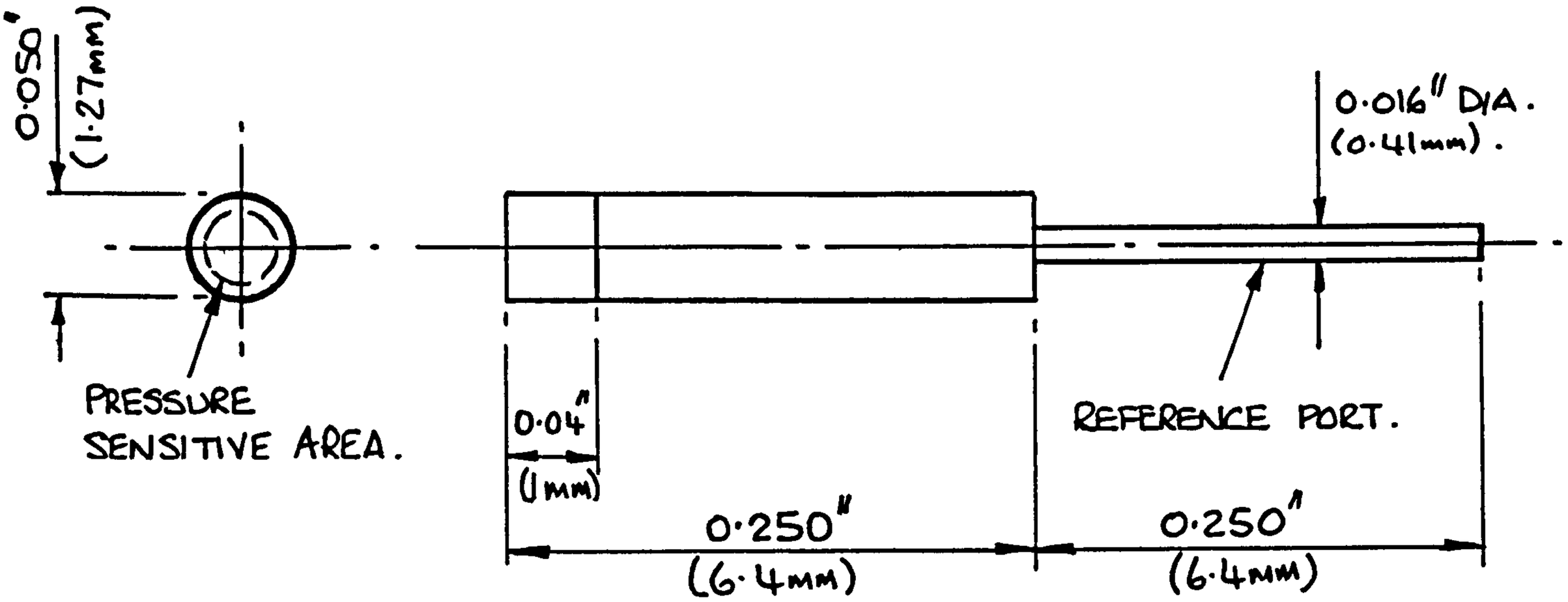

FIG. (9.3a) ENTRAN EPI-050-200 TRANSDUCER.

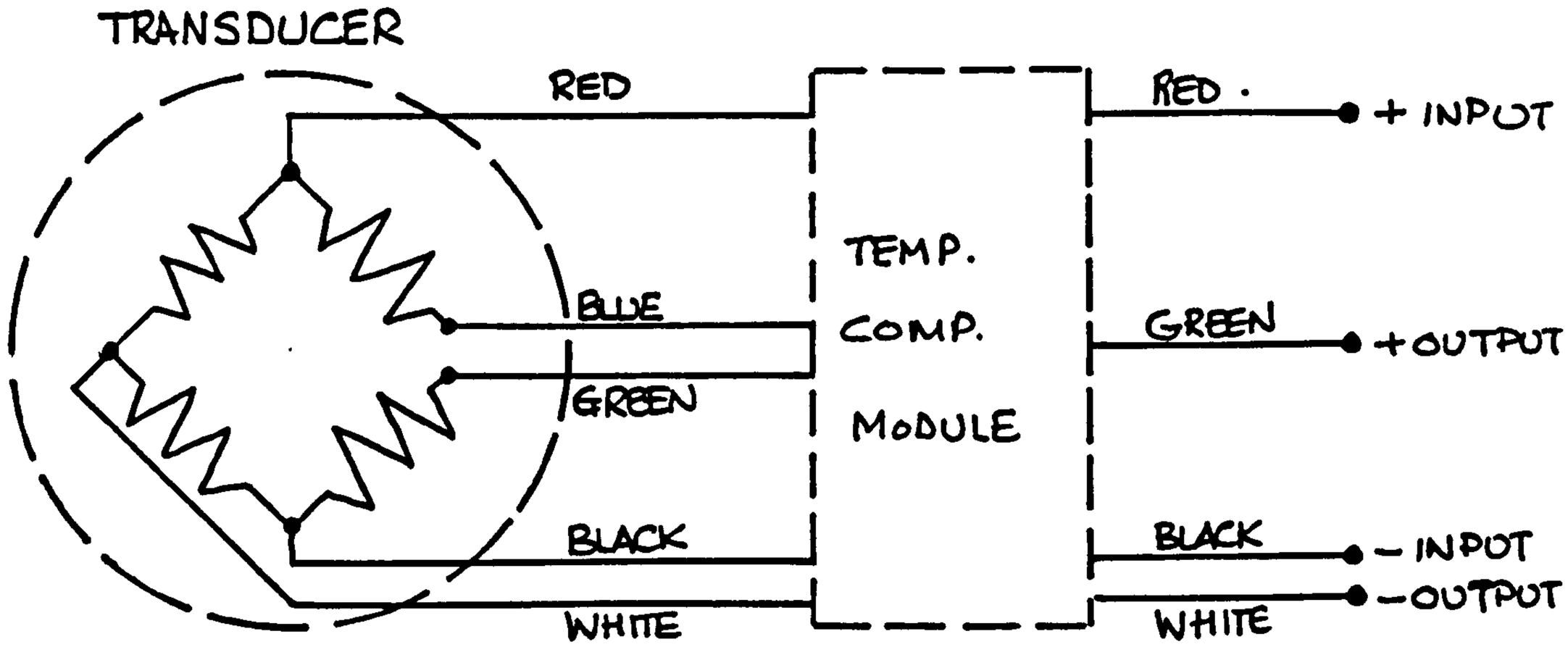

FIG. (9.3b) EPI-050-200 WIRING DIAGRAM.

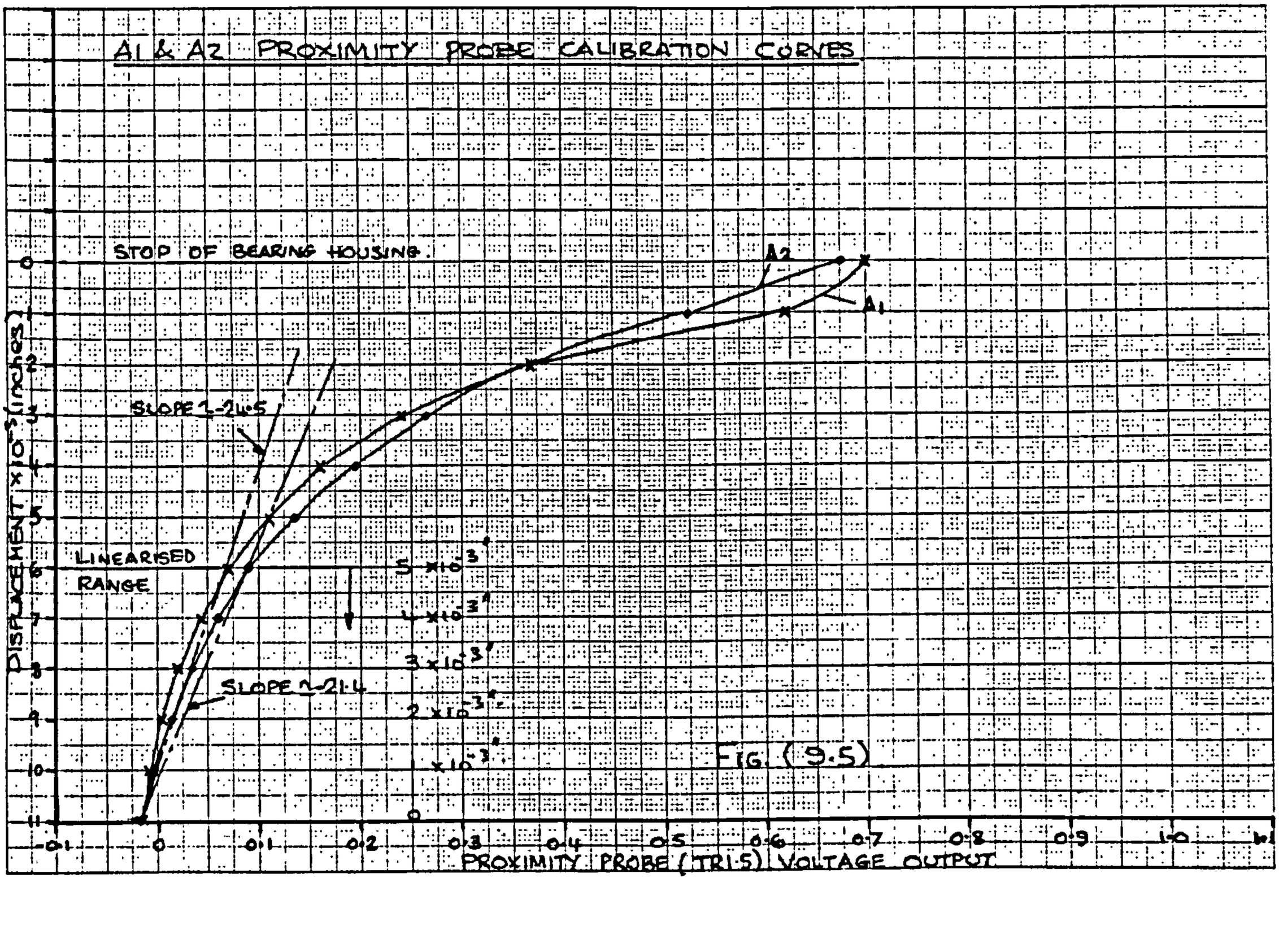
A1 & A2 PROXIMITY PROBE CALIBRATION CURVES
STOP OF BEARING HOUSING.
A2
A1
SLOPE ~ -24.5
SLOPE ~ -21.4
LINEARISED RANGE
DISPLACEMENT x10⁻³ (inches)
PROXIMITY PROBE (TR1.5) VOLTAGE OUTPUT

FIG. (9.5)

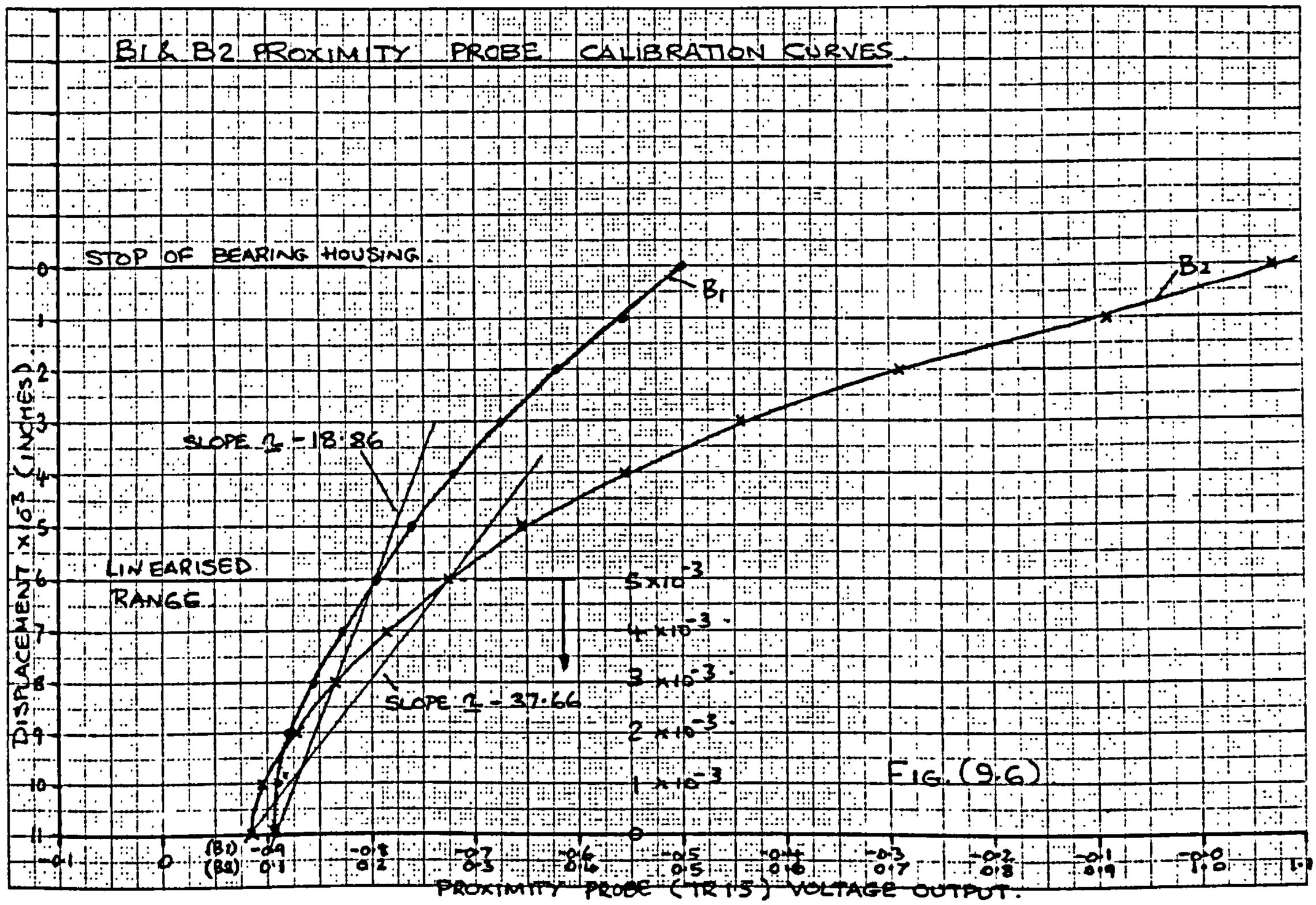
B1 & B2 PROXIMITY PROBE CALIBRATION CURVES.
STOP OF BEARING HOUSING.
B1
B2
SLOPE ~ -18.86
SLOPE ~ -37.66
LINEARISED RANGE
DISPLACEMENT x10⁻³ (INCHES)
PROXIMITY PROBE (TR1.5) VOLTAGE OUTPUT.

FIG. (9.6)

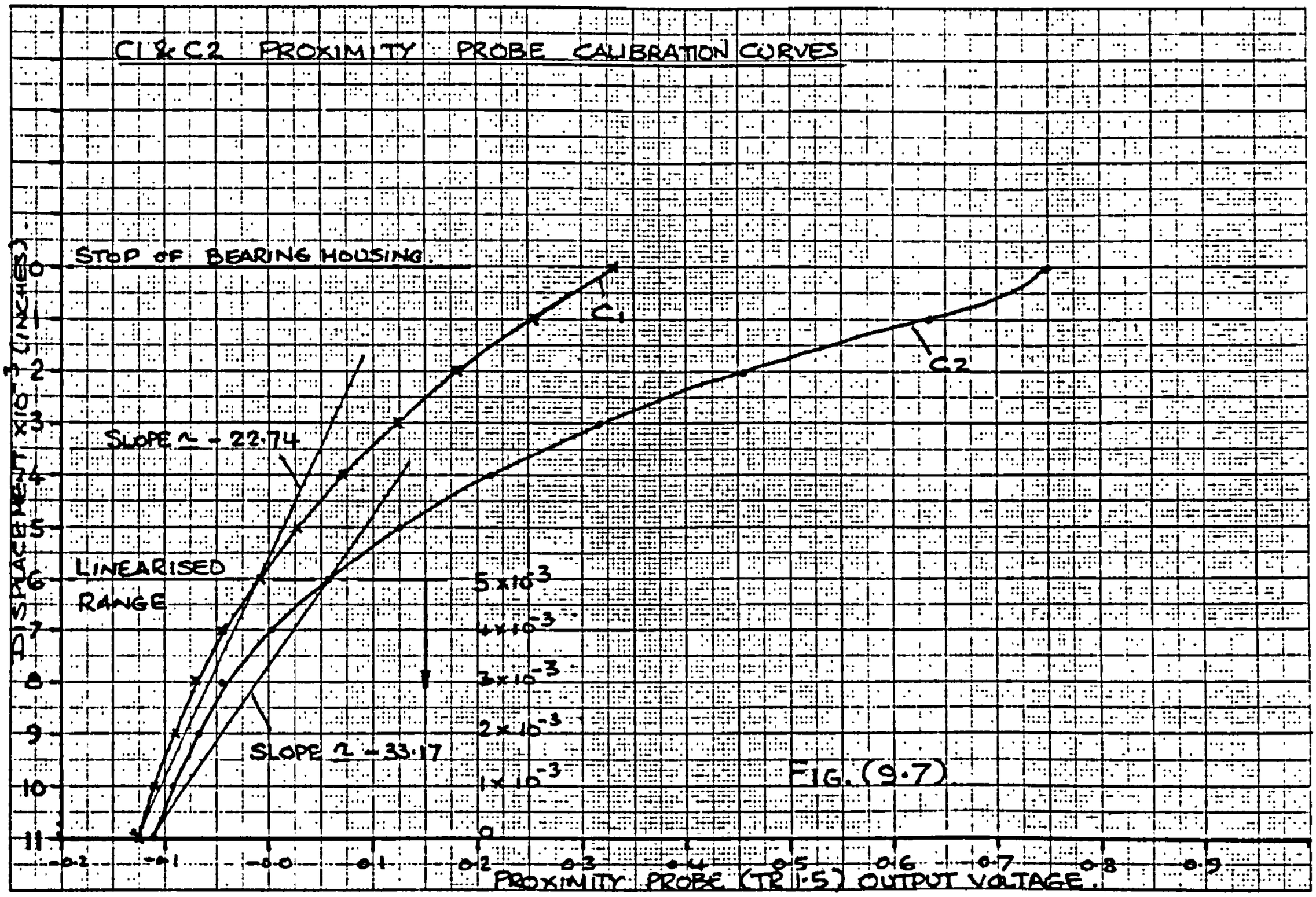
C1 & C2 PROXIMITY PROBE CALIBRATION CURVES
STOP OF BEARING HOUSING.
C1
C2
SLOPE ≃ - 22.74
LINEARISED
RANGE
SLOPE ≃ - 33.17
DISPLACEMENT X10⁻³ (INCHES)
0
1
2
3
4
5
6
7
8
9
10
11
5x10⁻³
4x10⁻³
3x10⁻³
2x10⁻³
1x10⁻³
0
-0·2
-0·1
-0·0
0·1
0·2
0·3
0·4
0·5
0·6
0·7
0·8
0·9
PROXIMITY PROBE (TR 1·5) OUTPUT VOLTAGE.

FIG. (9.7)

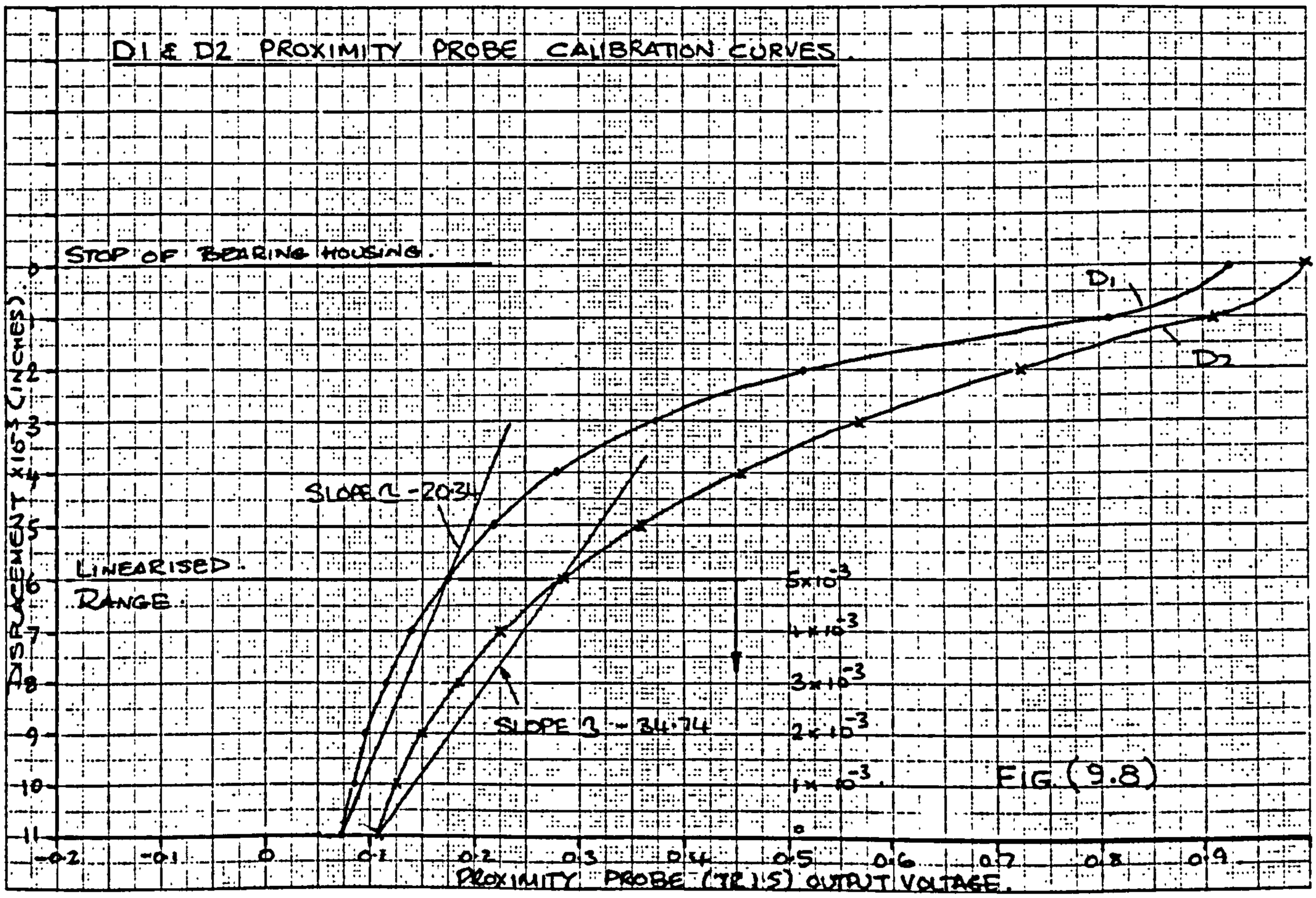
D1 & D2 PROXIMITY PROBE CALIBRATION CURVES.
STOP OF BEARING HOUSING.
D1
D2
SLOPE ≃ - 20·34
LINEARISED
RANGE.
SLOPE 3 ≃ - 34·74
DISPLACEMENT X10⁻³ (INCHES).
0
1
2
3
4
5
6
7
8
9
10
11
5x10⁻³
1x10⁻³
3x10⁻³
2x10⁻³
1x10⁻³.
0
-0·2
-0·1
0
0·1
0·2
0·3
0·4
0·5
0·6
0·7
0·8
0·9
PROXIMITY PROBE (TR 1·5) OUTPUT VOLTAGE.

FIG (9.8)

Reprinted from (73)

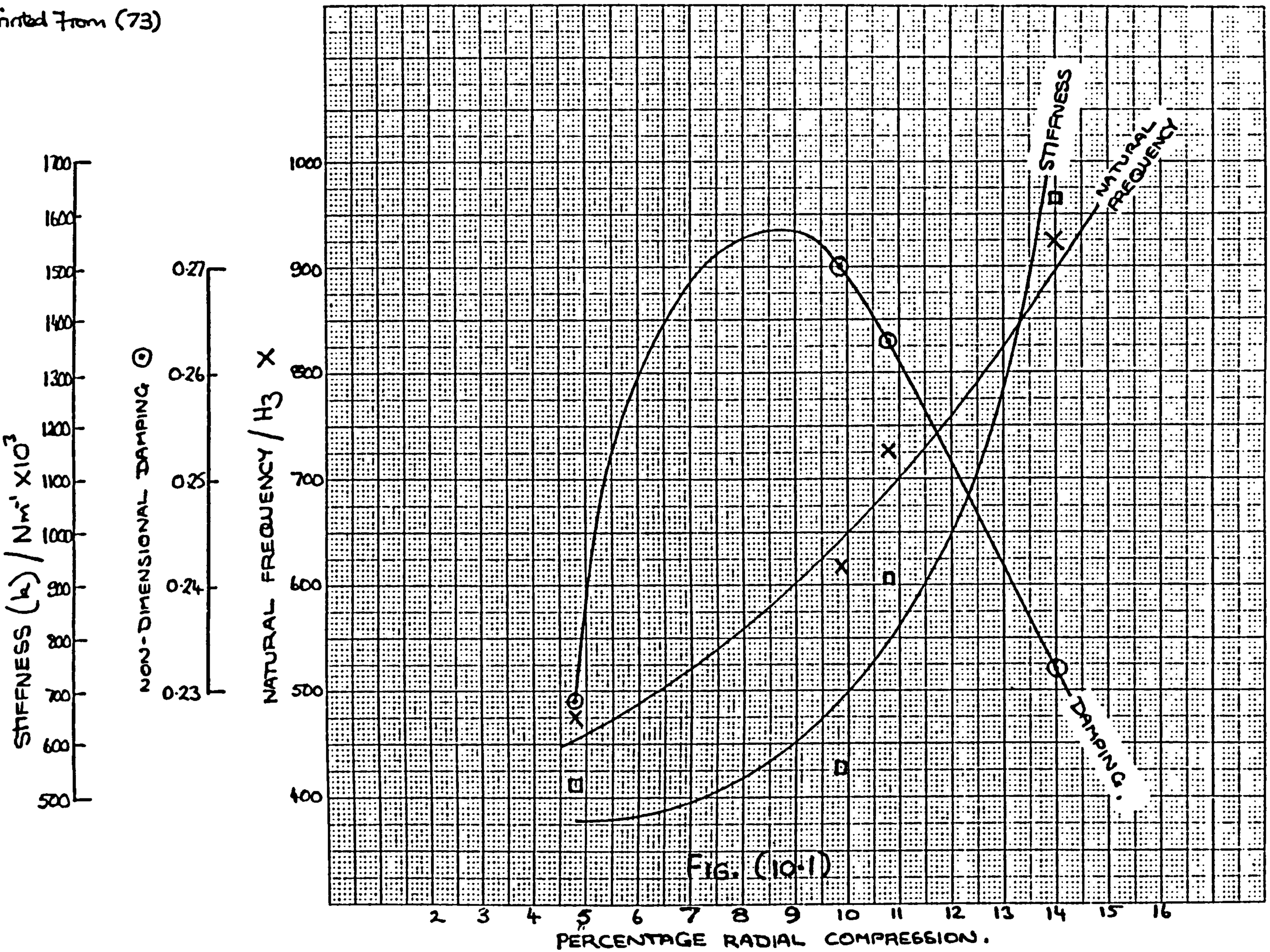

FIG. (10·1)

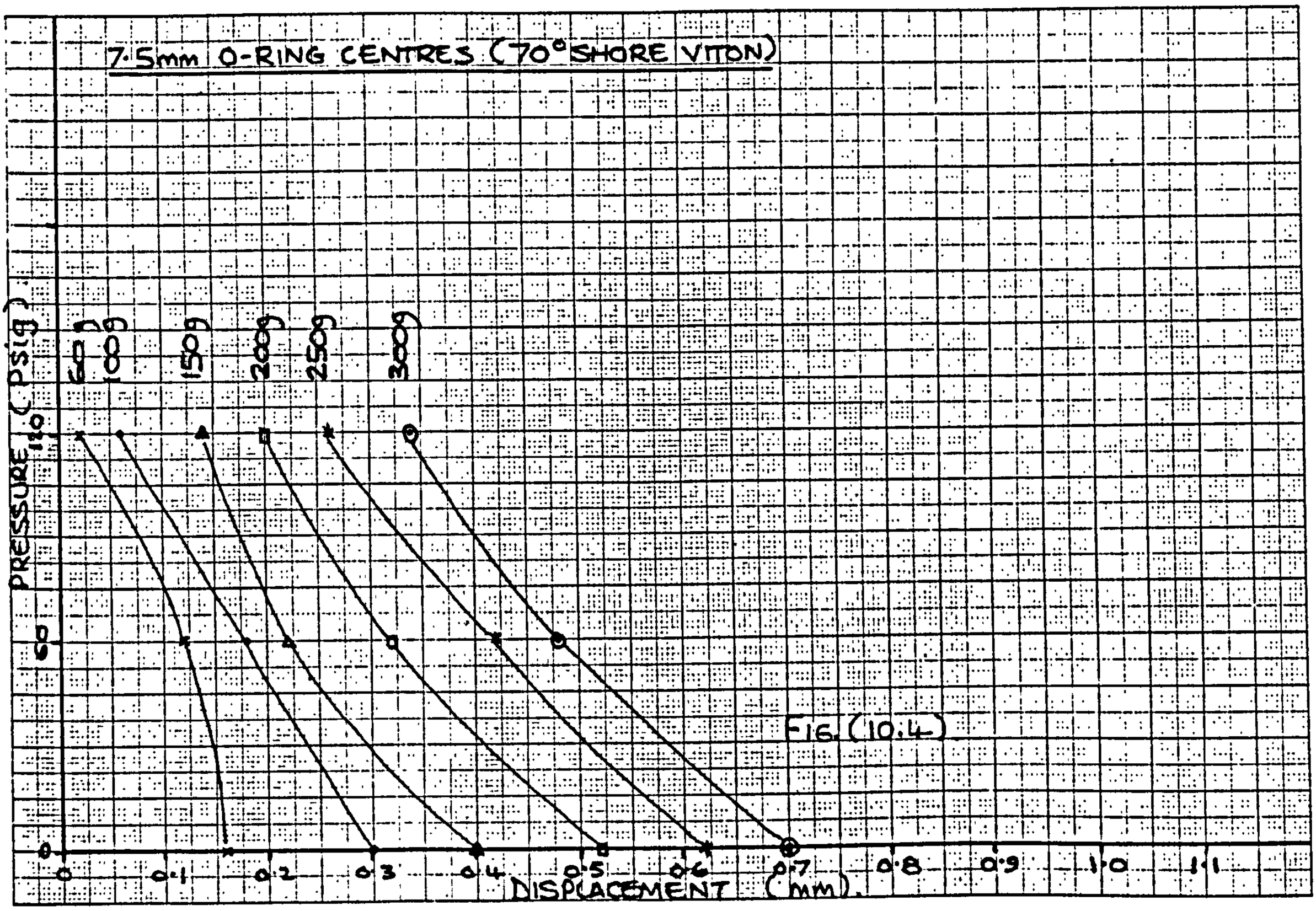

FIG. (10.4)

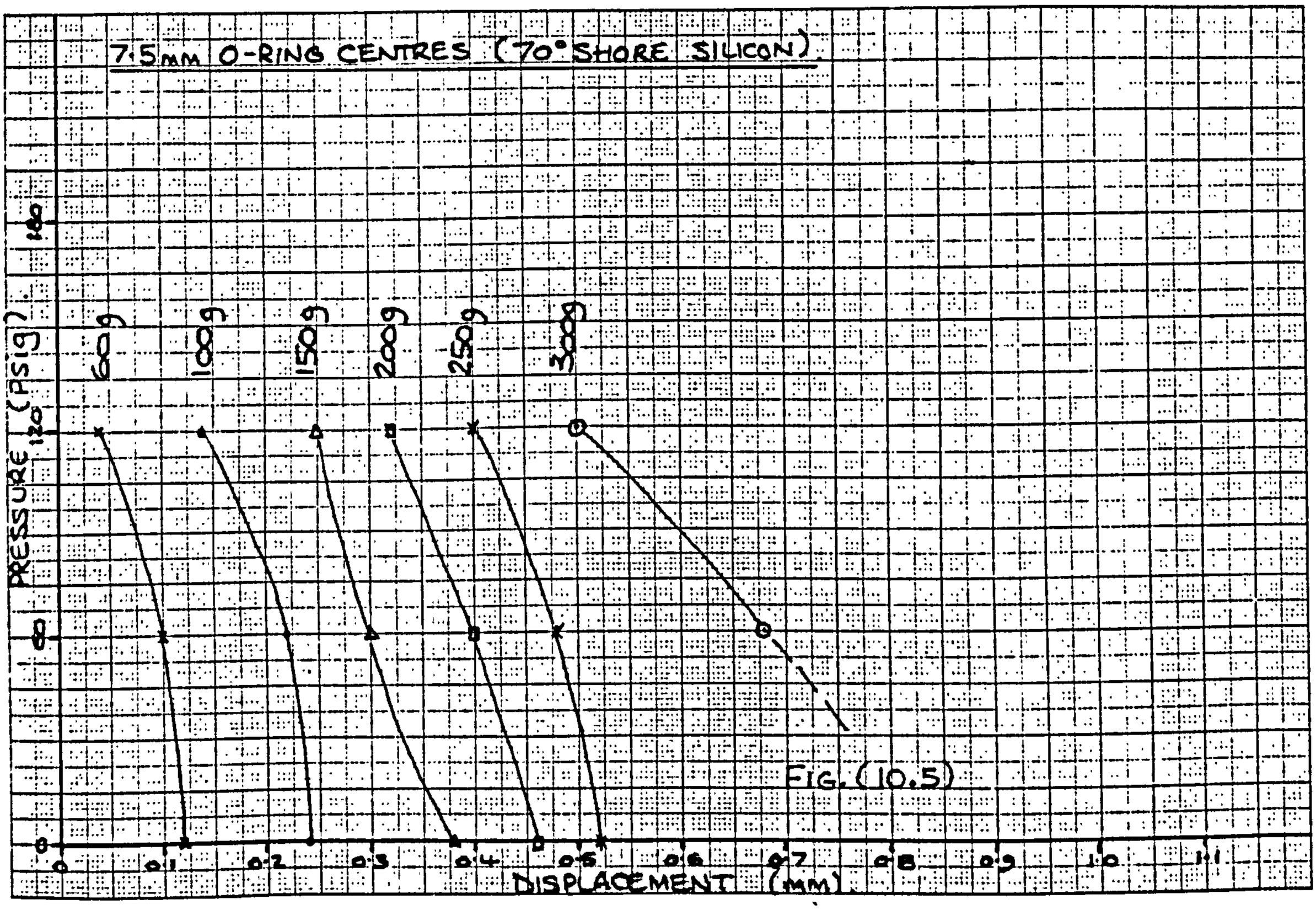

FIG. (10.5)

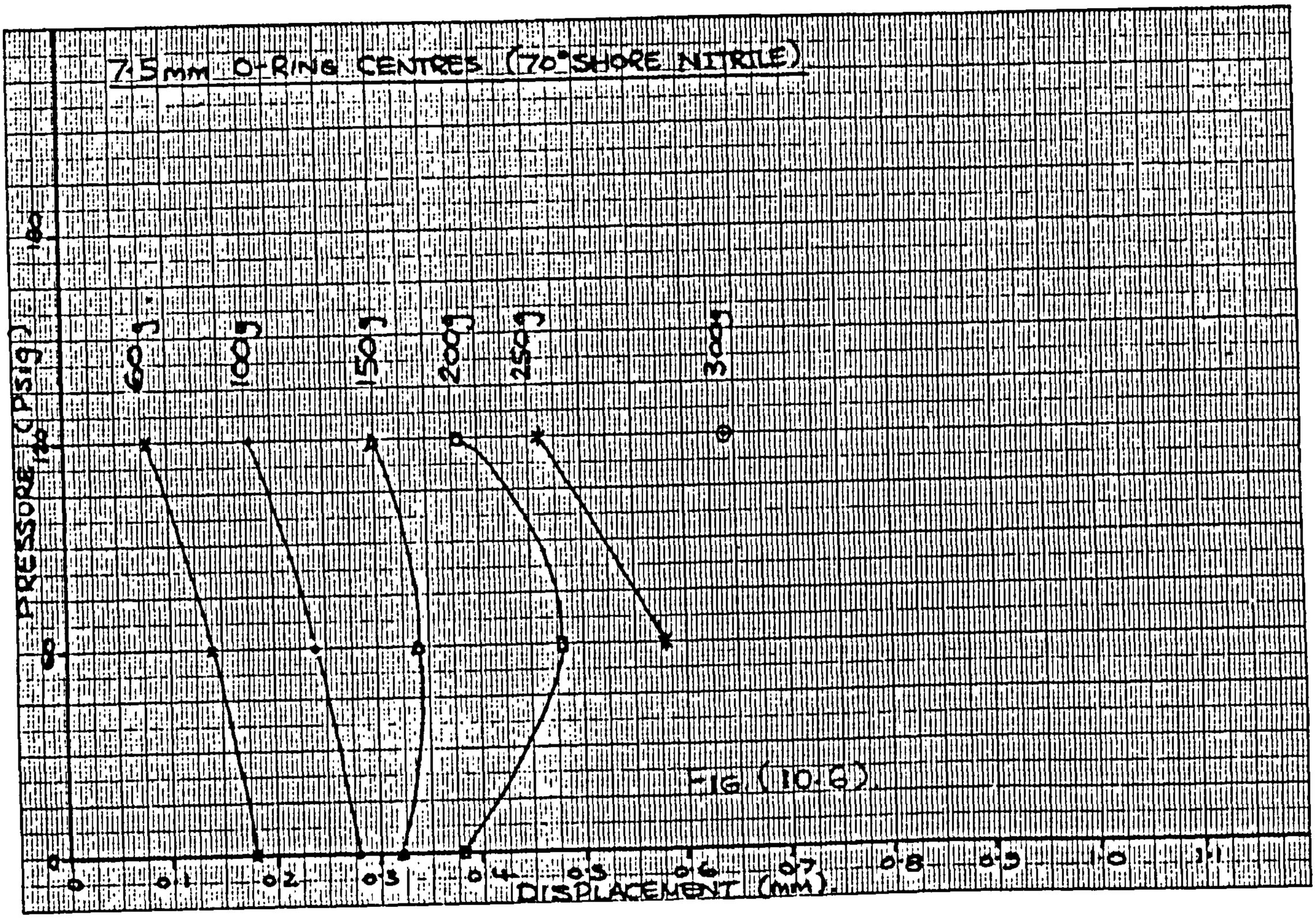

FIG. (10·6).

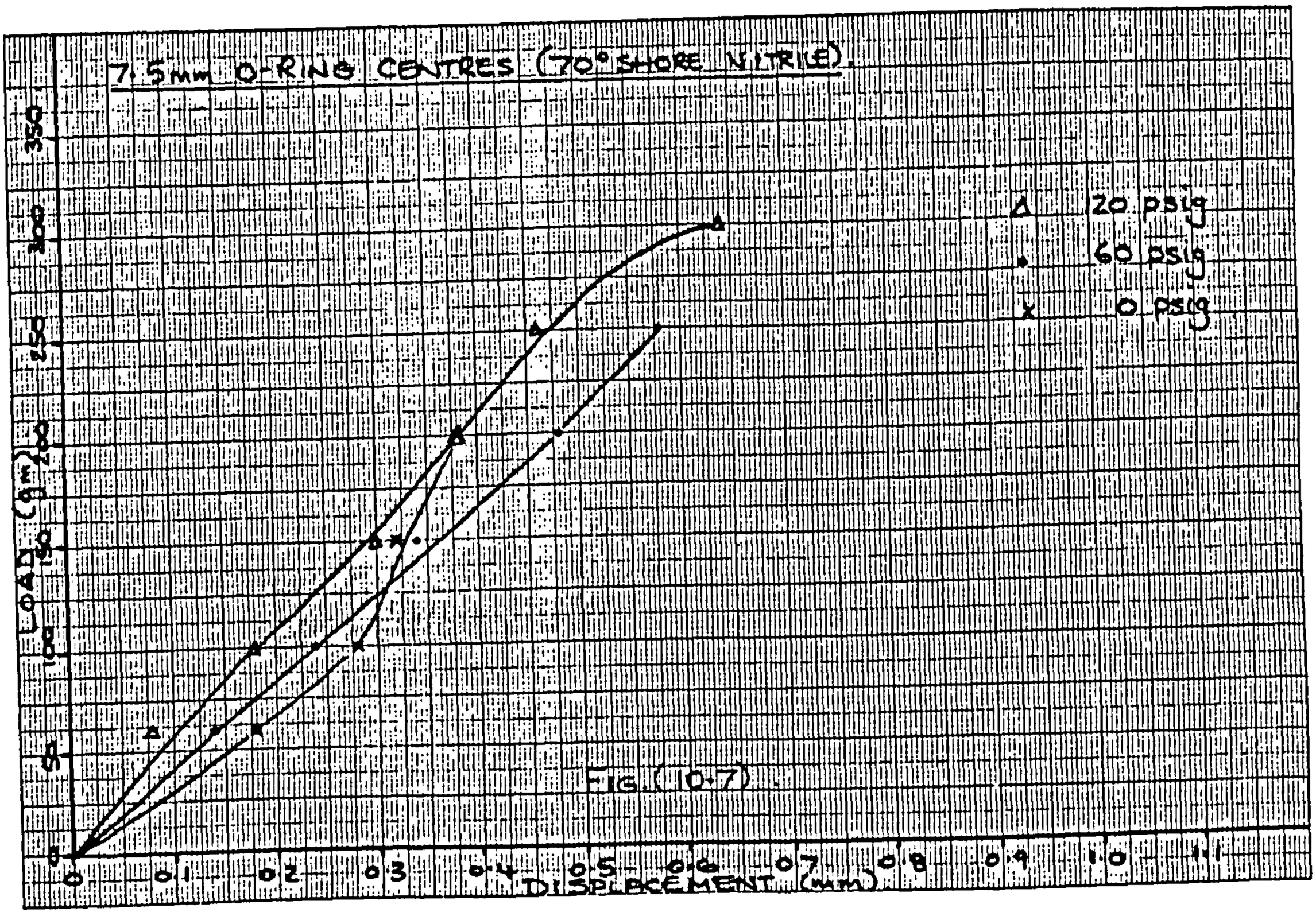

FIG. (10·7).

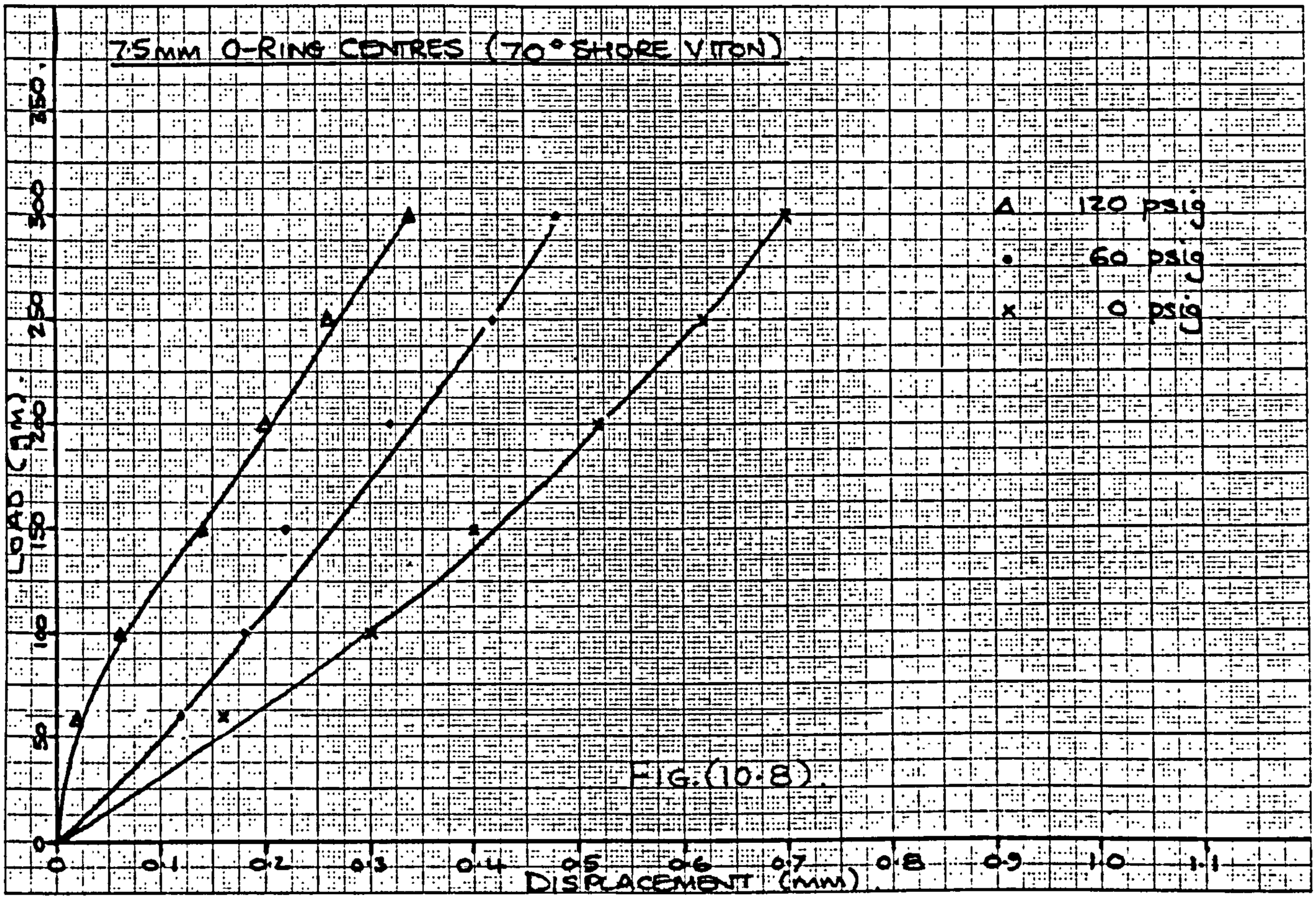

FIG.(10·8).

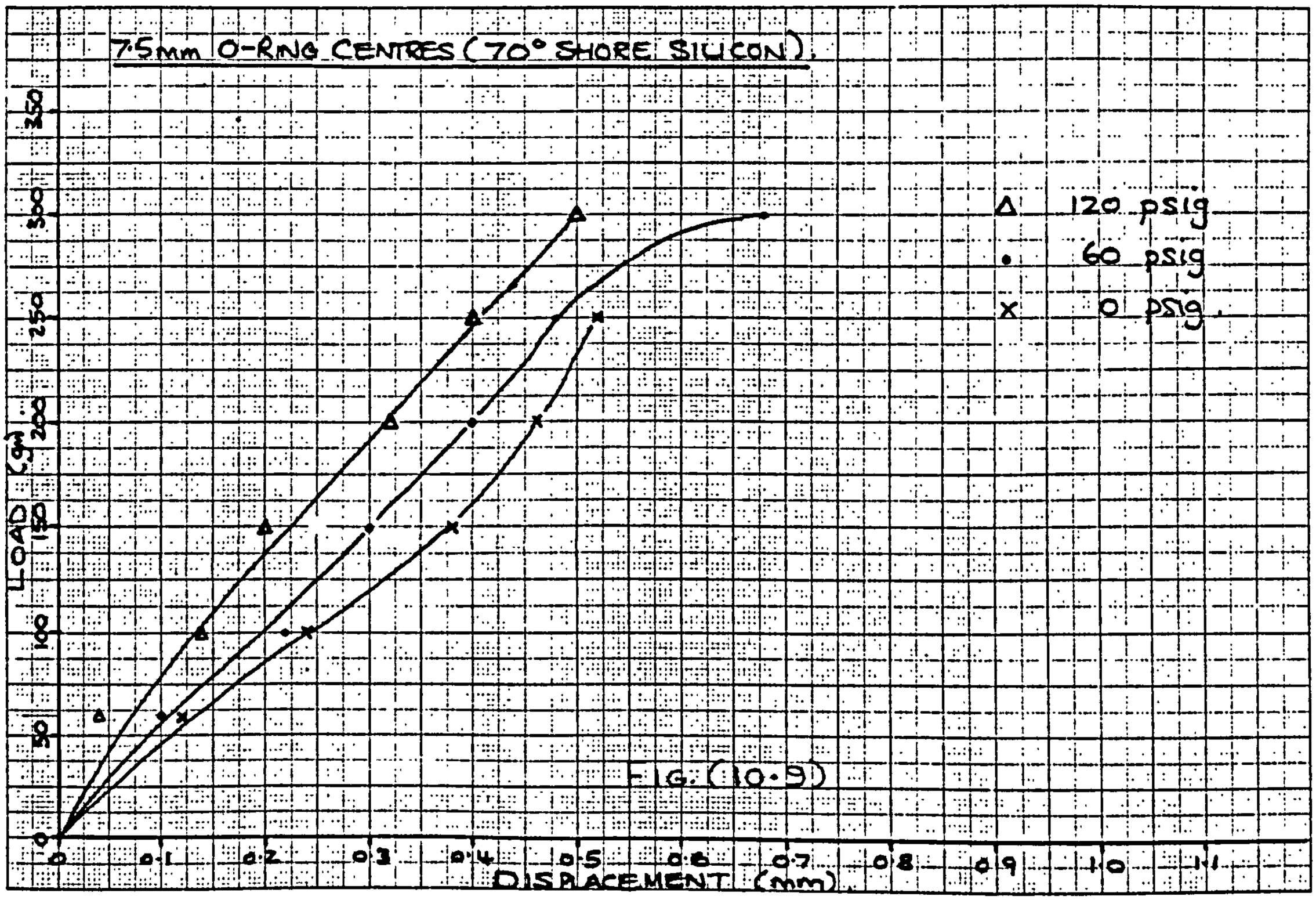

FIG.(10·9).

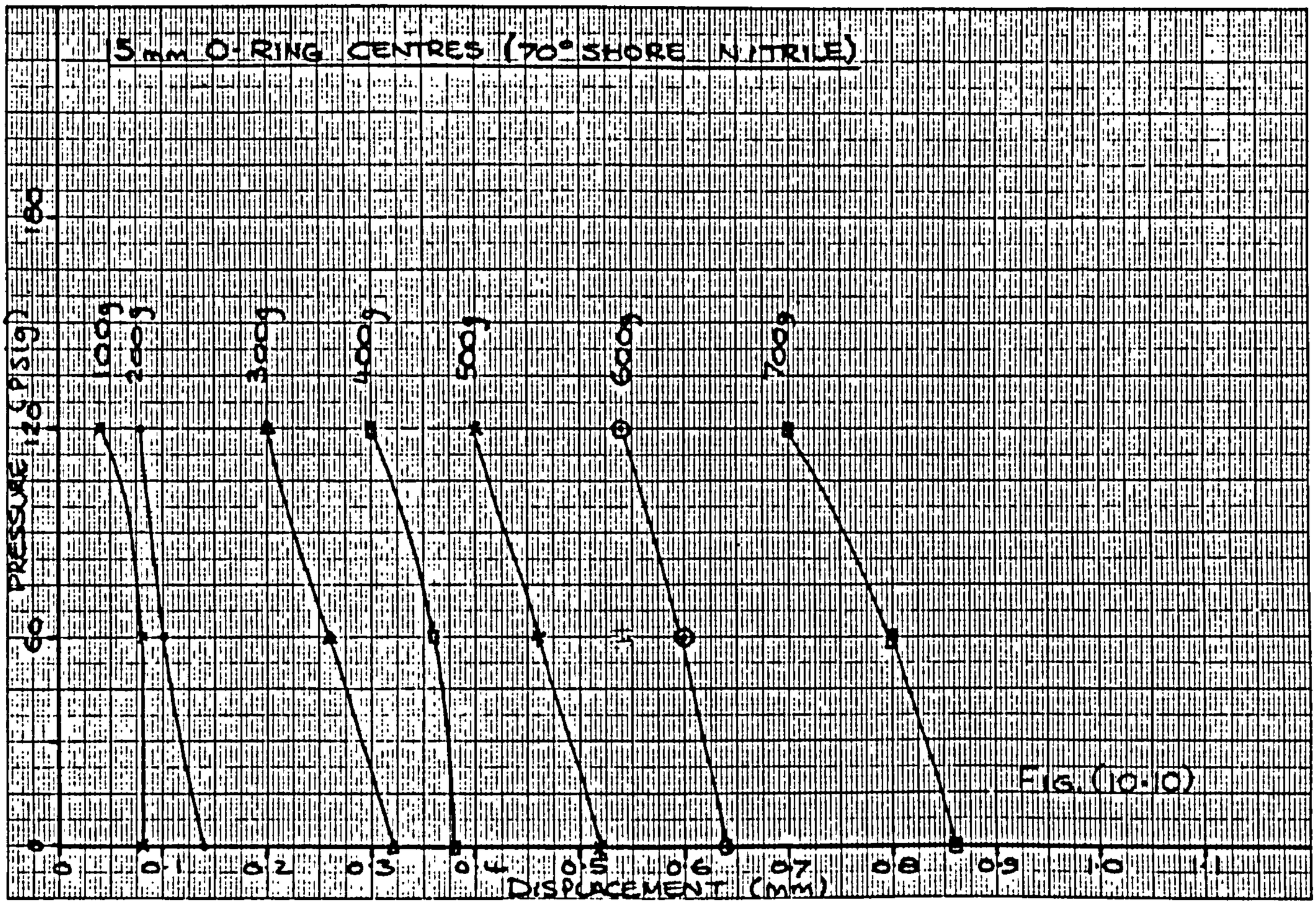

FIG. (10.10)

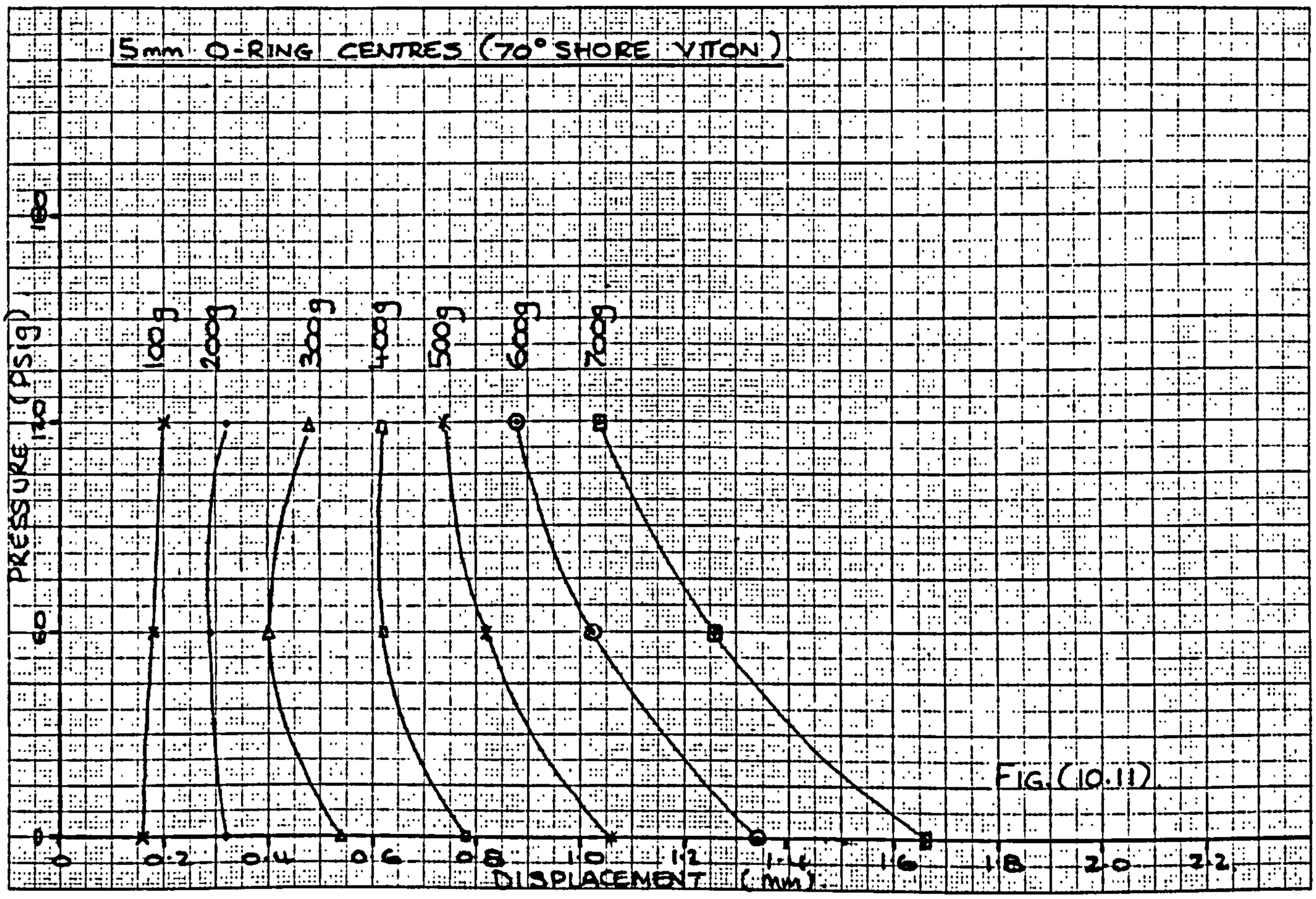

FIG. (10.11)

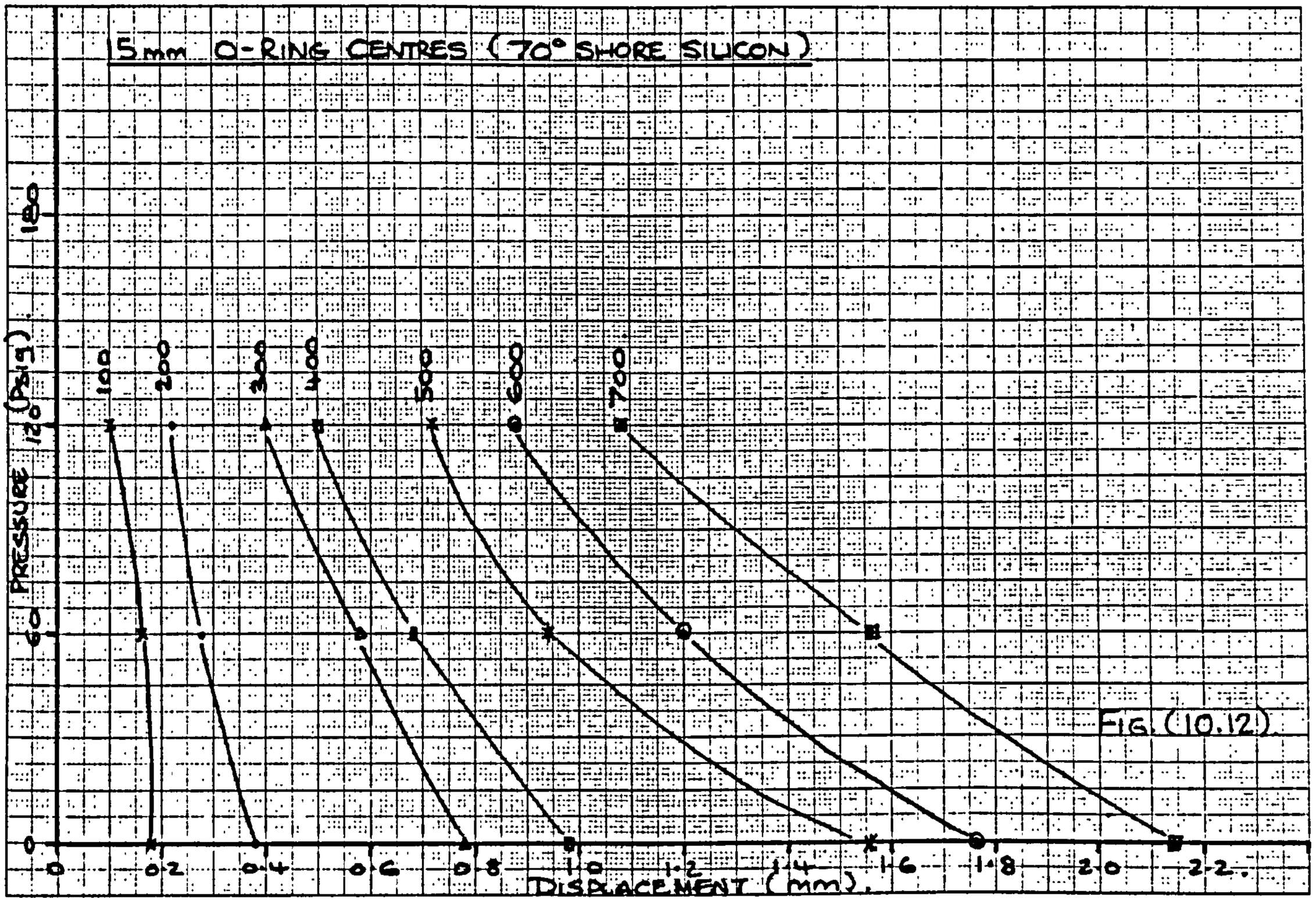

FIG. (10.12)

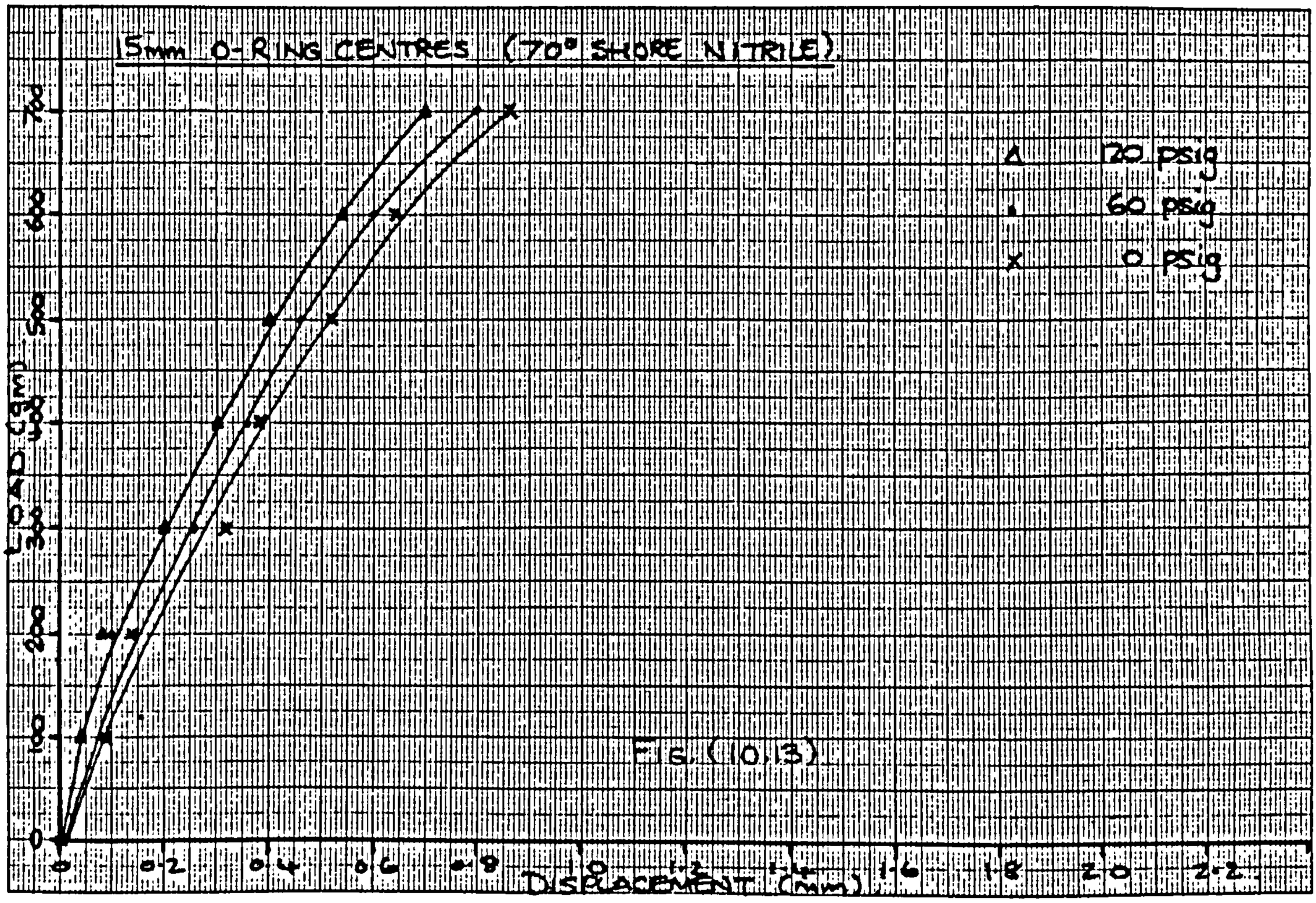

FIG. (10.13)

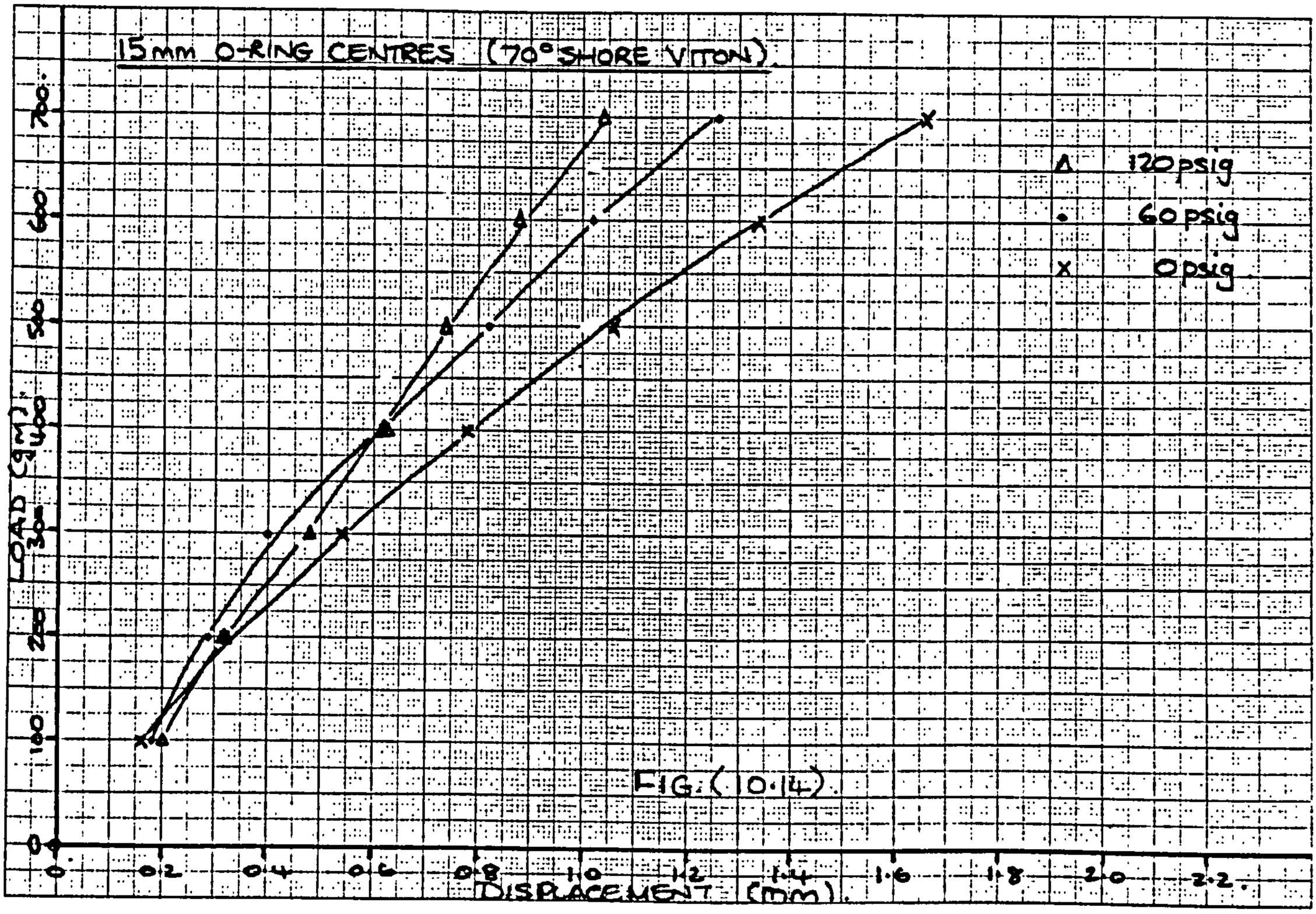

FIG: (10·14).

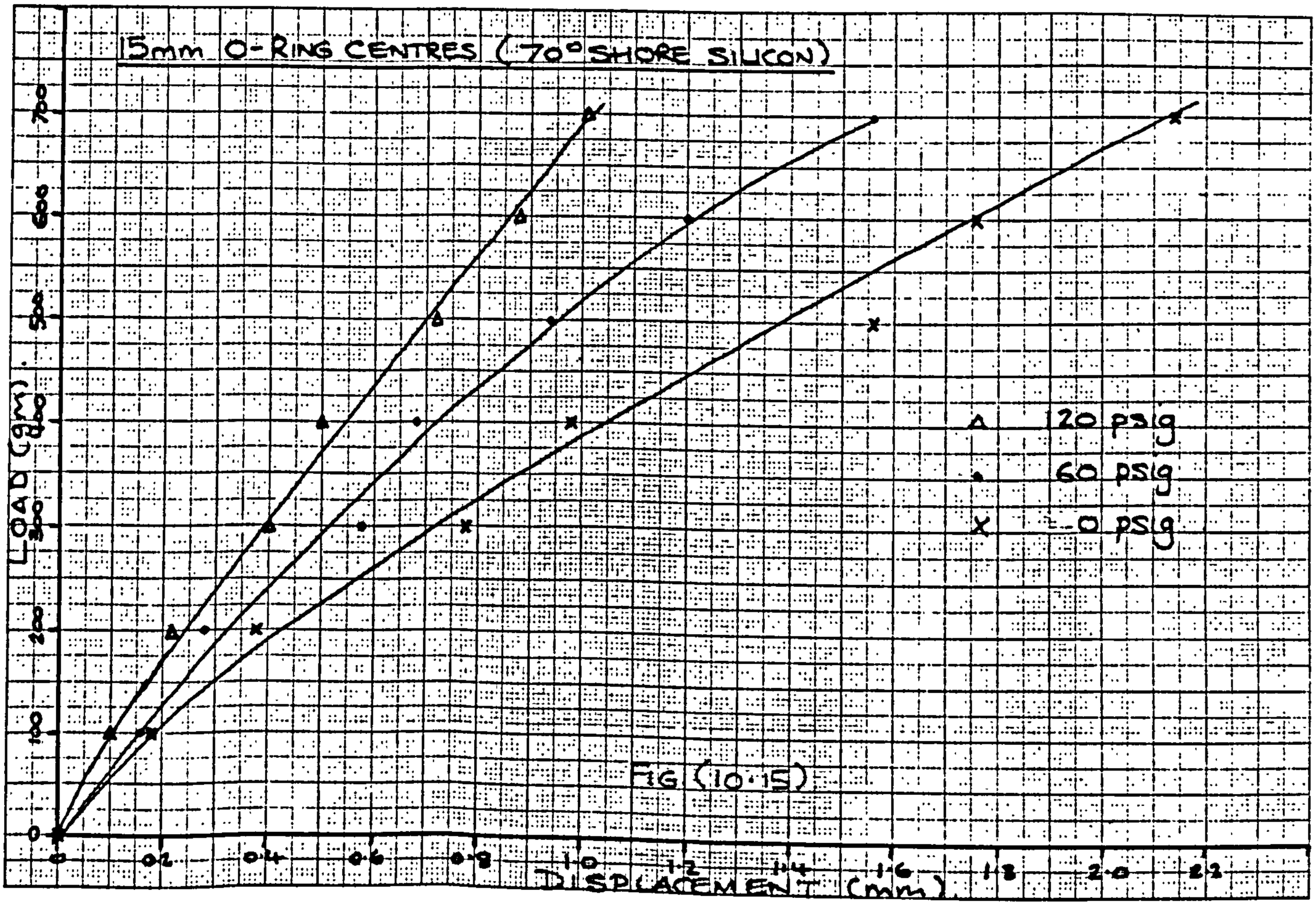

FIG (10·15)

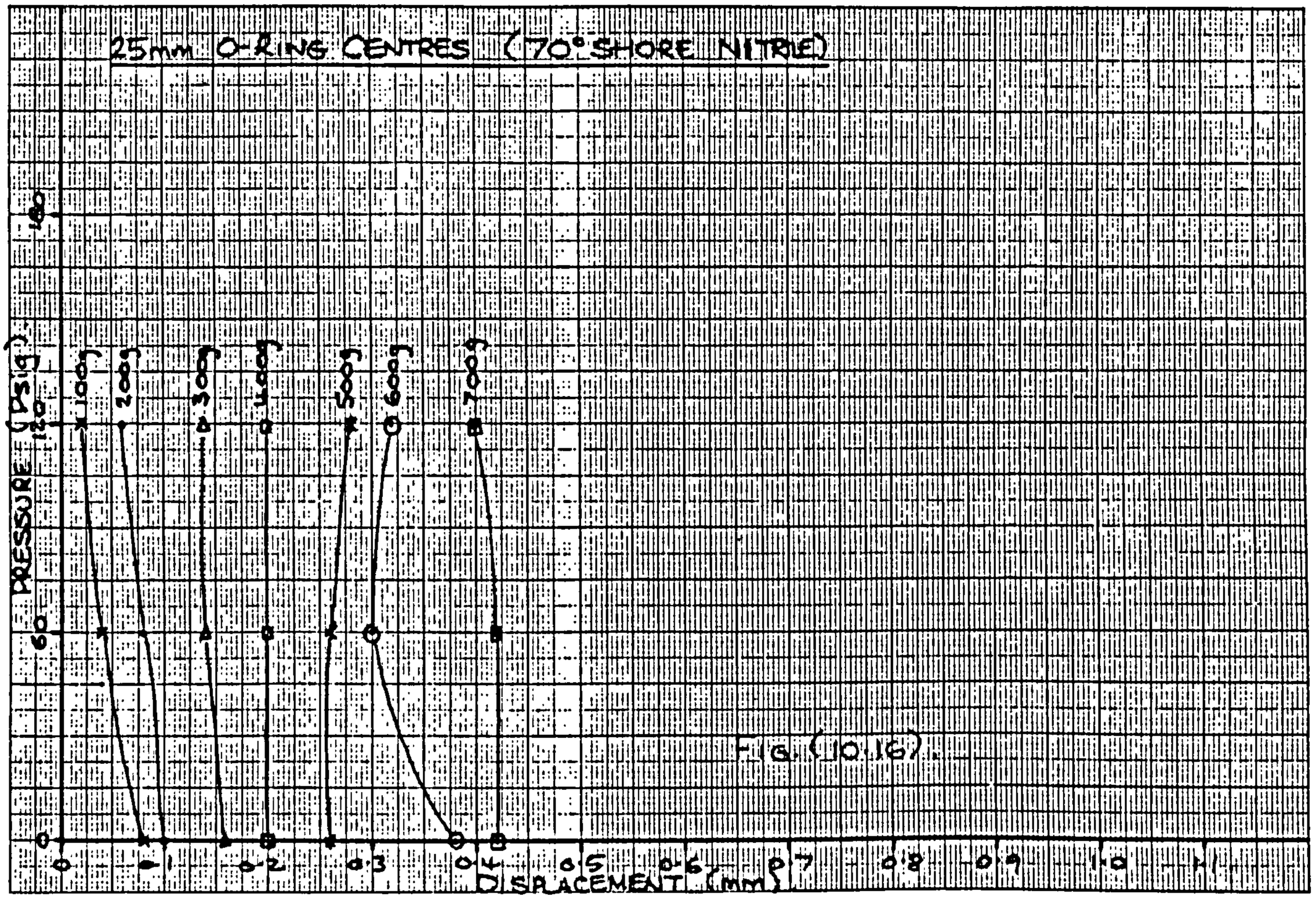

FIG. (10.16).

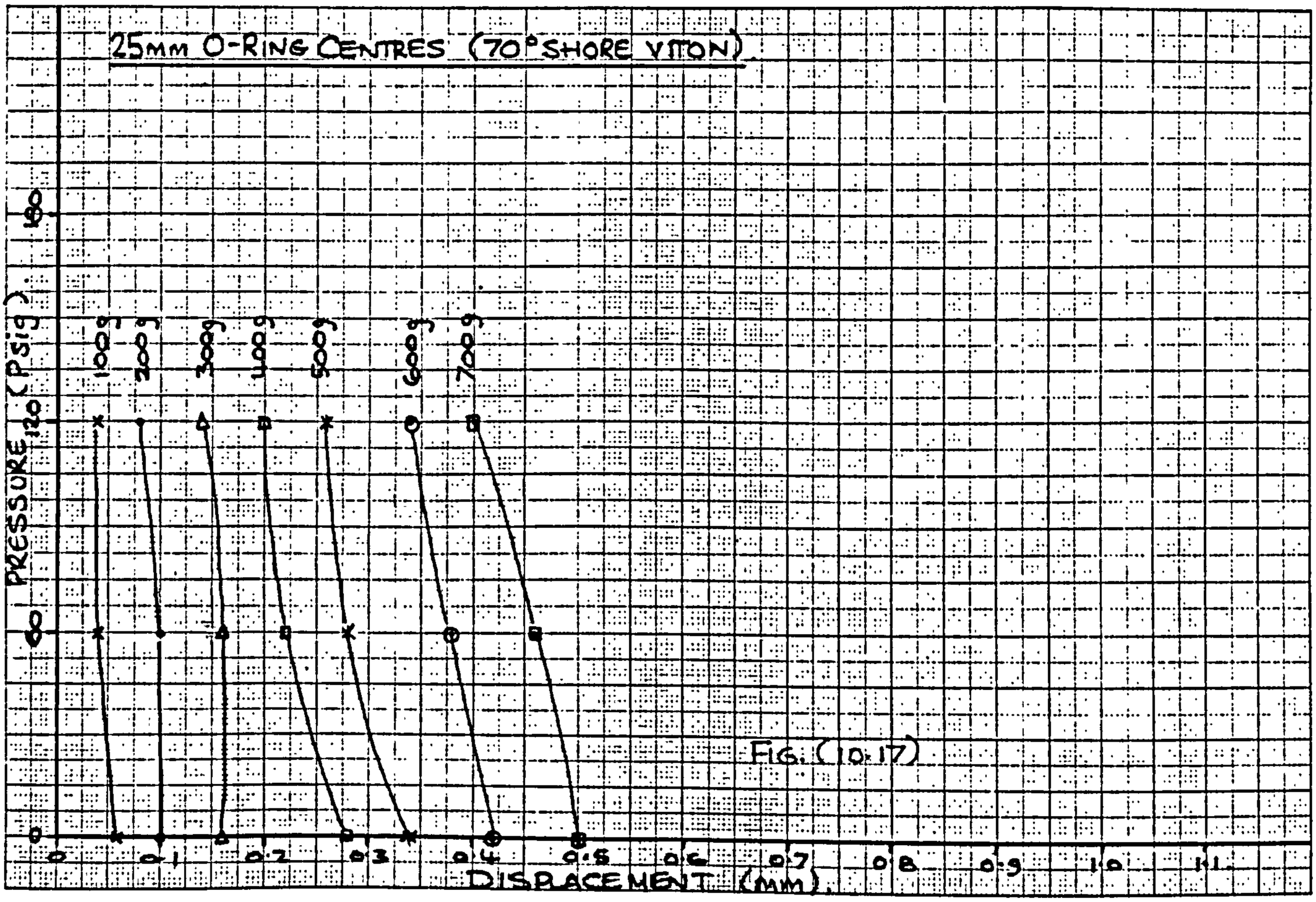

FIG. (10.17)

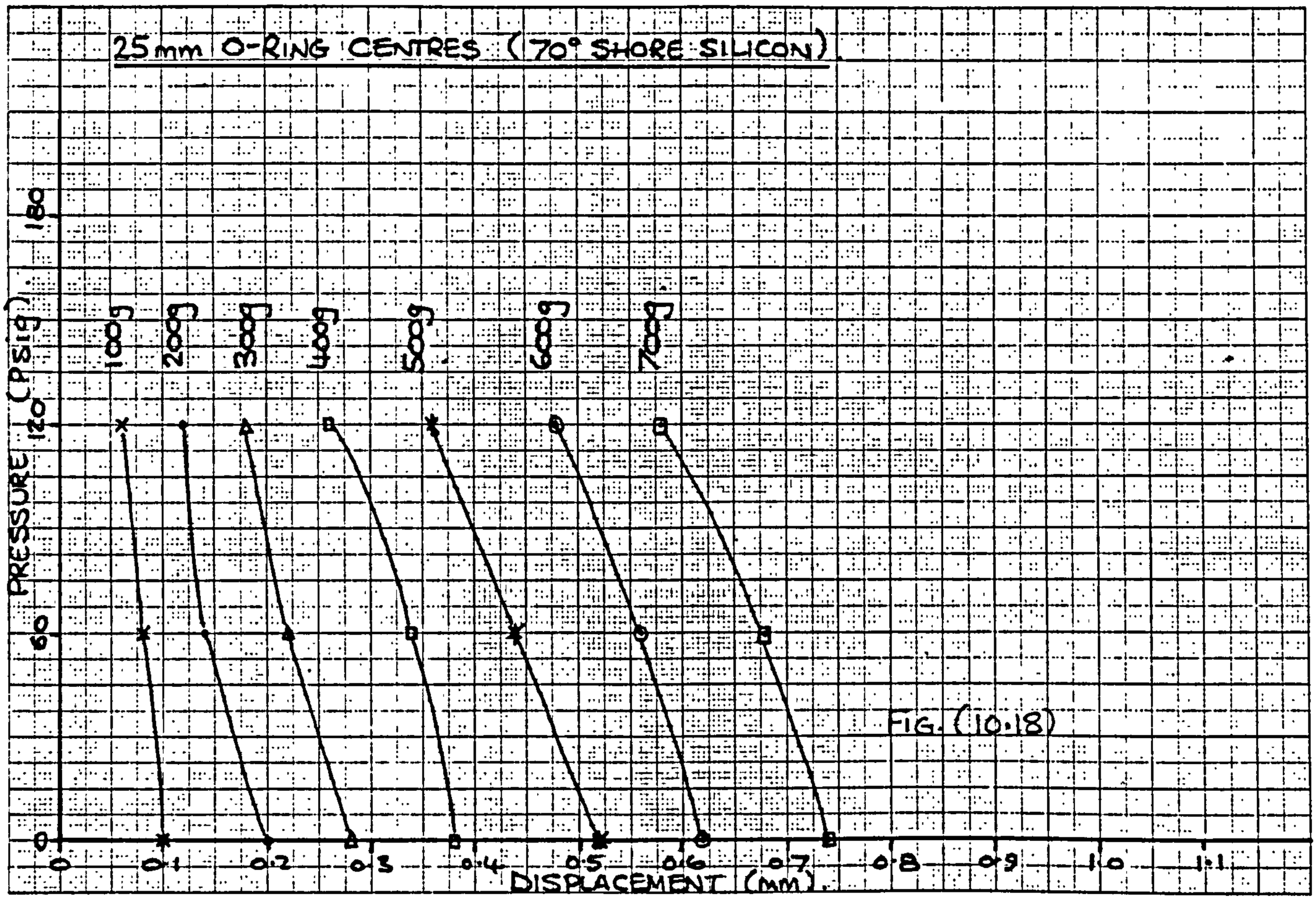

FIG. (10.18)

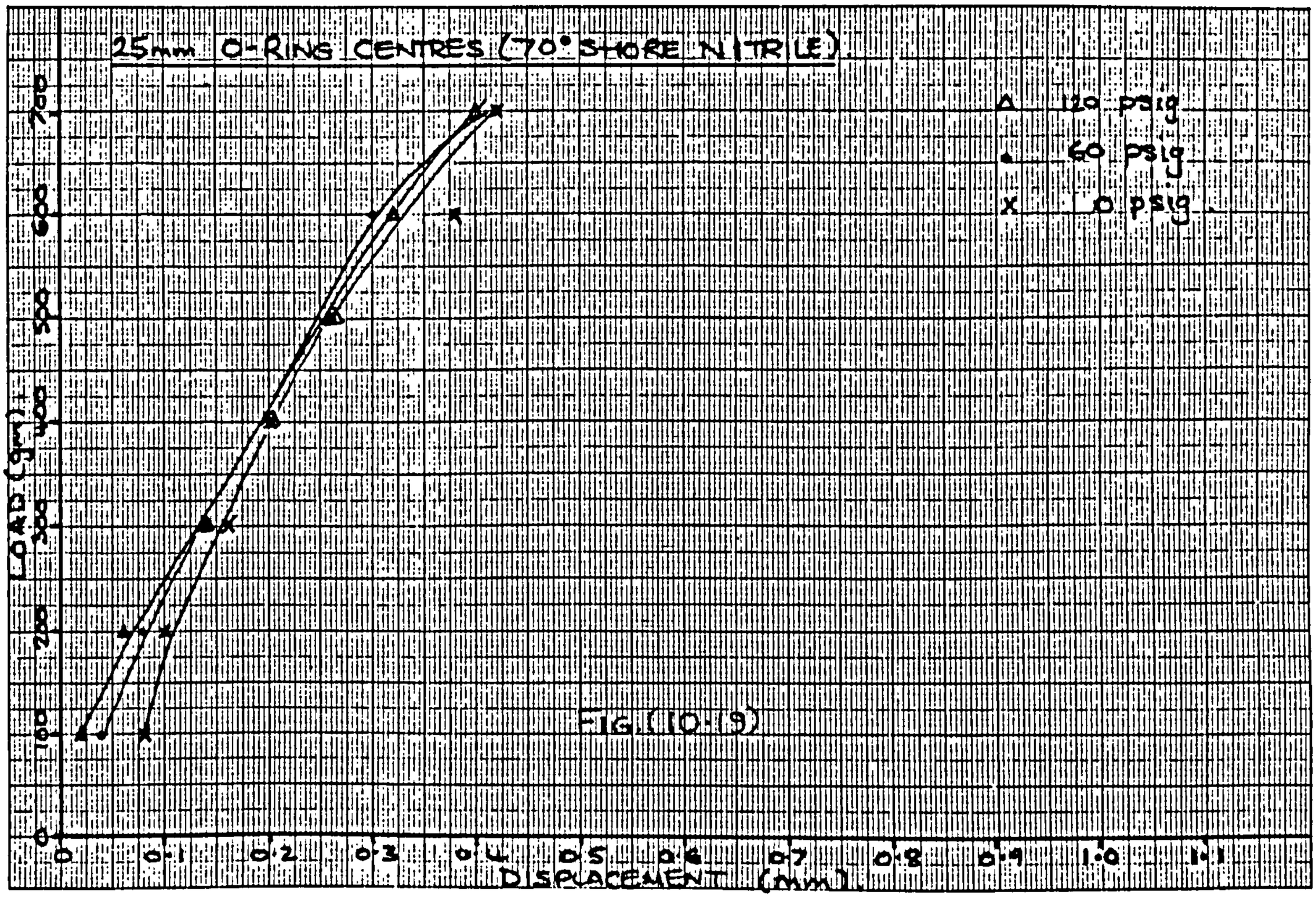

FIG. (10.19)

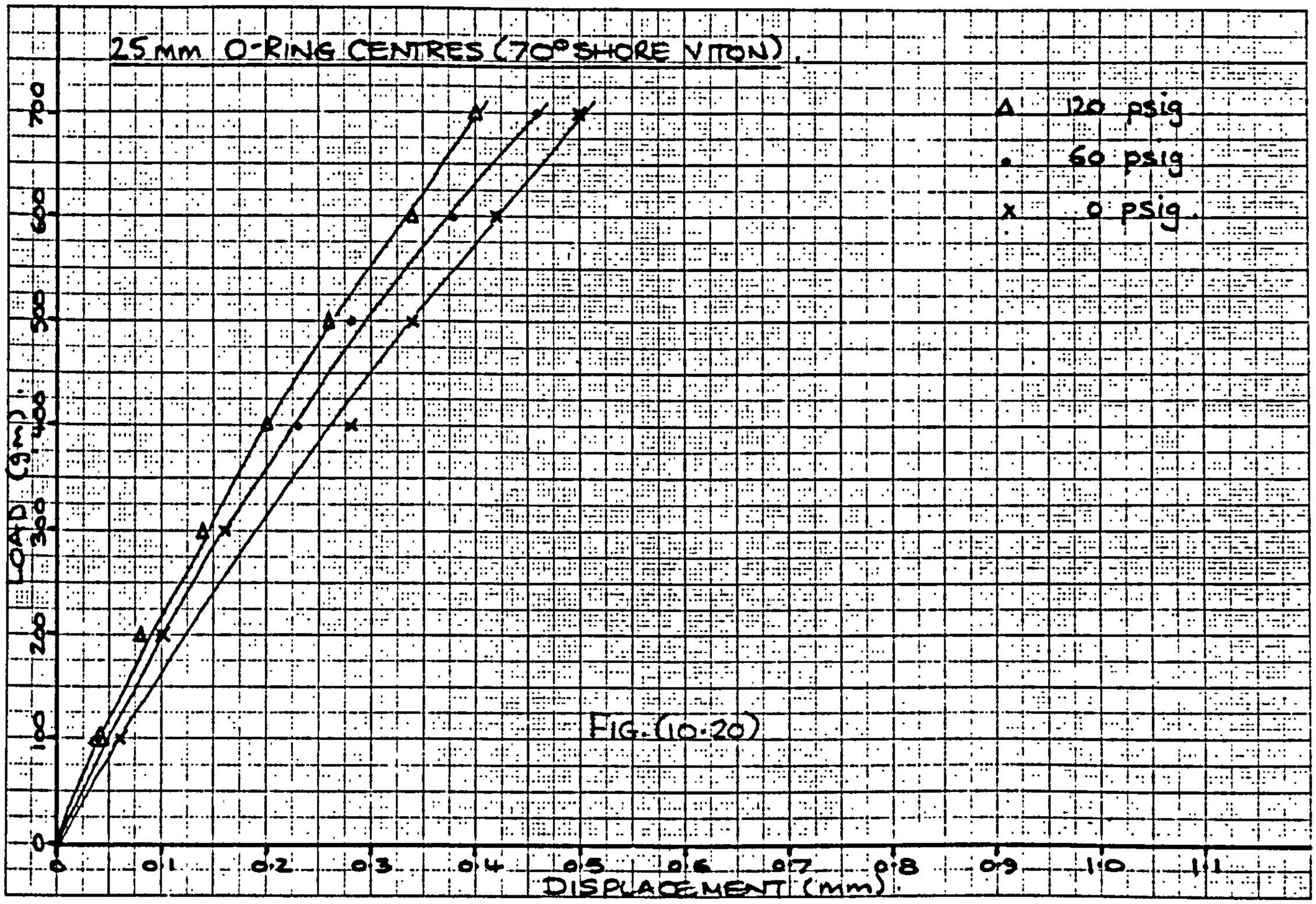

FIG. (10·20)

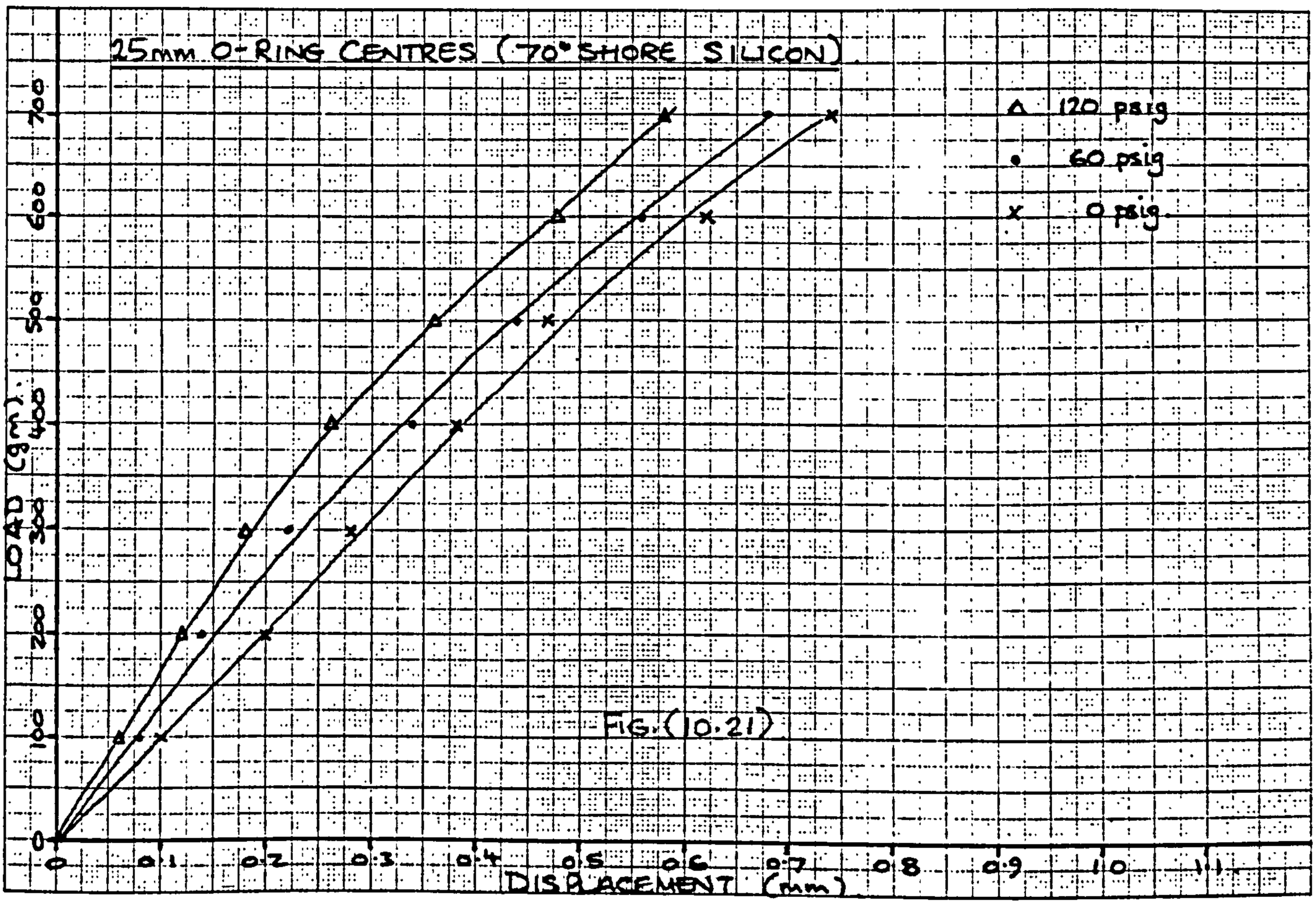

FIG. (10·21)

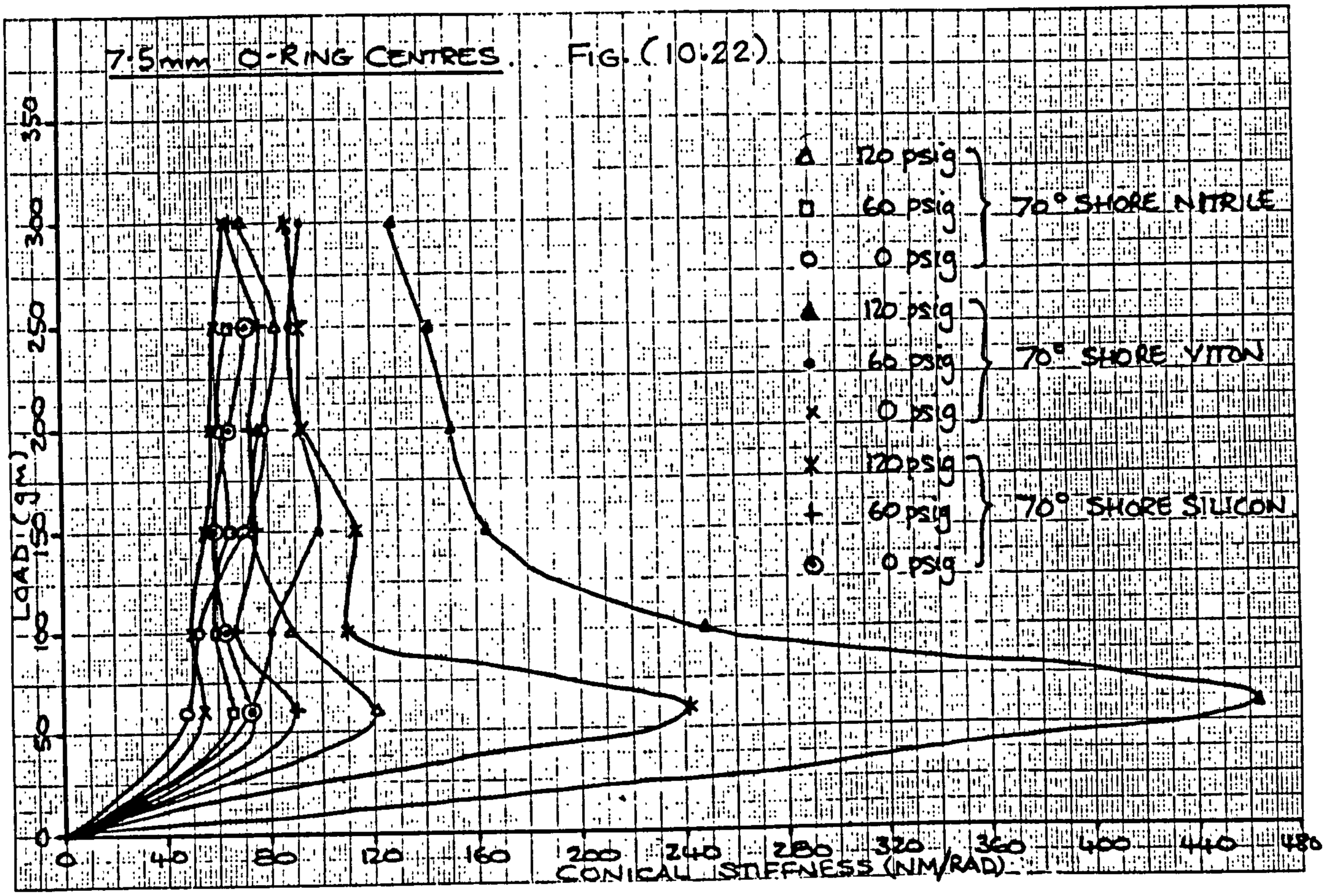
7·5mm O-RING CENTRES.
FIG. (10·22)
120 psig
60 psig
0 psig
70° SHORE NITRILE
120 psig
60 psig
0 psig
70° SHORE VITON
120 psig
60 psig
0 psig
70° SHORE SILICON
LOAD (GM)
0
50
100
150
200
250
300
350
0
40
80
120
160
200
240
280
320
360
400
440
480
CONICAL STIFFNESS (NM/RAD)

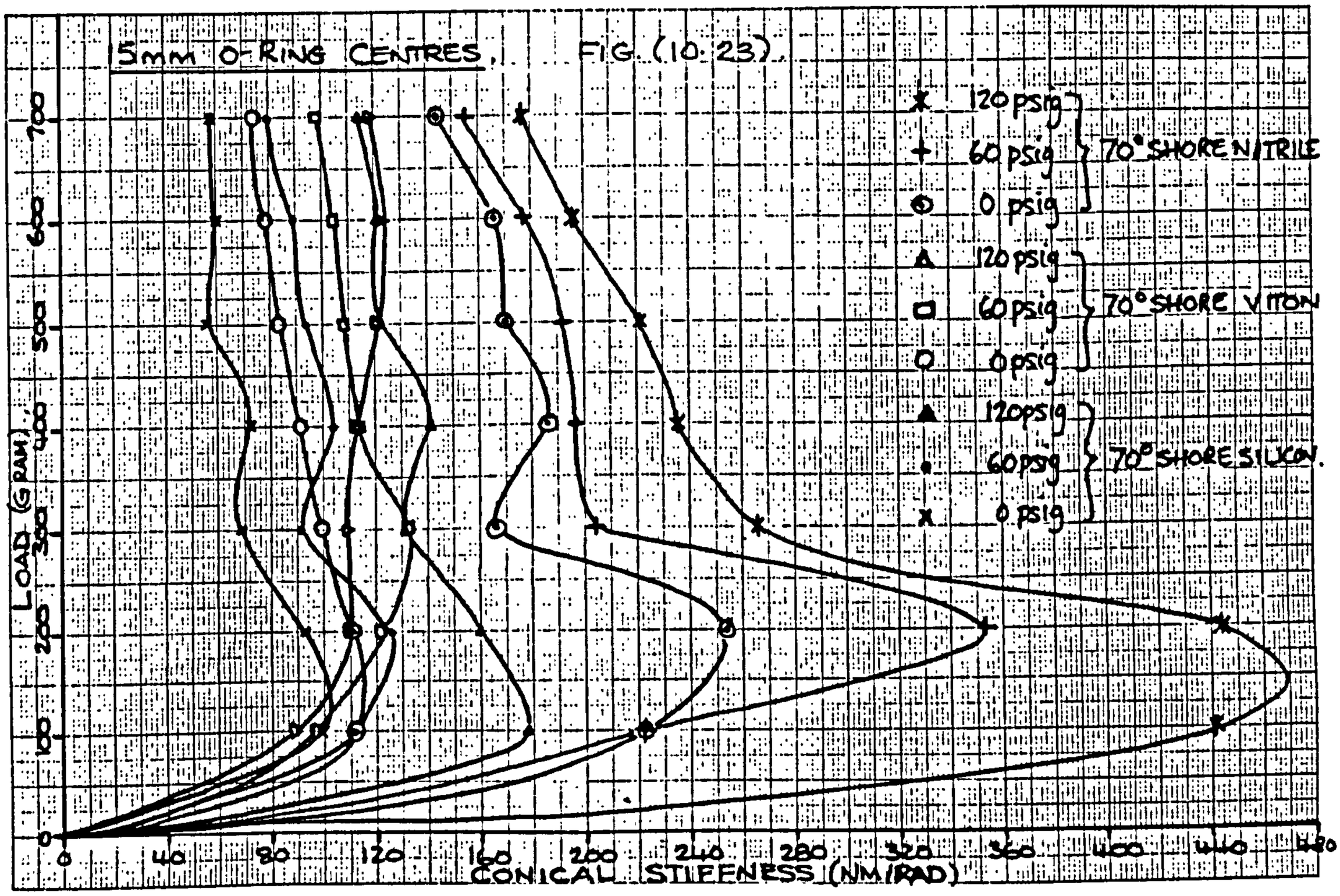
5mm O-RING CENTRES.
FIG. (10·23)
120 psig
60 psig
0 psig
70° SHORE NITRILE
120 psig
60 psig
0 psig
70° SHORE VITON
120psig
60psig
0 psig
70° SHORE SILICON.
LOAD (GRAM)
0
100
200
300
400
500
600
700
0
40
80
120
160
200
240
280
320
360
400
440
480
CONICAL STIFFNESS (NM/RAD)

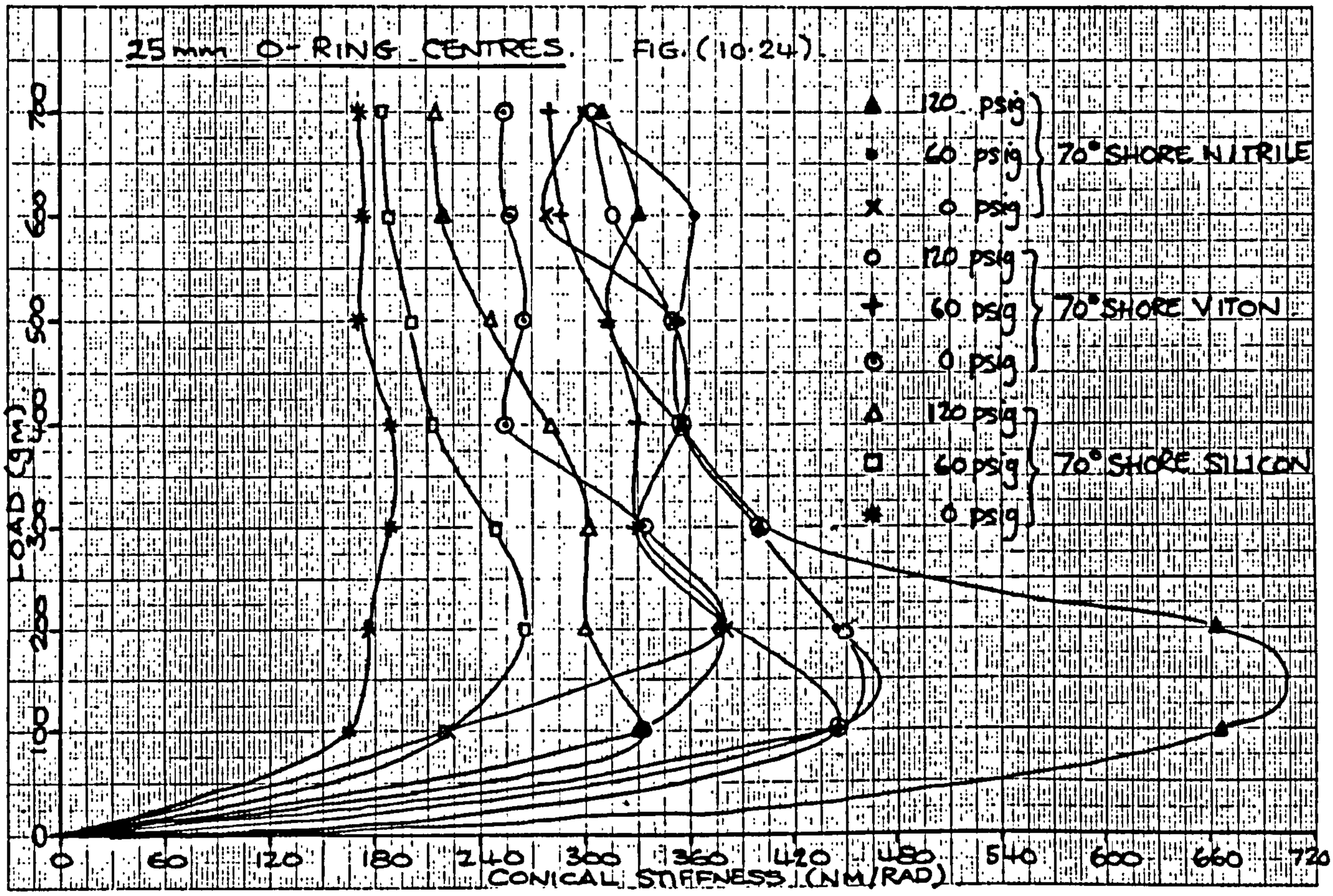
25 mm O-RING CENTRES.
FIG. (10·24)
120 psig
60 psig
0 psig
70° SHORE NITRILE
120 psig
60 psig
0 psig
70° SHORE VITON
120 psig
60 psig
0 psig
70° SHORE SILICON
LOAD (gm)
0
100
200
300
400
500
600
700
0
60
120
180
240
300
360
420
480
540
600
660
720
CONICAL STIFFNESS (NM/RAD)

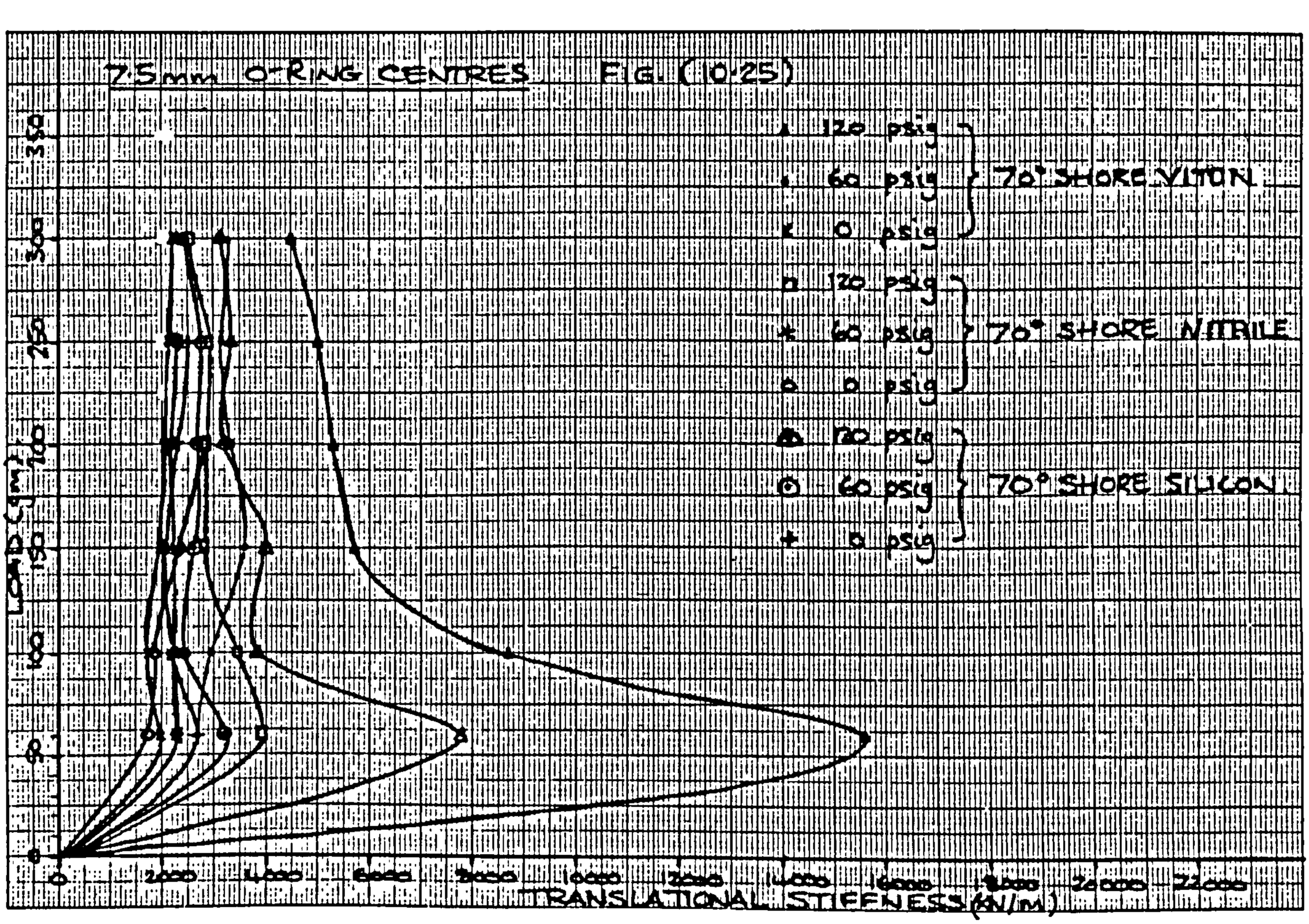
7·5 mm O-RING CENTRES
FIG. (10·25)
120 psig
60 psig
0 psig
70° SHORE VITON
120 psig
60 psig
0 psig
70° SHORE NITRILE
120 psig
60 psig
0 psig
70° SHORE SILICON
LOAD (gm)
0
50
100
150
200
250
300
350
0
2000
4000
6000
8000
10000
12000
14000
16000
18000
20000
22000
TRANSLATIONAL STIFFNESS (KN/M)

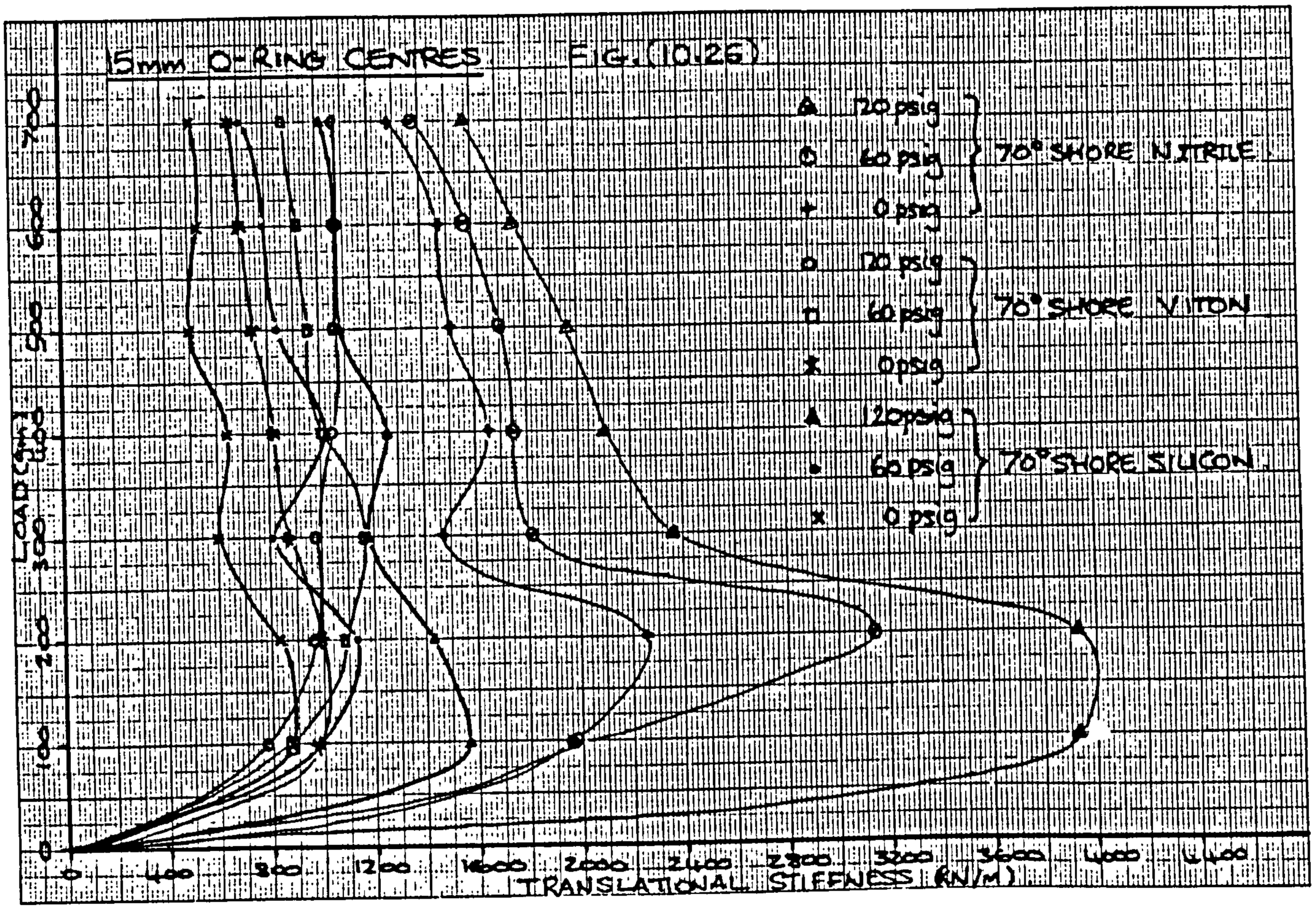
5mm O-RING CENTRES. FIG.(10.26)
LOAD (psig)
0
100
200
300
400
500
600
700
800
0
400
800
1200
1600
2000
2400
2800
3200
3600
4000
4400
TRANSLATIONAL STIFFNESS (KN/M)
120 psig
60 psig
0 psig
70° SHORE NITRILE.
120 psig
60 psig
0 psig
70° SHORE VITON.
120 psig
60 psig
0 psig
70° SHORE SILICON.

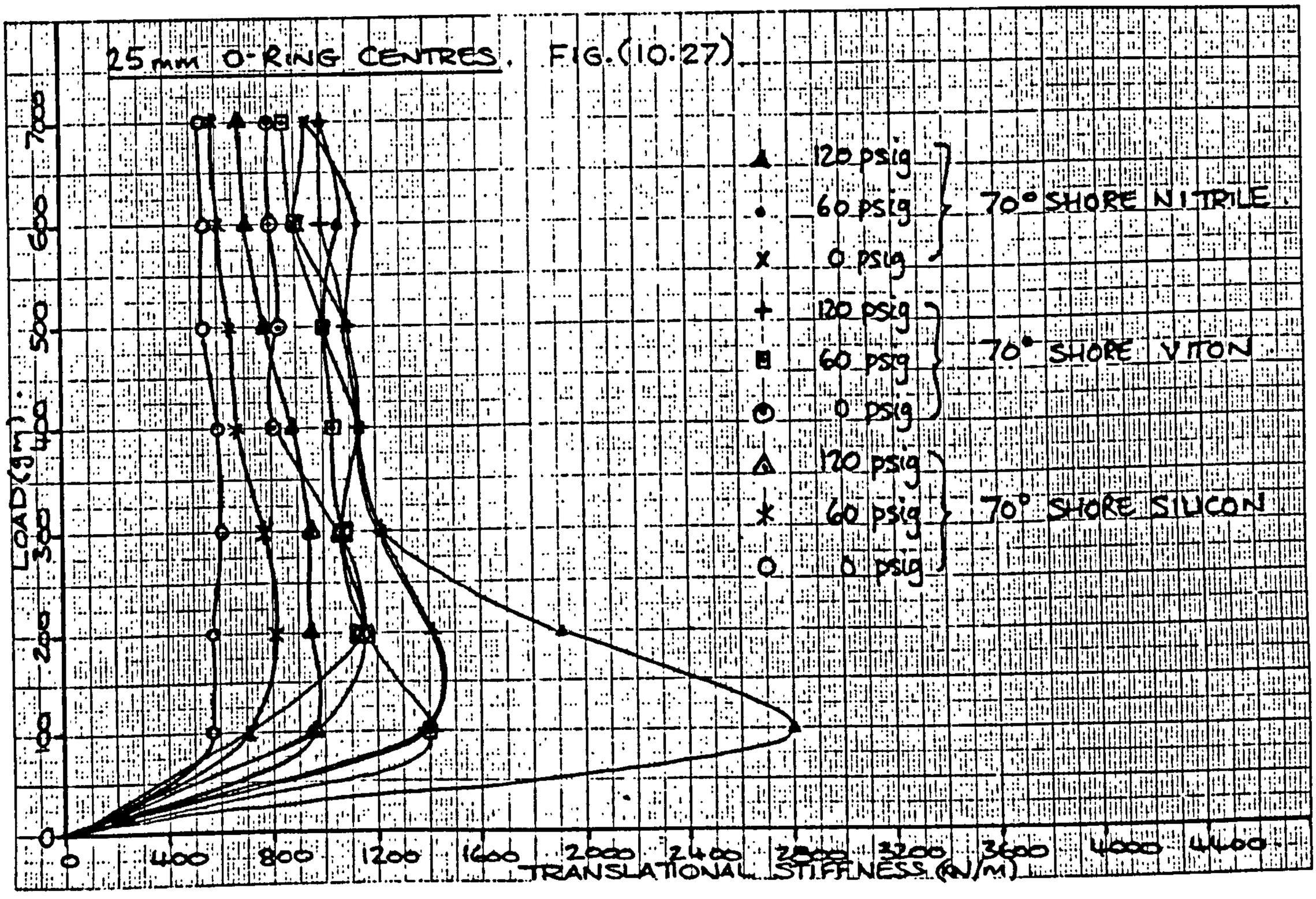
25mm O-RING CENTRES. FIG.(10.27)
LOAD (psig)
0
100
200
300
400
500
600
700
0
400
800
1200
1600
2000
2400
2800
3200
3600
4000
4400
TRANSLATIONAL STIFFNESS (KN/M)
120 psig
60 psig
0 psig
70° SHORE NITRILE.
120 psig
60 psig
0 psig
70° SHORE VITON.
120 psig
60 psig
0 psig
70° SHORE SILICON.

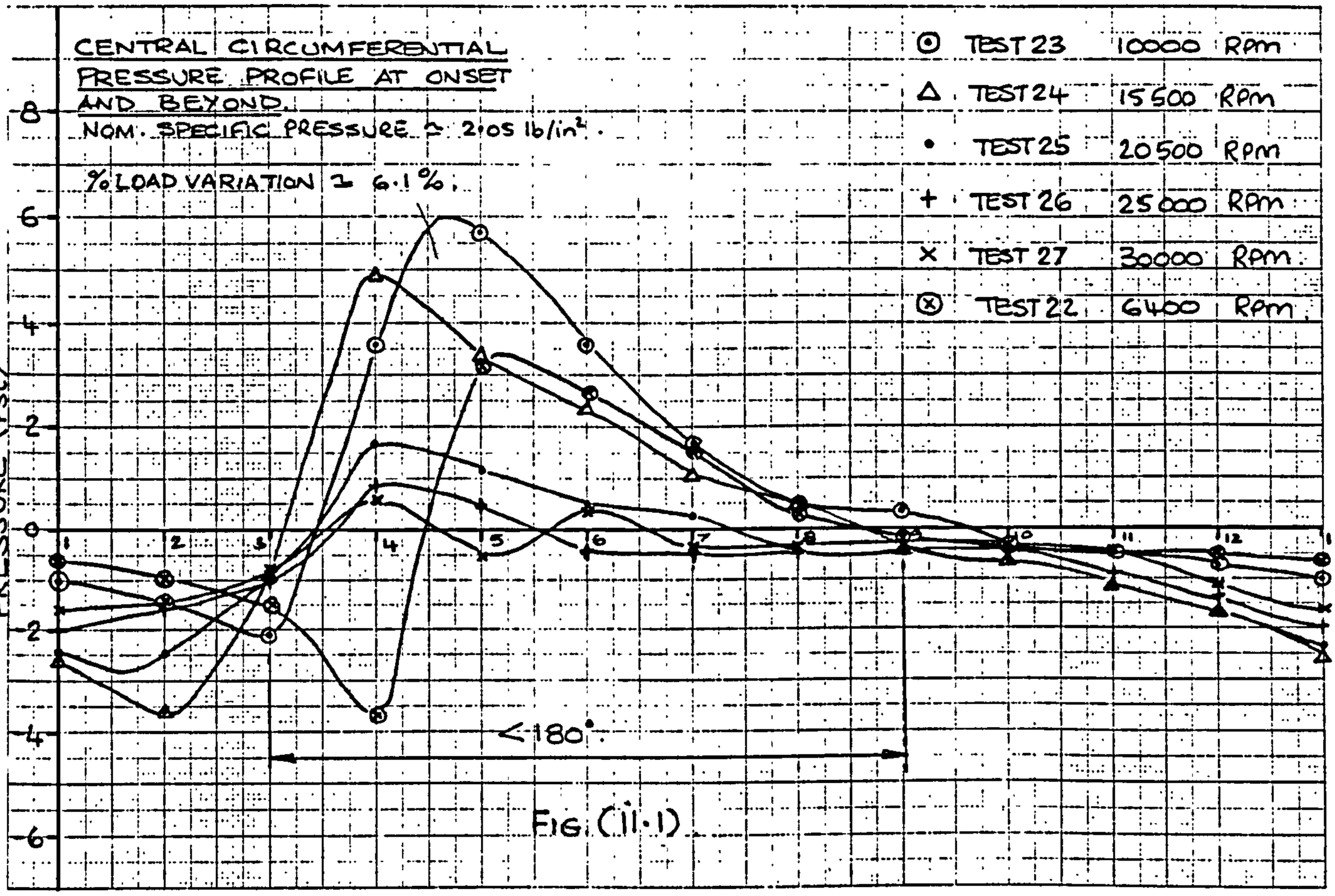

FIG. (11·1)

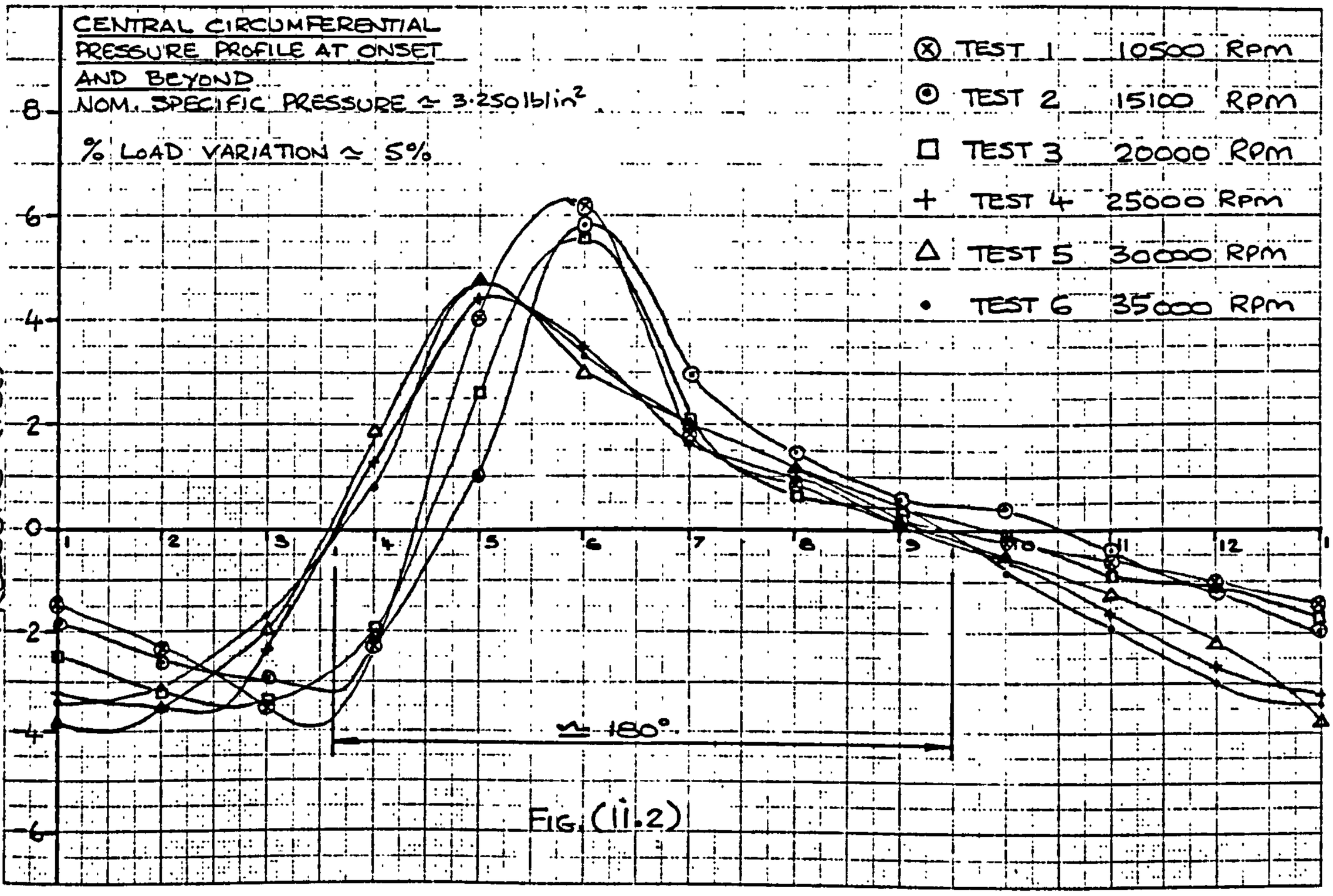

FIG. (11.2)

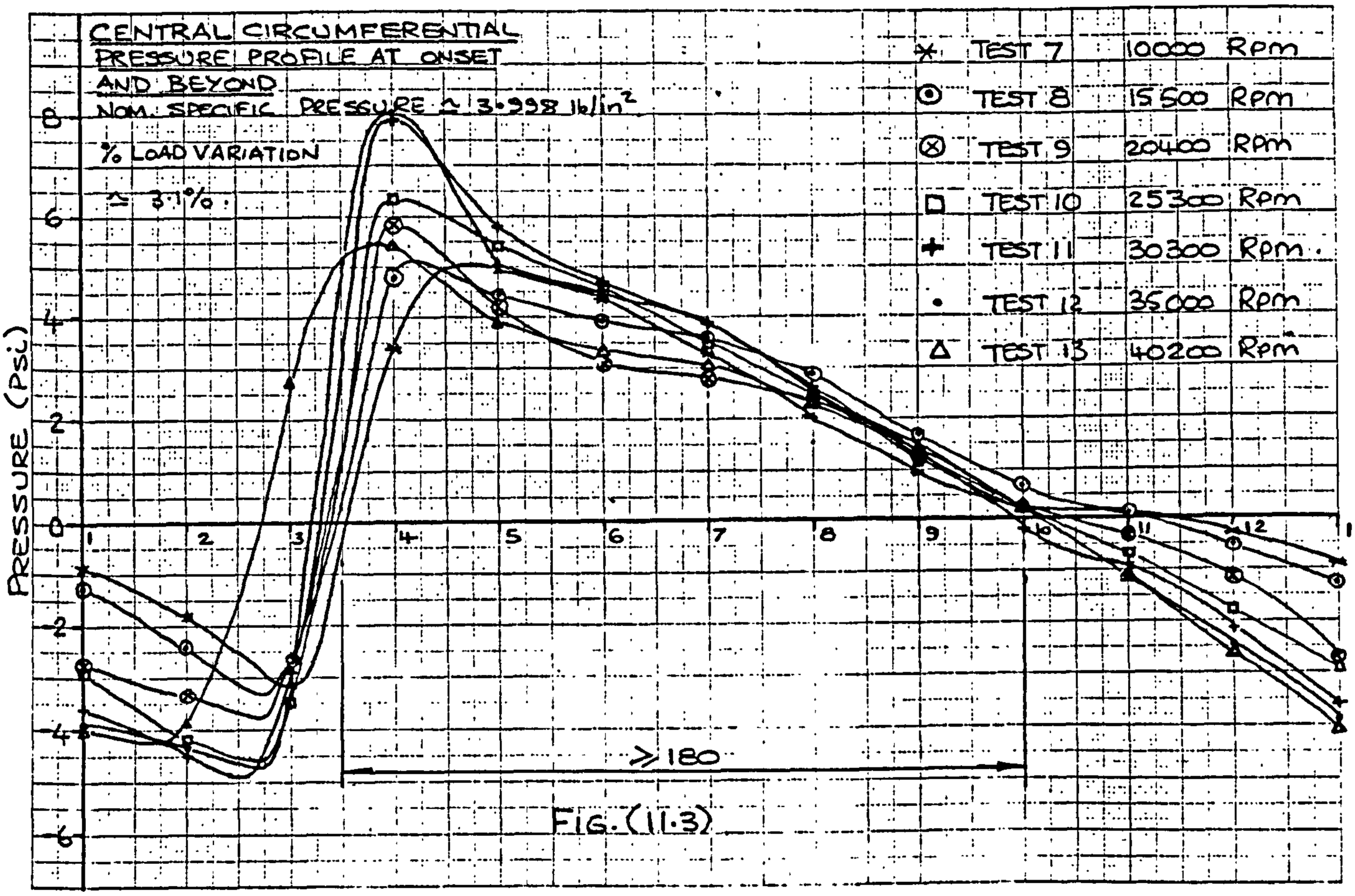

FIG. (11·3)

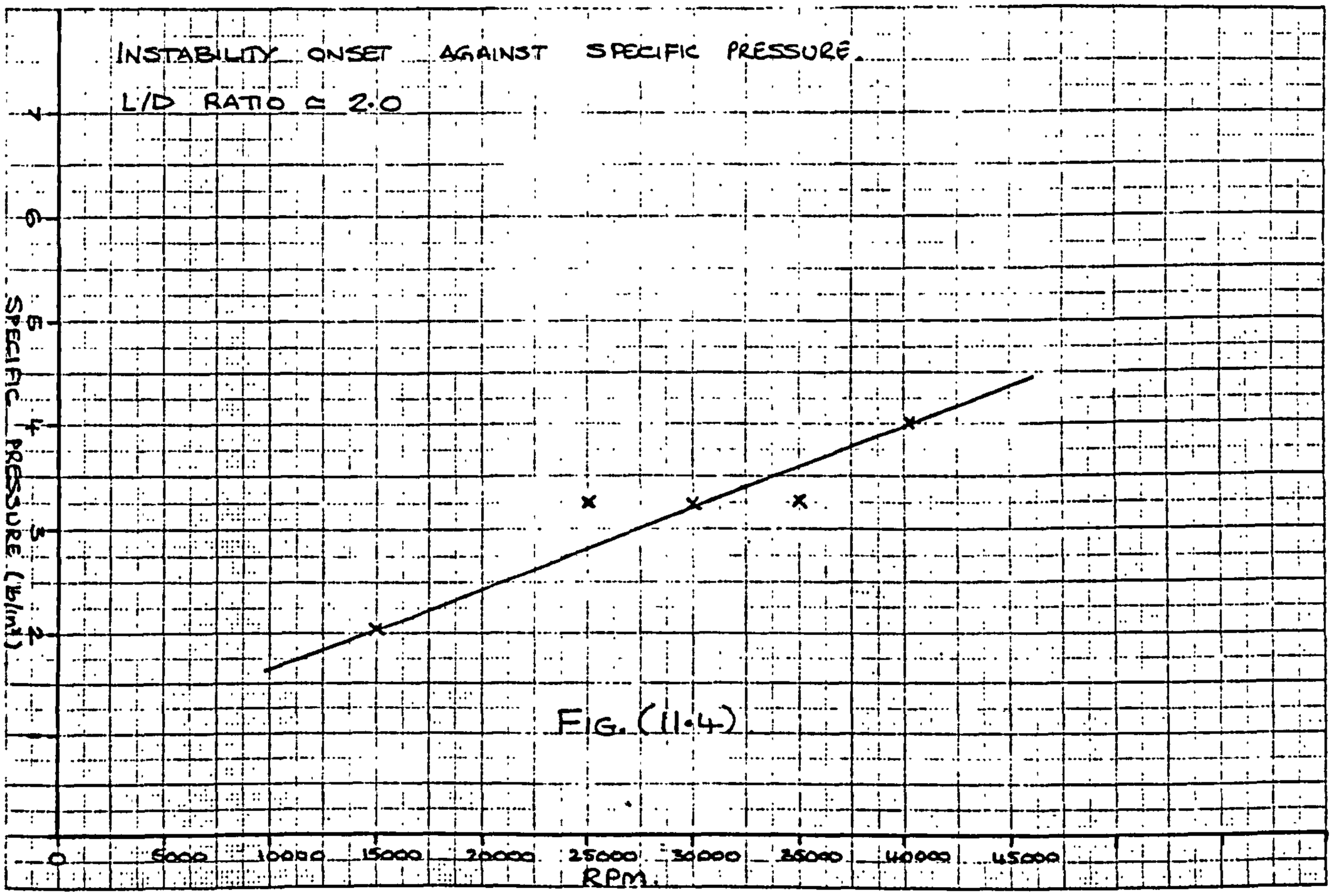

FIG. (11·4)

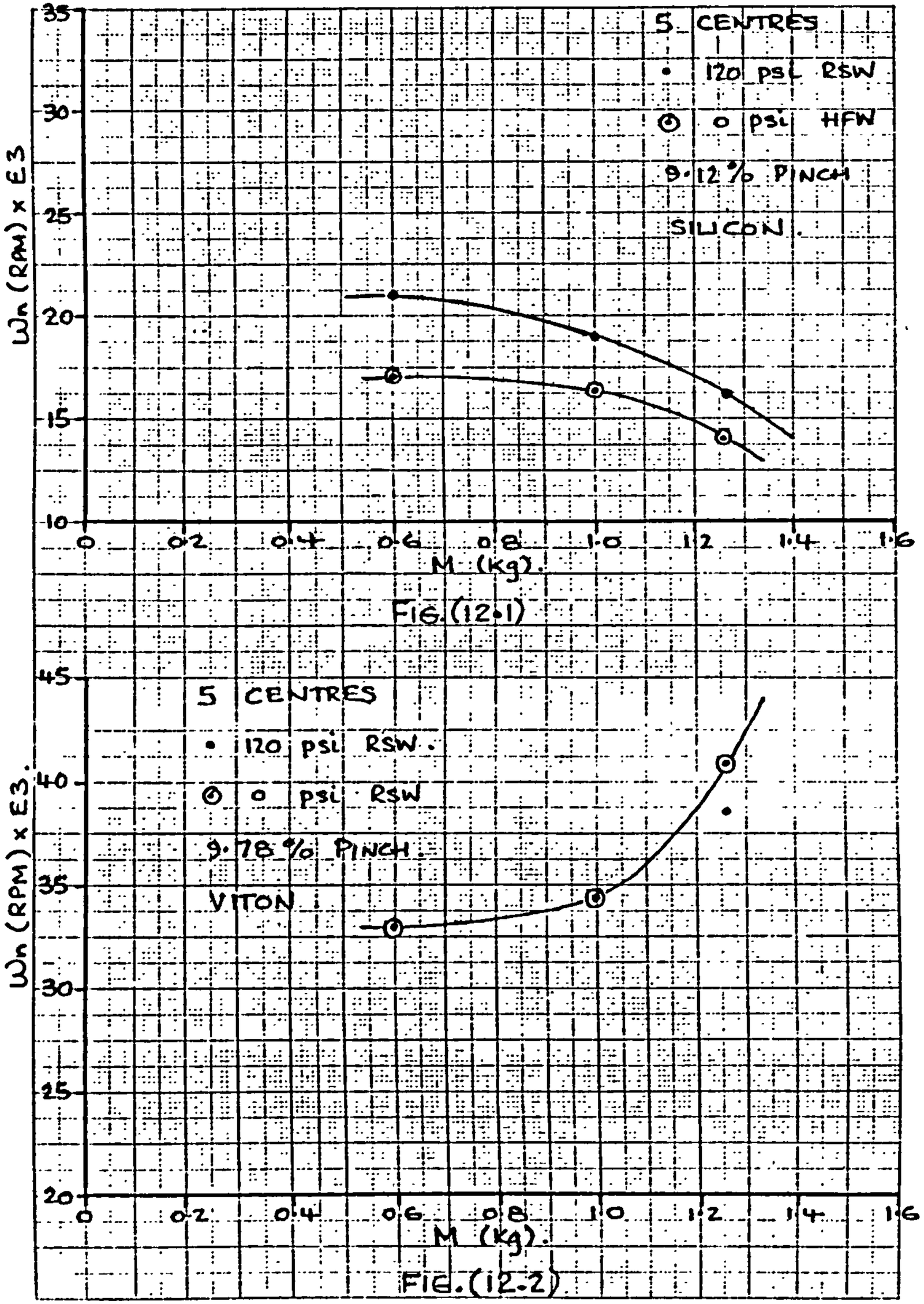

FIG.(12·1)

FIG.(12·2)

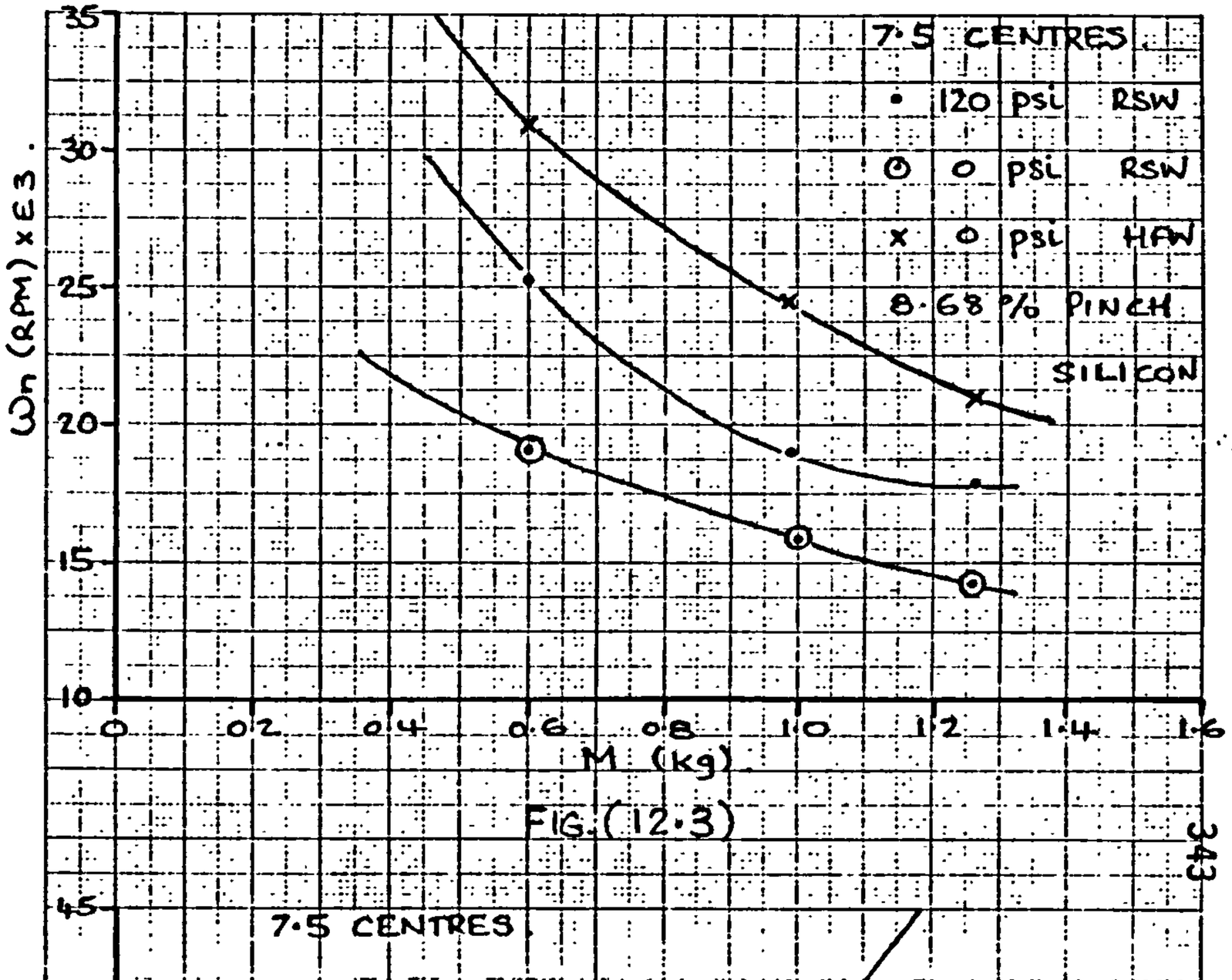

FIG.(12·3)

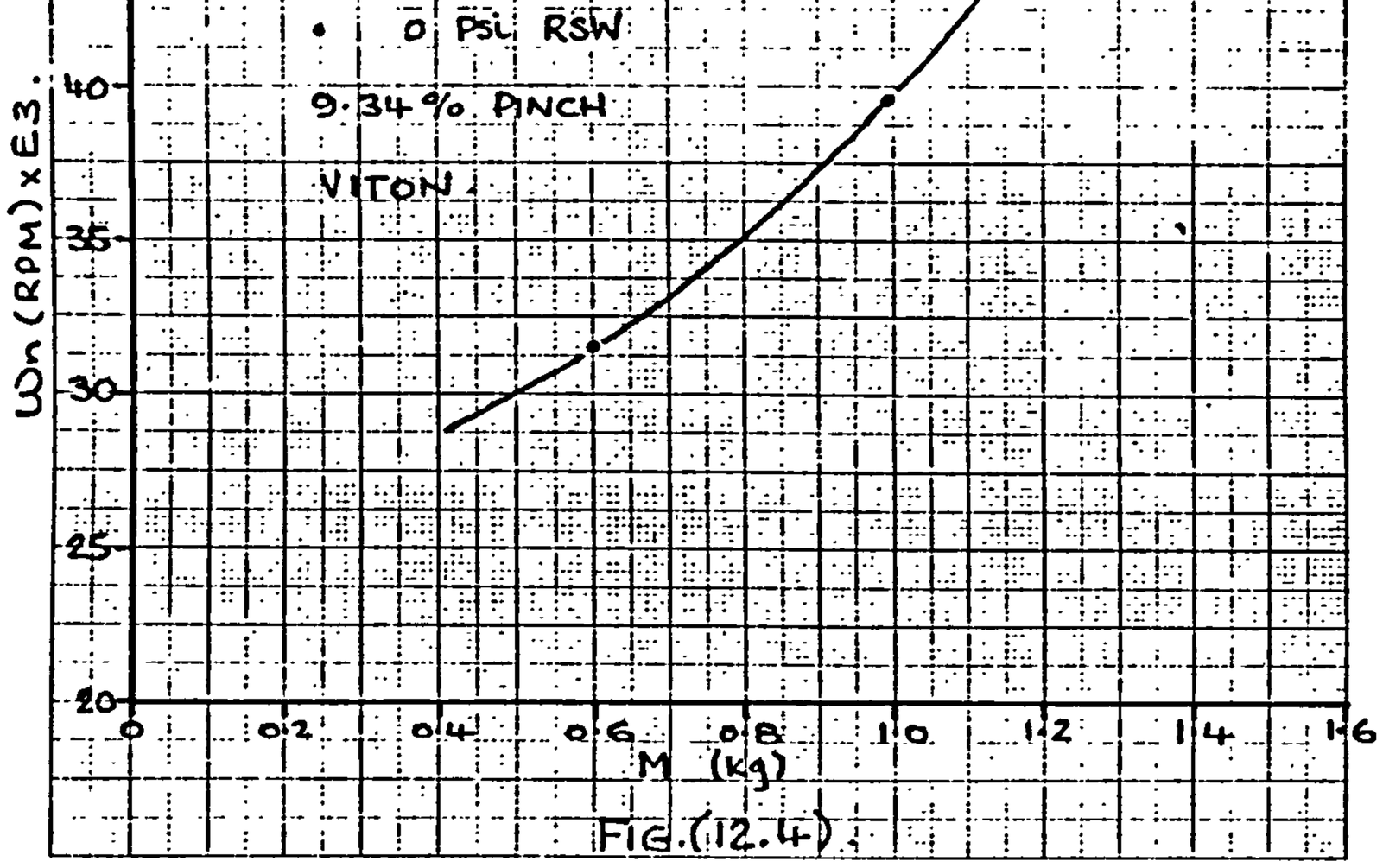

FIG.(12·4)

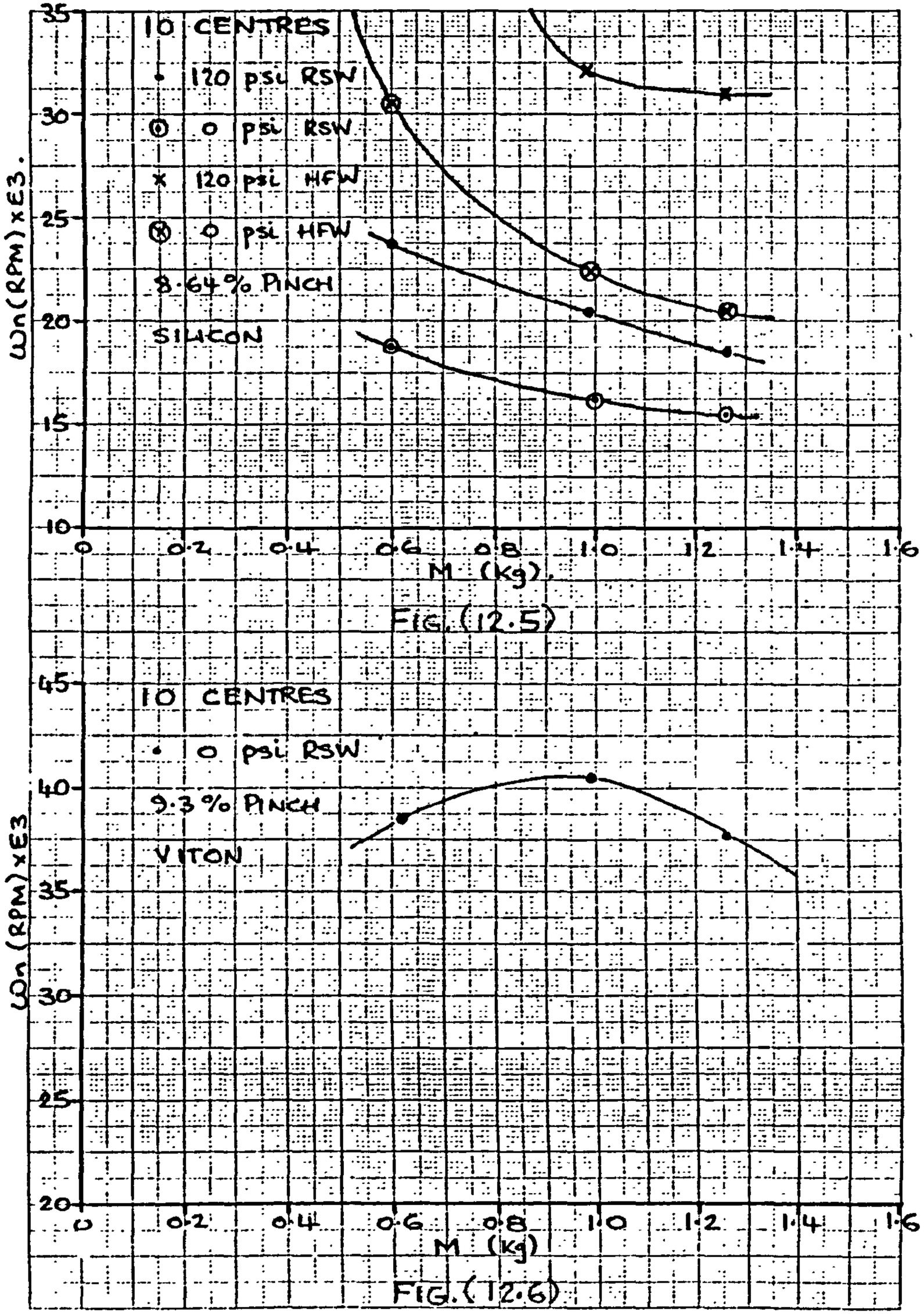

FIG. (12.5)

FIG. (12.6)

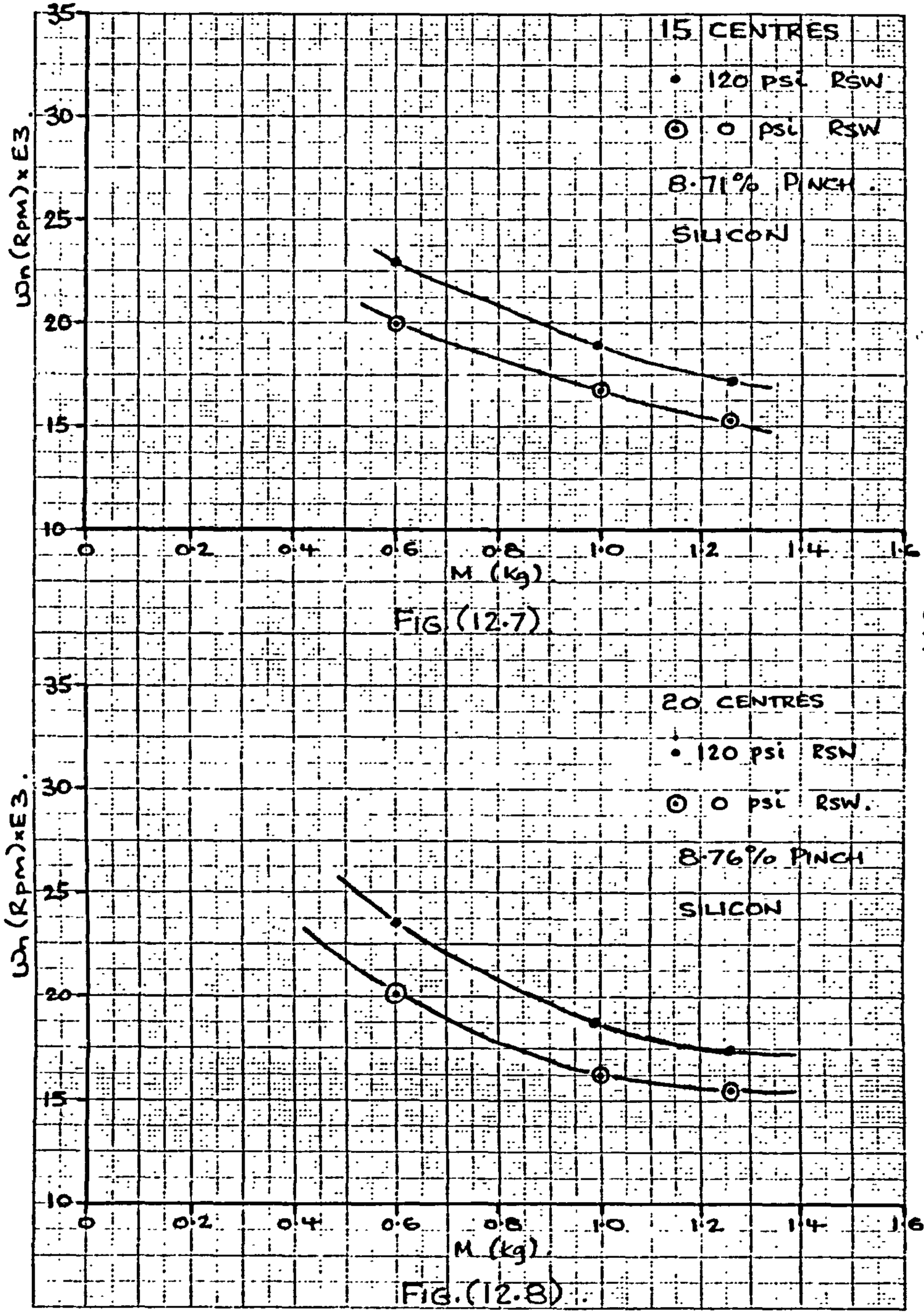

FIG (12.7)

FIG. (12.8)

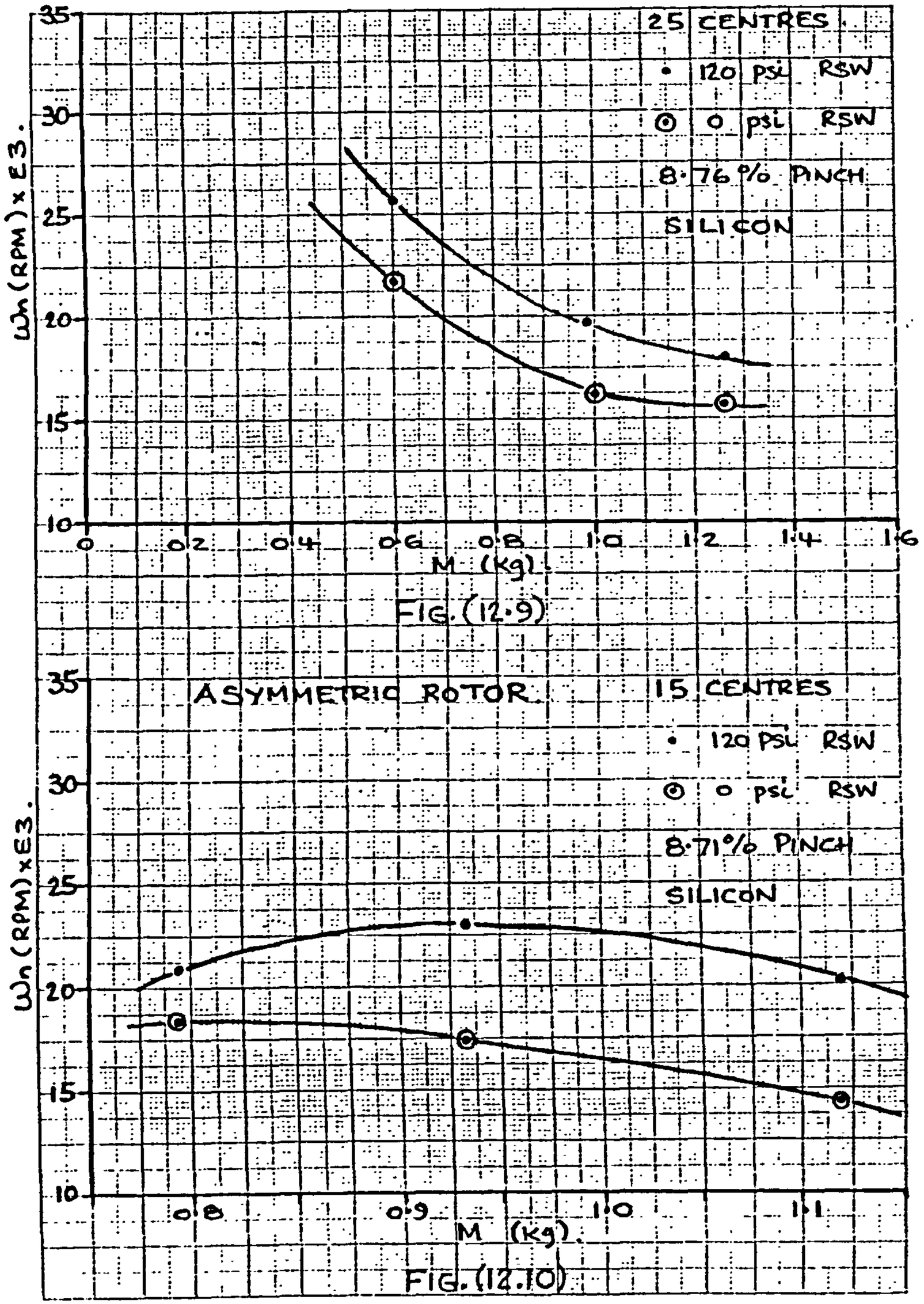

FIG. (12·9)

FIG. (12.10)

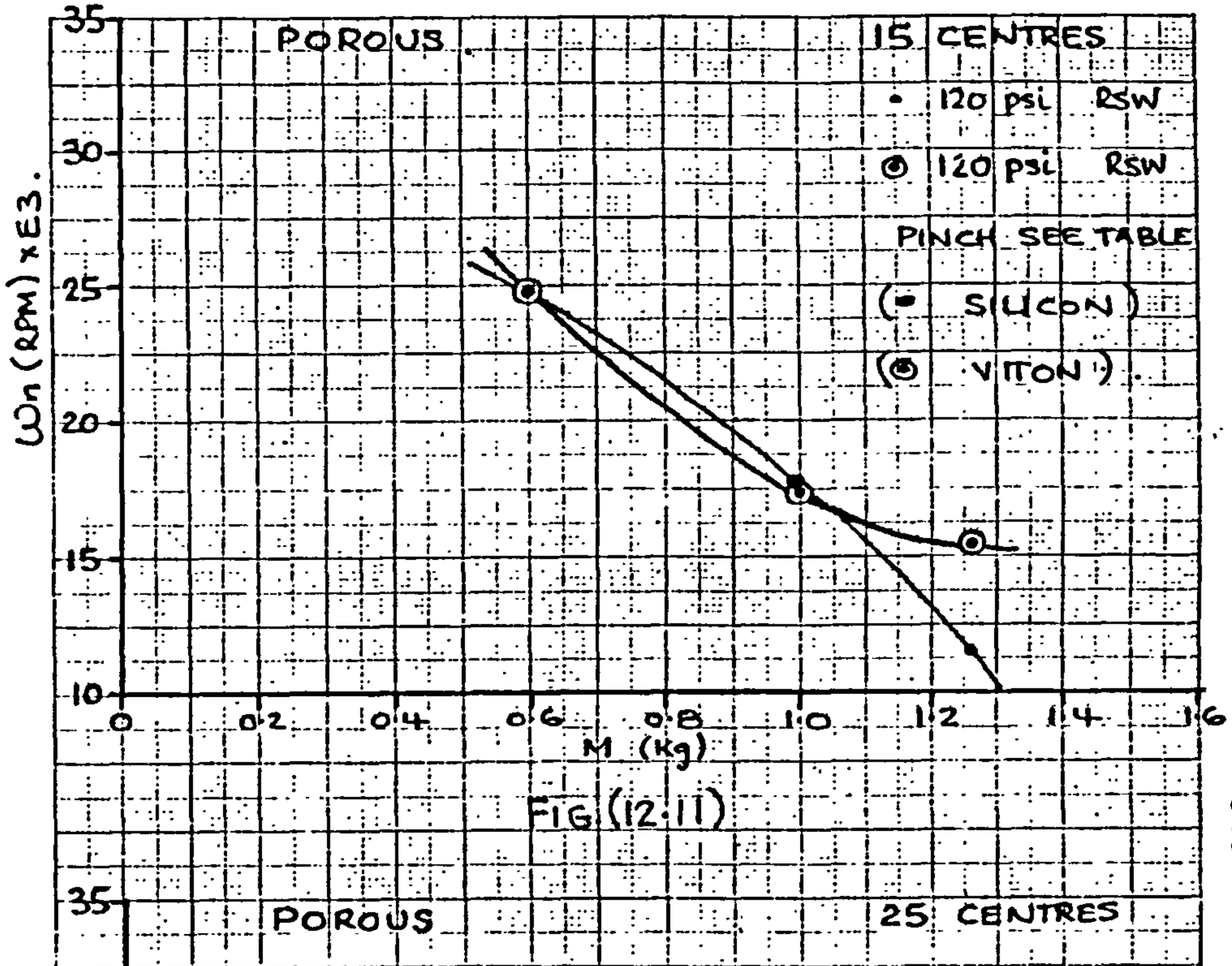

FIG (12·11)

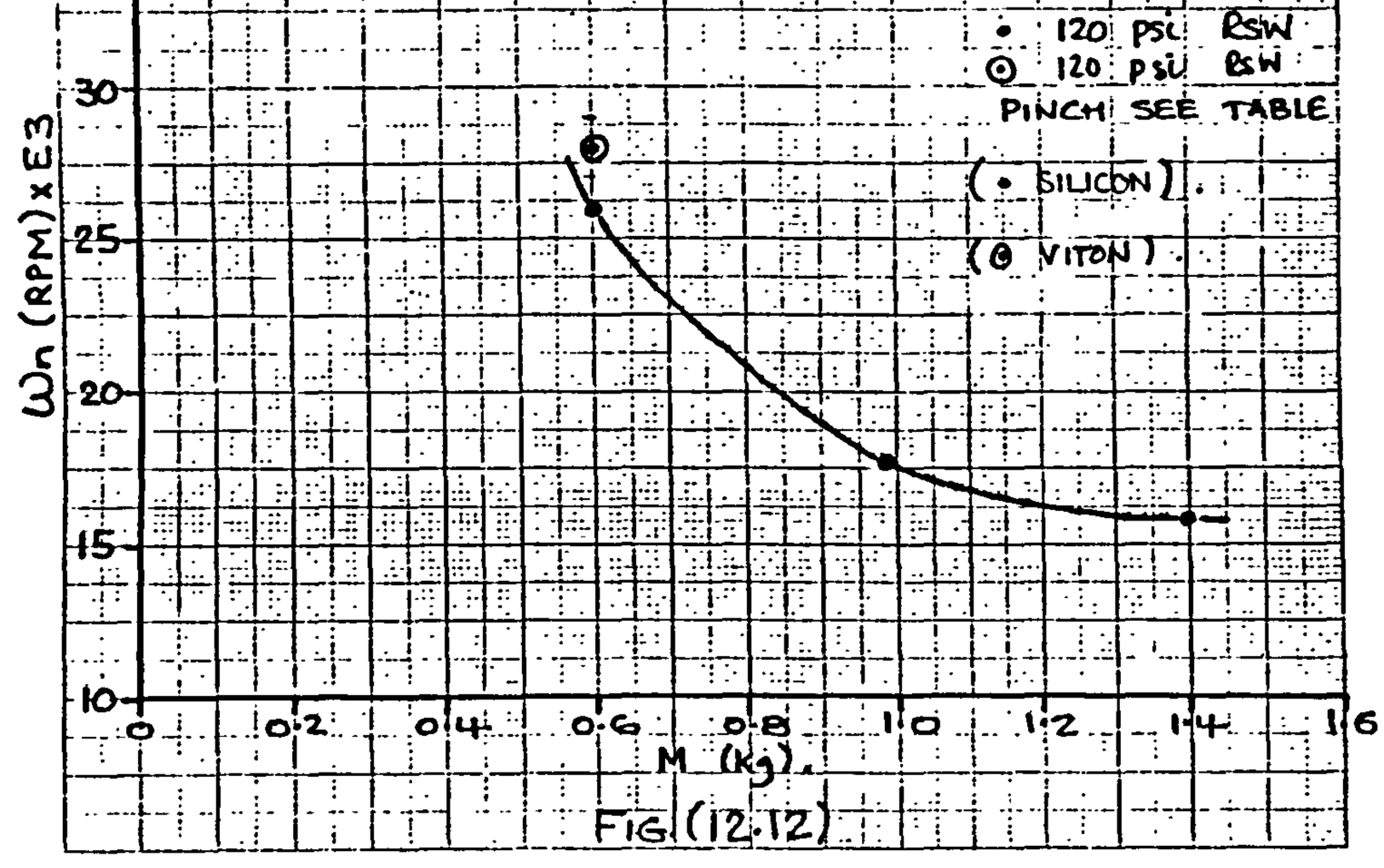

FIG. (12.12)

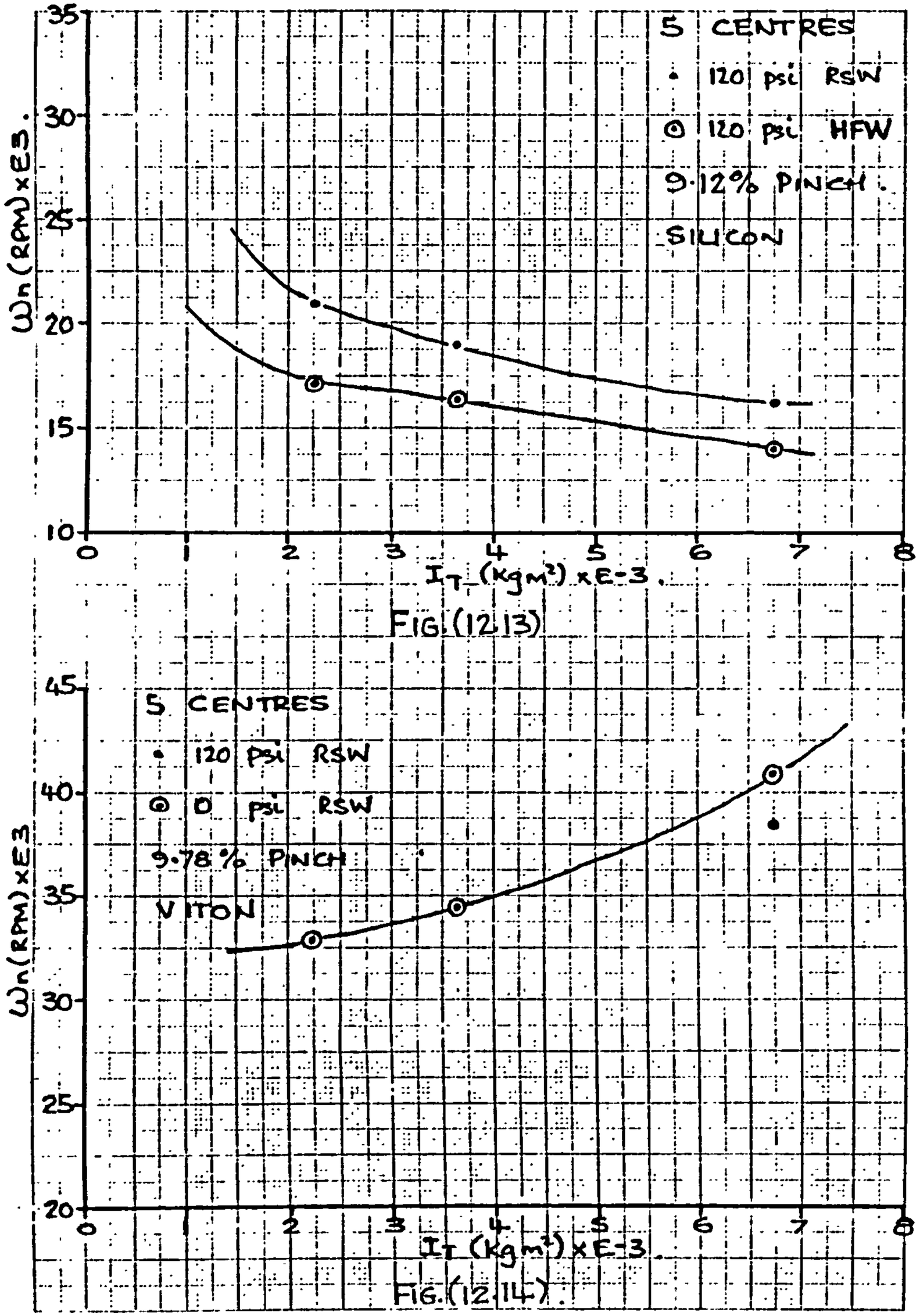

FIG (12.13)

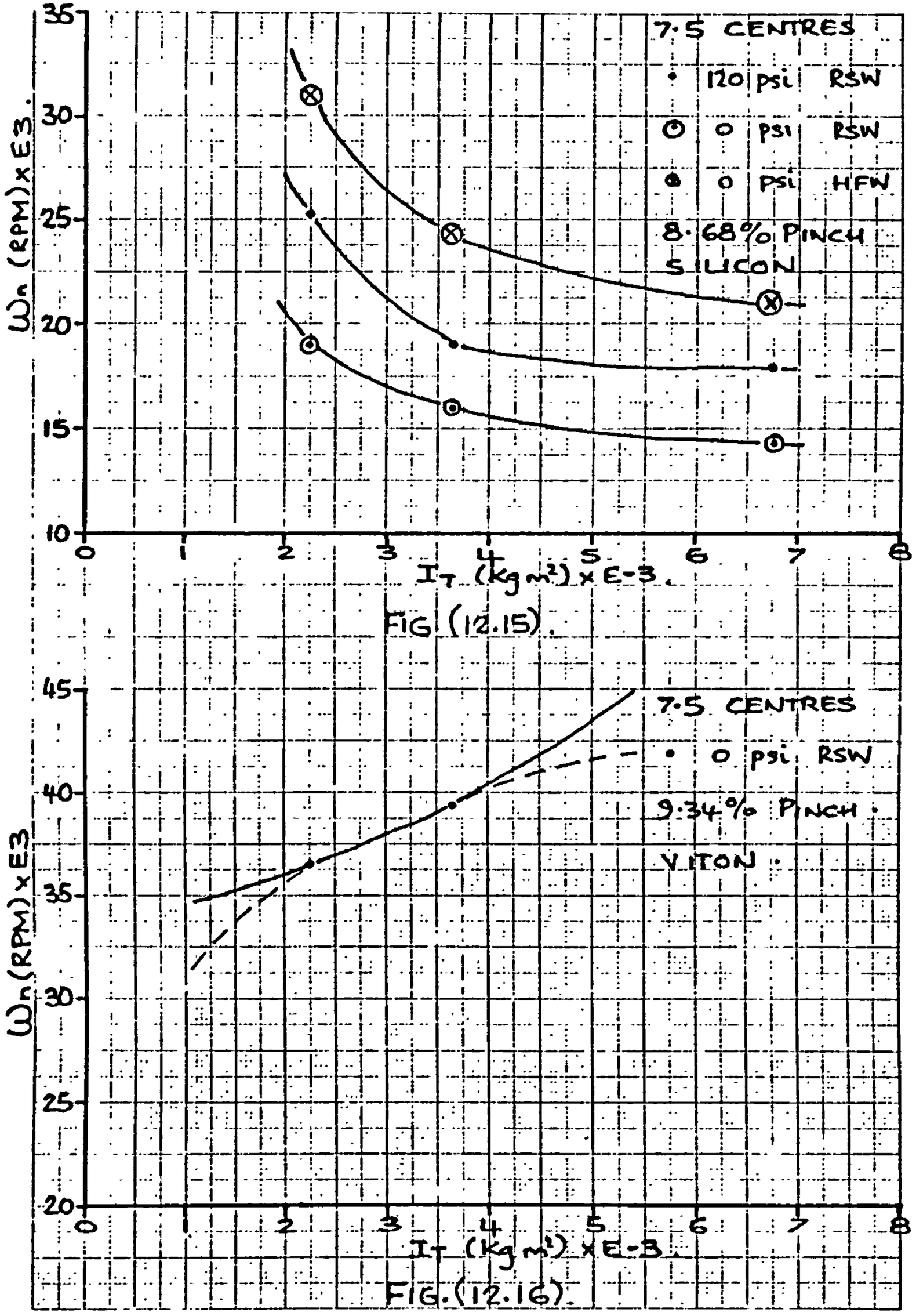

FIG (12.15).

FIG. (12.14).

FIG. (12.16).

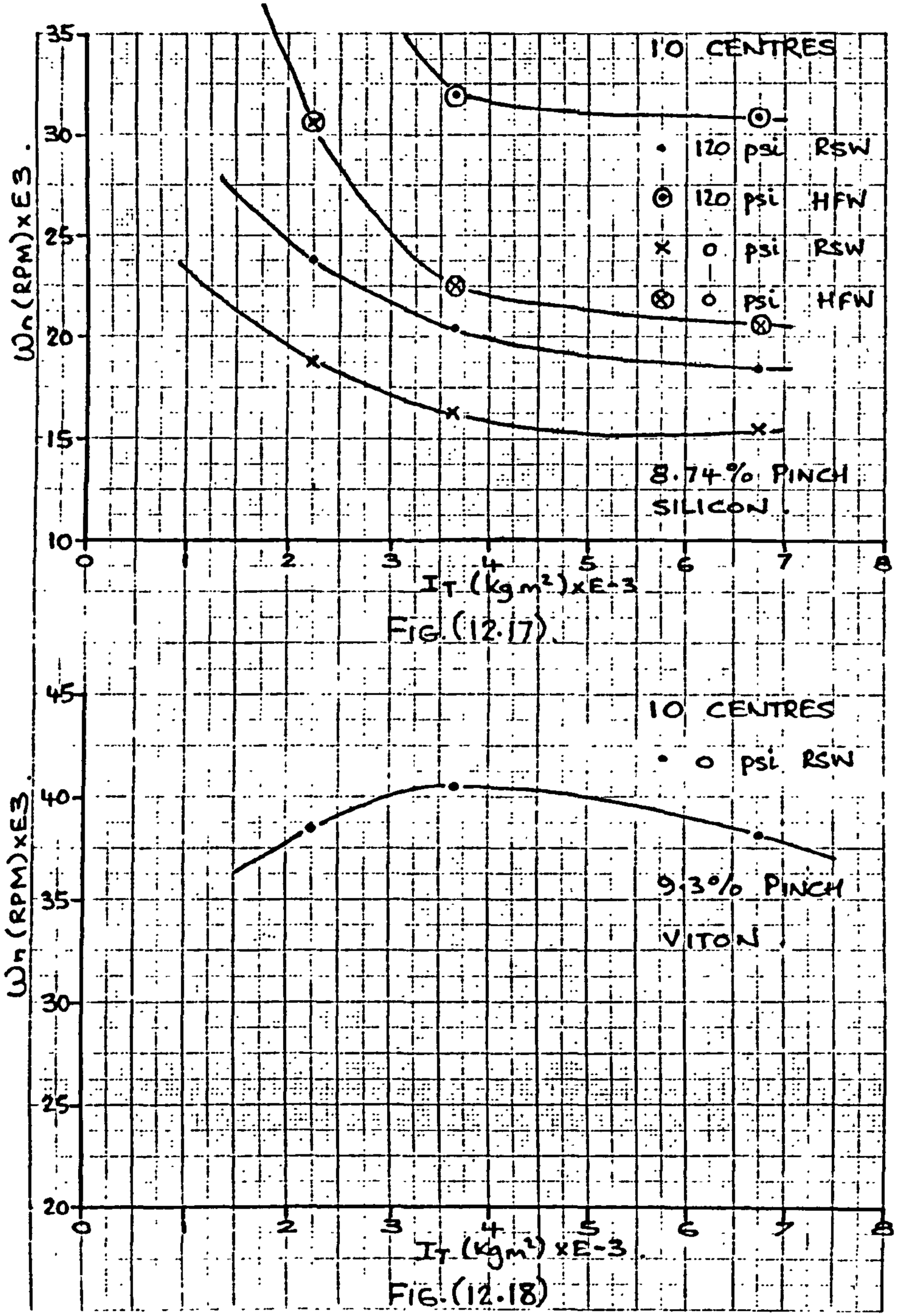

FIG. (12.17).

FIG. (12.18)

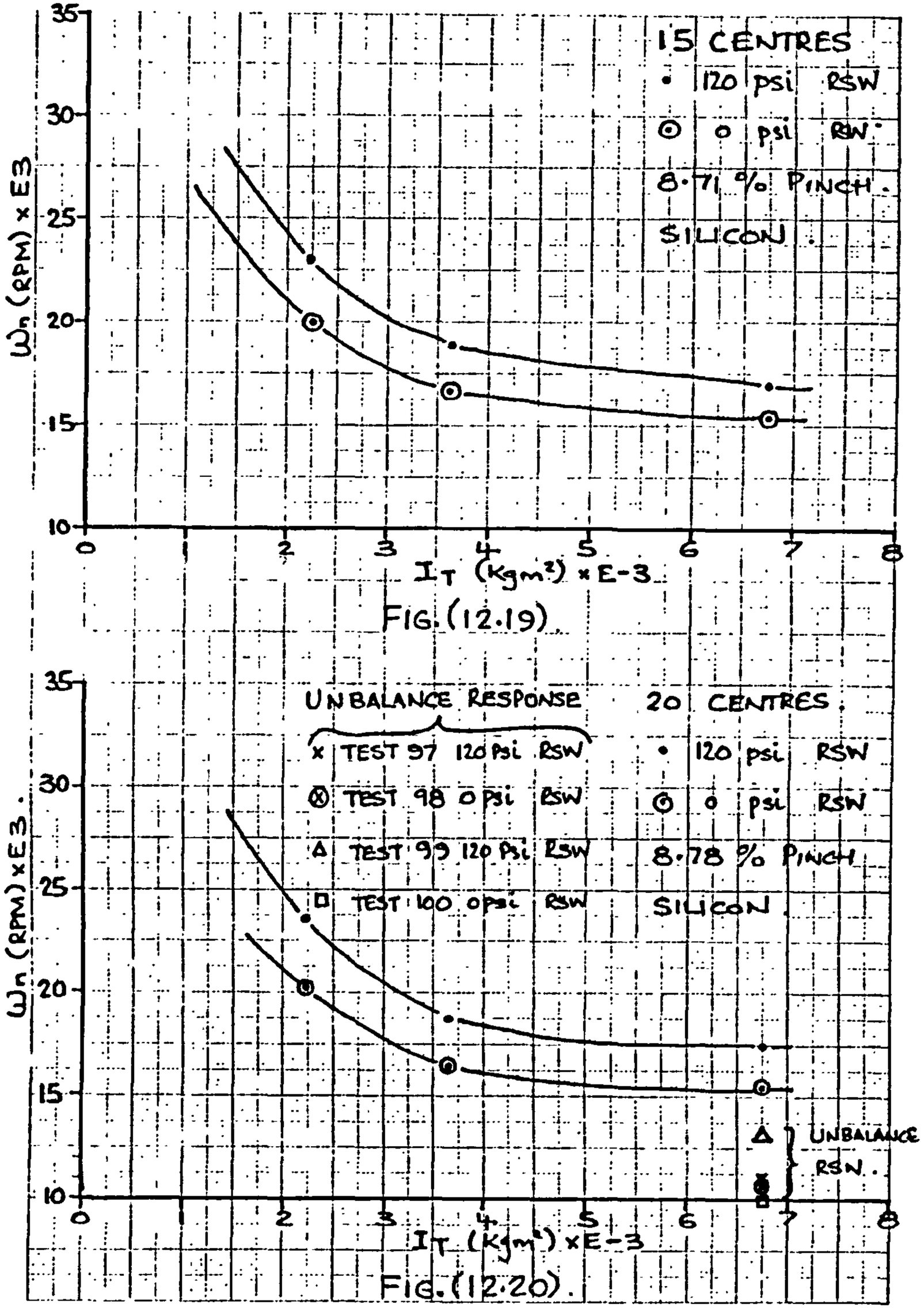

FIG. (12.19)

FIG. (12.20).

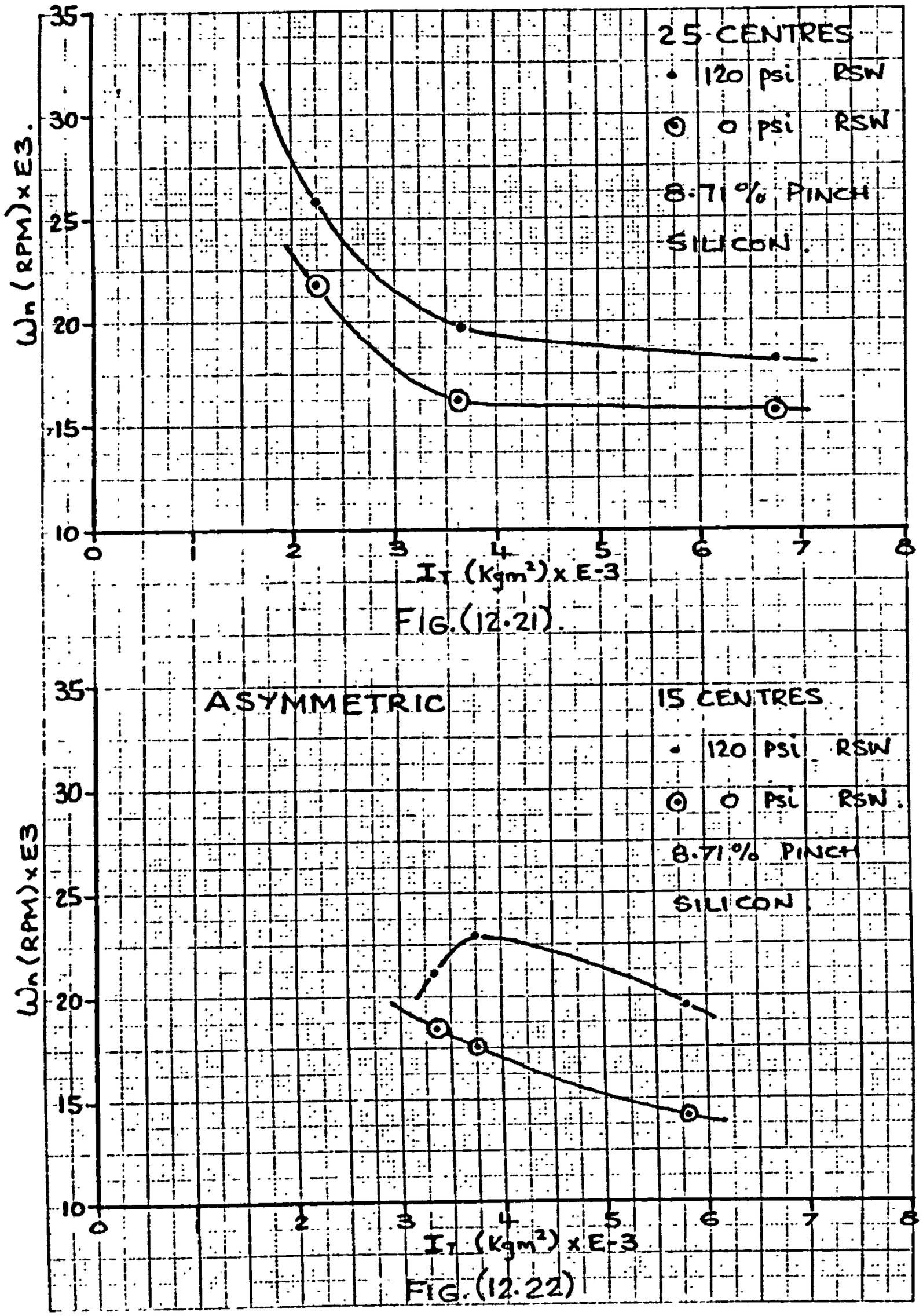

FIG. (12.21).

FIG. (12.22)

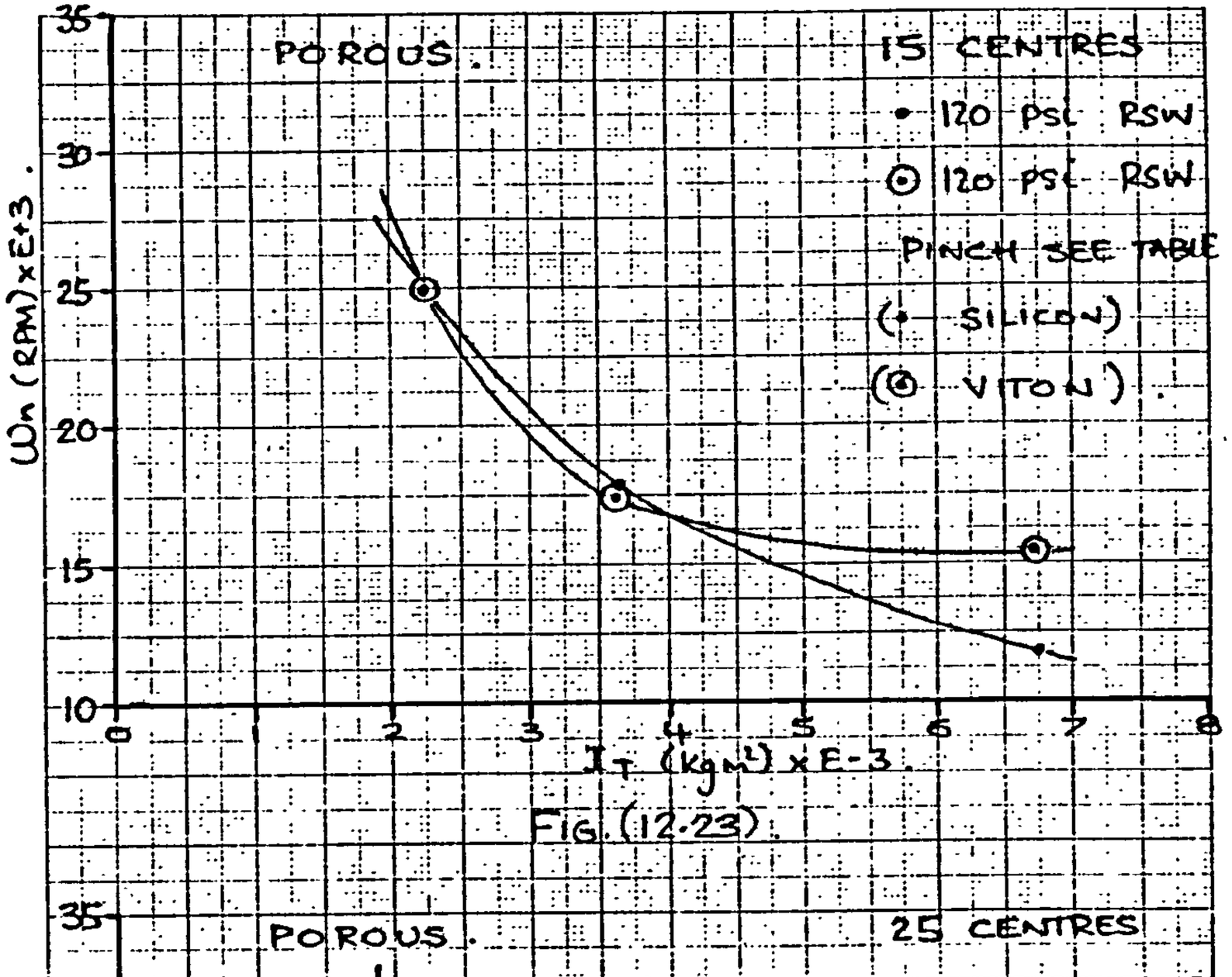

FIG. (12.23).

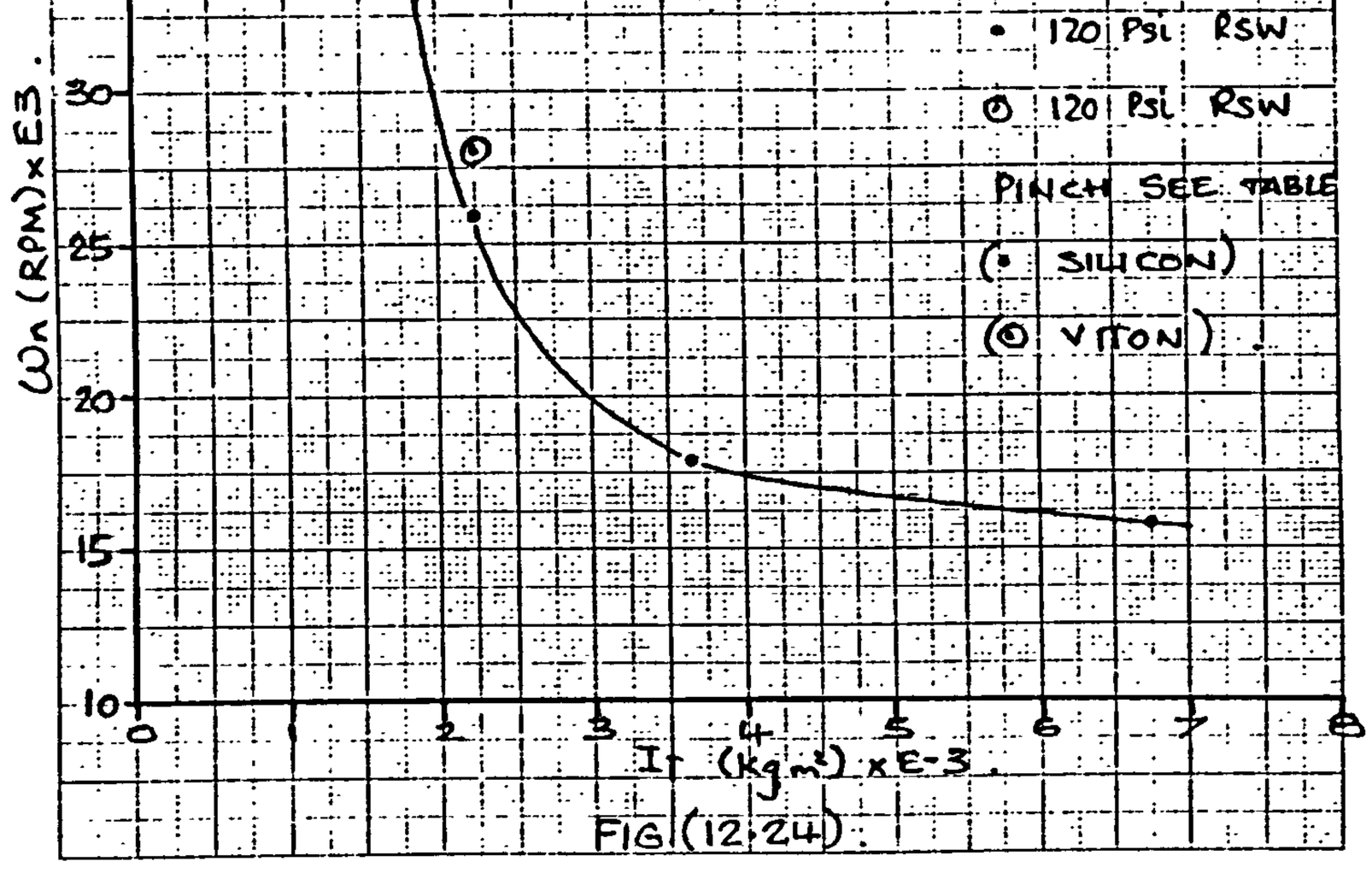

FIG (12.24).

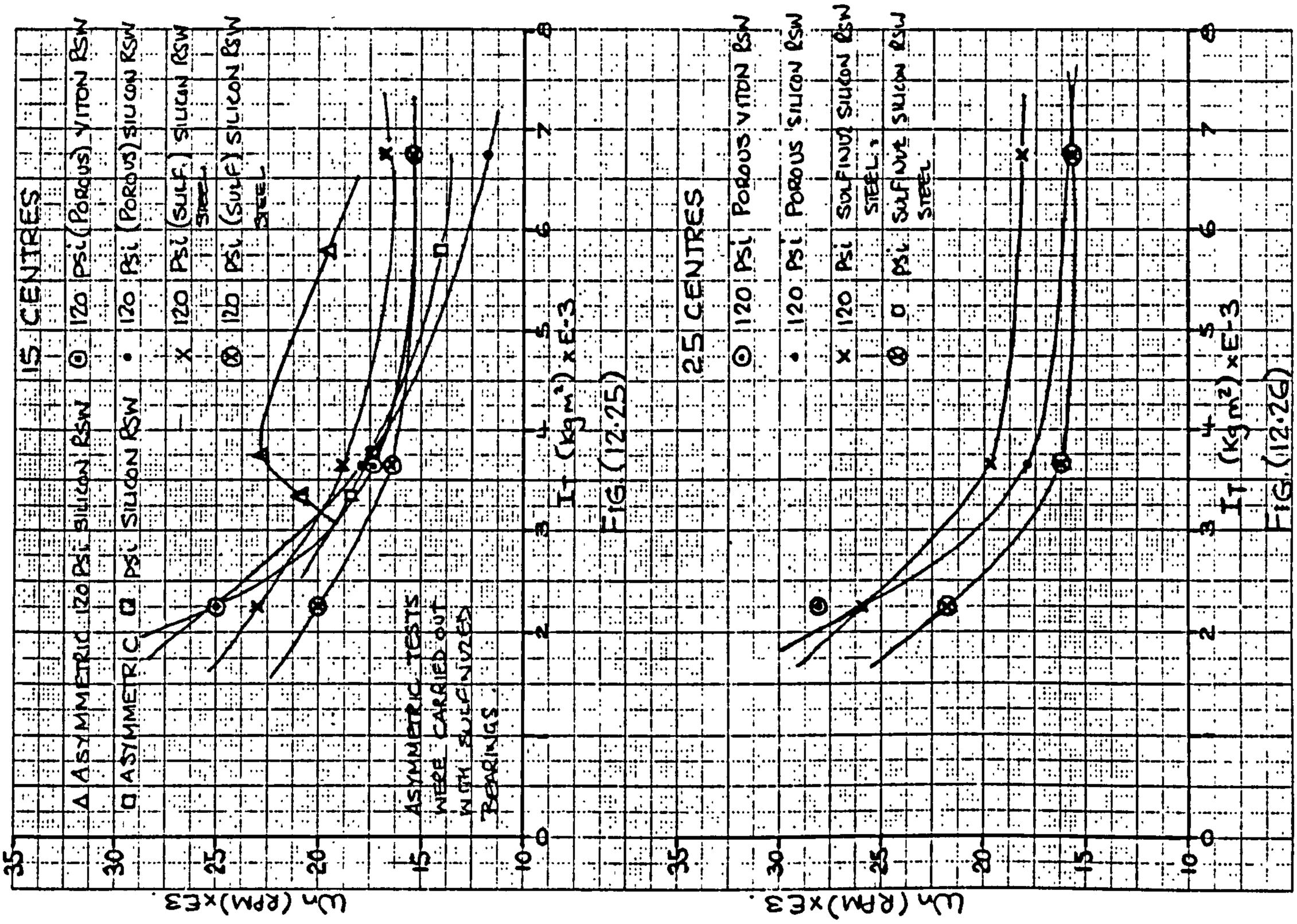
15 CENTRES
Δ ASYMMETRIC 120 PSI SILICON RSW
□ ASYMMETRIC □ PSI SILICON RSW
120 PSI (POROUS) VITON RSW
120 PSI (POROUS) SILICON RSW
120 PSI (SULF.) SILICON RSW STEEL
120 PSI (SULF.) SILICON RSW STEEL
ASYMMETRIC TESTS WERE CARRIED OUT WITH SULPHURIZED BEARINGS
FIG. (12.25)
25 CENTRES
120 PSI POROUS VITON RSW
120 PSI POROUS SILICON RSW
120 PSI SULFINUL SILICON RSW STEEL
0 PSI SULFINUL SILICON RSW STEEL
FIG. (12.26)
ω_h (RPM) x E3
IT (Kg m²) x E-3

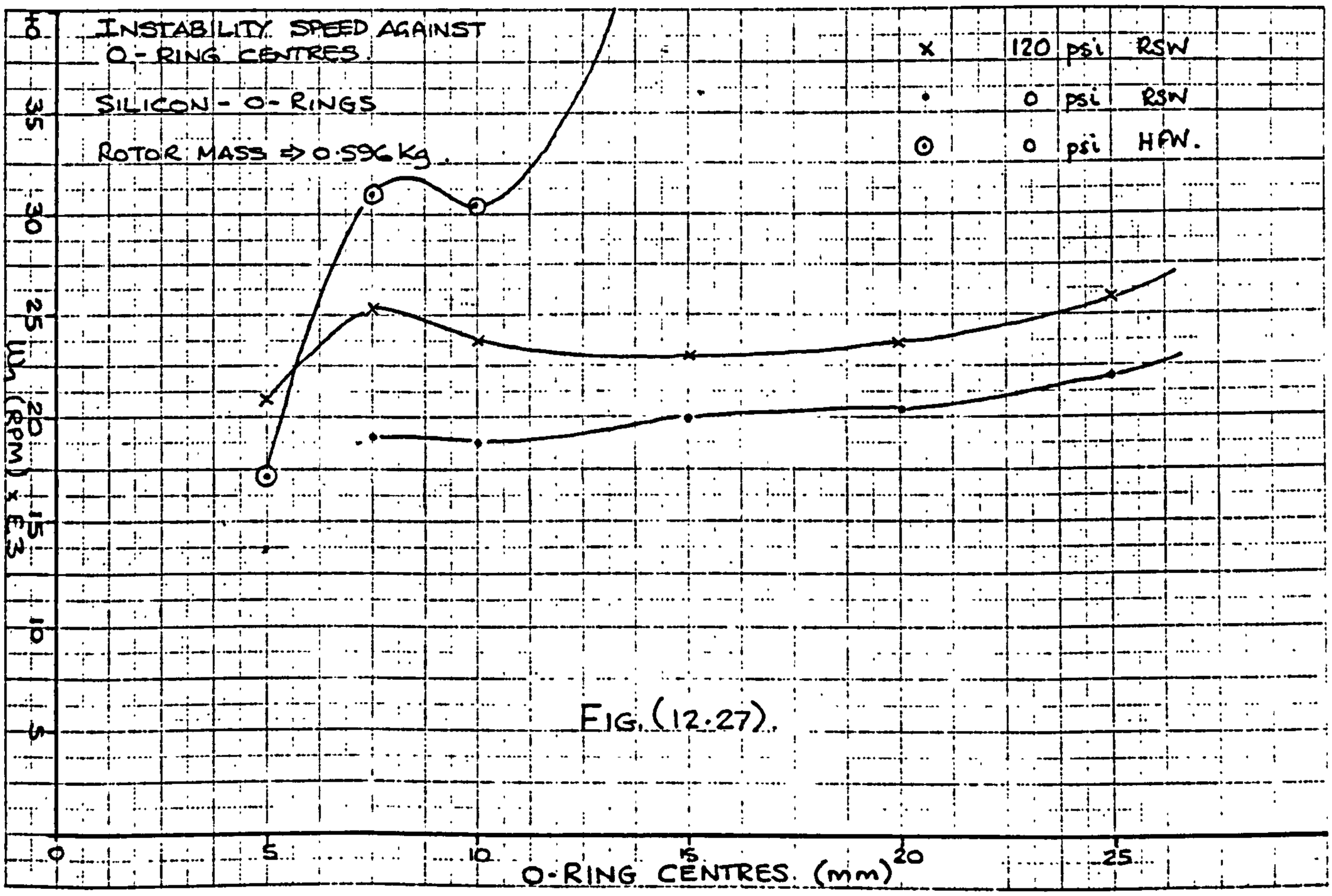
INSTABILITY SPEED AGAINST O-RING CENTRES.
SILICON - O - RINGS
ROTOR MASS ⇒ 0.596 Kg.
X 120 psi RSW
• 0 psi RSW
⊙ 0 psi HAW.
ω_h (RPM) x E3
O-RING CENTRES. (mm)
FIG. (12.27).

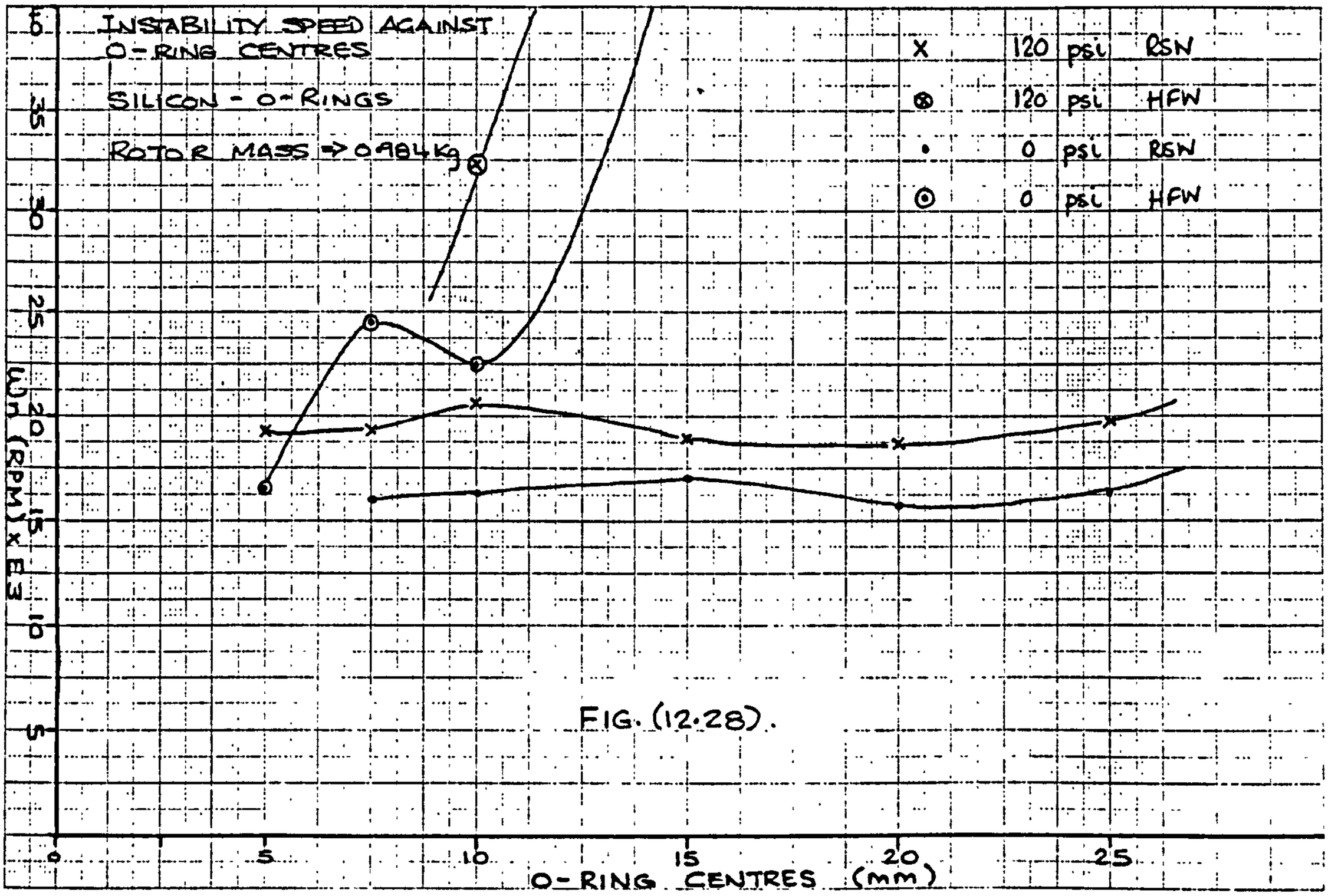

FIG. (12.28).

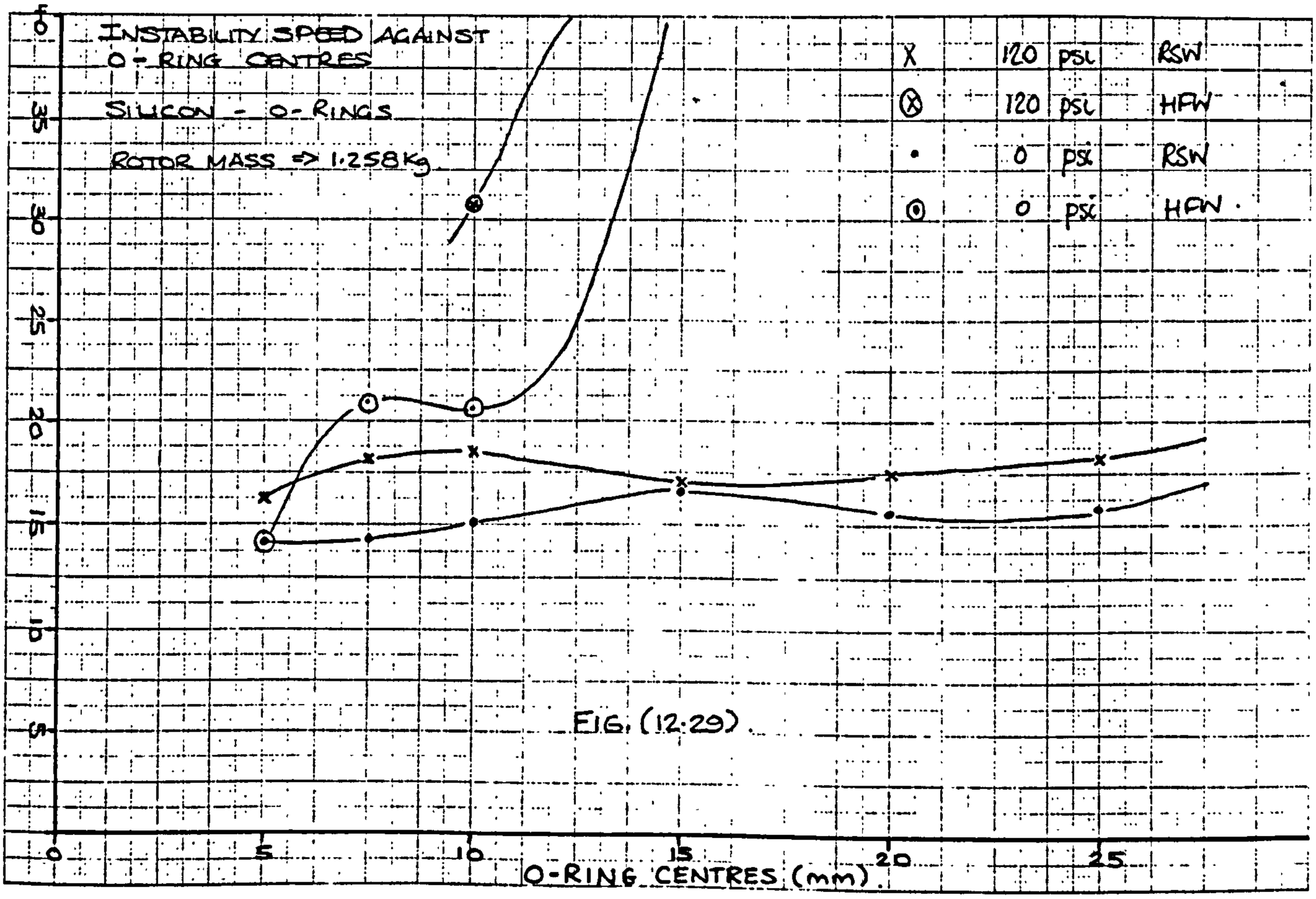

FIG. (12.29).

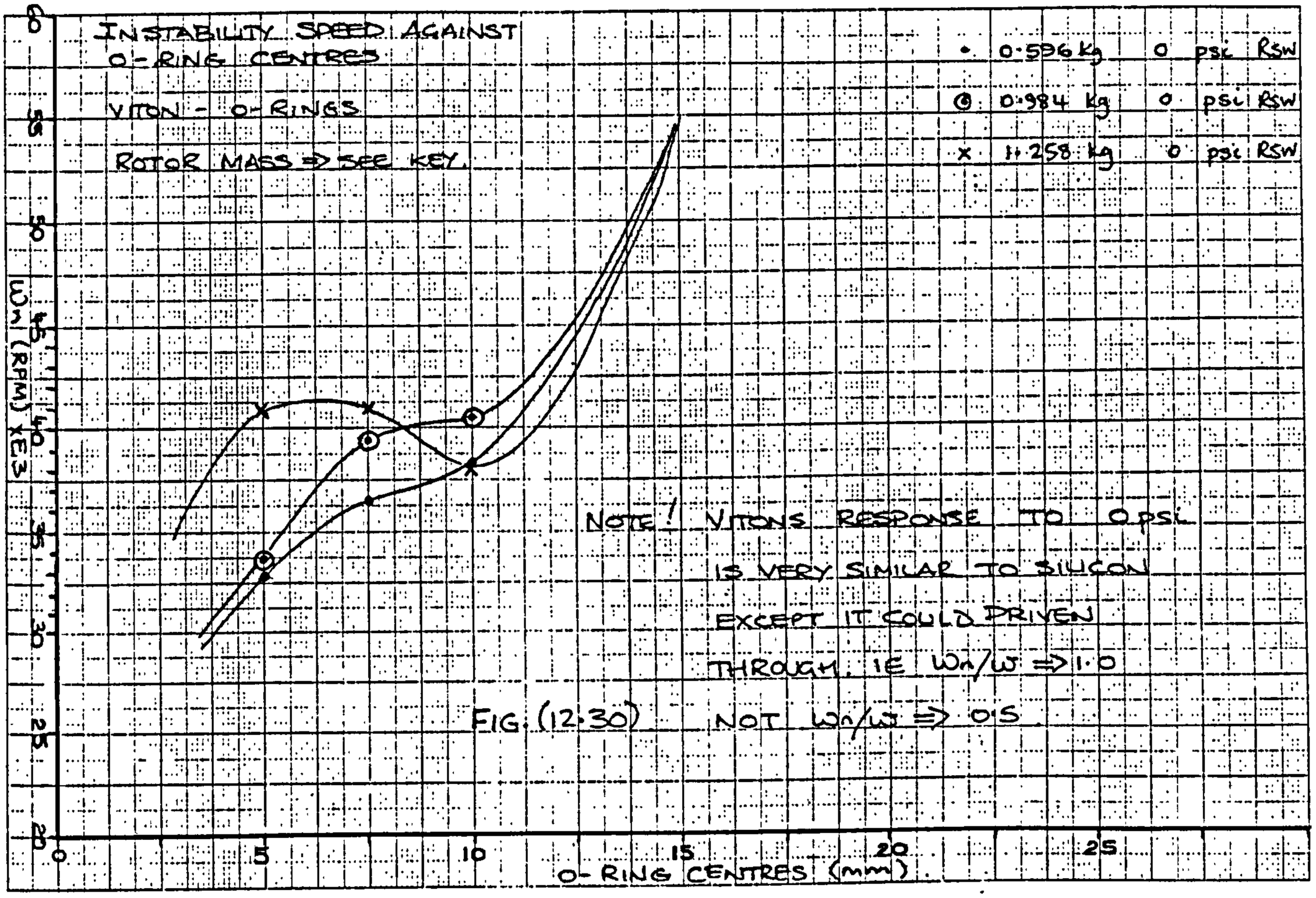

FIG. (12·30)

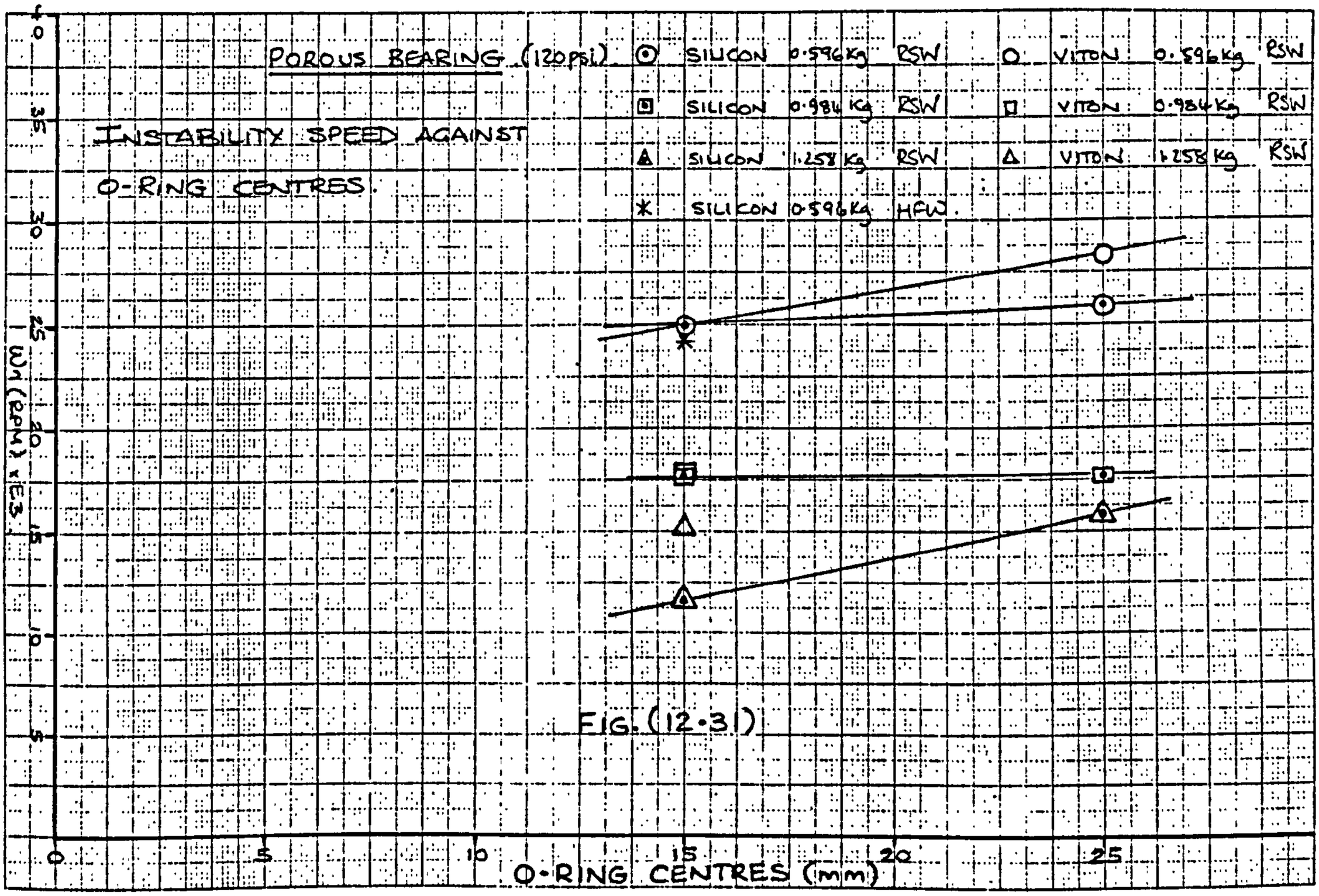

FIG. (12·31)

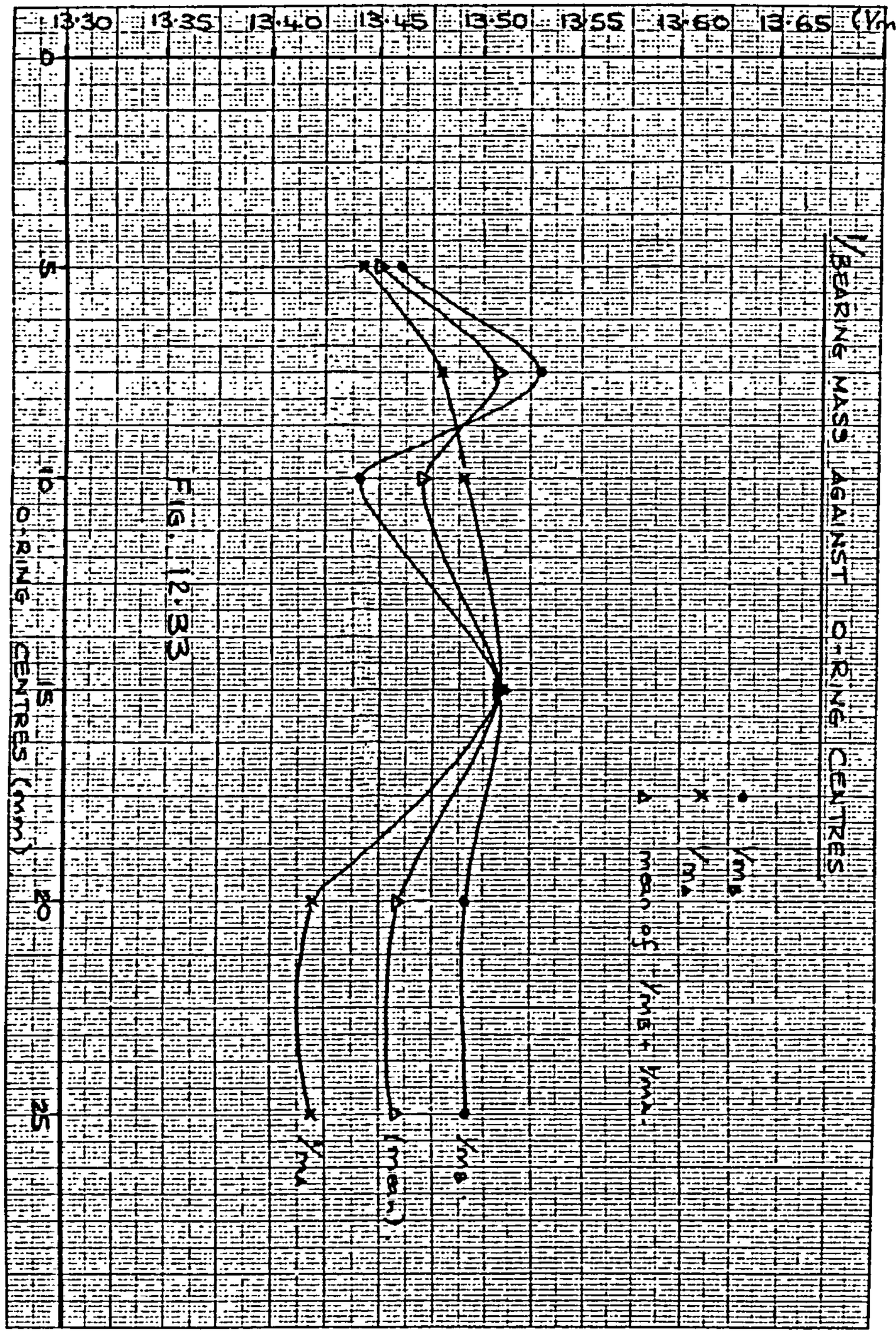

FIG. 12·33

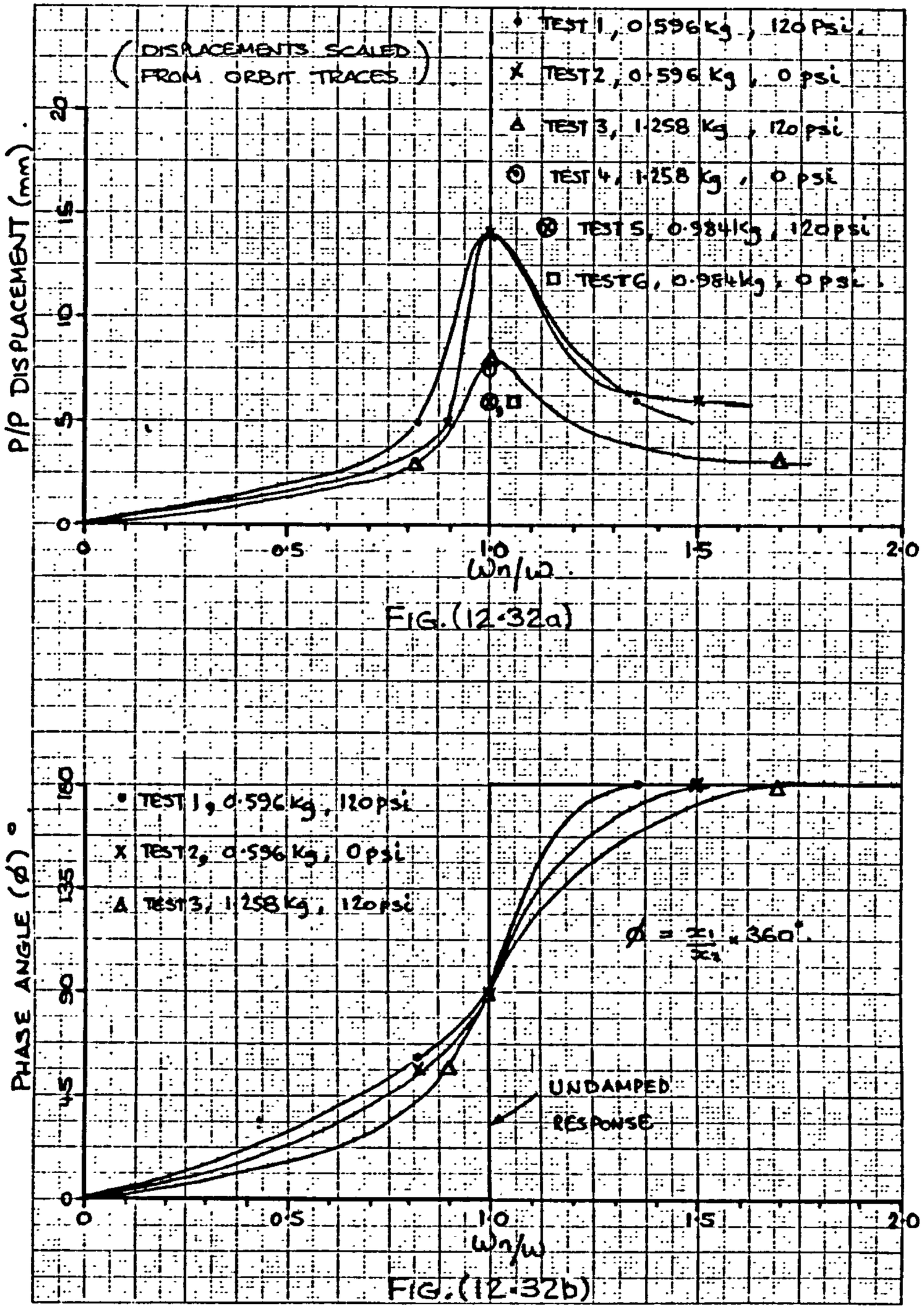

FIG. (12·32a)

FIG. (12·32b)

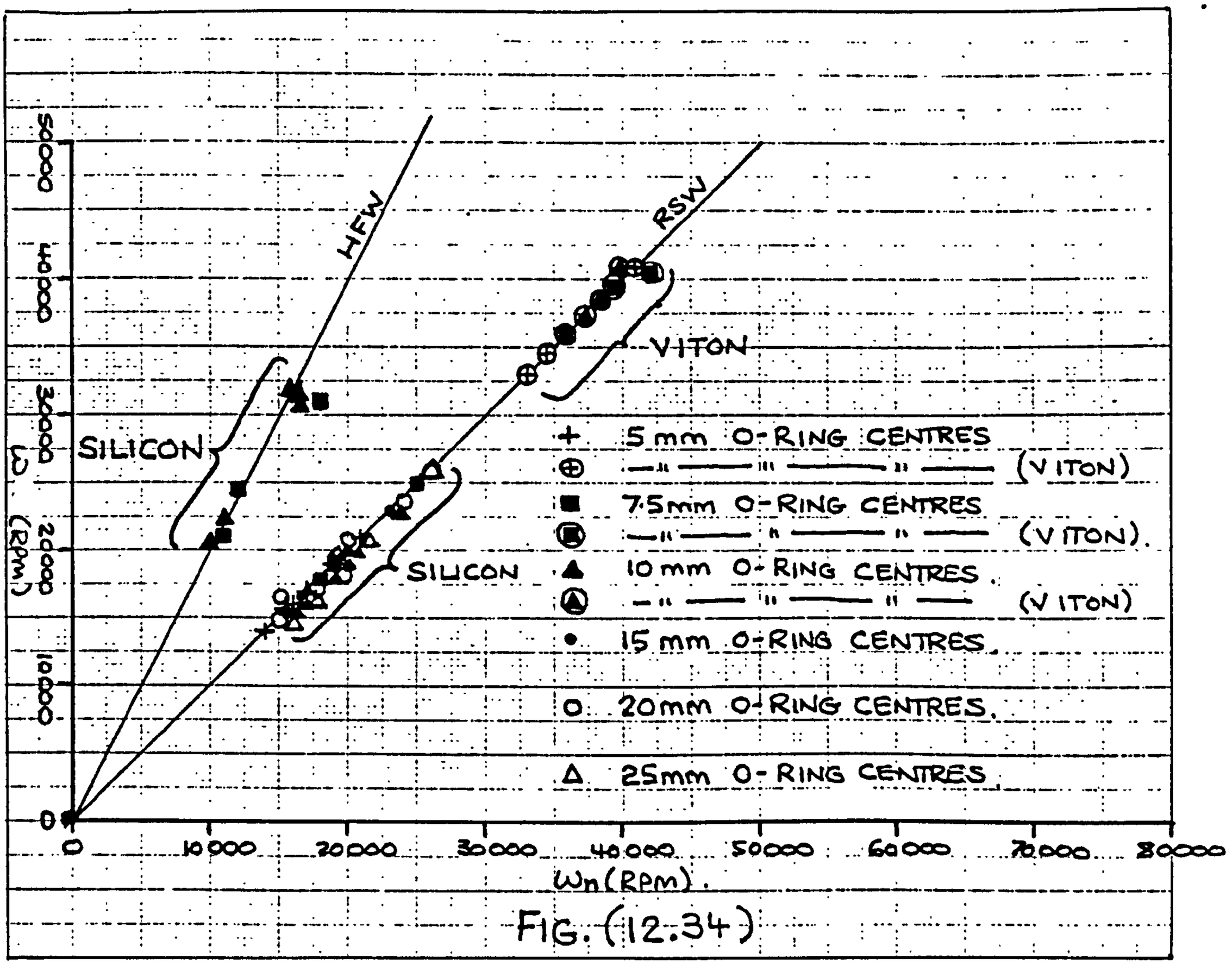
HFW
RSW
VITON
SILICON
SILICON
+ 5 mm O-RING CENTRES
⊕ —"— —"— —"— (VITON)
■ 7.5mm O-RING CENTRES
▣ —"— —"— —"— (VITON).
▲ 10 mm O-RING CENTRES.
▲ —"— —"— —"— (VITON)
• 15 mm O-RING CENTRES.
O 20mm O-RING CENTRES.
Δ 25mm O-RING CENTRES.
50000
40000
30000
20000
10000
0
ωn (RPM)
0
10000
20000
30000
40000
50000
60000
70000
80000
ωn (RPM).

FIG. (12.34)

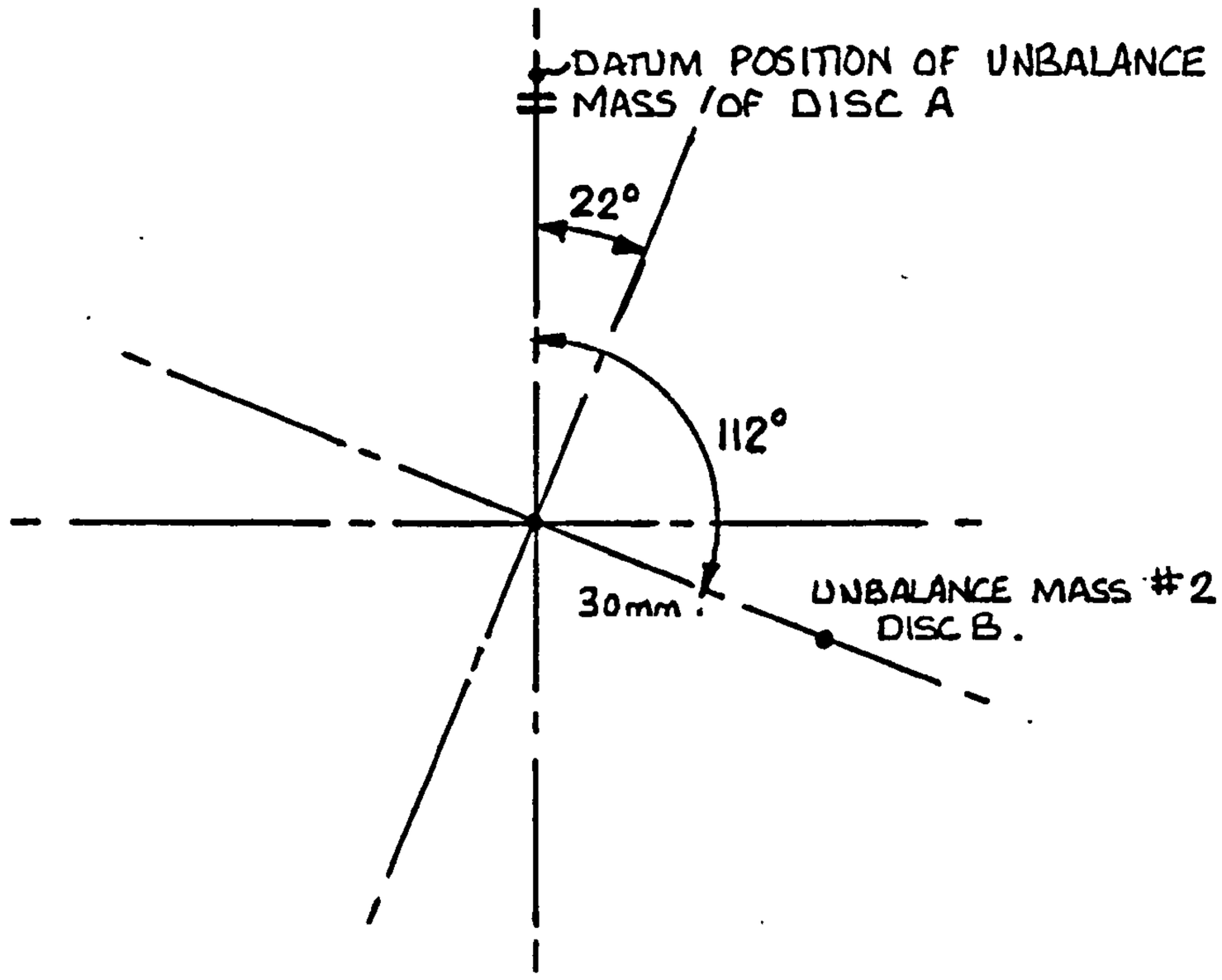

FIG (12.35 a) UNBALANCE MASS POSITION OF, FIRST COUPLE UNBALANCE

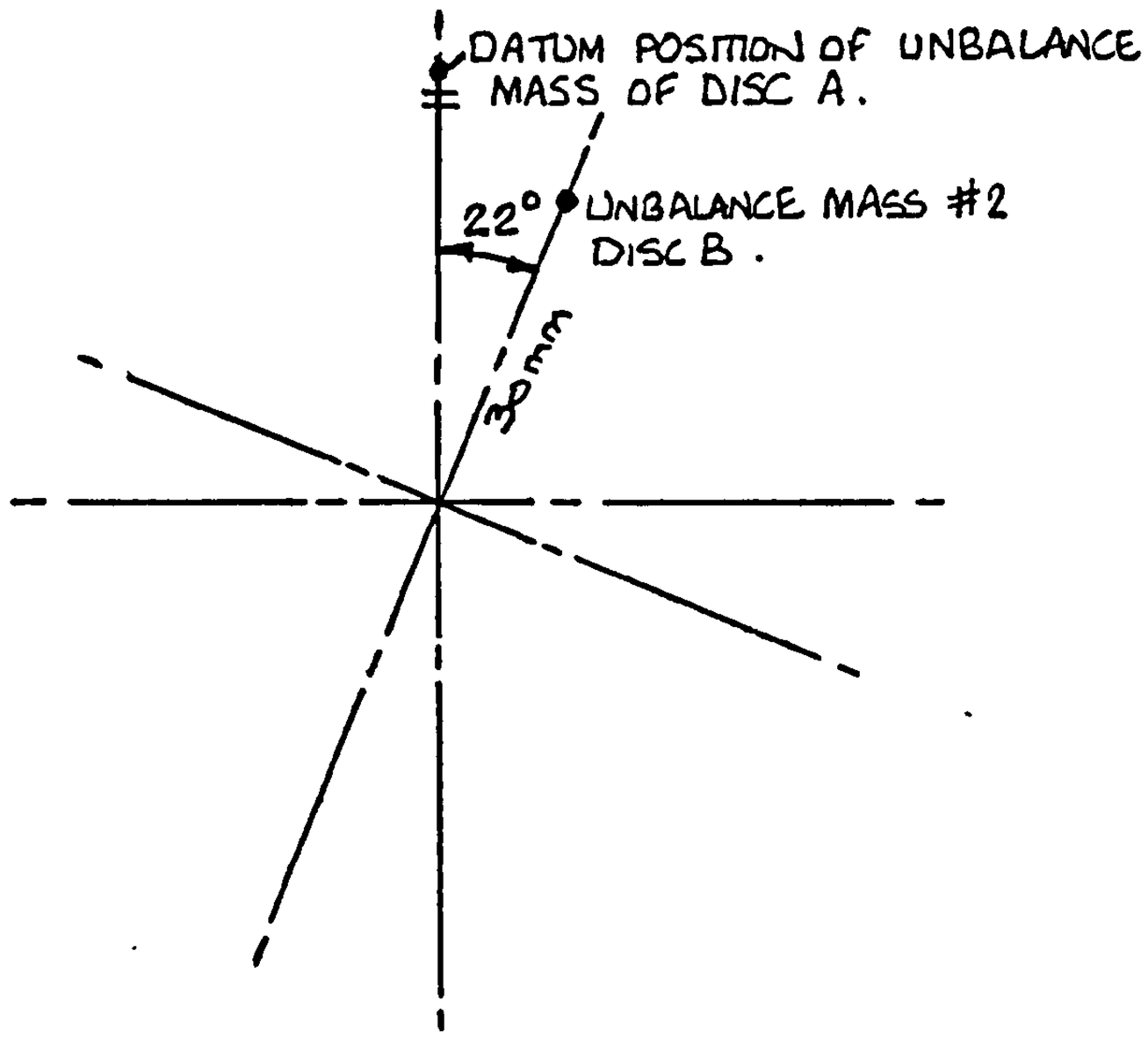

FIG (12.35 b) UNBALANCE MASS POSITION OF. SECOND COUPLE UNBALANCE.

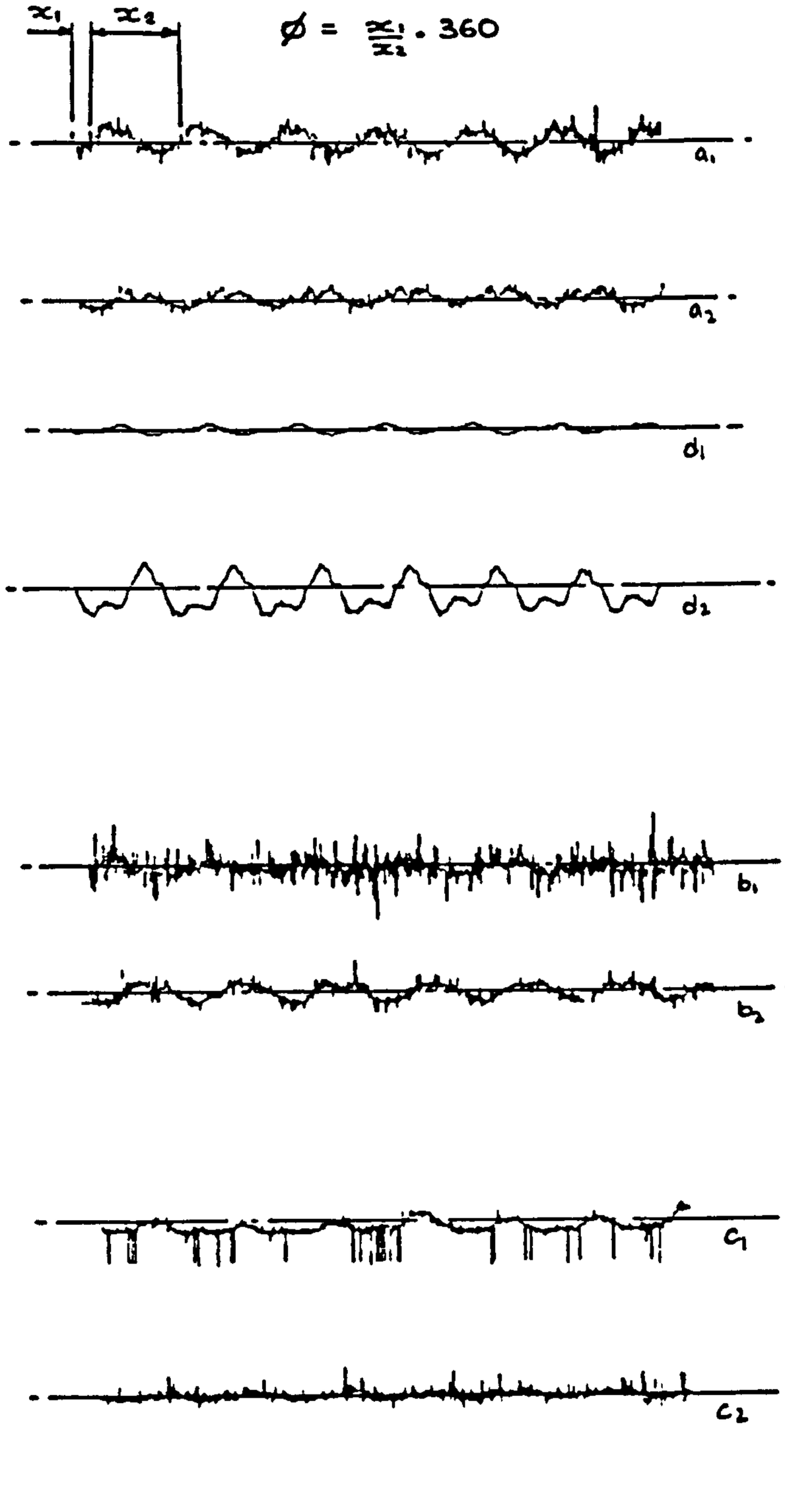

FIG.(12.36a) TEST I BELOW RSW 19000 RPM.

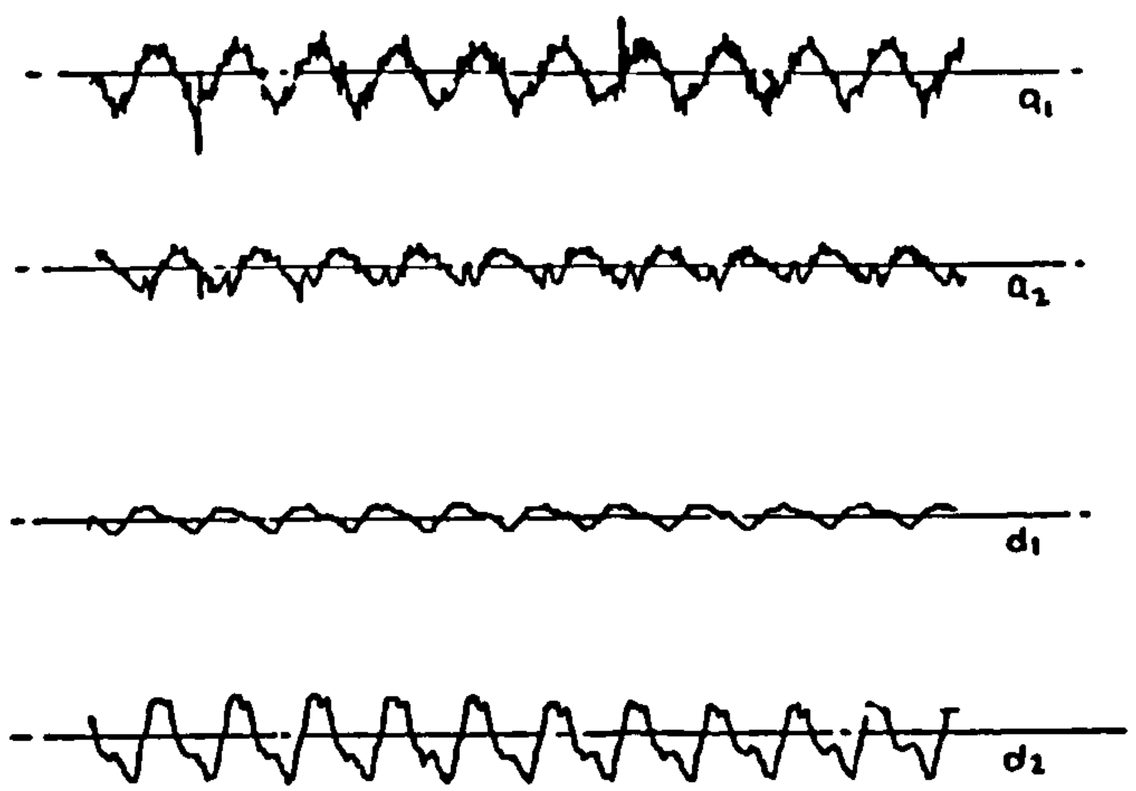

FIG. (12·36c) TEST 1 ABOVE RSW 31000 RPM

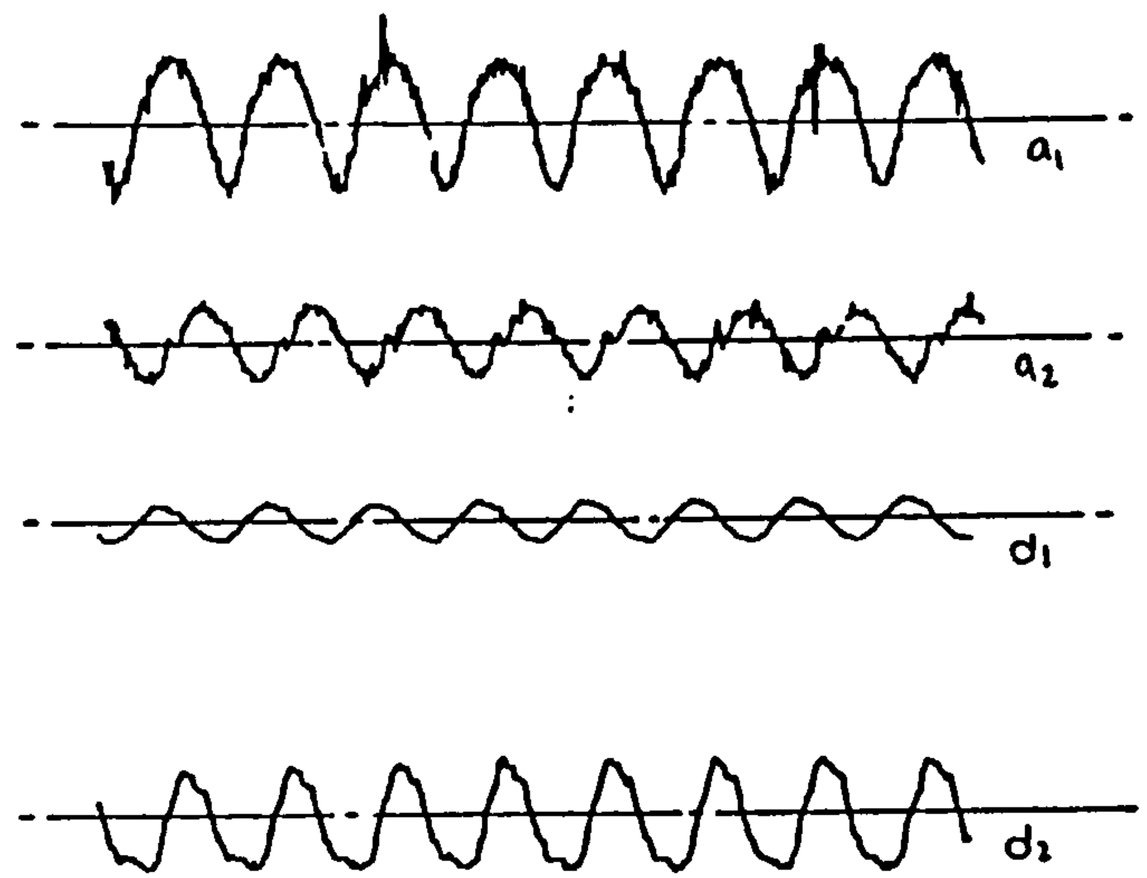

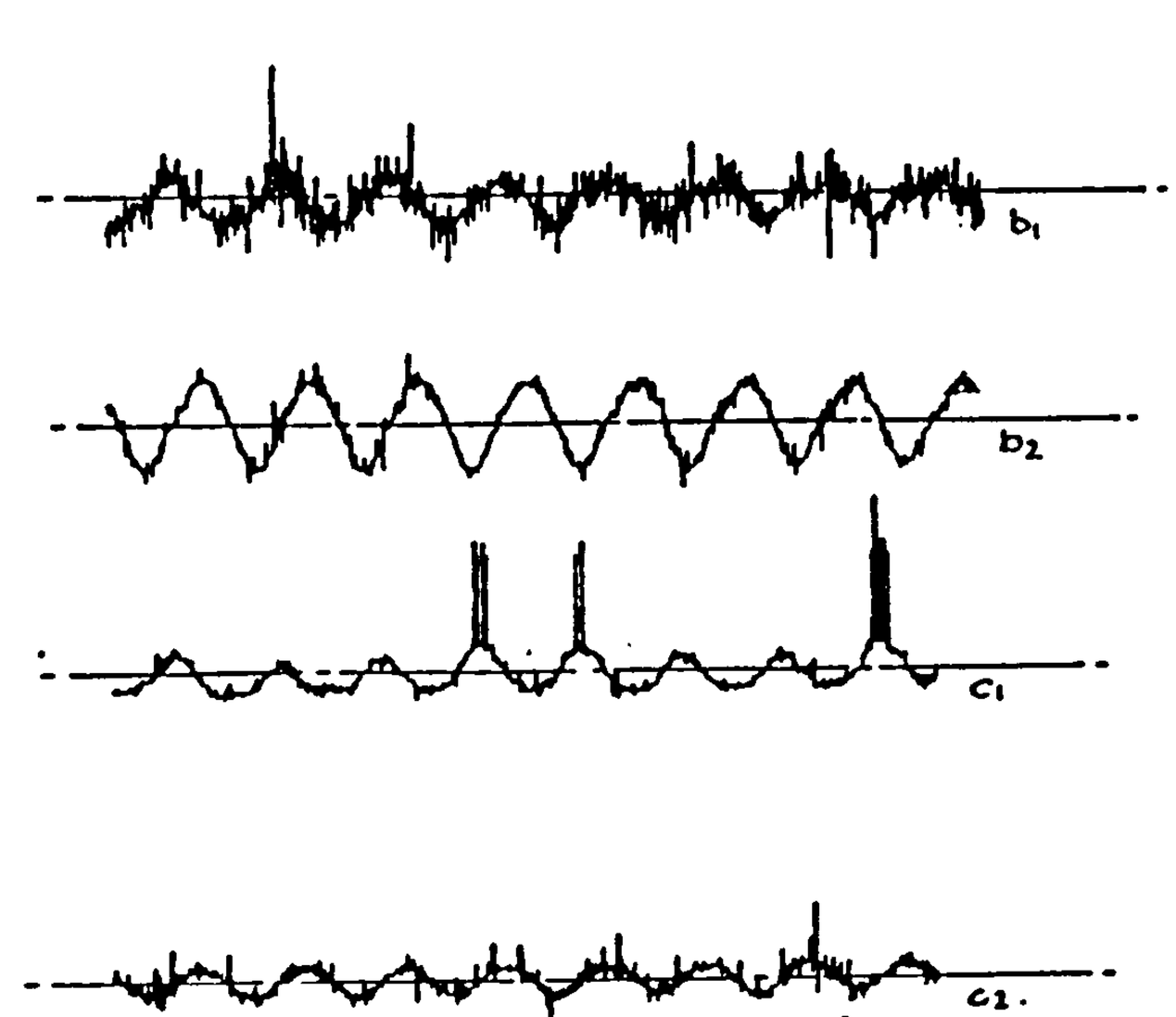

FIG. (12·36b) TEST 1 RSW 23000 RPM

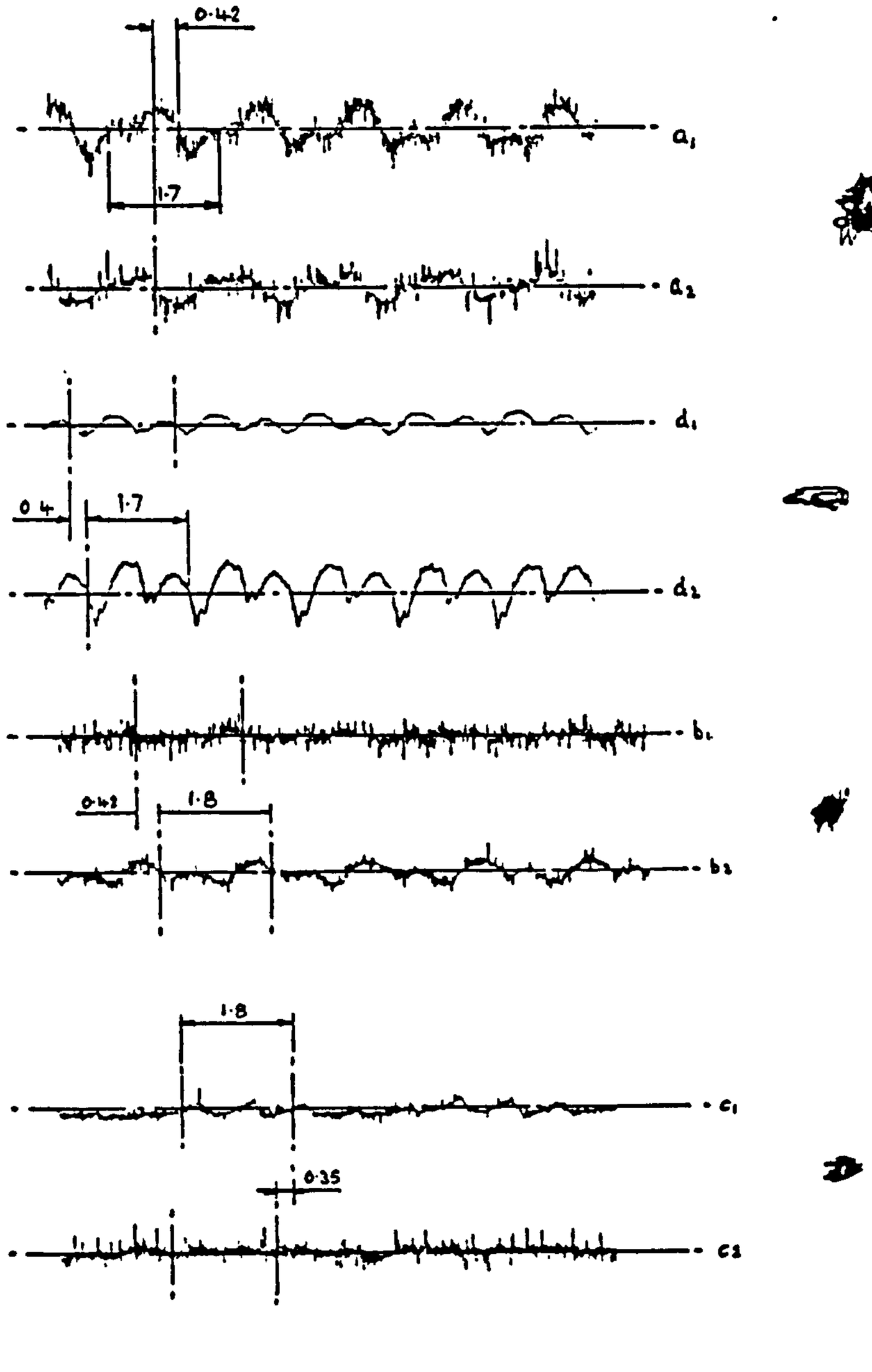

FIG(12.37) TEST 26a HFW 31000 RPM.

$L/D = 2{\cdot}0$ Shaft No. 1 $\left(\frac{D}{C}\right) \rightarrow \left(\frac{0{\cdot}9990}{0{\cdot}0014}\right) \rightarrow 713{\cdot}5714$ $R/C = 1427{\cdot}1428$ $\mu = 2\pi^2\left(\frac{R}{C}\right)\cdot\frac{\eta N'}{P}$

$N' = N/60$

Test	Speed Rpm	Temp T°C	$\eta 10^{-6}$ Reyns	W (lbf)	P Nom	P Actual	P/Pa	S	λ	ε_o	φ_o	$\eta N/P \times 10^{-7}$	μ
1	10500	21·5	2·633	5·038	3·250	2·522	0·1716	0·0930	0·1003	0·374	46·55	1·827	0·0026
2	15100	22·2	2·638	5·760		2·883	0·1961	0·1173	0·1445	0·369	45·79	2·303	0·0033
3	20000	22·9	2·642	5·767		2·886	0·1963	0·1554	0·1917	0·346	46·68	3·052	0·0043
4	25000	24·0	2·649	5·764		2·885	0·1963	0·1948	0·2402	0·318	47·55	3·826	0·0054
5	30000	25·4	2·658	5·531		2·768	0·1883	0·2444	0·2892	0·286	48·44	4·801	0·0068
6	35000	27·4	2·670	5·846		2·926	0·1991	0·2710	0·3390	0·229	54·13	5·323	0·0075
7	10000	21·4	2·633	7·921	3·998	3·965	0·2697	0·0564	0·0955	0·984	57·67	1·107	0·0016
8	15500	22·6	2·640	7·762		3·885	0·2643	0·0894	0·1484	0·650	56·10	1·756	0·0025
9	20400	23·3	2·645	7·366		3·687	0·2508	0·1218	0·1919	0·352	40·10	2·391	0·0034
10	25300	24·3	2·657	7·246		3·627	0·2467	0·1551	0·2404	0·365	7·44	3·046	0·0043
11	30300	25·6	2·659	7·161		3·584	0·2438	0·1889	0·2894	1·23	-71·86	3·710	0·0052
12	35000	27·2	2·669	7·386		3·697	0·2515	0·2145	0·3389	0·480	89·42	4·211	0·0059
13	40200	29·2	2·681	7·203		3·605	0·2452	0·2525	0·3890	0·831	73·37	4·958	0·0070
14	10000	20·1	2·625	9·369	4·969	4·689	0·3190	0·0475	0·0952	0·861	40·25	0·933	0·0013
15	15000	22·2	2·638	8·814		4·412	0·3001	0·0761	0·1435	0·610	49·95	1·495	0·0021
16	20000	23·6	2·646	8·775		4·392	0·2988	0·1023	0·1920	0·624	54·82	2·008	0·0028
17	25100	25·5	2·658	9·175		4·592	0·3124	0·1228	0·2410	0·939	55·29	2·422	0·0034
18	30300	27·1	2·668	9·594		4·802	0·3267	0·1414	0·2903	0·881	38·10	2·778	0·0039
19	35000	28·5	2·677	10·114		5·062	0·3444	0·1571	0·3400	0·828	47·10	3·085	0·0044
20	10900	21·9	2·636	12·702	6·911	6·357	0·4325	0·0384	0·1042	0·39	33·27	0·753	0·0011
21	15100	23·5	2·646	13·579		6·796	0·4623	0·0495	0·1438	0·384	20·67	0·980	0·0014

Units Are Imperial For Comparison With Raimondi's Results

Table (5·1)

L/D = 2·0 Shaft No. 2 $\left(\frac{D}{C}\right) \rightarrow \left(\frac{0{\cdot}9989}{0{\cdot}0015}\right) \rightarrow 665{\cdot}933$ $\mu = 2\pi^2 \left(\frac{R}{C}\right) \cdot \frac{\eta N'}{P}$ $N' = N/60$

Test	Speed Rpm	Temp T°C	$\eta 10^{-3}$ Reyns	W (lbf)	P Nom	P Actual	P/Pa	S	λ	ε_o	φ_o	$\eta N/P \times 10^{-7}$	μ
22	6400	20·2	2·625	4·181	2·052	2·0921	0·1423	0·0594	0·0531	0·445	64·29	1·338	0·0018
23	10000	20·9	2·630	4·184		2·0943	0·1425	0·0928	0·0831	0·161	38·16	2·093	0·0028
24	15500	22·0	2·636	4·192		2·0983	0·1427	0·1393	0·1249	0·270	-89·73	3·141	0·0041
25	20500	24·8	2·654	4·213		2·1088	0·1435	0·1907	0·1719	0·292	-65·67	4·300	0·0057
26	25000	34·8	2·716	4·085		2·0448	0·1391	0·2454	0·2145	0·974	-87·51	5·535	0·0073
27	30000	64·3	2·899	3·955		1·9797	0·1347	0·3788	0·3206	0·698	84·80	7·322	0·0096
28	6400	24·4	2·651	6·078	2·990	3·0423	0·2069	0·0412	0·0536			0·930	0·0012
29	10500	21·0	2·630	6·014		3·0103	0·2048	0·0678	0·0872			1·529	0·0020
30	15200	22·4	2·639	6·119		3·0629	0·2084	0·0968	0·1267			2·183	0·0029
31	6600	21·4	2·633	6·062	2·990	3·0343	0·2064	0·0423	0·0549	0·702	-76·17	0·955	0·0013
32	10500	21·6	2·634	6·180		3·0934	0·2104	0·0661	0·0874	0·342	22·79	1·490	0·0020
33	15200	22·3	2·638	6·108		3·0574	0·2080	0·0956	0·1250	0·196	78·70	2·157	0·0028
34	20200	23·0	2·643	5·997		3·0018	0·2042	0·1315	0·1687	0·178	84·92	2·964	0·0039
35	6500	27·8	2·672	7·798	3·929	3·9033	0·2655	0·0329	0·0549	0·519	29·10	0·742	0·0010
36	10500	21·5	2·633	7·945		3·9814	0·2708	0·0513	0·0873	0·425	29·13	1·157	0·0015
37	15750	21·8	2·635	7·883		3·9458	0·2684	0·0777	0·1311	0·185	39·43	1·753	0·0023
38	10400	22·9	2·642	9·701	4·867	4·8558	0·3303	0·0418	0·0868	0·509	21·93	0·943	0·0012
39	15200	24·4	2·651	9·751		4·8809	0·3320	0·0610	0·1273	0·413	35·99	1·376	0·0018
40	8200	22·7	2·641	11·498	5·805	5·7553	0·3915	0·0278	0·0684	0·500	39·78	0·627	0·0008
41	10700	22·7	2·641	11·619		5·8159	0·3956	0·0359	0·0893	0·488	38·94	0·810	0·0011
42	15300	24·6	2·653	11·699		5·8559	0·3984	0·0512	0·1282	0·388	61·04	1·155	0·0015
43	20000	25·8	2·660	11·708		5·8604	0·3987	0·0671	0·1681	0·519	58·42	1·513	0·0020
44	15300	23·1	2·643	13·201	6·743	6·6078	0·4495	0·0453	0·1278	0·702	15·20	1·020	0·0013
45	20000	24·8	2·654	13·036		6·5252	0·4439	0·0601	0·1677	0·582	18·40	1·356	0·0018
46	25200	25·5	2·658	12·821		6·4176	0·4366	0·0771	0·2116	0·515	24·50	1·740	0·0023
47	30100	27·5	2·671	12·861		6·4376	0·4379	0·0923	0·2540	0·493	22·03	2·082	0·0027
48	35000	29·4	2·682	12·955		6·4846	0·4411	0·1070	0·2966	0·477	29·90	2·413	0·0032

Units Are Imperial For Comparison With Raimondi's Results

Table (5·2)

L/D = 1·5 Shaft No. 4 $\left(\frac{D}{C}\right) \rightarrow \left(\frac{0{\cdot}99845}{0{\cdot}00195}\right) \rightarrow 512{\cdot}026$ $\mu = 2\pi^2 \left(\frac{R}{C}\right) \cdot \frac{\eta N'}{P}$ $N' = N/60$

Test	Speed Rpm	Temp T°C	$\eta 10^{-9}$ Reyns	W (lbf)	P Nom	P Actual	P/Pa	S	λ	ε_o	φ_o	$\eta N/P \times 10^{-7}$	μ
49	6500	20·9	2·630	4·101	2·739	2·738	0·1863	0·0273	0·0319	0·571	13·40	1·041	0·0011
50	10200	20·4	2·627	4·139		2·764	0·1880	0·0423	0·0500	0·560	35·30	1·616	0·0016
51	15200	20·8	2·629	4·231		2·825	0·1922	0·0618	0·0746	0·451	39·03	1·882	0·0019
52	8500	20·8	2·629	5·681	3·990	3·793	0·2580	0·0257	0·0417	0·672	18·74	0·982	0·0010
53	10200	20·7	2·628	5·698		3·805	0·2588	0·0308	0·0501	0·586	28·05	1·174	0·0012
54	15200	21·3	2·632	5·681		3·793	0·2580	0·0461	0·0747	0·497	27·05	1·758	0·0018
55	10300	21·7	2·635	7·665	5·241	5·118	0·3482	0·0232	0·0507	0·737	16·46	0·884	0·0009
56	15300	20·0	2·624	7·665		5·118	0·3482	0·0343	0·0750	0·700	21·67	1·307	0·0013
57	20200	21·0	2·630	7·693		5·137	0·3495	0·0454	0·0997	0·614	22·34	1·732	0·0018
58	10200	22·9	2·642	9·489	6·493	6·336	0·4310	0·0182	0·0493	0·730	14·59	0·695	0·0007
59	15200	22·1	2·637	9·411		6·284	0·4275	0·0275	0·0739	0·576	20·46	1·049	0·0011
60	20200	22·9	2·642	9·428		6·295	0·4282	0·0371	0·0997	0·531	22·92	1·413	0·0014
61	25300	23·8	2·648	9·561		6·384	0·4343	0·0453	0·1236	0·539	24·29	1·728	0·0018
62	15300	22·0	2·636	11·266	7·744	7·522	0·5117	0·0234	0·0753	0·897	9·99	0·894	0·0009
63	20200	22·9	2·642	11·276		7·529	0·5122	0·0310	0·0997	0·850	13·77	1·181	0·0012
64	25200	23·9	2·648	11·314		7·554	0·5139	0·0386	0·1246	0·795	13·21	1·472	0·0015
65	30200	25·2	2·656	11·400		7·612	0·5178	0·0461	0·1498	0·819	14·07	1·756	0·0018
66	15300	22·8	2·641	13·184	8·996	8·803	0·5988	0·0203	0·0765	0·948	8·15	0·765	0·0008
67	20200	23·4	2·645	13·223		8·829	0·6006	0·0262	0·0988	0·859	9·94	0·999	0·0010
68	25200	24·4	2·651	13·309		8·886	0·6045	0.0326	0·1238	0·850	10·81	1·243	0·0013
69	30000	25·7	2·659	13·380		8·934	0·6078	0·0390	0·1490	0·859	12·13	1·488	0·0015
70	35000	26·9	2·667	12·874		8·596	0·5848	0·0473	0·1738	0·740	13·79	1·810	0·0018

Units Are Imperial For Comparison With Raimondi's Results

Table (5·3)

L/D 1·0 Shaft No. 5 $\left(\frac{D}{C}\right) \rightarrow \left(\frac{0{\cdot}99905}{0{\cdot}00135}\right) \rightarrow 740{\cdot}04$ $\mu = 2\pi^2 \left(\frac{R}{C}\right) \cdot \frac{\eta N'}{P}$ $N' = N/60$

Test	Speed Rpm	Temp T°C	$\eta 10^{-6}$ Reyns	W (lbf)	P Nom	P Actual	P/Pa	S	λ	ε_o	φ_o	$\eta N/P$ $\times 10^{-7}$	μ
71	6500	19·0	2·618	4·033	4·103	4·037	0·2746	0·0385	0·0664	0·749	21·37	0·703	0·0010
72	10300	19·3	2·619	3·988		3·992	0·2716	0·0617	0·1053	0·500	12·80	1·126	0·0016
73	15200	19·9	2·620	4·116		4·120	0·2803	0·0882	0·1554	0·728	25·51	1·611	0·0024
74	6500	18·0	2·612	5·763	5·982	5·769	0·3943	0·0267	0·0662	0·945	9·63	0·491	0·0007
75	10300	18·3	2·614	5·682		5·687	0·3869	0·0432	0·1051	0·811	10·60	0·789	0·0012
76	15200	19·0	2·618	5·682		5·687	0·3869	0·0639	0·1553	0·824	14·87	1·166	0·0017
77	20200	20·0	2·624	5·692		5·697	0·3876	0·0849	0·2068	0·727	20·19	1·551	0·0023
78	6400	18·7	2·616	7·798	7·857	7·805	0·5310	0·0196	0·0653	0·865	10·46	0·358	0·0005
79	10200	18·9	2·617	7·762		7·769	0·5285	0·0314	0·1042	0·827	13·25	0·573	0·0008
80	15200	19·8	2·620	7·733		7·740	0·5265	0·0470	0·1554	0·879	18·17	0·858	0·0013
81	20200	20·8	2·629	7·756		7·763	0·5281	0·0624	0·2072	0·894	15·17	1·140	0·0017
82	10200	20·0	2·624	9·613	9·733	9·622	0·6546	0·0254	0·1044	0·990	10·87	0·464	0·0007
83	15200	20·9	2·629	9·646		9·655	0·6568	0·0378	0·1559	0·787	7·31	0·690	0·0010
84	20200	22·1	2·637	9·643		9·652	0·6566	0·0504	0·2078	0·631	9·96	0·920	0·0013
85	25100	23·3	2·645	9·606		9·615	0·6541	0·0630	0·2590	0·503	7·76	1·151	0·0017
86	10200	19·1	2·618	11·584	11·609	11·595	0·7888	0·0210	0·1042	0·945	8·44	0·384	0·0006
87	15200	20·4	2·627	11·496		11·507	0·7828	0·0317	0·1558	0·821	12·28	0·578	0·0008
88	20200	21·4	2·633	11·557		11·568	0·7869	0·0420	0·2075	0·732	7·96	0·766	0·0011
89	25200	23·6	2·646	11·581		11·592	0·7886	0·0525	0·2601	0·503	5·50	0·952	0·0014
90	30000	25·2	2·656	11·504		11·515	0·7833	0·0632	0·3109	0·572	14·56	1·140	0·0017
91	15100	22·5	2·640	13·386	13·485	13·399	0·9115	0·0222	0·1555	0·946	9·13	0·496	0·0007
92	20200	23·7	2·647	13·377		13·390	0·9109	0·0365	0·2086	0·944	16·99	0·666	0·0010
93	25200	25·1	2·656	13·465		13·478	0·9167	0·0453	0·2611	0·917	7·24	0·828	0·0012
94	30000	26·7	2·666	13·409		13·422	0·9131	0·0544	0·3120	0·895	21·40	0·933	0·0015

Units Are Imperial For Comparison With Raimondi's Results

Table (5·4)

TEST 1 LOAD 5·038 lbf SPEED 10500 Rpm L/D 2·0

PRESSURE PROFILE (lb/in²)					CIRCUMFERENTIAL STATION NUMBER						
1	2	3	4	5	6	7	8	9	10	11	12
0	0	0	0	0	0	0	0	0	0	0	0
-0·31	-0·41	-0·49	-0·54	-0·21	0·05	0·19	0·03	0·06	-0·11	-0·23	-0·33
-0·67	-1·08	-1·03	-1·17	1·06	1·83	0·65	0·12	0·14	-0.16	-0·29	-0·52
-1·23	-1·85	-2·25	-1·62	2·43	2·09	1·27	0·64	0·29	-0·14	-0·40	-0·80
-1·45	-2·28	-3·49	-2·25	4·10	6·30	1·82	0·96	0·32	-0·22	-0·48	-0·96
-1·18	-1·83	-2·65	-2·05	2·29	2·83	1·48	0·69	0·31	-0·15	-0·46	-0·79
-0·72	-1·09	-1·74	-1·62	1·16	2·03	0·90	0·16	0·12	-0·16	-0·31	-0·53
-0·29	-0·38	-0·25	-0·58	0·21	0·54	0·19	0·06	0·05	-0·13	-0·28	-0·32
0	0	0	0	0	0	0	0	0	0	0	0

Table (5·5)

TEST 2 LOAD 5·760 lbf SPEED 15100 Rpm L/D 2·0

PRESSURE PROFILE (lb/in²)					CIRCUMFERENTIAL STATION NUMBER						
1	2	3	4	5	6	7	8	9	10	11	12
0	0	0	0	0	0	0	0	0	0	0	0
-0·32	-0·54	-0·64	-0·79	-0·30	0·23	0·21	0·11	-0·04	-0·18	-0·25	-0·35
-0·92	-1·45	-1·41	-1·47	-0·26	1·24	1·07	0·31	0·13	-0·12	-0·26	-0·55
-1·27	-2·28	-2·54	-1·94	0·84	2·47	2·57	1·09	0·56	-0·06	-0·37	-0·85
-1·77	-2·64	-2·84	-2·24	0·99	5·87	2·95	1·49	0·60	0·05	-0·43	-1·03
-1·39	-1·94	-2·24	-1·81	0.75	2·48	2.38	1·08	0·50	-0·04	-0·37	-0·86
-0·82	-0·88	-1·26	-1·22	-0·12	1·22	1·05	0·30	0·17	-0·08	-0·28	-0·56
-0·34	-0·42	-0·28	-0·52	-0·20	0·27	0·13	0·02	0·12	-0·19	-0·26	-0·32
0	0	0	0	0	0	0	0	0	0	0	0

Table (5·6)

TEST 3 LOAD 5·767 lbf SPEED 20000 Rpm L/D 2·0

PRESSURE PROFILE (lb/in²)	CIRCUMFERENTIAL STATION NUMBER										
1	2	3	4	5	6	7	8	9	10	11	12
0	0	0	0	0	0	0	0	0	0	0	0
-0·44	-0·64	-0·74	-0·66	-0·55	0·21	-0·18	-0·05	-0·05	-0·21	-0·26	-0·39
-1·27	-1·80	-1·51	-1·08	0·16	1·21	0·76	0·22	0·09	-0·18	-0·30	-0·70
-1·45	-2·74	-2·36	-1·72	2·02	2·23	1·73	0·79	0·31	-0·16	-0·58	-1·19
-2·47	-3·13	-3·59	-2·08	2·58	5·81	2·07	0·89	0·38	-0·18	-0·79	-1·53
-1·91	-2·33	-2·10	-1·23	1·42	2·08	1·68	0·80	0·33	-0·19	-0·67	-1·23
-1·09	-1·66	-1·35	-0·81	0·63	1·30	0·81	0·19	0·10	-0·19	-0·42	-0·81
-0·37	-0·46	-0·39	-0·40	-0·25	0·29	0·08	-0·08	-0·13	-0·24	-0·28	-0·39
0	0	0	0	0	0	0	0	0	0	0	0

Table (5·7)

TEST 4 LOAD 5·764 lbf SPEED 25000 Rpm L/D 2·0

PRESSURE PROFILE (lb/in²)	CIRCUMFERENTIAL STATION NUMBER										
1	2	3	4	5	6	7	8	9	10	11	12
0	0	0	0	0	0	0	0	0	0	0	0
-0·42	-0·68	-0·73	-0·61	0·03	0·20	0·18	0·08	-0·06	-0·21	-0·30	-0·45
-1·53	-2·00	-1·54	-0·88	0·42	1·19	0·53	0·19	0·03	-0·23	-0·41	-1·05
-2·48	-3·09	-2·14	0·47	3·22	2·30	1·30	0·67	0·62	-0·38	-1·13	-2·00
-3·06	-3·50	-2·48	1·28	4·39	3·60	1·58	1·08	0·98	-0·52	-1·60	-2·63
-2·61	-2·81	-1·80	0·57	3·04	2·11	1·31	0·71	0·66	-0·42	-1·20	-2·05
-1·67	-1·58	-1·46	-0·78	1·20	1·15	0·78	0·18	0·06	-0·25	-0·59	-1·12
-0·33	-0·48	-0·59	-0·49	0·05	0·24	0·09	0·05	-0·13	-0·22	-0·29	-0·43
0	0	0	0	0	0	0	0	0	0	0	0

Table (5·8)

TEST 5 LOAD 5·531 lbf SPEED 30000 Rpm L/D 2·0

PRESSURE PROFILE (lb/in²) CIRCUMFERENTIAL STATION NUMBER											
1	2	3	4	5	6	7	8	9	10	11	12
0	0	0	0	0	0	0	0	0	0	0	0
-0·51	-0·76	-0·72	-0·45	0·11	0·24	0·15	0·07	-0·05	-0·20	-0·29	-0·45
-1·75	-2·25	-1·54	-0·54	0·52	1·18	0·70	0·21	0·14	-0·22	-0·45	-1·05
-1·97	-3·38	-1·81	0·91	3·66	2·53	1·67	0·77	0·24	-0·45	-1·13	-2·00
-3·75	-3·68	-2·08	1·92	4·78	2·87	2·06	1·20	0·26	-0·62	-1·60	-2·63
-1·83	-2·89	-1·62	0·76	2·95	2·59	1·71	0·83	0·22	-0·48	-1·20	-2·65
-1·54	-1·95	-1·38	-0·47	0·96	1·33	0·84	0·24	0·14	-0·23	-0·59	-1·12
-0·38	-0·49	-0·49	-0·24	0·09	0·28	0·11	0·04	-0·09	-0·20	-0·29	-0·43
0	0	0	0	0	0	0	0	0	0	0	0

Table (5·9)

TEST 6 LOAD 5·846 lbf SPEED 35000 Rpm L/D 2·0

PRESSURE PROFILE (lb/in²) CIRCUMFERENTIAL STATION NUMBER											
1	2	3	4	5	6	7	8	9	10	11	12
0	0	0	0	0	0	0	0	0	0	0	0
-0·47	-0·64	-0·56	-0·35	-0·13	0·14	0·16	0·07	-0·02	-0·19	-0·32	-0·49
-1·59	-1·84	-1·10	-0·41	1·02	1·39	0·64	0·22	0·12	-0·21	-0·51	-1·24
-2·35	-2·85	-1·52	0·21	3·38	2·40	1·69	0·80	0·18	-0·55	-1·37	-2·31
-3·42	-3·13	-1·86	0·82	4·71	3.36	2·08	0·97	0·54	-0·83	-1·93	-3·03
-2·60	-2·36	-1·39	0·23	3·46	2·71	1·77	0·84	0·19	-0·63	-1·42	-2·35
-1·43	-1·03	-0·91	-0·10	1·26	1·51	0·94	0·28	0·16	-0·31	-0·67	-1·30
-0·36	-0·47	-0·28	-0·15	-0·25	0·38	0·16	0.01	-0·09	-0·22	-0·30	-0·45
0	0	0	0	0	0	0	0	0	0	0	0

Table (5·10)

ROTOR TESTS

15 mm 'O'-Ring Centres (Symmetric Rotor)

Rotor Data (Silicon)

Test	Ps Psi	Mass Flow g/min	Mr kg	Disc Dia. EndA	Disc Dia. EndB	Ip kgm²	It kgm²	Ip/It	ω_n Rpm	ls (m)	Mode	φ Deg	ω_n/ω
1	120	15·56	0·596	0	0	9·503E-5	2·221E-3	0·0431	23000	0	RSW	90	1·0
2	0	0	0·596	0	0	9·503E-5	2·221E-3	0·0431	20000	0	RSW	90	1·0
3	120	15·56	1·258	90+	90+	6·516E-4	6·759E-3	0·0964	17000	0	RSW	90	1·0
4	0	0	1·258	90+	90+	6·516E-4	6·759E-3	0·0964	15500	0	RSW	90	1·0
5	120	15·56	0·984	60	60	2·492E-4	3·657E-3	0·0683	18900	0	RSW	90	1·0
6	0	0	0·984	60	60	2·492E-4	3·657E-3	0·0683	16700	0	RSW	90	1·0

Bearing Data Bearing Material - Sulfinuz Steel

	Clearance	Bore mm	Mb kg	Ip kgm²	It kgm²	Ip/It	O-Ring Material	% O-Ring Pinch
Bearing A	0·0007	29·9999	0·074	2·031E-5	1·830E-5	1·11	S70	8·71
Bearing B	0·0033	30·0025	0·074	2·031E-5	1·830E-5	1·11	S70	8·71

Table (12·1)

Rotor Data (Viton)

Test	Ps Psi	Mass Flow g/min	Mr kg	Disc Dia. EndA	Disc Dia. EndB	Ip kgm²	It kgm²	Ip/It	ω_n Rpm	ls (m)	Mode	φ Deg	ω_n/ω
7	120	15·56	0·596	0	0	9·503E-5	2·221E-3	0·0431	23000	0	NID	-	1·0
8	0	0	0·596	0	0				20000	0	NID	-	1·0
9	120	15·56	0·984	60	60	2·492E-4	3·651E-3	0·0683	18900	0	NID	-	1·0
10	0	0	0·984	60	60				16700	0	NID	-	1·0
11	120	15·56	1·258	90+	90+	6·516E-4	6·759E-3	0·0964	17000	0	NID	-	1·0
12	0	0	1·258	90+	90+				15300	0	NID	-	1·0

Bearing Data Bearing Material - Sulfinuz Steel

	Clearance	Bore mm	Mb kg	Ip kgm²	It kgm²	Ip/It	O-Ring Material	% O-Ring Pinch
Bearing A	0·0007	29·9999	0·074	2·031E-5	1·830E-5	1·11	V70	9·38
Bearing B	0·0033	30·0025	0·074	2·031E-5	1·830E-5	1·11	V70	9·38

Table (12·2)

5 mm 'O'-Ring Centres (Symmetric Rotor)

Rotor Data (Silicon)

Test	Ps Psi	Mass Flow g/min	Mr kg	Disc Dia. EndA	Disc Dia. EndB	Ip kgm²	It kgm²	Ip/It	ω_n Rpm	ls (m)	Mode	φ Deg.	ω_n/ω
13	120	23·71	0·596	0	0	9·503E-5	2·221E-3	0·0431	21000	0	RSW	90	1·0
14	0	0	0·596	0	0				17100	0	HFW	90	1·0
15	120	23·71	0·9844	60	60	2·492E-4	3·651E-3	0·0683	19000	0	RSW	90	1·0
16	0	0	0·9844	60	60				16400	0	HFW	90	1·0
17	120	23·71	1·258	90+	90+	6·516E-4	6·759E-4	0·0964	16200	0	RSW	90	1·0
18	0	0	1·258	90+	90+				14000		HFW	90	1·0

Bearing Data Bearing Material - Sulfinuz Steel

	Clearance	Bore mm	Mb kg	Ip kgm²	It kgm²	Ip/It	O-Ring Material	% O-Ring Pinch
Bearing A	0·0033	30·0025	0·0743	2·040E-5	1·838E-5	1·11	S70	9·30
Bearing B	0·0058	30·0050	0·0744	2·042E-5	1·840E-5	1·11	S70	8·93

Table (12·3)

Rotor Data (Viton)

Test	Ps Psi	Mass Flow g/min	Mr kg	Disc Dia. EndA	Disc Dia. EndB	Ip kgm²	It kgm²	Ip/It	ω_n Rpm	ls (m)	Mode	φ Deg.	ω_n/ω
19	120	23·71	0·596	0	0	9·503E-5	2·221E-3	0·0431	21000	0	NID	-	1·0
20	0	0	0·596	0	0				33000	0	RSW	90	1·0
21	120	23·71	0·9844	60	60	2·492E-4	3·651E-3	0·0683	18900	0	NID	-	1·0
22	0	0	0·9844	60	60				34500	0	RSW	90	1·0
23	120	23·71	1·258	90+	90+	6·516E-4	6·759E-3	0·0964	38600	0	RSW	90	1·0
24	0	0	1·258	90+	90+				41000	0	RSW	90	1·0

Bearing Data Bearing Material - Sulfinuz Steel

	Clearance	Bore mm	Mb kg	Ip kgm²	It kgm²	Ip/It	O-Ring Material	% O-Ring Pinch
Bearing A	0·0033	30·0025	0·0743	2·040E-5	1·838E-5	1·11	V70	9·96
Bearing B	0·0058	30·0050	0·0744	2·042E-5	1·840E-5	1·11	V70	9·60

Table (12·4)

7·5 mm 'O'-Ring Centres (Symmetric Rotor)

Rotor Data (Silicon)

Test	Ps Psi	Mass Flow g/min	Mr kg	Disc Dia. EndA	Disc Dia. EndB	Ip kgm²	It kgm²	Ip/It	ω_n Rpm	ls (m)	Mode	φ Deg.	ω_n/ω
25	120	15·56	0·596	0	0	9·503E-5	2·221E-3	0·0431	25200	0	RSW	90	1·0
26	0	0	0·596	0	0				19000	0	RSW	90	1·0
									31000		HFW	90	0·58
27	120	15·56	0·9844	60	60	2·492E-4	3·651E-3	0·0683	19000	0	RSW	90	1·0
28	0	0	0·9844	60	60				16000	0	RSW	90	1·0
									24400		HFW	90	0·49
29	120	15·56	1·258	90+	90+	6·516E-4	6·759E-3	0·0964	17900	0	RSW	90	1·0
30	0	0	1·258	90+	90+				14200	0	RSW	90	1·0
									21000	0	HFW	90	0·51

Bearing Data Bearing Material - Sulfinuz Steel

	Clearance	Bore mm	Mb kg	Ip kgm²	It kgm²	Ip/It	O-Ring Material	% O-Ring Pinch
Bearing A	0·0058	30·0050	0·0739	2·029E-5	1·828E-5	1·11	S70	8·79
Bearing B	0·0033	30·0025	0·0742	2·037E-5	1·835E-5	1·11	S70	8·57

Table (12·5)

Rotor Data (Viton)

Test	Ps Psi	Mass Flow g/min	Mr kg	Disc Dia. EndA	Disc Dia. EndB	Ip kgm²	It kgm²	Ip/It	ω_n Rpm	ls (m)	Mode	φ Deg.	ω_n/ω
31	120	15·56	0·596	0	0	9·503E-5	2·221E-3	0·0431	25200	0	NID	-	-
32	0	0	0·596	0	0				36500	0	RSW	90	1·0
33	120	15·56	0·9844	60	60	2·492E-4	3·651E-3	0·0683	19000	0	NID	-	-
34	0	0	0·9844	60	60				39600	0	RSW	90	1·0
35	120	15·56	1·258	90+	90+	6·516E-4	6·759E-3	0·0964	17900	0	NID	-	-
36	0	0	1·258	90+	90+				41000	0	RSW	90	1·0

Bearing Data Bearing Material - Sulfinuz Steel

	Clearance	Bore mm	Mb kg	Ip kgm²	It kgm²	Ip/It	O-Ring Material	% O-Ring Pinch
Bearing A	0·0058	30·0050	0·0739	2·029E-5	1·828E-5	1·11	V70	9·45
Bearing B	0·0033	30·0025	0·0742	2·037E-5	1·835E-5	1·11	V70	9·23

Table (12·6)

10 mm 'O'-Ring Centres (Symmetric Rotor)

Rotor Data (Silicon)

Test	Ps Psi	Mass Flow g/min	Mr kg	Disc Dia. EndA	Disc Dia. EndB	Ip kgm²	It kgm²	Ip/It	ω_n Rpm	ls (m)	Mode	φ Deg.	ω_n/ω
37	120	13·13	0·596	0	0	9·503E-5	2·221E-3	0·043	23800	0	RSW	90	1·0
38	0	0	0·596	0	0				18800	0	RSW	90	1·0
									30500		HFW	90	0·55
39	120	13·13	0·9844	60	60	2·492E-4	3·651E-3	0·0683	20400	0	RSW	90	1·0
									32000		HFW	90	0·49
40	0	0	0·9844	60	60				16300	0	RSW	90	1·0
									22400		HFW	90	0·52
41	120	13·13	1·258	90+	90+	6·516E-4	6·759E-3	0·0964	18400	0	RSW	90	1·0
									30900		HFW	90	0·54
42	0	0	1·258	90+	90+				15500	0	RSW	90	1·0
									20500		HFW	90	0·49

Bearing Data Bearing Material - Sulfinuz Steel

	Clearance	Bore mm	Mb kg	Ip kgm²	It kgm²	Ip/It	O-Ring Material	% O-Ring Pinch
Bearing A	0·0033	30·0025	0·0744	2·042E-5	1·840E-5	1·11	S70	8·71
Bearing B	0·0007	29·9999	0·0741	2·034E-5	1·833E-5	1·11	S70	8·57

Table (12·7)

Rotor Data (Viton)

Test	Ps Psi	Mass Flow g/min	Mr kg	Disc Dia. EndA	Disc Dia. EndB	Ip kgm²	It kgm²	Ip/It	ω_n Rpm	ls (m)	Mode	φ Deg.	ω_n/ω
43	120	13·13	0·596	0	0	9·503E-5	2·221E-3	0·043	23800	0	NID	-	-
44	0	0	0·596	0	0				38400	0	RSW	90	1·0
45	120	13·13	0·9844	60	60	2·492E-4	3·651E-3	0·0683	19000	0	NID	-	-
46	0	0	0·9844	60	60				40500	0	RSW	90	1·0
47	120	13·13	1·258	90+	90+	6·516E-4	6·759E-3	0·0964	17900	0	NID	-	-
48	0	0	1·258	90+	90+				37900	0	RSW	90	1·0

Bearing Data Bearing Material - Sulfinuz Steel

	Clearance	Bore mm	Mb kg	Ip kgm²	It kgm²	Ip/It	O-Ring Material	% O-Ring Pinch
Bearing A	0·0033	30·0025	0·0744	2·042E-5	1·840E-5	1·11	V70	9·38
Bearing B	0·0007	29·9999	0·0741	2·034E-5	1·833E-5	1·11	V70	9·23

Table (12·8)

20 mm 'O'-Ring Centres (Symmetric Rotor)

Rotor Data (Silicon)

Test	Ps Psi	Mass Flow g/min	Mr kg	Disc Dia. EndA	Disc Dia. EndB	Ip kgm²	It kgm²	Ip/It	ω_n Rpm	ls (m)	Mode	φ Deg.	ω_n/ω
49	120	18·84	0·596	0	0	9·503E-5	2·221E-3	0·043	23600	0	RSW	90	1·0
50	0	0	0·596	0	0				20100	0	RSW	90	1·0
51	120	18·84	0·9844	60	60	2·492E-4	3·651E-3	0·0683	18700	0	RSW	90	1·0
52	0	0	0·9844	60	60				16400	0	RSW	90	1·0
53	120	18·84	1·258	90+	90+	6·516E-4	6·759E-3	0·0964	17400	0	RSW	90	1·0
54	0	0	1·258	90+	90+				15600	0	RSW	90	1·0

Bearing Data Bearing Material - Sulfinuz Steel

	Clearance	Bore mm	Mb kg	Ip kgm²	It kgm²	Ip/It	O-Ring Material	% O-Ring Pinch
Bearing A	0·0033	30·0025	0·0741	2·034E-5	1·833E-5	1·11	S70	8·57
Bearing B	0·0033	30·0025	0·0745	2·045E-5	1·843E-5	1·11	S70	9·00

Table (12·9)

25 mm 'O'-Ring Centres (Symmetric Rotor)

Rotor Data (Silicon)

Test	Ps Psi	Mass Flow g/min	Mr kg	Disc Dia. EndA	Disc Dia. EndB	Ip kgm²	It kgm²	Ip/It	ω_n Rpm	ls (m)	Mode	φ Deg.	ω_n/ω
61	120	17·02	0·596	0	0	9·503E-5	2·221E-3	0·043	25800	0	RSW	90	1·0
62	0	0	0·596	0	0				21700	0	RSW	90	1·0
63	120	17·02	0·9844	60	60	2·492E-4	3·651E-3	0·0683	19800	0	RSW	90	1·0
64	0	0	0·9844	60	60				16200	0	RSW	90	1·0
65	120	17·02	1·258	90+	90+	6·516E-4	6·759E-3	0·0964	18100	0	RSW	90	1·0
66	0	0	1·258	90+	90+				15700	0	RSW	90	1·0

Bearing Data Bearing Material - Sulfinuz Steel

	Clearance	Bore mm	Mb kg	Ip kgm²	It kgm²	Ip/It	O-Ring Material	% O-Ring Pinch
Bearing A	0·0007	29·9999	0·0741	2·034E-5	1·833E-5	1·11	S70	8·71
Bearing B	0·0007	29·9999	0·0745	2·045E-5	1·843E-5	1·11	S70	8·80

Table (12·10)

NB Tests 55 - 60 and 67 - 72 were exploratory only, as other trends have indicated, no Instability was detected.

15 mm 'O'-Ring Centres (Symmetric Porous Bearing)

Rotor Data (Silicon)

Test	Ps Psi	Mass Flow g/min	Mr kg	Disc Dia. EndA	Disc Dia. EndB	Ip kgm²	It kgm²	Ip/It	ω_n Rpm	ls (m)	Mode	φ Deg.	ω_n/ω
73	120	59·57	0·596	0	0	9·503E-5	2·221E-3	0·043	24900	0	RSW	90	1·0
74	120	61·39	0·9844	60	60	2·492E-4	3·651E-3	0·0683	17800	0	RSW	90	1·0
									24500		HFW	90	1·0
75	120	61·39	1·258	90+	90+	6·516E-4	6·759E-3	0·0964	11500	0	RSW	90	1·0
											TD		

Bearing Data Bearing Material - Porous Phospher

	Clearance	Bore	Mb kg	Ip kgm²	It kgm²	Ip/It	O-Ring Material	% O-Ring Pinch
Bearing A	0·0008	30·0000	0·0663	1·852E-5	1·492E-5	1·242	S70	7·90
Bearing B	0·0008	30·0000	0·0663	1·852E-5	1·492E-5	1·242	S70	7·17

Table (12·11)

Rotor Data (Viton)

Test	Ps Psi	Mass Flow g/min	Mr Kg	Disc Dia. EndA	Disc Dia. EndB	Ip kgm²	It kgm²	Ip/It	ω_n Rpm	ls (m)	Mode	φ Deg.	ω_n/ω
76	120	41·94	0·596	0	0	9·503E-5	2·221E-3	0·043	25000	0	RSW	90	1·0
											TD	-	-
77	120	41·94	0·9844	60	60	2·492E-4	3·651E-3	0·0683	17500	0	RSW	90	1·0
											TD	-	-
78	120	41·94	1·258	90+	90+	6·516E-4	6·759E-3	0·0964	15500	0	RSW	90	1·0
											TD	-	-

Bearing Data Bearing Material - Porous Phospher

	Clearance	Bore	Mb kg	Ip kgm²	It kgm²	Ip/It	O-Ring Material	% O-Ring Pinch
Bearing A	0·0008	30·000	0·0663	1·852E-5	1·492E-5	1·242	V70	8·58
Bearing B	0·0008	30·000	0·0663	1·852E-5	1·492E-5	1·242	V70	7·85

Table (12·12)

25 mm 'O'-Ring Centres (Symmetric Porous Bearing)

Rotor Data (Silicon)

Test	Ps Psi	Mass Flow g/min	Mr kg	Disc Dia. EndA	Disc Dia. EndB	Ip kgm²	It kgm²	Ip/It	ω_n Rpm	ls (m)	Mode	φ Deg.	ω_n/ω
79	120	87·53	0·596	0	0	9·503E-5	2·221E-3	0·043	26000	0	RSW	90	1·0
80	120	87·53	0·9844	60	60	2·492E-4	3·651E-3	0·0683	17900	0	RSW TD	90	1·0
81	120	87·53	1·258	90+	90+	6·516E-4	6·759E-3	0·0964	15900	0	RSW TD	90	1·0

Bearing Data Bearing Material - Porous Phospher Bronze

	Clearance	Bore	Mb kg	Ip kgm²	It kgm²	Ip/It	O-Ring Material	% O-Ring Pinch
Bearing A	0·0008	30·0000	0·774	2·223E-5	1·772E-5	1·254	S70	5·63
Bearing B	0·0008	30·0000	0·0774	2·223E-5	1·772E-5	1·254	S70	6·95

Table (12·13)

Rotor Data (Viton)

Test	Ps Psi	Mass Flow g/min	Mr kg	Disc Dia. EndA	Disc Dia. EndB	Ip kgm²	It kgm²	Ip/It	ω_n Rpm	ls (m)	Mode	φ Deg.	ω_n/ω
82	120	87·53	0·596	0	0	9·503E-5	2·221E-3	0·043	28000	0	RSW	90	1·0
83	120	87·53	0·9844	60	60	2·492E-4	3·651E-3	0·0683	} Viton		Seized	-	
84	120	87·53	1·258	90	90	6·516E-4	6·759E-3	0·0964	} O-Ring Melted		Seized	-	

Bearing Data Bearing Material - Porous Phospher Bronze

	Clearance	Bore	Mb kg	Ip kgm²	It kgm²	Ip/It	O-Ring Material	% O-Ring Pinch
Bearing A	0·0008	30·0000	0·0774	2·223E-5	1·772E-5	1·254	V70	6·31
Bearing B	0·0008	30·0000	0·0774	2·223E-5	1·772E-5	1·254	V70	7·63

Table (12·14)

15 mm 'O'-Ring Centres (Assymetric Rotor)

Rotor Data (Silicon)

Test	Ps Psi	Mass Flow g/min	Mr kg	Disc Dia. EndA	Disc Dia. EndB	Ip kgm²	It kgm²	Ip/It	ω_n Rpm	ls (m)	Mode	φ Deg.	ω_n/ω
85	120	15·56	0·932	90	0	3·733E-4	3·744E-3	0·0997	22900	0·0285	RSW	90	1·0
86	0	0	0·932	90	0			0·0997	17500	0·0285	RSW	90	1·0
87	120	15·56	1·1213	90	60	4·504E-4	5·809E-3	0·0775	21000	0·0096	RSWA	90	1·0
									19400		RSWB	90	1·0
88	0	0	1·1213	90	60			0·0775	14600	0·0096	HFW	90	1·0
89	120	15·56	0·932	0	90	3·733E-4	3·744E-3	0·0997	22900	0·0285	RSW	90	1·0
90	0	0	0·932	0	90			0·0997	17500	0·0285	RSW	90	1·0
91	120	15·56	0·7951	60	0	1·721E-4	3·331E-3	0·052	21000	0·01995	RSWB	90	1·0
									22000		RSWA	90	1·0
92	0	0	0·7951	60	0			0·052	18400	0·01995	RSWB	90	1·0
									18900		RSWA	90	1·0
93	120	15·56	0·7954	0	60	1·721E-4	3·331E-3	0·052	28000	0·01995	RSWA	90	1·0
									22000		RSWB	90	1·0
94	0	0	0·7954	0	60			0·052	18400	0·01995	RSWA	90	1·0
									18900		RSWB	90	1·0
95	120	15·56	1·1211	60	90	4·504E-4	5·809E-3	0·0775	18400	0·0096	RSWB	90	1·0
									18900		RSWA	90	1·0
96	0	0	1·1211	60	90			0·0775	14200	0·0096	HFW	90	1·0

Bearing Data Bearing Material - Sulfinuz Steel

	Clearance	Bore	Mb kg	Ip kgm²	It kgm²	Ip/It	O-Ring Material	% O-Ring Pinch
Bearing A	0·0007	29·9999	0·0740	2·0313E-5	1·830E-5	1·11	S70	8·71
Bearing B	0·0033	30·0025	0·0740	2·0313E-5	1·830E-5	1·11	S70	8·71

Table (12·15)

20 mm 'O'-Ring Centres (Unbalance Response)

Rotor Data (Silicon)

Test	Ps Psi	Mass Flow g/min	Mr kg	Disc Dia. EndA	Disc Dia. EndB	Ip kgm²	It kgm²	Ip/It	ω_n Rpm	ls (m)	Mode	φ Deg.	ω_n/ω
97	120	18·84	1·258	90+	90+	6·516E-4	6·759E-3	0·0964	11060		RSW	90	1·0
98	0	0	1·258	90+	90+	6·516E-4	6·759E-3	0·0964	10800		RSW	90	1·0
									18000		TD	90	-
99	120	18·84	1·258	90+	90+	6·516E-4	6·759E-3	0·0964	13200		RSW	90	1·0
100	0	0	1·258	90+	90+	6·516E-4	6·759E-3	0·0964	10000		TD	90	1·0

Bearing Data Bearing Material - Sulfinuz Steel

	Clearance	Bore	Mb kg	Ip kgm²	It kgm²	Ip/It	O-Ring Material	% O-Ring Pinch
Bearing A	0·0033	30·0025	0·0741	2·042E-5	1·842E-5	1·11	S70	8·57
Bearing B	0·0033	30·0025	0·0745	2·037E-5	1·835E-5	1·11	S70	9·00

Table (12·16)

Plate (4·1)

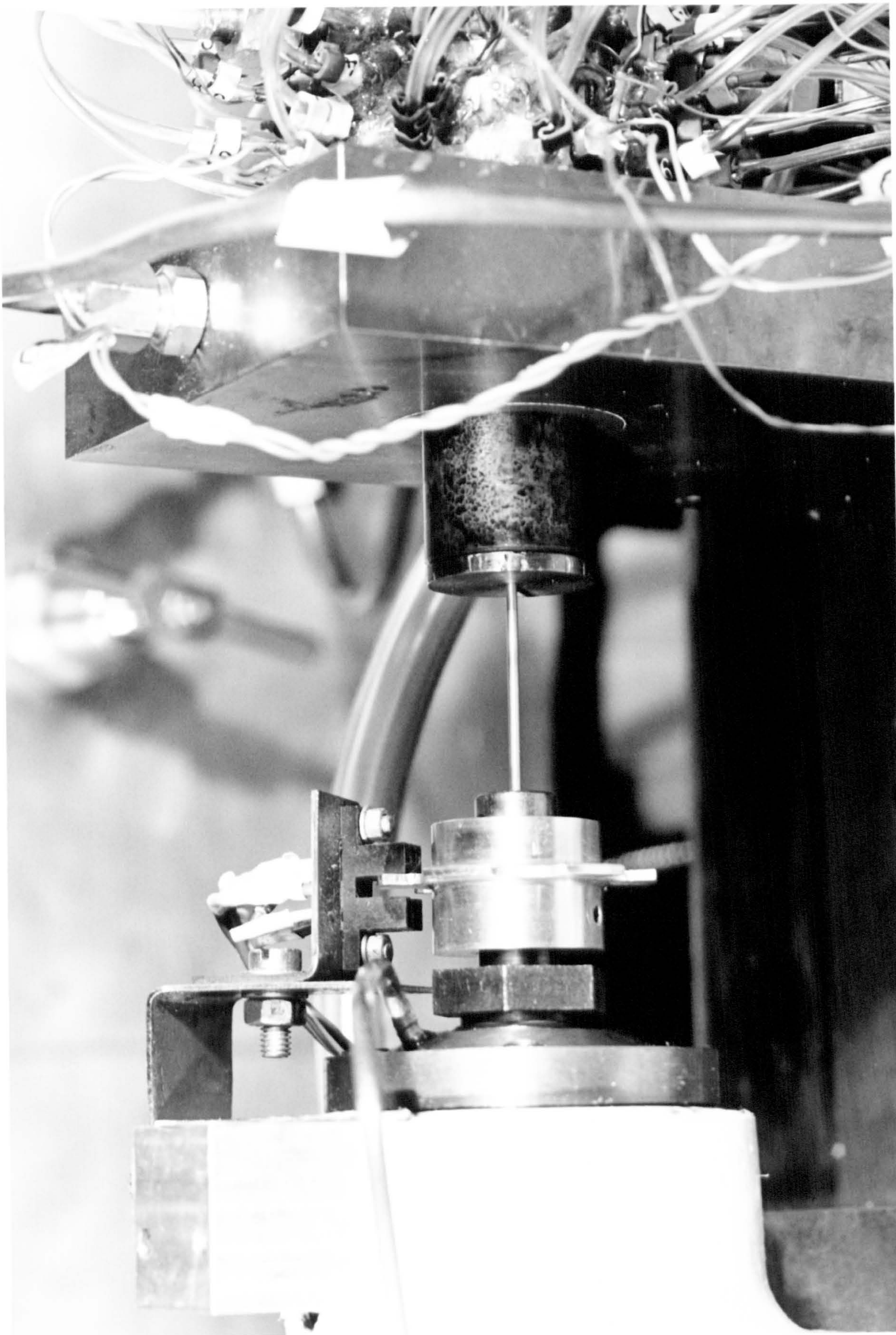

Plate (4·2)

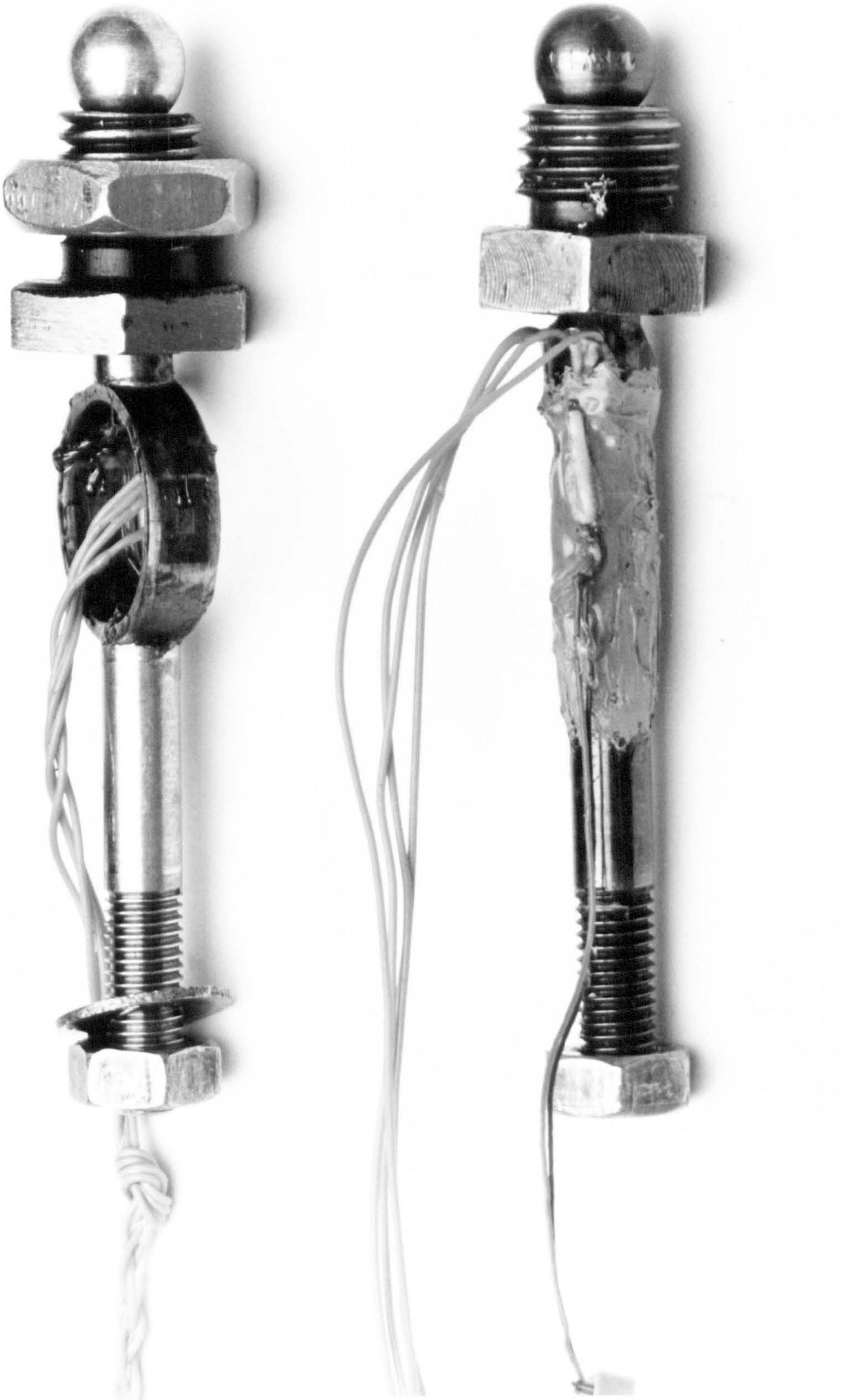

Plate (4·3)

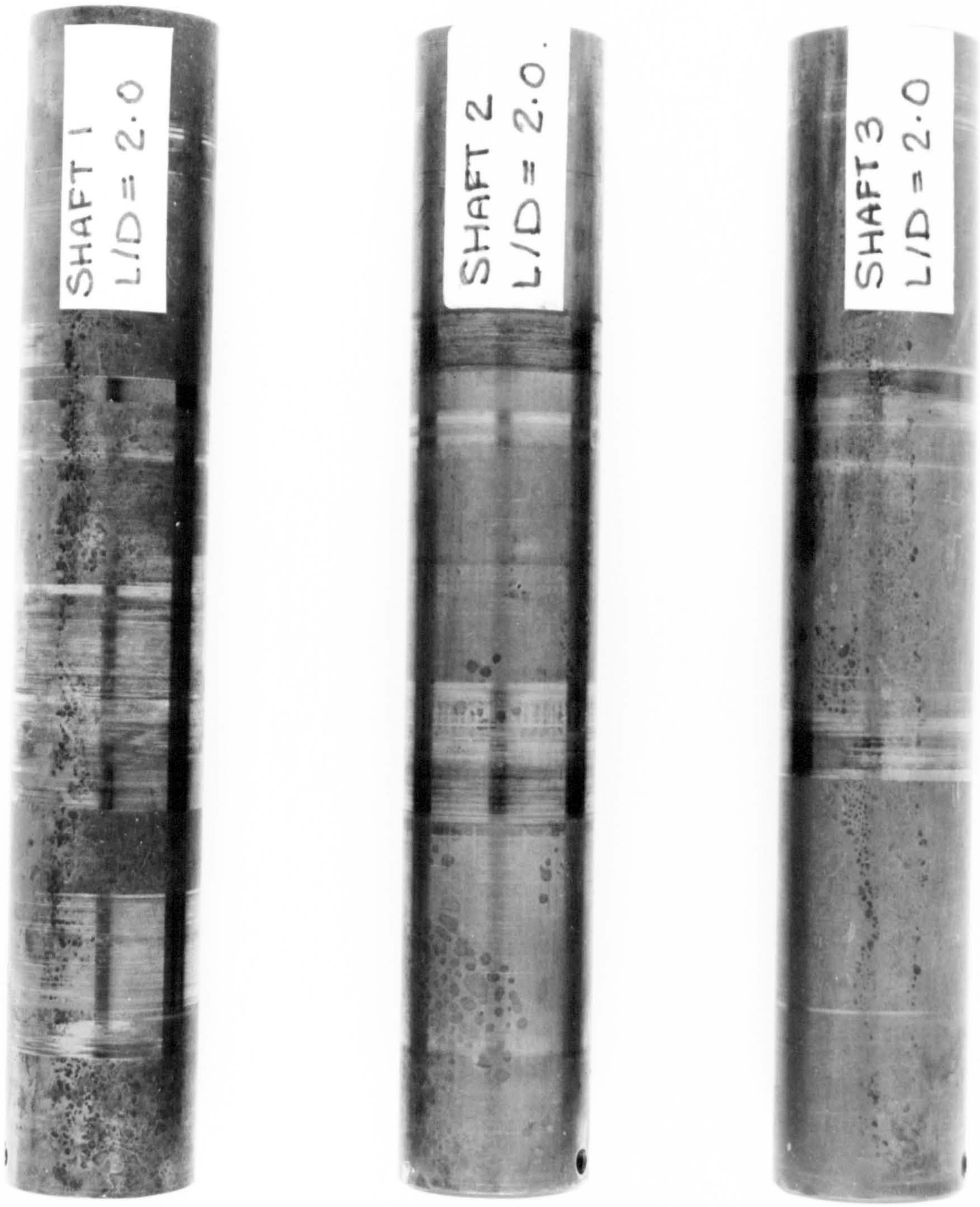

Plate (4.4)

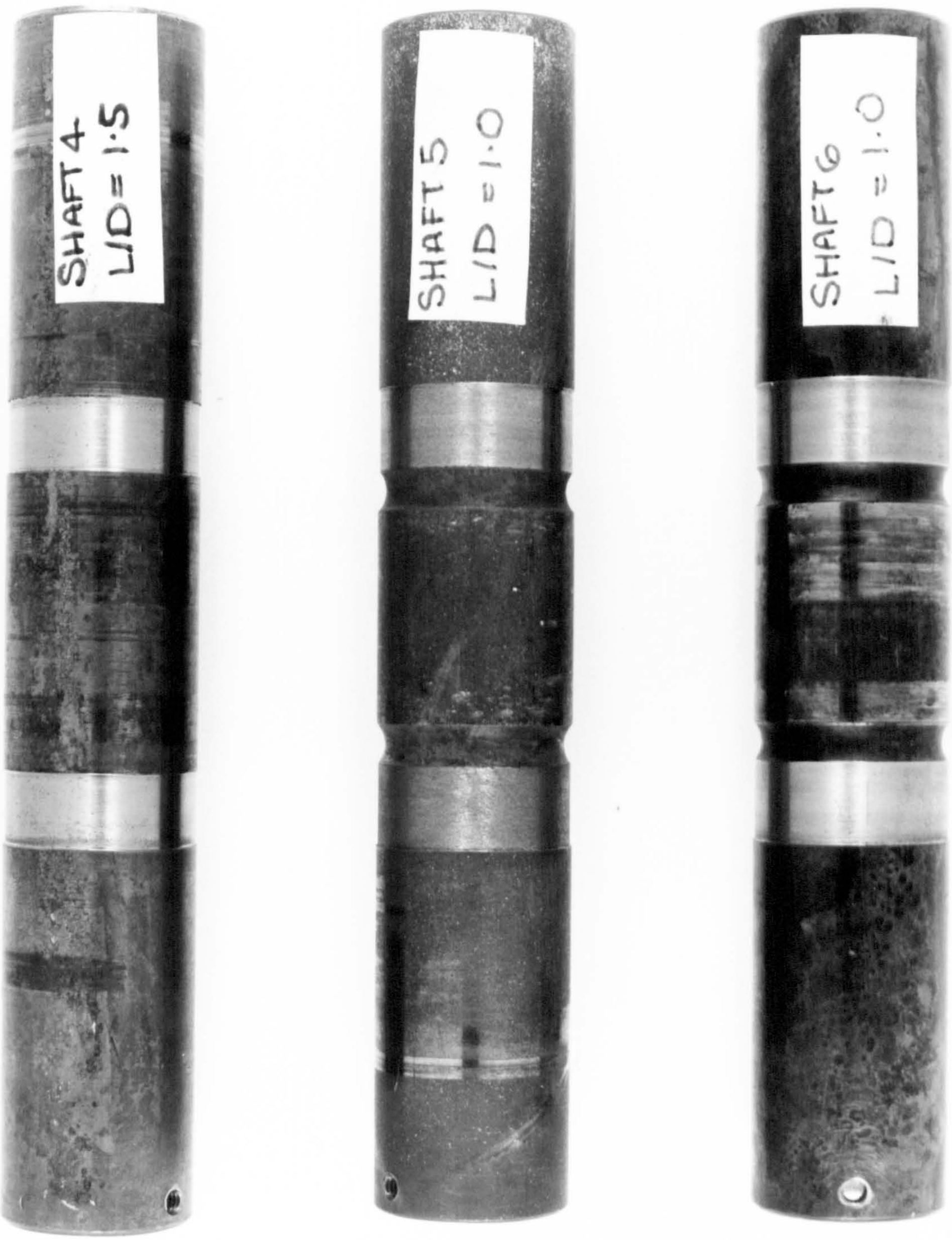

Plate (4·5)

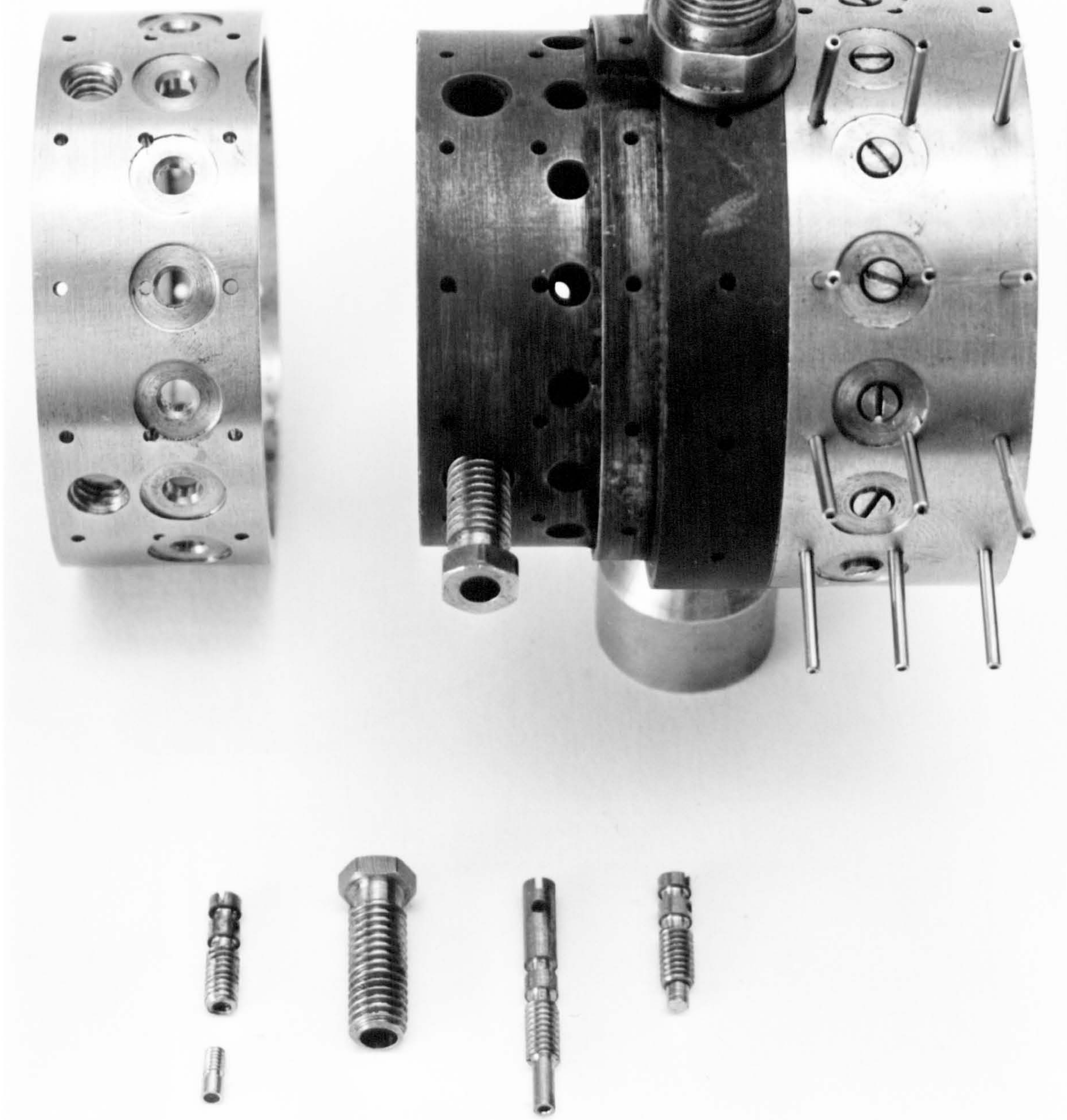

Plate (4·6)

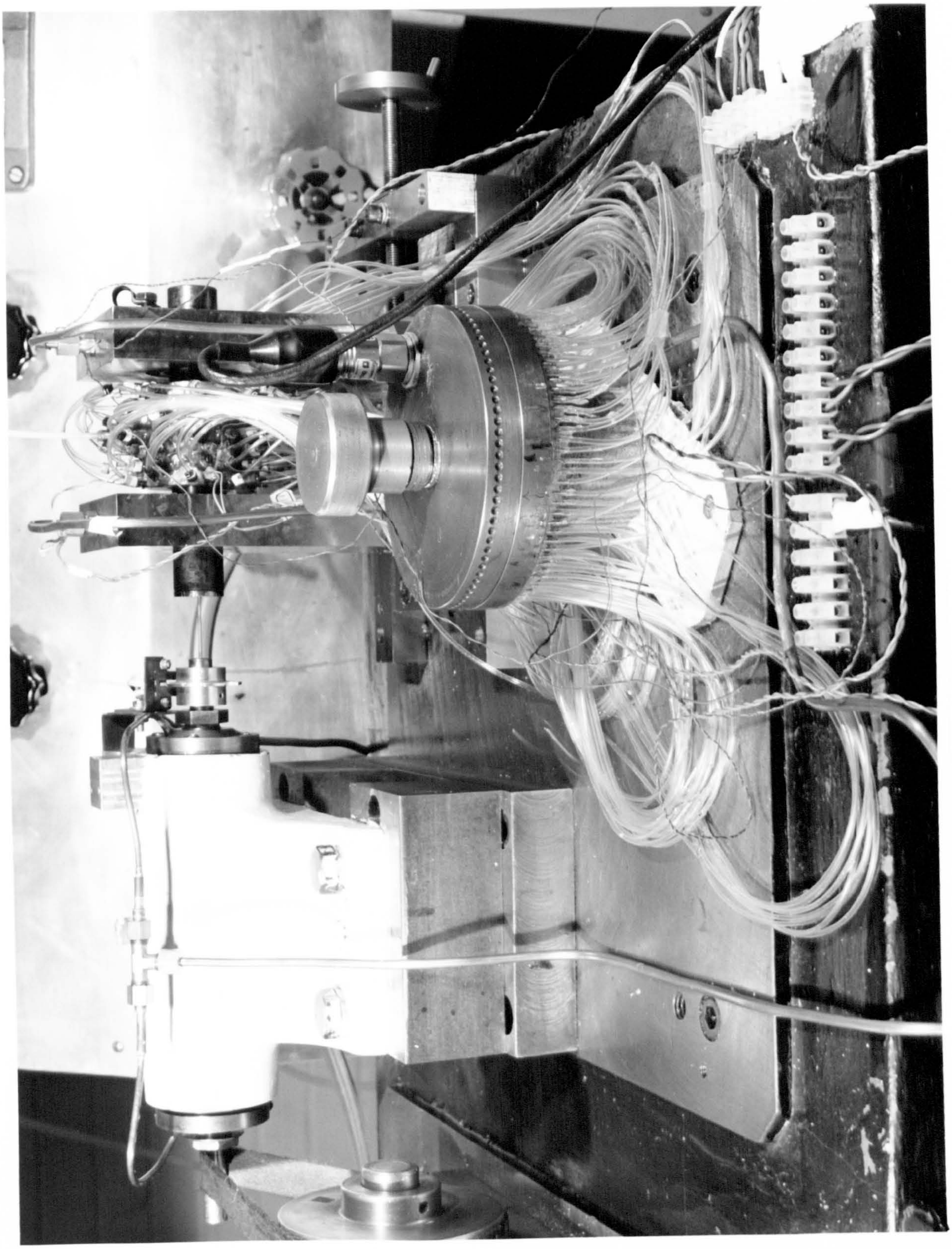

Plate (4.7)

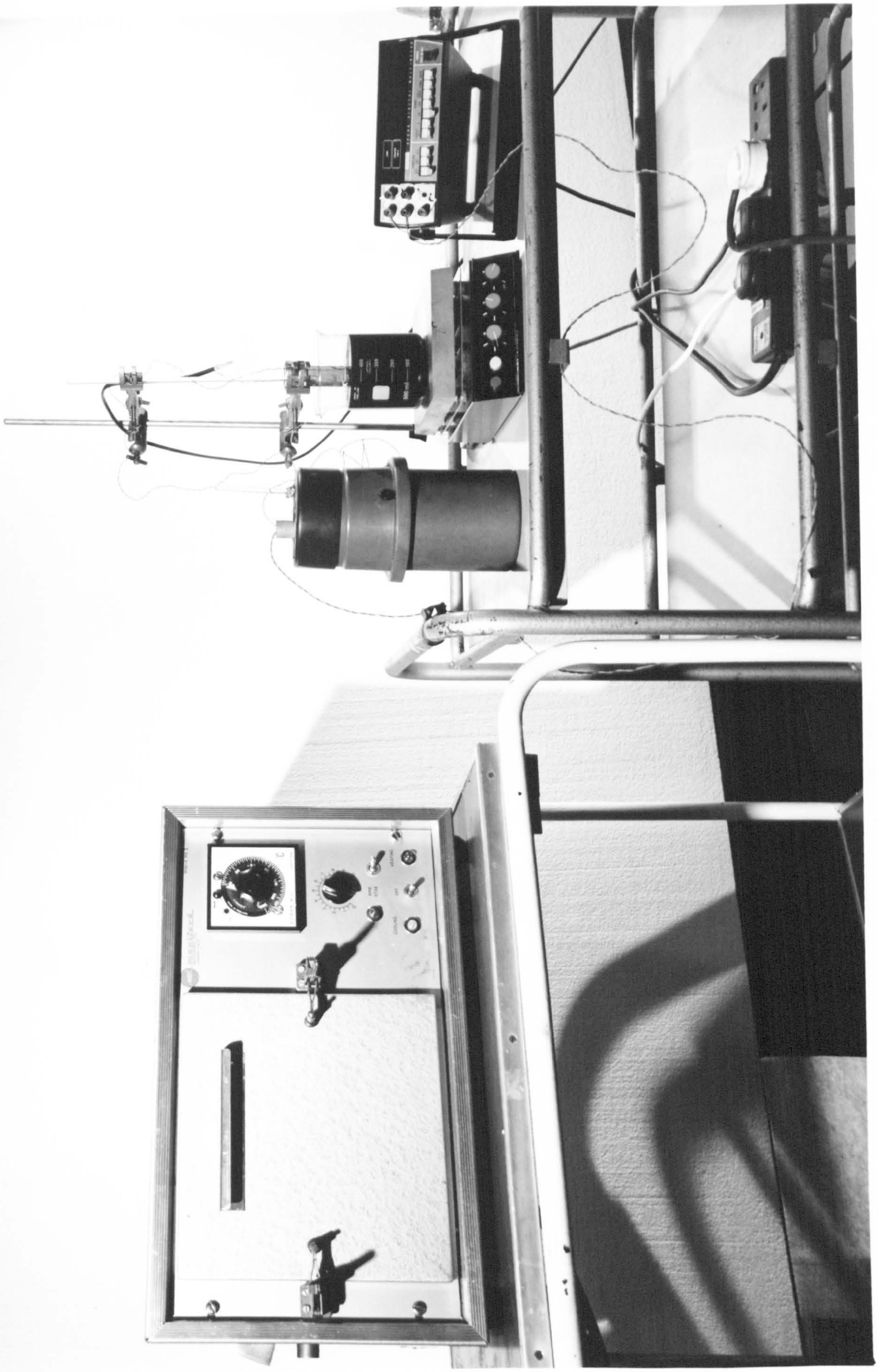

Plate (4·8)

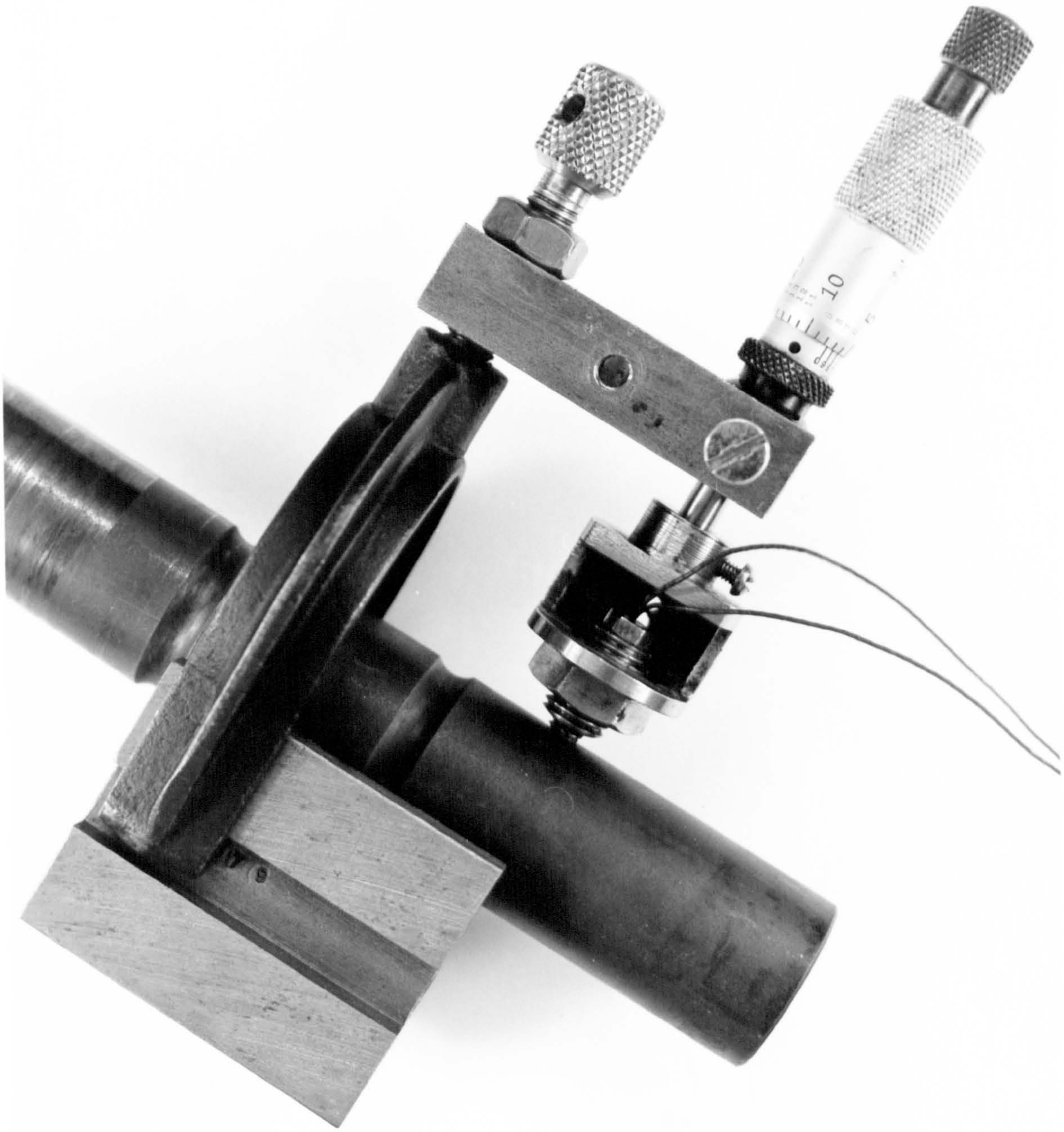

Plate (4·9)

Plate (8·1)

Plate 〈 8·2 〉

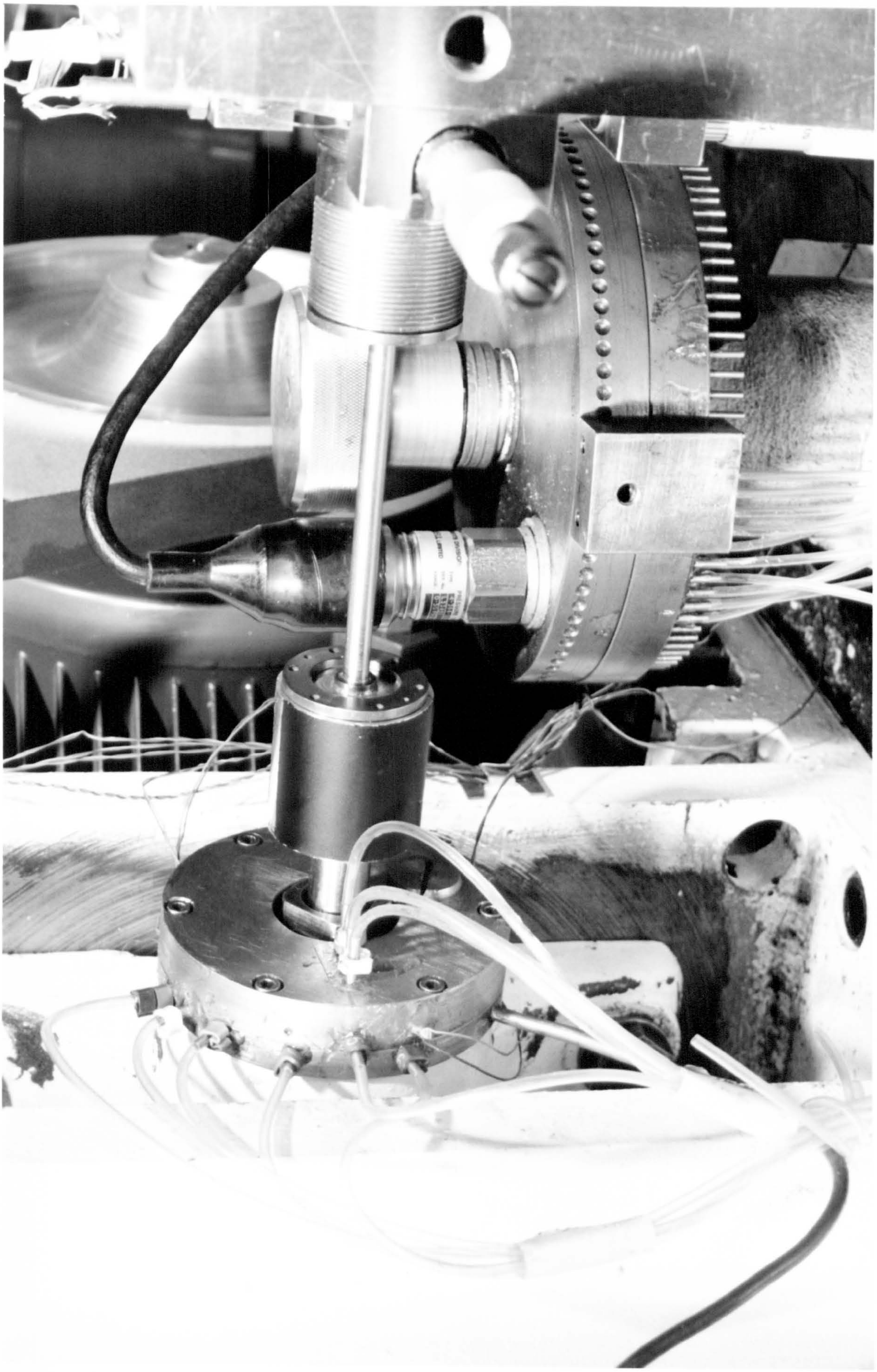

Plate (8·3)

Plate (8·4)

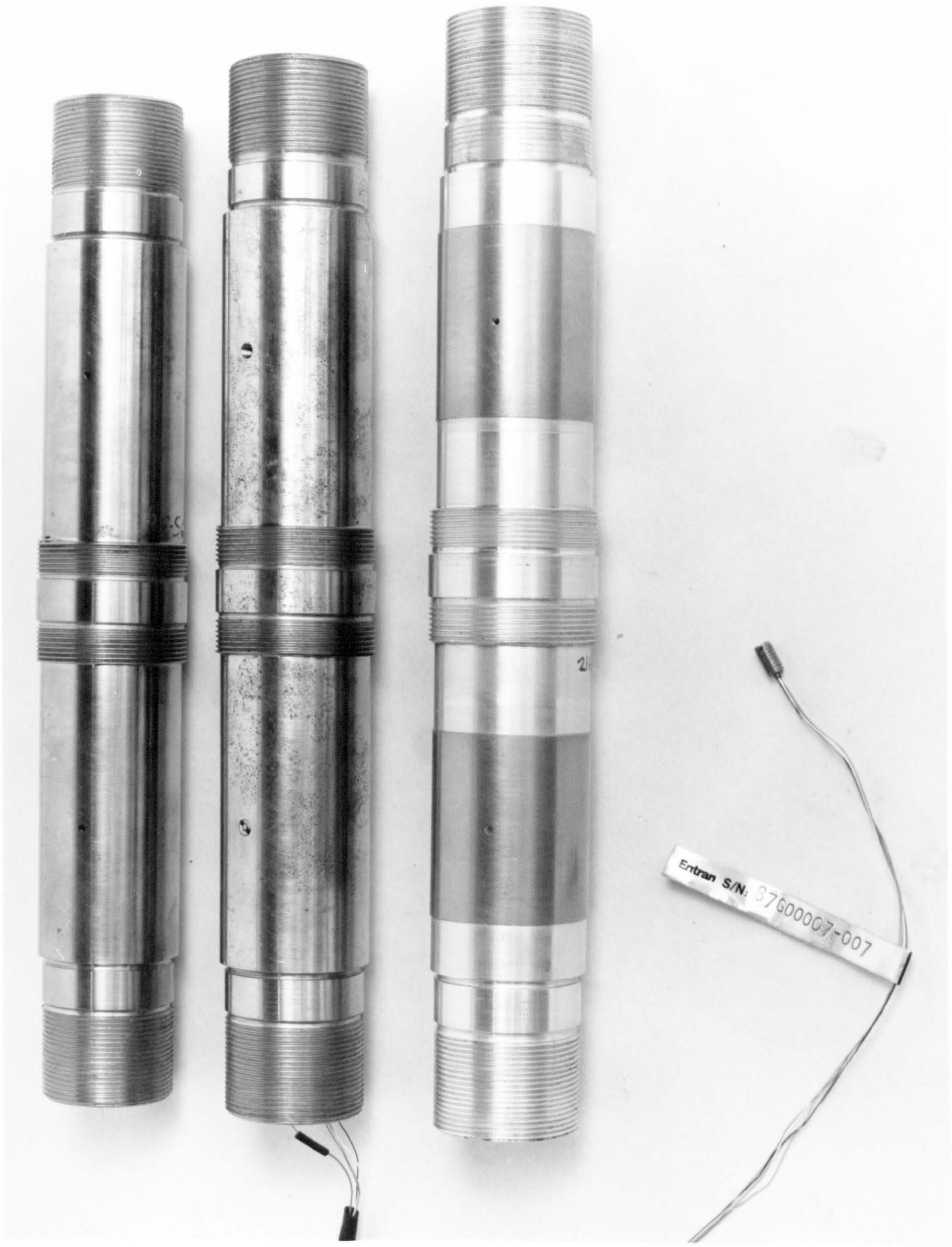

Plate (8.5)

Plate (8·6)

Plate (8·7)

Plate (8·8)

Plate 8.9)

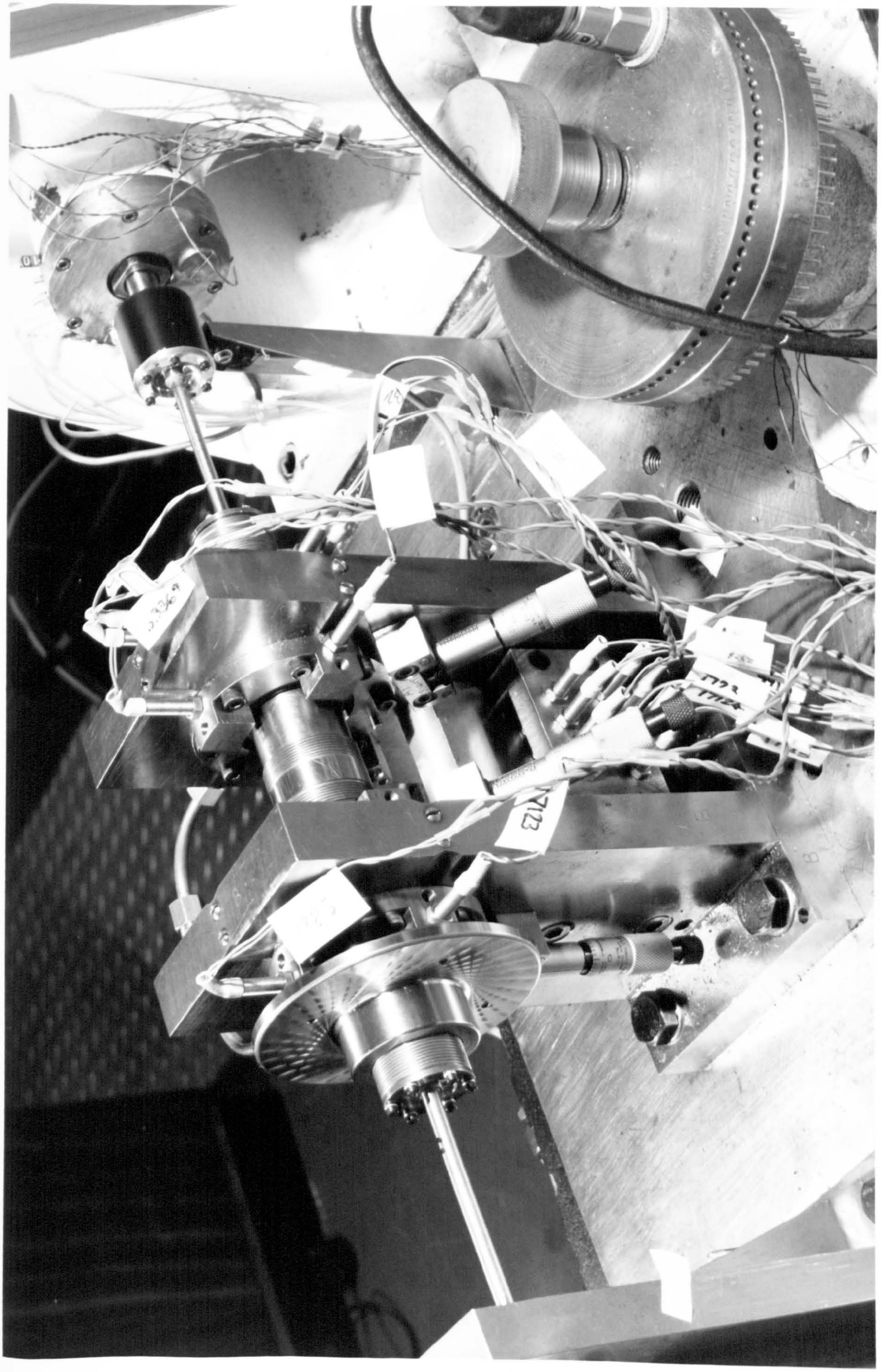

Plate ‹ 8·10 ›

Plate (8·11)

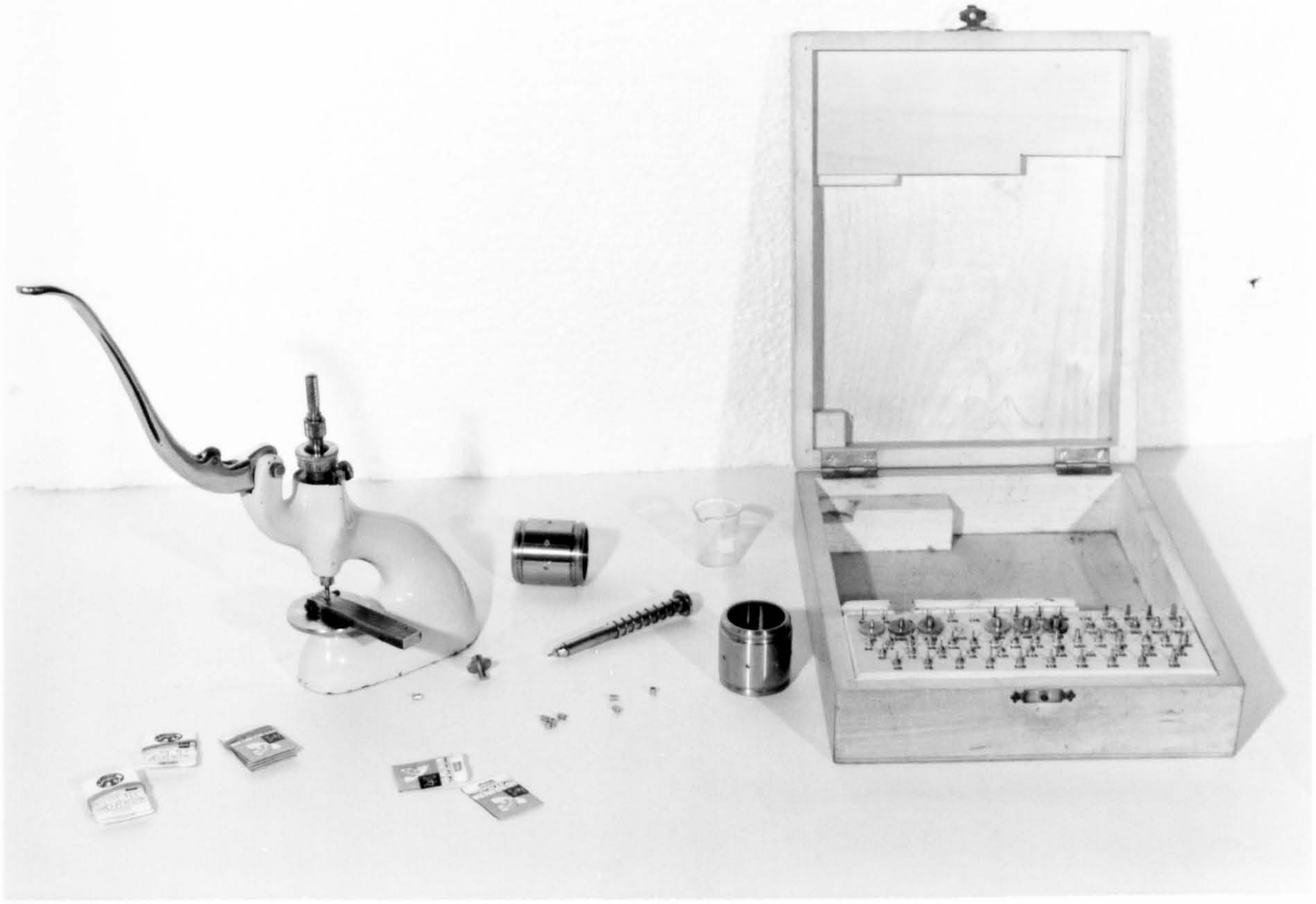

Plate (8·12)

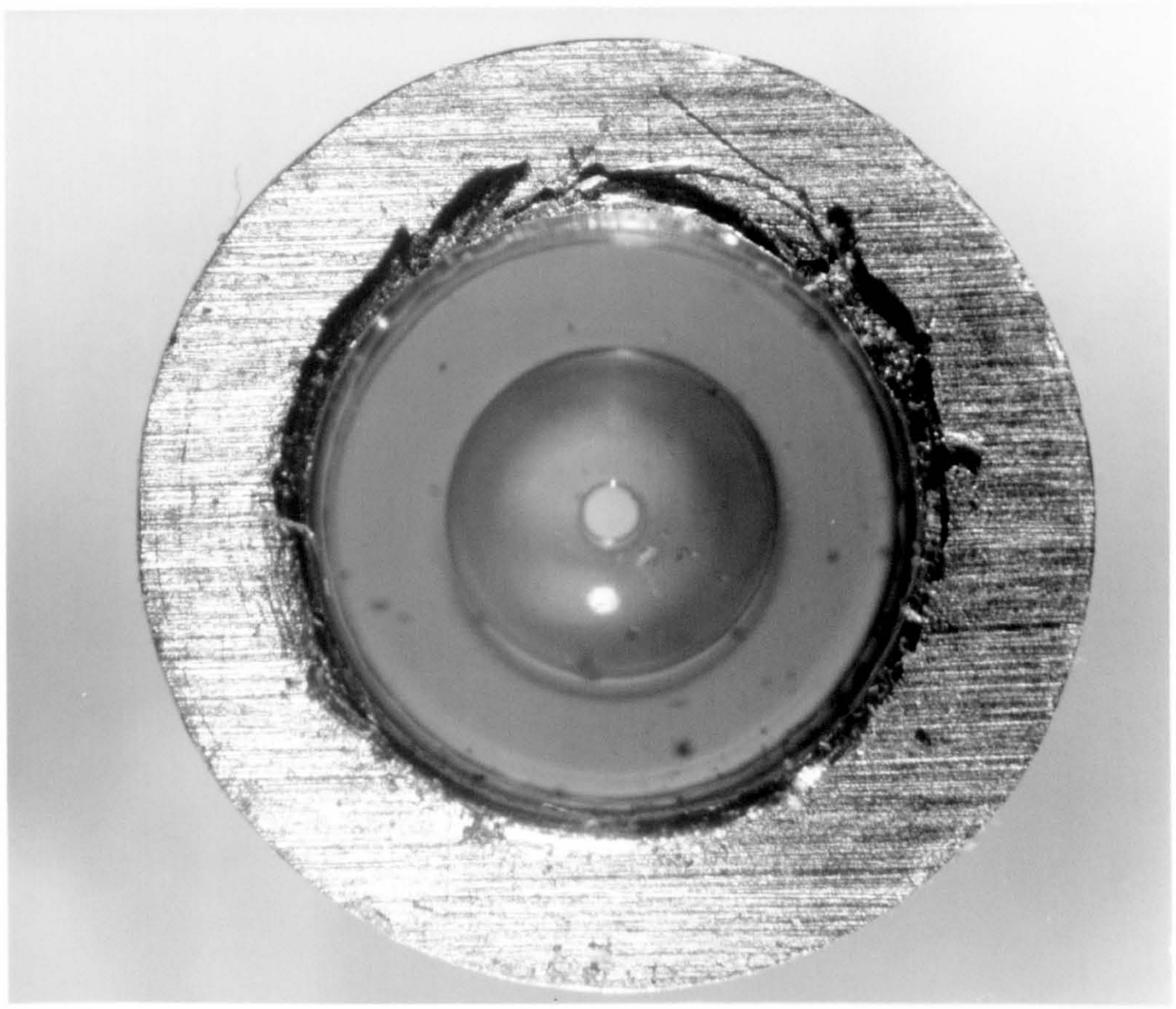

Plate (8·13)

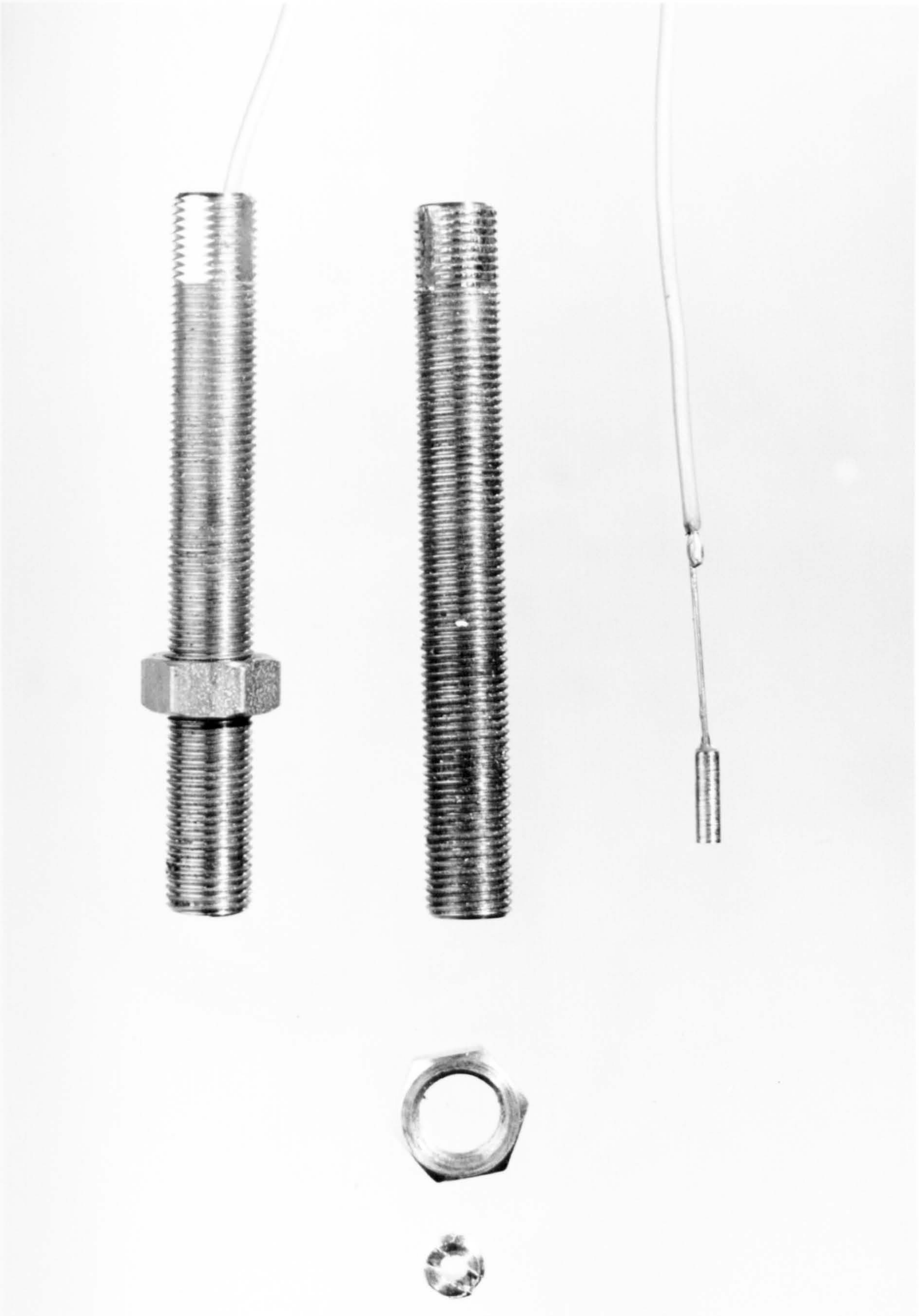

Plate (8.14)

Plate (8·15)

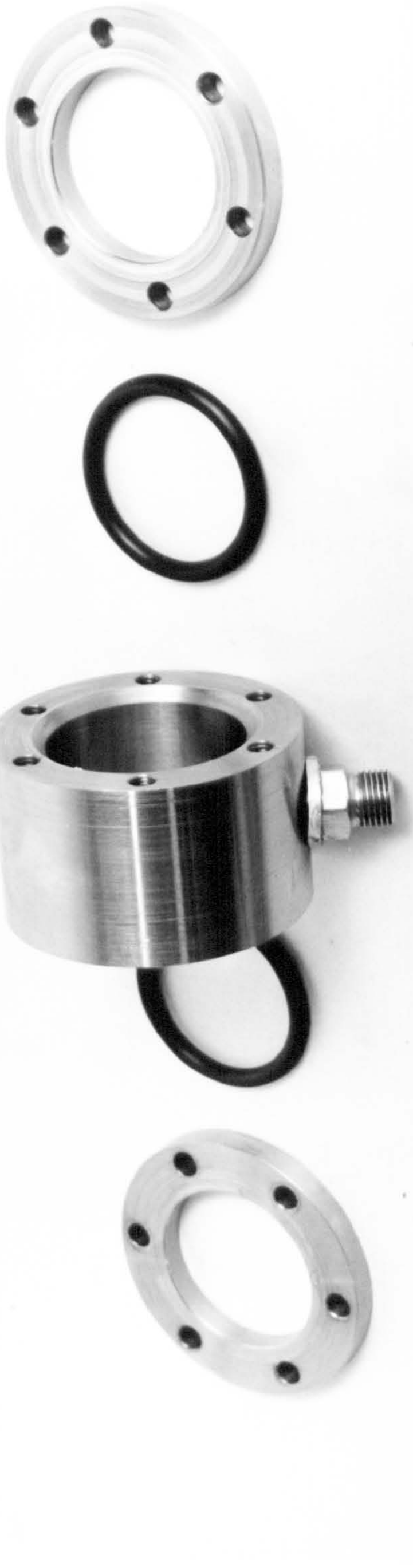

Plate (1.9)

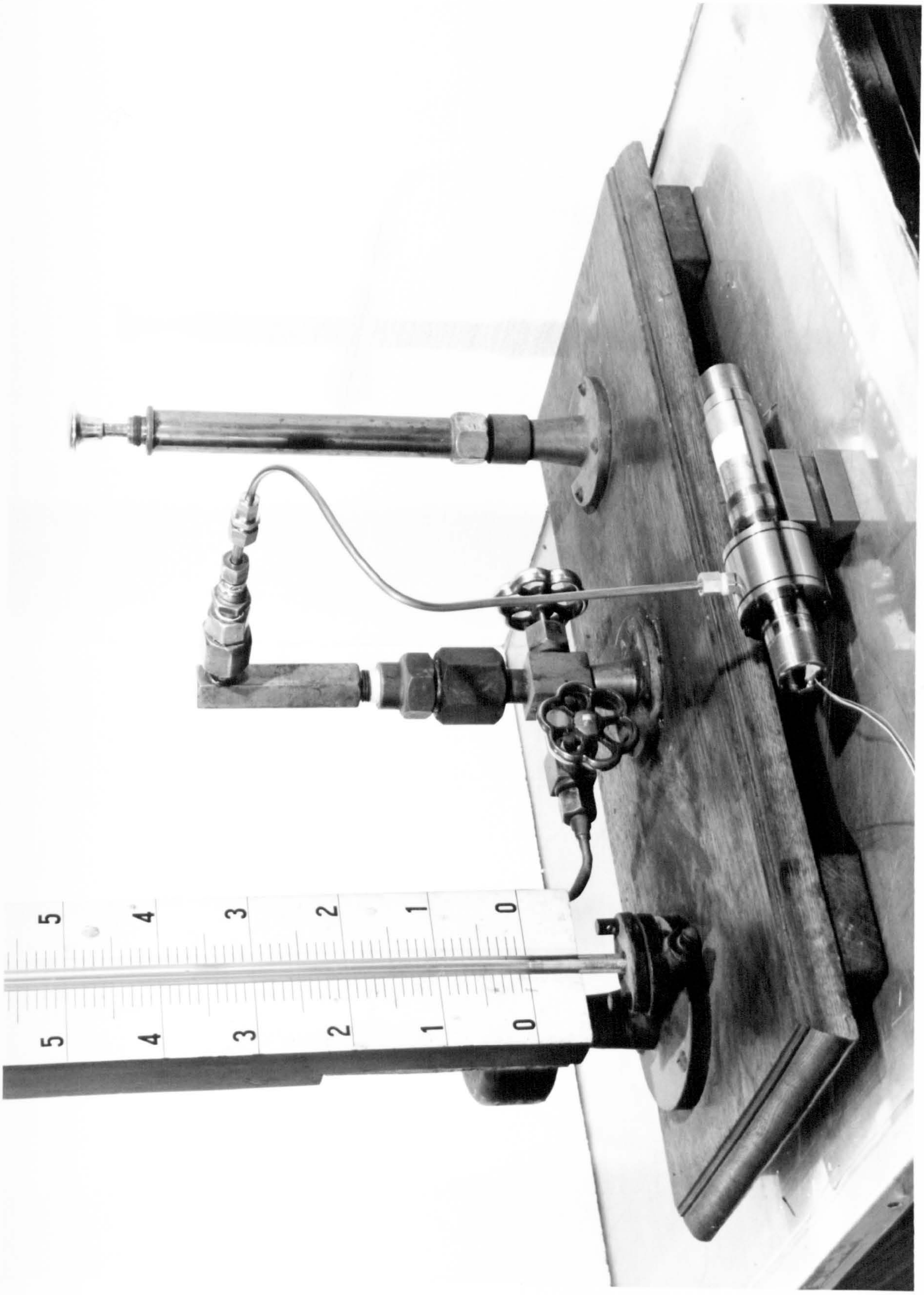

Plate (9.2)

Plate (9·3)